

**A LABORATORY EVALUATION OF ALIGNMENT
TOLERANCES FOR DOWEL BARS AND THEIR EFFECT ON
JOINT OPENING BEHAVIOR**

Final Report

**Submitted to
MICHIGAN DEPARTMENT OF TRANSPORTATION
Construction and Technology Division
Lansing, Michigan**

**by
Neeraj Buch (Principal Investigator)
Amit H. Varma (Co-Principal Investigator, Purdue University)
Milind L. Prabhu (Graduate Research Assistant)**

**Department of Civil and Environmental Engineering
Michigan State University
East Lansing, MI 48824-1226**

February 2007

Technical Report Documentation Page

1. Report No. RC-1487	2. Government Accession No.	3. Recipient's Catalog No.	
4. Title and Subtitle A Laboratory evaluation of alignment tolerances for dowel bars and their effect on joint opening behavior.		5. Report Date February 2007	
		6. Performing Organization Code	
7. Author(s) Neeraj Buch, Amit H. Varma and Milind L. Prabhu		8. Performing Organization Report No.	
9. Performing Organization Name Address Michigan State University Department of Civil and Environmental Engineering 3546 Engineering Building East Lansing, MI 48824		10. Work Unit No. (TRAIS)	
		11. Contract or Grant No.	
12. Sponsoring Agency Name and Address Michigan Department of Transportation Construction and Technology Division Lansing, Michigan		13. Type of Report and Period Covered	
		14. Sponsoring Agency Code	
15. Supplementary Notes			
16. Abstract This report presents an experimental and analytical investigation on the fundamental pullout behavior and joint opening behavior of misaligned dowel bars in concrete pavement joints. Experimental investigations were conducted to determine the fundamental joint opening behavior of concrete pavements, and to evaluate the effects of dowel misalignment on joint opening behavior. The parameters included in the experimental investigations were the number of dowel bars (1, 2, 3, or 5) at the joint, the dowel misalignment type (horizontal, vertical, and combined), misalignment magnitude (0, 1/36, 1/18, 1/12, 1/9 radians.), and uniformity across the joint. The effects of these parameters were evaluated on the joint opening behavior and structural distresses observed in the specimens. Numerous instrumented laboratory-scale specimens of pavement slabs with doweled joints were tested. The second task focused on the development of 3D finite element models for computing the complex stress states and resulting damage in concrete pavement joints with misaligned dowels, and their validation using experimental results. The concrete pavement is modeled using a damage-plasticity material model, which uses concepts of damaged plasticity formulation in compression and cracking combined with damage elasticity in tension. The longitudinal bond between the steel dowel and the concrete is modeled in two parts. (i) The longitudinal bond resulting from chemical adhesion, mechanical interlock, and static friction (in the aligned state) is modeled using spring elements. (ii) The longitudinal bond resulting from transverse interaction between steel dowels and the concrete pavement is modeled using surface-to-surface contact-interaction elements and associated friction models. The 3D finite element models are validated using results from the experimental investigations. These validated models provide significant insight into the 3D stress states and principal stresses that develop in concrete pavement joints with misaligned dowels. They are used to evaluate analytically the effects of misalignment type, magnitude, uniformity, and distribution on the 3D stress states and resulting damage in concrete pavements. The analytical results (3D stresses and strains) from the finite element analyses were considered to identify significant limit states and distresses in the concrete pavement joints. Parametric studies were conducted and recommendations on misalignment tolerances based on these parametric studies have been made. A preliminary investigation to capture the effects of misaligned dowel bars combined with wheel loads has also been carried out in this research study.			
17. key Words Rigid concrete pavements, finite element analysis, misaligned dowel bars, nonlinear concrete material model		18. Distribution Statement	
19. Security Classif. (of this report) Unclassified	20. Security Classif. (of this page) Unclassified	21. No of Pages 376	22. Price

ACKNOWLEDGMENTS

The research project was financially supported by the Michigan Department of Transportation. The project team would also like to acknowledge the technical support offered by the project technical assistance group (TAG).

DISCLAIMER

The contents of this report reflect the views of the authors. The contents do not necessarily reflect the views or policies of the Michigan Department of Transportation. This report does not constitute a standard, specification or regulation.

TABLE OF CONTENTS

LIST OF TABLES	vii
LIST OF FIGURES	xii
ABSTRACT	xx
CHAPTER 1	
INTRODUCTION	
1.1 Introduction.....	1
1.2 Problem statement.....	2
1.3 Research Objectives.....	2
1.4 Research Plan.....	4
1.5 Layout of the Thesis.....	5
CHAPTER 2	
LITERATURE REVIEW	
2.1 Introduction.....	7
2.2 Definitions of misalignment, various organizational specifications and construction practices	8
2.2.1 Definitions of misalignment	8
2.2.2 Specifications from various State Highway Authorities.....	11
2.2.3 Construction practices.....	14
2.3 Review of field studies.....	20
2.4 Review of laboratory investigations	23
2.5 Review of analytical studies	32
CHAPTER 3	
EXPERIMENTAL INVESTIGATIONS	
3.1 Introduction.....	46
3.2 Experimental plan	46
3.2.1 Dowel misalignment type	47
3.2.2 Dowel misalignment magnitude	47
3.2.3 Number of misaligned dowels	47
3.2.4 Orientation of misaligned mowel bars	47
3.3 Experimental test setup.....	53
3.4 Limitations and short comings of the test setup.....	57
3.5 Surveying technique and calculations.....	57
3.5.1 Derivation for measurement of vertical misalignment	58
3.5.2 Derivation for measurement of horizontal misalignment	62
3.6 Material specifications	69

3.7 Instrumentation and data acquisition system	74
3.8 Typical cycle for preparing and testing a specimen.....	78

CHAPTER 4

EXPERIMENTAL RESULTS AND EVALUATION

4.1 Introduction.....	81
4.2 Laboratory test results.....	81
4.2.1 Comparison within a type of misalignment.....	85
4.2.2 Comparisons between the orientation of misaligned dowel bars.....	102
4.2.3 Distresses observed in the test specimen	118
4.3 Summary of results	127
4.4 Pullout behavior of misaligned dowel bars.....	127
4.5 Dowel-concrete interaction.....	129

CHAPTER 5

DEVELOPMENT OF 3D FINITE ELEMENT MODELS

5.1 Introduction.....	131
5.2 Need for a 3D Finite element model.....	131
5.3 The 3D Finite element model – element selection.....	132
5.4 Material model – Behavior and Calibration.....	135
5.4.1 Types of concrete material models	135
5.4.1.1 The smeared cracking model	135
5.4.1.2 The cracking model for concrete	137
5.4.1.3 The concrete damage plasticity model.....	137
5.4.2 Features of concrete behavior	139
5.4.3 Input parameters for the concrete material model	143
5.4.4 Steel dowel bar material model.....	147
5.5 Development of the dowel – concrete interaction bond model	147
5.5.1 The longitudinal Bond Behavior.....	148
5.5.2 The transverse Interaction Behavior	150
5.6 Limitations and short comings of the FE model.....	151
5.7 Loading and boundary conditions.....	155
5.8 The 3D Finite element model results	156
5.9 Concluding remarks	167

CHAPTER 6

THREE DIMENSIONAL FINITE ELEMENT ANALYSIS RESULTS

6.1 Introduction.....	168
6.2 Material events or damage limit states.....	168

6.2.1 Additional discussion and limitations	172
6.3 Discussion of analytical and experimental results	175
6.3.1 Single dowel bar models	177
6.3.2 Two dowel bar models	178
6.3.3 Five dowel bar models	179
6.3.4 Concluding remarks on the 3D Finite element analytical models with events / material damage limit states.....	196
6.4 Analytical parametric study	197
6.5 Results and discussion	198
6.5.1 One misaligned dowel bar	198
6.5.2 Two misaligned dowel bars	201
6.5.3 Concluding remarks on the results of the analytical parametric studies.....	209
6.6 Conclusions and recommendations.....	210

CHAPTER 7

PRELIMINARY INVESTIGATION OF LOAD EFFECTS COMBINED WITH DOWEL MISALIGNMENTS

7.1 Introduction.....	212
7.2 Assumptions and limitations of the finite element model	212
7.3 Development of the finite element model.....	213
7.3.1 Dimensions of the analytical model.....	214
7.3.2 Material model input parameters	219
7.3.3 Interaction models.....	220
7.3.4 Loading and boundary conditions.....	224
7.4 Results and discussion	226
7.4.1 Single dowel bar model	227
7.4.2 Three dowel bar model	234
7.5 Concluding remarks	240

CHAPTER 8

SUMMARY, CONCLUSIONS, RECOMMENDATIONS AND FUTURE RESEARCH

8.1 Introduction.....	241
8.2 Summary and conclusions based on experimental investigations	241
8.3 Summary and conclusions based on analytical investigations	244
8.4 Summary and conclusions of parametric studies.....	246
8.5 Summary and conclusions based on the studies for misaligned dowels combined with wheel loading.....	246
8.6 Recommendations and future research	248

Appendices.....	250
Refereces.....	350

LIST OF TABLES

Table 2.1(a): Possible Effects of Translational type of Dowel Misalignment on Pavement Performance	9
Table 2.1(b): Possible Effects of Skew type of Dowel Misalignment on Pavement Performance	10
Table 2.2: DOT Tolerance Specifications	13
Table 2.3: Survey of Dowel Bar Installation Specifications.....	14
Table 2.4: Construction Factors affecting Misalignment	18
Table 2.5: Summary of Field Study Results	24
Table 3.2: Experimental Test Investigation Matrix	50
Table 3.3(a) Test Specimen of the single dowel bar experiments conducted.....	51
TABLE 3.3(b) Test Matrix of the two dowel bar experiments conducted	52
TABLE 3.3(c) Test Matrix of the three and five dowel bar experiments conducted	53
Table 3.5: Summary Table showing all angles for horizontal misalignment	66
Table 3.6: Mix Design of Concrete.....	70
Table 3.7: Concrete Properties.....	71
Table 5.1: Case I and Case II input parameters for the various models.....	151
Table 6.1(a) Test Matrix of the single dowel bar.....	175
Table 6.1(b) Test Matrix of the two dowel bars	176
Table 6.1(c) Test Matrix of the five dowel bars	176
Table 6.2(a): Summary of the pullout load – joint opening for cases I and II in the 1V18, 1H18 and 1C18 tests	181
Table 6.2(b): Summary of pullout load-joint opening for case (i) and (ii) in the 2V18NU, 2V18U and 2V18AM test	181
Table 6.2(c): Summary of pullout load-joint opening for case (i) and (ii) in the 2H18NU, 2H18U and 2H18AM test	182
Table 6.2(d): Summary of pullout load-joint opening for case (i) and (ii) in the 2C18NU, 2C18U and 2C18AM test.....	182
Table 6.2(e): Summary of the pullout load – joint opening for cases I and II in the 5V18NU and 5V18AM tests.....	183
Table 6.2(f): Summary of the pullout load – joint opening for cases I and II in the 5H18NU and 5H18AM tests.....	183
Table 6.2(g): Summary of the pullout load – joint opening for cases I and II in the 5C18NU and 5C18AM tests	183
Table 6.3: Summary of the Finite Element Analysis conducted	197
Table 6.4(a): Summary of the Damage Limit States and Joint Opening (in.) for Case I	199
Table 6.4(b): Summary of the Damage Limit States and Joint Opening (in.) for Case II	199
Table 6.5(a): Summary of the Damage Limit States and Joint Opening (in.) for Case I with Vertically Misaligned dowel bars	202
Table 6.5(b): Summary of the Damage Limit States and Joint Opening (in.) for Case II with Vertically Misaligned dowel bars	202
Table 6.6(a): Summary of the Damage Limit States and Joint Opening for Case I with Horizontally Misaligned dowel bars.....	206

Table 6.6(b): Summary of the Damage Limit States and Joint Opening for Case II with Horizontally Misaligned dowel bars.....	206
Table 7.1: Misalignment cases considered for single and three dowel bar loaded slabs	219
Table 7.2: Material input parameters for the single and three dowel bar finite element models.....	221
Table A-1. Mix Design Specifications.....	253
Table A-2: Concrete Specimen strength at 7 days.....	254
Table A-3. Description of Linear Variable Differential Transducer	257
Table A-4. Description of the Hydraulics (Actuators RC 156 and RC 256)	257
Table B-1. Misalignment Check Summary – One Dowel Tests.....	265
Table B-2. Misalignment Check Summary – Two Dowel Tests (North Dowel)	266
Table B-3. Misalignment Check Summary – Two Dowel Tests (South Dowel)	266
Table B-3. Misalignment Check Summary – Two Dowel Tests (South Dowel)	267
Table B-4. Misalignment Check Summary – Three and Five Dowel Tests	268
Table B-5. Horizontal Misalignment Summary – One Dowel Tests.....	269
Table B-6. Horizontal Misalignment Summary – Two Dowel Tests (North Dowel)	269
Table B-7. Horizontal Misalignment Summary – Two Dowel Tests (South Dowel)	270
Table B-8. Horizontal Misalignment Summary – Three and Five Dowel Tests	271
Table C-1: Dowel-Concrete Friction Coefficients; Material Properties used and limit states obtained from the analysis.	273
Table C-2: Summary of Material Failure / Damage Limit States from the analysis	273
Table C-3: Dowel-Concrete Friction Coefficients; Material Properties used and limit states obtained from the analysis.	274
Table C-4: Summary of Material Failure / Damage Limit States from the analysis	274
Table C-5: Dowel-Concrete Friction Coefficients; Material Properties used and limit states obtained from the analysis.	275
Table C-6: Summary of Material Failure / Damage Limit States from the analysis	275
Table C-7: Dowel-Concrete Friction Coefficients; Material Properties used and limit states obtained from the analysis.	276
Table C-8: Summary of Material Failure / Damage Limit States from the analysis	276
Table C-9: Dowel-Concrete Friction Coefficients; Material Properties used and limit states obtained from the analysis.	277
Table C-10: Summary of Material Failure / Damage Limit States from the analysis	277
Table C-11: Dowel-Concrete Friction Coefficients; Material Properties used and limit states obtained from the analysis.	278
Table C-12: Summary of Material Failure / Damage Limit States from the analysis	278
Table C-13: Dowel-Concrete Friction Coefficients; Material Properties used and limit states obtained from the analysis.	279
Table C-14: Summary of Material Failure / Damage Limit States from the analysis	279
Table C-15: Dowel-Concrete Friction Coefficients; Material Properties used and limit states obtained from the analysis.	280
Table C-16: Summary of Material Failure / Damage Limit States from the analysis	280
Table C-17: Dowel-Concrete Friction Coefficients; Material Properties used and limit states obtained from the analysis.	281
Table C-18: Summary of Material Failure / Damage Limit States from the analysis	281

Table C-19: Dowel-Concrete Friction Coefficients; Material Properties used and limit states obtained from the analysis.	282
Table C-20: Summary of Material Failure / Damage Limit States from the analysis	282
Table C-21: Dowel-Concrete Friction Coefficients; Material Properties used and limit states obtained from the analysis.	283
Table C-22: Summary of Material Failure / Damage Limit States from the analysis	283
Table C-23: Dowel-Concrete Friction Coefficients; Material Properties used and limit states obtained from the analysis.	284
Table C-24: Summary of Material Failure / Damage Limit States from the analysis	284
Table C-25: Dowel-Concrete Friction Coefficients; Material Properties used and limit states obtained from the analysis.	285
Table C-26: Summary of Material Failure / Damage Limit States from the analysis	285
Table C-27: Dowel-Concrete Friction Coefficients; Material Properties used and limit states obtained from the analysis.	286
Table C-28: Summary of Material Failure / Damage Limit States from the analysis	286
Table C-29: Dowel-Concrete Friction Coefficients; Material Properties used and limit states obtained from the analysis.	287
Table C-30: Summary of Material Failure / Damage Limit States from the analysis	287
Table C-31: Dowel-Concrete Friction Coefficients; Material Properties used and limit states obtained from the analysis.	288
Table C-32: Summary of Material Failure / Damage Limit States from the analysis	288
Table C-33: Dowel-Concrete Friction Coefficients; Material Properties used and limit states obtained from the analysis.	289
Table C-34: Summary of Material Failure / Damage Limit States from the analysis	289
Table C-35: Dowel-Concrete Friction Coefficients; Material Properties used and limit states obtained from the analysis.	290
Table C-36: Summary of Material Failure / Damage Limit States from the analysis	290
Table C-37: Dowel-Concrete Friction Coefficients; Material Properties used and limit states obtained from the analysis.	291
Table C-38: Summary of Material Failure / Damage Limit States from the analysis	291
Table C-39: Dowel-Concrete Friction Coefficients; Material Properties used and limit states obtained from the analysis.	292
Table C-40: Summary of Material Failure / Damage Limit States from the analysis	292
Table C-41: Dowel-Concrete Friction Coefficients; Material Properties used and limit states obtained from the analysis.	293
Table C-42: Summary of Material Failure / Damage Limit States from the analysis	293
Table C-43: Dowel-Concrete Friction Coefficients; Material Properties used and limit states obtained from the analysis.	294
Table C-44: Summary of Material Failure / Damage Limit States from the analysis	294
Table C-45: Dowel-Concrete Friction Coefficients; Material Properties used and limit states obtained from the analysis.	295
Table C-46: Summary of Material Failure / Damage Limit States from the analysis	295
Table C-47: Dowel-Concrete Friction Coefficients; Material Properties used and limit states obtained from the analysis.	296
Table C-48: Summary of Material Failure / Damage Limit States from the analysis	296

Table C-49: Dowel-Concrete Friction Coefficients; Material Properties used and limit states obtained from the analysis.	297
Table C-50: Summary of Material Failure / Damage Limit States from the analysis	297
Table C-51: Dowel-Concrete Friction Coefficients; Material Properties used and limit states obtained from the analysis.	298
Table C-52: Summary of Material Failure / Damage Limit States from the analysis	298
Table C-53: Dowel-Concrete Friction Coefficients; Material Properties used and limit states obtained from the analysis.	299
Table C-54: Summary of Material Failure / Damage Limit States from the analysis	299
Table C-55: Dowel-Concrete Friction Coefficients; Material Properties used and limit states obtained from the analysis.	300
Table C-56: Summary of Material Failure / Damage Limit States from the analysis	300
Table C-57: Dowel-Concrete Friction Coefficients; Material Properties used and limit states obtained from the analysis.	301
Table C-58: Summary of Material Failure / Damage Limit States from the analysis	301
Table C-59: Dowel-Concrete Friction Coefficients; Material Properties used and limit states obtained from the analysis.	302
Table C-60: Summary of Material Failure / Damage Limit States from the analysis	302
Table C-61: Dowel-Concrete Friction Coefficients; Material Properties used and limit states obtained from the analysis.	303
Table C-62: Summary of Material Failure / Damage Limit States from the analysis	303
Table C-63: Dowel-Concrete Friction Coefficients; Material Properties used and limit states obtained from the analysis.	304
Table C-64: Summary of Material Failure / Damage Limit States from the analysis	304
Table C-65: Dowel-Concrete Friction Coefficients; Material Properties used and limit states obtained from the analysis.	305
Table C-66: Summary of Material Failure / Damage Limit States from the analysis	305
Table C-67: Dowel-Concrete Friction Coefficients; Material Properties used and limit states obtained from the analysis.	306
Table C-68: Summary of Material Failure / Damage Limit States from the analysis	306
Table C-69: Dowel-Concrete Friction Coefficients; Material Properties used and limit states obtained from the analysis.	307
Table C-70: Summary of Material Failure / Damage Limit States from the analysis	307
Table C-71: Dowel-Concrete Friction Coefficients; Material Properties used and limit states obtained from the analysis.	308
Table C-72: Summary of Material Failure / Damage Limit States from the analysis	308
Table C-73: Dowel-Concrete Friction Coefficients; Material Properties used and limit states obtained from the analysis.	309
Table C-74: Summary of Material Failure / Damage Limit States from the analysis	309
Table C-75: Dowel-Concrete Friction Coefficients; Material Properties used and limit states obtained from the analysis.	310
Table C-76: Summary of Material Failure / Damage Limit States from the analysis	310
Table C-77: Dowel-Concrete Friction Coefficients; Material Properties used and limit states obtained from the analysis.	311
Table C-78: Summary of Material Failure / Damage Limit States from the analysis	311

Table C-79: Dowel-Concrete Friction Coefficients; Material Properties used and limit states obtained from the analysis.	312
Table C-80: Summary of Material Failure / Damage Limit States from the analysis	312
Table C-81: Dowel-Concrete Friction Coefficients; Material Properties used and limit states obtained from the analysis.	313
Table C-82: Summary of Material Failure / Damage Limit States from the analysis	313
Table C-83: Dowel-Concrete Friction Coefficients; Material Properties used and limit states obtained from the analysis.	314
Table C-84: Summary of Material Failure / Damage Limit States from the analysis	314
Table C-85: Dowel-Concrete Friction Coefficients; Material Properties used and limit states obtained from the analysis.	315
Table C-86: Summary of Material Failure / Damage Limit States from the analysis	315
Table C-87: Dowel-Concrete Friction Coefficients; Material Properties used and limit states obtained from the analysis.	316
Table C-88: Summary of Material Failure / Damage Limit States from the analysis	316
Table C-89: Dowel-Concrete Friction Coefficients; Material Properties used and limit states obtained from the analysis.	317
Table C-90: Summary of Material Failure / Damage Limit States from the analysis	317
Table C-91: Dowel-Concrete Friction Coefficients; Material Properties used and limit states obtained from the analysis.	318
Table C-92: Summary of Material Failure / Damage Limit States from the analysis	318
Table E-1: Comparison of the fine and coarse mesh joint opening and dowel pullout forces.....	349

LIST OF FIGURES

Figure 2.1: Typical components of a pavement cross section and truck loading.	7
Figure 2.2: Typical dowel basket assembly used as load transfer devices in JPCP	15
Figure 2.3: Dowel Bar Inserter (Source Gomaco Inc., www.gomaco.com).....	17
Figure 2.4: Various Non-Destructive Misalignment Measuring Devices	20
Figure 2.5: Pressure Exerted on a Loaded Dowel, Yoder (1975).....	33
Figure 3.1 Sign Convention for Orientation of the dowel bar (Clockwise (CW) – Positive)	48
Figure 3.2: Concrete slab specimen with misaligned dowel bars.....	49
Figure 3.3: Shop drawings showing the test setup dimensions for one and two dowel bar specimens.....	55
Figure 3.4: Photograph of the various components of the experimental set-up	56
Figure 3.5: Horizontal plane showing angles measured from center of base plate to misalignment.....	59
Figure 3.6: Vertical plane in the center of the plate.....	59
Figure 3.7: Horizontal plane showing angles measured from center of base plate to misalignment.....	61
Figure 3.8: Vertical plane in the center of the plate.....	61
Figure 3.9: Horizontal plane showing angles measured from center of base plate to misalignment.....	63
Figure 3.10: Vertical plane in the center of the plate.....	64
Figure 3.11: Angles in the vertical plane, after forcing the misalignment of H.	64
Figure 3.12: Showing the final computation of the horizontal misalignment	65
Figure 3.13: Horizontal plane showing angles measured from center of base plate to misalignment.....	66
Figure 3.14: Vertical plane in the center of the plate.....	67
Figure 3.15: Angles in the vertical plane, after forcing the misalignment of H.	68
Figure 3.16: Showing the final computation of the horizontal misalignment	69
Figure 3.17: Concrete Hardened Properties Test Setup.....	71
Figure 3.18: Standard ½ in. Round Tension Test specimen with 2 in. gage length (ASTM E8-99)	72
Figure 3.19: Stages of Coupon Testing.....	73
Figure 3.20: Typical Stress-Strain Curve for a coupon	73
Figure 3.21: Closeup of Instruments (website: www.omega.com and www.beiduncan.com)	75
Figure 3.22: Typical Instruments and cylinders used in the tests.....	76
Figure 3.23: Five Dowel Instrumentation Setup.....	77
Figure 3.24: Typical cycle of specimen preparation and testing	80
Figure 4.1: Typical Bond Stress versus Joint Opening curve.....	85
Figure 4.2: Comparison of pullout force vs. joint opening behavior for specimens with a single vertically misaligned dowel bar	87
Figure 4.3: Comparison of pullout force vs. joint opening behavior for specimens with two vertically misaligned dowel bars having non-uniform (NU) orientation.....	88
Figure 4.4: Comparison of pullout force vs. joint opening behavior for specimens with two vertically misaligned dowel bars and uniform (U) orientation.....	88

Figure 4.5: Comparison of pullout force vs. joint opening behavior for specimens with two vertically misaligned dowel bars and alternate (AM) orientation	89
Figure 4.6: Comparison of pullout force per bar vs. joint opening behavior for specimens with three vertically misaligned dowel bars	89
Figure 4.7: Comparison of pullout force per bar vs. joint opening behavior for specimens with five vertically misaligned dowel bars (5A, 5V18NU and 5V18AM).....	90
Figure 4.8: Comparison of pullout force per bar for vertically misaligned dowel bars at ¼ in joint opening	90
Figure 4.9: Comparison of pullout force per bar for vertically misaligned dowel bars at ½ in. joint opening	91
Figure 4.10: Comparison of pullout force vs. joint opening behavior for specimens with a single horizontally misaligned dowel bar	93
Figure 4.11: Comparison of pullout force vs. joint opening behavior for specimens with two horizontally misaligned dowel bars having non-uniform (NU) orientation	93
Figure 4.12: Comparison of pullout force vs. joint opening behavior for specimens with two horizontally misaligned dowel bars having uniform (U) orientation.....	94
Figure 4.13: Comparison of pullout force vs. joint opening behavior for specimens with two horizontally misaligned dowel bars having alternate (AM) orientation	94
Figure 4.14: Comparison of pullout force per bar vs. joint opening behavior for specimens with three horizontally misaligned dowel bars	95
Figure 4.15: Comparison of pullout force per bar vs. joint opening behavior for specimens with five horizontally misaligned dowel bars (5A, 5H18NU and 5H18AM). 95	
Figure 4.16: Comparison of pullout force per bar for horizontally misaligned dowel bars at ¼ in. joint opening	96
Figure 4.17: Comparison of pullout force per bar for horizontally misaligned dowel bars at ½ in. joint opening	96
Figure 4.18: Comparison of pullout force vs. joint opening behavior for specimens with a single combined misaligned dowel bar.....	98
Figure 4.19: Comparison of pullout force vs. joint opening behavior for specimens with two combined misaligned dowel bars having non-uniform (NU) orientation.....	99
Figure 4.20: Comparison of pullout force vs. joint opening behavior for specimens with two combined misaligned dowel bars having non-uniform (U) orientation.....	99
Figure 4.21: Comparison of pullout force vs. joint opening behavior for specimens with two combined misaligned dowel bars having alternate (AM) orientation.....	100
Figure 4.22: Comparison of pullout force vs. joint opening behavior for specimens with three combined misaligned dowel bars.....	100
Figure 4.23: Comparison of pullout force vs. joint opening behavior for specimens with five combined misaligned dowel bars (5A, 5C18NU and 5C18AM).....	101
Figure 4.24: Comparison of pullout force per bar for combined misaligned dowel bars at ¼ in. joint opening	101
Figure 4.25: Comparison of pullout force per bar for combined misaligned dowel bars at ½ in. joint opening	102
Figure 4.26: Comparison of pullout force vs. joint opening curves of 2-dowel ½ in. Horizontal Misalignment (2H18NU, 2H18U, and 2H18AM)	104
Figure 4.27 Comparison of pullout force vs. joint opening curves of 2-dowel ½ in. Vertical Misalignment (2V18NU, 2V18U, and 2V18AM)	105

Figure 4.28: Comparison of pullout force vs. joint opening curves of 2-dowel ½ in. Combined Misalignment (2C18NU, 2C18U, and 2C18AM)	105
Figure 4.29: Comparison of pullout force vs. joint opening curves of 2-dowel ¾ in. Horizontal Misalignment (2H12NU and 2H12AM).....	106
Figure 4.30: Comparison of pullout force vs. joint opening curves of 2-dowel ¾ in. Vertical Misalignment (2V12NU and 2V12AM).....	106
Figure 4.31 Comparison of pullout load vs. joint opening curves of 2-dowel ¾ in. Combined Misalignment (2C12NU and 2C12AM).....	107
Figure 4.32 Comparison of pullout load vs. joint opening curves of 5H18NU and 5H18AM	107
Figure 4.33 Comparison of pullout force vs. joint opening curves of 5V18NU and 5V18AM	108
Figure 4.34 Comparison of pullout force vs. joint opening curves of 5C18NU and 5C18AM	108
Figure 4.35 Comparison of pullout force vs. joint opening curves of 1H18 and 2-dowel ½ in. Horizontal Misalignment (2H18NU, 2H18U, 2H18AM).....	110
Figure 4.36 Comparison of pullout force vs. joint opening curves of 1H9 and 2-dowel 1 in. Horizontal Misalignment (2H9NU, 2H9U).....	110
Figure 4.37 Comparison of pullout force vs. joint opening curves of 3H18NU and 5H18NU	111
Figure 4.38: Comparison of pullout force vs. joint opening curves of 1V18 and 2-dowel ½ in. Vertical Misalignment (2V18NU, 2V18U, 2V18AM).....	112
Figure 4.39 Comparison of pullout force vs. joint opening curves of 1V9 and 2-dowel 1 in. Vertical Misalignment (2V9NU, 2V9U)	112
Figure 4.40 Comparison of pullout force vs. joint opening curves of 3V18NU and 5V18NU	113
Figure 4.41: Comparison of pullout force vs. joint opening curves of 1C18 and 2-dowel ½ in. Combined Misalignment (2C18NU, 2C18U).....	114
Figure 4.42: Comparison of pullout force vs. joint opening curves of 1C9 and 2-dowel 1 in. Combined Misalignment (2C9NU, 2C9U).....	115
Figure 4.43 Comparison of pullout force vs. joint opening curves of 3C18NU and 5C18NU	115
Figure 4.44: Comparison of loads at ¼ in. across different tests of misalignment.....	116
Figure 4.45: Comparison of loads at ½ in. across different tests of misalignment.....	117
Figure 4.46: Vertical Uplift (2V9NU)	119
Figure 4.47: Diagrammatic representation of Crack in 5V18NU.....	119
Figure 4.48: Spalling in the 2H9U test	120
Figure 4.49: Joint opening as a function of distance along the joint (2H1U).....	121
Figure 4.50: Cracking in 2H12NU.....	122
Figure 4.51: Crack pattern and Initial dimensions in 2H9NU	123
Figure 4.52: Cracking in 2C12NU.....	125
Figure 4.53: Corner Cracking in 2C9NU on west side.....	126
Figure 4.54: Aligned dowel bar in concrete pavement slab.....	128
Figure 4.55: Misaligned dowel bar in a concrete pavement slab.....	128
Figure 4.56: Forces on a misaligned dowel and surrounding concrete.....	130
Figure 5.1: Abaqus Solid element Library (Abaqus User Manual 2004).....	133

Figure 5.2: Finite Element Model discretization of the concrete slab and dowel bar. ...	134
Figure 5.3: Uniaxial behavior of plain concrete (Abaqus User Manual 2004).....	136
Figure 5.4: Typical concrete uniaxial stress –strain curve in tension and compression (Abaqus User Manual 2004).....	138
Figure 5.5: A plasticity hardening model for concrete (Chen and Han, 1995).....	140
Figure 5.6: Schematic of yield surface and flow in the meridinal plane. (Abaqus User Manual 2004).....	141
Figure 5.8: Typical uniaxial compressive strength of concrete, Collins et al (1992).....	144
Figure 5.9: Typical Post failure Stress – Displacement curve using fracture energy criterion.....	145
Figure 5.10: Typical tensile post failure stress-strain curves using the fracture energy criterion.....	146
Figure 5.11: Spring model derived from the control test specimen (aligned single dowel bar).....	149
Figure 5.12: Distribution of spring forces along half length of the dowel bar	149
Figure 5.13: Typical spring forces (lbs) at ¼ in joint opening in the 1V18 model.....	150
Figure 5.14 Summary of the Pullout force per bar at debonding limit state (A) and the debonding stress for the aligned and misaligned test cases	153
Figure 5.15: Step I – Dead (gravity / self weight) Load due to the concrete and dowel	155
Figure 5.16: Step II – Displacement Control step simulating joint opening	156
Figure 5.17: Comparison of finite element results and experimental data for a single misaligned 1/18 radians dowel bar.	158
Figure 5.18: Comparison of finite element results and experimental data for two vertically misaligned 1/18 radians dowel bar.	160
Figure 5.19: Comparison of finite element results and experimental data for two horizontally misaligned 1/18 radians dowel bar.	162
Figure 5.20: Comparison of finite element results and experimental data for five vertically misaligned 1/18 radians dowel bar.	164
Figure 5.21: Comparison of finite element results and experimental data for five horizontally misaligned 1/18 radians dowel bar.	165
Figure 5.22: Typical stress contours at material damage / limit state (C) in the FE model for Case I input parameters at 0.05 in. joint opening.....	166
Figure 6.1: Typical location of initial slip state (A) for single and two aligned dowel bars	169
Figure 6.2: Identification of various limit states on the concrete compression – tension stress-strain curves.....	172
Figure 6.3: Comparison of the FEM model with the experimental data for a single dowel bar specimen	185
Figure 6.4: Comparison of FEM and experimental data for a two dowel bars with vertical misalignment.....	187
Figure 6.5: Comparison of FEM and experimental data for a two dowel bars with horizontal misalignment.....	189
Figure 6.6: Comparison of FEM and experimental data for a two dowel bars with combined misalignment.....	191
Figure 6.7: Comparison of FEM and experimental data for five dowel bars with vertical misalignment.....	193

Figure 6.8: Comparison of FEM and experimental data for five dowel bars with horizontal misalignment.....	194
Figure 6.9: Comparison of FEM and experimental data for five dowel bars with combined misalignment.....	196
Figure 6.10: Summary of Joint Opening Behavior and Limit States of single misaligned dowel bars.....	200
Figure 6.12: Case II analysis summary of Joint Opening Behavior and Limit States of two vertically misaligned dowel bars.....	204
Figure 6.13: Case I analysis summary of Joint Opening Behavior and Limit States of two horizontally misaligned dowel bars.....	207
Figure 6.14: Case II analysis summary of Joint Opening Behavior and Limit States of two horizontally misaligned dowel bars.....	208
Figure 7.1: Dimensions and location of various parts of the pavement slab and wheel base in the finite element model.....	216
Figure 7.2: Spring Force vs. Joint Opening behavior used in the finite element models.....	222
Figure 7.3: Typical constraint conditions used for the finite element model.....	223
Figure 7.4: Typical Boundary and Loading conditions on the pavement system.....	226
Figure 7.5: Loaded and unloaded sides of the concrete slab.....	227
Figure 7.6: Compressive stress zones in the concrete for 1V72 FE model.....	229
Figure 7.7 Compressive stress zones in the concrete for 1H72 FE model.....	229
Figure 7.8 Results at location (i) and (ii) for single vertically misaligned dowel bar at 1/8" joint opening.....	230
Figure 7.9 Results at location (i) and (ii) for single horizontally misaligned dowel bar at 1/8" joint opening.....	232
Figure 7.10: Stress concentration zones formed in concrete due to misaligned dowel bars and at joint opening (1/8 in).....	235
Figure 7.11: Formation of bearing stress zones in the concrete due to load application.....	236
Figure 7.12: Stress concentration zones formed in concrete due to misaligned dowel bars and at joint opening (1/8 in).....	237
Figure 7.13: Formation of bearing stress zones in the concrete due to load application.....	238
Figure 7.14: Compressive stresses in the three dowel bar FE models.....	239
Figure A-1. Cross section of the small mold for pullout test.....	251
Figure A-2. Plan of the small mold with outside dimensions.....	251
Figure A-3. Typical sectional view of the big mold.....	252
Figure A-4. Typical plan view of mold with 5 dowel bars.....	252
Figure A-5. Calibration of 1.5 in. slider-1.....	258
Figure A-6. Calibration of 1.5 in. slider-2.....	258
Figure A-7. Calibration of 1.0 in. slider-1.....	258
Figure A-8. Calibration of 1.0 in. slider-2.....	258
Figure A-9. Calibration of 1.0 in. slider-3.....	259
Figure A-10. Calibration of 1.0 in. slider-4.....	259
Figure A-11. Calibration of LVDT-1.....	259
Figure A-12. Calibration of LVDT-2.....	259
Figure A-13. Calibration of LVDT-3.....	260
Figure A-14. Calibration of RC156 Actuator 1.....	260
Figure A-15. Calibration of RC256 Actuator 1.....	260

Figure A-16. Calibration of RC156 Actuator 2	260
Figure A-17. Calibration of RC256 Actuator 2	261
Figure A-18. Data Flow	262
Figure C-1: Comparison of the FEM model with the experimental data for 1A specimen	273
Figure C-2: Comparison of the FEM model with the experimental data for 1V18 specimen	274
Figure C-3: Comparison of the FEM model with the experimental data for 1V36 specimen	275
Figure C-4: Comparison of the FEM model with the experimental data for 1V72 specimen	276
Figure C-5: Comparison of the FEM model with the experimental data for 1H18 specimen	277
Figure C-6: Comparison of the FEM model with the experimental data for 1H36 specimen	278
Figure C-7: Comparison of the FEM model with the experimental data for 1H72 specimen	279
Figure C-8: Comparison of the FEM model with the experimental data for 1C18 specimen	280
Figure C-9: Comparison of the FEM model with the experimental data for 1C36 specimen	281
Figure C-10: Comparison of the FEM model with the experimental data for 2A specimen	282
Figure C-11: Comparison of the FEM model with the experimental data for 2V18NU specimen	283
Figure C-12: Comparison of the FEM model with the experimental data for 2V18U specimen	284
Figure C-13: Comparison of the FEM model with the experimental data for 2V18AM specimen	285
Figure C-14: Comparison of the FEM model with the experimental data for 2V36NU specimen	286
Figure C-15: Comparison of the FEM model with the experimental data for 2V36U specimen	287
Figure C-16: Comparison of the FEM model with the experimental data for 2V36AM specimen	288
Figure C-17: Comparison of the FEM model with the experimental data for 2V72NU specimen	289
Figure C-18: Comparison of the FEM model with the experimental data for 2V72U specimen	290
Figure C-19: Comparison of the FEM model with the experimental data for 2V72AM specimen	291
Figure C-20: Comparison of the FEM model with the experimental data for 2H18NU specimen	292
Figure C-21: Comparison of the FEM model with the experimental data for 2H18U specimen	293

Figure C-22: Comparison of the FEM model with the experimental data for 2H18AM specimen	294
Figure C-23: Comparison of the FEM model with the experimental data for 2H36NU specimen	295
Figure C-24: Comparison of the FEM model with the experimental data for 2H36U specimen	296
Figure C-25: Comparison of the FEM model with the experimental data for 2H36AM specimen	297
Figure C-26: Comparison of the FEM model with the experimental data for 2H72NU specimen	298
Figure C-27: Comparison of the FEM model with the experimental data for 2H72U specimen	299
Figure C-28: Comparison of the FEM model with the experimental data for 2H72AM specimen	300
Figure C-29: Comparison of the FEM model with the experimental data for 2C18NU specimen	301
Figure C-30: Comparison of the FEM model with the experimental data for 2C18U specimen	302
Figure C-31: Comparison of the FEM model with the experimental data for 2C18AM specimen	303
Figure C-32: Comparison of the FEM model with the experimental data for 2C36NU specimen	304
Figure C-33: Comparison of the FEM model with the experimental data for 3A specimen	305
Figure C-34: Comparison of the FEM model with the experimental data for 3V18NU specimen	306
Figure C-35: Comparison of the FEM model with the experimental data for 3H18NU specimen	307
Figure C-36: Comparison of the FEM model with the experimental data for 3C18NU specimen	308
Figure C-37: Comparison of the FEM model with the experimental data for 5A specimen	309
Figure C-38: Comparison of the FEM model with the experimental data for 5V18NU specimen	310
Figure C-39: Comparison of the FEM model with the experimental data for 5V18AM specimen	311
Figure C-40: Comparison of the FEM model with the experimental data for 5V36AM specimen	312
Figure C-41: Comparison of the FEM model with the experimental data for 5H18NU specimen	313
Figure C-42: Comparison of the FEM model with the experimental data for 5H18AM specimen	314
Figure C-43: Comparison of the FEM model with the experimental data for 5H36AM specimen	315
Figure C-44: Comparison of the FEM model with the experimental data for 5C18NU specimen	316

Figure C-45: Comparison of the FEM model with the experimental data for 5C18AM specimen	317
Figure C-46: Comparison of the FEM model with the experimental data for 5C36AM specimen	318
Figure D-1: Stress and Strains for 3A slab model at joint opening of 1/8 in.....	321
Figure D-2: Stresses and Strains for 3A model after load application	322
Figure D-3: Stress and Strains for 3V36NU slab model at joint opening of 1/8 in.....	324
Figure D-4: Stresses and Strains for 3V36NU model after load application.....	325
Figure D-5: Stress and Strains for 3V36AM slab model at joint opening of 1/8 in.	327
Figure D-6: Stresses and Strains for 3V72NU model after load application.....	328
Figure D-7: Stress and Strains for 3V36AM slab model at joint opening of 1/8 in.	330
Figure D-8: Stresses and Strains for 3V36AM model after load application	331
Figure D-9: Stress and Strains for 3V72AM slab model at joint opening of 1/8 in.	333
Figure D-10: Stresses and Strains for 3V72AM model after load application	334
Figure D-11: Stress and Strains for 3H36NU slab model at joint opening of 1/8 in.....	336
Figure D-12: Stresses and Strains for 3H36NU model after load application.....	337
Figure D-13: Stress and Strains for 3H72NU slab model at joint opening of 1/8 in.....	339
Figure D-14: Stresses and Strains for 3H72NU model after load application.....	340
Figure D-15: Stress and Strains for 3H36AM slab model at joint opening of 1/8 in.	342
Figure D-16: Stresses and Strains for 3H36AM model after load application	343
Figure D-17: Stress and Strains for 3H72AM slab model at joint opening of 1/8 in.	345
Figure D-18: Stresses and Strains for 3H72AM model after load application	346
Figure E-1: Comparison of dowel pullout force-joint opening behavior for the 2V18NU coarse and fine mesh finite element model.....	349

ABSTRACT

This report presents an experimental and analytical investigation on the fundamental pullout behavior and joint opening behavior of misaligned dowel bars in concrete pavement joints. Experimental investigations were conducted to determine the fundamental joint opening behavior of concrete pavements, and to evaluate the effects of dowel misalignment on joint opening behavior. The parameters included in the experimental investigations were the number of dowel bars (1, 2, 3, or 5) at the joint, the dowel misalignment type (horizontal, vertical, and combined), misalignment magnitude (0, $1/36$, $1/18$, $1/12$, $1/9$ radians.), and uniformity across the joint. The effects of these parameters were evaluated on the joint opening behavior and structural distresses observed in the specimens. Numerous instrumented laboratory-scale specimens of pavement slabs with doweled joints were tested. The second task focused on the development of 3D finite element models for computing the complex stress states and resulting damage in concrete pavement joints with misaligned dowels, and their validation using experimental results. The concrete pavement is modeled using a damage-plasticity material model, which uses concepts of damaged plasticity formulation in compression and cracking combined with damage elasticity in tension. The longitudinal bond between the steel dowel and the concrete is modeled in two parts. (i) The longitudinal bond resulting from chemical adhesion, mechanical interlock, and static friction (in the aligned state) is modeled using spring elements. (ii) The longitudinal bond resulting from transverse interaction between steel dowels and the concrete pavement is modeled using surface-to-surface contact-interaction elements and associated friction models. The 3D finite element models are validated using results from the experimental

investigations. These validated models provide significant insight into the 3D stress states and principal stresses that develop in concrete pavement joints with misaligned dowels. They are used to evaluate analytically the effects of misalignment type, magnitude, uniformity, and distribution on the 3D stress states and resulting damage in concrete pavements. The analytical results (3D stresses and strains) from the finite element analyses were considered to identify significant limit states and distresses in the concrete pavement joints. Parametric studies were conducted and recommendations on misalignment tolerances based on these parametric studies have been made. A preliminary investigation to capture the effects of misaligned dowel bars combined with wheel loads has also been carried out in this research study.

CHAPTER 1

INTRODUCTION

1.1 INTRODUCTION

Jointed Plain Concrete pavements (JPCP) have been widely used in the United States and many developing countries both for roadways and airport runways because of their durability and low maintenance requirements. One of the main features of the JPCP is the doweled contraction joint, spaced at 10 – 20 ft intervals to permit contraction of the slabs and control crack locations. To ensure long term performance of highway pavements subjected to heavy traffic mechanical load transfer devices such as dowel bars are necessary. Dowel bars are placed across joints to provide additional load transfer without restricting horizontal joint movement. They also assist in maintaining the horizontal and vertical alignment of slabs.

From a construction view point, it is important to install the dowel bars properly, i.e., in the horizontal plane and parallel to the pavement centerline. Dowel bars can become misaligned during construction. The misaligned dowel bars restrain the horizontal movement of the joint which leads to joint locking. This causes the effective length of the concrete slabs to increase which increases the stresses due to applied thermal and wheel loads causing transverse slab cracking, corner breaks, and joint spalling (Tayabji 1986).

1.2 PROBLEM STATEMENT

The Michigan Department of Transportation (MDOT) specifications require that the dowel bars should provide adequate load transfer across transverse joints, while allowing horizontal movement without significant restraint. These dowel bars are installed during construction using factory fabricated dowel basket assemblies. DOTs also have recently started using dowel bar inserters (DBI) that mechanically insert the dowels into the “green” or fresh (plastic) concrete during construction. The DOTs use the same allowable misalignment tolerances for dowels placed using basket assemblies or dowel bar inserters as given in the construction specifications. The basis of these misalignment tolerances in the specifications needs to be investigated.

There is sparse experimental data documenting the behavior, effects, and distresses caused by the presence of misaligned dowel bars in a concrete pavement joints. Computational models developed in previous studies to investigate the effects of dowel misalignment had several limitations and assumptions. The experimental investigation and companion finite element models developed in this study will play an important role in the process of developing tolerances for dowel misalignment in jointed concrete pavements.

1.3 RESEARCH OBJECTIVES

The objectives of this research are:

- 1) To investigate experimentally the fundamental *pullout behavior* of misaligned dowel bars in plain concrete pavements subjected to thermal expansion (joint opening only).

- 2) To investigate experimentally the behavior and distress of pavement joints with multiple misaligned dowel bars subjected to *joint opening*.
- 3) To develop and calibrate 3D finite element analytical models that can be used to predict the joint opening behavior and evaluate the distresses of concrete pavement joints with misaligned dowel bars.
- 4) Conduct parametric studies to evaluate the behavior and potential distress of in-situ pavement joint with multiple misaligned dowel bars.

The experimental investigations cannot provide detailed information regarding the localized interaction between the dowel bar and the surrounding concrete. Hence computational models were developed based on the laboratory investigations and validated using experimental results. The computational models and results provide a deeper understanding of the mechanics of dowel-concrete interaction, the 3D stresses, and the distress (damage) produced by misaligned dowels in the pavement specimens. The computational models were 3D finite element models developed using ABAQUS, which is a commercially available finite element software (ABAQUS 2004).

1.4 RESEARCH PLAN

The research objectives were achieved by systematically conducting the following tasks:

- 1) Task I: Pullout Behavior of single misaligned dowel bars

Task-1 focused on the fundamental pullout behavior of a misaligned dowel bar in a concrete pavement joint. The pullout behavior of single dowel bars with various misalignment types and magnitudes were determined experimentally. Three-dimensional (3D) finite element models were developed to investigate the pullout behavior of single

misaligned dowel bars from the experimental investigation. The experimental results were used to further calibrate and verify the overall behavior predicted by the finite element models.

2) Task 2: Opening behavior of joints with multiple misaligned dowel bars

Task-2 focused on the joint opening behavior of concrete pavement joints with multiple misaligned dowel bars. Experimental investigations were conducted to determine the joint opening behavior of concrete pavement joints with uniformly, non-uniformly or alternately misaligned dowel bars. Three dimensional finite element models were developed and calibrated to predict the overall force – joint opening behavior and to provide insight into the localized stresses and observed distresses. The calibrated models were used to further investigate the behavior of ‘realistic’ concrete pavement joints with possible and ‘typical’ dowel bar misalignments. The behavior of these pavement joints were examined for the cases of uniform, non-uniform and random dowel bar misalignments.

1.5 LAYOUT OF THE REPORT

This report, “Experimental and Analytical Investigations of the Mechanistic Effects of Dowel Misalignment in Jointed Concrete Pavements” is outlined as follows:

Chapter 2 contains a detailed literature review of the technical papers, reports and thesis on experimental and analytical studies of dowel bars. This chapter defines misalignment and discusses various construction practices. It discusses the ways for measuring misalignment in the field. The experimental studies conducted by researchers,

their test setups and limitations are also presented in this chapter. A detailed study of the various 2D and 3D finite element models that were developed over the years for rigid pavements is presented. This defines the current state-of-the-art and identifies the modeling strategies used by other researchers in the rigid pavement design field.

Chapter 3 provides a detailed description of the experimental plan and procedure, the test matrix, research parameters such as misalignment magnitudes, type and orientation. The nomenclature used to identify the laboratory test specimens and the finite element models are explained. The instrumentation, hydraulics and data acquisition used in the experimental investigation and their calibration and accuracy are presented.

Chapter 4 presents the results of the experimental investigations. Various cases of dowel pullout forces vs. joint opening behavior are compared to identify trends from the experimental results. A hypothesis regarding the mechanics of dowel misalignment and its impact on surrounding concrete is presented. This chapter also presents a rationale for developing computational models that can be calibrated and validated using data from the experimental investigation.

Chapter 5 shows the development of the 3D finite element model. The ABAQUS concrete damage plasticity model was used in this research study. The features and detailed description of this model including various parameters are presented in this chapter. The development and calibration of the model for the bond between the dowel bar and surrounding concrete is presented. This chapter also includes some comparisons of the overall dowel pullout force-joint opening behavior from the experiment and analysis to verify the model.

Chapter 6 presents a detailed discussion on the various material failure or damage limit states that occur in the analytical models. The chapter presents results from the 3D finite element analyses and parametric studies evaluating effects of various misalignment parameters on the joint behavior. Some recommendations on the misalignment tolerances are made based upon the results of the parametric study.

Chapter 7 presents some preliminary investigations of the effects of wheel loads combined with dowel misalignments and joint opening. This chapter focuses on the development of the finite element model, the loading and boundary conditions and the effects of dowel misalignment and wheel load on joint opening behavior.

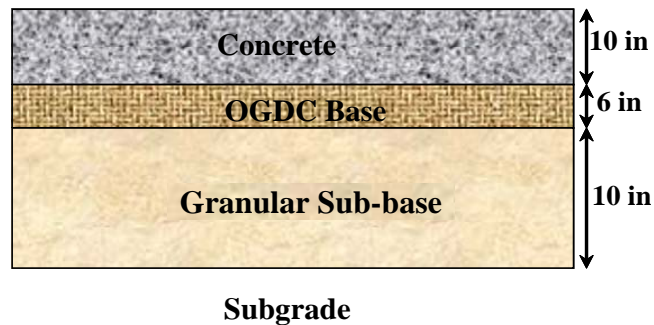
Chapter 8 presents the summary and conclusions of this research study. It includes the conclusions from the experimental and analytical investigations and recommendations for future work.

CHAPTER 2

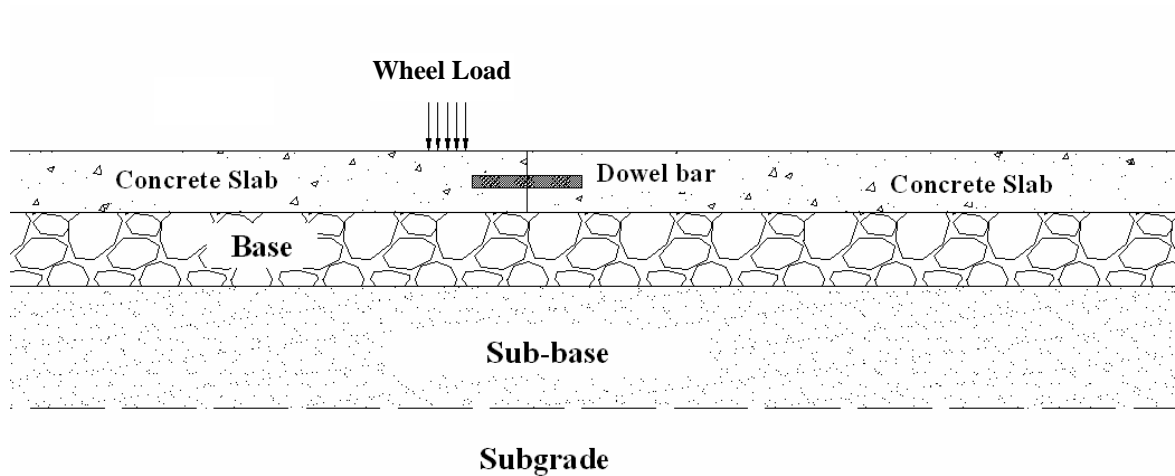
LITERATURE REVIEW

2.1 INTRODUCTION

In general a Jointed Plain Concrete Pavement (JPCP) consists of several components, as shown in figure 2.1 (Davids, 1998)



(a) Typical pavement cross-section



(b) Typical Pavement and loading in longitudinal direction

Figure 2.1: Typical components of a pavement cross section and truck loading.

JPCPs are constructed with contraction joints to accommodate slab movements due to temperature and moisture variations. A combination of steel dowel bars and aggregate interlock are used across joints to maintain continuity between slabs. In this chapter a comprehensive literature review is presented on all aspects of experimental investigation and numerical modeling of dowel bar misalignments.

2.2 DEFINITIONS OF MISALIGNMENT, VARIOUS ORGANIZATIONAL SPECIFICATIONS AND CONSTRUCTION PRACTICES

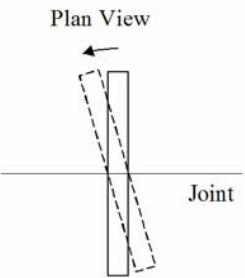
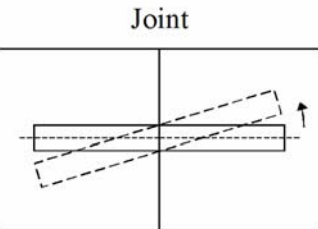
2.2.1 DEFINITIONS OF MISALIGNMENT

There are two basic types of dowel misalignments that can occur in concrete pavements, namely, the skew and translation type of misalignment. Table 2.1 shows the misalignment types and the effect of these misalignments on the pavement performance. The distresses observed include spalling, cracking and loss of load transfer efficiency. Distresses exhibited are attributable to high levels of stress or deflection (Snyder 1989) and they tend to appear in the vicinity of slab edges and corners. Excessive dowel-concrete bearing stresses may also result in spalling and faulting of concrete surrounding the dowel bars at the joint (Ionnides et al. 1990). From the information provided in table 2.1, the skew types of misalignments are more detrimental and they can cause all three types of distresses at the pavement joints. This research focuses on the effects of the skew type of misalignments.

Table 2.1(a): Possible Effects of Translational type of Dowel Misalignment on Pavement Performance

Type of Alignment		Effect on			Distress Observed
Translation		Spalling	Cracking	Load Transfer	
Horizontal	<p>Plan View</p>	-	-	Yes	Depends on magnitude of Translation
Longitudinal	<p>Plan View</p>	-	-	Yes	
Vertical	<p>Section View</p>	Yes	-	Yes	

Table 2.1(b): Possible Effects of Skew type of Dowel Misalignment on Pavement Performance

Type of Alignment		Effect on			Distress Observed
Skew		Spalling	Cracking	Load Transfer	
Horizontal	 <p>Plan View</p> <p>Joint</p>	Yes	Yes	Yes	Horizontal rotation or Vertical uplift, depending on magnitude of skew
Vertical	 <p>Joint</p> <p>Section View</p>	Yes	Yes	Yes	
Combined	Horizontal + Vertical	Yes	Yes	Yes	

2.2.2 SPECIFICATIONS FROM VARIOUS STATE HIGHWAY AUTHORITIES

The American Concrete Paving Association (ACPA) recommends that dowel bars should be used to provide added mechanical load transfer where truck traffic exceeds 120 per day or accumulated design traffic exceeds 4-5 million ESALs. This truck traffic loading condition will require at least an 8 in. thick slab and for most highways, dowels are recommended for 8 in. thick slabs or greater (ACPA 2004).

The American Association of State Highway and Transportation Officials (AASHTO), provisions for joint design include the following parameters; the dowel diameter, embedment length, spacing of joints and dowels so as to limit and control the magnitude of stresses developing in each bar and the deflections in the surrounding concrete. Current DOT practices for dowel and joint design (AASHTO 1993 and Mechanical Empirical Pavement Design Guide), are based on experience and the thumb rule that the diameter of the dowel should be equal to $1/8^{\text{th}}$ of slab thickness. FHWA (1990), Federal Highway Administration, recommends a minimum dowel diameter of $1\frac{1}{4}$ in. for highways. ACPA (1991) recommends a dowel diameter of $1\frac{1}{4}$ in. for pavements less than 10 in. thick and $1\frac{1}{2}$ in. for pavements greater than 10 in. thick. The NCHRP 1-37A mechanical empirical design guide methodology is based on the bearing stress of the dowel bar on the surrounding concrete with the dowel bar diameter being a key parameter in the design.

Various highway agencies have their own specific permissible limits. No clear consensus exists as to the level of practical limits on dowel placement tolerances. The Pennsylvania DOT specifies an allowable tolerance of $\frac{1}{4}$ in. per 18 in. of dowel length in both the horizontal and vertical directions. The Tennessee DOT investigated

misalignment dowels by uncovering dowels in freshly placed concrete and by core drilling in hardened concrete. The recommended limits on horizontal and vertical skew were $\frac{1}{2}$ in. The Michigan DOT recommends the use of Billet steel grade 40 made dowel bars. The dowel bars coated with epoxy have to be placed at 12 in ($\pm \frac{1}{2}$ in.) centers. As per MDOT specifications, Standard R-40, after the load transfer assembly is set in place, dowel bars shall remain aligned parallel with each other and within $\frac{1}{4}$ in. anywhere along the length in both the horizontal and vertical planes of the pavement. Indiana DOT and Iowa DOT have specified that dowel bars shall remain aligned parallel with each other and within $\pm \frac{1}{8}$ in. tolerance limits. Misalignment tolerance specifications for various DOTs have been summarized in table 2.2. A survey of some DOTs, as shown in table 2.3, showed that they have specified some tolerances irrespective of whether the dowel has been placed using a DBI or a basket assembly

Table 2.2: DOT Tolerance Specifications

State	Tolerance	
	Dowel Basket Assembly	Dowel Bar Inserter
Michigan (2004)	<p>Misalignment: Dowel bars shall remain aligned (parallel) with each other and $\pm 1/8$ in. in both horizontal and vertical planes.</p> <p>Transverse Location and Depth: Dowels shall be placed middepth $\pm 1/2$ in. Dowels shall be centered 1 ft $\pm 1/2$ in.</p>	<p>Misalignment: $\pm 1/4$ in. over the length of the bar in the horizontal and vertical planes.</p> <p>Longitudinal Location: ± 2 in. of planned longitudinal location.</p>
Wisconsin (2004)	<p>Hold dowel bars in the correct position and alignment using an engineer-approved device during construction</p>	<p>Misalignment: Parallel to the pavement surface and centerline $\pm 1/2$ in. over 18 in.</p> <p>Transverse Location and Depth: ± 1 in. of the planned transverse location and depth.</p> <p>Longitudinal Location: ± 2 in. of planned longitudinal location.</p>
Ohio (2005)	<p>Misalignment: $\pm 1/4$ in. per foot.</p> <p>Transverse Location and Depth: Centerline of individual dowels shall be parallel to each other, the surface and the centerline of the slab. Dowels shall be $\pm 1/2$ in. on centers. Dowels shall be placed mid-depth of the slab.</p>	
Iowa (2005)	<p>Misalignment: $\pm 1/8$ in. over 18 in.</p> <p>Transverse Location and Depth: Centerline of individual dowels shall be parallel to the other dowels in the assembly $\pm 1/8$ in. Spacing between dowels shall be 1 ft $\pm 1/4$ in. Each assembly shall be placed so that the bars are in a horizontal plane at $T/2 \pm 1/2$ in.</p>	N/A
California	<p>Misalignment: ± 0.354 in. over 18 in. in both horizontal and vertical directions.</p> <p>Transverse Location and Depth: Parallel with the pavement lane centerline and surface of the pavement at mid-pavement depth. Transverse location ± 1 in. from planned location.</p> <p>Longitudinal Location: ± 2 in. of planned longitudinal location.</p>	
Illinois (2002)	<p>Misalignment: $\pm 1/8$ in. over 1 ft. in the horizontal and vertical planes.</p> <p>Transverse Location and Depth: Dowels, when used, shall be held in position parallel to the surface and centerline of the slab by metal devices.</p>	

Table 2.3: Survey of Dowel Bar Installation Specifications

SHA* / DOT	Basket (% used)	DBI (% used)	Misalignment Tolerance		Quality Control of Misalignment
			DBI	Basket	
Alabama	Yes (100)	No (0)	None	¼ in. over 12 in.	Field Inspection
Colorado	Yes (25)	Yes (75)	Not specific		No requirement
Florida	Yes (100)	No (0)	None	½ in. over 18 in.	Contractor's responsibility
Nevada	Yes (75)	Yes (25)	½ in. over 18 in.		Coring. Also evaluating the the usefulness of MITSCAN
North Carolina	Yes (75)	Yes (25)	½ in. over 18 in.	0.25 in., 0.75 in. opposing skew	MITSCAN
Ohio	Yes (75)	Yes (25)	None	None	Pachometer or coring
Pennsylvania	Yes (25)	Yes (75)	¼ in. over dowel length		Alignment verified prior to concrete placement. Baskets assumed to be rigid.
Virginia	Yes (75)	Yes (25)	Not specific		No requirement
Washington	Yes (75)	Yes (25)	½ in. over 18 in.		Developing specs for MITSCAN
Wisconsin	Yes (50)	Yes (50)	½ in. over 18 in.		Not specific

*SHA: State Highway Association

2.2.3 CONSTRUCTION PRACTICES

Pavements are constructed using fixed form paving and slipform paving. Fixed form paving is used generally for small jobs, complicated geometry pavements, or variable width pavements, while slipform paving is used for larger jobs that require high

production rates. There are two main methods of dowel bar placement in the field: dowel basket assembly and dowel bar inserter (DBI). Slipform paving can accommodate both the methods of dowel bar placement while fixed form paving can accommodate dowel baskets only.

Dowel Baskets

Dowel baskets are simple truss structures used to hold dowel bars at the appropriate height before Portland Cement Concrete (PCC) placement. Typically, dowel baskets span an entire lane width and are fabricated from thick gauge wire. They are left in place after the PCC is placed but do not contribute to the pavement structure. When using dowel baskets, the dowels must be aligned and the dowel basket firmly anchored to the base course. The FHWA recommends that the dowel baskets be secured with steel stakes with a minimum diameter of 0.3 in. embedded at least 4 in. in stabilized bases, 6 in. in treated permeable bases and 10 in. in untreated bases or subgrade. Further, a minimum of 8 stakes per basket is recommended. Figure 2.2 illustrates a typical dowel basket assembly. The dowels come precoated with lubricant from the manufacturer and are welded on alternate sides

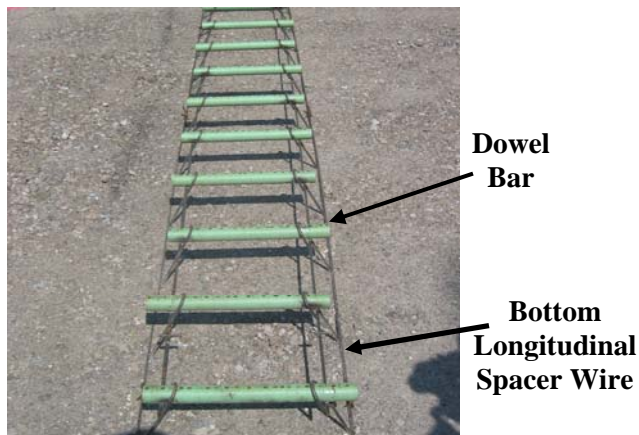


Figure 2.2: Typical dowel basket assembly used as load transfer devices in JPCP

Dowel Bar Inserter

The dowel bar inserter is a device which mounts behind the slipform paver. The DBI can accommodate different dowel spacings, dowel depths, skewed or square contraction joints, etc. as shown in figure 2.3.

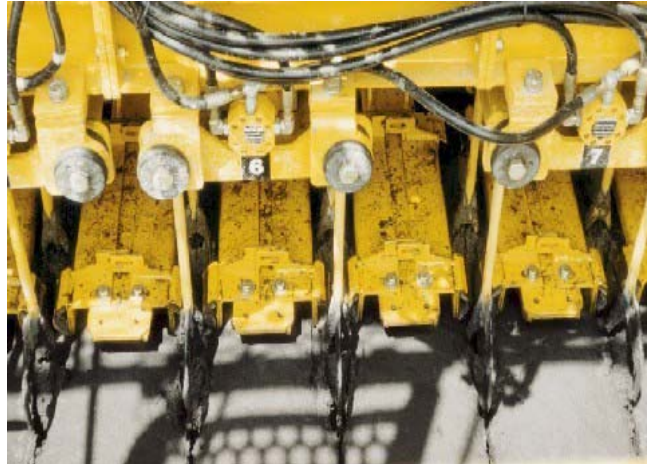


(a) Typical Slipform Paver with inbuilt Dowel Bar Inserter



(b) Dowel Bar Magazine in position

Figure 2.3: Dowel Bar Inserter (Source Gomaco Inc., www.gomaco.com)



(c) Insertion into Plastic Concrete

Figure 2.3 (cont'd).

When the desired joint location is reached, an automated insertion cycle is activated. A pan mounted dowel distributor shifts allowing the dowels to drop from the magazine through the pan onto the fresh concrete. The vibration-isolated “inserting fork assemblies” then vibrate the bars until they have reached their proper depth in the concrete. Mounted on rubber-isolated beams, the vibrating forks reconsolidate the concrete as the forks are pulled out of the slab. Once the forks have cleared the concrete, the vibration is stopped and DBI and the pan are retracted. Because the dowels are being vibrated intensely and are inserted down to their final resting place under the weight of the dowel inserter assembly and light hydraulic pressure, the concrete has enough time to flow around the bar rather than being displaced (Gomaco, Inc).

Factors affecting misalignment

With either method, care and attention towards many details are required to achieve proper dowel bar alignment (Yu 2005). For dowel baskets, the most critical factor appears to be the manner in which the baskets are secured on the subbase or base prior to paving. If the baskets are not adequately pinned down, the baskets may be shoved,

rotated, or pulled apart during paving, resulting in extreme dowel bar misalignments. The baskets may also get bent during handling or during concrete placement.

For DBI construction, the critical factors are the proper adjustment of the DBI and PCC mix design. When using a DBI, mix optimization is extremely important to ensure the dowel bars do not become displaced after insertion. PCC mix for DBI construction must be stable enough to hold the bars in place without displacing them during paving. Construction factors that may affect misalignment as identified by Tayabji (1986) have been summarized in table 2.4.

Table 2.4: Construction Factors affecting Misalignment*

Dowel Baskets	Dowel Bar Inserter
<ul style="list-style-type: none"> • Basket rigidity • Quality control during basket fabrication • Care during basket transportation and placement • Fastening of basket to subbase • Location of saw-cut over basket • Paving operation • Field inspection during construction 	<ul style="list-style-type: none"> • Implanting machine operation • Strike-off after dowel placement • Consolidation (vibration) after dowel placement • Location of saw-cut over implanted dowels • Field inspection during construction

*Ref: Tayabji (1986)

Quality Control of Misalignment

There are a few destructive and non-destructive methods used for the detection and measurement of dowel bar misalignment in the field: coring, the pachometer and covermeter, the Ground Penetrating Radar (GPR), and the MIT Scan-2. Coring is the only destructive method among the detection methods and by far, it is the most accurate method but its use is limited. The various devices used in measuring misalignment of dowel bars after construction are shown in figure 2.4.

Pachometer and Covermeter

These are battery-operated magnetic detection devices, which are mainly intended to measure the depth of reinforcement in concrete, and to detect the position of rebars. Its use has been extended to pavements to detect the location of dowel bars. The device emits an electromagnetic field and detects disturbances in the field caused by embedded metals.

Ground Penetrating Radar

The Ground Penetrating Radar (GPR) uses a radio wave source to transmit a pulse of electromagnetic energy into a subsurface (in this case, concrete pavement). The amplitude and arrival time of the reflected electromagnetic pulse (which originates from the top of the dowel) is recorded for analysis (determination of spatial location of the dowel). The GPR signal is characterized primarily by changes in reflection amplitude and changes in the arrival time of specific reflections. The GPR record consists of a continuous graphic display of reflected energy over a preset time interval. The depth to the dowel can then be determined if the propagation velocity, and electromagnetic energy through concrete are known or estimated.

MIT Scan-2

The MIT Scan-2 is a state-of-the-art device for measuring the position of metal bars embedded in concrete. The MIT Scan-2 is based on the magnetic imaging tomography technology and utilizes an array of sensitive detectors and sophisticated data analysis algorithms to produce very accurate results. The device emits a weak, pulsating magnetic signal and detects the transient magnetic response signal induced in metal bars. The methods of magnetic imaging tomography are then used to determine the position of the

metal bars. Unlike other devices that have been used in the past, which are general-purpose instruments adapted to the dowel bar detection application, the MIT Scan-2 was developed specifically for measuring dowel and tie bar alignments. As a result, the device is simple to operate, efficient, and provides real-time results in the field.



(a) Typical Pachometer



(b) Ground Penetrating Radar (GPR)



(c) Close up of MIT Scan-2



(d) Typical Run of MIT Scan-2 in Field

Figure 2.4: Various Non-Destructive Misalignment Measuring Devices

2.3 REVIEW OF FIELD STUDIES

Donahue (2003) in his report on dowel bar placement accuracy with a DBI, carried out field investigation (measurements of alignment) using ground penetrating radar. The findings in his report categorized the misalignments into three groups of skew: $\leq \frac{1}{2}$ in.,

$\frac{1}{2}$ in. $-\leq 1$ in. and > 1 in. Dowel baskets had 70% higher incidence of horizontal dowel misalignments > 1 in. compared to the DBI. Average horizontal skew was 0.49 in. in the DBI and 0.51 in. in the basket assembly. Average vertical skew occurrence was higher in the DBI method compared to using the dowel baskets, but both within acceptable standards close to 90% of $\frac{1}{2}$ in. skew limit. Neither case had occurrences of misalignments over 1 in.

Donahue (2003) states that translation, both horizontal and vertical, does not have as significant an impact as skew. He states that longitudinal translation is a measure of the bar's effective length on the approach and leave slabs. It is not realistic to expect every 18 in. bar to straddle a joint with 9 in. on either side, but it is expected that a bar have at least 6 in. on each side to ensure that it can adequately provide load transfer across the slabs. A study conducted in the late 1950's concluded that the dowel embedment length required to provide full load transfer is five or more times the bar diameter (Teller 1959). A study by Minnesota DOT (Burnham 1999) indicated that an embedment length of only 2.5 in. is sufficient to keep faulting at an acceptable level of $\frac{1}{4}$ in. and provide load transfer efficiency (LTE) with less variability.

Burati et al. (1983), carried out statistical analysis of the visual surveys and actual measurements recorded of the dowel alignment with an electronic metal detector for both the basket assembly and implanted projects. The visual testing was carried out to record any distress type, rate of occurrence, severity, location of distress, general condition of pavement and any relevant visual imperfections. The metal detector was used to measure the horizontal misalignments. They found that there was no significant difference between the basket assembly and implanted assembly with respect to the joint related

distress. Spalling and raveling was noticeable on the metal inserter projects. The metal insert joints appeared to be the cause of spalling as there was much evidence of corroded insert segments. Strangely, they came up with no statistical proof that either the basket assembly or implanted projects are superior. Though, the overall results, viewed with much skepticism showed that the dowels in the implanted projects, on the average, were better horizontally aligned than the dowels in the basket assembly.

Okamoto et al. (CTL, Inc.) (1989) summarized field evaluations of Texas, Wisconsin and Idaho highways, for both the dowel basket assemblies pinned to the subbase and Guntert & Zimmerman dowel bar inserter joints. Dowel bar depth was generally consistent with both methods of construction. The average depth maintained was plus or minus one inch of slab mid depth. They found that the range of dowel depths at individual joints were 0.8 in. to 0.4 in. for inserter and basket assembly, respectively. The vertical misalignment was generally consistent for both types of construction, though the average ranged from 0.1 in. to 0.2 in per foot. At locations where inserters were used nearly 60% of the dowels were tilted forward (or backwards) in the direction of paving, for the Wisconsin project. For horizontal misalignments, the accuracy was estimated at approximately $\frac{1}{4}$ in. to $\frac{1}{2}$ in./ft. Also, the direction of paving did not affect the direction of horizontal misalignment. Both uniform and asymmetric horizontal misalignments were observed. Coring data and radar output were used to measure the longitudinal displacement. In Wisconsin, the percentage of dowel displaced were 9.3% and 7.5% for inserter and basket assemblies respectively.

The overall performance and distress of in-service concrete pavements are functions of: (a) the pavement design, (b) environmental conditions including thermal

gradients, (c) joint spacing, (d) applied loads and number of passes (e) the dowel misalignments, (f) material quality and (g) construction. The tolerance limits for dowel misalignment will depend on the other parameters (a - d mentioned here) and the required number of passes (design life) before pavement failure occurs in terms of the distress (spalling, cracking) or performance (load transfer efficiency < 70%). In “in-service” pavements, the structural distresses are probably a combination of the basic types of misalignments. The type and magnitude of skew will impact the concrete-dowel bearing stress which leads to higher cumulative damage at a joint.

Table 2.5 summarizes the results of some of the older and recent field studies comparing the two dowel bar placement methods, i.e. basket assemblies and DBIs, with respect to misalignments and distresses observed.

2.4 REVIEW OF LABORATORY INVESTIGATIONS

Laboratory investigation to study the impact of misaligned dowel bars was started as early as 1938 by Smith and Benham. They conducted laboratory tests of small slab sections incorporating joint and dowels spaced at 12 in. on centers. In these tests, 3/4 in. diameter dowels were placed at different levels of misalignment and loading was applied at 28 days to open the joint. Results indicated that for 6 in. thick slab sections, an alignment error in excess of 1 in. caused spalling when joints were opened 3/4 in. For a 5 in. thick slab section, an alignment error of 1/4 in. caused slight spalling. Tests also showed that if the joint was not opened more than 1/2 in., alignment errors upto 1.5 in. could be tolerated without spalling. Generally, the load required to open a contraction

Table 2.5: Summary of Field Study Results

Reference Study and Test Section	Specifications, Method of Measurement and Parameters Monitored	Findings/Conclusions
<p>Georgia DOT (Gary Fowler, 1983)</p> <ul style="list-style-type: none"> • M-5020 Richmond: Baskets • I-16 Bulloch paved in 1976: DBI • APD-056 Forsyth: DBI Contractor tried placing dowels after the paver had passed resulting in extra finishing, dowel depressions filled with grout, and poor riding surface. The implanter was positioned ahead of the paver after a short period. • Three interstate projects with dowels implanted and two projects with baskets 	<p>Dowels 1.25 in. diameter, 18 in. long, 15 in. c/c, joint spacing 20 ft</p> <p>Tolerance: H, V of ± 1 in. for translation</p> <p>Rotational misalignment was 1-1/8 in. H and 9/16 in. V</p> <p>Method: Coring, Electronic Metal Detector</p> <p>Parameters:</p> <ul style="list-style-type: none"> • Depth • Longitudinal alignment • Vertical and horizontal rotation 	<ul style="list-style-type: none"> • 1st project that used an implanter met the specifications in most cases and compared closely to the accuracy of one reference job that utilized baskets. • Utilization of baskets did not eliminate all problems of rotation and especially the problem of longitudinal alignment. • Longitudinal displacement is affected at least as much by location of the sawed joint as it is by actual dowel movement. • Most difficult factor to control with implanting seemed to be the vertical height of dowel. • No dowel related pavement distress occurred in either of the projects. • All dowels were working. The dowel bar paint is ineffective as a coating on the working end of the dowel. However, it does aid in breaking the concrete bond of the dowel.
<p>Missouri DOT (John Donahue, May 2003)</p> <p>US 60 JPCP construction project near Van Buren (G&Z DBI, Baskets)</p>	<p>Tolerance: Be parallel to the subgrade and parallel to the line of the joint</p> <p>Misalignment: $\pm 1/2$ in. over 18 in.</p> <p>Transverse location: ± 1 in.</p> <p>Longitudinal translation: ± 2 in.</p> <p>Method: Ground penetrating radar (GPR), handheld pachometer</p> <p>Parameters:</p> <ul style="list-style-type: none"> • Dowel Skew • Dowel Translation • Dowel depth 	<ul style="list-style-type: none"> • Both tend to have moderate horizontal skew tendencies with the DBI performing a little better. • Both have very good control of vertical skew with the baskets holding a slight edge in performance. • Both have few serious occurrences of high opposite skew between dowel bars in the same joint. • For depth, DBI was more consistent than baskets with respect to surface evaluation. • Average depth and average depth standard deviation was acceptable for both.
<p>Burati et.al.,(1983)</p> <p>Alabama pavements</p>	<p>Method: Electronic Metal Detector</p> <p>Parameters:</p> <ul style="list-style-type: none"> • Absolute horizontal rotation • Absolute longitudinal displacement 	<ul style="list-style-type: none"> • No significant difference between DBI and basket projects with respect to joint-related distress. • No significant difference between DBI and basket projects with respect to joint-related distress.

Table 2.5 (contd.)

Reference Study and Test Section	Specifications, Method of Measurement and Parameters Monitored	Findings/Conclusions
<p>Burati et.al.,(1983) Alabama pavements</p>	<ul style="list-style-type: none"> • Absolute horizontal displacement 	<ul style="list-style-type: none"> • Overall results indicated that the dowels in the implanted projects, on the average, were better aligned than were the dowels in the basket projects. But contractor difference and inconsistency might have contributed to the difference. • Overall results indicated that the dowels in the implanted projects, on the average, were better aligned than were the dowels in the basket projects. But contractor difference and inconsistency might have contributed to the difference. • Individual dowel position had no effect on the alignment achieved. • No effect from pavement grade on dowel alignment or distress was found. • No correlation between misalignment types and distress was found. • Absolute horizontal rotation values were virtually the same for both implanted and basket projects. • Absolute longitudinal and horizontal displacements were noticeably better in implanted projects.
<p>James Parry (Wisconsin DOT) (1987) Three projects each using DBI and baskets on I-90 at Janesville in 1987</p>	<p>Tolerance: Depth of dowel: ½ in. above the mid-depth Vertical/Rotation: ± ½ in. over full length Longitudinal translation: ± 3 in. in either direction</p> <p>Method: Coring</p> <p>Parameters:</p> <ul style="list-style-type: none"> • Average depth • Vertical rotation • Horizontal rotation • Ride quality • Voids • Missing dowels 	<ul style="list-style-type: none"> • DBI is capable of consistent satisfactory placement of dowel bars with respect to average depth, vertical and horizontal rotation. • Initial setup of the DBI with respect to depth of dowel placement is critical at the start of each project, and dowel depths should be verified by probing through the fresh concrete. • Accurate marking for sawing joints is important. • Having a magnetic rebar locator available on all doweled PCC construction projects would be useful in aligning sawn joints with the dowel bars and in identifying missing dowels. • Ride quality of 4.6 can be achieved on DBI projects with minimum grinding. • Improved consolidation is required on both projects. • Problems with missing dowels on existing DBI projects appear to be infrequent and isolated, but this problem should be monitored on future projects.

Table 2.5 (contd.)

Reference Study and Test Section	Specifications, Method of Measurement and Parameters Monitored	Findings/Conclusions
<p>Bock, Okamoto (1988) I-86, Idaho (Gomaca DBI) I-45, Texas (Baskets, DBI) I-90, Wisconsin (Baskets, DBI)</p>	<p>ID-1.25 in., 18 in. long @ 12 in. c/c. 10 in. PCC, random joint spacing Tolerance: $\pm \frac{1}{4}$ in. per 12 in. TX-1.25 in., 22 in. long @ 12 in. c/c. 10 in. PCC, 15 ft. joint spacing WI-1.25 in., 18 in. long @ 12 in. c/c. 10 in. PCC, random joint spacing Tolerance: Dowel depth: mid-depth ± 1 in. Misalignment: $\pm \frac{1}{2}$ in. per 18 in. Horizontal Translation: ± 1 in. Parameters:</p> <ul style="list-style-type: none"> • Average depth • Vertical Misalignment • Horizontal Misalignment • Longitudinal Displacement (qualitative) 	<ul style="list-style-type: none"> • DBI performed well compared to baskets. • Based on dowel depth, longitudinal displacement, vertical tilt, and horizontal skew, there is no significant difference between DBI and baskets. • Distribution of tilt is more symmetrical for basket joints than inserter joints, indicating that vertical misalignment may not be independent of paving direction. • Horizontal misalignment seems to be independent of paving direction. • Occurrence of longitudinal translation is similar for both types of joints.
<p>Okamoto (1987) I-45, South of Dallas, Texas</p>	<p>Method: Ground penetrating radar, Coring Parameters:</p> <ul style="list-style-type: none"> • Average depth • Vertical Misalignment • Horizontal Misalignment • Longitudinal Displacement (qualitative) 	<ul style="list-style-type: none"> • Overall, the dowels in the inserter sections tended to be misaligned slightly downward in the leave direction. • Displacement can be introduced if the joint location is not marked correctly for sawing, or if the saw cut does not follow the marked joint location. • Average dowel depths appear to be uniform for both methods. • DBI performance is better than basket in terms of both degree of vertical misalignment and variability of vertical misalignment with each joint. • If other sources of variability, such as accuracy of joint locating and sawing are assumed to be constant, it appears that more longitudinal displacement was detected in the DBI sections than basket sections. Number of occurrences was, however, small in comparison to the number of dowels evaluated.

Table 2.5: (contd.) Summary of Field Study Results

Reference Study and Test Section	Specifications, Method of Measurement and Parameters Monitored	Findings/Conclusions
<p>Yu, Khazanovich (2003) One section each using DBI and baskets, totaling 100 joints each, on I-15 reconstruction project near Victorville, California</p>	<p>Tolerance: Horizontal and vertical misalignment: $\pm \frac{1}{4}$ in. per 1 ft Lateral dowel position: ± 1 in. Method: MIT Scan-2 Parameters: Horizontal and vertical misalignment</p>	<ul style="list-style-type: none"> • Dowel alignment in the DBI section is no worse than that in the basket section. • In terms of number of bars misaligned, the basket section performed better (15.2 % vs 19.1 %) • In terms of the risk of the improper dowel alignment causing joint problems, the DBI section may be better because the greater percentage of the out-of-spec bars in the DBI section was due entirely to the higher percentage of misaligned bars in the 0.35 to 0.6 in. range. • In both of the more severe misalignment categories (0.6 to 0.8 in.; and >0.8 in.), the basket section had a higher percentage of misaligned bars than the DBI section.

joint by $\frac{1}{2}$ in. did not exceed 3,000 lb per dowel. Also, the load necessary to close an expansion joint to a width of 0.25 in. in no case exceeded 4000 lbs per bar.

Segner and Cobb (1967), tested slab sections 6 ft wide, 5-1/2 ft long, and 10 in. thick. Dowels used were 1.25 in. diameter and 16 in. long. Testing was done at 2 and 7 days. The dowel bar alignment errors in any plane resulted in an increase in the load required to produce a joint opening of $\frac{1}{2}$ in. and $\frac{3}{4}$ in. A dowel bar alignment error on the order of $\frac{1}{4}$ in. does not require an appreciable increase in the load to produce these joint opening. Their observation indicated that any misalignment in the vertical and oblique (combined misalignment) plane was more critical than the horizontal plane in terms of the load required to produce a joint opening of $\frac{1}{2}$ in. and $\frac{3}{4}$ in. A dowel bar misalignment greater than $\frac{1}{4}$ in. produced severe increase in the load required to produce a corresponding joint opening.

Significant spalling failures were observed for a 3 in. horizontally and 1 in. vertically misaligned dowel bar for a joint opening of 0.9 in. A spalling type failure defines one that pulls, breaks or chips out concrete in the immediate vicinity of the contraction joint. The failure results in large wedge-shaped “chunk” of concrete being torn out of the top of the slab. Another type of failure that occurred with the dowel misaligned specimens was the local crushing of concrete around the periphery of the dowels. This crushing or bearing type failure around the dowels was more severe in the specimens tested at 2 days than those tested at 7 days. This was expected since the additional age probably provided for an increase in the bearing strength of concrete. The crushing of the concrete around the dowels undoubtedly increases slightly the diameter of the dowel cavity in the slab. This increase in the dowel cavity provided some slop or

room for the movement between the dowel and the cavity walls in addition to that provided by the dowel grease which probably loosened the effects of dowel misalignment to some extent.

Load required to open a joint by $\frac{1}{2}$ in. for a 1 in. vertical misalignment of a dowel was about 4,000 lbs and for a 1 in. horizontal misalignment of a dowel the load was about 2,000 lb for the same joint opening. Spalling was produced for a vertical misalignment of 3 in. at a joint opening of about 0.9 in as indicated above.

Tayabji (1989) conducted laboratory study of misaligned dowel bars using a slab section of 3ft wide by 7ft. The depths of the slab sections were 8 in. and 10 in. with misalignment levels (per 18 in length) being 0, $\frac{1}{4}$, $\frac{1}{2}$, 1, 2 and 4 in. Both categories of misalignment, i.e. horizontal and vertical, were carried out. Pullout loads were applied gradually and uniformly to obtain a joint opening of 0.25 in. in about 1 minute. Chairs were used to keep the dowel bars in place and a $\frac{1}{8}$ in. thick steel plate used to form the joint. Typical relationship between joint opening and pullout load were shown. A large portion of the pullout load is required to open the joint 0.01 in. After the joint was opened to about 0.05 in, there is no further increase in the pullout load.

For each of the tests that they performed, they applied pullout load three times. After each pullout, the slab was pushed back to close the joint and the pullout test was repeated. The maximum pullout load was always obtained under the first test. For the second and third test, the maximum pullout load obtained was less than half that obtained for the first test. Maximum average pullout load for the various misalignments of single dowel bar in an 8 in. slab with max joint opening of 0.25 in. was 1237 lbs.

Testing of a pair of misaligned dowel bars with the same level of misalignment was carried out but the misalignment was in the opposite direction to cancel out any tendency of pulled slab to tilt horizontally or vertically. Both the 8 in. thick and 10 in. thick slab sections were tested with the load applied gradually and uniformly to obtain a joint opening of 0.25 in. In their tests they observed that there was an increase in the pullout load with increased level of dowel misalignment. The absolute magnitude of pullout force was 1000 lbs for dowel misalignments less than 1 in. The magnitude of the pullout load increased to 4000 lbs when the dowel misalignment exceeded 1 in. A very important fact worth mentioning was that there was no spalling around the dowel bars at the joint face for specimens having dowels with misalignments less than 1 in.

Weaver et al. (1970) carried out laboratory studies on the effects of the misalignment of dowel bars. The concept they used was that the effect of a misaligned dowel bar in a joint when opening or closing can be studied in a joint containing a single dowel bar, aligned normal to the joint, by the application of a shear force across the joint in a direction parallel to the plane of the joint. This method of study had the advantage that specimens containing precisely aligned dowel bars were produced easily and tested by varying the deflection across the joint. As a result of change in magnitude of the shear force applied to the joint, of known width (a) and deflection (Δ), a series of equivalent misalignments $\frac{\Delta}{a}$ were simulated until failure eventually occurred.

The authors tested joints of various widths with plane and interlocking joint faces. Tests were conducted on 10 in. thick specimens and 1 in. dowel diameters. Dowel bars were coated over half their length with a bond preventing compound and joints were produced using brass or steel sheets. The joints were loaded initially to an equivalent

misalignment of 4%, then unloaded and reloaded to the same equivalent misalignment. This was followed by 2 similar cycles but to an equivalent misalignment of 8%, which were followed by a cycle to 16%. The second and fourth cycles were performed as checks on the results of the first and third cycles. Relationships between dowel bar rigidity, $\left(\lambda = \frac{P}{\Delta}\right)$, and equivalent misalignment were plotted for various joint widths and overall they all exhibited the same characteristic shape. On initial application of the load to the joint, high dowel bar rigidity is noted, which rapidly decreases until an equivalent misalignment of 3% is reached and then it becomes a constant. A very important observation from the comparison of the results stated that as the joint width is increased the dowel bar rigidity decreased. The measured rigidity of dowel bars in a joint increased up to an age of 7 days and then little difference was detected between specimens of ages 7 and 28 days.

They observed that when a joint is loaded with a shear force, the concrete in the face of the joint around the uncoated half of the dowel bar is stressed in a complex fashion. The tensile strains across the horizontal axis through the dowel bar increased until at a strain of about 100×10^{-6} was reached and cracking occurred. After cracking occurred they found that the load - deflection curve became linear, the dowel bar rigidity was constant and the width of the crack recorded as strain in the joint face increased linearly. When a crack originates at the dowel bar due to traffic or misalignment, the condition is stable and will not progress until the load or effect of misalignment is exceeded; progression of cracks to the surface of the specimen were noted at equivalent misalignments of 25%.

The experimental and field investigations could not provide any information on the internal stresses that developed due to misaligned dowel bars. The field and experimental studies did not provide any knowledge on the mechanics of dowel-concrete interaction and how the distresses were produced due to misaligned dowel bars. A comprehensive study on some of the analytical investigations carried out in the past and recent years is presented in the next section.

2.5 REVIEW OF ANALYTICAL STUDIES

The determination of stresses and deflections, using analytical finite element methods, in concrete pavements with joints containing dowel bars as load transfer devices has been investigated in detail since the late 1970s. Analytical solutions and theories presented in the 1930s by Westergaard (1926) based on many simplified assumptions presented equations of stresses and displacements of infinite length slabs resting on a Winkler foundations and static loads.

The stress analysis of dowels is based upon the work presented by Timoshenko (1925). Dowel bar stresses result from shear, bending and bearing. These stresses can be analyzed analytically to determine factors that affect load-transfer characteristics. According to Timoshenko (1925), a dowel bar encased in concrete will deflect as shown in figure 2.5. When a load is applied at the end of the dowel bar it will deflect downward exerting pressure at the lower face of the dowel for a distance designated as A to B in figure 2.5.

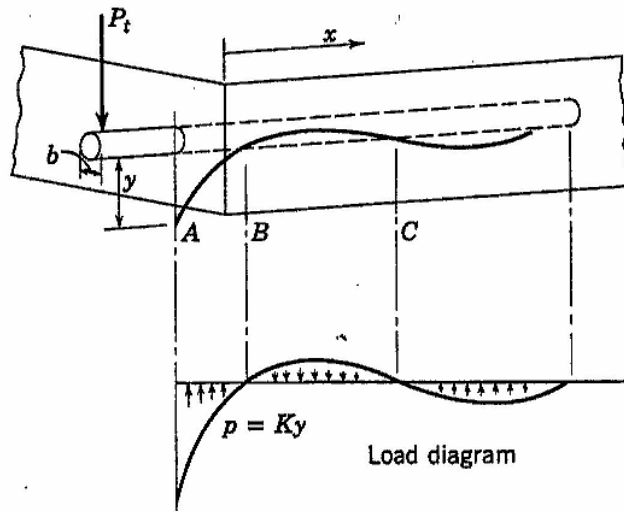


Figure 2.5: Pressure Exerted on a Loaded Dowel, Yoder (1975).

At this point of contra flexure, resulting bearing stress is on the top of the dowel and then at some distance beyond this, bearing again on the bottom of the dowel bar. For the purpose of analysis, it is necessary to assume that the dowel bar is infinite in length, extending into an elastic body. This assumption, can however, be simplified by neglecting the small pressures exerted on the bar at some distance on the elastic body.

Bradbury (1938) and Friberg (1940) have presented mathematical analysis of dowel design, which are all based upon the principles presented by Timoshenko. The relative stiffness of the bar embedded in concrete is given by

$$\beta = 4 \sqrt{\frac{K b}{4 E I}} \dots \dots \dots \text{Equation 2.1}$$

where,

K = modulus of dowel support (pci) = 300,000 to 1,500,000 pci

b = diameter of the dowel

E = modulus of elasticity of the dowel

I = moment of inertia of the dowel

According to Timoshenko, the deflection of the bar resulting from the load P_t is:

$$y = \frac{e^{-\beta x}}{2 \beta^2 EI} [P_t \cos(\beta x) - \beta M_o (\cos \beta x - \sin \beta x)] \dots\dots\dots \text{Equation 2.2}$$

where,

e = natural logarithm base

x = distance along dowel from face of concrete

M_o = bending moment on dowel at face of concrete

P_t = transferred load

Friberg (1940) adopted the above equation to dowels for design purpose. Bending moment and shear in the dowel can be expressed as following equations

$$-EI \frac{d^2 y}{dx^2} = M = -\frac{e^{-\beta x}}{\beta} [P_t \sin \beta x - \beta M_o (\sin \beta x + \cos \beta x)] \dots\dots\dots \text{Equation 2.3}$$

$$\frac{dM}{dx} = V = -e^{-\beta x} [(2 \beta M_o - P_t) \sin \beta x + P_t \cos \beta x] \dots\dots \text{Equation 2.4}$$

If the joint-width opening is designated z and since the concrete is very stiff compared to the steel bar, the moment at the dowel – concrete interface as:

$$M_o = -\frac{P_t z}{2} \dots\dots\dots \text{Equation 2.5}$$

for $x = 0$, and $M_o = -\frac{P_t z}{2}$ the deflection of the dowel joint is

$$y_o = \frac{P_t}{4 \beta^3 EI} (2 + \beta z) \dots\dots\dots \text{Equation 2.6}$$

The bearing pressure on concrete at the joint face is

$$\sigma = Ky_0 = \frac{P_t}{4 \beta^3 EI} (2 + \beta z) \dots\dots\dots \text{Equation 2.7}$$

Maximum moment occurs where the shear is equal to zero $\left(\frac{dM}{dx} = 0\right)$ and can be

written as
$$M = -\frac{P_t e^{-\beta x}}{2 \beta} \sqrt{1 + (1 + \beta z)^2} \dots\dots\dots \text{Equation 2.8}$$

The above equations for bearing pressure and maximum moment are directly applicable to stress computations. In each case P_t is the transferred load on the dowel and is less than the design load as a portion of the load is transferred by the pavement to the subgrade.

The bearing stress on the concrete at the face of the joint is critical for the proper function of the dowel bar in concrete. If the bearing stress on the concrete becomes too large the concrete will begin to break away where it contacts the dowel bar. Repetitive high-stress loadings of the dowel bar concrete interface will create a void. This void creates an additional amount of deflection in the system before the dowel bar begins to take on the applied load. This additional deflection creates a loss in the efficiency of the dowel bar to transfer load across the joint. This loss in efficiency must now be carried by the subgrade, which puts additional stress on the subgrade and creates the possibility for differential settlement of the adjacent slabs.

The bearing stress at the face of the joint is given as

$$\sigma = Ky_0 = \frac{P_t}{4 \beta^3 EI} (2 + \beta z) \dots\dots\dots \text{Equation 2.9}$$

The bearing stress on the concrete should be less than the crushing of concrete. According to the American Concrete Institute (ACI) Committee 325 (1956), the allowable bearing stress on the concrete is equivalent to

$$\sigma_a = \left(\frac{4-b}{3} \right) f'_c \dots\dots\dots \text{Equation 2.10}$$

where,

σ_a = allowable bearing stress (psi)

b = dowel bar width, i.e., diameter (in.)

f'_c = compressive strength of concrete (psi)

This equation provides a factor of safety of approximately three. The dowel bars immediately under the applied load assume a major portion of the load with other dowel bars assuming progressively lesser amounts of load. According to the theoretical analysis, maximum negative moment occurs at a distance of $1.8 l$ from the load, where l is the radius of relative stiffness.

Finite element methods were first employed to model response of rigid pavements in the 1970's. The fast growth of computer capabilities has enabled researchers to make use of the complicated computational techniques into many engineering applications. Finite element analysis has proved to be one such tool that has been molded into a powerful tool to solve complex pavement engineering problems. The following is a summary of the various studies that have been conducted using finite element analysis to model the dowel bar and the dowel – concrete interaction in JPCP joints.

Tabatabaie, et al. (1979), developed a 2D finite element program that is commercially available, modified later and still used, called ILLISLAB written in Fortran IV. This FEM code uses elastic material properties, can model load transfer systems such

as dowel bars and aggregate interlock and effects of using different types of base layers and variety of traffic loading on the slab system. The concrete slab and the base are modeled using elastic homogenous medium thick plates. The subgrade is modeled as a Winkler foundation using springs and dashpots. The dowel bars are modeled as beam elements and the relative deformation between the dowel bar and surrounding concrete was incorporated using spring elements. The authors compared and verified the accuracy of the finite element program with analytical solutions found before 1978, i.e., Westergaards (1926) equations and the Pickett and Ray charts.

Majidzadeh, et al. (1981), presented the development of stress analysis model called RIGMUL. Features of their model were variables such as slab thickness, effects of curling, warping and load transfer across joints, etc. The authors coupled finite element plate theory with multilayer elastic layer theory using two layer rigid slabs for concrete resting on three semi-infinite layers of elastic solid foundation. The model was verified by comparing results for different loading conditions from Westergaard's theory. RIGMUL was capable of analyzing load transfer effects of aligned dowel bars between slabs. The authors after conducting many parametric studies, concluded with engineering judgment and experience that their model worked well for cases with change in dowel bar diameter and spacing on the slab stresses and displacements.

Kukreti et al. (1992) presented a finite element procedure for the dynamic analysis of rigid airport pavements with discontinuities. Their overall aim was to model the dynamic interaction between the aircraft and a rigid pavement. To model the concrete pavement, rectangular, thin plate elements, having three degrees of freedom at each of the four corner nodes, namely vertical displacement and rotations about the in-plane, x and y,

axes. The discontinuities in the pavement such as joints were represented as vertical spring elements connecting two nodes having the same global coordinates in the mesh. They assumed that the load is transferred across the joint by shear. The equivalent spring stiffness is dependent on the dowel properties, dowel spacing, joint opening and dowel concrete interaction. They identified the interaction between the dowel and concrete as a parameter known as modulus of dowel support. The subgrade was modeled as a Winkler foundation consisting of a uniformly distributed springs and dashpots. To verify their model, parametric studies were carried out by varying mesh type, loading condition, slab thickness, changing modulus of dowel support and modulus of subgrade reaction. By changing the modulus of dowel support from 3×10^5 to 8×10^6 psi/in., the load transfer efficiency increased from 50 – 87%, meaning that by increasing the modulus of dowel support, the concrete supporting the dowel bar became more rigid. Increasing the slab thickness from 8 – 24 in., the load transfer efficiency decreased from 77 – 63%. This is due to the fact that the equivalent spring stiffness of the joint became smaller relative to the slab thickness. They did not study the effects on load transfer efficiency due to misalignment of dowel bars, slab curling or warping due to temperature gradients.

Channakeshava et al. (1993), presented a nonlinear finite element analysis of dowel jointed concrete pavement. Material nonlinearity, geometric nonlinearity and nonlinear loading conditions were considered by the authors. Nonlinear concrete cracking in tension, yielding in compression and nonlinear response of subgrade soils were considered in the material nonlinearities. The variables considered in the model were loss of support due to pumping of the material, expansion and curling of slabs under temperature gradients and the resulting joint closure and partial loss of support were

incorporated in the model as geometric nonlinearities. Behavior of nonlinear concrete material under static loading and effects due to loss of support and temperature curling were considered. To accurately model the nonlinear behavior of concrete, the authors identified the following four parameters that have to be calibrated; the uniaxial strength of concrete in compression (f'_c); uniaxial strength of concrete in tension (f'_t); equal biaxial compressive strength of concrete (f_{bc}) and point on the failure envelope corresponding to the hydrostatic and deviatoric stresses. The subgrade was represented as a set of three orthogonal springs. These springs were capable of resisting the compressive forces to prevent lift-offs and to simulate in-plane frictional effects between the subgrade and pavement slab (not considered in this paper). To simulate loss of support the authors assumed that the subgrade springs loose their stiffness over a certain width of the pavement adjacent to the joint; different widths were assumed in their analysis. For the dowel bars, beam elements were used and only elastic behavior was assumed. In order to simulate small gaps around the dowel (dowel looseness), interface spring elements connecting the beam nodes and isoparametric quadratic solid element concrete nodes were used. To model the dowel concrete interface, a localized joint response analysis was performed. The authors stated that the dowel bars embedded in concrete on either side of the joint bear against concrete in shear as the slab is loaded. The bearing strength of concrete is limited and due to the repetition of heavy loads, high level of stresses is induced on the concrete around the dowel at the joint. Their study did not consider the effects of misaligned dowel bars as the finite element meshes had to be coarse for computational efficiency. The authors concluded that load (shear) transfer efficiency of

the joint is reduced due to the local deformations of concrete around the dowels at the joint due to high stress concentrations.

Guo et al. (1995), presented a component dowel bar model to simulate the doweled joint in Portland Cement Concrete (PCC) pavements. The model developed by the authors is a further modification to the dowel concrete interaction models used by Tabatabaie et al. (1979) and Nishizawa et al. (1989). The component dowel bar model consists of two bending beams of finite length, embedded in concrete connected by a shear – bending beam. To verify the accuracy of their model the authors compared the model to results obtained from JSLAB, developed by Tayabji and Colley. The results for longitudinal edge stresses and bending moments of the dowel bars predicted were found to be in close comparison with both the analytical and experimental results.

Zaman et al. (1995), developed a finite element algorithm to model the multiple jointed concrete pavements to moving aircraft loads. The authors presented a special joint element developed to accurately model the dowel pavement joints based on contact theory. They idealized the finite element model using rectangular thin plate elements and the soil using Winkler springs and dashpots. For the dowel bars, massless plane frame elements were considered with the dowel – concrete interaction represented by contact elements between the dowel bar and concrete. For simulating aggregate interlock, vertical spring elements were used. In the model and parametric studies they did not consider misaligned dowel bars as a load transfer mechanism. The contact element between the dowel and surrounding concrete was developed based on the Lagrangian Multiplier Method. In their model they assumed one side of dowel to be fully embedded in the pavement and not allowed to move, whereas the other side is allowed to move vertically

or slide simulating dowel looseness. The contact forces developed in the embedded end are normal and tangential forces, and similar forces are developed on the free end. The Coulomb friction law was used in addition to the tangential forces. The plane frame element considered has three degrees of freedom per node, namely, vertical deflection and rotations about in-plane axes. The contact elements used are such that common points between the dowel and surrounding concrete are in contact. The authors verified the accuracy of their model with parametric studies to understand the contact element behavior. A specific study on dowel looseness showed that the joint efficiency decreases from 99 – 70% with an increase in dowel looseness from 0 – 0.005 in.

Kuo et al. (1995), developed a 3D finite element model called 3DPAVE to analyze many complex factors that influence the concrete pavement using Abaqus. Factors such as base thickness and stiffness, interface bond and friction, slab curling and warping due to temperature and moisture gradients were considered. Using C3D20R and C3D27R, a bilinear quadratic three dimensional continuum element, they were able to model the temperature gradient through the depth of the slab. Interface elements were used to model the separation between the concrete and the underlying layers. Using Abaqus infinite elements the subgrade was modeled as an elastic foundation. Straight dowel bars were modeled as beam elements to model dowel load transfer mechanism. Aggregate interlock at the joints was modeled using shear springs. The 3DPAVE model was validated with full scale field test data such as the AASHO Road test, PCA Tests and the Arlington Road test. The authors presented results obtained from the 3DPAVE model that matched well with the above tests in terms of measured stress and strains, deflections at load position, etc.

Bhatti et al. (1998), presented a finite element model for nonlinear analysis of jointed concrete pavement that allows for modeling of nonlinear concrete material properties, behavior under cyclic loading and nonlinear fatigue damage accumulation. The concrete slab was modeled as a nine noded quadrilateral element formulated using the Mindlin approach for thick plates. The elements they used allowed for accurate monitoring of cracks and fatigue propagation through the thickness of the concrete pavement. The subgrade was modeled as Winkler foundation that can resist only the compressive stresses and involves the pumping of materials due to cyclic loading. The dowel bar was considered as a beam element that accounts for shear deformations. As the slab is loaded at the joint there is relative deformation between the dowel bar and the adjacent concrete slabs as a result of which additional deformations such as deflections, shear forces and bending moments takes place. To account for this generalized springs capable of supporting both axial and rotational deformations were used attached to the ends of the beam element. To assess the model, the authors used examples and validated the results obtained by other finite element programs and analytical solutions. They modeled the slabs such that the dowel bars were straight and did not include any misalignment.

Davids et al. (1998, 1999, 2000, 2003) developed a user friendly three dimensional finite element program that is freely available to a pavement design engineer. The program called EverFE can model multiple slabs with varied loading conditions, dowel mis-location, nonlinear thermal and shrinkage gradients, nonlinear horizontal shear stress transfer between the slabs and base, etc. Twenty noded quadratic hexahedral elements are used to discretize the slab and base layers. The dense liquid

foundation is discretized using eight noded quadratic elements that are meshed with the bottommost layer of the solid elements. The dowel bars are modeled using embedded flexural finite elements. The dowel slab interaction is captured by springs sandwiched between the dowel and slab and the dowel support moduli or the spring stiffness is specified by the user. A note by the author says that dowel bar misalignment solutions are not included in the algorithm and also, the localized stresses in the concrete surrounding the dowels may not be accurately predicted when the embedded length formulation is used. Numerous parametric studies were conducted by changing the dowel concrete spring stiffnesses and load transfer efficiency to ascertain the robustness of the finite element code.

Khazanovich et al. (2001), in a feasibility study for the Michigan Department of Transportation, built 2D finite element models with elastic material properties to explain and understand the pullout behavior of a single and joint opening behavior of multiple dowel bars. They used the general purpose commercially available finite element package ABAQUS. Various cases of misaligned dowel orientation and magnitudes were studied. Their models did predict that the presence of dowel misalignment can significantly affect joint opening behavior and cause subsequent increase in stresses around the dowel in the surrounding concrete pavement at the joint. After carefully examining the model developed by the authors, it was found that the models were based on several assumptions and limitations. To model the dowel concrete interaction, special contact interface elements were used. An initial contact pressure between the dowel and concrete was introduced by assigning a change in dowel temperature. The analytical relationship

between the pullout force and joint opening could not be validated with experimental results.

Kim et al. (2003), presented various aspects of the structural behavior of doweled joints in load transfer using nonlinear three dimensional finite element methods. They basically considered two concrete slab segments connected by dowel and supported by layers of continuum three dimensional solid elements. In the paper presented they state that by using solid continuum elements they were able to capture the severe deformation of the slabs compared to the classical plate elements. Also using solid elements as supporting layers (subgrade), a better representation of the materials was seen compared to using Winkler foundation made of springs and dashpots. Beam elements were used to model the dowels which were primarily considered straight with no misalignment. The dowel beam elements were directly connected to solid elements for an intact joint. The dowel elements were embedded in the solid concrete elements so the interaction between the dowel and slab is through mechanical contact. To simulate the loose dowels, a gap contact algorithm was considered. This approach assumes that there is a physical gap between the dowel bar and concrete. As the dowel bar deforms, the gap closes and the bar bears on the surrounding concrete transferring stresses. A parametric study was conducted on load levels (single wheel and multiple wheels), dowel spacing, slab thickness, dowel looseness, etc. Their analyses clearly showed that thicker slabs engage more dowels in load transfer. The load transfer ratio was found to decrease with an increase in applied wheel load for multiple wheel slabs. Without a doubt, they were able to show that dowel looseness, with small gaps between the dowel and surrounding

concrete, reduces the load transfer efficiency significantly and magnified the bending stresses.

Rarely has any one in the past studied or investigated experimentally and analytically the behavior of misaligned dowel bars. The purpose of this research is to examine and incorporate the effects of misaligned dowel bars and use the knowledge gained from previous literature to better model a joint in a concrete pavement system.

CHAPTER 3

EXPERIMENTAL INVESTIGATIONS

3.1 INTRODUCTION

A comprehensive laboratory experimental investigation was carried out to study the joint opening behavior of misaligned dowel bars placed in contraction joints. The instrumented pavement slab specimens were subjected to simulated thermal joint expansion and the various distresses that occurred due to misalignment were documented. This chapter presents the experimental plan, definition, type and sign convention of misalignment used in this research study. A complete description of the test setup, the surveying techniques used and an example of the calculations to demonstrate the misalignment calculation is shown. The casting process including MDOT approved concrete mix design and fresh and hardened properties of concrete are presented. Additionally, a description of the various test equipment, instrumentation and data acquisition system is presented.

3.2 EXPERIMENTAL PLAN

An extensive experimental investigation was carried out to study the effects of skew type misalignment on the opening of transverse joints subjected to thermal expansion. The effects of the following parameters on the joint opening characteristics were investigated:

- Dowel misalignment types
- Varying the dowel misalignment magnitude
- Varying the number of dowels misaligned in a test specimen
- The orientation of misalignment

3.2.1 DOWEL MISALIGNMENT TYPE

There are three types of skew misalignments, namely, the vertical, horizontal and combined misalignment types, as shown in table 2.1(b). The combined form of misalignment, formed with equal magnitude of skew in the vertical and horizontal direction, was also considered.

3.2.2 DOWEL MISALIGNMENT MAGNITUDE

The misalignment magnitude in the test specimens were measured over half the length of the dowel bar (9 in.). The misalignment magnitudes that were considered were 0 (aligned), $\frac{1}{4}$ in., $\frac{1}{2}$ in., $\frac{3}{4}$ in. and 1 in. The misalignment magnitudes were considered as skew angles measured in radians. A misalignment of $\frac{1}{18}$ radians translated to a misalignment magnitude of $\frac{1}{2}$ in. measured over 9 in. length of the dowel bar. Similarly, $\frac{1}{9}$ radians, $\frac{1}{12}$ radians and $\frac{1}{36}$ radians relate to a misalignment magnitude of 1 in., $\frac{3}{4}$ in. and $\frac{1}{4}$ in. measured over 9 in. length of the dowel bar, respectively.

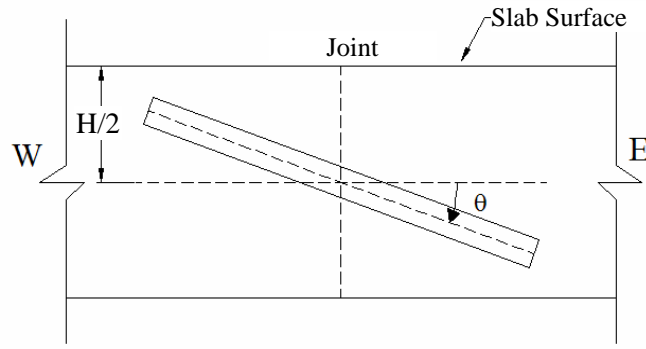
3.2.3 NUMBER OF MISALIGNED DOWELS

As shown in table 3.2, the one-, two-, three- and five- dowels were considered in the test matrix. The tests were carried out in two slab sizes, explained later in the experimental test setup. The smaller slab (overall dimensions 48 in. x 48 in. x 10 in.) could accommodate one- and two- dowel bars. The larger slab (overall dimensions 96 in. x 72 in. x 10 in.) could accommodate three- and five- dowel bars. The dowel bars in each test specimen could be all aligned or misaligned or have a certain misalignment orientation.

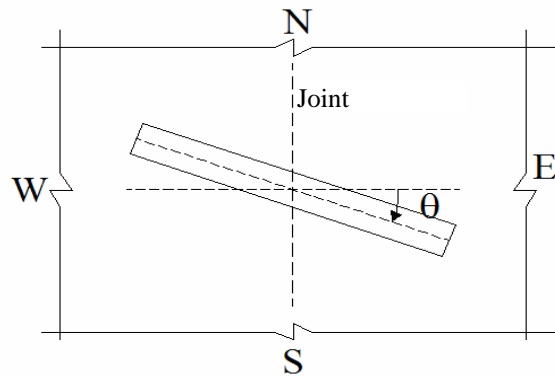
3.2.4 ORIENTATION OF MISALIGNED DOWEL BARS

In the case of multiple misaligned dowel bars in a test specimen, the orientation of a dowel bar with the adjacent bars was considered. The orientation of a dowel was

measured with respect to the skew angle. For example in a test specimen, all the dowel bars could be misaligned having uniform skew, non-uniform skew or alternate skew angles. The sign convention for measuring the skew angle is shown in figure 3.1, a clockwise skew (CW) is considered positive and counter-clockwise skew (CCW) is considered negative angle of orientation.



(a) Slab Specimen - Section View



(b) Slab Specimen - Plan View

FIGURE 3.1 Sign Convention for Orientation of the dowel bar (Clockwise (CW) – Positive)

Therefore, in case of a test specimen with non-uniform misaligned dowel bars, shown in figure 3.2 (a), the bars will have opposite angles of skew with respect to each other. In case of uniform misaligned dowel bar test specimen, shown in figure 3.2 (b), the dowel bars will have the same angle of skew with respect to each other and for alternate misaligned dowel bars, shown in figure 3.2 (c), an aligned dowel bar is placed adjacent to

the misaligned dowel bar and the misaligned dowel bars in the test specimen will have opposite skew with respect to each other.

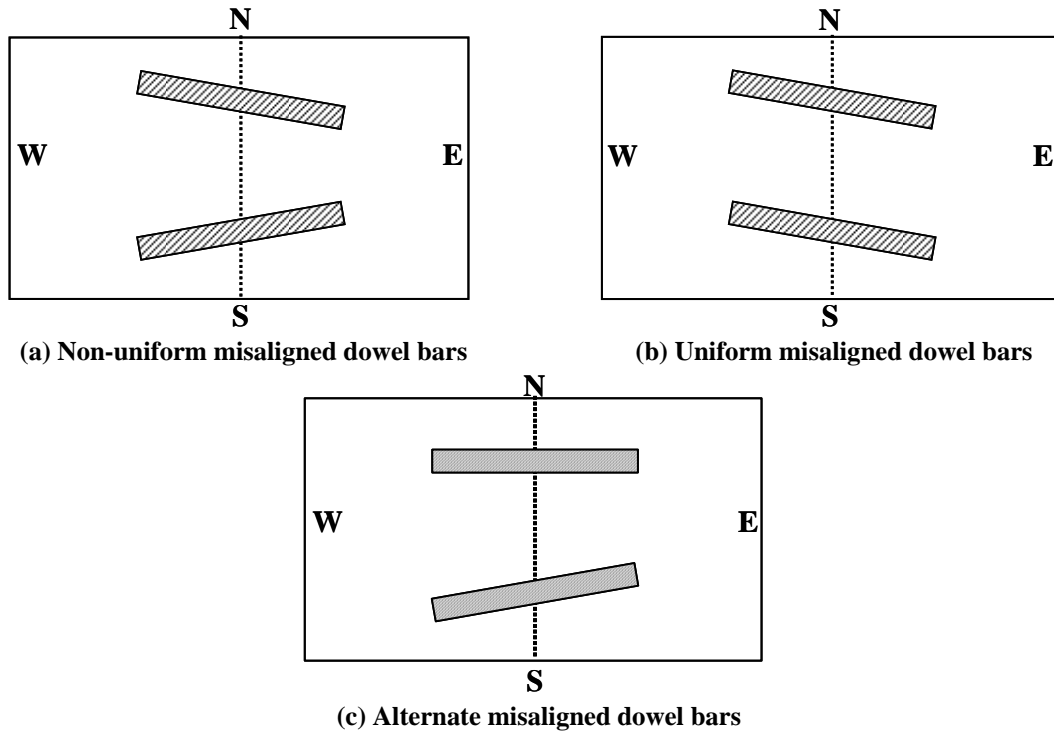


Figure 3.2: Concrete slab specimen with misaligned dowel bars

A nomenclature was developed to identify a test specimen. The specimen identification (ID), for example, 2V18NU, consisted first of the number of dowel bars in a test specimen, one-, two-, three- or five-. The second letter is the misalignment type, aligned (A), vertical (V), horizontal (H) or combined (C). The numbers following the misalignment type is the misalignment magnitude measured in radians (18 represents $\frac{1}{18}$ radians, $\frac{1}{2}$ in. magnitude of misalignment measured over 9 in. length). In case of multiple dowel bars test specimen, following the misalignment magnitude is the misalignment orientation, NU (Non-Uniform), U (Uniform) and AM (alternate misaligned).

Table 3.2, shows the experimental matrix that was developed for the laboratory investigation. In all, 67 laboratory tests on slab specimens were carried out which included limited repetitions.

Table 3.2: Experimental Test Investigation Matrix

Orientation	Magnitude		1 bar	2 bars			3 bars	5 bars	
	(in in.)	(in rad.)		U	NU	AM	NU	AM	NU
Aligned	0	0	x	x			x	x	
Vertical (V)	1	9	x	x	x				
	3/4	12	x		x	x			
	1/2	18	x	x	x	x	x	x	x
	1/4	36	x	x	x			x	
Horizontal (H)	1	9	x	x	x				
	3/4	12	x		x	x			
	1/2	18	x	x	x	x	x	x	x
	1/4	36	x	x	x			x	
Combined (C)	1	9	x	x	x				
	3/4	12	x		x	x			
	1/2	18	x	x	x	x	x	x	x
	1/4	36	x		x			x	
Total			13	9	13	6	3	6	4

Table 3.3 (a), (b) and (c), presents the slab specimen dimensions, the number of dowels in a test specimen, specimen ID, misalignment type and misalignment magnitude measured in radians.

TABLE 3.3(a) Test Specimen of the single dowel bar experiments conducted

Slab Dimensions	Number of Dowels	ID	Misalignment	Magnitude (in rad.)	Magnitude (in in.)
2 slabs each (48 in. x 24 in. x 10 in.)	1	1A	Aligned	0	0
		1V9	Vertical	$\frac{1}{9}$	1 in. over 9 in.
		1V12		$\frac{1}{12}$	$\frac{3}{4}$ in. over 9 in.
		1V18		$\frac{1}{18}$	$\frac{1}{2}$ in. over 9 in.
		1V36		$\frac{1}{36}$	$\frac{1}{4}$ in. over 9 in.
		1H9		Horizontal	$\frac{1}{9}$
		1H12	$\frac{1}{12}$		$\frac{3}{4}$ in. over 9 in.
		1H18	$\frac{1}{18}$		$\frac{1}{2}$ in. over 9 in.
		1H36	$\frac{1}{36}$		$\frac{1}{4}$ in. over 9 in.
		1C9	Combined	$\frac{1}{9}$	1 in. over 9 in.
		1C12		$\frac{1}{12}$	$\frac{3}{4}$ in. over 9 in.
		1C18		$\frac{1}{18}$	$\frac{1}{2}$ in. over 9 in.
		1C36		$\frac{1}{36}$	$\frac{1}{4}$ in. over 9 in.

TABLE 3.3(b) Test Matrix of the two dowel bar experiments conducted

Slab Dimensions	Number of Dowels	ID	Misalignment	Magnitude (in rad.)	Magnitude (in in.)
2 slabs each (48 in. x 24 in. x 10 in.)	2 (Uniform)	2A	Aligned	0	None
		2V9U	Vertical	$+\frac{1}{9}; +\frac{1}{9}$	1 in. over 9 in.
		2V18U		$+\frac{1}{18}; +\frac{1}{18}$	$\frac{1}{2}$ in. over 9 in.
		2V36U		$+\frac{1}{36}; +\frac{1}{36}$	$\frac{1}{4}$ in. over 9 in.
		2H9U	Horizontal	$+\frac{1}{9}; +\frac{1}{9}$	1 in. over 9 in.
		2H18U		$+\frac{1}{18}; +\frac{1}{18}$	$\frac{1}{2}$ in. over 9 in.
		2H36U		$+\frac{1}{36}; +\frac{1}{36}$	$\frac{1}{4}$ in. over 9 in.
		2C9U	Combined	$+\frac{1}{9}; +\frac{1}{9}$	1 in. over 9 in.
		2C18U		$+\frac{1}{18}; +\frac{1}{18}$	$\frac{1}{2}$ in. over 9 in.
	2 (Non - Uniform)	2V9NU	Vertical	$+\frac{1}{9}; -\frac{1}{9}$	1 in. over 9 in.
		2V12NU		$+\frac{1}{12}; -\frac{1}{12}$	$\frac{3}{4}$ in. over 9 in.
		2V18NU		$+\frac{1}{18}; -\frac{1}{18}$	$\frac{1}{2}$ in. over 9 in.
		2V36NU		$+\frac{1}{36}; -\frac{1}{36}$	$\frac{1}{4}$ in. over 9 in.
		2H9NU	Horizontal	$+\frac{1}{9}; -\frac{1}{9}$	1 in. over 9 in.
		2H12NU		$+\frac{1}{12}; -\frac{1}{12}$	$\frac{3}{4}$ in. over 9 in.
		2H18NU		$+\frac{1}{18}; -\frac{1}{18}$	$\frac{1}{2}$ in. over 9 in.
		2H36NU		$+\frac{1}{36}; -\frac{1}{36}$	$\frac{1}{4}$ in. over 9 in.
		2C9NU	Combined	$+\frac{1}{9}; -\frac{1}{9}$	1 in. over 9 in.
		2C12NU		$+\frac{1}{12}; -\frac{1}{12}$	$\frac{3}{4}$ in. over 9 in.
		2C18NU		$+\frac{1}{18}; -\frac{1}{18}$	$\frac{1}{2}$ in. over 9 in.
		2C36NU		$+\frac{1}{36}; -\frac{1}{36}$	$\frac{1}{4}$ in. over 9 in.
	2 (One Bar Misaligned)	2V12AM	Vertical	$\frac{1}{12}; 0$	$\frac{3}{4}$ in. over 9 in.
		2V18AM		$\frac{1}{18}; 0$	$\frac{1}{2}$ in. over 9 in.
		2H12AM	Horizontal	$\frac{1}{12}; 0$	$\frac{3}{4}$ in. over 9 in.
		2H18AM		$\frac{1}{18}; 0$	$\frac{1}{2}$ in. over 9 in.
		2C12AM	Combined	$\frac{1}{12}; 0$	$\frac{3}{4}$ in. over 9 in.
		2C18AM		$\frac{1}{18}; 0$	$\frac{1}{2}$ in. over 9 in.

TABLE 3.3(c) Test Matrix of the three and five dowel bar experiments conducted

Slab Dimensions	Number of Dowels	ID	Misalignment	Magnitude (in rad.)	Magnitude (in in.)
2 slabs each (96 in. x 36 in. x 10 in.)	3 (Non - Uniform)	3V18NU	Vertical	$+\frac{1}{18}; -\frac{1}{18};$ $+\frac{1}{18}$	$\frac{1}{2}$ in. over 9 in.
		3H18NU	Horizontal		
		3C18NU	Combined		
	5 (Non - Uniform)	5V18NU	Vertical	$+\frac{1}{18}; -\frac{1}{18};$ $+\frac{1}{18}; -\frac{1}{18};$ $+\frac{1}{18}$	$\frac{1}{2}$ in. over 9 in.
		5H18NU	Horizontal		
		5C18NU	Combined		
	5 (Alternate Misaligned)	5V18AM	Vertical	$+\frac{1}{18}; 0;$ $-\frac{1}{18}; 0;$ $+\frac{1}{18}$	$\frac{1}{2}$ in. over 9 in.
		5H18AM	Horizontal		
		5C18AM	Combined		

3.3 EXPERIMENTAL TEST SETUP

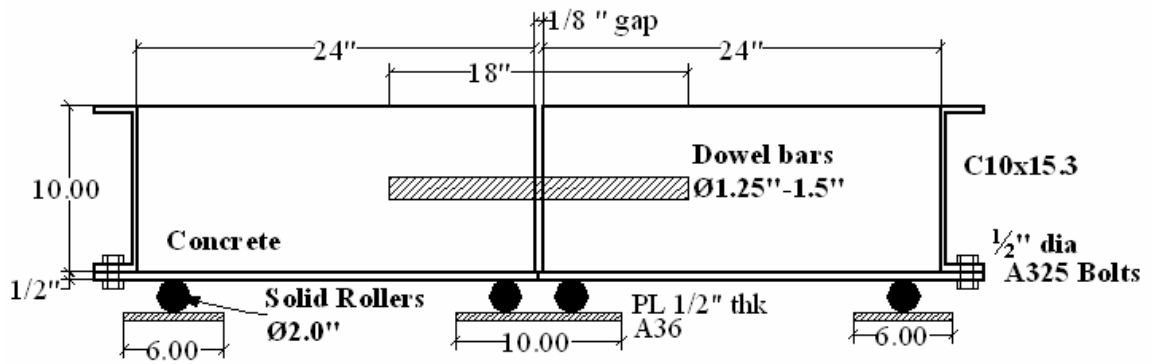
Each laboratory scale pavement specimen consisted of two concrete slabs connected at the joint using steel dowel bars. The steel dowels are smooth round bars 1.25 in. in diameter, 18 in. in length and placed at the mid-depth of the slab. The embedded length is 9 in. on either side of the joint. In case of multiple dowel bars, the bars are placed at 12 in. on center. The number of dowel bars at a joint, the misalignment type, magnitude and uniformity was varied as shown in the experimental plan, tables 3.2 and 3.3.

The test specimen molds were made from structural steel sections and designed using specifications described in the AISC Steel Manual. The test mold consisted, from

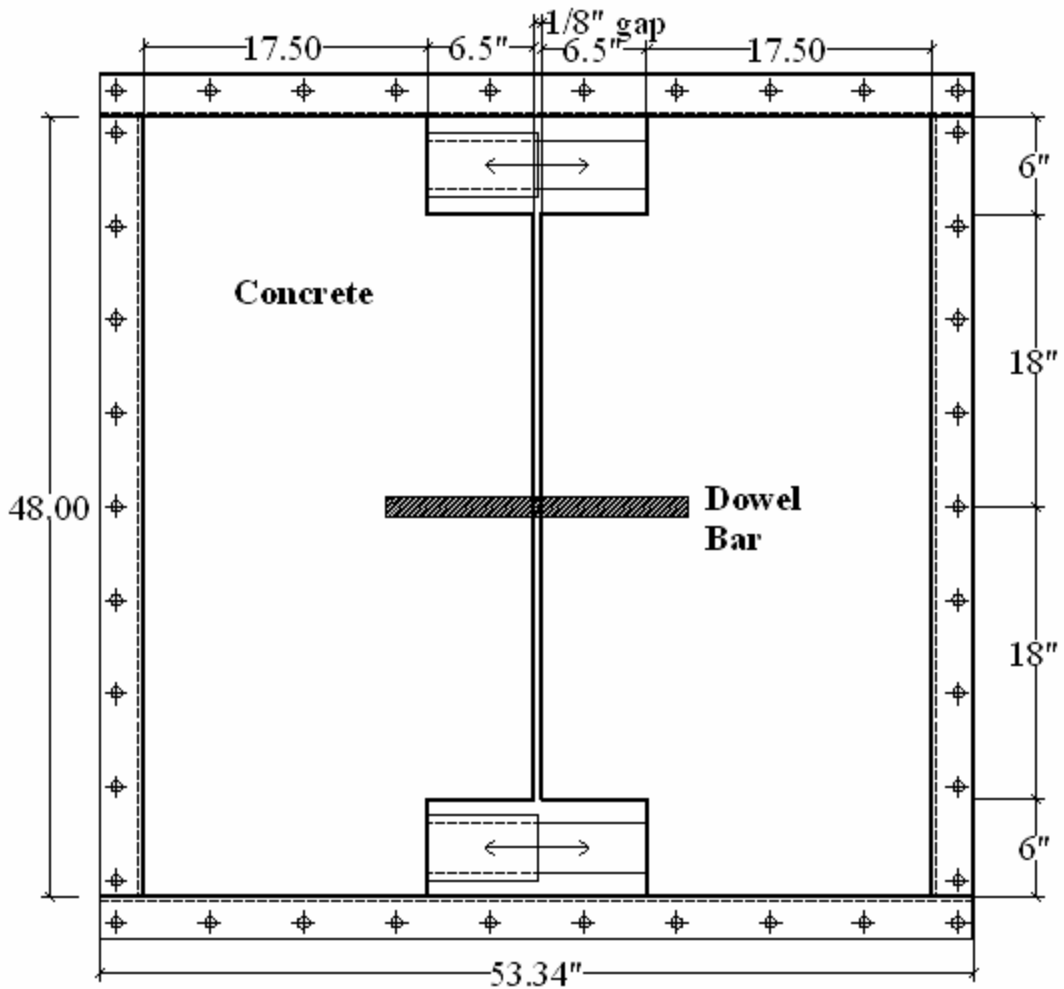
ground up, of ½ in. thick steel base plates which had 2 in. diameter solid rollers placed over it. The solid rollers supported a structural steel base plate of ½ in. thickness. The base rails, solid rollers and bottom of the base plate were treated with a special mill finish to obtain a smooth frictionless surface. The structural steel C10x15 channels made up the sides of the mold. The structural steel channels parallel to the joint were left in place during the duration of the test whereas the channels perpendicular to the joint were removed after concrete set.

To form the contraction joint between the two slab specimens, a 1/8 in. thick aluminum separator plate with pre-fabricated holes at mid-height and 12 in. center were used. This aluminum plate was left in place after casting the concrete and it does not hinder the experiment or separation of the slab in any way. A box cut-out made of ¼ in. steel plate was fabricated and placed on either side of the joint. After concrete set and the mold was stripped, hydraulic cylinders were placed in the box cut outs.

To hold the steel dowel bars in alignment before and during the casting process, a simple U shaped hanging assembly was developed. This assembly was primarily made of a light weight structural steel channel section with a 3/8 in. slot drilled along the length. A 3/8 in. diameter threaded steel bar was bent into a U shape to hold the dowel bar. This threaded U shape was then bolted to the supporting steel channel through the slot. The overall dimensions of one and two dowel bars concrete slab test specimen is shown in figure 3.3. Figure 3.4 shows the details of the slab specimen mold, U-shape hanging assembly in the test setup and a cast specimen.

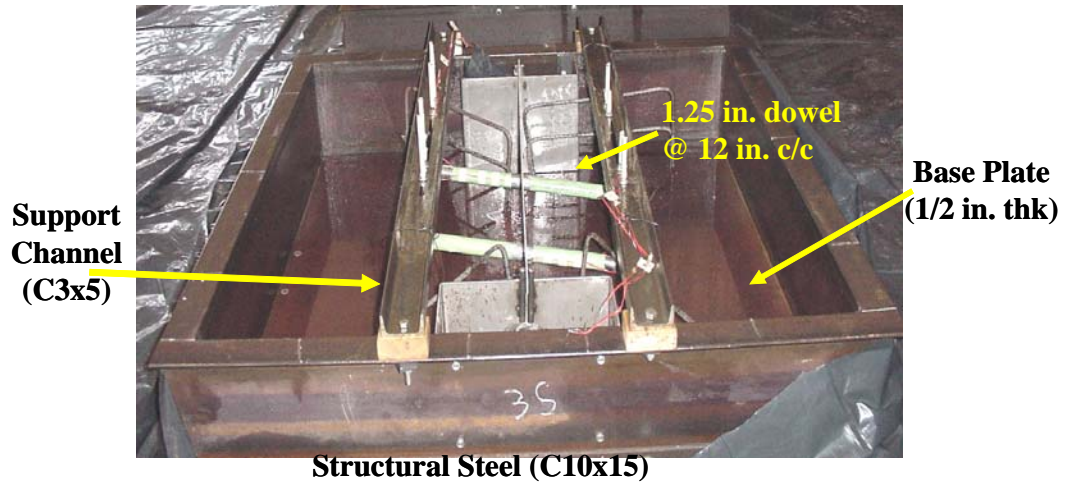


(a) Cross Section view of test setup

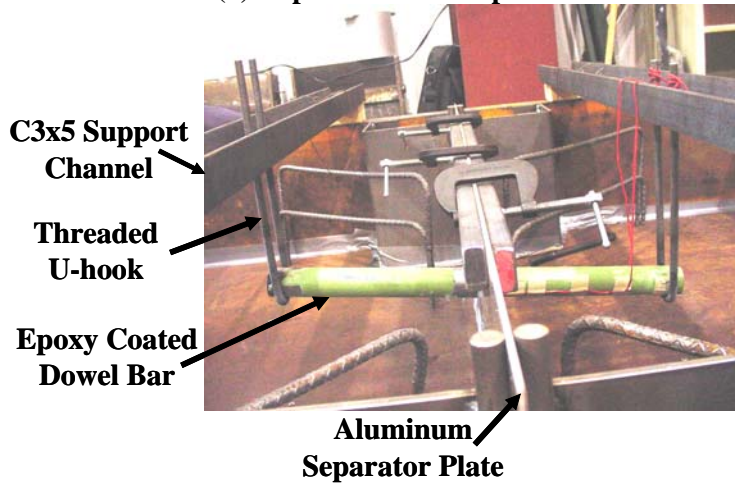


(b) Plan view of the test setup dimensions

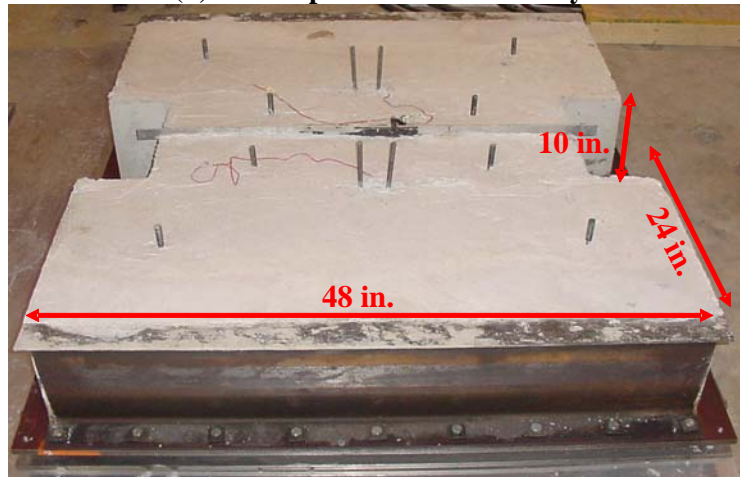
Figure 3.3: Shop drawings showing the test setup dimensions for one and two dowel bar specimens



(a) Experimental Setup



(b) Close up of U-hook Assembly



(c) Cast Specimen (48 in. x 24 in. x 10 in.)

Figure 3.4: Photograph of the various components of the experimental set-up

Misalignment accuracy was measured using surveying techniques and instruments such as the total electronic station. Details of the surveying calculations and an example demonstrating the misalignment calculation are shown in a later section of this chapter. The test setup shown in figures 3.3 and 3.4 and dimensions given in table 3.3(c) was modified to study the effects of joint opening on a 12 in. thick slab with five dowel bars of 1.5 in. diameter and placed 12 in. on centers.

3.4 LIMITATIONS AND SHORT COMINGS OF THE TEST SETUP

The research study focuses on the joint opening behavior of concrete pavement slabs with misaligned dowel bars. The joint in the slab specimens was created using a 1/8 in. aluminum separator plate to eliminate effects of aggregate interlock. Joint design is primarily based on the strength of concrete, diameter of dowels and modulus of dowel support.

The scaled test specimens were subjected to controlled joint opening which are related to the thermal expansion of the concrete slabs in the field. The slab specimens in the experimental investigation were cast in steel molds to eliminate effects due to base friction and isolate distresses caused due to misaligned dowel bars. No axle wheel loads are considered in this phase of the experimental investigation but they will be included in future research on a full pavement cross-section.

3.5 SURVEYING TECHNIQUE AND CALCULATIONS

Accurate misalignments of the dowel bars in the test setup were achieved using simple surveying techniques. A Total Electronic Station (Theodolite) was used to measure the

various angles formed between the dowel bar and the horizontal and vertical planes of the mold. To measure one misalignment angle, two theodolite stations were used.

Each misalignment of the dowel bar in the test setup achieved using the theodolite was cross-checked with a tape measure before preparing the specimen to receive concrete. The derivation to achieve the desired misalignments is explained along with sample calculations.

3.5.1 DERIVATION FOR MEASUREMENT OF VERTICAL MISALIGNMENT

Notations:

L = Distance between Station A and Station B

Horizontal Angles

θ_a = from Station A to the base plate (center of the base plate)

θ_b = from Station B to base plate (center of the base plate)

Vertical Angles

α_a = from Station A to the base plate (at the level of the base plate)

α_b = from Station B to base plate (at the level of the base plate)

β_a = from Station A to the dowel bar (at the level of the center of dowel bar)

β_b = from Station B to the dowel bar (at the level of the center of dowel bar)

A = Station A

B = Station B

C = Base Plate (center)

D = dowel bar (center)

E = height at eye level (center)

Referring to figure 3.5, in the horizontal plane,

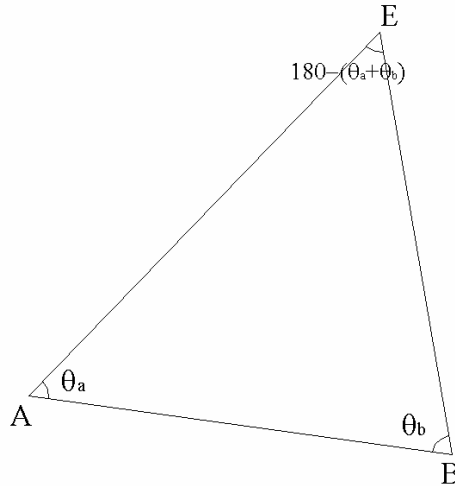


Figure 3.5: Horizontal plane showing angles measured from center of base plate to misalignment

For $\triangle ABE$, refer figure 3.5:

Using Sine Rule,

$$AE = L \operatorname{Cosec}[\theta_a + \theta_b] \operatorname{Sin}[\theta_b]$$

Now with respect to the dowel at the center of the plate:

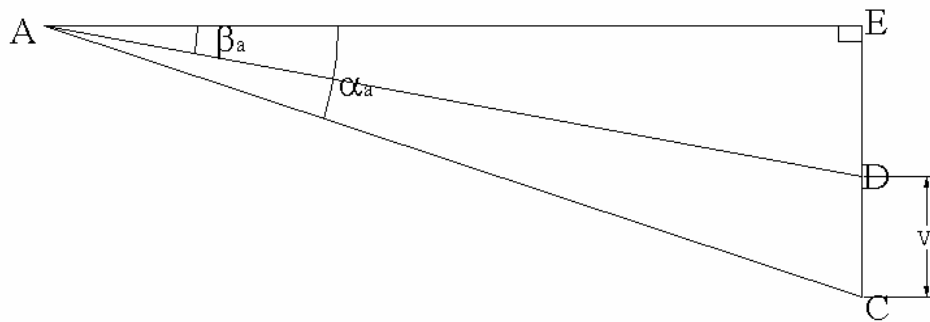


Figure 3.6: Vertical plane in the center of the plate

The vertical height from the eye level to the base plate is

$$EC = AE \tan[\alpha_a]$$

The vertical height from the eye level to the center of the dowel bar is:

$$ED = AE \tan[\beta_a]$$

The difference in the height taken from the eye level to the base plate and the center line of the dowel bar will give us the vertical height,

$$V = EC - ED$$

Therefore, vertical misalignment = V – 5 in. (mid height of the dowel).

Sample Calculations for Vertical Misalignment of ½ in:

The sample calculations shows are for a vertical misalignment of ½ in on the East Side of the test setup. The same set of calculation is carried out on the West Side.

Table 3.4: Summary Table showing the various angles

Location	WEST SIDE (L = 10.4')				EAST SIDE (L = 9.2')			
	Theodolite			Theoretical	Theodolite			Theoretical
	Degrees	Minutes	Seconds	Degrees	Degrees	Minutes	Seconds	Degrees
θ_a	62	37	0	62.617	25	12	40	25.211
θ_b	27	53	50	27.897	74	51	0	74.850
α_a	322	27	30	322.458	333	44	20	333.739
α_b	337	52	40	337.878	331	47	20	331.789
β_a	319	12	20	319.206	335	39	40	335.661
β_b	333	15	10	333.253	314	32	10	314.536

Referring to figure 3.7;

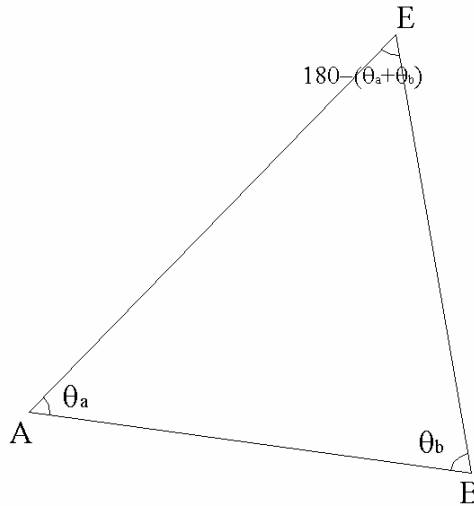


Figure 3.7: Horizontal plane showing angles measured from center of base plate to misalignment

For $\triangle ABE$:

Using Sine Rule,

$$AE = L \operatorname{Cosec}[\theta_a + \theta_b] \operatorname{Sin}[\theta_b] = 108.227 \text{ in.}$$

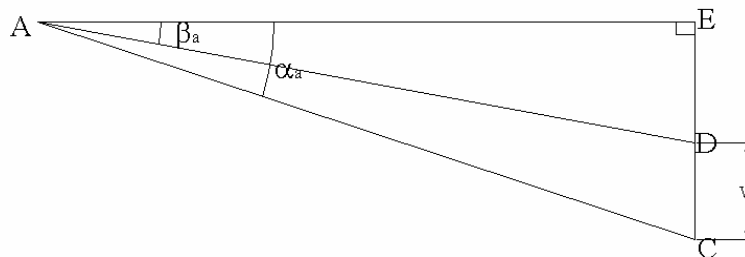


Figure 3.8: Vertical plane in the center of the plate

The vertical height from the eye level to the base plate is:

$$EC = AE \tan[\alpha_a] = 53.397 \text{ in.}$$

The vertical height from the eye level to the bottom edge of the dowel bar is:

$$ED = AE \tan[\beta_a] = 48.9549 \text{ in.}$$

The difference in the height taken from the eye level to the base plate and dowel bar will give us the distance from the base plate to the bottom edge of the dowel bar,

$$V = EC - ED = 4.4429 \text{ in.}$$

A perfectly aligned bar will be at (base plate to center line of dowel bar) = 5 in.

Misalignment = 5 - 4.4429 = 0.557 in. vertical misalignment.

3.5.2 DERIVATION FOR MEASUREMENT OF HORIZONTAL MISALIGNMENT

Notations:

L = Distance between Station A and Station B

Horizontal Angles

θ_a = from Station A to the base plate (center of the base plate)

θ_b = from Station B to base plate (center of the base plate)

γ_a = from Station A to the base plate (horizontal misalignment on the base plate)

γ_b = from Station B to base plate (horizontal misalignment on the base plate)

Vertical Angles

α_a = from Station A to the base plate (at the level of the base plate)

α_b = from Station B to base plate (at the level of the base plate)

β_a = from Station A to the dowel bar (at the level of the center of dowel bar)

β_b = from Station B to the dowel bar (at the level of the center of dowel bar)

A = Station A

B = Station B

C = Base Plate (center)

D = dowel bar (center)

E = height at eye level (center)

E = height at eye level (misaligned)

C' = Base Plate (misaligned)

D = dowel bar (misaligned)

In the following surveying description we are assuming two important measurements:

1. The height of each of the stations is same
2. The two stations are parallel to the horizontal misalignments.

Referring to figure 3.9, in the horizontal plane,

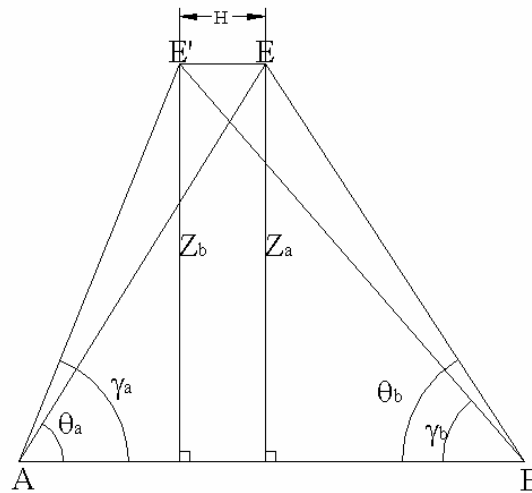


Figure 3.9: Horizontal plane showing angles measured from center of base plate to misalignment

For $\triangle ABE$, figure 3.9:

Using Sine Rule,

$$AE = L \operatorname{Cosec}[\theta_a + \theta_b] \operatorname{Sin}[\theta_b]$$

$$BE' = L \operatorname{Cosec}[\gamma_a + \gamma_b] \operatorname{Sin}[\gamma_a]$$

To make sure that the two stations are parallel, we compare the perpendicular distances,

Z_a and Z_b :

$$Z_a = AE \operatorname{Sin}[\theta_a] \quad \& \quad Z_b = BE' \operatorname{Sin}[\gamma_b]$$

If, $Z_a \cong Z_b$, then the two stations are parallel to the horizontal misalignment.

Now with respect to the dowel at the center of the plate:

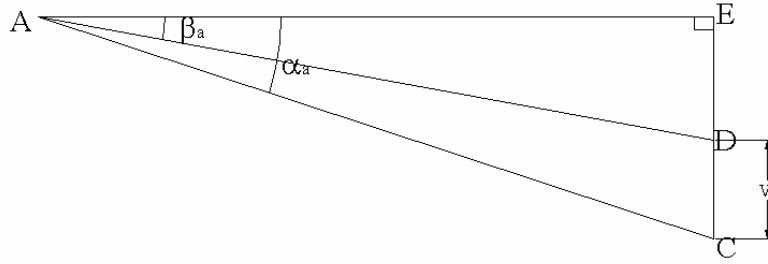


Figure 3.10: Vertical plane in the center of the plate

The vertical height from the eye level to the base plate is, figure 3.10:

$$EC = AE \tan[\alpha_a]$$

The vertical height from the eye level to the center of the dowel bar is

$$ED = AE \tan[\beta_a]$$

The difference in the height taken from the eye level to the base plate and the center line of the dowel bar will give us the vertical height,

$$V = EC - ED$$

Therefore, vertical misalignment = $V - 5$ in. (mid height of the dowel)

Now to check after forcing a misalignment, H, the vertical distance of the dowel bar from the base plate

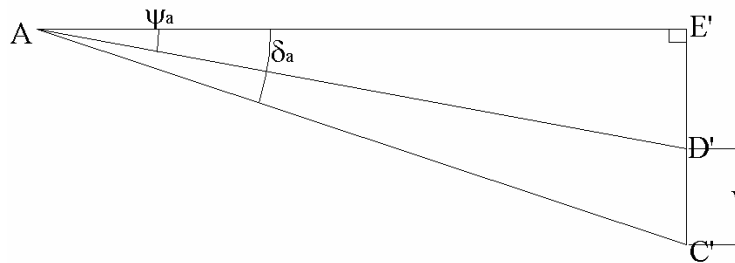


Figure 3.11: Angles in the vertical plane, after forcing the misalignment of H.

The vertical height from the eye level to the base plate is, figure 3.11:

$$E'C' = AE' \tan[\delta_a]$$

The vertical height from the eye level to the center of the dowel bar is

$$E'D' = AE' \tan[\psi_a]$$

The difference in the height taken from the eye level to the base plate and the center line of the dowel bar will give us the vertical height

$$V' = E'C' - E'D'$$

Therefore, vertical misalignment after forcing the misalignment in the horizontal plane should be = $V' - 5$ in. (mid height of the dowel)

For $\triangle ABE'$, in horizontal plane,

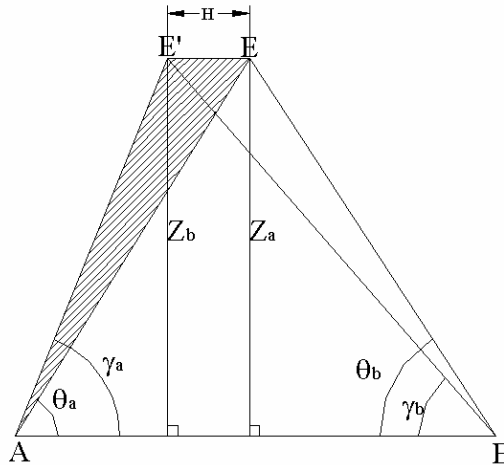


Figure3.12: Showing the final computation of the horizontal misalignment

$$AE' = Z \operatorname{Cosec}[\gamma_a]$$

Using cosine rule for $\triangle AEE'$, figure 3.11:

$$H = \sqrt{(AE)^2 + (AE')^2 - 2 (AE) (AE') \operatorname{Cos}[\theta_a - \gamma_a]}$$

The H obtained is then compared with tape measure as a final check.

Sample Calculation for Horizontal Misalignment of ½ in:

Table 3.5: Summary Table showing all angles for horizontal misalignment

Location	NORTH WEST SIDE (L = 5.7')				SOUTH EAST SIDE (L = 5.2')			
	Theodolite			Theoretical	Theodolite			Theoretical
	Degrees	Minutes	Seconds	Degrees	Degrees	Minutes	Seconds	Degrees
θ_a	56	58	40	56.978	57	30	40	57.511
θ_b	49	0	20	49.006	53	19	0	53.317
γ_a	57	30	0	57.500	57	6	40	57.111
γ_b	48	41	40	48.694	53	47	30	53.792
α_a	317	58	30	317.975	319	53	20	319.889
α_b	321	0	30	321.008	321	30	0	321.500
β_a	321	6	40	321.111	323	13	40	323.228
β_b	324	5	10	324.086	324	52	0	324.867
δ_a	317	52	40	317.878	320	3	50	320.064
δ_b	321	11	0	321.183	321	22	20	321.372
ψ_a	321	0	30	321.008	323	24	0	323.400
ψ_b	324	17	50	324.297	324	42	0	324.700

Referring to figure 3.13, in the horizontal plane,

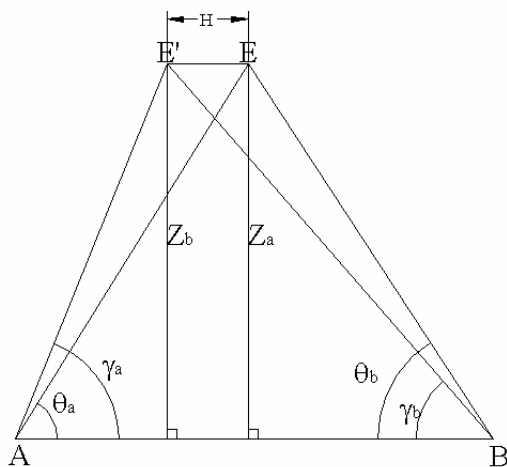


Figure 3.13: Horizontal plane showing angles measured from center of base plate to misalignment

For $\triangle ABE$, figure 3.13:

Using Sine Rule,

$$AE = L \operatorname{Cosec}[\theta_a + \theta_b] \operatorname{Sin}[\theta_b] = 53.54 \text{ in.}$$

$$BE' = L \operatorname{Cosec}[\gamma_a + \gamma_b] \operatorname{Sin}[\gamma_a] = 56.09 \text{ in}$$

To make sure that the two stations are parallel, we compare the perpendicular distances,

Z_a and Z_b :

$$Z_a = AE \operatorname{Sin}[\theta_a] = 45.16 \text{ in.} \quad \& \quad Z_b = BE' \operatorname{Sin}[\gamma_b] = 45.27 \text{ in.}$$

If, $Z_a \cong Z_b$, then the two stations are parallel to the horizontal misalignment.

Now with respect to the dowel at the center of the plate:

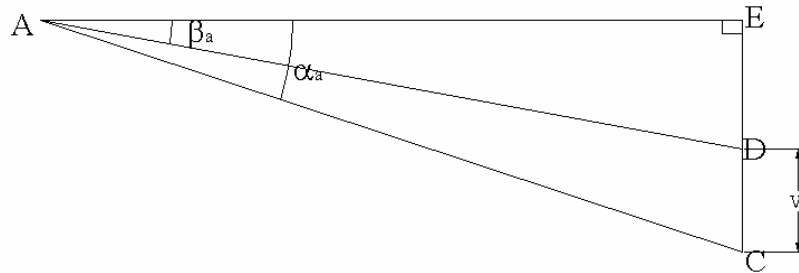


Figure 3.14: Vertical plane in the center of the plate

The vertical height from the eye level to the base plate is, figure 3.14

$$EC = AE \tan[\alpha_a] = 45.10 \text{ in.}$$

The vertical height from the eye level to the center of the dowel bar is

$$ED = AE \tan[\beta_a] = 40.01 \text{ in.}$$

The difference in the height taken from the eye level to the base plate and the center line of the dowel bar will give us the vertical height,

$$V = EC - ED = 5.09 \text{ in.}$$

Therefore, vertical misalignment = $V - 5 \text{ in. (mid height of the dowel)} = 0.09 \text{ in}$

Now to check after forcing a misalignment, H, the vertical distance of the dowel bar from the base plate

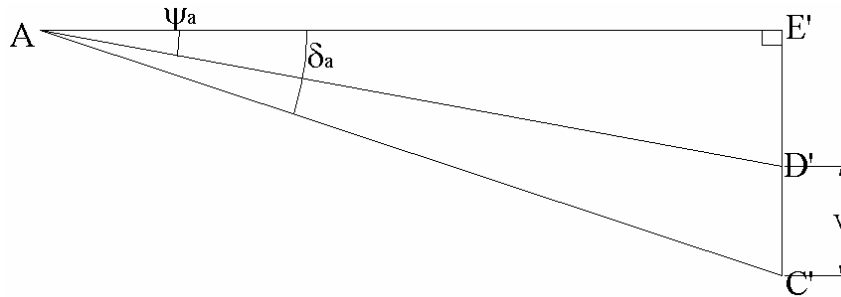


Figure 3.15: Angles in the vertical plane, after forcing the misalignment of H.

The vertical height from the eye level to the base plate is, figure 3.15:

$$E'C' = AE' \tan[\delta_a] = 45.12 \text{ in.}$$

The vertical height from the eye level to the center of the dowel bar is

$$E'D' = AE' \tan[\psi_a] = 40.02 \text{ in.}$$

The difference in the height taken from the eye level to the base plate and the center line of the dowel bar will give us the vertical height,

$$V' = E'C' - E'D' = 5.09 \text{ in.}$$

Therefore, vertical misalignment after forcing the misalignment in the horizontal plane should be = $V' - 5 \text{ in. (mid height of the dowel)} = 0.09 \text{ in.}$

For $\triangle ABE'$, in horizontal plane,

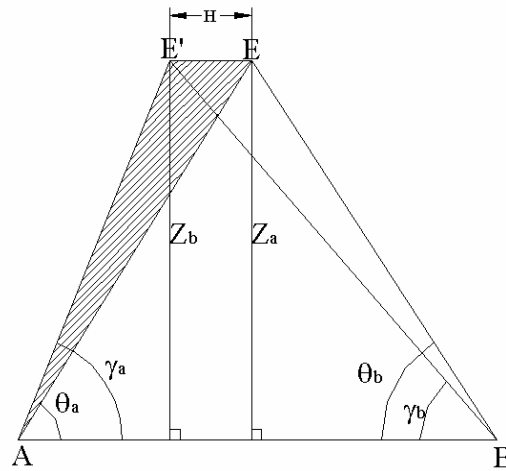


Figure 3.16: Showing the final computation of the horizontal misalignment

$$AE' = Z \text{ Co sec}[\gamma_a] = 53.89 \text{ in.}$$

Using cosine rule for $\triangle AEE'$, figure 3.15

$$H = \sqrt{(AE)^2 + (AE')^2 - 2 (AE) (AE') \text{Cos}[\theta_a - \gamma_a]} = 0.5168 \text{ in.}$$

The H obtained is then compared with tape measure as a final check.

In the next section, material specifications such as the M-DOT approved mix design, fresh and hardened properties of concrete specimens, coupon strengths of the steel dowel bar carried out as per ASTM specifications that were documented are presented.

3.6 MATERIAL SPECIFICATIONS

The concrete used in the fabrication of the pavement slab specimens was a MDOT pavement mix grade P1 supplied by a local pre-approved ready mix plant. The mix design is summarized in table 3.6.

Table 3.6: Mix Design of Concrete

Source of Concrete: Plant 14-East Lansing			
Material	Class: Source	SSD Weight (lb/yd ³)	Yield, ft ³
Cement	ASTM C-150 Type I: Essroc	564	2.87
Fine Aggregate	2NS: Builders Aggregates (#34-86)	1275	7.65
Coarse Aggregate	6AA: MLO LS(#71-3)	1720	10.81
Water		256	4.1
Air Content		6.5 %	1.77
		Total	27.2
Admixtures added:			
ASTM C-494A Water Reducer Type A	MB 200 N	3.0 oz/c	
ASTM C-260 Air Entrainer	MB Microair	1.2 oz/c	
Desired Plastic Concrete Properties			
	Slump	3 in.	
	Concrete Unit Weight	142 pcf	
	Air Content	6.5 %	

Fresh and hardened properties of concrete were documented. Concrete cylinders (4 in. diameter x 8 in. length) and flexural beams (4 in. x 4 in. x 14 in.) were cast during the slab specimen construction. During the slab specimen casting, fresh concrete properties such as slump (3.6 in. average), air content (6.1 % average), unit weight (144.8 pcf average) and temperature (70.8 °F) were recorded. The hardened properties were measured at 3-days, 7-days and 28-days corresponding to the day at which demolding took place, day of testing and target compressive strength is achieved, respectively. To measure the compressive strength of concrete, split tensile strength and flexural strength an average was taken of 3 cylinders, 2 cylinders and 2 beams, respectively. The specimens were tested in accordance with ASTM specifications, as shown in Table 3.7 and figure 3.17.

Table 3.7: Concrete Properties

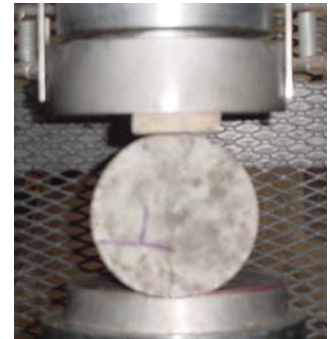
Type of Test	Property Measured	ASTM Standard
Fresh Concrete	Slump (in.)	ASTM C143
	Unit Weight (pcf)	ASTM C138
	Air Content (%)	ASTM C138
	Temperature (°F)	ASTM C1064
Hardened Concrete	Compressive Strength (psi)	ASTM C39
	Split Tensile Strength (psi)	ASTM C496
	Flexural Strength (psi)	ASTM C78



(a) Compression



(b) Flexure

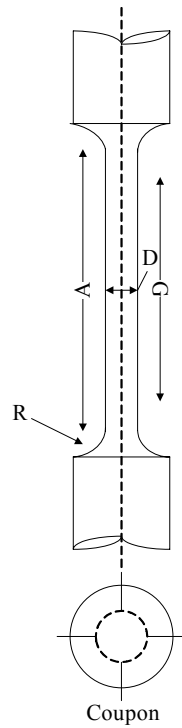


(c) Split Tension

Figure 3.17: Concrete Hardened Properties Test Setup

The dowel bars used in the tests were made from billet steel grade 40 as per AASHTO M31 specification which says that the minimum yield strength and minimum ultimate strength of the steel coupons should be 40 ksi and 70 ksi respectively. The dowel bars were epoxy coated as per AASHTO M254 and MDOT specifications and obtained from the same heat and batch as far as possible. Tensile coupon tests were fabricated as shown in figure 3.18, according to ASTM E8-99. Using an MTS testing machine, the

yield strength, the ultimate strength and the elastic modulus of steel was determined, figure 3.19 and 3.20. The average yield strength, ultimate tensile strength and elastic modulus of steel obtained were 69 ksi, 95 ksi and 30,270 ksi, respectively.



Legend:

- D= nominal diameter = 0.500 in.
- A= length of reduced section = $2\frac{1}{4}$ in.
- G = gage length = 2.000 ± 0.005 in.
- R = radius of fillet = $\frac{3}{8}$ in.

Figure 3.18: Standard $\frac{1}{2}$ in. Round Tension Test specimen with 2 in. gage length (ASTM E8-99)

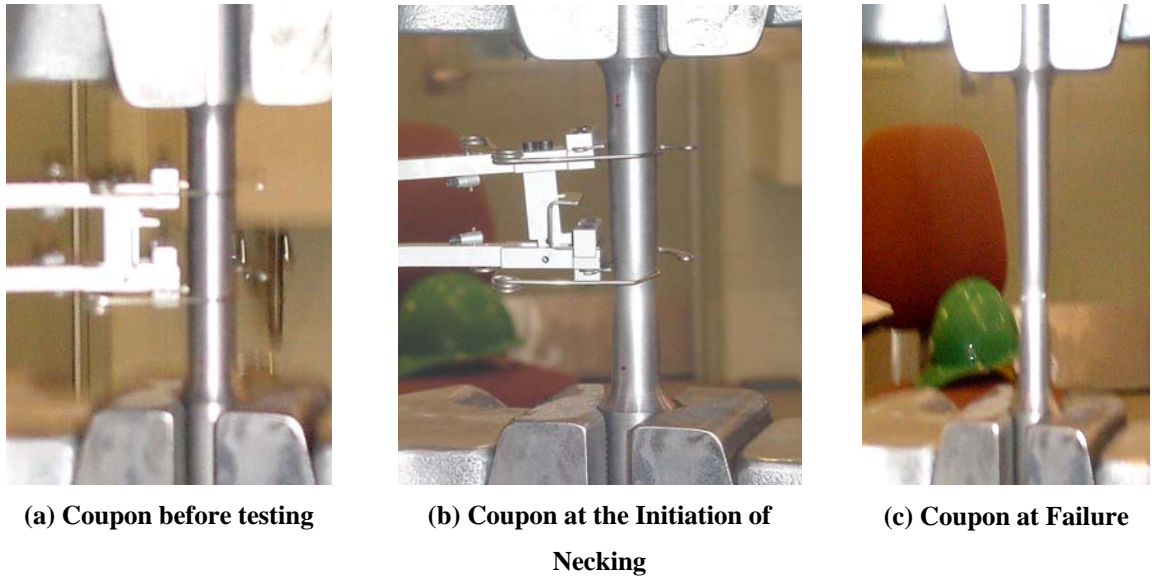


Figure 3.19: Stages of Coupon Testing

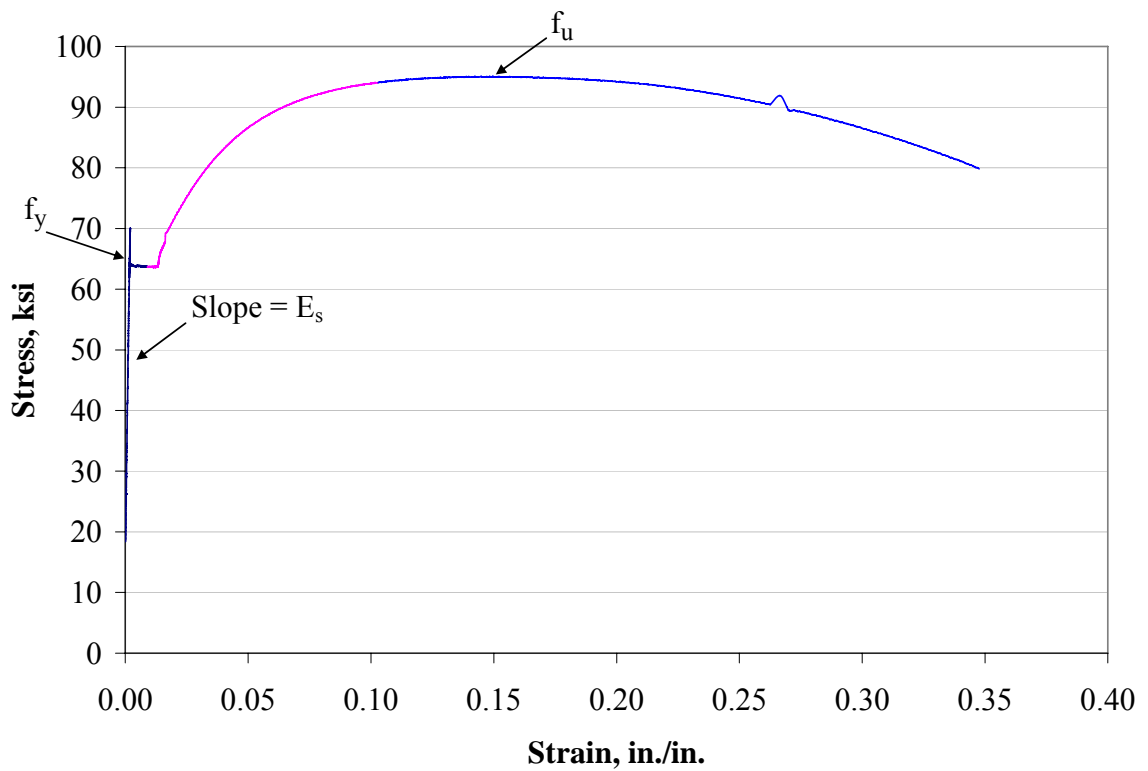


Figure 3.20: Typical Stress-Strain Curve for a coupon

3.7 INSTRUMENTATION AND DATA ACQUISITION SYSTEM

The translational and longitudinal joint opening, uplift and the force applied to push the slabs apart were measured using various instruments. Linear Variable Displacement Transducers (LVDT) and spring-return linear motion sensors (potentiometers) were used to measure various displacements occurring in the slab specimens. Special brackets were designed to hold these instruments plumb and in place during the test. The LVDTs (Omega LD610-15) were a 1.5 in. stroke LVDT placed strategically on top of the dowel bar to measure longitudinal only joint openings. Linear displacement potentiometers (Duncan Electronics 9610 and 9615) of 1.0 in. and 1.5 in. stroke lengths were used to measure the longitudinal joint opening, vertical uplift of the slabs and any translational displacements causing non-uniform joint openings in the slabs. Two pressure transducers (Omega PX303-015G5V) were placed close to the hydraulic cylinders to measure the force that was being applied to cause joint opening. The LVDTs, sliders and pressure transducers used during the testing of the specimens are shown in figure 3.21.

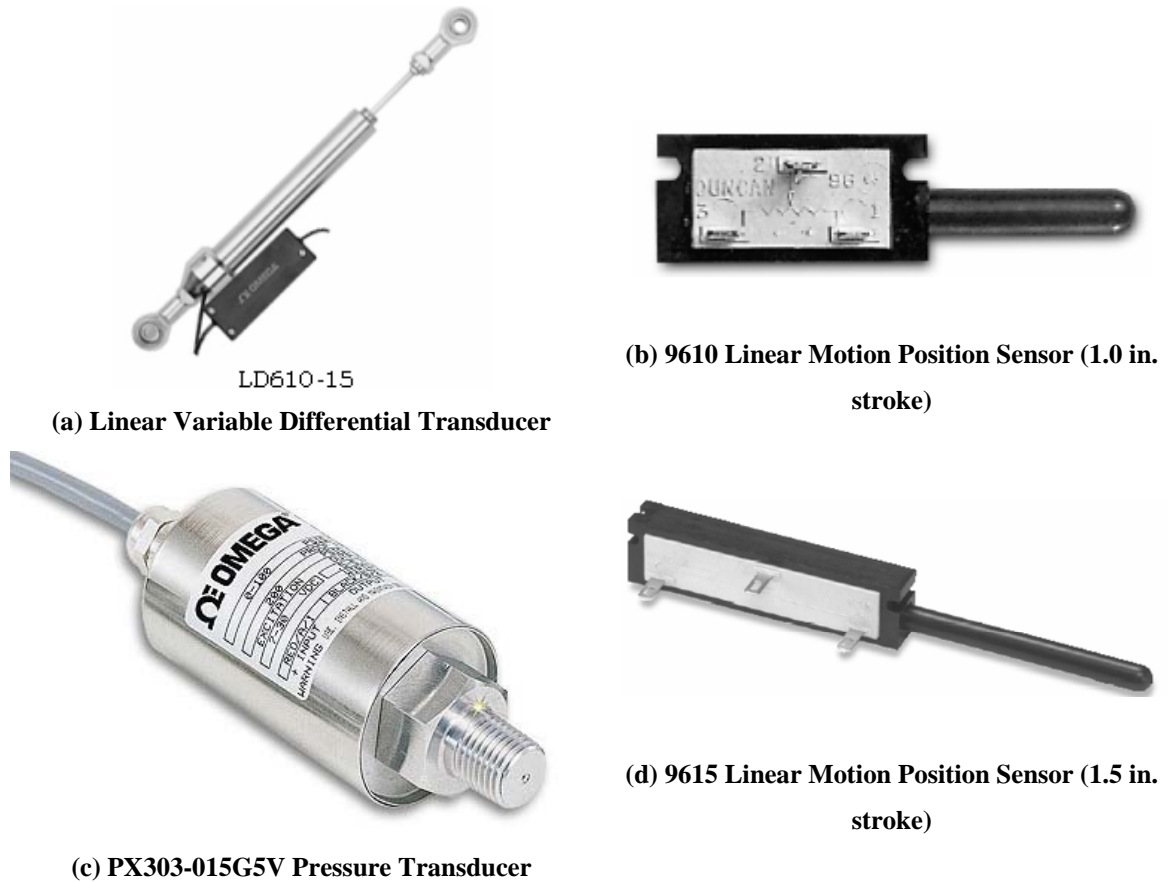


Figure 3.21: Closeup of Instruments (website: www.omega.com and www.beiduncan.com)

The pullout load was applied using two similar hydraulic cylinders and hand pumps supplied by Enerpac. These cylinders were placed in the box cut out on either side of the slab specimen. For the smaller slab configuration two RC156 (15 ton – 6 in piston stroke) and for the larger slab RC256 (25 ton – 6 in piston stroke) hydraulic cylinders were used. The pressure flow through the hydraulic cylinders was controlled using split flow and needle valves to apply a continuous monotonic loading at a rate of 20 lbs./min. followed by an opening rate of 0.02 in./min. The linear displacement potentiometers and the LVDTs had a measurement sensitivity of 0.02 in. and 4.5×10^{-3} in. Some typical photographs of the enerpac hand pump, hydraulic jacks, lvdts and sliders mounted on special designed brackets are shown in figure 3.22.

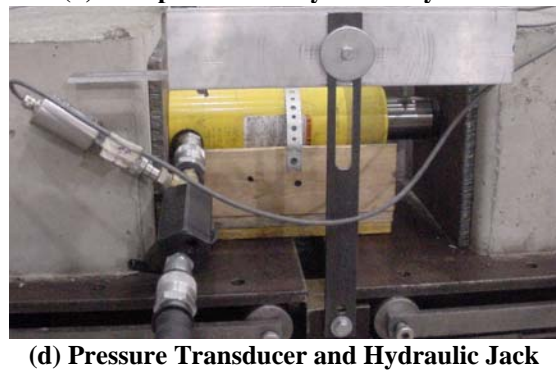
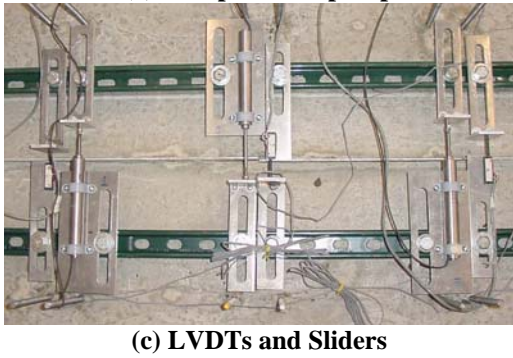
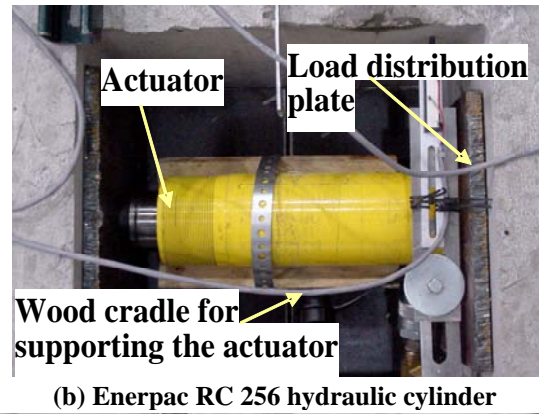
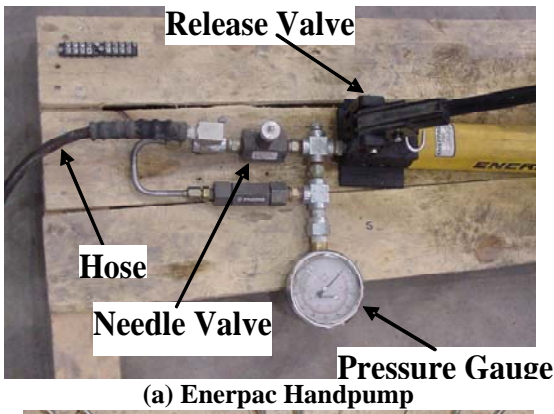
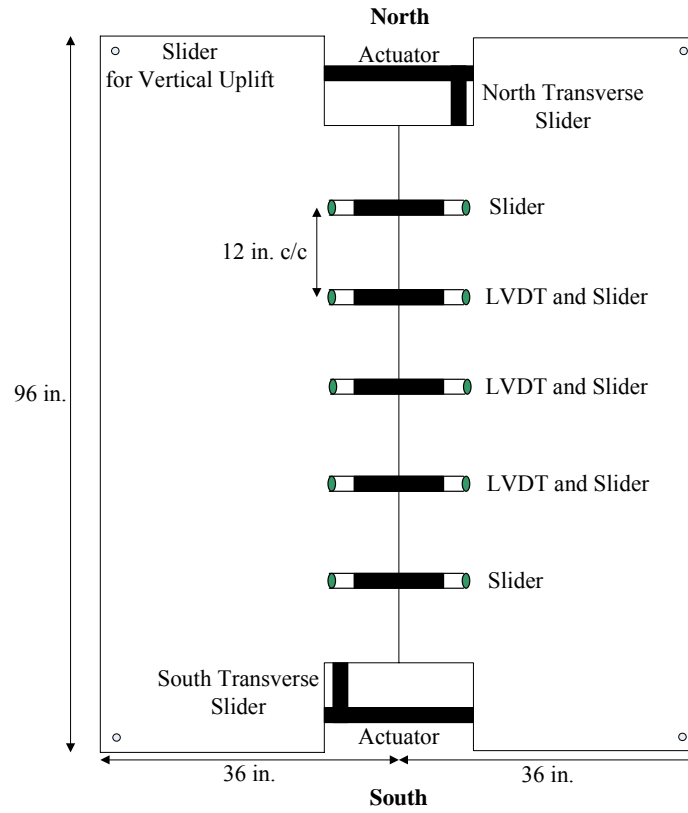
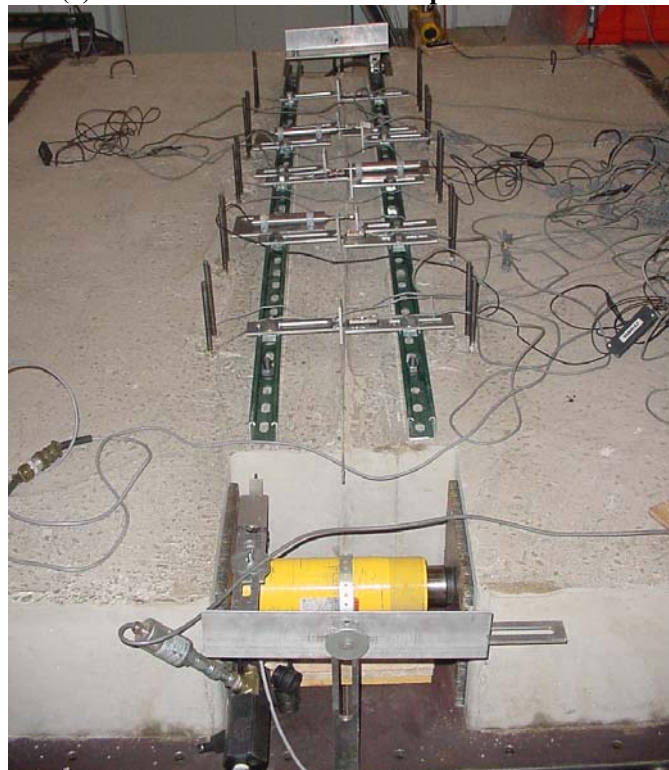


Figure 3.22: Typical Instruments and cylinders used in the tests

All the instruments used during the test were calibrated and the calibrated graph was used to scale the analog signals in the data acquisition system software. The calibration data is provided in Appendix A. The data from various instruments was collected at the rate of nearly 6 – 12 scans per second, using an array of National Instruments Data Acquisition cards. Custom built software called Little General was used to collect and process the data that was later imported into Microsoft Excel for data analysis.



(a) Plan of Instrumentation Setup for 5-dowel test



(b) Actual setup of instrumentation on the slab specimen
Figure 3.23: Five Dowel Instrumentation Setup

3.8 TYPICAL CYCLE FOR PREPARING AND TESTING A SPECIMEN

A typical cycle in fabricating and testing a specimen in the laboratory involved, cleaning and assembling the mold; rough misalignment, surveying and final preparation before casting; casting and material testing and finally demolding and setting up instrumentation and hydraulic cylinders before testing. A typical preparation and testing cycle would take 14 days. All slabs were tested on the 7th day after casting, giving 7 days for preparation time for the next slab specimen.

Step 1: Cleaning and assembling the mold – The mold and all the structural steel sections were first cleaned, placed and assembled. The smooth polished surfaces of the base rails, solid steel rollers and bottom of the base plate were cleaned using rubbing alcohol solution. This was done to remove any debris or small pieces of concrete and to provide a smooth frictionless surface between the base rails, rollers and base plates when the slabs were moved apart. The molds were assembled as per the shop drawings mentioned earlier.

Step 2: Rough Misalignment, surveying and final preparation – Once the assembled mold was placed on the solid rollers, the next step was to thread the rods through the threaded U shapes and the holes fabricated in the 1/8 in thick aluminum separator plate. Using the base plate and the sides of the structural steel sections, a rough misalignment as per the desired combination was achieved using tape measures. After rough misalignment, one side of the dowel bar was greased using MDOT certified grease / bond breaking agent. The other side of the dowel bar was welded using small tack welds to the threaded U shapes. This assembly of the dowels is basically a controlled misalignment provided by a basket assembly.

Accurate dowel misalignments were achieved using two total electronic stations (theodolites), a reference point (the base plate and sides of the mold), trigonometric principles and surveying techniques as explained earlier. The accuracy of the surveying instruments (0.005 radians) was adequate for determining the dowel misalignment angles. The maximum error between the measured and theoretical values of misalignment was $\pm \frac{1}{16}$ in. On the day of casting, a mold release agent was applied to the insides of the steel mold for easy demolding of the slab specimen.

Step 3: Casting and Material Testing – Concrete was supplied by a local ready mix plant approved by MDOT. Fresh concrete properties such as slump, air content, temperature, etc were recorded. Test specimens such as beams and cylinders were cast along with the test specimen for quality control of the MDOT approved paving mix. These beams and cylinder specimens were cured in a temperature controlled curing room and were tested at 3 days – when the specimen is demolded, 7 days – on day of specimen testing and 28 days.

Step 4: Demolding, setting up instrumentation and hydraulic cylinders, testing – The test specimens after casting were covered using plastic sheets and demolded after 3 days of curing. The specimens were demolded after ascertaining that the concrete has achieved at least 50% of the target 28-day uniaxial compressive strength (3500 psi).

A protocol was maintained during the entire testing regime: to continuously measure the induced load in the dowel bar due to joint opening of up to 1 in. The total load measured as the joint opened was divided by the number of dowels in the test specimen. The specimens were tested by pushing apart the concrete slabs using hydraulic actuators. The actuators applied a controlled monotonic longitudinal loading. The

hydraulic pressures in the actuators were synchronized using the split flow and needle valves. The concrete slabs were pushed apart very slowly at the approximate load rate of 20 lbs/min. followed by the opening displacement rate of approximately 0.02 in./min.



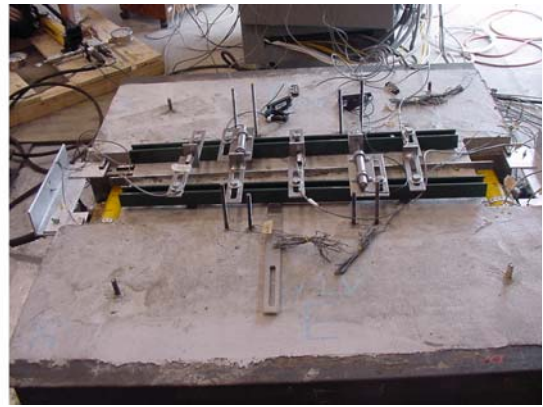
(a) Assembled Mold



(b) Surveying



(c) Casting of specimen



(d) Instrumented Slab

Figure 3.24: Typical cycle of specimen preparation and testing

In chapter 4, the results from the experimental investigations are presented. The types and severity of structural distresses observed during the laboratory investigation are also summarized in the next chapter.

CHAPTER 4

EXPERIMENTAL RESULTS AND EVALUATION

4.1 INTRODUCTION

This chapter presents results on the laboratory tests that were conducted on the concrete pavement specimens. A comparison of the dowel pullout force vs. joint opening behavior between the test specimens has been presented. Observations of structural distresses such as spalling around misaligned dowels at the joint face in the concrete, cracking and uplift of some test specimens with high misalignment magnitudes have been presented in this chapter.

4.2 LABORATORY TEST RESULTS

Table 4.1 presents the complete test matrix for the experimental investigation. As mentioned in Chapter 3, the parameters considered in the experimental investigations include (i) the number of dowel bars, (ii) the dowel misalignment type, (iii) magnitude and (iv) uniformity of the dowel bars. Additionally, Table 4.1 summarizes the structural distresses that were observed during the testing of the laboratory specimens.

TABLE 4.1(a): Test Matrix of the single dowel bar experiments conducted

Slab Dimensions	Number of Dowels	ID	Misalignment	Distresses Observed
2 slabs each 1220 x 610 x 250 mm	1	1A	Aligned	None
		1V9	Vertical	None
		1V12		
		1V18		
		1V36		
		1H9	Horizontal	None
		1H12		
		1H18		
		1H36		
		1C9	Combined	Spalling at end
		1C12		None
		1C18		None
		1C36		None

TABLE 4.1(b): Test Matrix of the two dowel bar experiments conducted

Slab Dimensions	Number of Dowels	ID	Misalignment	Distress Observed
2 slabs each 1220 x 610 x 250 mm	2 (Uniform)	2A	Aligned	None
		2V9U	Vertical	Spalling at end
		2V18U		None
		2H9U	Horizontal	Spalling at end
		2H18U		None
		2C9U	Combined	Spalling at end
		2C18U		None
	2 (Non - Uniform)	2V9NU	Vertical	Spalling at end
		2V12NU		Spalling at end
		2V18NU		Spalling at end
		2V36NU		Spalling at end
		2H9NU	Horizontal	Spalling and Transverse Cracking @ 0.67 in. joint opening
		2H12NU		Spalling and Transverse Cracking @ 0.7 in. joint opening
		2H18NU		Spalling at end
		2H36NU		Spalling at end
		2C9NU	Combined	Spalling and Transverse Cracking @ 0.43 in. joint opening
		2C12NU		Spalling and Transverse Cracking @ 0.95 in. joint opening
	2C18NU	Spalling at end		
	2C36NU	Spalling at end		
	2 (One Bar Misaligned)	2V12AM	Vertical	None
		2V18AM		None
		2H12AM	Horizontal	None
		2H18AM		None
		2C12AM	Combined	None
		2C18AM		None

TABLE 4.1(c) Test Matrix of the three and five dowel bar experiments conducted

Slab Dimensions	Number of Dowels	ID	Misalignment	Distresses Observed
2 slabs each 2440 x 915 x 250 mm	3 (Non - Uniform)	3V18NU	Vertical	Spalling around the dowel bars
		3H18NU	Horizontal	
		3C18NU	Combined	
	5 (Non - Uniform)	5V18NU	Vertical	Spalling @ 0.9 in. joint opening
		5H18NU	Horizontal	Spalling and Transverse Cracking @ 0.86 in. joint opening
		5C18NU	Combined	Spalling and Transverse Cracking @ 0.86 in. joint opening
	5 (Alternate Misaligned)	5V18AM	Vertical	Spalling around the outer and center dowel bars
		5H18AM	Horizontal	
		5C18AM	Combined	

The pullout behavior of dowel bars, as shown in Figure 4.1, is characterized by two distinct regions: (a) the initial fully bonded region (OA) and (b) the debonded / post – slip behavior region (AC). The bond stress τ , is then calculated by dividing the load by the circumferential area of the dowel bar ($\pi*1.25*9$). The magnitude of the bond stress at the point of debonding or initial slip is denoted as the initial slip/debonding stress (τ_b), and is calculated using the following equation:

$$\text{Bond Stress: } \tau_b = \frac{F_b}{\pi DL}$$

where F_b is the force at initial slip/debonding in lbs, D is the dowel bar diameter in inches and L is the embedment length of the dowel bar (9 in.).

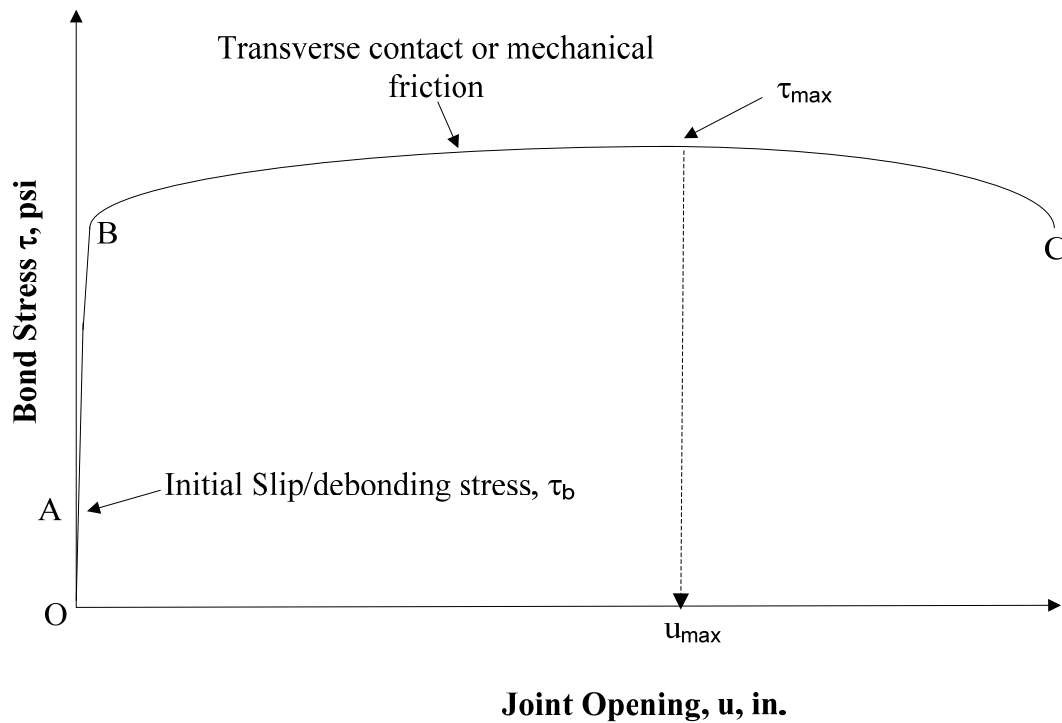


Figure 4.1: Typical Bond Stress versus Joint Opening curve

4.2.1 COMPARISON WITHIN A TYPE OF MISALIGNMENT

Vertically Misaligned dowel bar specimens

Figure 4.2 illustrates the comparisons of dowel pullout force per dowel bar vs. joint behavior for the one dowel (1A, 1V36, 1V18, 1V12 and 1V9) test specimens. Figures 4.3 through 4.5 present the comparisons of pullout force per dowel vs. joint opening behavior

of two dowels having non-uniform (2A, 2V36NU, 2V18NU, 2V12NU and 2V9NU), uniform (2A, 2V18U and 2V9U) and alternate misalignment (2V18AM and 2V12AM) orientations, respectively. Figures 4.6 and 4.7 present the comparisons of pullout force per dowel vs. joint opening behavior for three (3A and 3V18NU) and five (5A, 5V18NU, 5V18AM) dowel bar specimens, respectively. Figures 4.8 and 4.9 present the amount of dowel pullout force required to open the joint to $\frac{1}{4}$ in. and $\frac{1}{2}$ in. respectively.

In the case of a single misaligned dowel bar, figure 4.2, a clear trend is observed in the post slip behavior. The amount of dowel pullout force required to open a joint increases as the misalignment magnitude is increased, from an aligned to a misalignment magnitude of $\frac{1}{9}$ radians. From figures 4.8 and 4.9, an increasing trend in the dowel pullout force both at $\frac{1}{4}$ in. and $\frac{1}{2}$ in. joint opening is observed. As the misalignment magnitude was increased, the amount force required to open the joint also increased.

In the two misaligned dowel bars test specimens, shown in figures 4.3 through 4.5, due to misalignment, the dowel pullout force per bar vs. joint opening behavior increases to a peak value and then plateaus as the joint is opened up to the end of the test. This trend was specially observed in the test specimens containing the non-uniform oriented dowel bars. The 2V9NU test specimen required the maximum amount of dowel pullout force, approximately 2900 lbs and 3400 lbs, to open a joint to $\frac{1}{4}$ in. and $\frac{1}{2}$ in., respectively.

The results obtained for three and five dowel test specimens are shown in figures 4.6 and 4.7. From the dowel pullout force vs. joint opening behavior of 3V18NU and 5V18NU test specimens, it is clear that the slabs were undergoing restraint as the slabs were pushed apart. This was due to the fact that all the dowel bars in the test specimens

were misaligned with non-uniform orientation of misalignment causing joint locking. In the case of the 5V18NU test specimen, figure 4.9, at a dowel pullout force of 4000 lbs and joint opening of 0.85 in. the test specimen failed due to cracking of the slab.

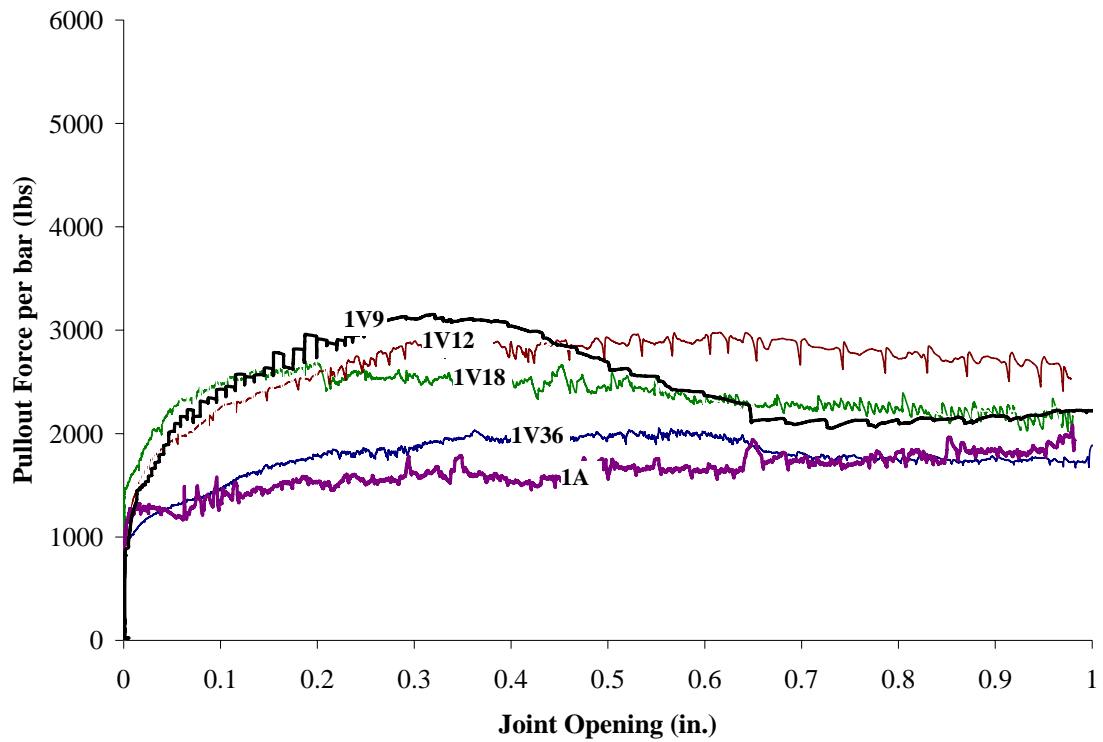


Figure 4.2: Comparison of pullout force vs. joint opening behavior for specimens with a single vertically misaligned dowel bar

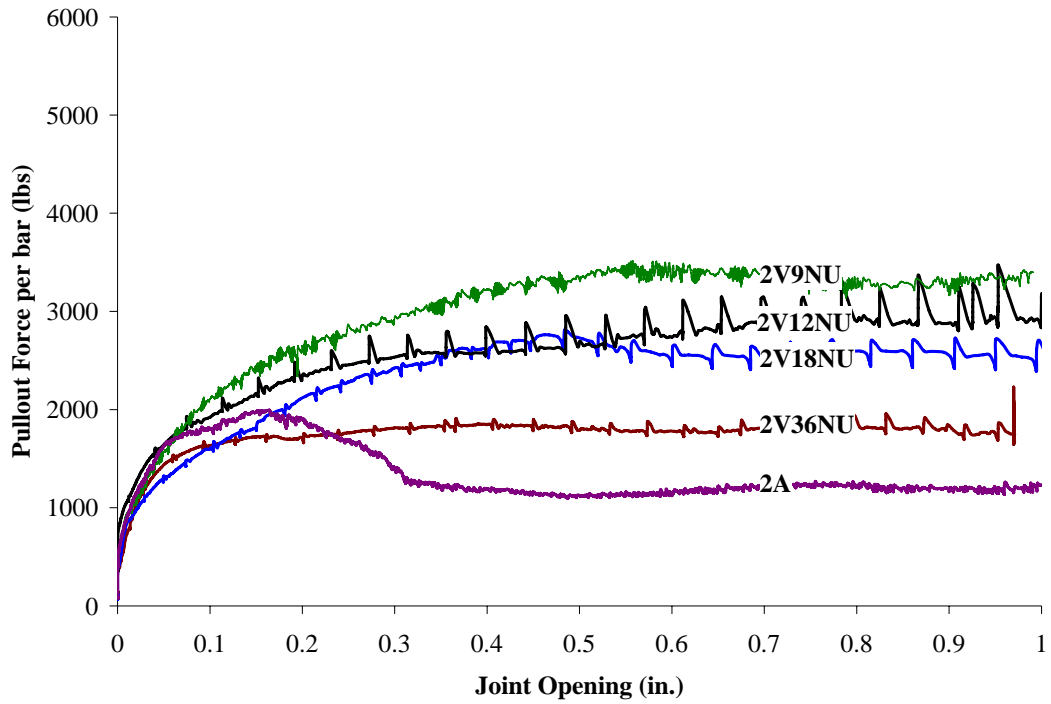


Figure 4.3: Comparison of pullout force vs. joint opening behavior for specimens with two vertically misaligned dowel bars having non-uniform (NU) orientation

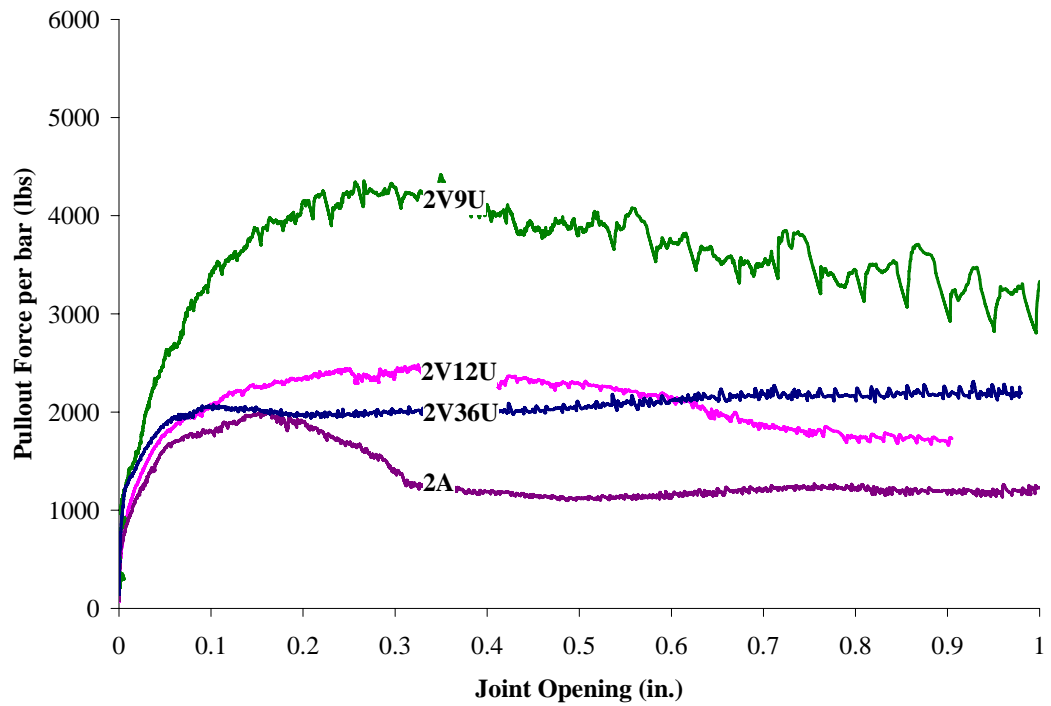


Figure 4.4: Comparison of pullout force vs. joint opening behavior for specimens with two vertically misaligned dowel bars and uniform (U) orientation

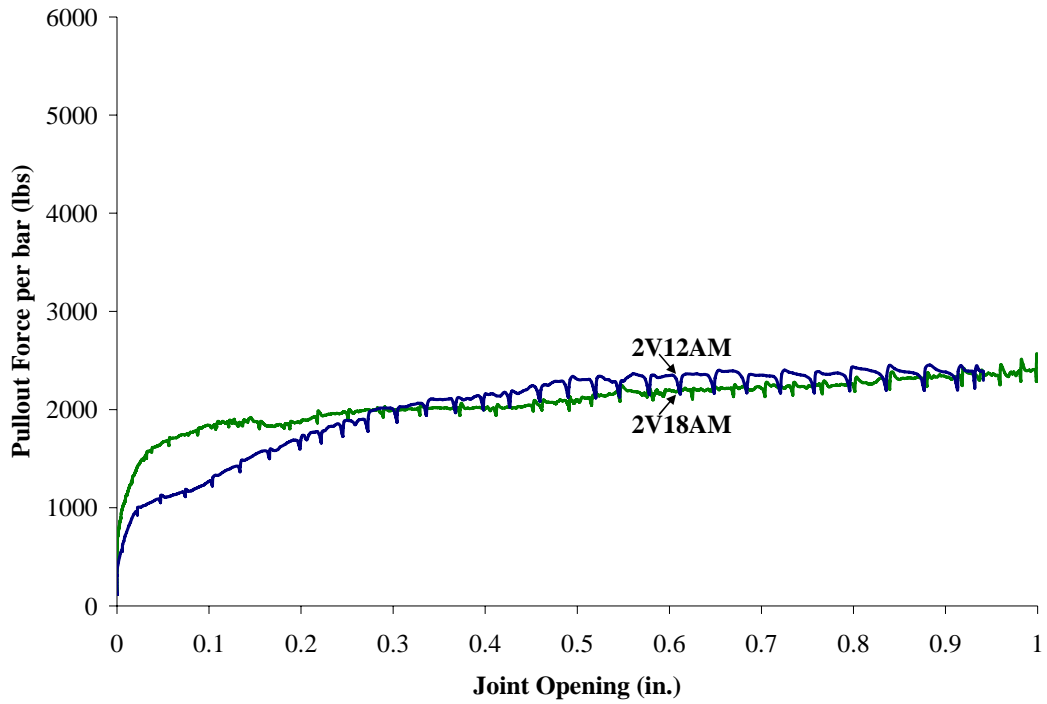


Figure 4.5: Comparison of pullout force vs. joint opening behavior for specimens with two vertically misaligned dowel bars and alternate (AM) orientation

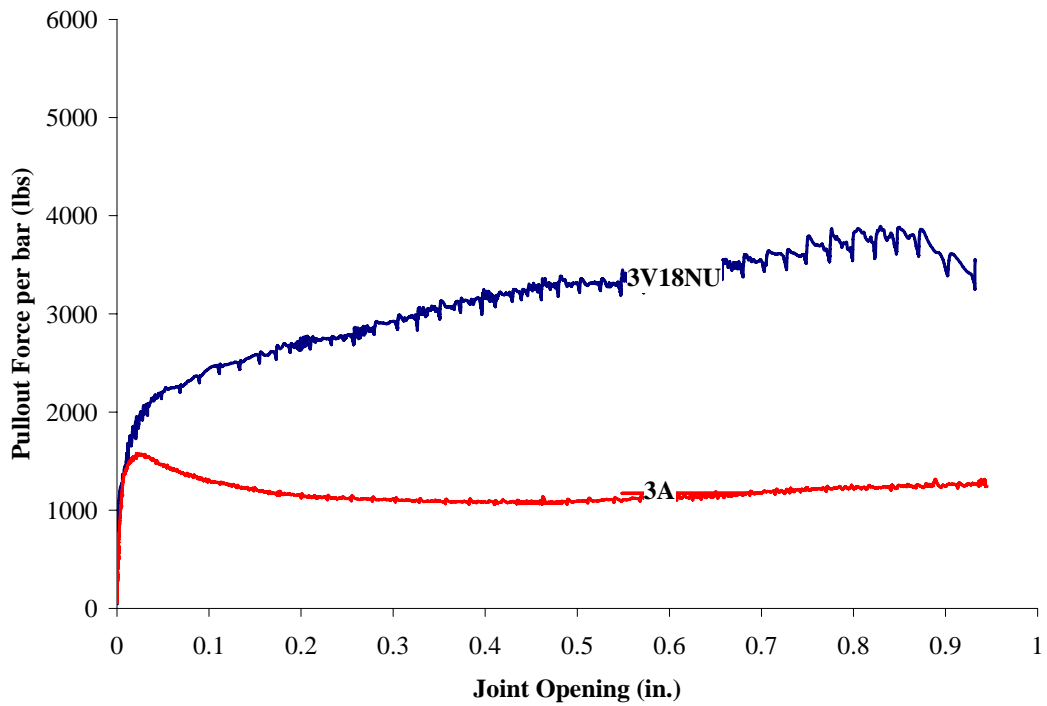


Figure 4.6: Comparison of pullout force per bar vs. joint opening behavior for specimens with three vertically misaligned dowel bars

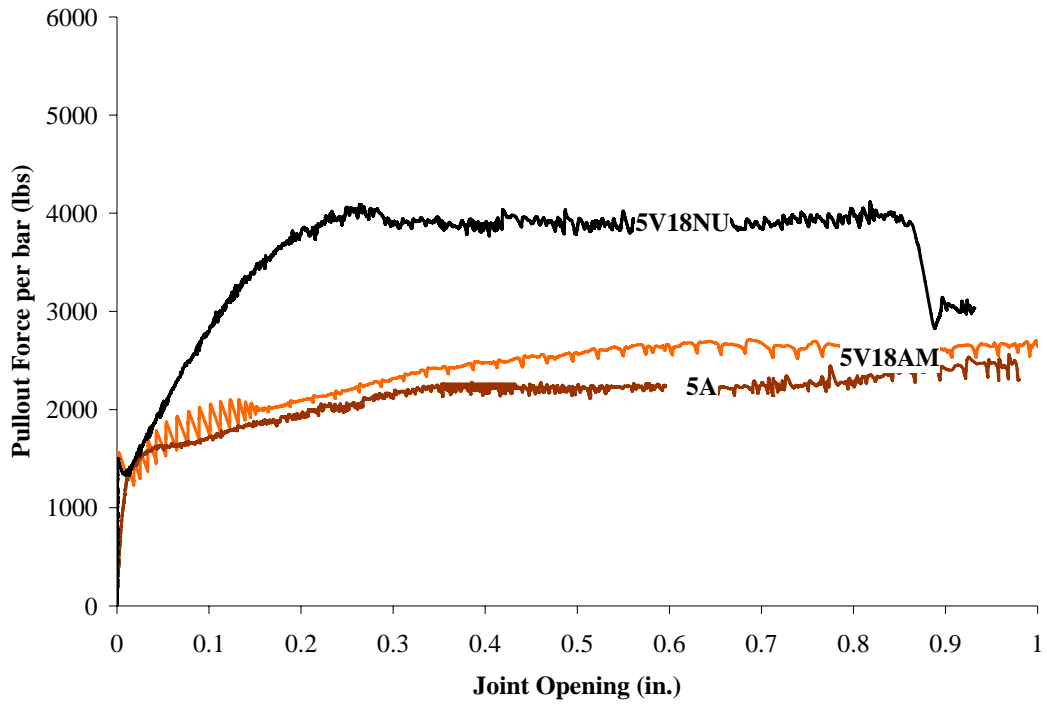


Figure 4.7: Comparison of pullout force per bar vs. joint opening behavior for specimens with five vertically misaligned dowel bars (5A, 5V18NU and 5V18AM)

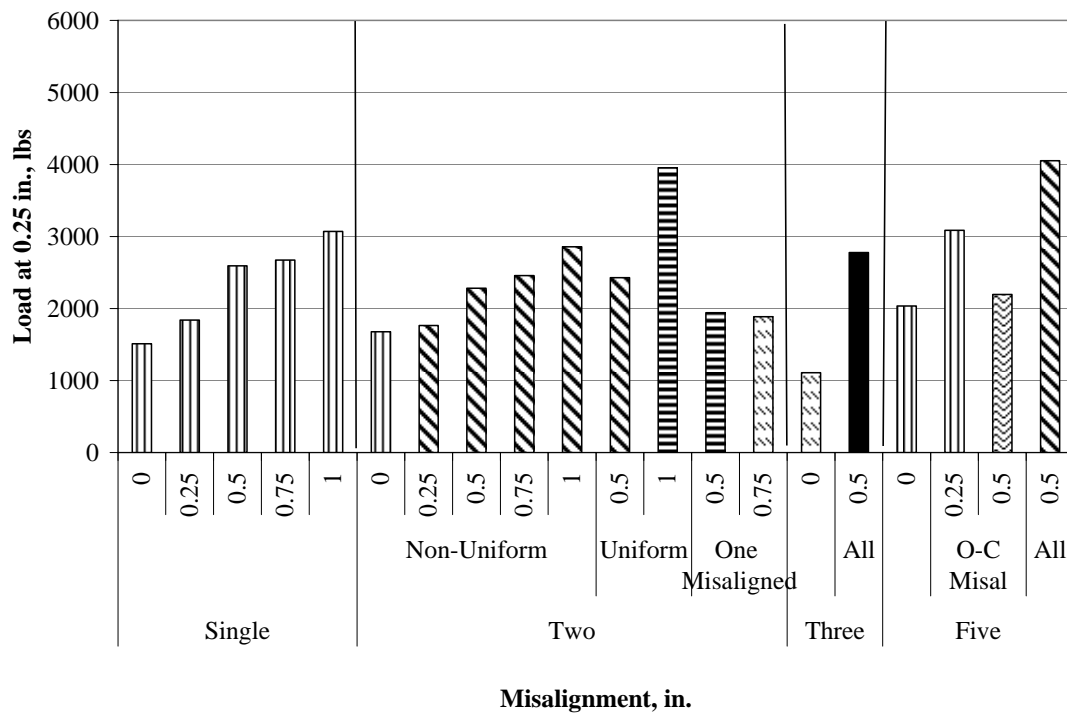


Figure 4.8: Comparison of pullout force per bar for vertically misaligned dowel bars at ¼ in joint opening

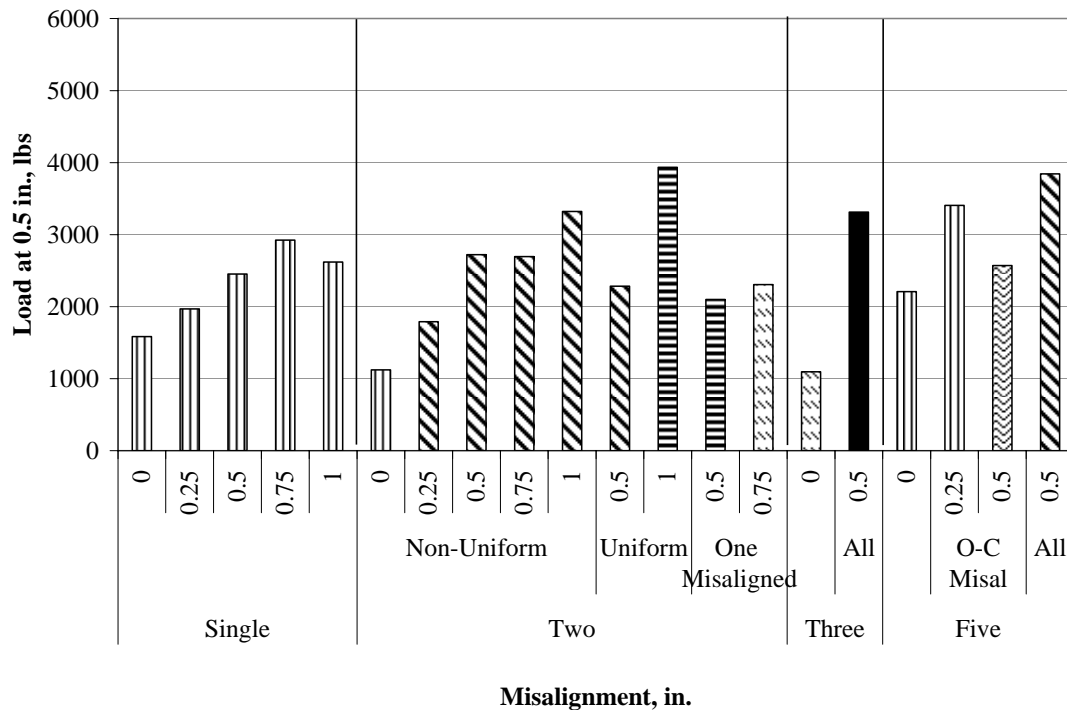


Figure 4.9: Comparison of pullout force per bar for vertically misaligned dowel bars at ½ in. joint opening

Horizontally Misaligned dowel bar specimens

Figure 4.10 illustrates the comparisons of dowel pullout force per dowel bar vs. joint behavior for the one dowel (1A, 1H36, 1H18, 1H12 and 1H9) test specimens. Figures 4.11 through 4.13 present the comparisons of pullout force per dowel vs. joint opening behavior of two dowels having non-uniform (2A, 2H36NU, 2H18NU, 2H12NU and 2H9NU), uniform (2A, 2H18U, 2H12U and 2H9U) and alternate misalignment (2H18AM and 2H12AM) orientations, respectively. Figures 4.14 and 4.15 present the comparison of the pullout force per dowel vs. joint opening behavior for three and five dowel bars respectively. Figures 4.16 and 4.17 present the amount of dowel pullout force required to open the joint to ¼ in. and ½ in. respectively.

Figure 4.10 shows the joint opening behavior for the single horizontally misaligned dowel bar test specimen. The overall magnitude of dowel pullout force

required to open a joint increased as the misalignment magnitude increases from an aligned to a misalignment magnitude of $\frac{1}{9}$ radians. In case of 1H9 test specimen, the dowel pullout force reaches a peak value of 3000 lbs at a joint opening of $\frac{1}{4}$ in. and 3500 lbs at a joint opening of $\frac{1}{2}$ in. as shown in figures 4.16 and 4.17.

In the two horizontally misaligned dowel bar test specimens, figures 4.11 through 4.13, due to misalignment, the dowel pullout force per bar vs. joint opening behavior increases to a certain peak value and then plateaus to the end of the test. Test specimens, 2H12NU and 2H9NU exhibited excessive spalling at joint in the concrete surrounding the misaligned dowel bars. The test specimens failed due to slab cracking at 0.7 in. joint opening.

In the three and five dowel test specimens, figures 4.16 and 4.17, the post slip behavior of the test specimen was characterized by an increasing dowel pullout force per bar. Structural distresses such as spalling in the concrete surrounding the misaligned dowel bars were observed in all the test specimens as mentioned in Table 4.1(c). Of the three and five dowel bar test specimens, maximum dowel pullout force of 3150 lbs and 3200 lbs corresponding to a joint opening of $\frac{1}{4}$ in. and $\frac{1}{2}$ in. was observed in the 5H18AM test specimen.

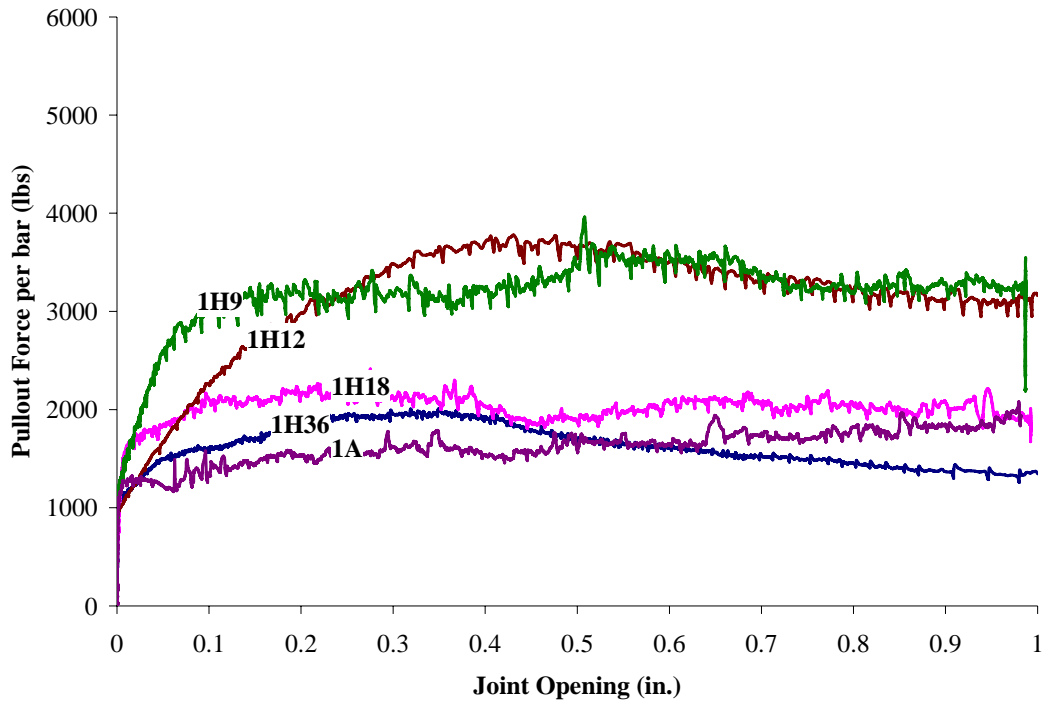


Figure 4.10: Comparison of pullout force vs. joint opening behavior for specimens with a single horizontally misaligned dowel bar

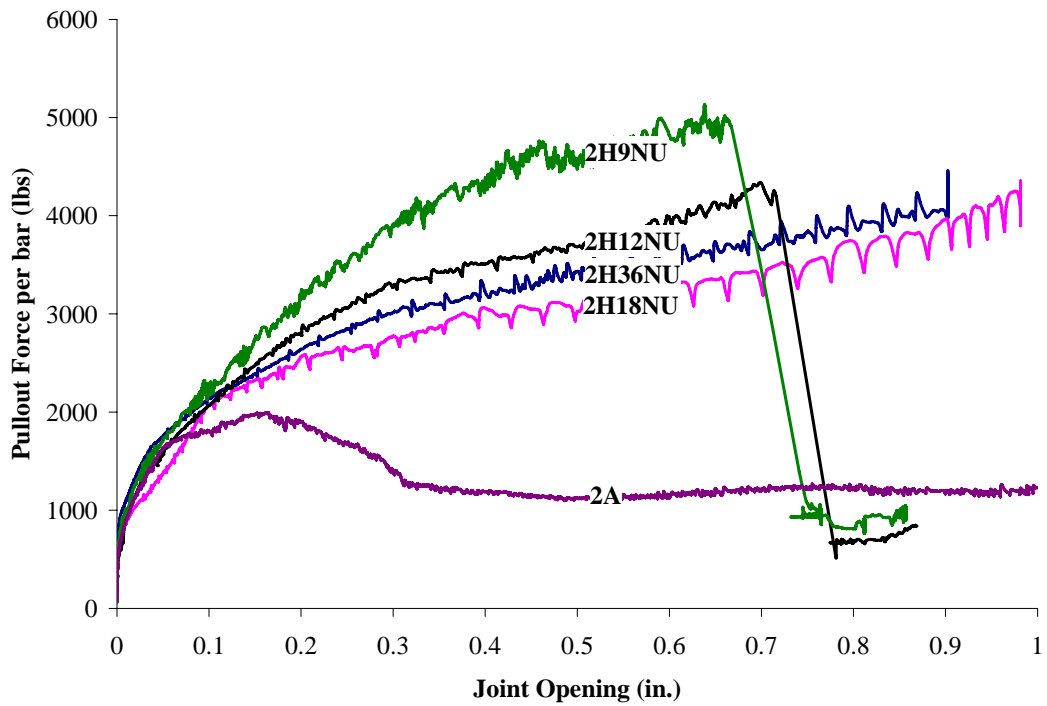


Figure 4.11: Comparison of pullout force vs. joint opening behavior for specimens with two horizontally misaligned dowel bars having non-uniform (NU) orientation

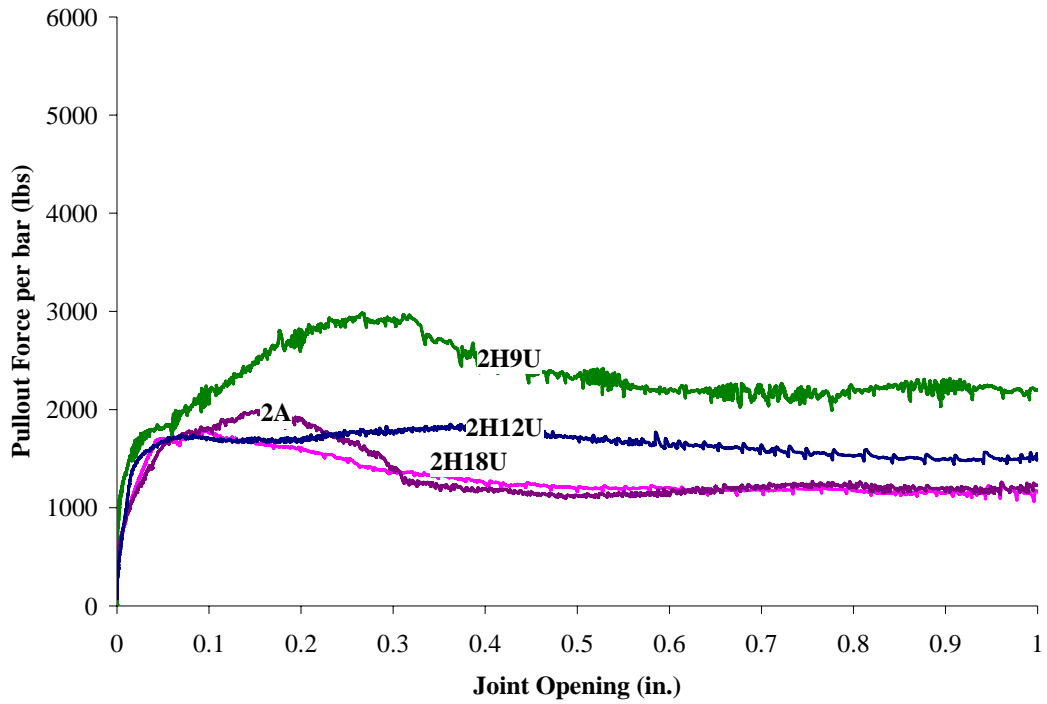


Figure 4.12: Comparison of pullout force vs. joint opening behavior for specimens with two horizontally misaligned dowel bars having uniform (U) orientation

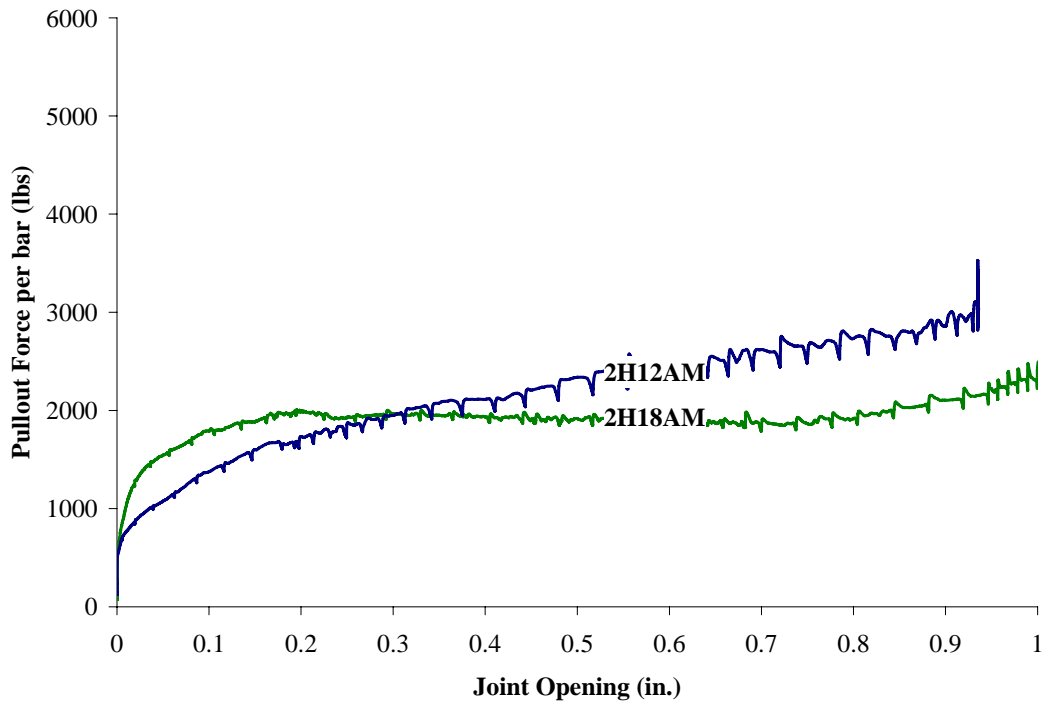


Figure 4.13: Comparison of pullout force vs. joint opening behavior for specimens with two horizontally misaligned dowel bars having alternate (AM) orientation

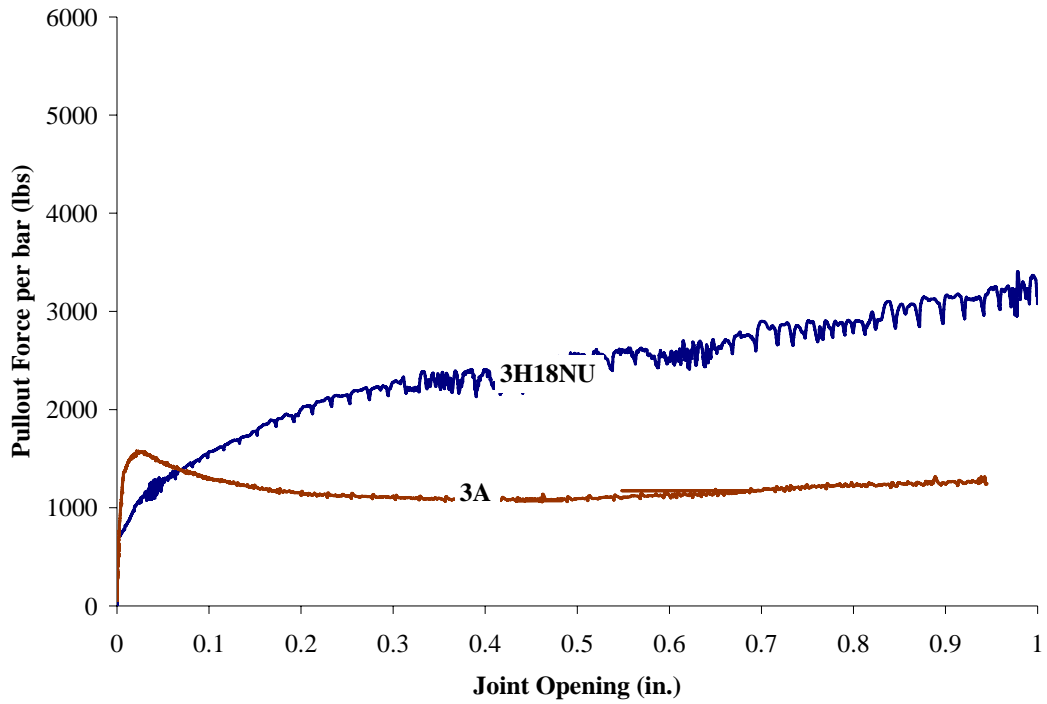


Figure 4.14: Comparison of pullout force per bar vs. joint opening behavior for specimens with three horizontally misaligned dowel bars

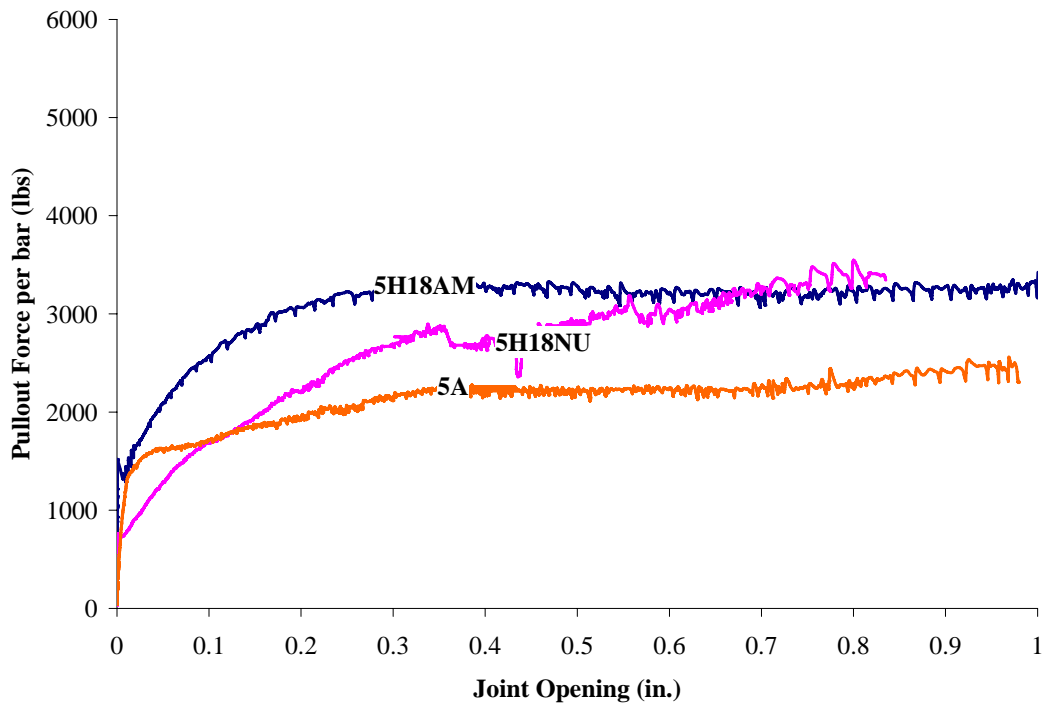


Figure 4.15: Comparison of pullout force per bar vs. joint opening behavior for specimens with five horizontally misaligned dowel bars (5A, 5H18NU and 5H18AM)

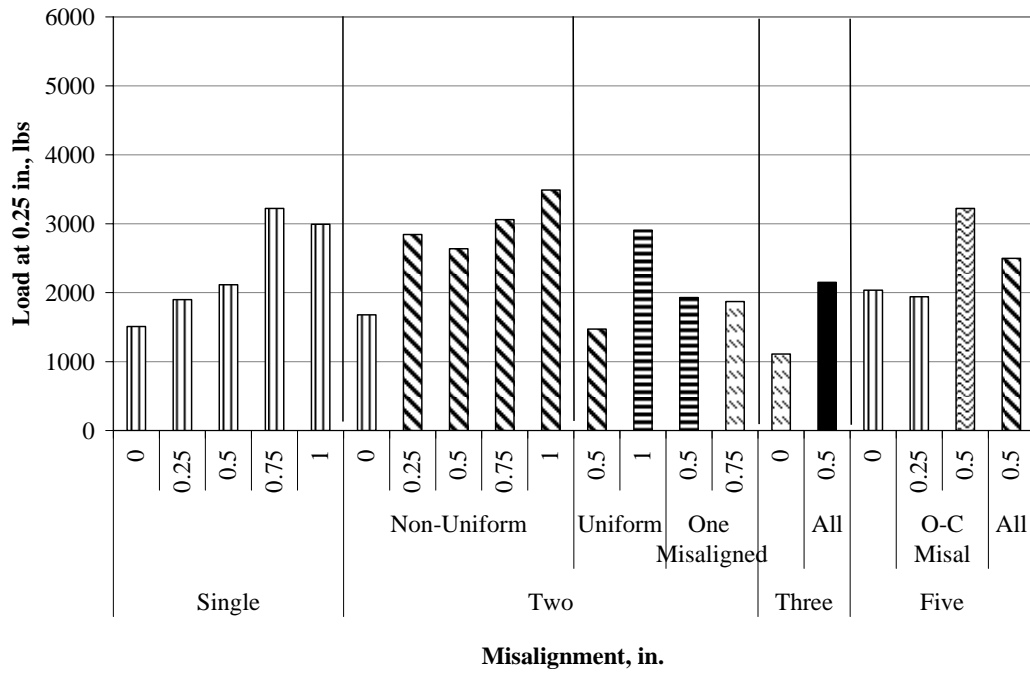


Figure 4.16: Comparison of pullout force per bar for horizontally misaligned dowel bars at 1/4 in. joint opening

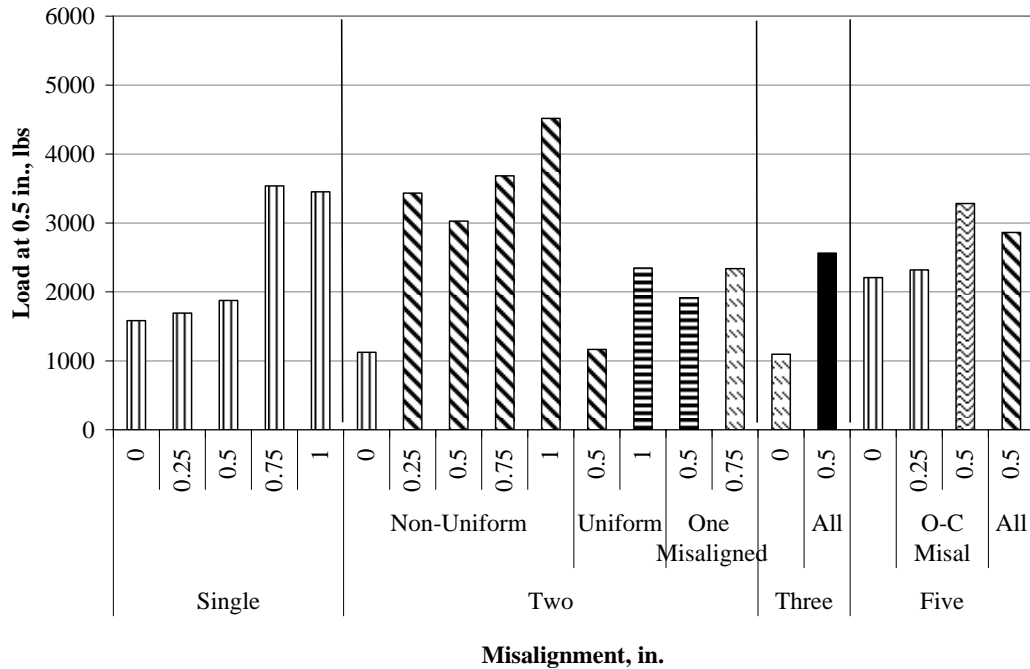


Figure 4.17: Comparison of pullout force per bar for horizontally misaligned dowel bars at 1/2 in. joint opening

Combined Misalignment type dowel bar specimens

Figure 4.18 illustrates the comparisons of dowel pullout force per dowel bar vs. joint opening behavior for the one dowel (1A, 1C36, 1C18, 1C12 and 1C9) test specimens. Figures 4.19 through 4.21 present the comparisons of pullout force per dowel vs. joint opening behavior of two dowels having non-uniform (2A, 2C36NU, 2C18NU, 2C12NU and 2C9NU), uniform (2A, 2C18U and 2C9U) and alternate misalignment (2C18AM and 2C12AM) orientations, respectively. Figures 4.22 and 4.23 present the comparison of the pullout force per dowel vs. joint opening behavior for three and five dowel bars respectively. Figures 4.24 and 4.25 present the amount of dowel pullout force required to open the joint to ¼ in. and ½ in. respectively.

Figure 4.18, shows the joint opening behavior for test specimens with a single dowel bar having combined misalignment type. For each of the test specimens, the amount of dowel pullout force required increased with increase in joint opening. In case of 1C9 test specimen, the dowel pullout force reached a peak value of 3500 lbs at a joint opening of 0.35 in. as shown in figure 4.18.

In the two dowel bar test specimens with combined misalignment, figures 4.19 through 4.21, due to misalignment the dowel pullout force per bar vs. joint opening behavior increases to a peak value and then a plateau or a sudden drop in the force due to structural distresses was observed. The dowel pullout force per bar dropped sharply in test specimen 2C9NU at a joint opening of 0.95 in. Some spalling around the misaligned dowel bars at the joint face was also observed at dowel pullout force of 5500 lbs per bar and joint opening of 0.45 in.

In the three and five dowel test specimens, figures 4.22 and 4.23, the post slip behavior of the test specimen was characterized by an increase in the dowel pullout force per bar. Spalling of the concrete surrounding the misaligned dowel bars was observed in all the test specimens as mentioned in Table 4.1(c). In test specimen 5C18NU a significant amount of spalling was observed at a pullout force of 4250 lbs and 0.6 in. joint opening and the test specimen failed due to brittle cracking of concrete at 0.85 in. joint opening, as shown in figure 4.23.

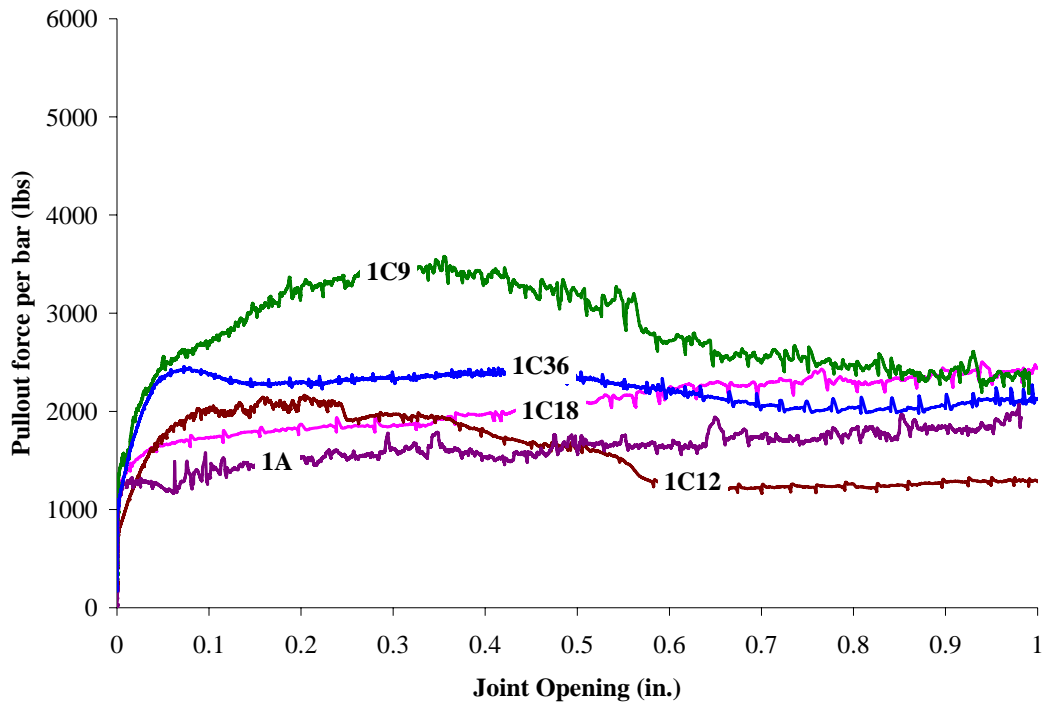


Figure 4.18: Comparison of pullout force vs. joint opening behavior for specimens with a single combined misaligned dowel bar

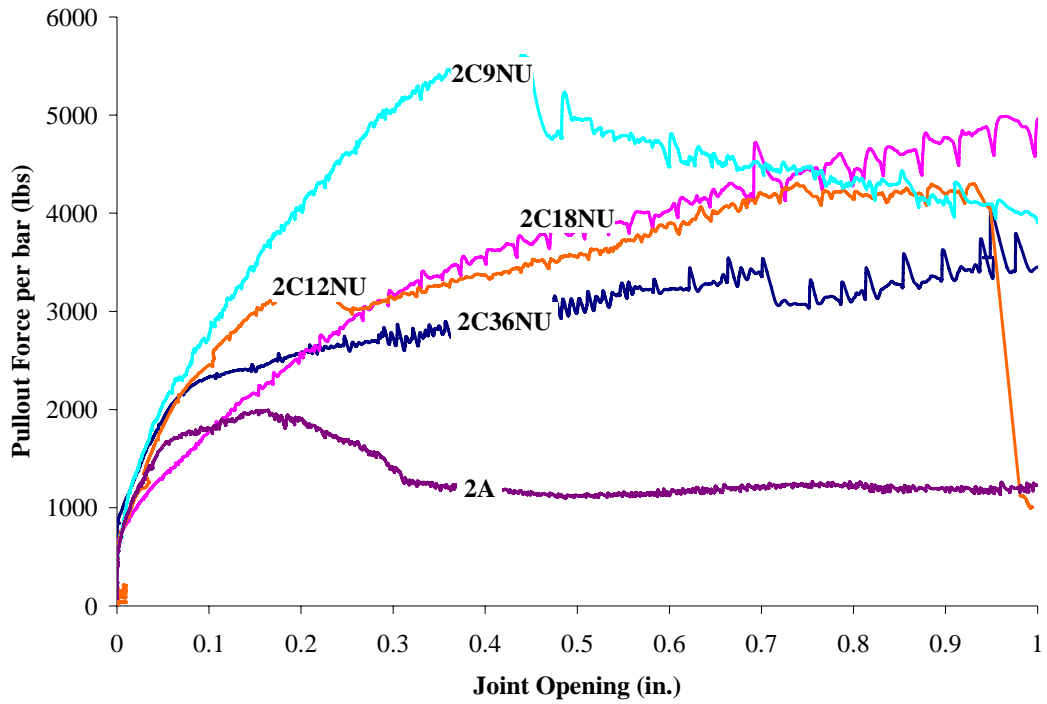


Figure 4.19: Comparison of pullout force vs. joint opening behavior for specimens with two combined misaligned dowel bars having non-uniform (NU) orientation

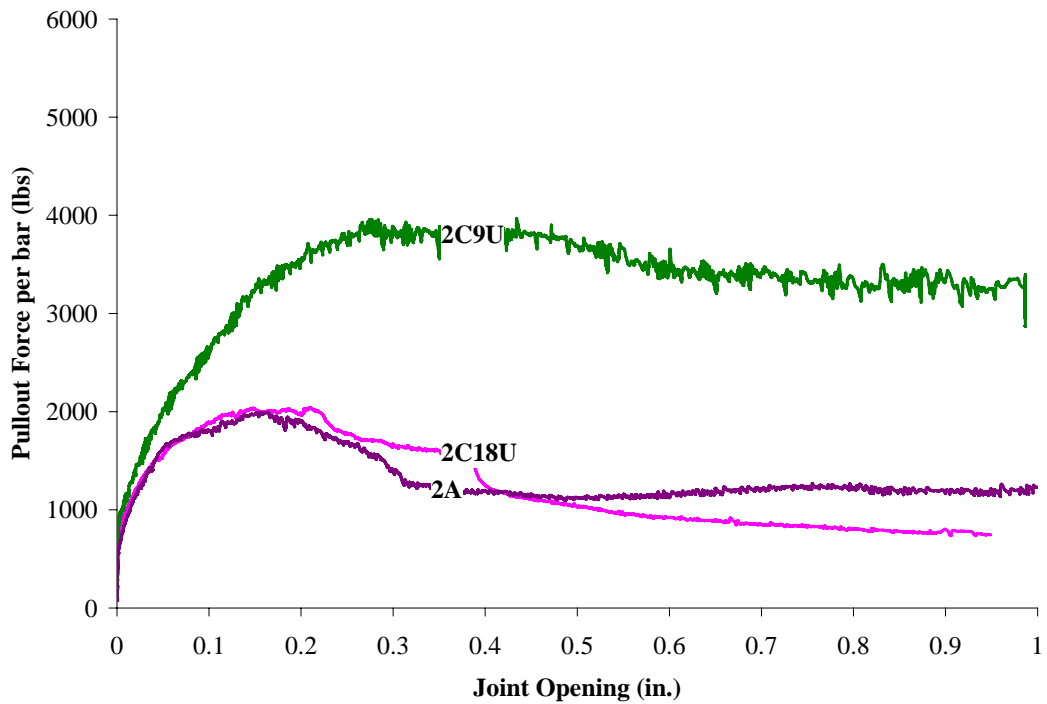


Figure 4.20: Comparison of pullout force vs. joint opening behavior for specimens with two combined misaligned dowel bars having non-uniform (U) orientation

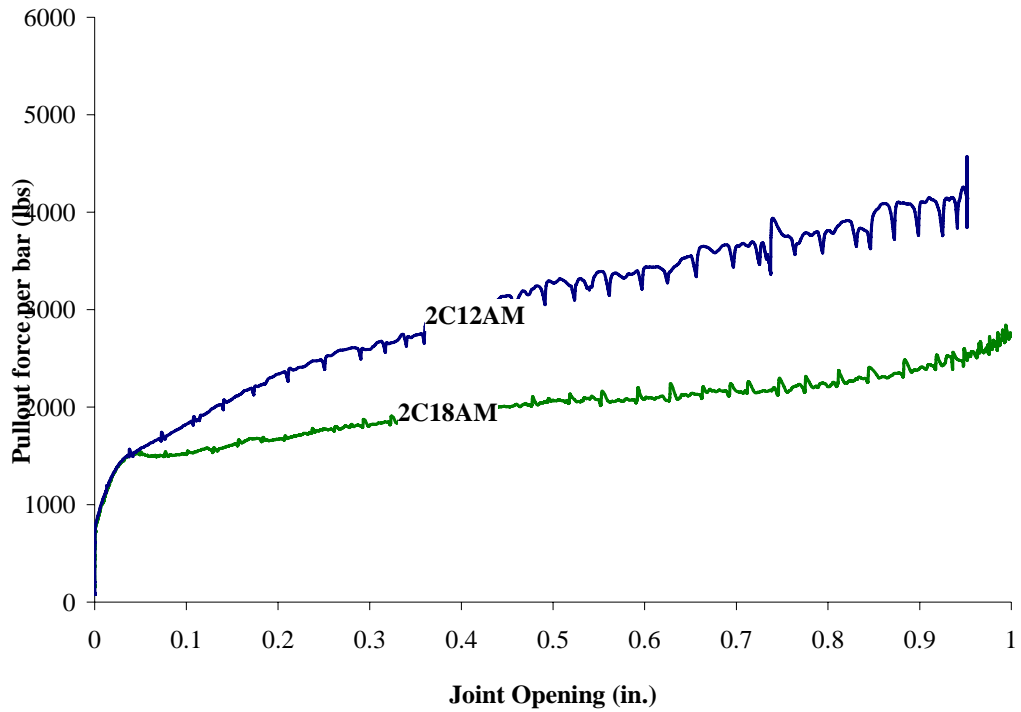


Figure 4.21: Comparison of pullout force vs. joint opening behavior for specimens with two combined misaligned dowel bars having alternate (AM) orientation

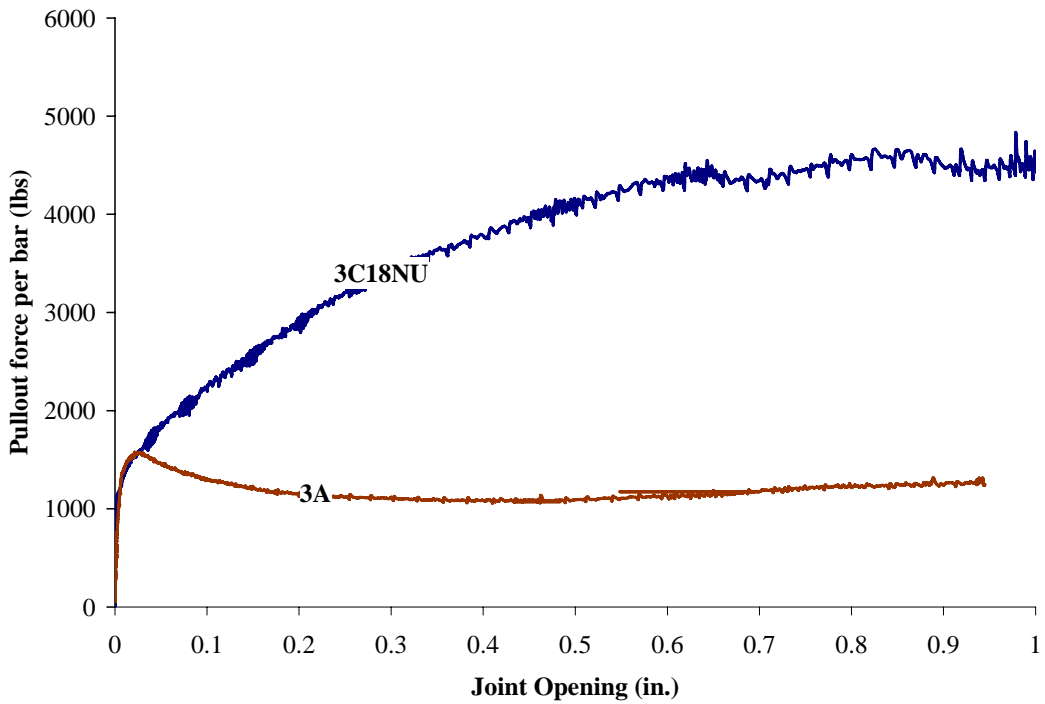


Figure 4.22: Comparison of pullout force vs. joint opening behavior for specimens with three combined misaligned dowel bars

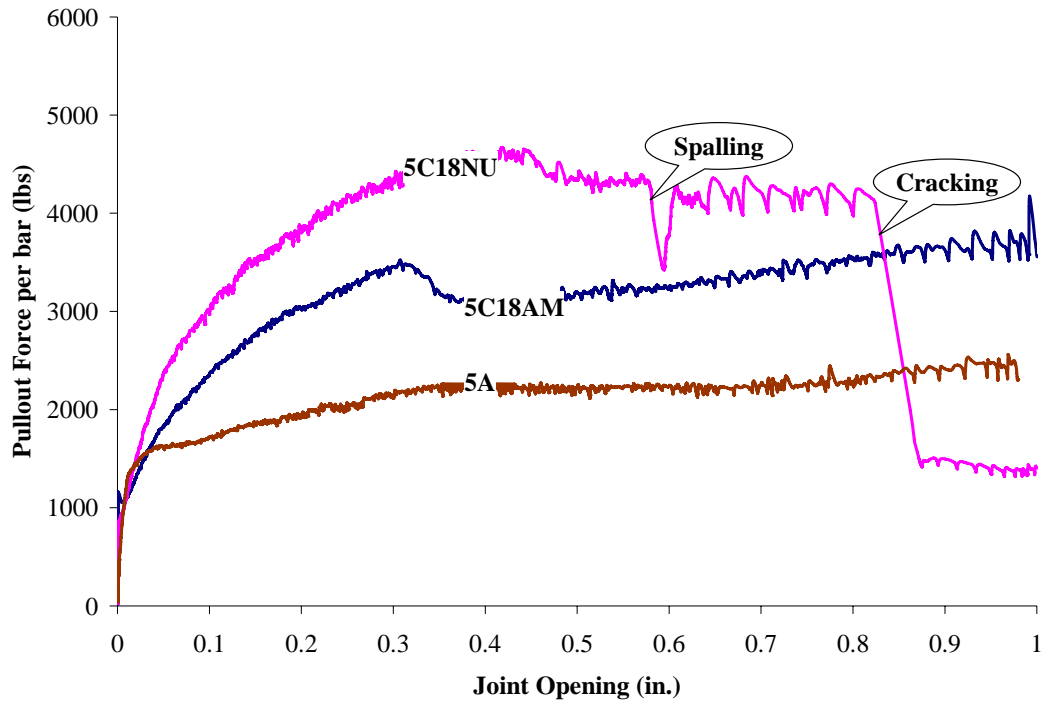


Figure 4.23: Comparison of pullout force vs. joint opening behavior for specimens with five combined misaligned dowel bars (5A, 5C18NU and 5C18AM)

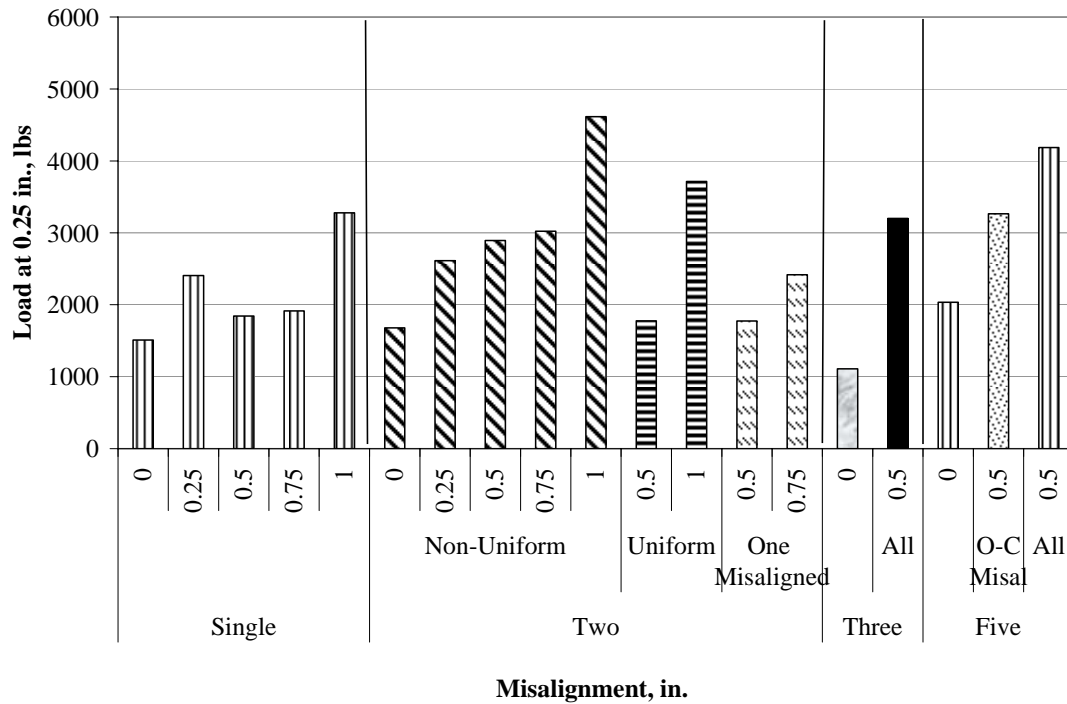


Figure 4.24: Comparison of pullout force per bar for combined misaligned dowel bars at ¼ in. joint opening

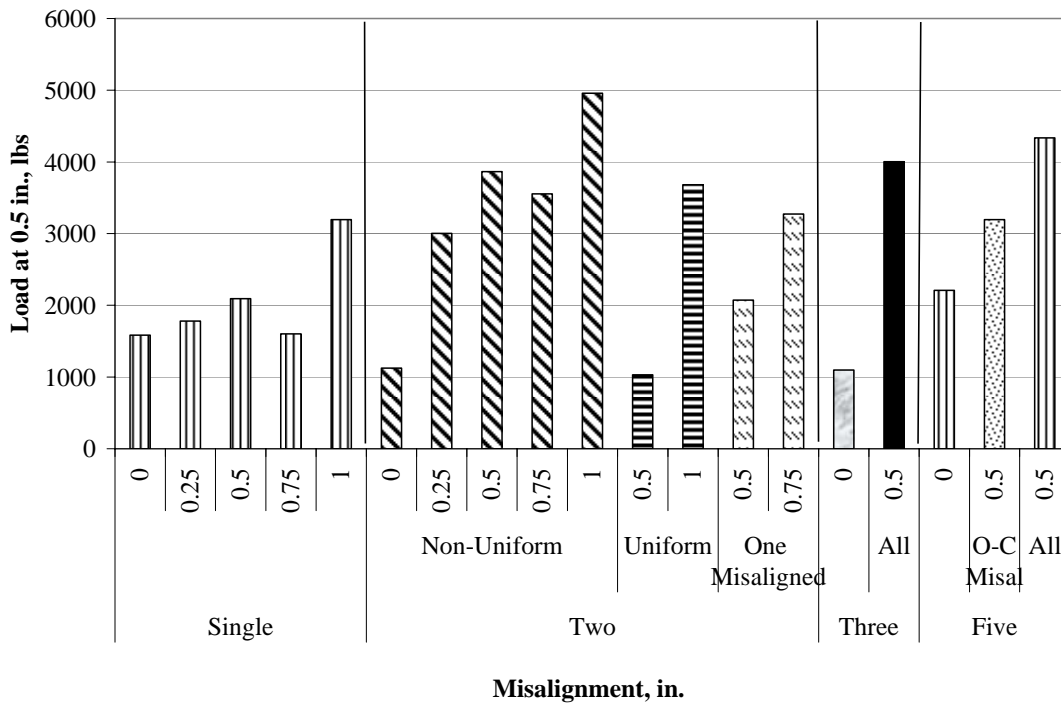


Figure 4.25: Comparison of pullout force per bar for combined misaligned dowel bars at 1/2 in. joint opening

4.2.2 COMPARISONS BETWEEN THE ORIENTATION OF MISALIGNED DOWEL BARS

The orientation of dowel bars in a multiple dowel bar test specimen could be one of three types, namely, non-uniform orientation (NU), uniform orientation (U) and alternate misaligned (AM). Comparison of the behavior between results of test specimens with same magnitude of misalignment, number of dowels in a test specimen, etc. have been presented.

Same Magnitude of misalignment

Figures 4.26 compares the pullout behavior of test specimens with two horizontally misaligned dowel bars of 1/18 radians misalignment magnitude and having different orientations. The dowel pullout force per dowel in the 2H18NU test specimen due to its

non-uniform orientation of misaligned dowels requires higher dowel pullout force compared to the 2H18AM and the 2H18U test specimens. A similar trend is observed in the results obtained from the joint opening behavior of 2V18NU, 2V18AM and 2V18U test specimens as shown in figure 4.27 and 2C18NU, 2C18AM and 2C18U test specimens shown in figure 4.28. The dowel pullout force vs. joint opening behavior for 1/12 radians magnitude of misalignment as shown in figures 4.29 through 4.31, show the same trend as observed in the 1/18 radians misaligned dowel bars. For the specimens with 1/12 radians with all three types of misalignments, the force required to open a joint with non-uniform orientation of misalignment is overall higher compared to the alternate misaligned dowel bars.

In the five dowel bar test specimens, comparison of the results were made with respect to the 1/18 radians magnitude and misalignment type. The alternate misaligned dowel bars in horizontally misaligned test specimen, 5H18AM, yielded higher values of pullout force compared to the no-uniform, 5H18NU, misaligned dowel bars, shown in figure 4.32. In results obtained from test specimens with vertical and combined misalignments, the forces in the specimens with non-uniform misaligned bars were higher compared to the alternate misalignment, as shown in figures 4.33 and 4.34.

In general, it can be concluded that for a given misalignment magnitude, the load induced per dowel increases as the number of dowels misaligned increases. Overall, it indicates that irrespective of the dowel misalignment type (vertical, horizontal or combined) and magnitude (1/18 radians, 1/12 radians), the force required to open the joint in a pavement slab with non-uniform misaligned dowel bars is higher compared to

alternate and uniform orientation of misalignments. Generally, more spalling was observed in test specimens with non-uniform orientation of dowel bars.

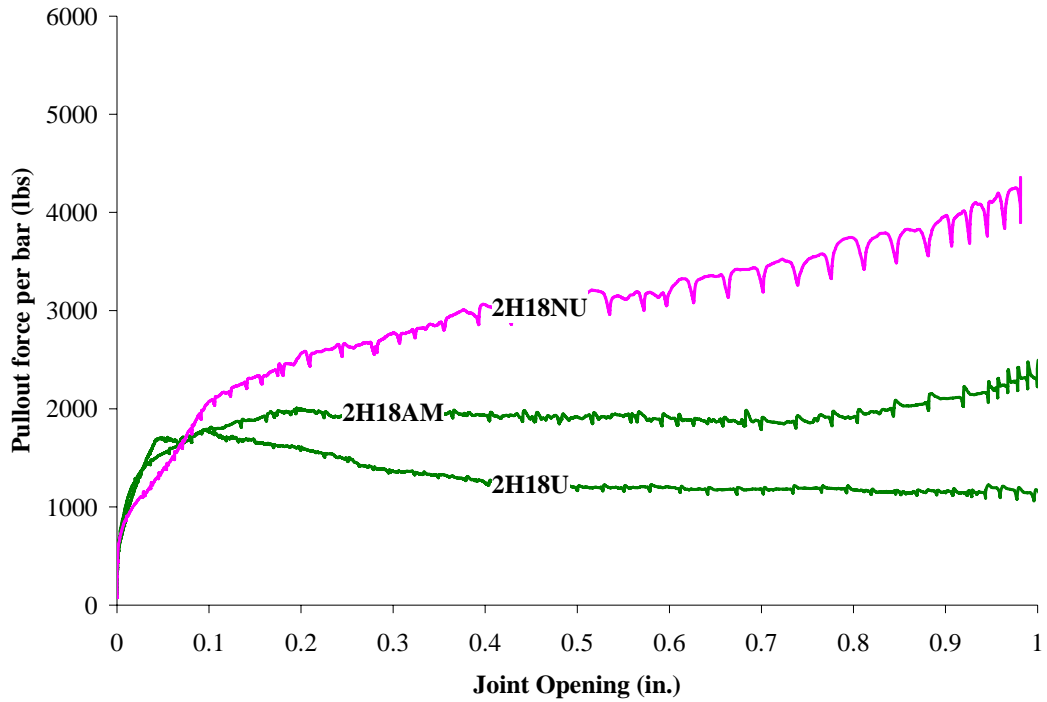


Figure 4.26: Comparison of pullout force vs. joint opening curves of 2-dowel ½ in. Horizontal Misalignment (2H18NU, 2H18U, and 2H18AM)

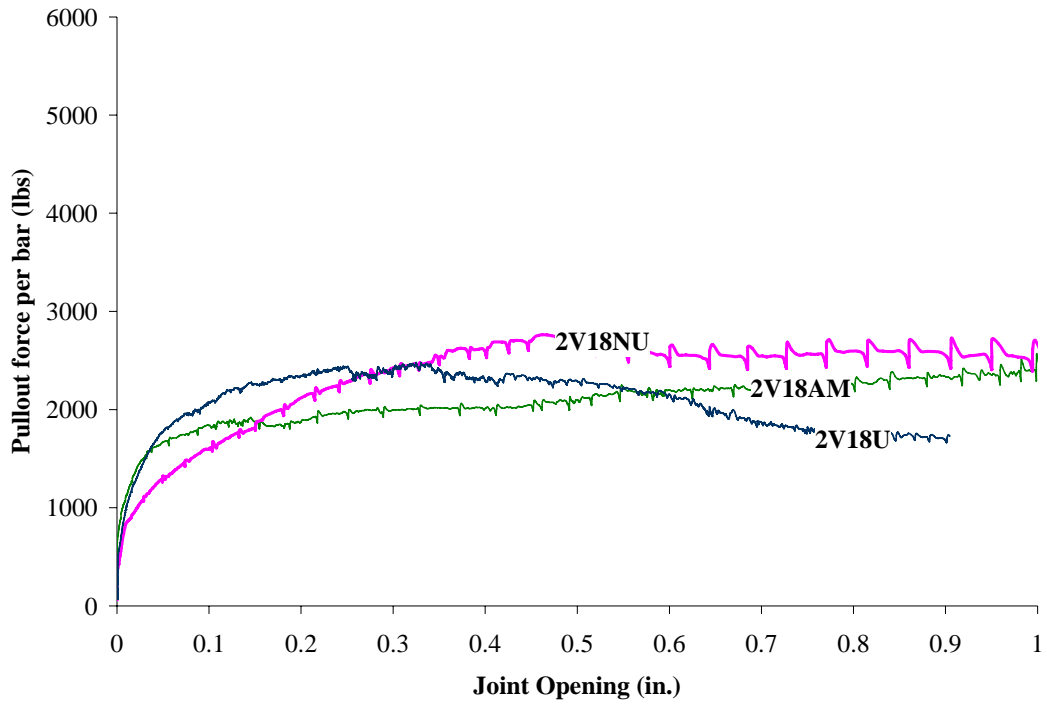


Figure 4.27 Comparison of pullout force vs. joint opening curves of 2-dowel 1/2 in. Vertical Misalignment (2V18NU, 2V18U, and 2V18AM)

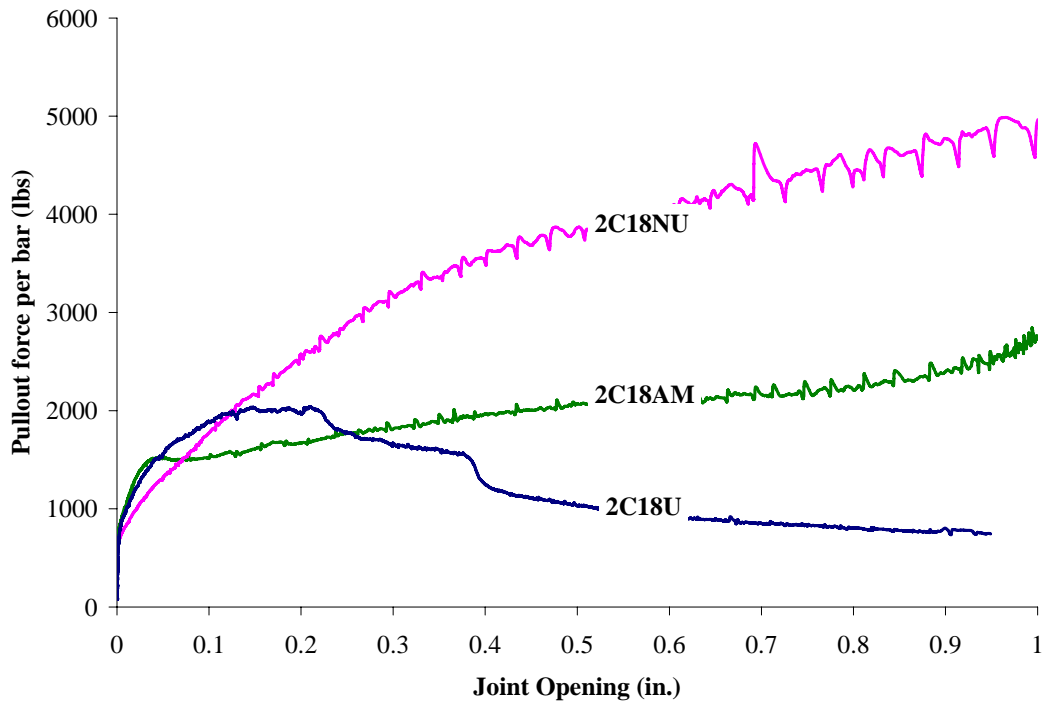


Figure 4.28: Comparison of pullout force vs. joint opening curves of 2-dowel 1/2 in. Combined Misalignment (2C18NU, 2C18U, and 2C18AM)

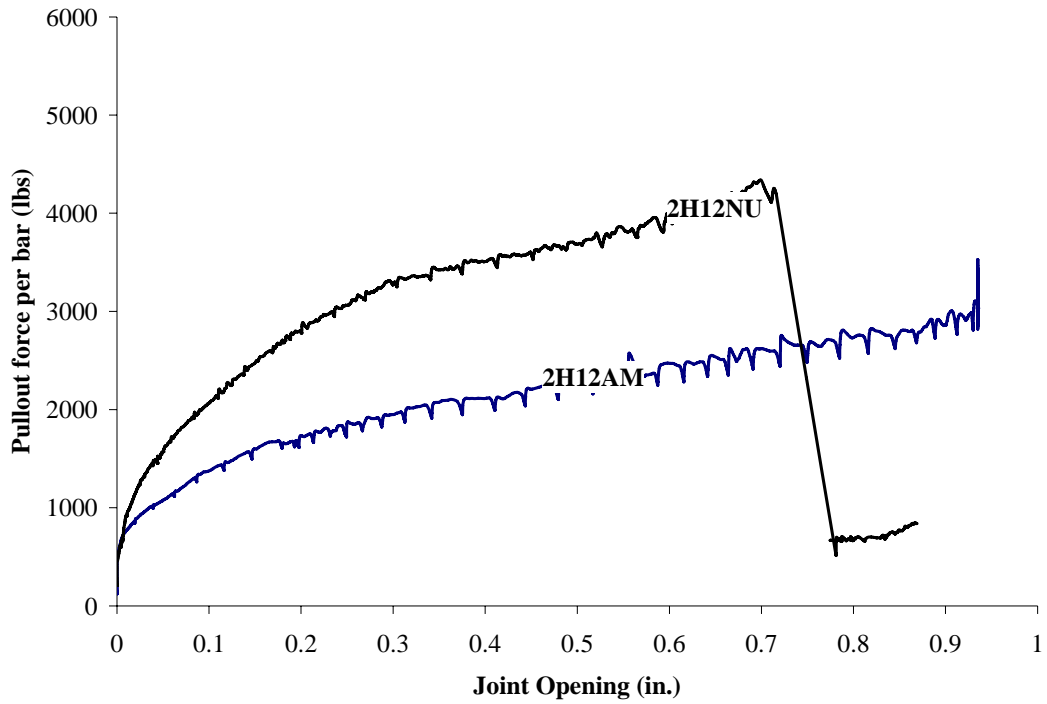


Figure 4.29: Comparison of pullout force vs. joint opening curves of 2-dowel $\frac{3}{4}$ in. Horizontal Misalignment (2H12NU and 2H12AM)

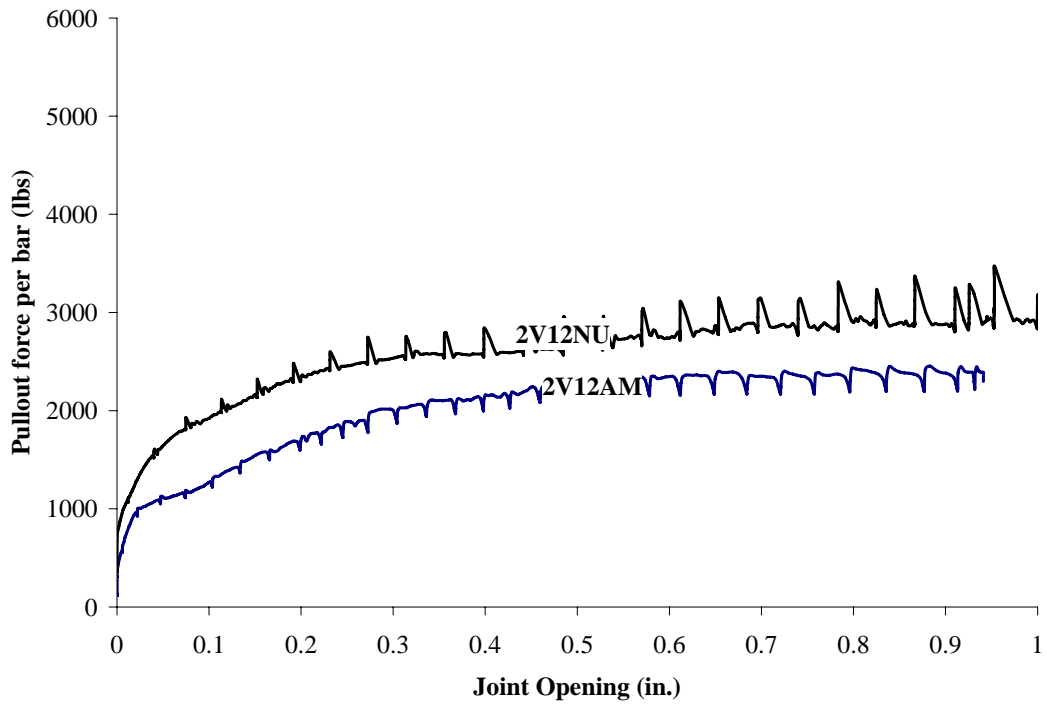


Figure 4.30: Comparison of pullout force vs. joint opening curves of 2-dowel $\frac{3}{4}$ in. Vertical Misalignment (2V12NU and 2V12AM)

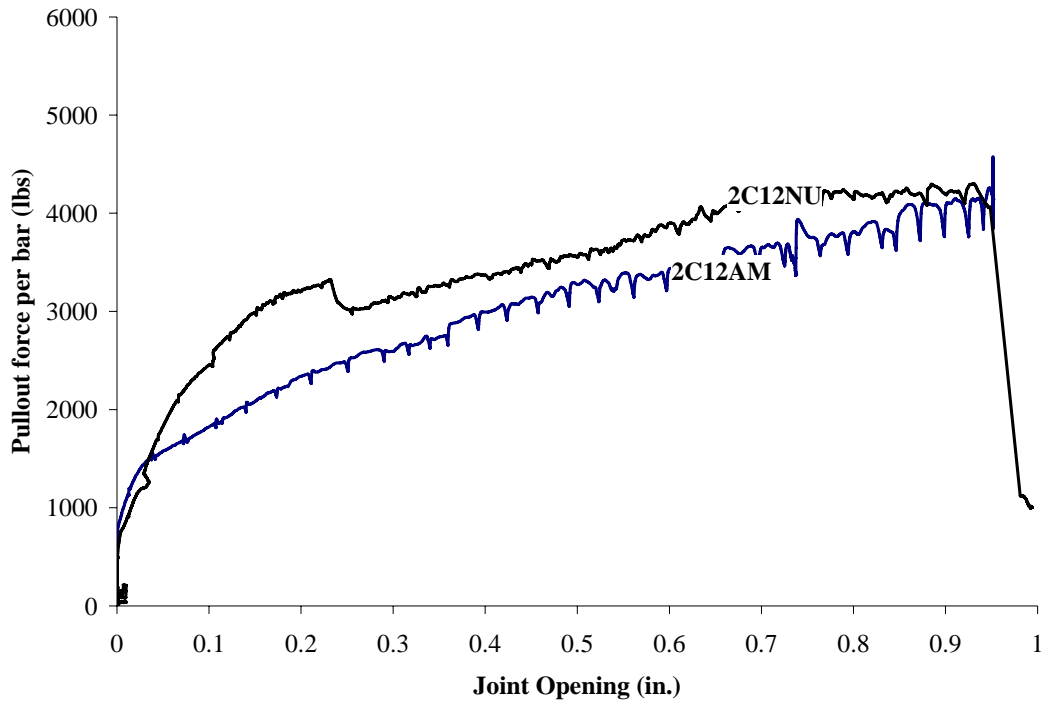


Figure 4.31 Comparison of pullout load vs. joint opening curves of 2-dowel $\frac{3}{4}$ in. Combined Misalignment (2C12NU and 2C12AM)

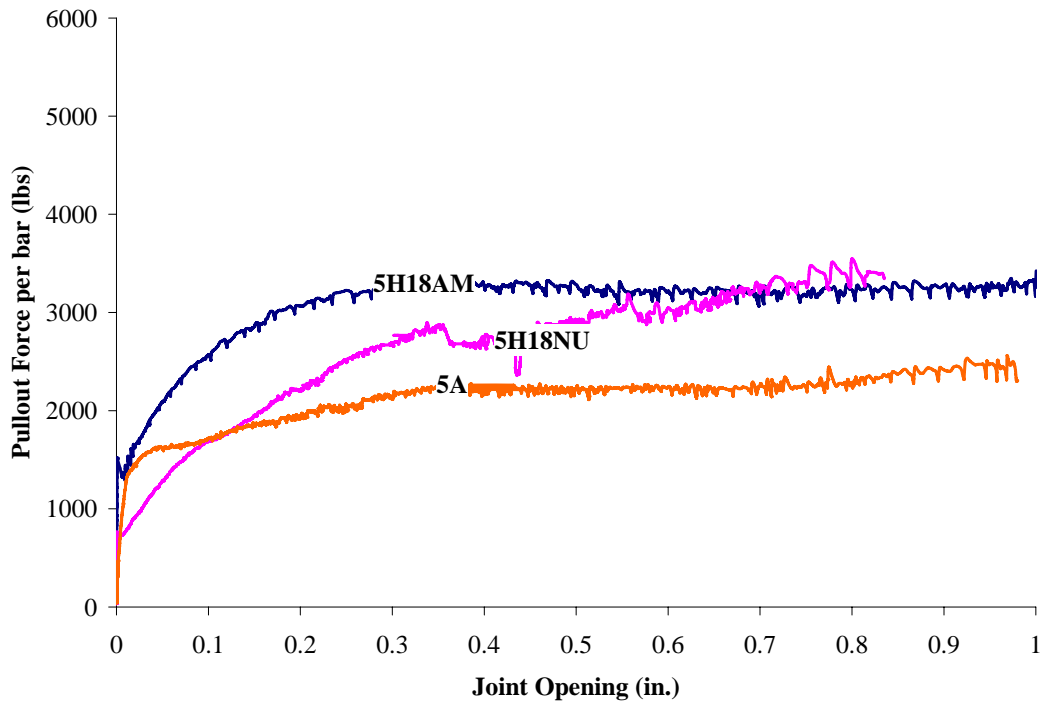


Figure 4.32 Comparison of pullout load vs. joint opening curves of 5H18NU and 5H18AM

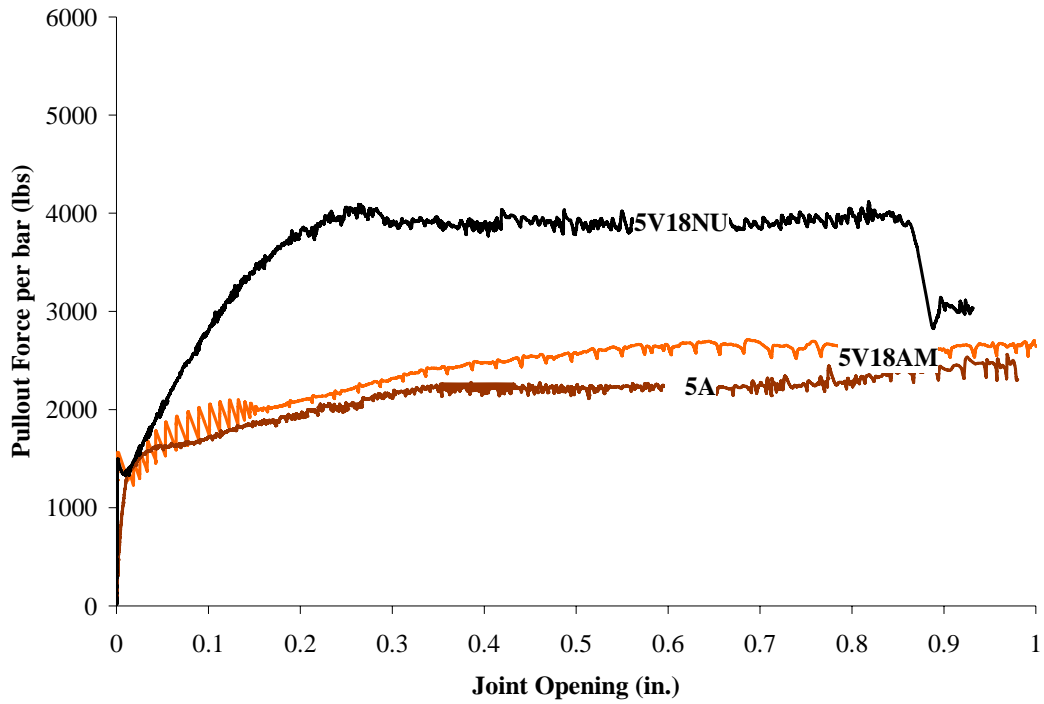


Figure 4.33 Comparison of pullout force vs. joint opening curves of 5V18NU and 5V18AM

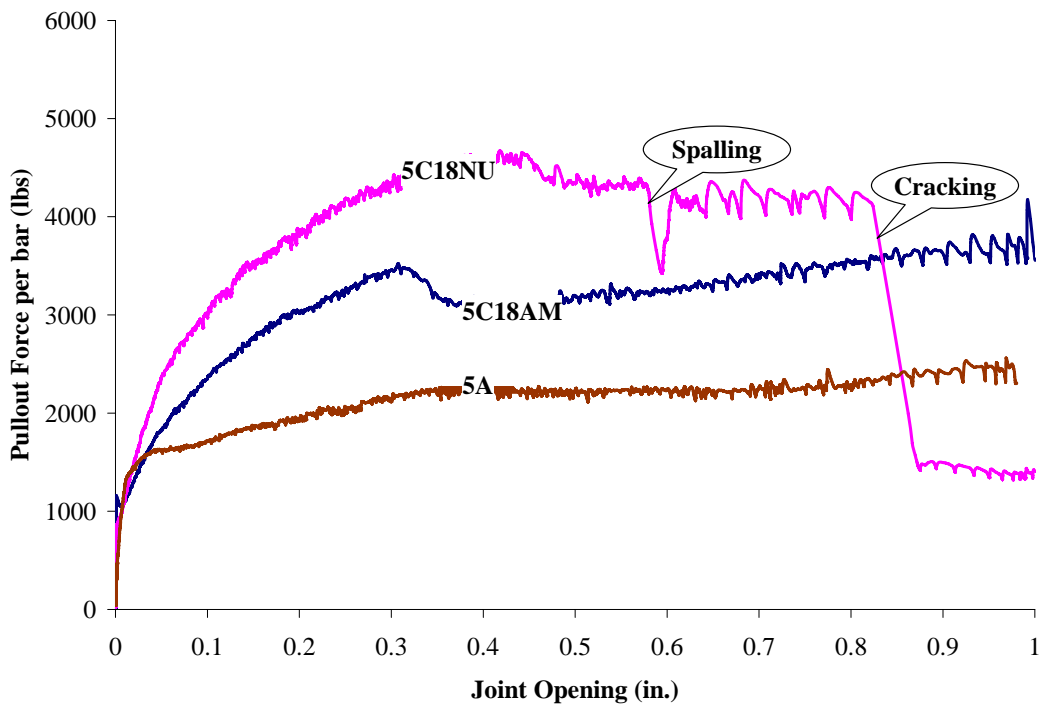


Figure 4.34 Comparison of pullout force vs. joint opening curves of 5C18NU and 5C18AM

Number of Dowels in Test Specimen Size

A comparison of the pullout force per dowel vs. joint opening behavior of one vs. two dowels and three vs. five dowels is presented in this section. Basically, the comparison is made due to difference in specimen size and concrete volume. The smaller specimen could accommodate one or two dowel bars whereas the larger specimen could accommodate three and five dowels.

Horizontal Misalignment

Figure 4.35 and 4.36 compare the results obtained for the test specimens with one and two dowel bars having horizontal misalignment of $1/18$ radians and $1/9$ radians respectively. In figure 4.35, the pullout force per bar to produce joint opening was higher in the 2H18NU followed by the 1H18 and the 2H18U test results. A similar trend was observed in figure 4.36, that illustrates the pullout force per bar in the 2H9NU was greater than the 1H9 and the 2H9U test results. In the slab specimen containing three and five dowel bars, the pullout force per dowel required by the 5H18NU test specimen was consistently higher compared to the results obtained for the 3H18NU test specimen, shown in figure 4.37.

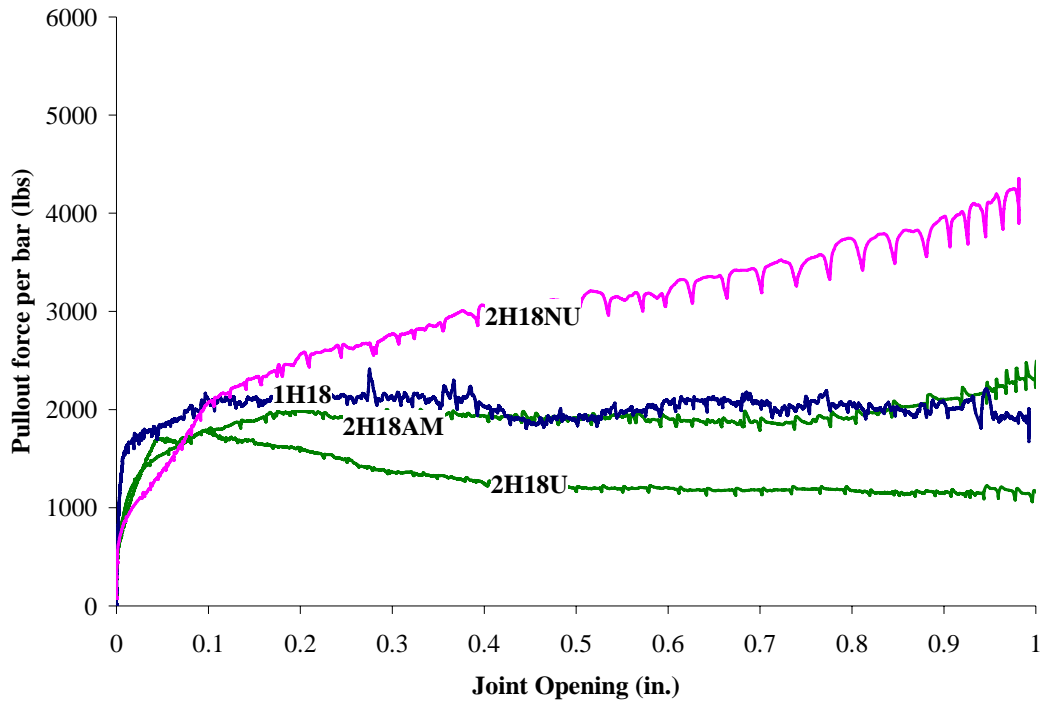


Figure 4.35 Comparison of pullout force vs. joint opening curves of 1H18 and 2-dowel 1/2 in. Horizontal Misalignment (2H18NU, 2H18U, 2H18AM)

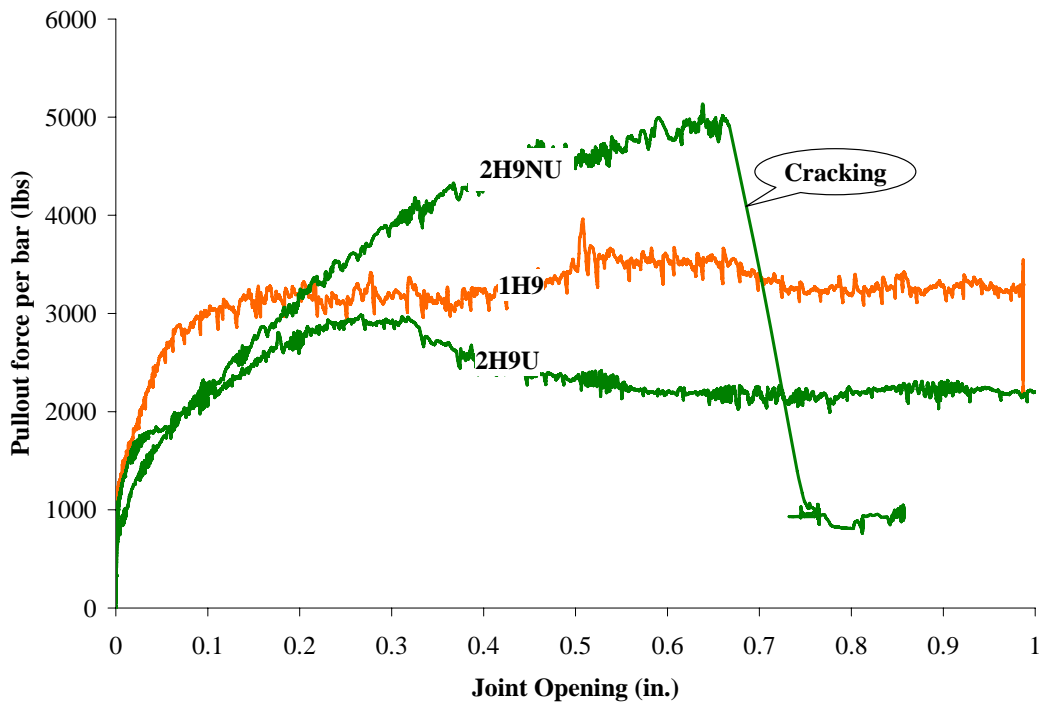


Figure 4.36 Comparison of pullout force vs. joint opening curves of 1H9 and 2-dowel 1 in. Horizontal Misalignment (2H9NU, 2H9U)

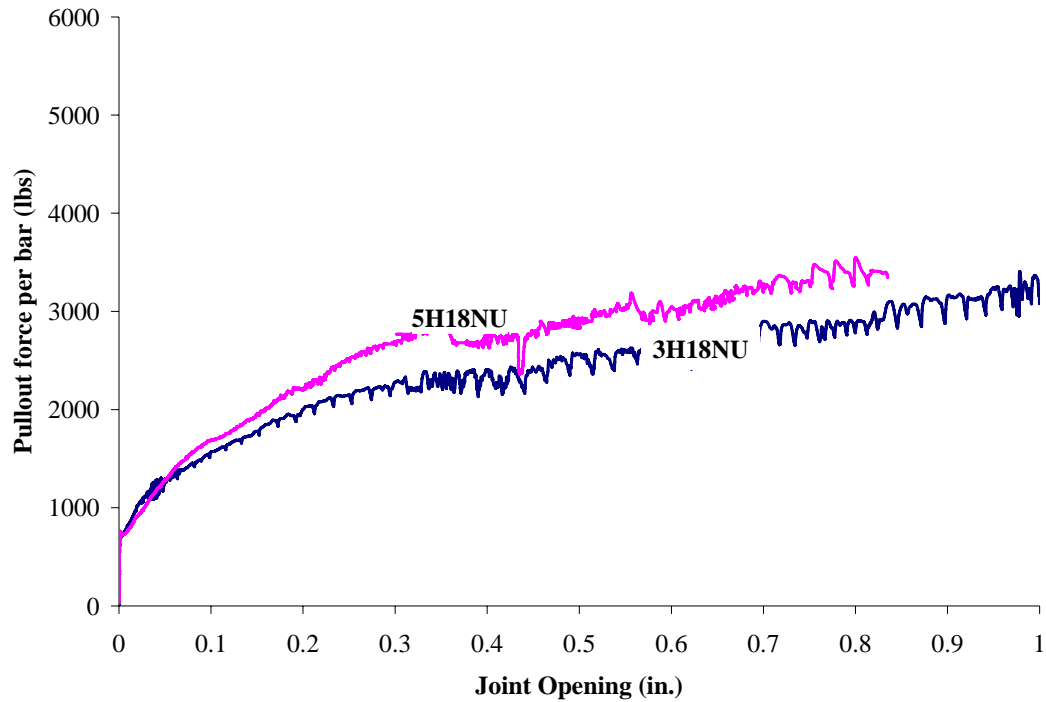


Figure 4.37 Comparison of pullout force vs. joint opening curves of 3H18NU and 5H18NU

Vertical Misalignment:

Figure 4.38 and 4.39 compare the results obtained for the test specimens with one and two dowel bars having vertical misalignment of 1/18 radians and 1/9 radians, respectively. In figure 4.38, similar to the horizontally misaligned dowel bar specimens, the pullout force per bar to produce joint opening was higher in the 2V18NU followed by the 1V18 and the 2V18U test results. In Figure 4.39, the post slip behavior with vertically misaligned bars with a magnitude of 1/9 radians shows that the pullout force per bar in the 2V9U was greater than the 2V9NU followed by the 1V9 test results. In the slab specimen containing three and five dowel bars, the pullout force per dowel required by the 5V18NU test specimen was consistently higher compared to the results obtained for the 3V18NU test specimen, shown in figure 4.40. The 5V18NU test specimen failed due cracking of the concrete slab towards the end of the test.

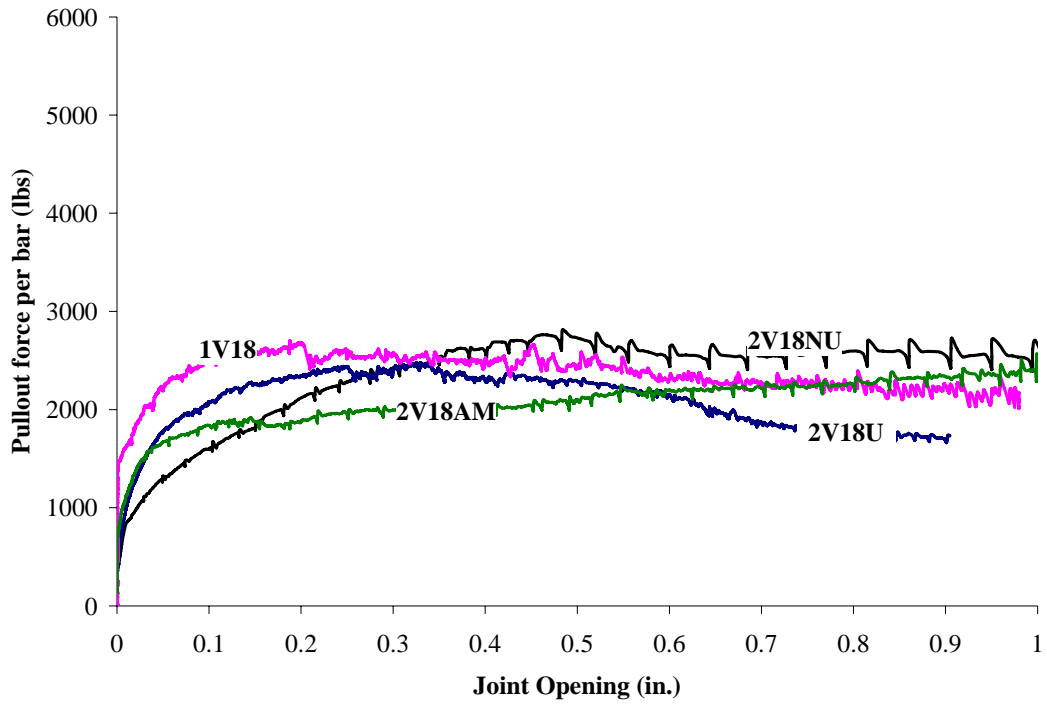


Figure 4.38: Comparison of pullout force vs. joint opening curves of 1V18 and 2-dowel 1/2 in. Vertical Misalignment (2V18NU, 2V18U, 2V18AM)

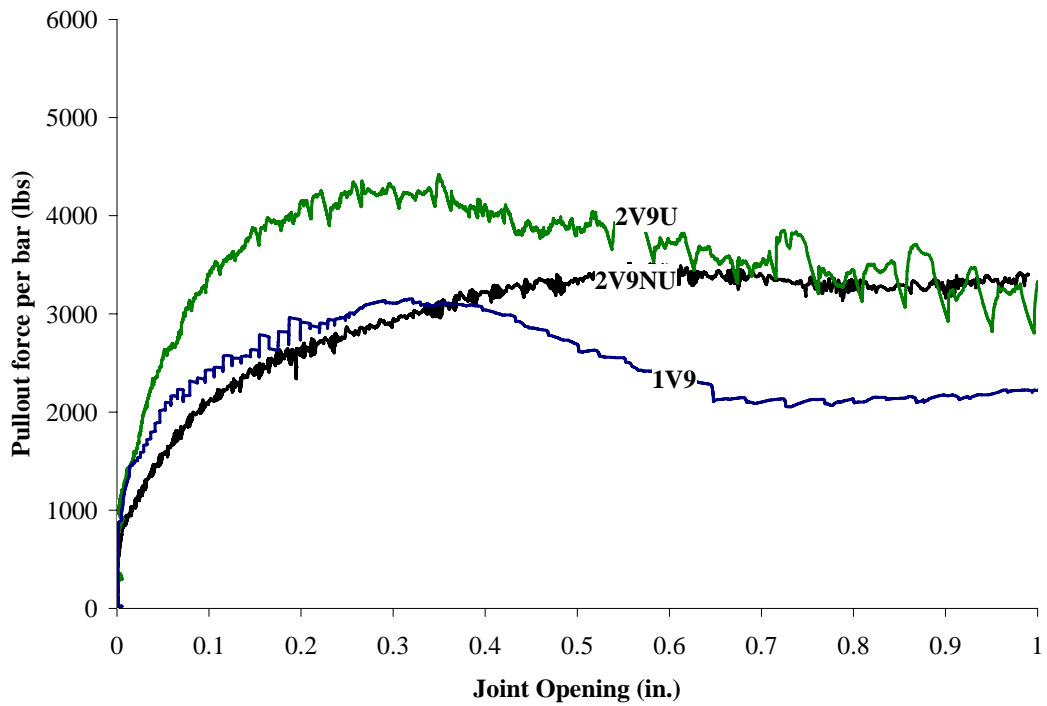


Figure 4.39 Comparison of pullout force vs. joint opening curves of 1V9 and 2-dowel 1 in. Vertical Misalignment (2V9NU, 2V9U)

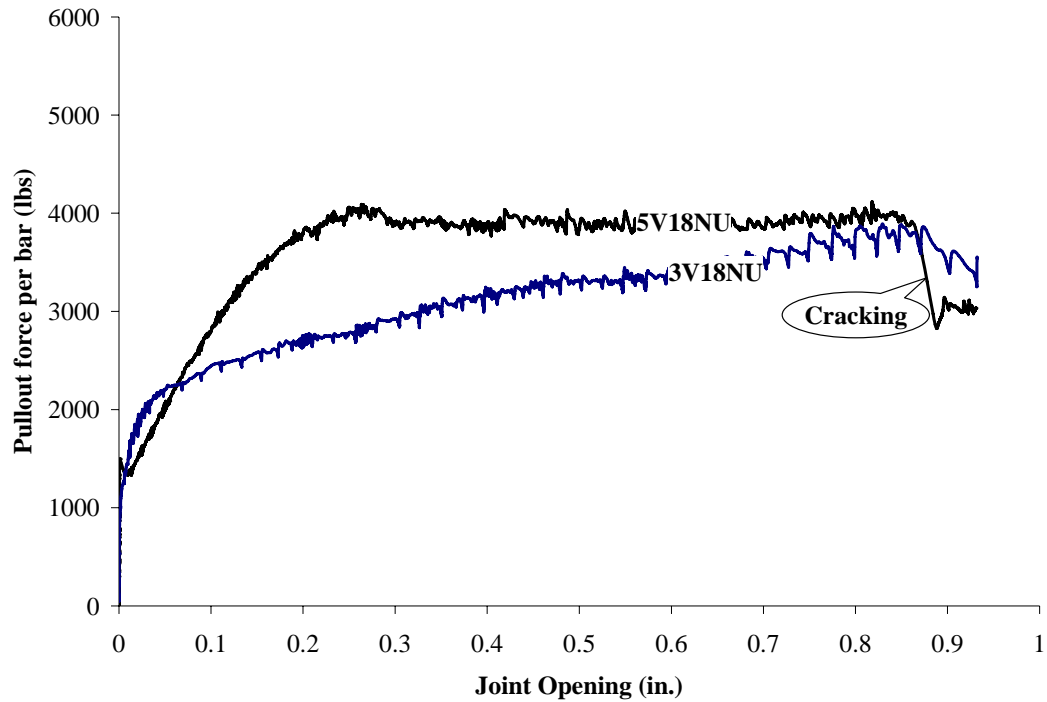


Figure 4.40 Comparison of pullout force vs. joint opening curves of 3V18NU and 5V18NU

Combined Misalignment

Figure 4.41 and 4.42 compare the results obtained for the test specimens with one and two dowel bars having a combined misalignment type of $1/18$ radians and $1/9$ radians, respectively. In figure 4.41, a trend similar to the horizontal and vertical misaligned dowel bars is seen. The pullout force per bar to produce joint opening in the 2C18NU test specimen is much higher followed by the 1C18 and the 2C18U test results. In figure 4.42, the post slip behavior with vertically misaligned bars with a magnitude of $1/9$ radians shows that the pullout force per bar in the 2C9NU was greater than the 2C9U and the 1C9 test results. In the slab specimen containing three and five dowel bars, the pullout force per dowel required by the 5C18NU test specimen was higher compared to the results obtained for the 3C18NU test specimen, shown in figure 4.43. Most of the test

specimens with multiple combined misalignment type showed spalling in the concrete around the dowel bars at the joint. The 5C18NU test specimen failed due to significant spalling and finally cracking of the concrete slab at a very high joint opening.

A comparison of the loads at $\frac{1}{4}$ and $\frac{1}{2}$ in. joint openings for different misalignment scenario has been presented in figures 4.44 and 4.45.

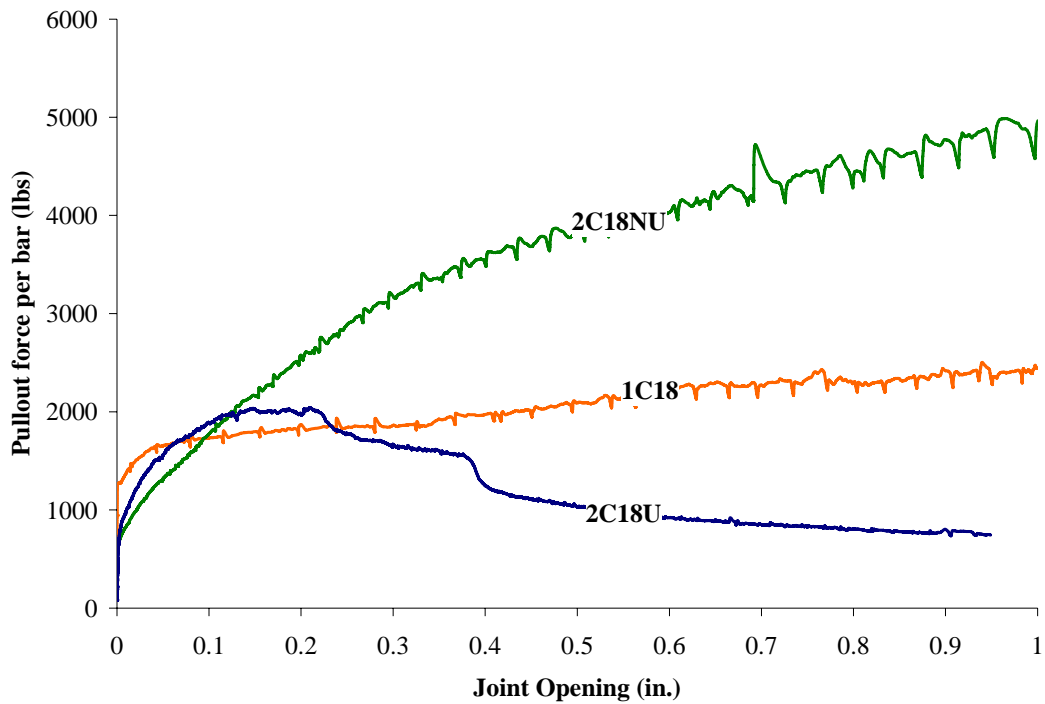


Figure 4.41: Comparison of pullout force vs. joint opening curves of 1C18 and 2-dowel $\frac{1}{2}$ in. Combined Misalignment (2C18NU, 2C18U)

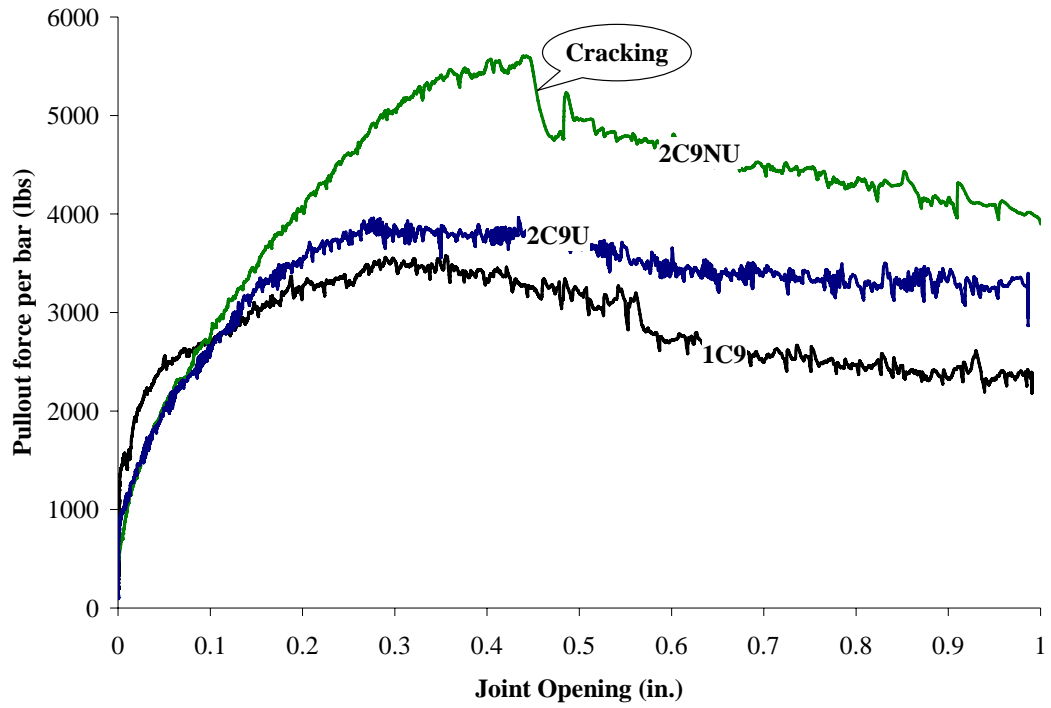


Figure 4.42: Comparison of pullout force vs. joint opening curves of 1C9 and 2-dowel 1 in. Combined Misalignment (2C9NU, 2C9U)

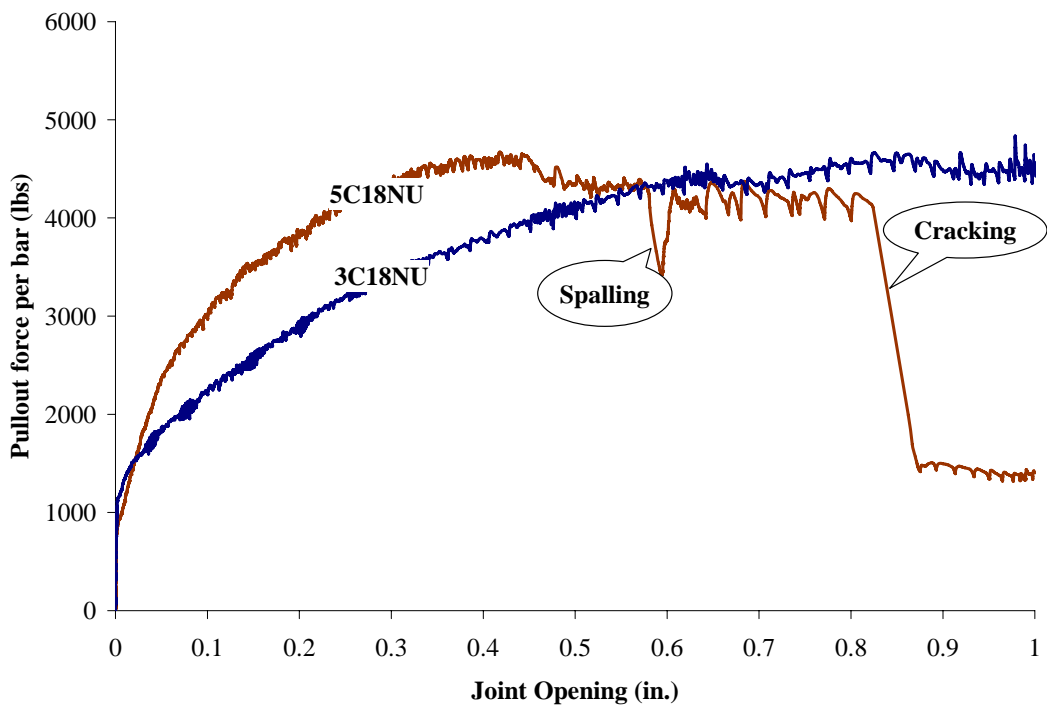


Figure 4.43 Comparison of pullout force vs. joint opening curves of 3C18NU and 5C18NU

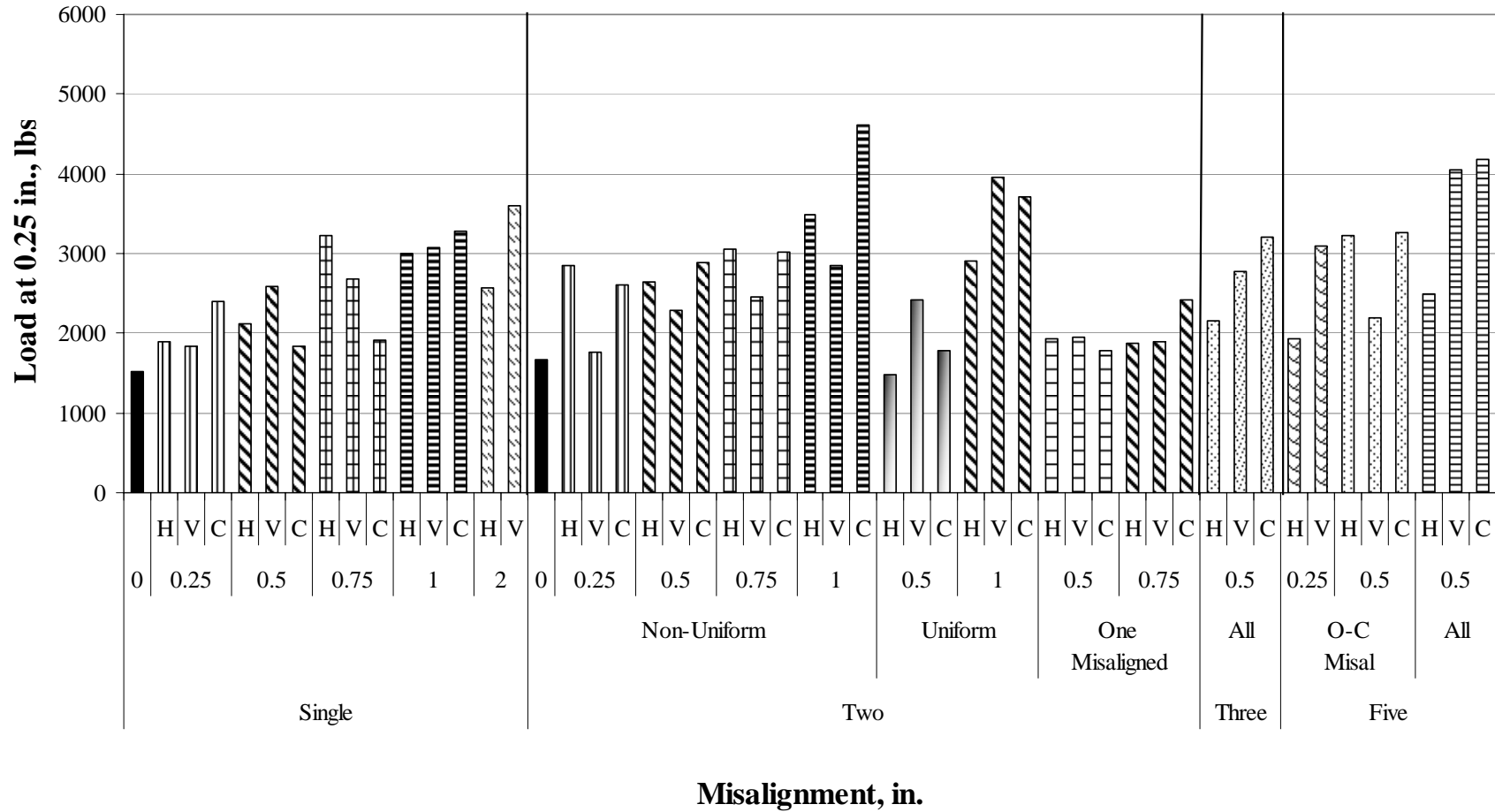


Figure 4.44: Comparison of loads at ¼ in. across different tests of misalignment

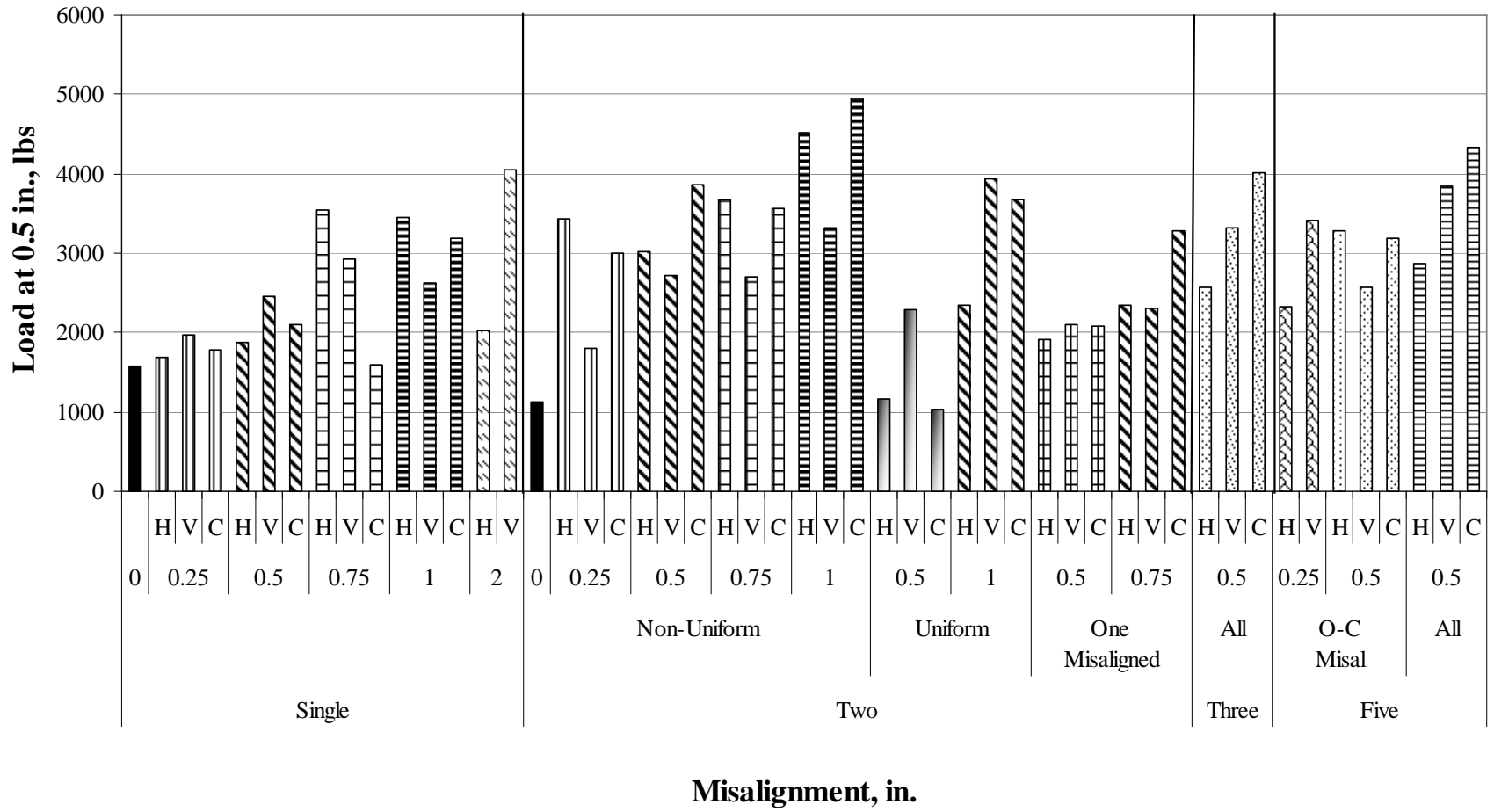


Figure 4.45: Comparison of loads at 1/2 in. across different tests of misalignment

4.2.3 DISTRESSES OBSERVED IN THE TEST SPECIMENS

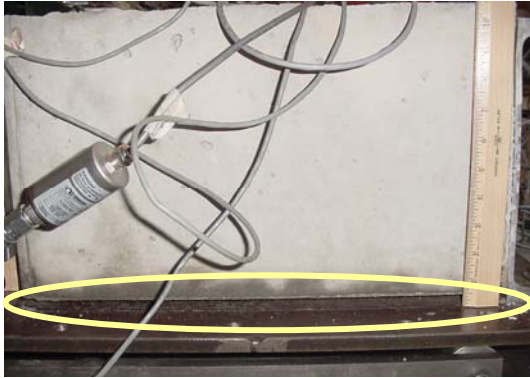
The distresses observed in all the test specimens during the laboratory investigation can be found in Table 4.1 (a), (b) and (c). Some of the “significant” structural distresses such as spalling of concrete, crack patterns, specimen uplift and slab rotation that were documented during the experimental investigation are presented in this section.

Vertically Misaligned Test Specimens

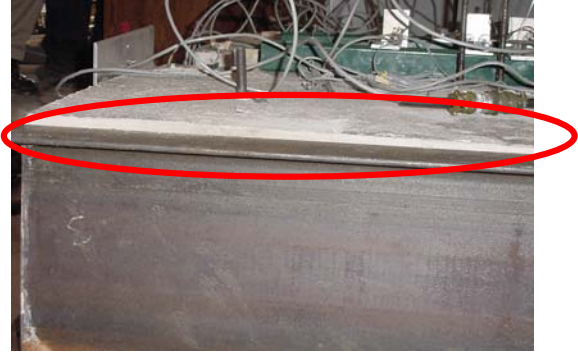
The visual observations in the vertical misaligned dowel bar test specimens are presented below. No distresses such as spalling were observed in the one dowel bar test specimens. In the two, three and five dowel test specimens, different orientation of misaligned dowel bars resulted in different types of distresses such as spalling at the dowel-concrete interface, vertical uplift and cracking of the concrete specimens.

In the 2V9NU test, in addition to surface spalling, the northwest and southeast ends of the slabs lifted up (the ungreased of the two dowel bars). Figure 4.46 (a) gives a diagrammatic representation of the uplift and figures 4.46 (b) and (c) corresponds to the actual vertical uplift at the NW and SE corners of the slab. A similar observation was made in the 2V12NU and 2V18NU test specimens but the magnitude of uplift was not measured.

Cracking of the slab in later stages of the test (at joint openings higher than ½ in.) was observed in the 5V18NU test, shown in figure 4.47. As further load was applied, the crack continued to open, pushing the two halves of the slab apart rather than opening the joint. Thus the test was terminated at a joint opening of 0.93 in.



(b) NW side



(c) SE side

Figure 4.46: Vertical Uplift (2V9NU)

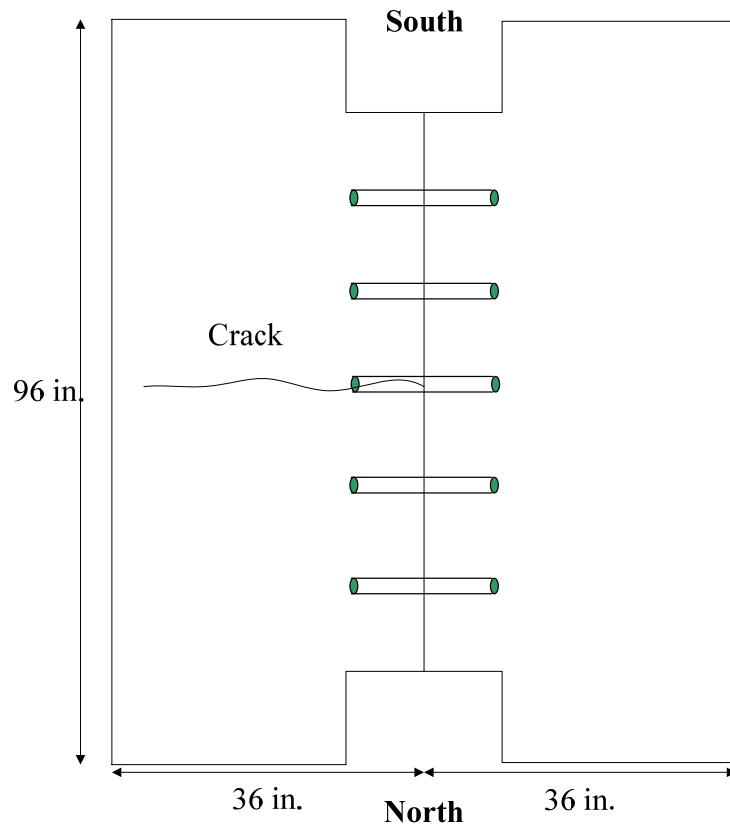


Figure 4.47: Diagrammatic representation of Crack in 5V18NU

Horizontal Misalignment Test Specimens

This section discusses the visual observations documented during the horizontal misalignment tests. In the two, three and five dowel bar test specimens, different combination of misalignment orientation resulted in different distresses such as spalling at the dowel-concrete interface, non-uniform joint opening, and cracking. Spalling was the predominant distress in these tests. The spalls ranged from 2 in. by 2 in. to more than half-depth of the slab. Typical illustrations of spalling and non-uniform joint opening observed in the 2H9U test are shown in figures 4.48 and 4.49, respectively.

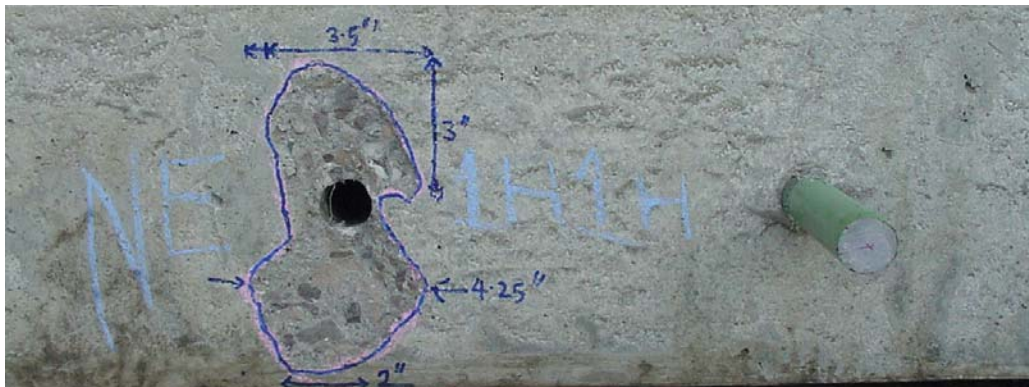


Figure 4.48: Spalling in the 2H9U test

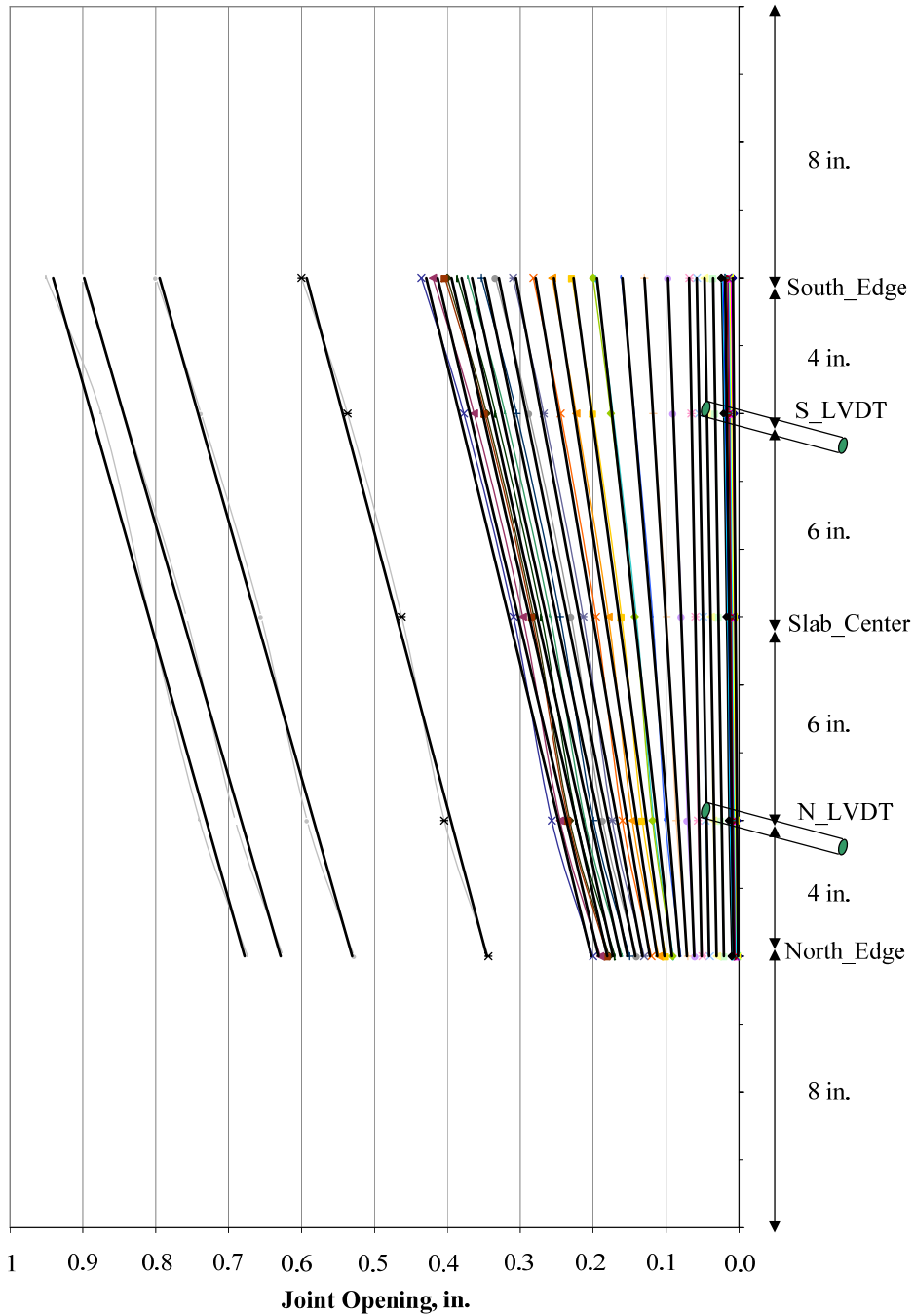
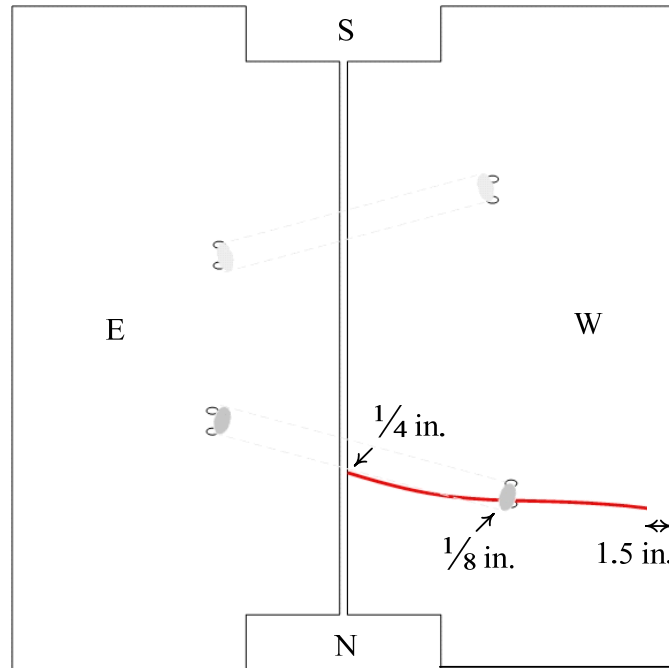


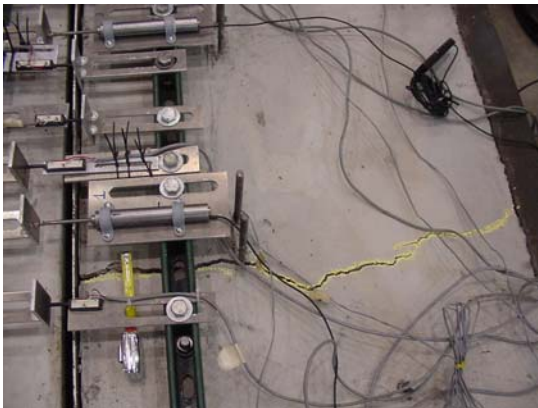
Figure 4.49: Joint opening as a function of distance along the joint (2H1U)

Cracking in the 2H12NU test: At a joint opening of 0.716 in., cracking occurred in the west slab, which resulted in a sudden drop of load from 4198 to 515 lbs, shown in figure 4.11. One full depth crack appeared instantaneously and it split the west slab into two

parts at the dowel bar on the north side. The location of the crack pattern and cracked test specimen is shown in figure 4.50.



(a) Crack Pattern and Initial dimensions



(b) Crack initiation



(c) Crack at end of test

Figure 4.50: Cracking in 2H12NU

Cracking in the 2H9NU test: At a joint opening of 0.668 in., cracking occurred in the west slab, which resulted in a sudden drop in load from 4891 to 1476 lbs. One full depth

crack appeared instantaneously and it split the west slab into two parts at the position of the dowel bar on the north side. The dimensions and position of the crack are shown in figure 4.51. Since the pattern is to the similar to the 2H9NU test, the photographs have not been provided here.

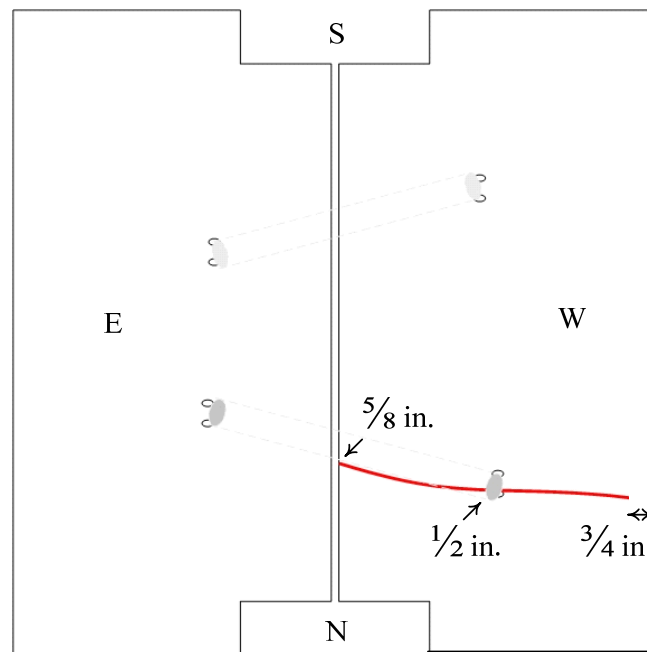


Figure 4.51: Crack pattern and Initial dimensions in 2H9NU

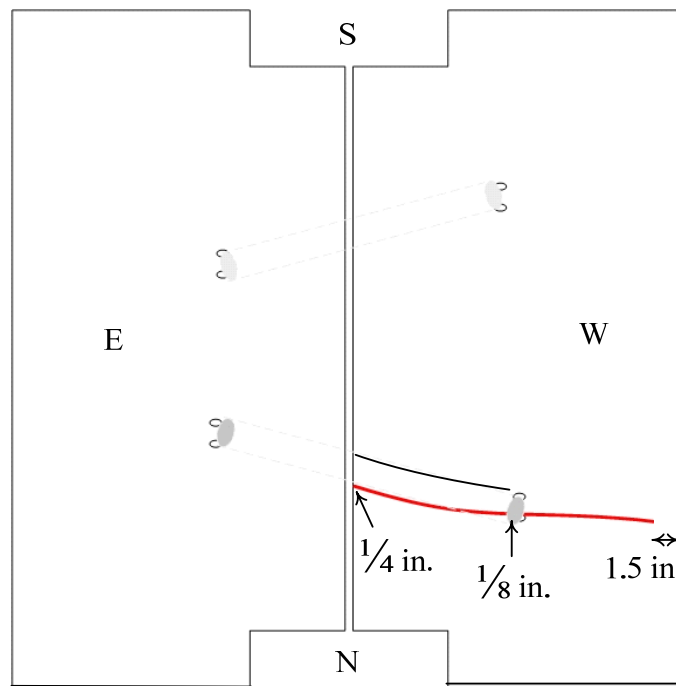
The sudden drop in pressure is captured in the load versus joint opening curve as seen in figure 4.11. As further load was applied, the crack continued to open, pushing the concrete pieces apart rather than opening the joint. Thus the test was stopped at a joint opening of 0.857 in. and the crack width at the joint at the end of the test was $\frac{3}{4}$ in.

Combined Misalignment Test Specimens

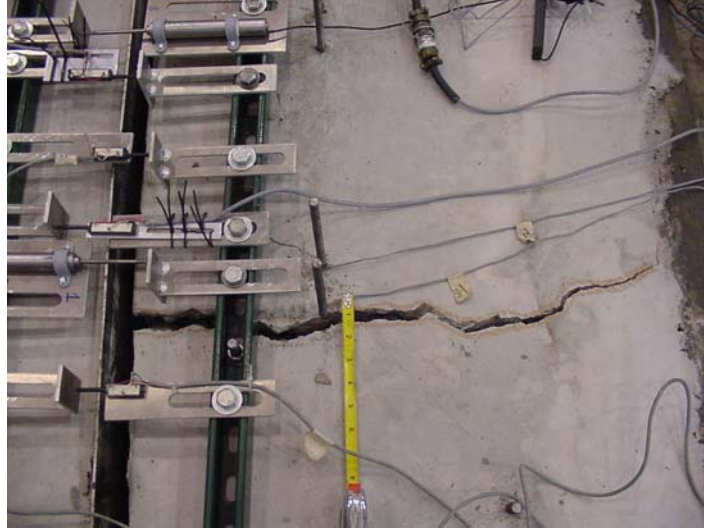
In the single dowel bar test specimens, the only distress observed was spalling at the dowel-concrete interface in the 1C9 test specimen. In the two, three, and five dowel tests, different orientation of misaligned dowel bars resulted in different distresses such as

spalling at the dowel-concrete interface, non-uniform joint opening, and cracking. Spalling was the predominant distress in these tests. The spalls ranged from 2 in. by 2 in. to more than half-depth of the slab. Cracking of slabs observed in the 2C12NU and 2C9NU tests are described below.

Cracking in the 2C12NU test: At a joint opening of 0.949 in., cracking occurred in the west slab, which resulted in a sudden drop of load from 4060 to 1124 lbs, shown in figure 4.19. Two cracks formed on the concrete above the north dowel bar, the schematics of the crack pattern are shown in figure 4.52. One of the cracks was a full-depth crack that appeared instantaneously and split the west slab into two part at the position of the dowel bar on the north side.



(a) Crack Pattern and Initial dimensions



(b) Crack initiation on top of the north dowel

Figure 4.52: Cracking in 2C12NU

Cracking in the 2C9NU test: At a joint opening of 0.447 in., two closely spaced cracks formed in the west slab near the south box cutout, which resulted in a sudden drop of load from 5550 to 4691 lbs, shown in figure 4.19. On further separation of the slabs, it was seen that the crack observed at the surface was a result of the crack that was initiated near the south dowel bar. At the surface, the cracks did not open significantly, but at the west joint face, the crack propagated from one dowel bar to the other. No further cracks were formed. The schematics of the crack pattern and actual cracks are shown in figure 4.53.



(a) Corner cracks observed in the test specimen



(c) Concrete spalling and cracking around misaligned dowel bar in test specimen

Figure 4.53: Corner Cracking in 2C9NU on west side

Cracking in the 5C18NU test: At a joint opening of 0.58 in., spalling occurred near the outer dowels which resulted in a drop in pressure. Cracking of the slab in later stages of the test (at joint openings higher than $\frac{1}{2}$ in.) was also observed. At a joint opening of 0.824 in., a hairline crack occurred in the east slab, near the center dowel bar, the location similar to the location in the 5V18NU test. This crack resulted in a drop in load from 4108 to 1568 lbs, shown in figure 4.23.

The results obtained in the experimental investigation indicate that the distress in the concrete surrounding the misaligned dowel bars depends on the magnitude, orientation and uniformity of misalignment. It is hypothesized that the same effects will be observed when the slab thickness is increased to 12 in. with 1.5 in. diameter dowel bars.

4.3 SUMMARY OF RESULTS

To summarize the results of the laboratory investigations:

- In general, for a given misalignment type, as the magnitude of misalignment was increased, the amount of pullout force per bar to produce joint opening also increased. Test specimens with non-uniform orientation of misaligned dowels required a higher force per bar to produce joint opening compared to the alternate or the uniform orientation of misaligned dowel bars.
- For a given misalignment magnitude, the load induced per dowel to produce joint opening increased as the number of misaligned dowels increased.
- The results indicate that irrespective of the dowel misalignment type (vertical, horizontal or combined) and magnitude (shown in the 1/18 radians and 1/12 radians), the force required to open the joint in a pavement slab with non-uniform misaligned dowel bars is higher as compared to alternate and uniform orientation of misalignments.
- Structural distress such as spalling was observed in the test specimens with non-uniform orientation of dowel bars. Test specimens especially with greater than 1/12 radians non-uniform misalignment magnitude exhibited cracking.

4.4 PULLOUT BEHAVIOR OF MISALIGNED DOWEL BARS

It is hypothesized that an initial bond exists between the dowel and the hardening concrete. This bond is present due to (i) the volumetric changes in the hydrating cement paste and (ii) irregularities along dowel surface. This initial bond generates contact stresses at the dowel concrete interface. These contact stresses generate frictional and axial forces in the dowel bar that resist the free axial movement of the pavement slab

when exposed to thermal expansion and contraction. There are no bearing stresses produced in the concrete during dowel pullout in the case of an aligned dowel bar subjected to pure thermal expansion, as shown in figure 4.54.



Figure 4.54: Aligned dowel bar in concrete pavement slab

However, bearing stresses and frictional shear stresses are produced at the dowel-concrete interface, for joints with misaligned dowel bars, as shown in figure 4.55.

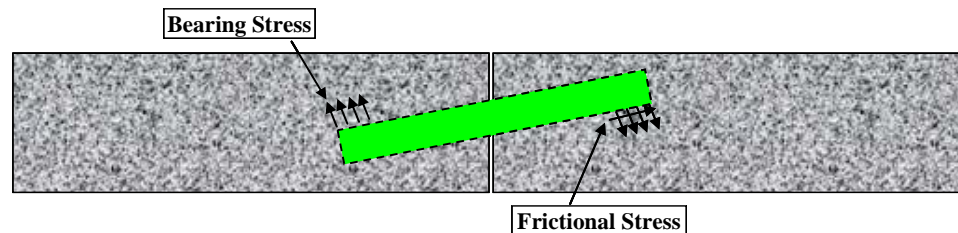


Figure 4.55: Misaligned dowel bar in a concrete pavement slab

Furthermore, as the joint opens due to thermal expansion, the bond between the dowel and concrete is a function of the kinematic friction between the two contacting surfaces. Each of the misalignment type, magnitude, and orientation would cause a certain stress state zone at the interface along the length of the bar and at the joint, which cannot be studied directly through lab observations/tests. There is a need to conduct an analytical study on the dowel concrete interaction to understand the joint opening behavior of misaligned dowel bars.

4.5 DOWEL-CONCRETE INTERACTION

The experimental results presented in the previous sections provide basic information regarding the overall joint opening behavior of concrete pavements with aligned or misaligned dowel bars. The pullout force per dowel-joint opening response of all pavement specimens consists of two regions: (1) the initial fully bonded region, and (2) the post-slip debonded region. In the initial fully bonded region, the load applied across the joint increases without any slip or joint opening. Slip occurs after the pullout force per dowel increases beyond a certain threshold value (1124 lbs -1574 lbs). In the post-slip region, as the joint is opened to 1 in., the pullout force per dowel undergoes hardening (increases) and softening (decreases) depending on the misalignment type, magnitude, and distribution. The effects of these parameters on the post-slip joint opening behavior have been presented in the previous section.

The pullout force per dowel-joint opening behavior of the pavement specimens can be used to estimate averaged bond shear stress-slip strain behavior of the dowel-concrete interfaces. The averaged bond shear stress can be estimated as the pullout force per dowel divided by the surface area ($\pi \times 1.25 \times 9 \text{ in}^2$) of the greased (debonding) side of the dowel. The slip strain can be estimated by dividing the joint opening by the embedded length (9 in.) of the greased side of the dowel. The averaged bond shear stress-slip strain responses for specimens 1A and 2A (with zero misalignment) provide information regarding the overall longitudinal bond interaction between straight (aligned) dowels and the surrounding concrete; see Figure 4.56(a). The averaged bond shear stress-slip strain responses for the remaining specimens provide information regarding the overall longitudinal bond between the misaligned dowel and the surrounding concrete,

while including the effects of friction and bearing stresses (from dowel misalignment); see Figure 4.56(b). For all specimens, slip occurred after the pullout force per dowel increased above 1124 lbs -1574 lbs, which corresponds to average bond shear stress (τ_b) of 30.0 psi to 43.0 psi.

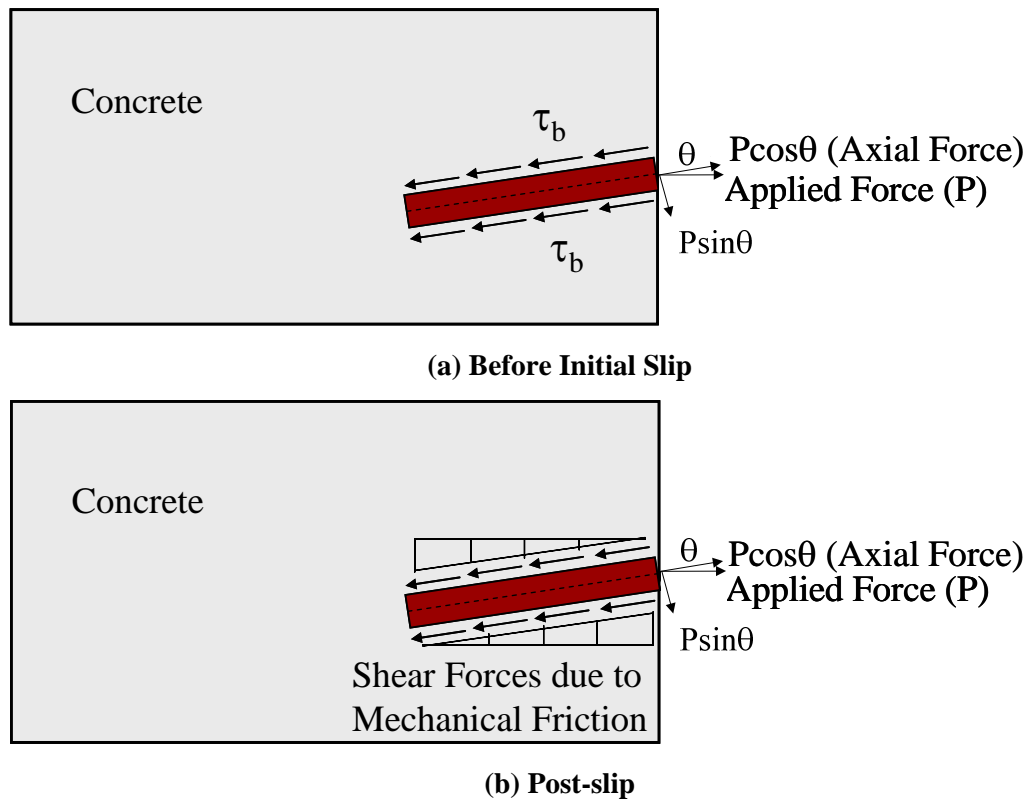


Figure 4.56: Forces on a misaligned dowel and surrounding concrete

In chapter 5, the assumptions made and the results from the three dimensional finite element models are presented.

CHAPTER 5

DEVELOPMENT OF 3D FINITE ELEMENT MODELS

5.1 INTRODUCTION

This chapter presents the development of the three dimensional (3D) nonlinear finite element models for the concrete pavement specimens. The input parameters for the steel dowel and concrete material model are presented. The development and calibration of the 3D finite element model for the pullout behavior of single and multiple misaligned dowel bars are also presented in this chapter.

5.2 NEED FOR A 3D FINITE ELEMENT MODEL

The experimental results presented in chapter 4 provide basic information regarding the overall joint opening behavior of concrete pavements with aligned or misaligned dowel bars. The experimental results indicate that the force-joint opening behavior consists of two regions: (i) the initial fully bonded region, and (ii) the post-slip debonded region. Initial slip occurs when the load applied across the joint increases beyond the threshold limit corresponding to the average bond stress (τ_b). The post-slip (debonded) region includes hardening and softening behavior corresponding to increase or decrease in the load applied across the joint depending on the misalignment type, magnitude and distribution of dowel bars. The experimental results indicate that larger misalignment results in larger pullout forces, which can potentially lead to spalling or cracking type distress around the dowel bars in some cases.

A major limitation of the experimental investigations is that they cannot provide detailed information or insight regarding the interaction between the dowel bar and the surrounding concrete. The experimental results and observations do not provide direct knowledge regarding: (a) the longitudinal bond and transverse (bearing) interaction between the dowel and the concrete slabs; (b) the complex 3D stress states in the concrete and (c) the structural distresses produced by stress concentrations and excessive stresses in the concrete surrounding the dowel bars. In light of these limitations analytical models and results will provide a better understanding of the mechanics of dowel concrete interaction, the 3D stresses and the distress (damage) produced due to misaligned dowels in the pavement slabs.

5.3 THE 3D FINITE ELEMENT MODEL – ELEMENT SELECTION

The concrete pavement specimens are modeled as two concrete slabs connected at the joint using 1.25 in. diameter steel dowel bars. The dowel bar is placed in the center of the joint at mid depth. In case of multiple dowel bar specimens, the dowel bars are placed at a distance of 12 in. on center. Three dimensional (3D) first order reduced integration continuum elements (C3D8R - Bricks) are used to model the concrete slab and the steel dowel bars. These elements are versatile and can be used in models for simple linear analysis or for complex nonlinear analyses involving contact, plasticity and large deformations. The typical solid elements in Abaqus are shown in figure 5.1. A typical mesh discretization of the concrete and dowel bar is shown in figure 5.2.

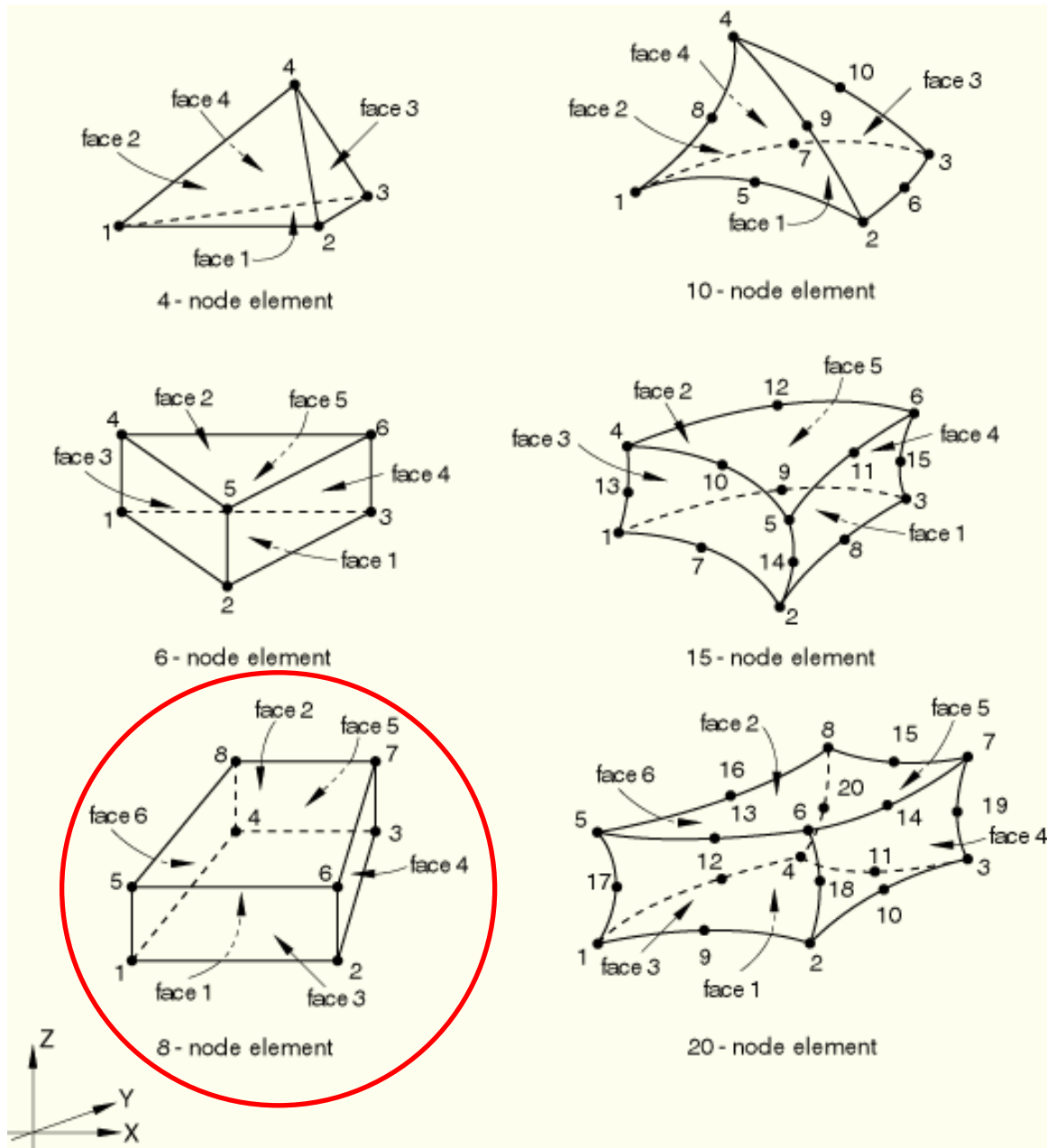
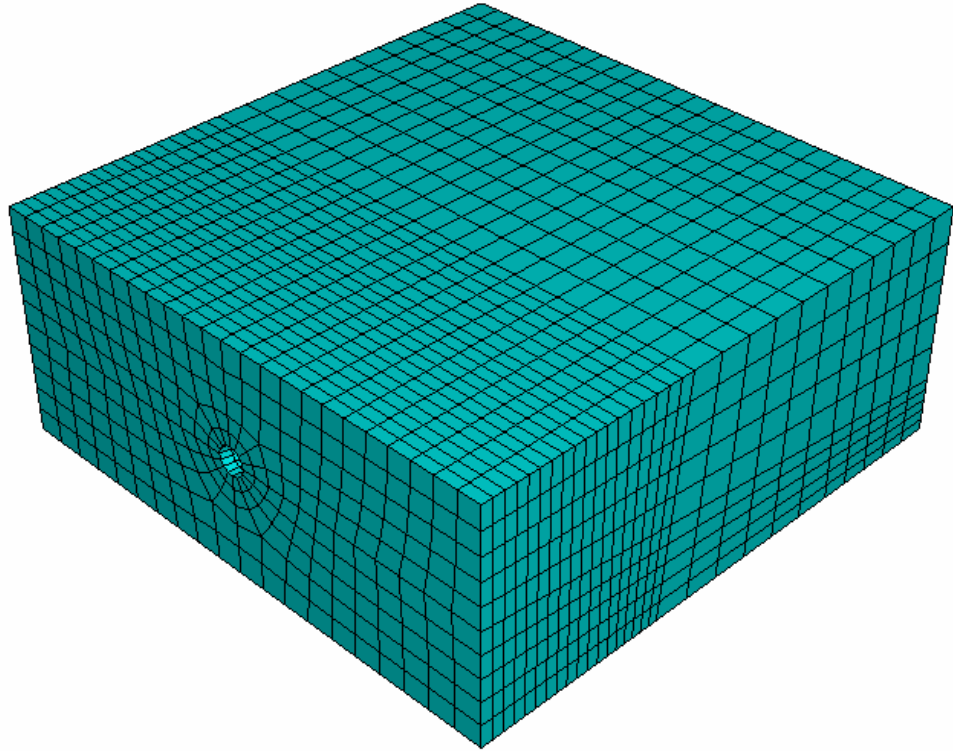
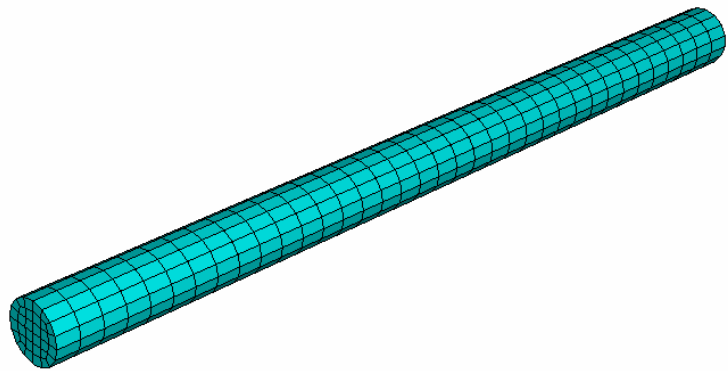


Figure 5.1: Abaqus Solid element Library (Abaqus User Manual 2004)



(a) Concrete Slab discretized using brick elements for a single dowel bar



(b) Dowel bar (Dia 1.25in. and 18 in. length) discretized using brick elements

Figure 5.2: Finite Element Model discretization of the concrete slab and dowel bar.

5.4 MATERIAL MODEL – BEHAVIOR AND CALIBRATION

The three dimensional (3D) finite element models were developed using Abaqus because it includes a robust concrete damage plasticity and cracking model that is needed for this research. The concrete elements were modeled with the nonlinear concrete damaged plasticity material model. The steel elements were provided with isotropic multiaxial elastic material model.

5.4.1 TYPES OF CONCRETE MATERIAL MODELS

There are currently three concrete models to model plain and reinforced concrete in Abaqus (2004). These include the smeared cracking model, the concrete damage plasticity model and the cracking model for concrete.

5.4.1.1 The Smeared Cracking Model

This model is appropriate for modeling the behavior of concrete structures subjected to *monotonic loading* under fairly low confining pressures (less than four to five times the uniaxial compressive stress). This model assumes cracking as the main failure mechanism. Cracking is assumed to occur when the stresses reach the failure surface defined in the *p-q plane* also called the crack detection surface and *p-* is the first stress invariant and *q-* is the second stress invariant of the deviatoric stress. This model assumes a smeared cracking approach, which does not track the individual micro cracks at each numerical integration point. The presence of a crack affects the stresses and material stiffness associated with that integration point. The model uses a multi-axial plasticity model when the stresses are compressive. This model uses a two parameter

Drucker-Prager yield surface, associated flow rule and isotropic hardening. As the model assumes an associative flow rule, it simplifies the actual behavior and over predicts the inelastic strain when concrete is strained beyond the ultimate stress point.

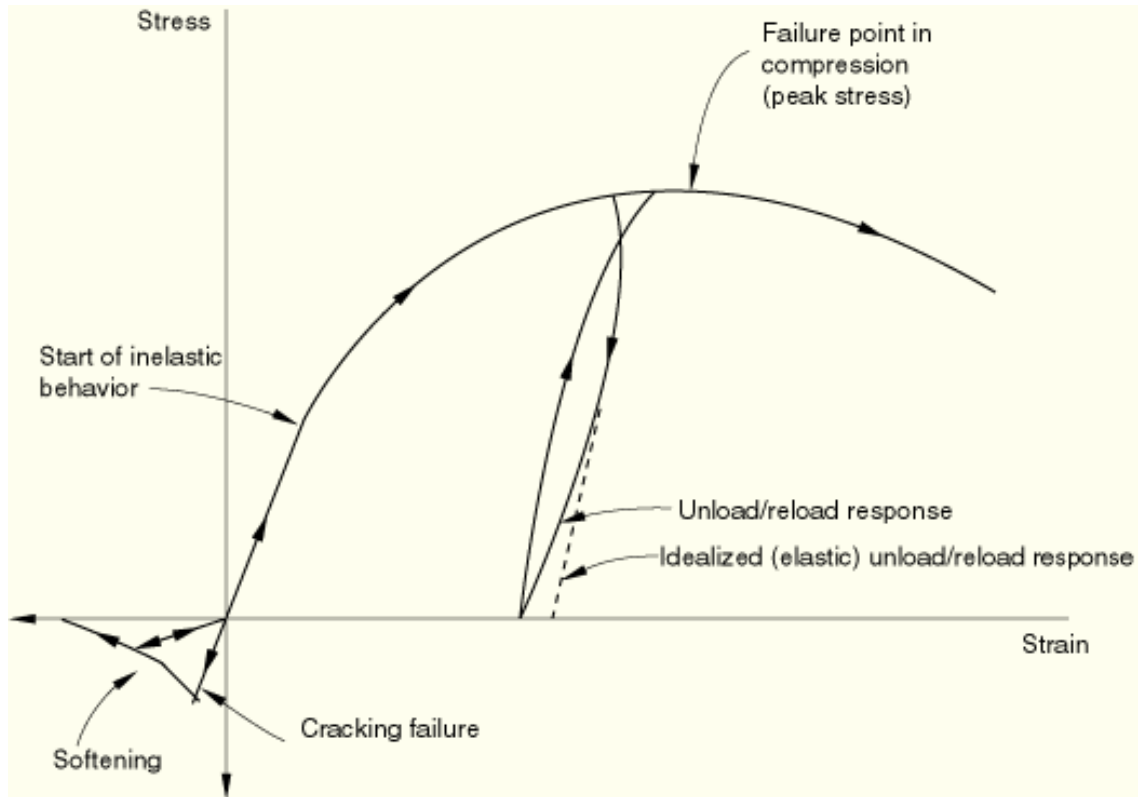


Figure 5.3: Uniaxial behavior of plain concrete (Abaqus User Manual 2004)

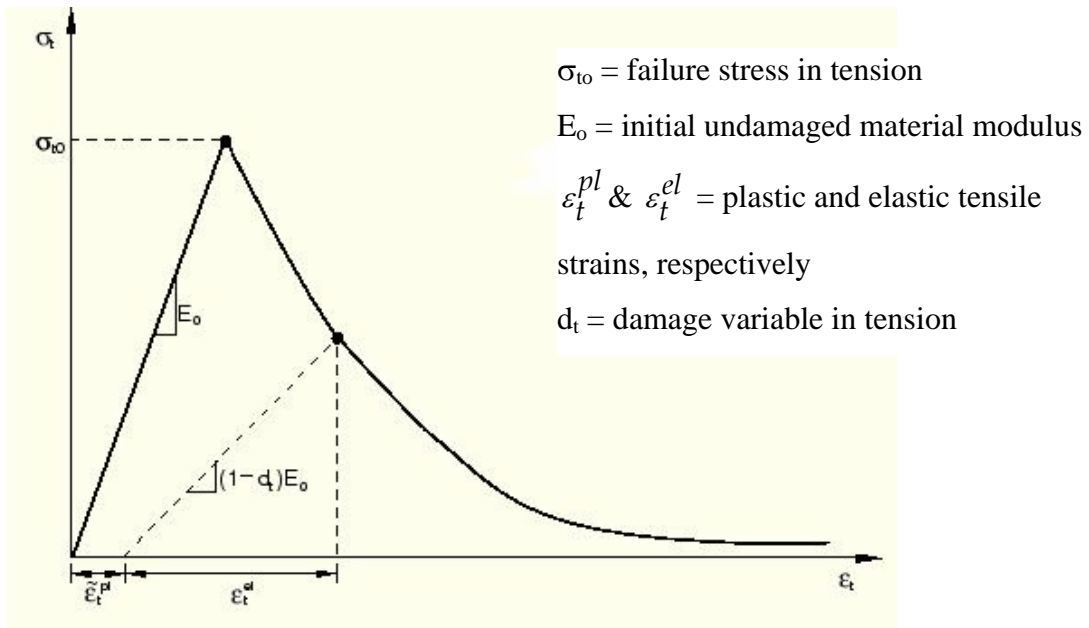
As shown in figure 5.3, as the compression stresses increases, the material undergoes inelastic straining in the form of hardening followed by eventual softening. Upon unloading the model assumes an idealized elastic unloading and re-loading response. In reality the unloading response of the material is slightly softer than the initial elastic response. This model makes no attempt to predict the cyclic or dynamic response as it was developed primarily for applications related to monotonically applied loading.

5.4.1.2 The Cracking Model for Concrete

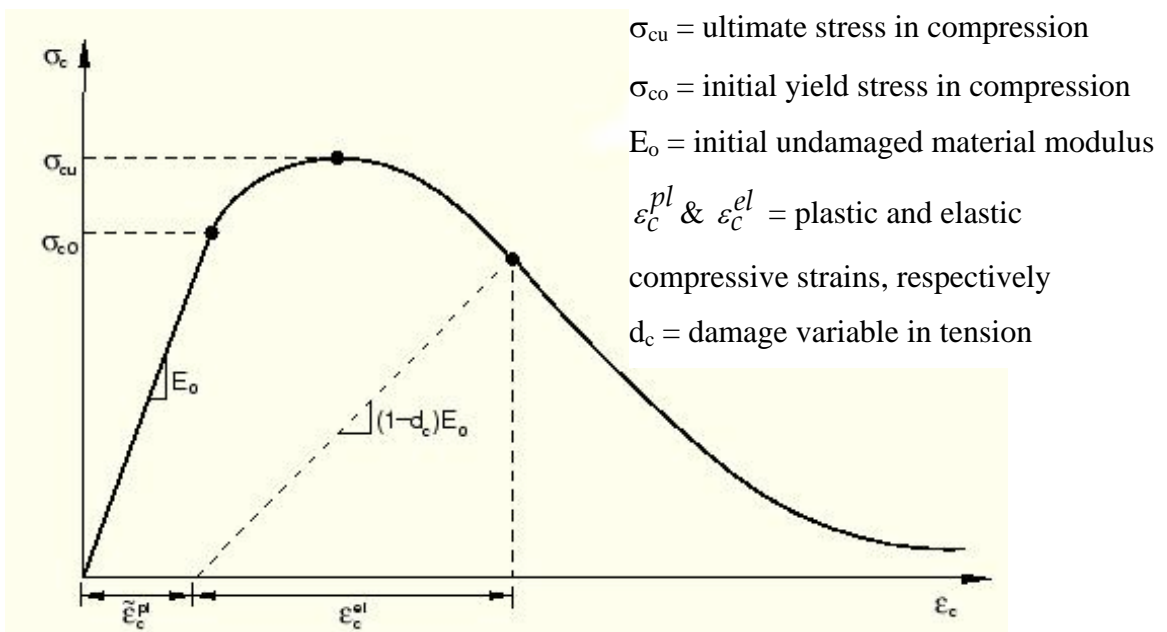
This model is used for modeling concrete structures subjected to dynamic loading only. The primary failure mechanism is dominated by tensile cracking of concrete. In compression, the model behaves linear elastic. The specialty of this model is that it allows removal of elements after failure. Failure is defined similar to the smeared cracking model in terms of crack to determine the discontinuous behavior of concrete. The model uses a simple Rankine criterion which states that crack forms when the maximum tensile stress exceeds the tensile strength of the material.

5.4.1.3 The Concrete Damage Plasticity Model

This concrete model is very versatile and capable of predicting the behavior of concrete structures subjected to monotonic, cyclic and / or dynamic loading. It assumes two main failure mechanisms, i.e., tensile cracking and compressive crushing of the concrete material. In compression, the model uses a multi-axial plasticity model with non-associated flow and an isotropic scalar hardening. The model in tension uses a multi-axial damage elasticity model. The equivalent tensile and compressive strains, PEEQT and PEEQ, as the hardening variables control the evolution of the yield surface. The model behavior in uniaxial tension and compression is shown in figure 5.4. The input parameters for the material model are explained in detail in the latter sections of this chapter.



(a) Uniaxial Tensile Loading



(b) Uniaxial compressive loading

Figure 5.4: Typical concrete uniaxial stress –strain curve in tension and compression (Abaqus User Manual 2004)

5.4.2 FEATURES OF CONCRETE BEHAVIOR

Concrete is a composite material that consists of coarse aggregates and a continuous cement paste and fine aggregate particles. Its mechanical behavior is complex due to the structure of the composite material. The stress-strain behavior is influenced by the development of micro- and macro-cracking of the material. The constitutive behavior of concrete under various loading conditions has been well documented in the published literature. A variety of constitutive models have been proposed for concrete, the Mohr-Coulomb model, the Drucker-Prager model, William-Warnke model, Ottosen model, etc. The aim of these models is to mathematically reproduce the stress-strain behavior of concrete.

Concrete exhibits a nonlinear stress-strain behavior during loading and has a significant irreversible strain upon loading. Under confining pressures and compressive loading, concrete shows ductile behavior. These irreversible deformations in concrete are modeled using the theory of plasticity. There are three basic assumptions in any plasticity model (Chen and Han, 1995):

- (i) An initial yield surface in the stress space that defines the stress levels at which plastic deformation begins.
- (ii) A flow rule which is related to a plastic potential function and gives an incremental plastic stress-strain relation.
- (iii) A hardening rule that defines the change of loading surface as well as the change of the hardening properties of the material during the course of plastic flow.

The concrete models typically differ from each other in the shape of the failure and loading surfaces, the hardening rule, and the flow rule. As shown in figure 5.5, in the hydrostatic plane (details about this can be found in Chen & Han 1995), the failure surface encloses all the loading surfaces and serves as a bounding surface which is assumed to remain unchanged during loading. The initial yield surface has a closed shape. During hardening, the loading surface expands and changes its shape from the initial yield surface to the final shape that matches with the failure surface.

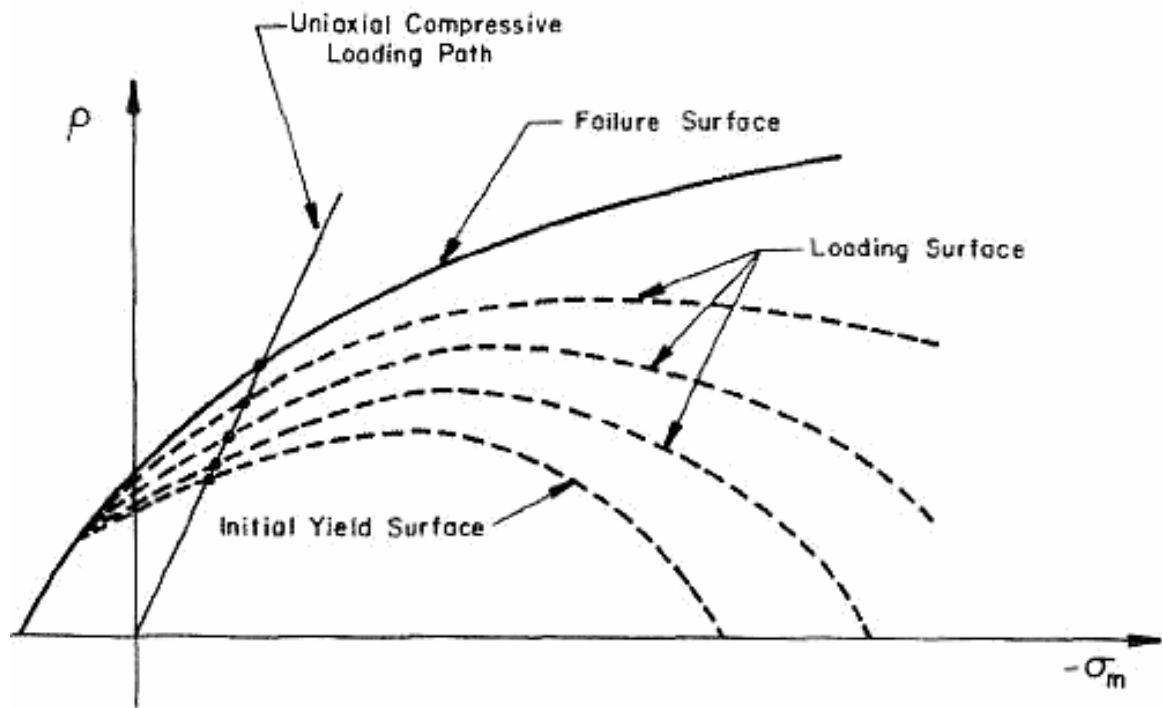


Figure 5.5: A plasticity hardening model for concrete (Chen and Han, 1995)

Concrete exhibits nonlinear volume change during hardening. Experimental results have indicated that under compressive loadings, inelastic volume contraction occurs at the beginning of yielding and volume dilation occurs at 75 to 90% of ultimate

(f_c) stress. This basically violates the associated flow rule and a plastic potential function other than the yield surface is used for the flow rule.

A schematic of hardening and flow for the linear Drucker Prager model in the deviatoric plane (details about this can be found in Chen & Han 1995) is shown in figure 5.6. The associated flow rule assumes that the material friction angle β to be equal to the material dilation angle ψ . For granular materials and concrete, the non-associated flow rule is assumed in the p - q plane, in the sense that the flow is assumed to be normal to the yield surface in the Π plane but at an angle ψ to the q -axis in the p - q plane, where $\psi < \beta$. If $\psi > 0$, the material dilates, hence ψ is referred to as the dilation angle. This flow potential is continuous and smooth and it ensures that the flow direction is defined uniquely.

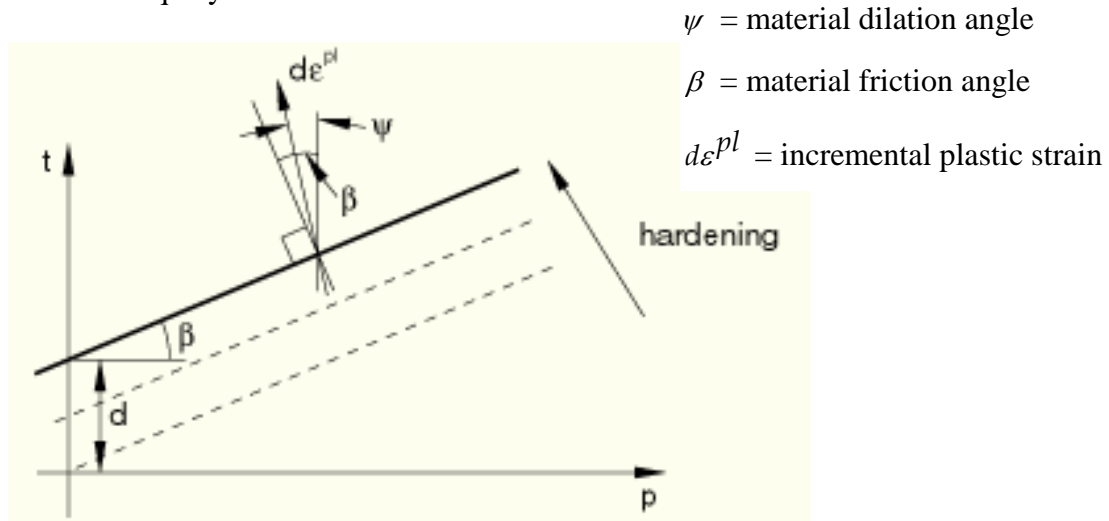


Figure 5.6: Schematic of yield surface and flow in the meridional plane. (Abaqus User Manual 2004)

The concrete damage plasticity model was used in this research study. It uses the following definitions for the yield surface and the flow potential.

Yield Surface: The plastic damage concrete model uses a yield condition based on the yield function proposed by Lubliner et al (1989) and incorporates the modifications

proposed by Lee and Fenves (1998) to account for the different evolution of strength under tension and compression. In terms of effective stresses, the yield function takes the form:

$$F(\bar{\sigma}, \tilde{\varepsilon}^{pl}) = \frac{1}{1-\alpha} (\bar{q} - 3\alpha\bar{p} + \beta(\tilde{\varepsilon}^{pl}) \langle \hat{\sigma}_{\max} \rangle - \gamma \langle -\hat{\sigma}_{\max} \rangle) - \bar{\sigma}_c(\tilde{\varepsilon}_c^{pl}) = 0$$

.....Equation 5.1

where,

$$\bar{p} = \frac{1}{3} \bar{\sigma} : I \text{ is the effective hydrostatic pressure;}$$

$$q = \sqrt{\frac{3}{2} \bar{S} : \bar{S}} \text{ is the Mises equivalent stress, where } \bar{S} = \bar{p}I + \bar{\sigma} \text{ is the deviatoric}$$

part of the effective stress tensor $\bar{\sigma}$;

$$\alpha = \frac{\left(\frac{\sigma_{bo}}{\sigma_{co}}\right) - 1}{2\left(\frac{\sigma_{bo}}{\sigma_{co}}\right) - 1}; 0 \leq \alpha \leq 0.5 ; \gamma = \frac{3(1 - K_c)}{2K_c - 1}; \beta = \frac{\bar{\sigma}_c(\tilde{\varepsilon}_c^{pl})}{\bar{\sigma}_t(\tilde{\varepsilon}_t^{pl})} (1 - \alpha) - (1 + \alpha)$$

where α and γ are material constants.

$$\frac{\sigma_{bo}}{\sigma_{co}} = \text{ratio of the initial equibiaxial compressive yield stress to initial uniaxial}$$

compressive yield stress (experimental values range from 1.10 to 1.16 from Lubliner et al (1998));

K_c = ratio of the second stress invariant on the tensile meridian to that on the compressive meridian at initial yield for any given value of pressure invariant p. Note that the value of K_c (default 2/3) should vary $0.5 < K_c < 1$

$$\hat{\sigma}_{\max} = \text{max principal effective stress}$$

The evolution of the yield surface is controlled by two hardening variables, $\tilde{\varepsilon}_t^{pl}$ and $\tilde{\varepsilon}_c^{pl}$ which are defined as the equivalent tensile (PEEQT) and compressive strains (PEEQ) that are linked to the failure mechanisms in tension and compression respectively.

Flow Rule and Potential: The concrete damaged plasticity model assumes non-associated potential plastic flow. This flow potential, which is continuous and smooth, ensures that the flow direction is always uniquely defined. The flow potential G used for this model is the Drucker-Prager hyperbolic function:

$$G = \sqrt{(\varepsilon \sigma_{to} \tan \psi)^2 + \bar{q}^2} - \bar{p} \tan \psi \quad \dots\dots\dots \text{Equation 5.2}$$

where,

ψ = the dilation angle measure in the $p - q$ plane at high confining pressure (measured in degrees)

σ_{to} = the uniaxial tensile stress at failure

ε = eccentricity parameter, defining the rate at which the function approaches the asymptote, default is 0.1.

The flow rule is given as, $d\varepsilon_{ij}^{pl} = d\lambda \frac{\partial G}{\partial \sigma_{ij}}$ Equation 5.3

The input parameters that were considered for the nonlinear concrete damage plasticity material and isotropic elastic material model for steel is presented in the next section

5.4.3 INPUT PARAMETERS FOR THE CONCRETE MATERIAL MODEL

The input parameters required for the defining concrete material model are: (i) the uniaxial compression stress- strain curve; (ii) the uniaxial tension stiffening stress–strain curve, (iii) the volumetric dilation angle ψ , (iv) the biaxial compression strength ratio

σ_{bc} , and (v) the ratio of tensile-to-compressive meridian K . These input parameters for the model are defined as follows:

The uniaxial compression stress-strain curve was defined using the experimentally measured properties such as; elastic modulus E_c and compressive strength f'_c and the modified Popovic's empirical stress-strain model recommended by Collins et al. (1992). A typical uniaxial compressive stress-strain curve for 3500 psi concrete is shown in figure 5.8.

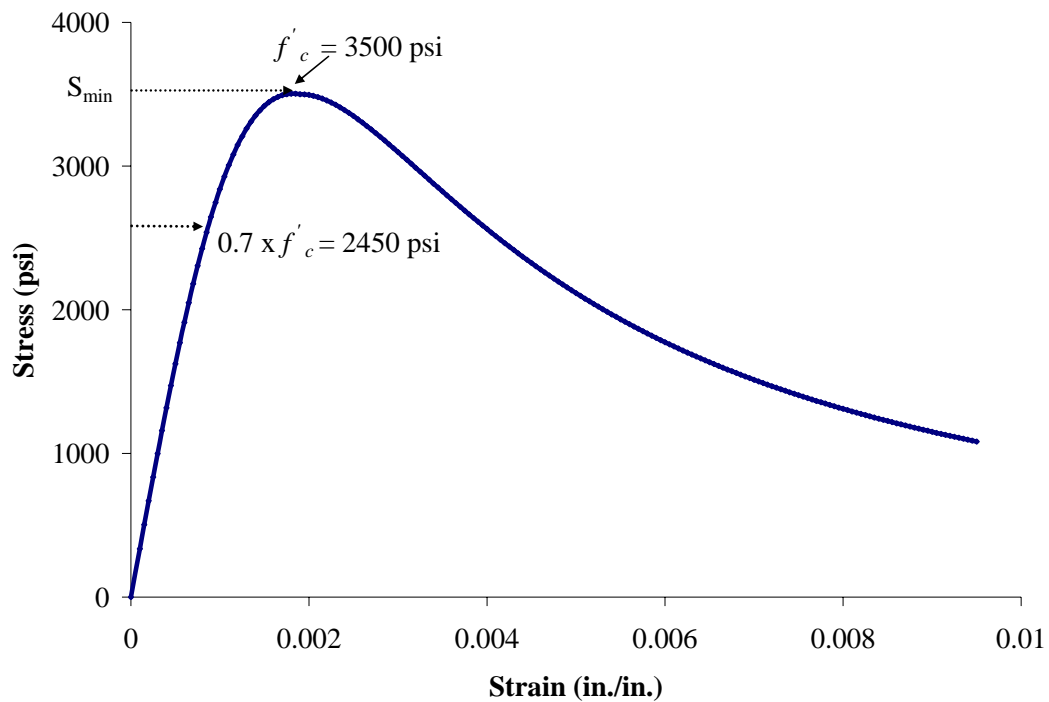


Figure 5.8: Typical uniaxial compressive strength of concrete, Collins et al (1992)

The tension stiffening stress-strain curve was developed using the fracture energy criterion, Abaqus (2004). The post failure response of concrete in the model can be defined using a stress-strain response. The post failure stress-strain response usually causes mesh sensitivity and is not recommended when there is no steel reinforcement to

arrest cracking of the concrete material. Instead, the Hillerborg (1976) approach of using fracture energy criterion to model the post failure response is used. Hillerborg defines the energy required to open a unit area of crack, G_f as a material parameter, using brittle fracture concepts. In this approach the model uses the stress-displacement response, shown in figure 5.9, instead of the stress-strain response to predict the cracking behavior of concrete. Using this concept, fracture energy, G_f , and the failure stress, σ_{t0} are defined in a tabular form. The model assumes a linear loss of strength after cracking.

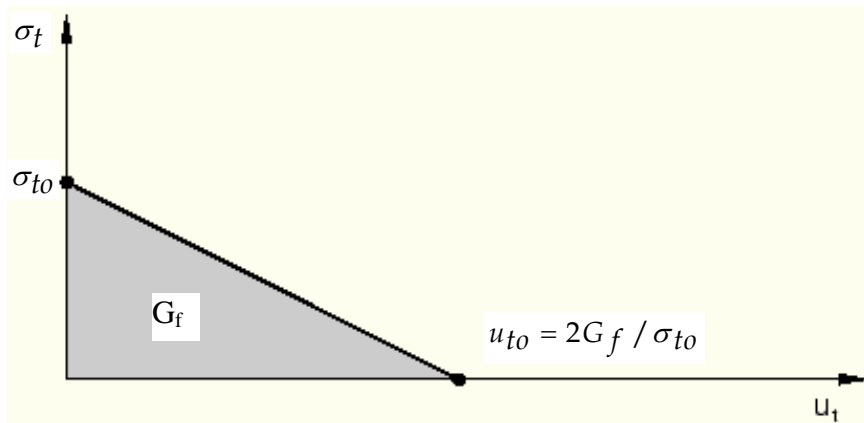


Figure 5.9: Typical Post failure Stress – Displacement curve using fracture energy criterion

Typical values of G_f range from 0.22 lb/in for normal concrete (compressive strength = 2850 psi) to 0.67 lb/in for high strength concrete (compressive strength = 5700 psi). The model calculates the strain in the element by using the elemental characteristic length. Abaqus calculates the cracking displacement at which complete loss of strength takes place using the equation, $u_{t0} = 2G_f / \sigma_{t0}$. The model then automatically converts these cracking displacement values to equivalent plastic displacement and then equivalent plastic strains using the characteristic element length. A simple analysis of the typical values obtained from laboratory split cylinder tensile tests and the G_f calculated using the respective cylinder compressive strength is shown in figure 5.10. G_f is the area under the

stress-displacement curve and its sensitivity depends on both the tensile failure stress and the uniaxial compressive strength of concrete.

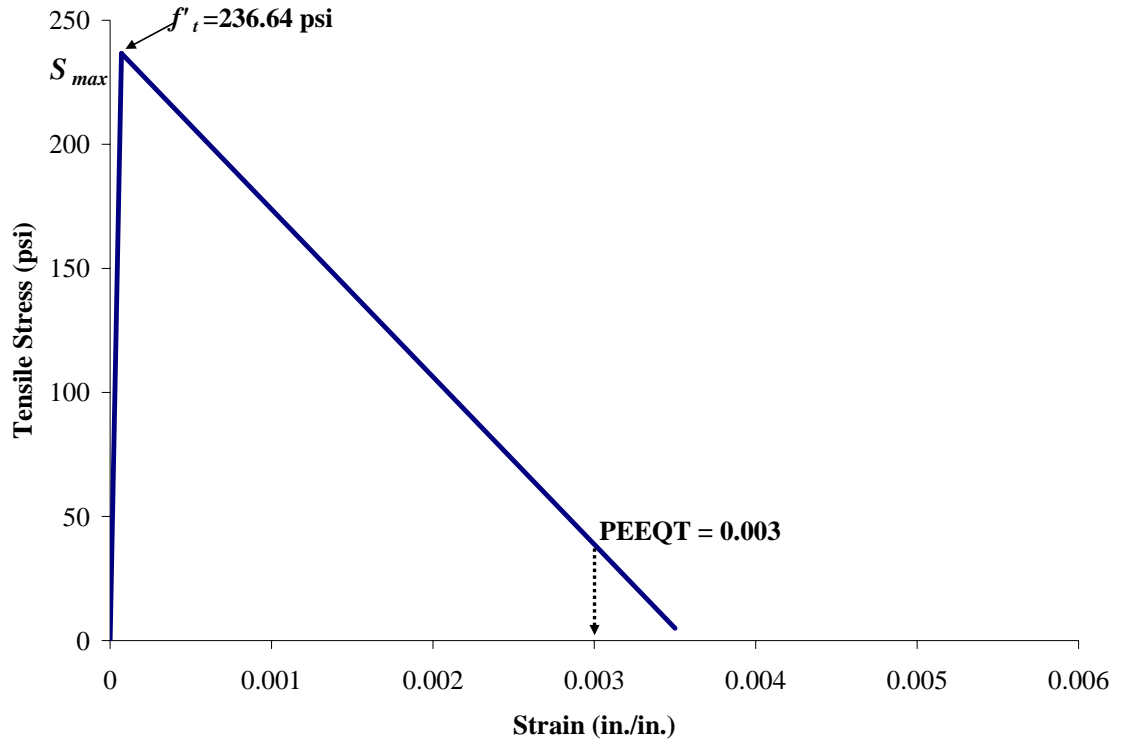


Figure 5.10: Typical tensile post failure stress-strain curves using the fracture energy criterion

The calculations for the dilation angle involved complex mathematical derivations and assumptions using the yield surface of the concrete damage plasticity model. From the data for axial and lateral stress-strain in multiaxial state given by Palaniswamy et al (1974) and Chadappa et al (1999, 2001), the dilation angle for unconfined concrete was assumed to be 15 degrees (15°). The biaxial stress ratio and the tensile-to-compressive meridian ratio were assumed to be equal to 1.16, and 0.667, respectively based on recommendations of Kupfer and Gerstle (1976) and Chen and Han (1995).

5.4.4 STEEL DOWEL BAR MATERIAL MODEL

The steel dowel bars were modeled using an isotropic elastic multiaxial material model. The elastic modulus, E_s , was based on results of standard ASTM (A370-97a) uniaxial tension tests on coupons fabricated from the billet steel grade M60 dowel bars. The measured elastic modulus was equal to 29,000 ksi, the yield stress and ultimate stress were equal to 68 ksi and 94.56 ksi, respectively. The yield and ultimate stresses were not required because the results of preliminary finite element analysis indicated that the dowel bar remained elastic throughout the experimental investigation.

5.5 DEVELOPMENT OF THE DOWEL – CONCRETE INTERACTION BOND MODEL

The longitudinal and transverse interactions between the dowel bars and the concrete slabs were modeled using two models: the first model focused on the longitudinal bond between the steel and concrete due to irregularities on the dowel surface and static friction. The second model focused on the transverse interaction between the steel dowel and surrounding concrete resulting in large contact or bearing stresses and additional friction bond in the longitudinal direction due to the normal (bearing) stresses and coulomb friction coefficients. The behavior of the spring elements and contact interactions, how it was calibrated to the pullout vs. joint opening behavior is presented in the next section.

5.5.1 THE LONGITUDINAL BOND BEHAVIOR

The behavior of the pavement specimens with aligned dowels is dominated by the longitudinal bond between the dowel bars and the concrete. The transverse interaction

between the dowel bar and concrete does not participate in the behavior of the joint with aligned dowel bars. Hence the longitudinal bond behavior was calibrated using the experimental results (pullout force – joint opening data) from aligned dowel bar tests (1A, 2A and 5A) as follows. Spring elements with nonlinear force-deformation relations in the longitudinal direction were used to model the longitudinal bond between the dowel bar and surrounding concrete nodes of the finite element model. The relative displacement (joint opening) across the spring element is the change in length of the spring between the initial and current position. The pullout load vs. joint opening behavior from the experiment is converted to the average bond stress over half length (9 in.) of the dowel bar using the relation, average bond stress = pullout force / circumferential area along ($\pi \times 1.25 \times 9 \text{ in}^2$) length. The average bond stress is then converted to the force in the spring by assuming a tributary area at the point of connectivity. The springs elements are assigned between the coinciding nodes of the dowel bar and concrete. These coinciding nodes are oriented along four diametrically opposite lines, as shown in figure 5.11 and 5.12. In the model, the force vs. the relative spring displacement is applied on both sides of the doweled joint. Typical forces in the spring elements are shown in figure 5.13.

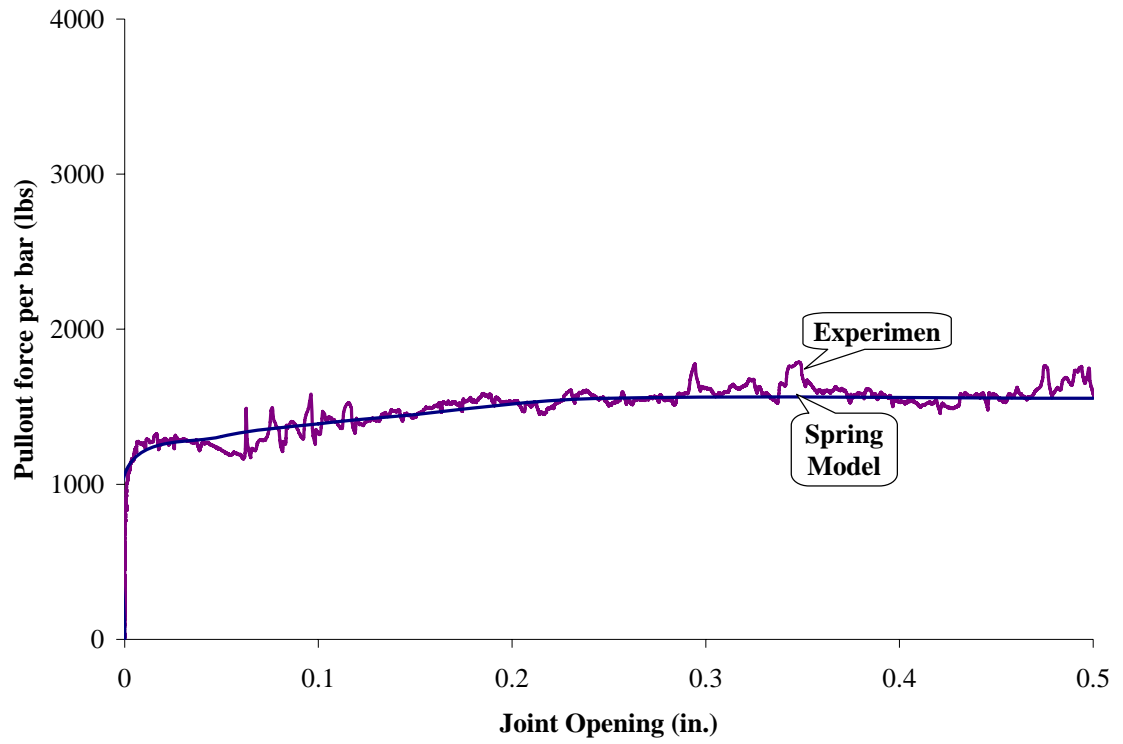


Figure 5.11: Spring model derived from the control test specimen (aligned single dowel bar).

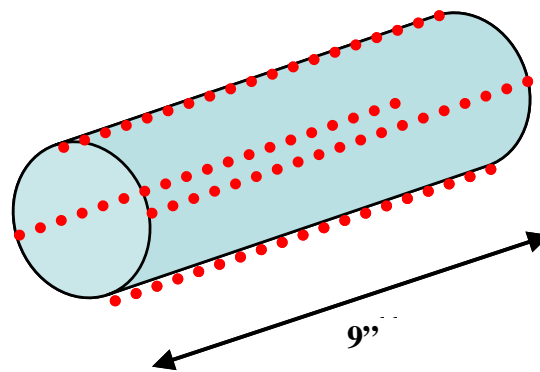


Figure 5.12: Distribution of spring forces along half length of the dowel bar

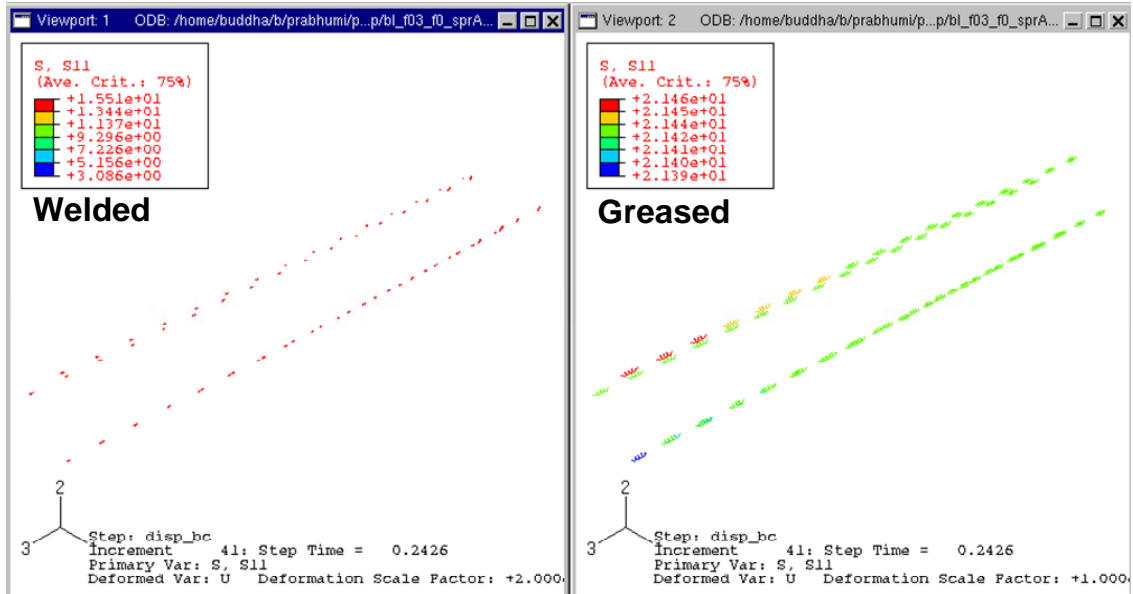


Figure 5.13: Typical spring forces (lbs) at ¼ in joint opening in the 1V18 model

5.5.2 THE TRANSVERSE INTERACTION BEHAVIOR

The second model focuses on the transverse interactions between the steel dowel, the concrete slab and the resulting frictional bond. The transverse interaction was modeled using special surface-to-surface contact elements. These elements model hard contact behavior with coulomb friction. The hard surface contact results in large bearing (normal) stresses at contact locations, and the coulomb friction model permits slip only if the applied shear is greater than the normal stress multiplied by the friction coefficient. Thus, the transverse interaction model includes additional longitudinal bond resulting from coulomb friction and large localized bearing stresses.

Two cases of coefficient of friction were considered for the greased and uncoated side of the dowel bar. In each misalignment model study, two cases with different input parameters were considered. Case I correspond to the use of idealized friction coefficients (0.0 and 0.3 on the greased and uncoated sides, respectively) and idealized

material properties (uniaxial compressive strength (f'_c) of 3500 psi & tensile strength (f'_t) of 236 psi. Case II corresponds to the use of friction coefficients measured by Shoukry (2003) (0.076 and 0.384 for greased and ungreased sides, respectively) and measured material properties of the hardened concrete specimens collected during actual laboratory tests. The idealized (Case I) and measured (Case II) compressive and tensile strengths and frictional coefficients for the various cases is shown in Table 5.1

Table 5.1: Case I and Case II input parameters for the various models

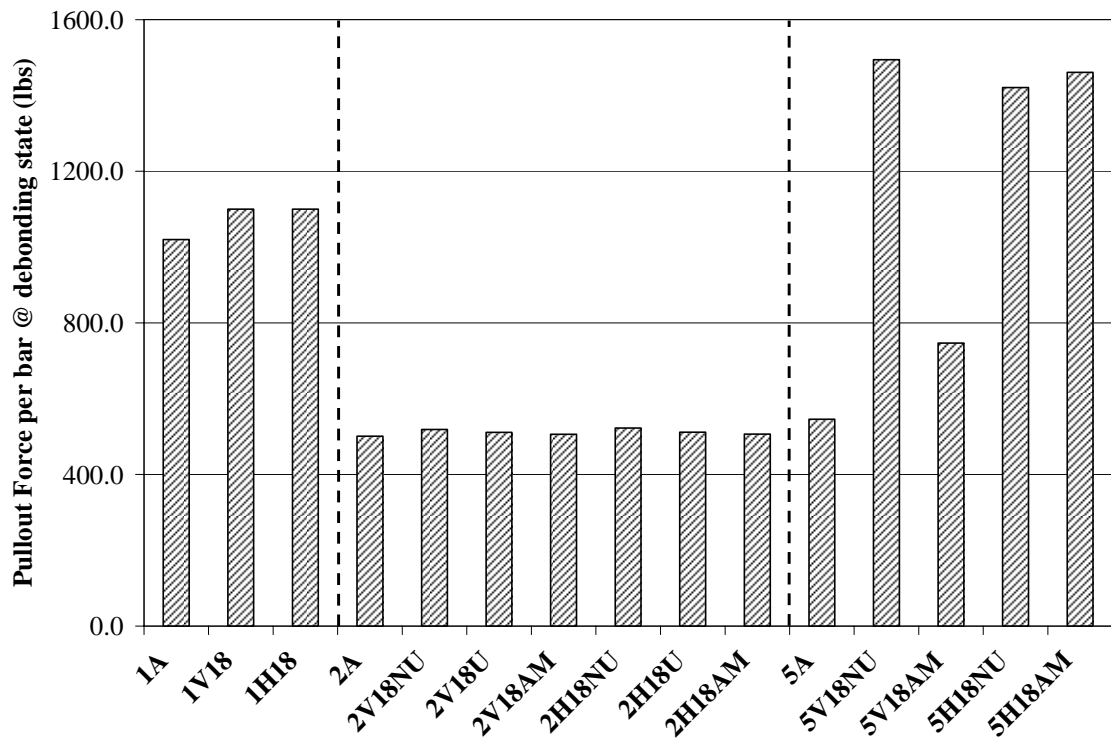
	Case I	Case II
• Uniaxial Compressive Strength (f'_c)	3500 psi	Data obtained from cylinder tests (Appendix A)
• Tensile Strength (f'_t)	236.64 psi	
• Friction coefficient on greased side	0.0	0.076
• Friction coefficient on welded side	0.30	0.384

5.6 LIMITATIONS AND SHORT COMINGS OF THE FE MODEL

The pullout force per dowel-joint opening behavior of all specimens consisted of two regions: an initial fully bonded region and a post-slip debonded region. The initial bond (corresponding to the debond stress τ_b) is caused by a variety of reasons including chemical adhesion, mechanical interlock between the dowel surface and concrete, shrinkage of concrete around the dowel bars, etc. This initial bond behavior can be highly variable depending on the concrete mix design, water content, surface finish of the dowel bar, friction between dowel surface and surrounding concrete, and various other parameters. Figure 5.14 shows the variation of the initial debond stress (τ_b) for various pavement specimens. This variability in the initial debond stress is typical for longitudinal bond between steel (embedded) and concrete. It is difficult to model

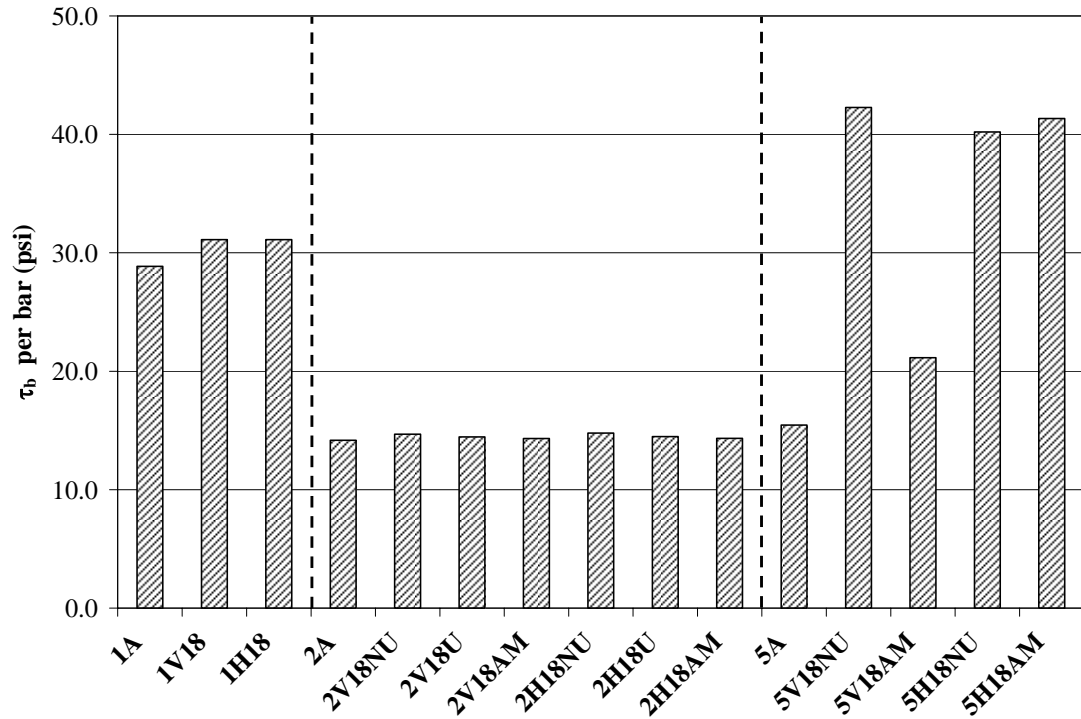
deterministically due to the variable nature of the problem. Probabilistic or stochastic modeling was beyond of the scope of the research.

The analytical approach consisted of using the experimental results for pavement specimens (1A, 2A, and 5A) with fully aligned dowel bars to define the spring model for the longitudinal bond between the dowel surface and the concrete. The underlying assumption is that specimens with no misalignment have only longitudinal bond behavior. There is no transverse (bearing) interaction and corresponding friction addition to the longitudinal bond of these specimens.



(a) Pullout force per bar just at debonding

Figure 5.14: Summary of the Pullout force per bar at debonding limit state (A) and the debonding stress for the aligned and misaligned test cases



(b) Debonding Stress in the dowel bar

Figure 5.14 (cont'd).

The 3D finite element models were developed using ABAQUS, a commercially available FEA software. The experimental results were used to define the model input parameters, for example, (i) the longitudinal bond was defined using the results for specimens with aligned bars, (ii) the steel and concrete material properties were defined based on material test results, and (iii) the friction coefficient between the dowel surface and surrounding concrete were defined using the experimental results of Shoukry et al (2003). These models were used to predict the joint opening behavior of the specimens with misaligned dowel bars with different misalignment type, magnitude, and distribution. The joint opening behavior results predicted for these specimens were compared directly with the experimental results, without any additional modification or calibration.

The comparisons focused on the overall pullout force per dowel-joint opening behavior predicted by the models and measured experimentally. The localized multiaxial stresses and strains computed by the models at the sites of stress concentration could not be verified because the corresponding measurements were not performed during the experiments. These stress concentration sites are located inside the concrete specimens at the interface of dowel and concrete. The sensors required to measure such local stresses and strains were not embedded in the specimens. Additionally, non-destructive techniques were not used to monitor the formation of distresses within the concrete specimens at the dowel-concrete interfaces. These are major limitations of the experimental approach used in this research, and should be addressed by future research.

It is important to note that pavement joint opening occurs due to thermal movements induced by changes in ambient conditions. It is a cyclic, time-varying phenomenon that depends completely on the weather (ambient) conditions. This research does not consider the effects of: (i) joint locking due to thermal gradients, (ii) friction at the base of the pavement specimens from the underlying base layers, or (iii) cyclic joint opening behavior. This is a major limitation of the research project.

Since joint opening is a cyclic, time-varying phenomenon, the problem becomes one of cyclic material fatigue at the distress (stress concentration) locations. This was not the focus of the research. The fatigue stress or strain – life relationships for pavements with misaligned dowel bars have not been addressed or developed. This is a major limitation that needs future research.

5.7 LOADING AND BOUNDARY CONDITIONS

The loading and boundary conditions are designed to simulate the experimental behavior of the tested specimens. They are applied in two steps. The first step applies loads due to the dead load (gravity load / self weight) of the two sides of the concrete slab and the dowel are applied as body force and the concrete base is assumed to be fixed from translation, as shown in figure 5.15. This step is used to generate the appropriate contact forces between the dowel and concrete interfaces and activate the Coulomb friction model. The second step uses a displacement control approach to pull each side of the pavement specimen in the opposite direction by 0.25 in., thereby giving a total joint opening of 0.5 in. In this step, the model is supported and restrained from out of plane movements, using support (roller) lines, as shown in figure 5.16.

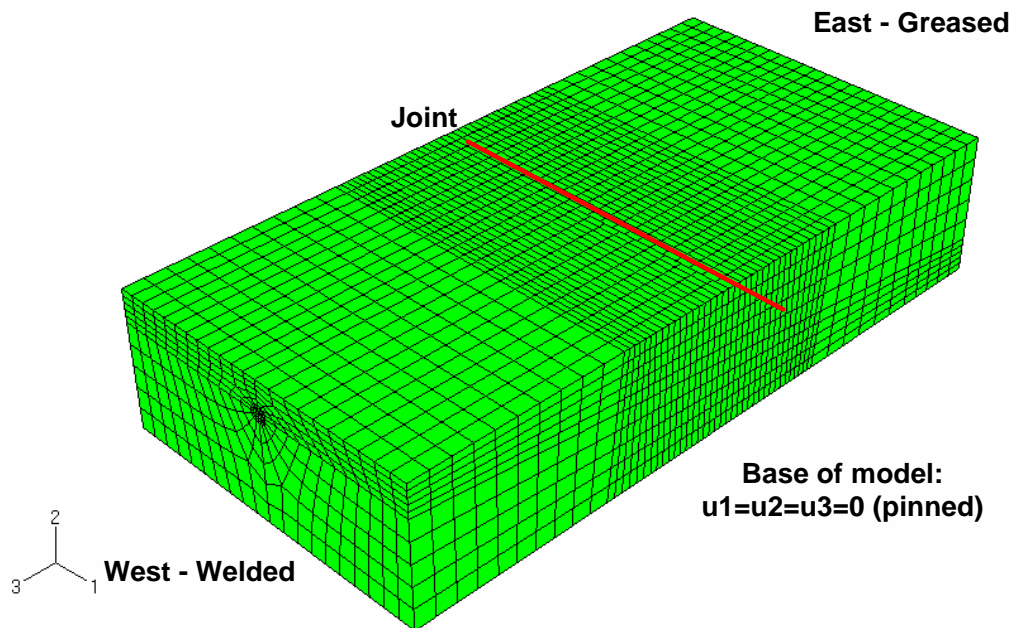


Figure 5.15: Step I – Dead (gravity / self weight) Load due to the concrete and dowel

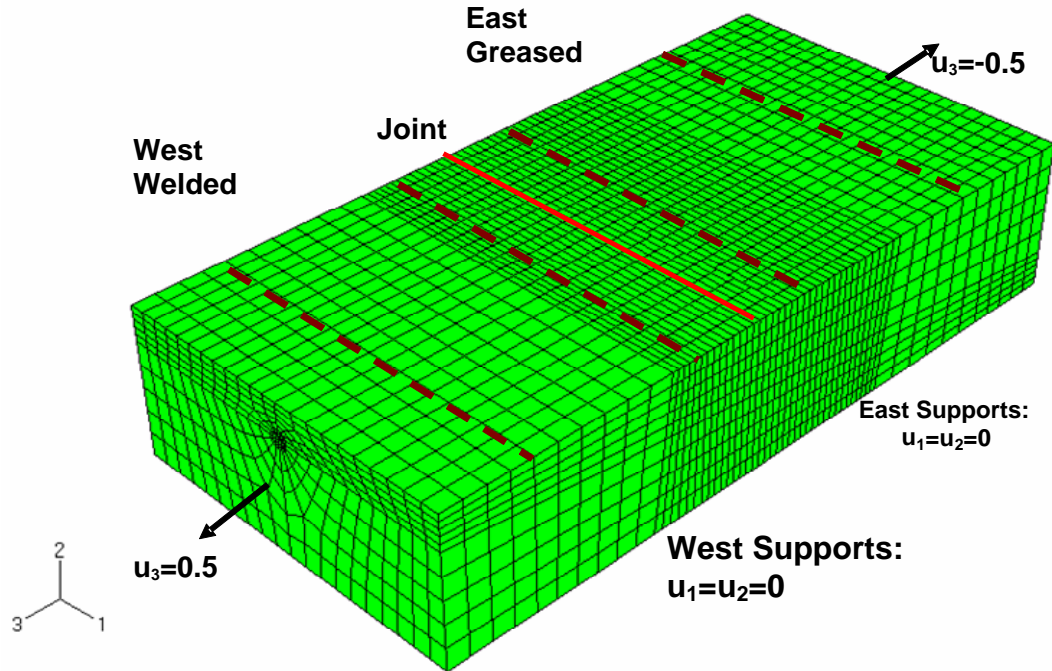
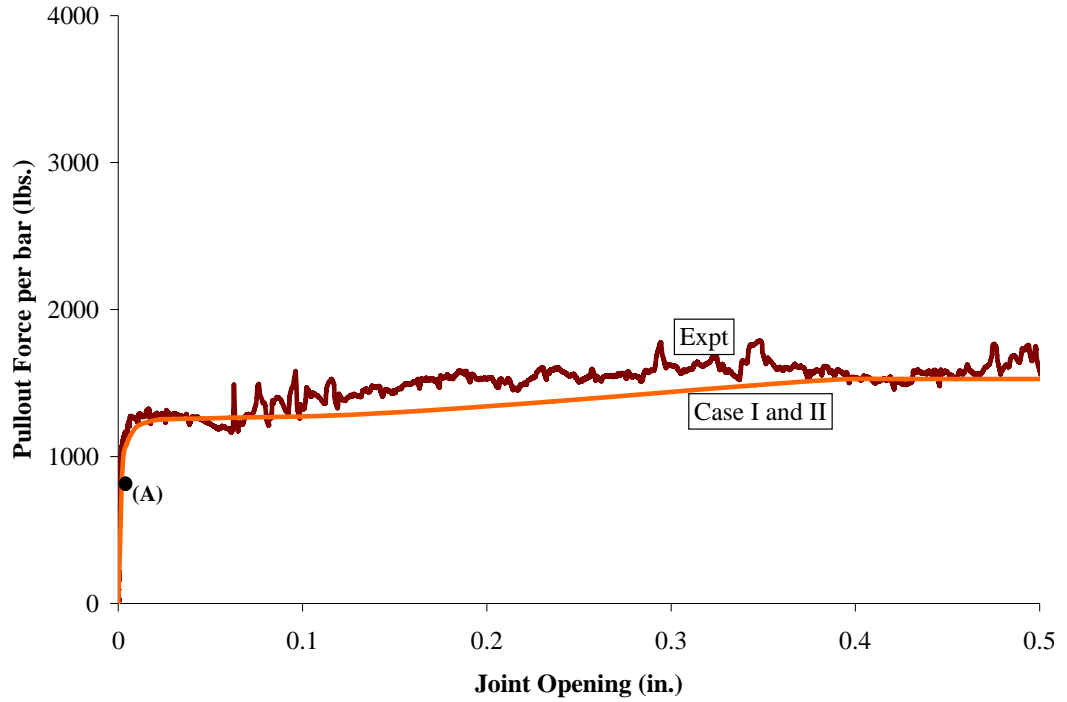


Figure 5.16: Step II – Displacement Control step simulating joint opening

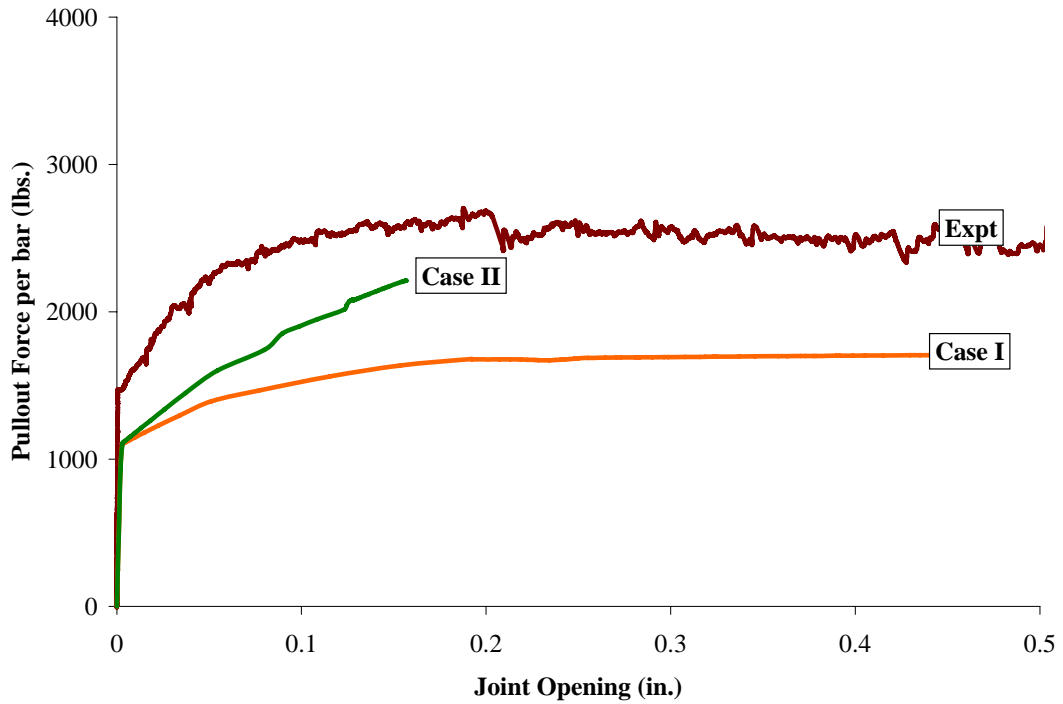
5.8 THE 3D FINITE ELEMENT MODEL RESULTS

The results from the 3D finite element analyses include the pullout force-joint opening behavior of the concrete specimens and the complex state of multiaxial (3D) stresses and strains in the model. Figure 5.17 compares the experimental and analytical pullout force-joint opening behavior for the single dowel specimens. These specimens are listed in table 4.1 (a). Figures 5.18 and 5.19 compare the experimental and analytical pullout force-joint opening behavior for specimens with two dowels misaligned vertically or horizontally, respectively. Similarly, figures 5.20 and 5.21 compare the experimental and analytical pullout force-joint opening behavior for specimens with five dowels misaligned vertically or horizontally, respectively. In Figures 5.17 through 5.21, Cases I and II correspond to the use of idealized and experimentally established static friction coefficients and material properties as explained earlier. In several cases, the post slip

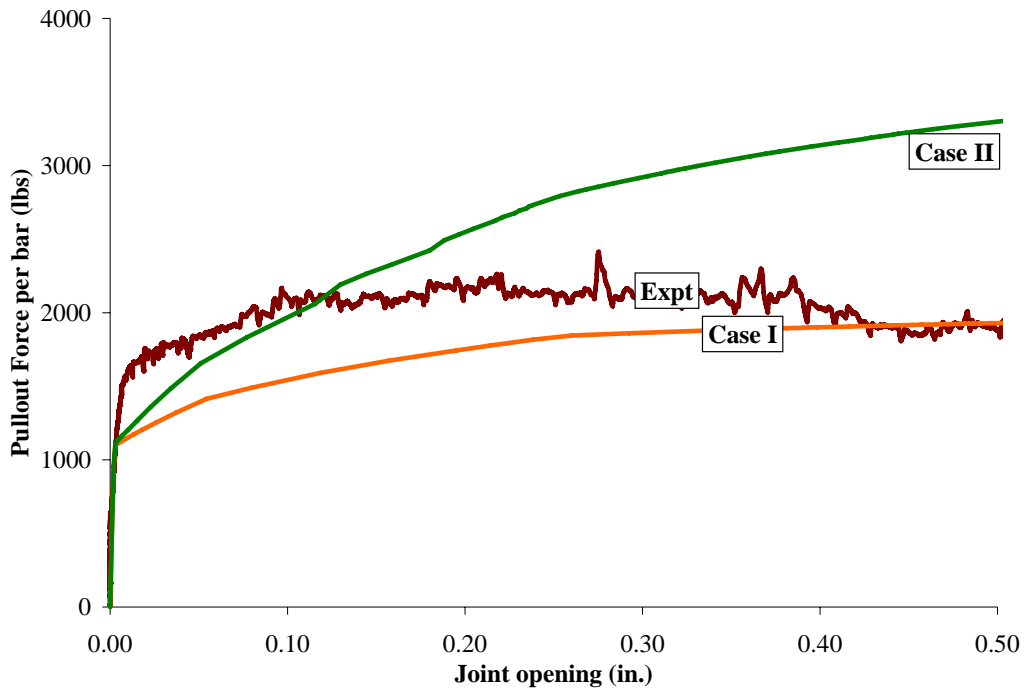
behavior of the pullout force obtained from the analyses using case I and II parameters bound the dowel pullout force obtained from the experiments.



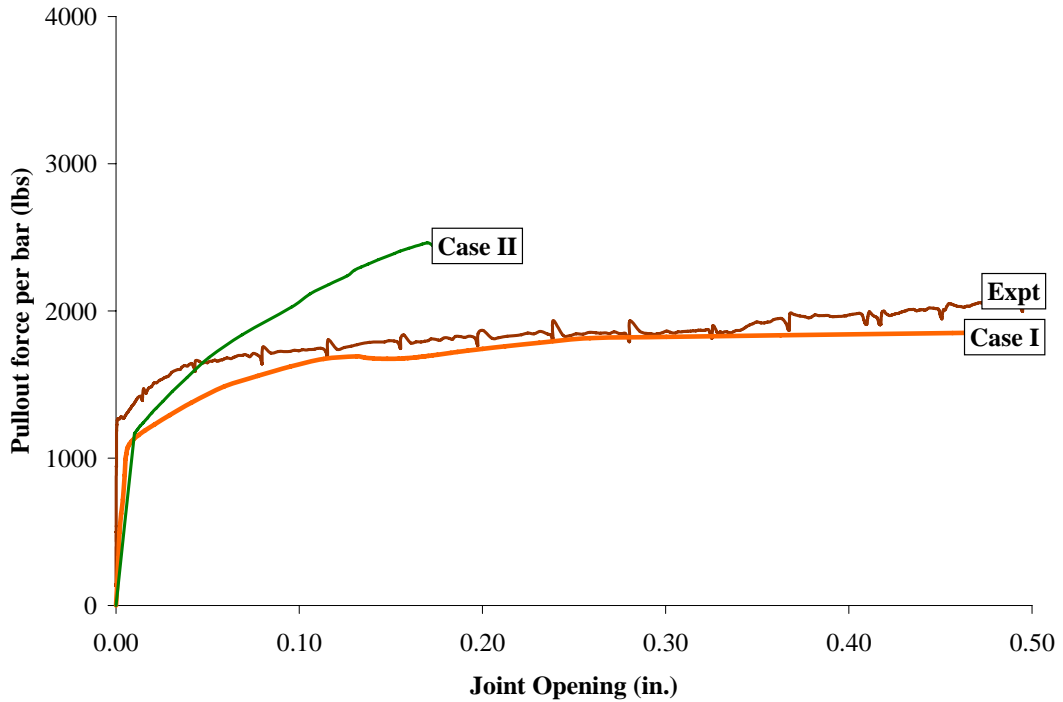
(a) Comparison of 1A model



(b) Comparison of 1V18 model

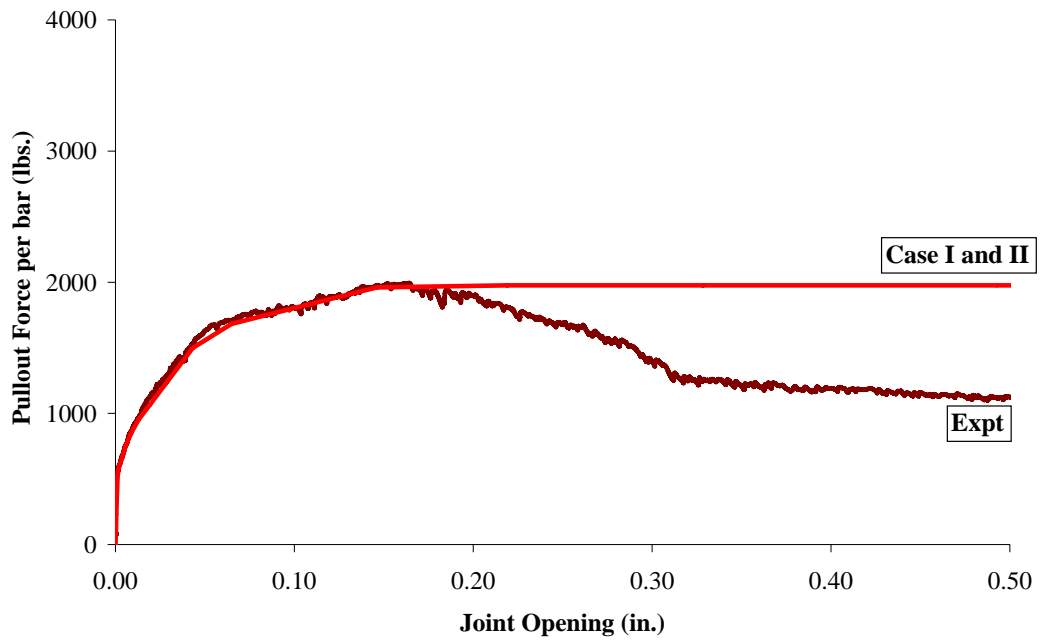


(c) Comparison of 1H18 model

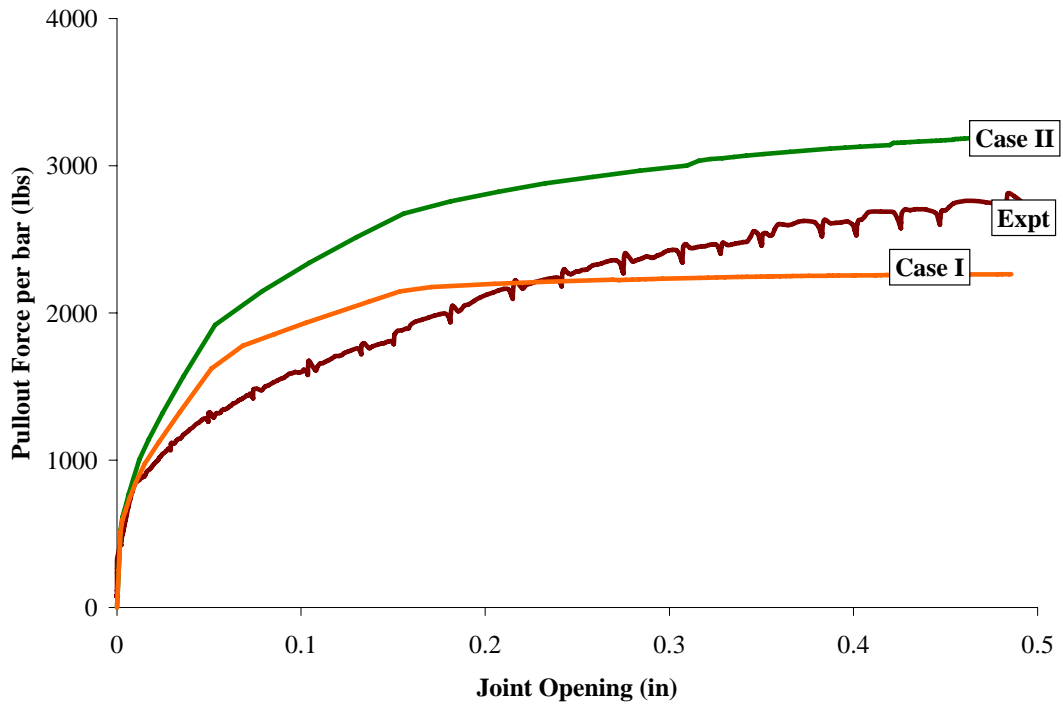


(d) Comparison of 1C18 model

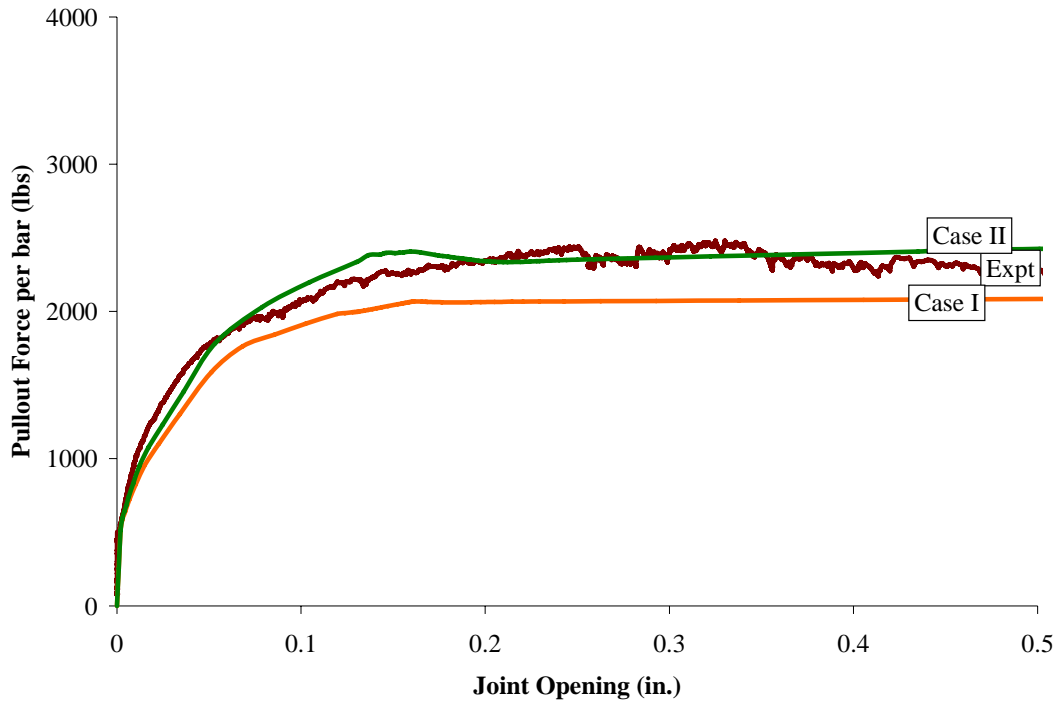
Figure 5.17: Comparison of finite element results and experimental data for a single misaligned 1/18 radians dowel bar.



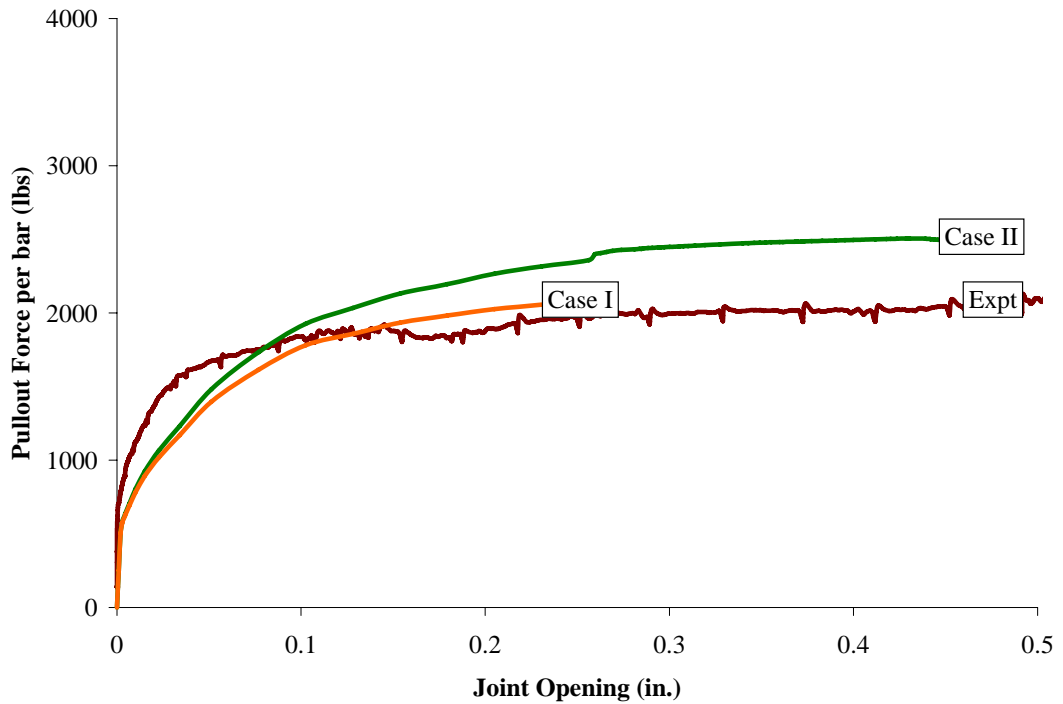
(a) Comparison of 2A model



(b) Comparison of 2V18NU model

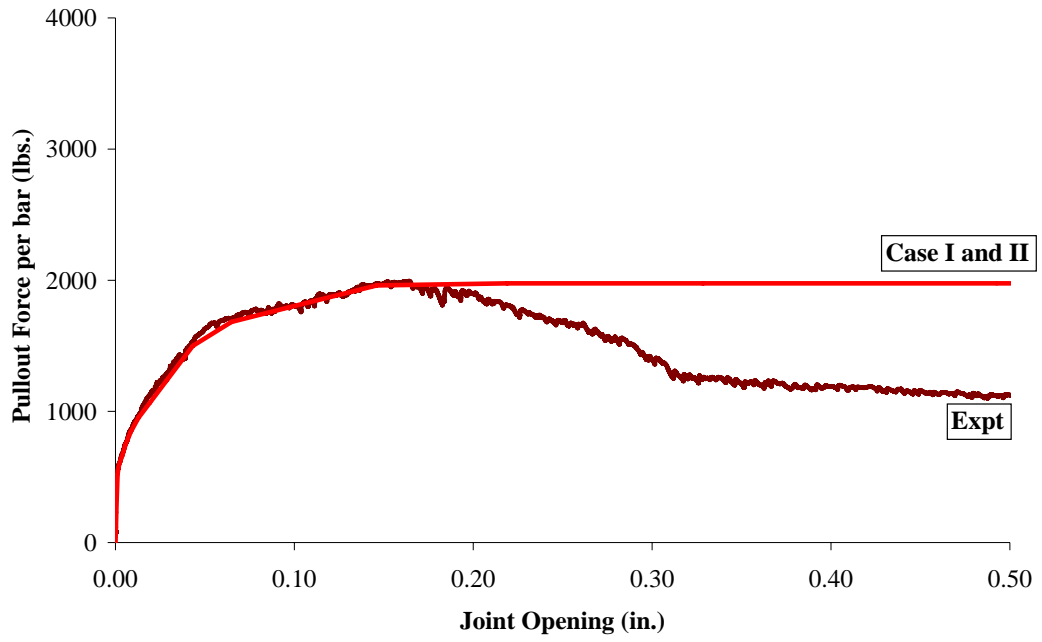


(c) Comparison of 2V18U model

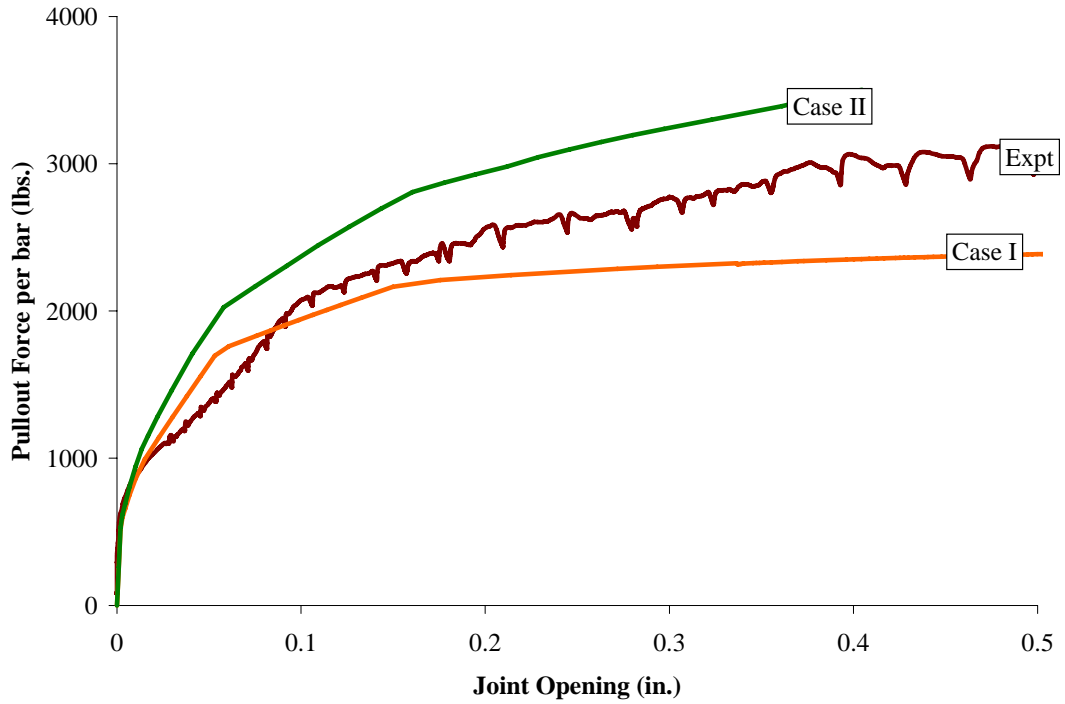


(d) Comparison of 2V18AM model

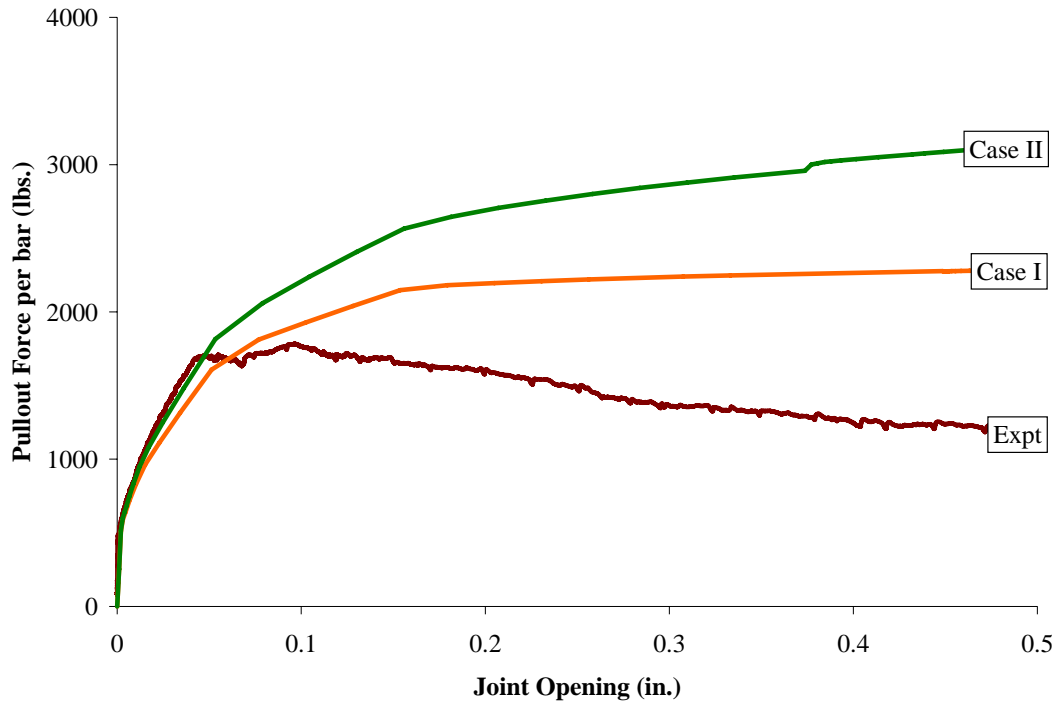
Figure 5.18: Comparison of finite element results and experimental data for two vertically misaligned 1/18 radians dowel bar.



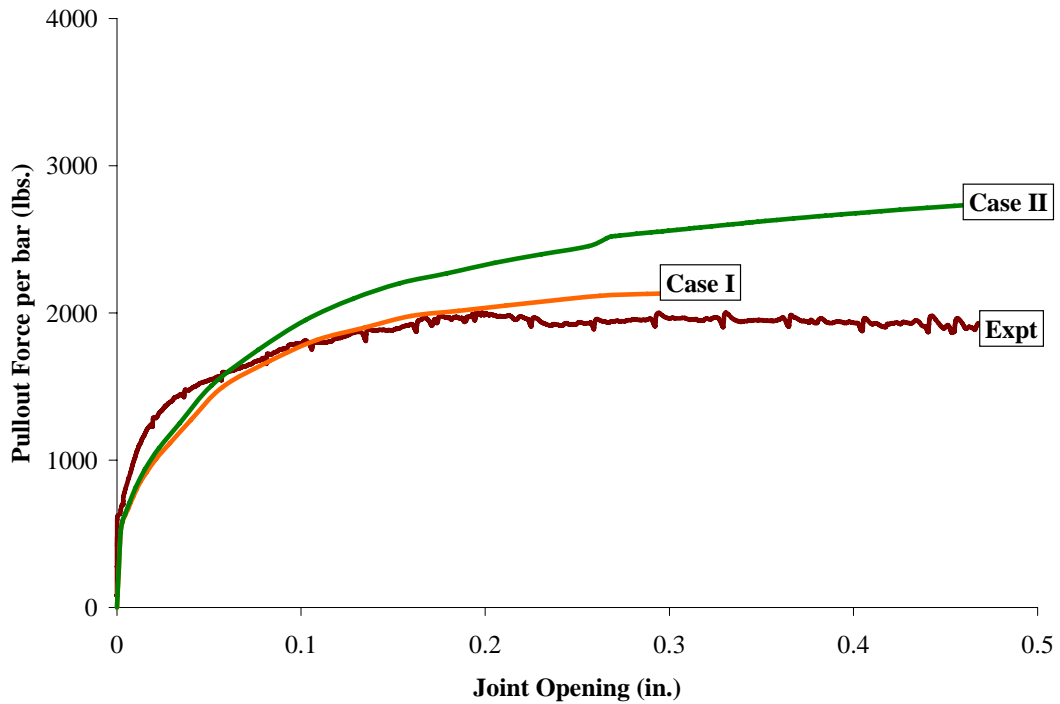
(a) Comparison of 2A model



(b) Comparison of 2H18NU model

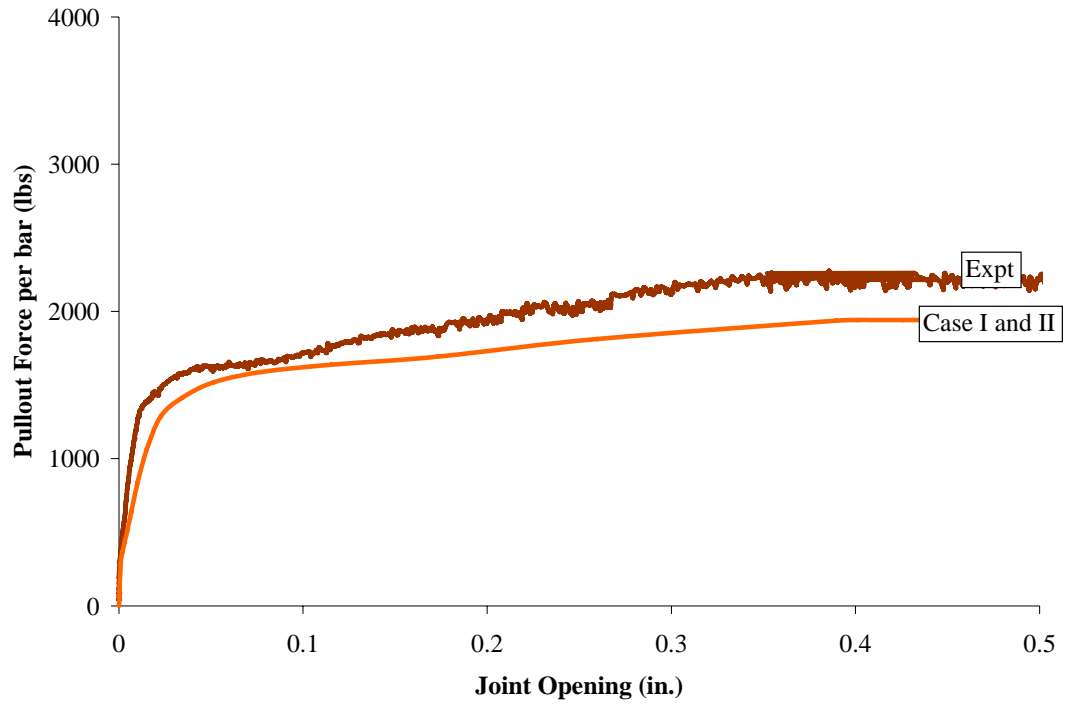


(c) Comparison of 2H18U model

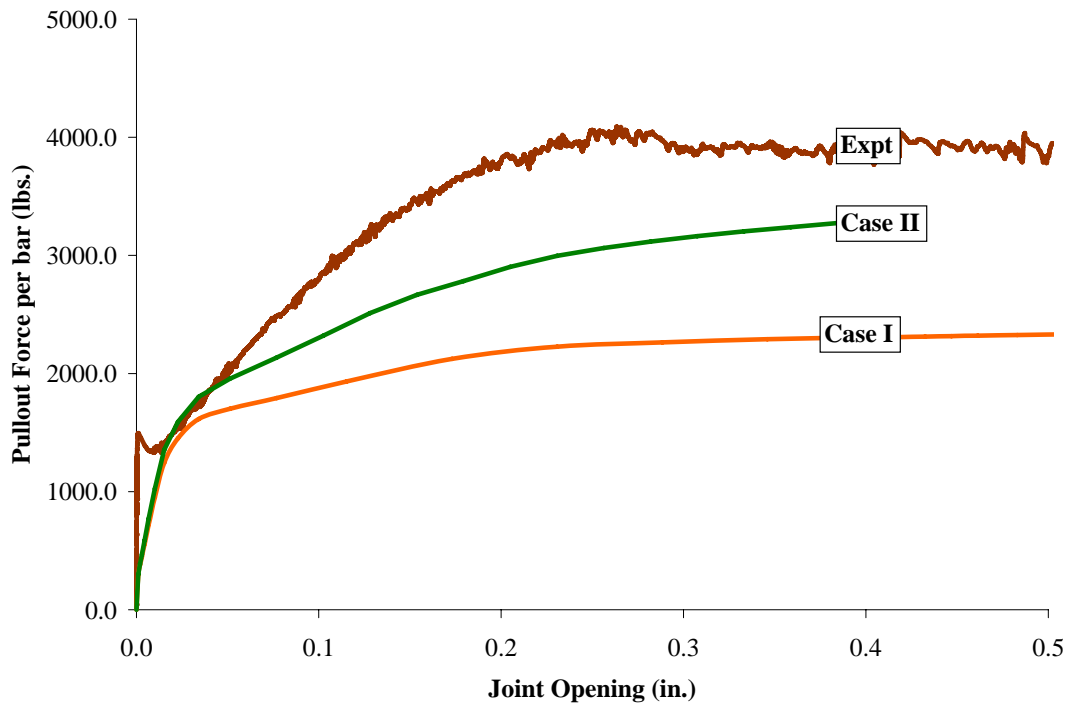


(d) Comparison of 2H18AM model

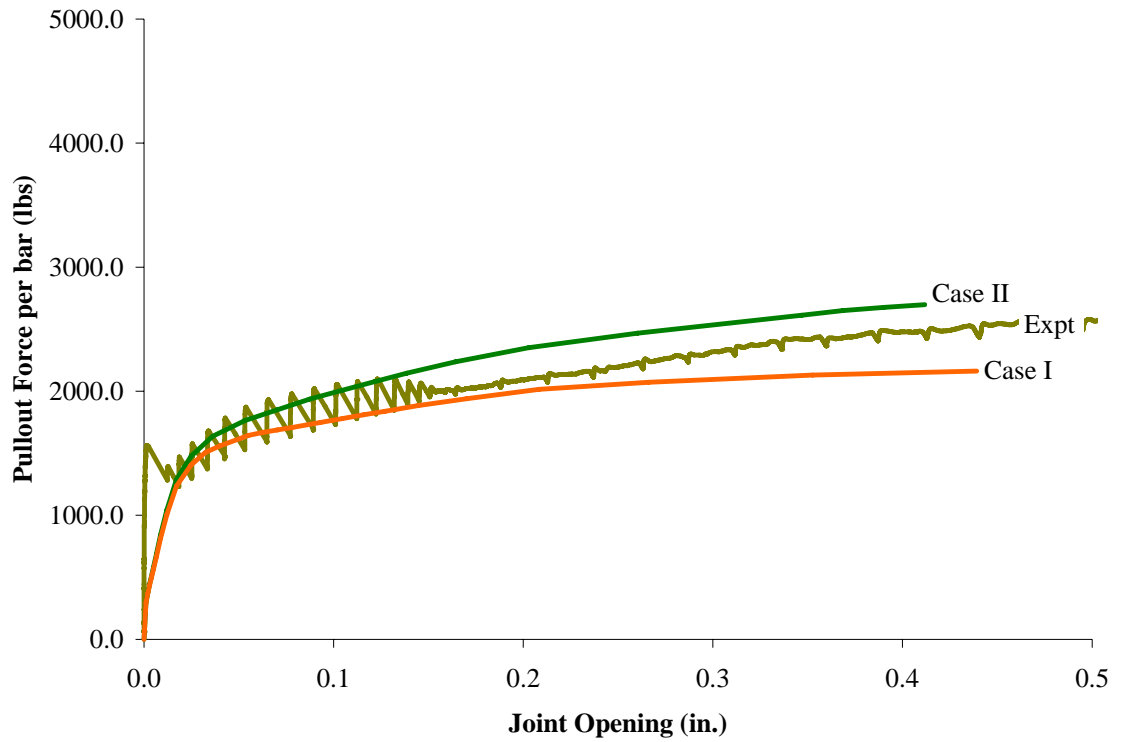
Figure 5.19: Comparison of finite element results and experimental data for two horizontally misaligned 1/18 radians dowel bar.



(a) Comparison of 5A model

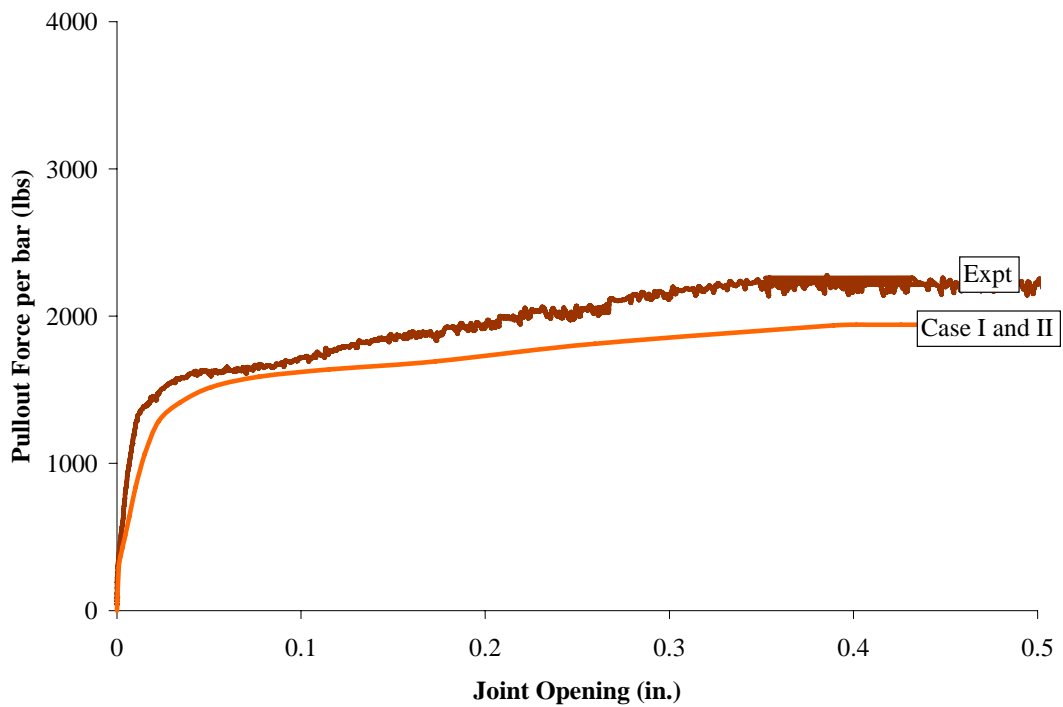


(b) Comparison of 5V18NU model

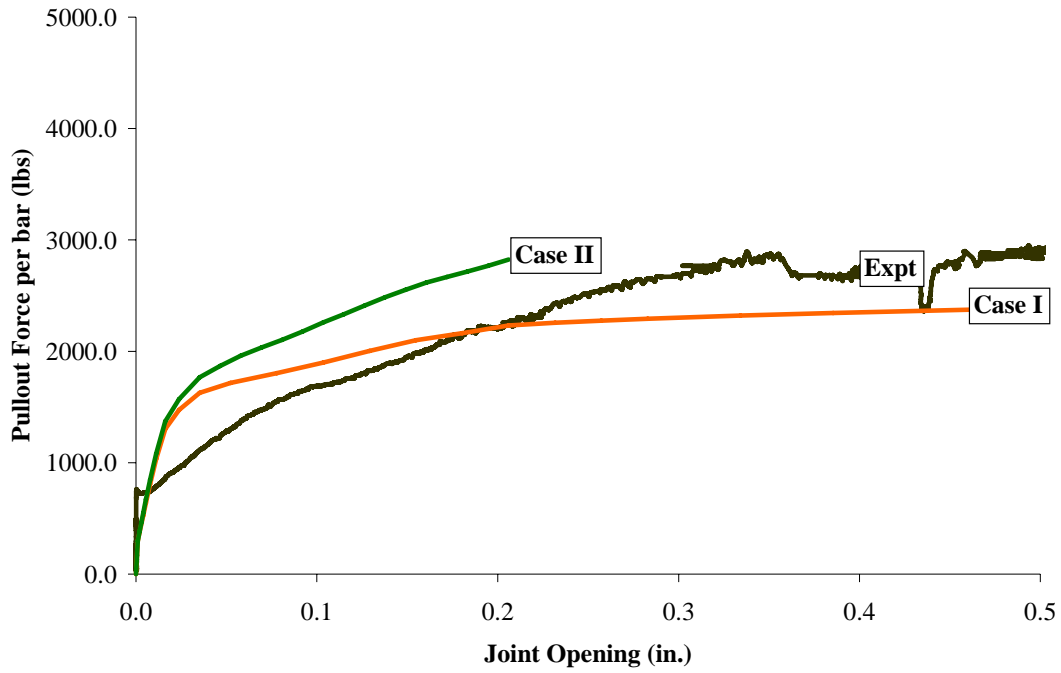


(c) Comparison of 5V18AM model

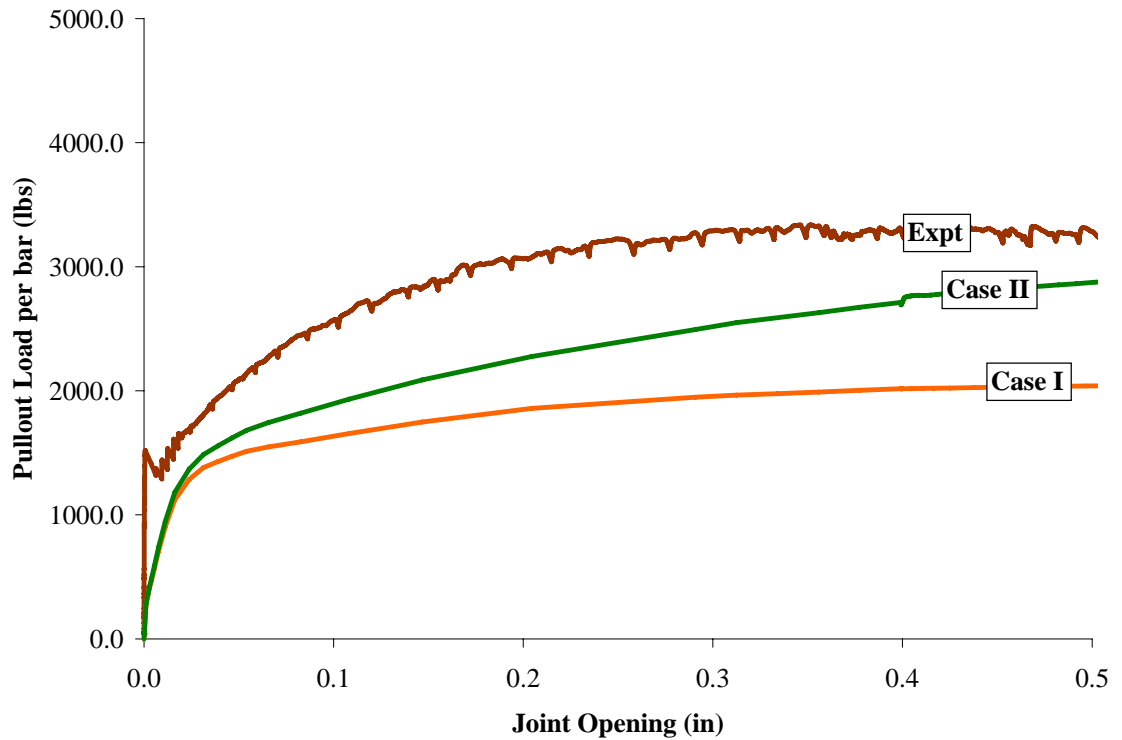
Figure 5.20: Comparison of finite element results and experimental data for five vertically misaligned 1/18 radians dowel bar.



(a) Comparison of 5A model



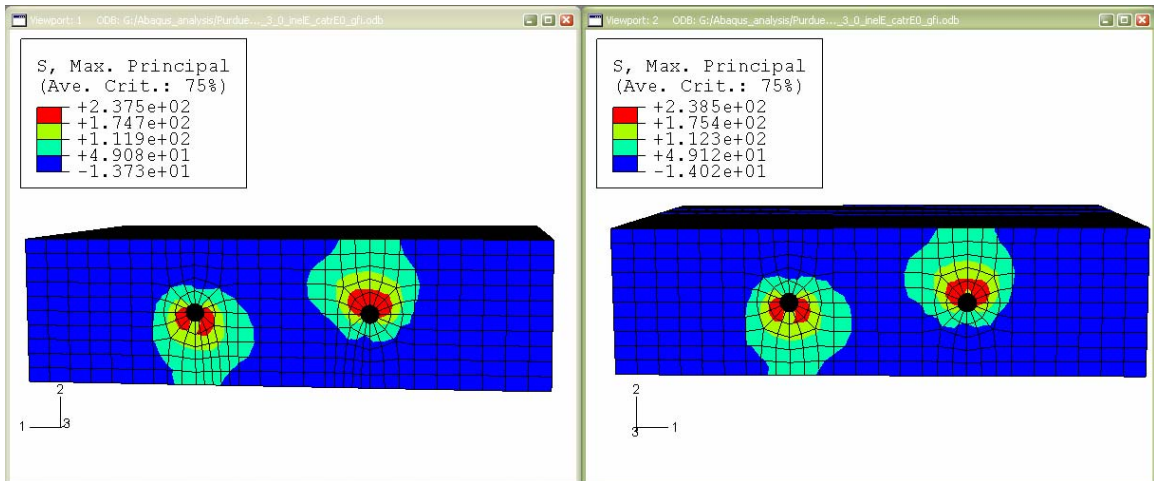
(b) Comparison of 5H18NU model



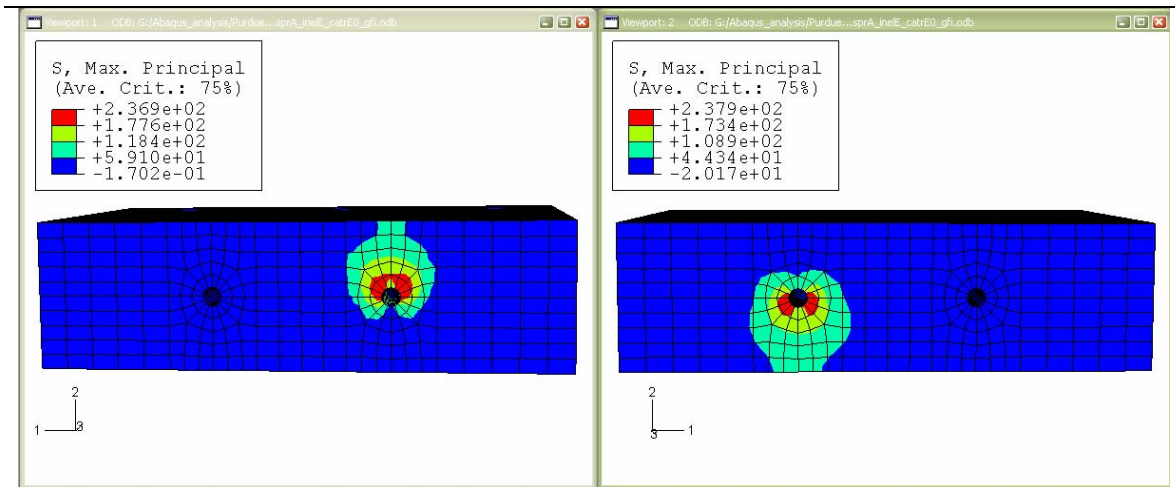
(c) Comparison of 5H18AM model

Figure 5.21: Comparison of finite element results and experimental data for five horizontally misaligned 1/18 radians dowel bar.

In all the finite element models, stress concentration zones occurred in the concrete at the joint face around misaligned dowel bars. For example, Figure 5.22(a) shows the stress concentrations in the test specimen, 2V18NU with non-uniformly misaligned dowel bars. Figure 5.22(b) shows the stress concentrations around test specimen, 2V18AM with alternate misaligned dowel bars. The joint opening in both cases is 0.05 in with case I input parameters.



(a) S_{max} Stress contours at the face of the joint for the 2V18NU model



(b) S_{max} Stress contours at the face of the joint for the 2V18AM model

Figure 5.22: Typical stress contours at material damage / limit state (C) in the FE model for Case I input parameters at 0.05 in. joint opening

5.9 CONCLUDING REMARKS

The comparisons in figures 5.17- 5.21 indicate that the analytical results compare favorably with the experimental results. Cases I and II generally bound the experimental results. However, neither the experimental nor the analytical pullout force-opening curves provide insight or knowledge regarding the 3D stress states and limit states or distress in the concrete pavement specimens. Hence, the analytical results (3D stresses and strains) from the finite element analyses were evaluated further to identify significant limit states and distresses in the concrete pavement joints. The protocol for defining the material failure / limit states is further explained in chapter 6.

CHAPTER 6

THREE DIMENSIONAL FINITE ELEMENT ANALYSIS RESULTS

6.1 INTRODUCTION

This chapter identifies the various events, i.e., the material damage limit states that occur in the pavement specimen models during the analysis. These events are identified using the analytical results and indicated on the predicted force-joint opening responses to help understand evolution of behavior. This chapter also presents the results from the analytical parametric studies including the overall force-joint opening responses and the events that occur at the dowel-joint interface. All the analytical results and experimental results from chapter 3 were used to establish limits for dowel misalignment.

6.2 MATERIAL EVENTS OR DAMAGE LIMIT STATES

The analytical results (3D stresses and strains) from the finite element analyses were used to identify significant events or damage limit states occurring in the concrete material at the dowel-pavement interface.

The following events or damage limit states were identified based on the material 3D stress state results:

- (A) Debonding / initial slip state (τ_b)
- (B) Onset of concrete material inelasticity or cracking
- (C) Maximum principal stresses (S_{max}) exceeds the concrete tensile (f'_t) strength
- (D) Minimum principal stresses (S_{min}) exceeds the concrete compressive (f'_c) strength
- (E) Significant crushing (compressive inelastic strains)

(F) Significant cracking (tensile cracking strains).

These events / damage limit states are indicated on the analytically predicted pullout force-joint opening behavior plots and are further explained below.

Event (A) Debonding / Initial slip state (τ_b) - The debonding / initial slip state (τ_b) is defined as the point where debonding occurs between the dowel and the concrete slab and the joint opening begins. The initial joint opening is approximately 0.003 in. This is the only limit state corroborated by experimental measurements and analytical results. It should be noted that the debonding state is a change in longitudinal bond from sticking to slipping or static to kinematic bond, as shown in figure 6.1.

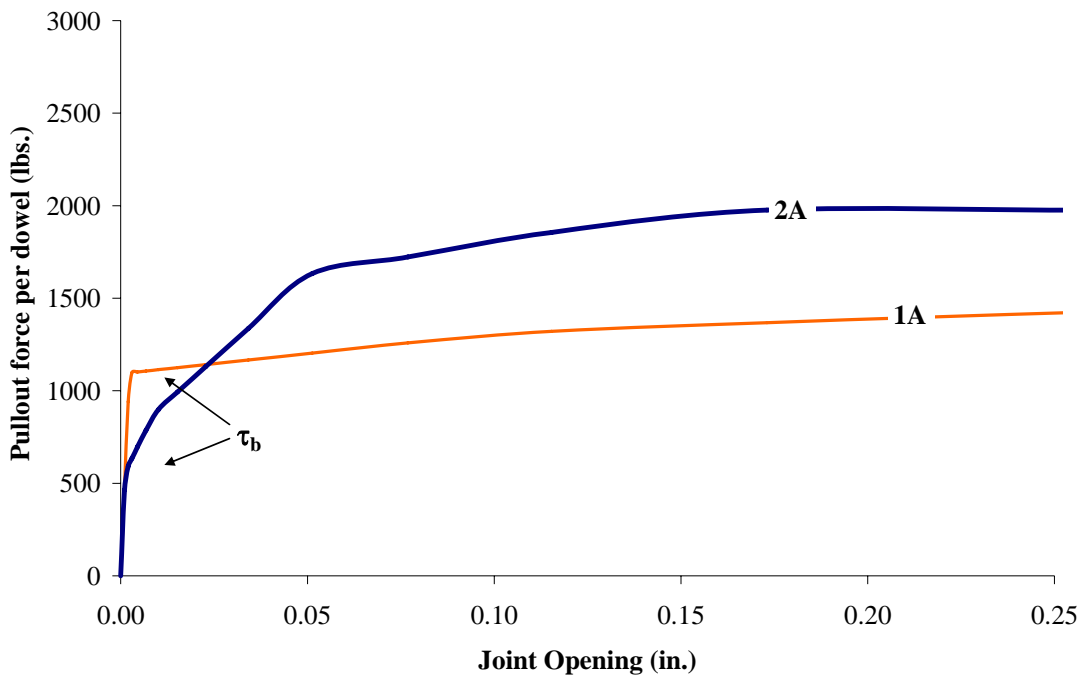


Figure 6.1: Typical location of initial slip state (A) for single and two aligned dowel bars

Event B occurs when the inelastic plastic strain in compression (PEEQ) and tension (PEEQT) values predicted by the finite element analysis became non-zero. PEEQ

and PEEQT are computed from the 3D finite element analysis results and they represent the effective lumped plastic strains in compression and tension, respectively. Concrete inelasticity or cracking initiates when these PEEQ and PEEQT values become non-zero. The initiation of concrete inelasticity ($PEEQ > 0$) and concrete cracking ($PEEQT > 0$) were first considered individually. However, they were always found to occur almost instantaneously. Hence, they were combined into one event limit state (B).

Events (C) and (D) pertains to the Principal Stress States (S_{max} and S_{min}) computed from the finite element analysis results. Event C occurs when the maximum principal stress (S_{max}) exceeds the concrete tensile strength (f'_t), see figure 6.2. This does not necessarily indicate cracking in a multiaxial stress state. Event D occurs when the minimum principal stress (S_{min}) exceeds the concrete compressive strength (f'_c), shown in figure 6.2. This does not necessarily mean crushing in a multiaxial stress state.

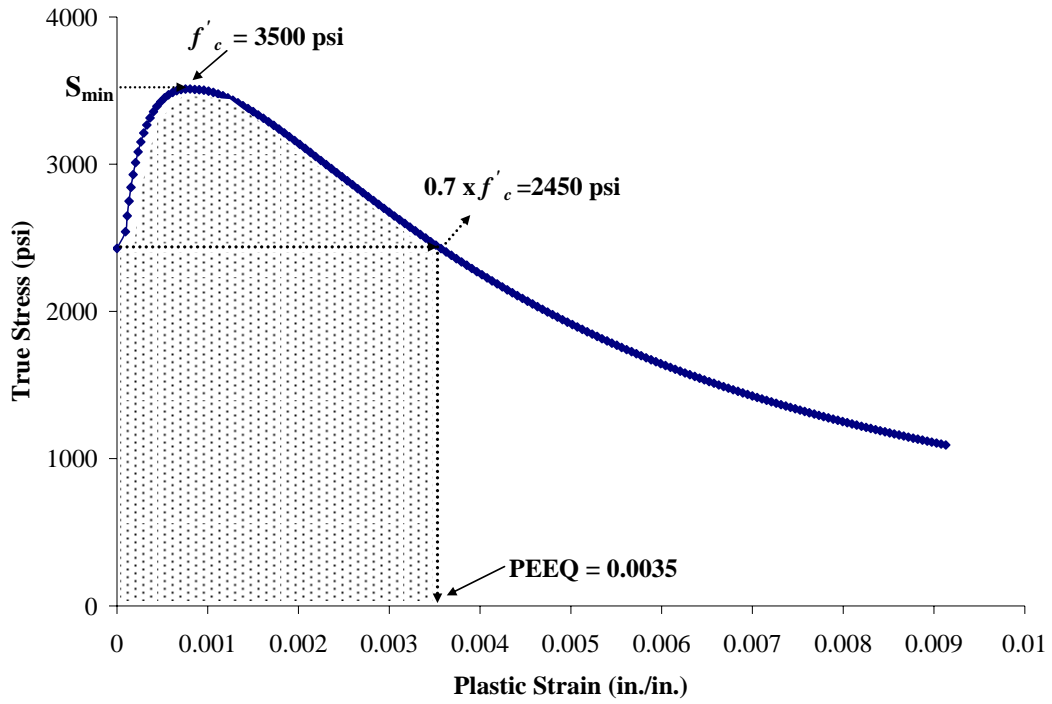
Event (E) represents significant crushing strain at the material point. It was assumed to occur when the effective plastic strain (PEEQ) exceeds 0.0035. PEEQ represents the total inelastic strain at the material point, which is resolved into the directional plastic strain tensor according to the non-associated flow rule. It is related to the uniaxial inelastic stress-strain behavior of the material. Figure 6.2(b) shows the uniaxial compressive stress-strain curve of concrete. This curve is used to calibrate the multiaxial flow rule in compression. This $PEEQ = 0.0035$ in the multiaxial strain state corresponds to the same magnitude of inelastic strain in compression. The value of $PEEQ = 0.0035$ was chosen to represent significant crushing at the material point. This value accounts for the inherent ductility of the material (shaded region in figure 6.2(b)) and the localized nature of the stress state.

Event (F) represents significant cracking strain at a material point was assumed to occur when the effective lumped plastic strain in tension (PEEQT) at a material point exceeded 0.003. PEEQT is similar to PEEQ with the exception that it is in tension. PEEQT is related to the uniaxial tension stress-cracking strain behavior of the material. The multiaxial behavior in tension is calibrated to the uniaxial stress-cracking strain behavior of the material. Thus, PEEQT=0.003 in a multiaxial strain state corresponds to the same magnitude of inelastic cracking strain state in uniaxial tension. The value of PEEQT=0.003, was chosen to represent significant cracking at the material point. This value is approximately ten times the initial cracking strain. It accounts for the material ductility and the highly localized nature of stresses.

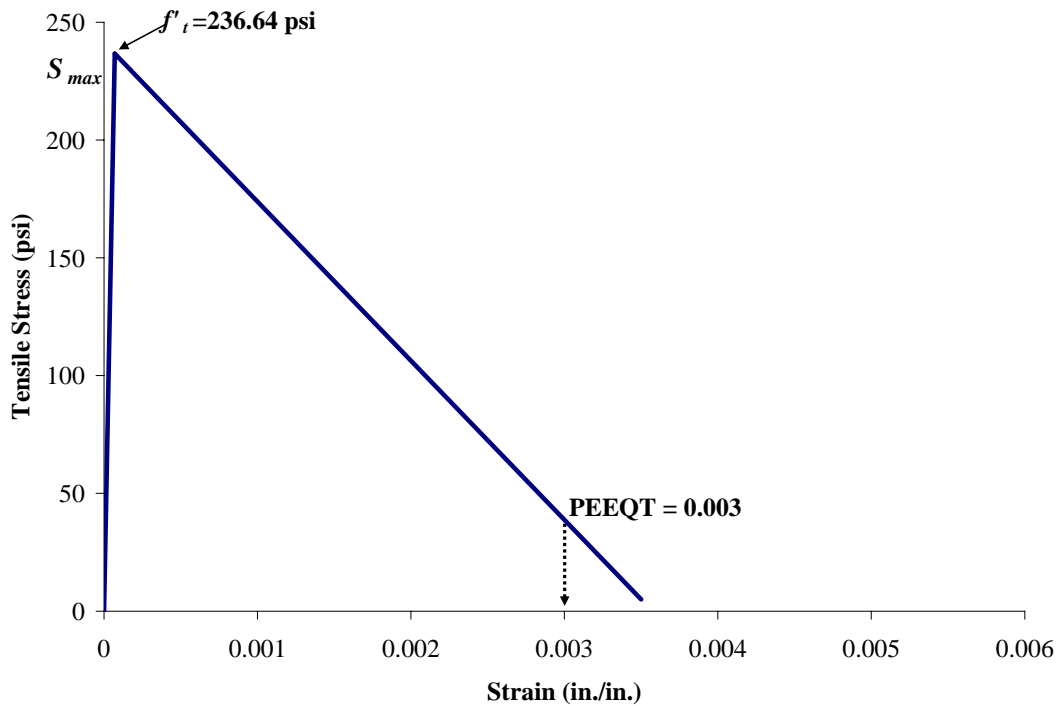
6.2.1 ADDITIONAL DISCUSSION AND LIMITATIONS

Verification and Implications of Local Events

The localized multiaxial stresses and strains and events (A – F) predicted by the numerical models could not be validated experimentally. The experimental results focused on the overall force per dowel – joint opening behavior of the pavement specimens. The stresses and strains at the dowel-concrete interfaces were not measured because they were highly localized and deep inside the concrete pavement specimens. The localized material distresses at the dowel-concrete interfaces due to the stress concentrations were also not measured using acoustic-emission or other non-destructive techniques. These are the major limitations of the experimental research, and they should be addressed by future researchers.



(a) Limit states (B), (D) and (E) on the compressive stress-strain curve



(b) Limit states (B), (C) and (F) on the tensile stress-strain curve

Figure 6.2: Identification of various limit states on the concrete compression – tension stress-strain curves

As shown in later sections 6.3 and so on, the occurrence of events (A – F) helps gain significant insight into the behavior and distresses of pavements with misaligned dowel bars. However, since the localized multiaxial stresses, strain, and events (A – F) could not be validated experimentally, they should be considered cautiously by the readers. The discussion in the following sections (6.3 and so on) implies that the events (A – F) occurred in the numerical finite element models. They do not imply or suggest that the events occur at the same joint opening in real pavement specimens. However, it is logically assumed that these distresses and events (A – F) will occur eventually in the experimental or real pavement specimens. The relative occurrence of these events for pavement specimens with different misaligned dowel bars is probably more important than their absolute joint opening values.

Discussion and Implication of Events (E) and (F)

Events (E) and (F) represent the occurrence of significant crushing and cracking plastic strains, respectively, at a material point in the numerical model. These events were chosen because the stresses and strains at the dowel-concrete interfaces have significant concentration due to dowel misalignment. As mentioned earlier in Section 5.6, joint opening is a cyclic time-varying phenomenon that will lead to fatigue failure (crack initiation) at the material point over several fatigue cycles. According to strain-life fatigue criteria (Bannantine et al. 1992), the occurrence of significant plastic strains at the material points is the major cause leading to low-cycle fatigue failure. Such fatigue strain-life equations have not yet been developed for dowel-concrete interfaces, and are a topic for future research. Without this information, it is difficult to establish a logical quantitative limit for ‘significant’ crushing or cracking plastic strains.

It is important to note that events (E) and (F) do not imply that the corresponding plastic values represent quantitatively ‘significant’ or ‘failure’ or ‘limiting’ strains because that can be established only by developing fatigue strain – life equations. Events E and F represent ‘milestones’ indicating that the material point has reached cumulative plastic strain values equal to 0.0035 and 0.003, respectively. That is the extent of implications from events E and F, nothing more. The values of 0.0035 and 0.003 were chosen arbitrarily as explained earlier. Other milestones can be chosen or used by future researchers.

The selection of events (E) and (F) was based on the cumulative plastic strain at the material point because according to the theory of plasticity, this cumulative plastic strain (PEEQ or PEEQT) has the most direct correlation with the corresponding uniaxial plastic strains in compression or tension (ABAQUS – theory manual). When the multiaxial cumulative plastic strain reaches a certain value, for example, PEEQ=0.0035, it corresponds to the same exact level of plastic strain in the uniaxial case, for example, 0.0035. No other parameter has similar exact correlations in the multiaxial and uniaxial states. The volumetric plastic strain energy was considered (area under plastic stress-strain curve, Figure 6.2 above) but not selected because it has a weaker correlation between the multiaxial and uniaxial cases. Additionally, it would require an inconsistent shift in the post-processing of the results to focus on volumetric strain energy rather than cumulative plastic strains, which is the basis for other events, for example, event B. Additionally, in the absence of a calibrated fatigue strain – life equation, both parameters (cumulative plastic strain and volumetric strain energy) imply qualitative ‘behavior’, i.e., ‘significant’ crushing or cracking, rather than quantitative assessment of fatigue life.

6.3 DISCUSSION OF ANALYTICAL AND EXPERIMENTAL RESULTS

The results from the 3D finite element analyses include the pullout force-joint opening behavior of the concrete specimens and the complex state of multiaxial (3D) stresses and strains in the model. These results can be used to identify events of damage limit states that occur in the material during the force-joint opening behavior. This section presents the results from the finite element analyses of pavement specimen models with one, two or five dowel bars at the joint. The models focuses on specimens with misalignment magnitude equal to 1/18 radians to enable greater understanding and insight. Tables 6.1(a), (b) and (c) show the specimen identification of the typical finite element models that are going to be discussed. The results from the analytical models and experimental data for the tests conducted in this research are presented in Appendix C.

Table 6.1(a) Test Matrix of the single dowel bar

Slab Dimensions	Number of Dowels	ID	Misalignment	Magnitude (in rad.)	Magnitude (in in.)
2 slabs each 24 x 24 x 10 in.	1	1A	Aligned	0	0
		1V18	Vertical	1/18	½ in. over 9 in. length of dowel
		1H18	Horizontal		
		1C18	Combined		

Table 6.1(b) Test Matrix of the two dowel bars

Slab Dimensions	Number of Dowels	ID	Misalignment	Magnitude (in rad.)	Magnitude (in in.)
2 slabs each 36 x 24 x 10 in.	2 Aligned	2A	Aligned	0	0
	2 (Uniform)	2V18U	Vertical	$+\frac{1}{18}; +\frac{1}{18}$	+ ½ in; +½ in. over 9 in. length
		2H18U	Horizontal		
		2C18U	Combined		
	2 (Non - Uniform)	2V18NU	Vertical	$+\frac{1}{18}; -\frac{1}{18}$	+ ½ in; -½ in. over 9 in. length
		2H18NU	Horizontal		
		2C18NU	Combined		
	2 (One Bar Misaligned)	2V18AM	Vertical	$\frac{1}{18}; 0$	+ ½ in; 0 over 9 in. length
		2H18AM	Horizontal		
		2C18AM	Combined		

Table 6.1(c) Test Matrix of the five dowel bars

Slab Dimensions	Number of Dowels	ID	Misalignment	Magnitude (in rad.)	Magnitude (in in.)
2 slabs each 72 x 36 x 10 in.	5 Aligned	5A	Aligned	0	0
	5 (Non - Uniform)	5V18NU	Vertical	$+\frac{1}{18}; -\frac{1}{18}; +\frac{1}{18}; -\frac{1}{18}; +\frac{1}{18}$	+ ½ in; - ½ in; + ½ in; - ½ in; + ½ in over 9 in. length
		5H18NU	Horizontal		
		5C18NU	Combined		
	5 (Alternate Bar Misaligned)	5V18AM	Vertical	$\frac{1}{18}; 0; -\frac{1}{18}; 0; \frac{1}{18}$	+ ½ in; 0; - ½ in; 0; + ½ in over 9 in. length
		5H18AM	Horizontal		
		5C18AM	Combined		

Figure 6.3 compares the experimentally measured and analytically predicted pullout force-joint opening behavior for single dowel specimens. Figures 6.4 and 6.5 compare the experimentally measured and analytically predicted pullout force-joint opening behavior for specimens with two dowels misaligned vertically or horizontally, respectively. Similarly, figures 6.6 and 6.7 compare the experimentally measured and analytically

predicted pullout force-joint opening behavior for specimens with five dowels misaligned vertically or horizontally, respectively. In figures 6.3 through 6.7, Cases I and II correspond to the use of idealized and experimentally established static friction coefficients and material properties, as explained earlier in section 5.4.3.

6.3.1 SINGLE DOWEL BAR MODELS

Figures 6.3 (a-d) compare the experimental and analytical pullout force-joint opening results for the single dowel bar specimens. These figures include the analytical results for cases I and II and identify the events / damage limit states (A) to (F) on the analytical results. As shown in figure 6.3(a), for specimen 1A, only the debonding event occurs in the analytical models. No other events or material damage limit states were observed, confirming the hypothesis that an aligned dowel bar gives the best performance in a pavement joint.

Table 6.2(a) presents the joint opening and the pullout forces for the various events or damage limit states (B) to (F) as they occur during the force-joint opening behavior of the analysis of specimens 1V18 and 1H18. Both the cases I and II are included in Table 6.2(a). For specimen 1V18, event (E) occurs for case II at joint opening = 0.349 in. and a dowel pullout force = 2675.23 lbs. Event (F) is not reached in the analysis of specimen 1V18. For specimen, 1H18, shown in figure 6.3(c), events or damage limit states (B - F) all occur at nearly the same joint opening for cases I and II. The analytical results indicate that the event (F) occurs prior to (E), which indicates that significant cracking occurs before significant crushing. For specimen, 1C18, shown in figure 6.3(d), events or damage limit states (B-C) and (B-E) occur for cases I and II.

Table 6.2(a) presents the pullout force and joint opening at which these events or damage limit states occur in the FE model.

6.3.2 TWO DOWEL BAR MODELS

Figure 6.4(a-d) compares the experimental and analytical results, i.e., force-joint opening responses for the two dowel bar specimens with vertical misalignment magnitude of 1/18 radians only. These include specimens with aligned dowels (2A), non-uniform (2V18NU), uniform (2V18U) and alternate misalignments (2V18AM).

As shown in figure 6.4(a), both the experimental and analytical results for specimen 2A indicate the occurrence of only the debonding limit state (event A). For specimen 2V18NU, shown in figure 6.4(b), the analytical results indicate that all the events / material damage limit states (A-F) occur for case (I) analysis. Case II analysis results show that event / material damage limit state (E) occurs but the event / material damage limit state (D) ($S_{min} > f'_c$) does not occur. This is because inelasticity occurs due to multiaxial stresses with $S_{min} < f'_c$. Events (B) and (E) occur but event (D) which focused on ($S_{min} > f'_c$) does not occur. This indicates that inelastic strain event or damage limit states (E, F) should be emphasized over the principal stress limit states (C, D) due to the multiaxial nature of the stress state. For specimen 2V18U, for both cases I and II, only events or damage limit states (A)-(C) occur in the finite element models as shown in figure 6.4(c). This means that very little material damage or inelasticity occurs in this specimen. Similar trend in the formation of events / damage limit states are observed in the 2V18AM specimen, as shown in figure 6.4(d).

Figure 6.5(a-d) compares the experimental and analytical force-joint opening results for the two dowel bar specimens with horizontal misalignment magnitude 1/18

radians only. These include specimens with aligned dowels (2A), non-uniform (2H18NU), uniform (2H18U) and alternate misalignments (2H18AM). As shown in figure 6.5(b), for specimen 2H18NU, all events / material damage limit states (A-F) occur for case I and II analysis. For specimen 2H18U, events / material damage limit states (A-E) occur in the analysis of case I whereas all the events / material damage limit states (A-F) occurs in case II, as shown in figure 6.5(c). In specimen 2H18AM, figure 6.5(d), all the events / damage limit states (A-F) occur in case I and II analysis.

Figure 6.6(a-d) compares the experimental and analytical force-joint opening results for the two dowel bar specimens with combined misalignment magnitude of 1/18 radians only. The results shown are for analysis of specimens with aligned dowels (2A), non-uniform (2C18NU), uniform (2C18U) and alternate misalignments (2C18AM). As shown in figure 6.6(b), for specimen 2C18NU, all events / material damage limit states (A-F) occur for case I and II analysis. For specimen 2C18U, events / material damage limit states (A-D) occur in the analysis of case I whereas all the events / material damage limit states (A-F) occurs in case II, as shown in figure 6.6(c). In specimen 2C18AM, figure 6.6(d), all the events / damage limit states (A-F) occur in case I and II analysis.

Table 6.2(b), (c) and (d) present the joint opening and pullout force for the various events / damage limit states (A) to (F) as they occur in the analysis for two dowel bars having vertical, horizontal and combined type of misalignments, respectively.

6.3.3 FIVE DOWEL BAR MODELS

Figure 6.7(a-c) compares the experimental and analytical force-joint opening results for the five dowel bar specimens with vertical misalignment magnitude of 1/18 radians only. These include specimens with aligned dowels (5A), non-uniform (5V18NU) and alternate

misalignments (5V18AM). As shown in figure 6.7(b) and 6.7(c), for specimen 5V18NU and 5V18AM respectively, all events / damage limit states (A-F) occur for case I and II analyses. These results indicate that the specimen will fail significantly in cracking and crushing at the dowel-concrete interfaces.

Figures 6.8(a-c) compares the experimental and analytical force-joint opening results for the five dowel bar specimens with horizontal misalignment magnitude $1/18$ radians only. These include specimens with aligned dowels (5A), non-uniform (5H18NU) and alternate misalignments (5H18AM). As shown in figure 6.8(b), for specimen 5H18NU, all events / damage limit states (A-F) occur for case I and for case II analysis, events / damage limit states from A-D occur. For specimen 5H18AM, figure 6.8(c), all the events / damage limit states (A-F) occur in the case I and II analyses.

Figure 6.9(a-c) compares the experimental and analytical force-joint opening results for the five dowel bar specimens with combined misalignment magnitude of $1/18$ radians only. These include specimens with aligned dowels (5A), non-uniform (5C18NU) and alternate misalignments (5C18AM). As shown in figure 6.9(b) and (c), for specimen 5C18NU and 5C18AM respectively, all events / damage limit states (A-F) occur for case I and II analyses. These results indicate that the specimen will fail significantly in cracking and crushing at the dowel-concrete interfaces. The joint opening and pullout forces per bar are presented in tables 6.2(e), (f) and (g), for five dowels with vertical, horizontal and combined misalignments respectively.

Table 6.2(a): Summary of the pullout load – joint opening for cases I and II in the 1V18, 1H18 and 1C18 tests

Events	1V18				1H18				1C18			
	Joint Opening (in)		Pullout Load (lbs)		Joint Opening (in)		Pullout Load (lbs)		Joint Opening (in)		Pullout Load (lbs)	
	(I)	(II)	(I)	(II)	(I)	(II)	(I)	(II)	(I)	(II)	(I)	(II)
(B)	0.015	0.038	1180.0	1450	0.018	0.034	1200.0	1480.0	0.012	0.014	1160.0	1240.0
(C)	0.115	-	1560.0	-	0.018	0.051	1200.0	1660.0	0.016	0.014	1190.0	1240.0
(D)	-	0.148	-	2170	0.214	0.228	1780.0	2680.0	-	0.116	-	2180.0
(E)	-	-	-	-	0.535	0.425	1940.0	3180.0	-	0.126	-	2240.0
(F)	-	-	-	-	0.260	0.217	1840.0	2620.0	-	-	-	-

Table 6.2(b): Summary of pullout load-joint opening for case (i) and (ii) in the 2V18NU, 2V18U and 2V18AM test

Events	2V18NU				2V18U				2V18AM			
	Joint Opening (in)		Pullout Load (lbs)		Joint Opening (in)		Pullout Load (lbs)		Joint Opening (in)		Pullout Load (lbs)	
	(I)	(II)	(I)	(II)	(I)	(II)	(I)	(II)	(I)	(II)	(I)	(II)
(B)	0.010	0.021	846.00	1002.53	0.015	0.012	957.78	947.95	0.002	0.002	505.34	507.34
(C)	0.023	0.025	112.82	1321.06	0.034	0.025	1302.88	1229.25	0.015	0.015	893.57	925.84
(D)	0.339	0.552	2244.78	3247.22	-	-	-	-	0.051	0.034	1397.25	1232.84
(E)	0.337	0.335	2244.09	3059.84	-	-	-	-	-	-	-	-
(F)	0.269	0.233	2225.76	2880.03	-	-	-	-	-	-	-	-

Table 6.2(c): Summary of pullout load-joint opening for case (i) and (ii) in the 2H18NU, 2H18U and 2H18AM test

Events	2H18NU				2H18U				2H18AM			
	Joint Opening (in)		Pullout Load (lbs)		Joint Opening (in)		Pullout Load (lbs)		Joint Opening (in)		Pullout Load (lbs)	
	(I)	(II)	(I)	(II)	(I)	(II)	(I)	(II)	(I)	(II)	(I)	(II)
(B)	0.010	0.010	859.91	943.06	0.016	0.012	963.53	949.91	0.013	0.015	852.68	937.34
(C)	0.023	0.022	1141.23	1279.29	0.034	0.0362	1314.26	1481.65	0.040	0.034	1272.77	1251.89
(D)	0.214	0.280	2243.57	3139.88	0.333	0.374	2247.57	2957.96	0.262	0.266	2116.95	2507.60
(E)	0.293	0.297	2299.83	3236.9	0.5452	0.492	2297.17	3128.53	-	0.348	-	2619.57
(F)	0.272	0.246	2285.39	3098.24	0.4101	0.335	2267.68	2912.34	0.288	0.256	2129.46	2454.00

Table 6.2(d): Summary of pullout load-joint opening for case (i) and (ii) in the 2C18NU, 2C18U and 2C18AM test

Events	2C18NU				2C18U				2C18AM			
	Joint Opening (in)		Pullout Load (lbs)		Joint Opening (in)		Pullout Load (lbs)		Joint Opening (in)		Pullout Load (lbs)	
	(I)	(II)	(I)	(II)	(I)	(II)	(I)	(II)	(I)	(II)	(I)	(II)
(B)	0.014	0.014	935.0	1025.0	0.0038	0.0098	530.65	735.0	0.0097	0.009	794.0	805.0
(C)	0.017	0.017	1070.0	1225.0	0.0075	0.015	615.0	980.0	0.018	0.026	980.0	1195.0
(D)	0.154	0.205	2330.0	3225.0	0.534	0.253	1125.0	1165.0	0.179	0.200	2095.0	2455.0
(E)	0.231	0.239	2415.0	3330.0	-	0.126	-	2410.0	-	0.259	-	2605.0
(F)	0.202	0.205	2395.0	3225.0	-	-	-	-	0.227	0.200	2175.0	2455.0

Table 6.2(e): Summary of the pullout load – joint opening for cases I and II in the 5V18NU and 5V18AM tests

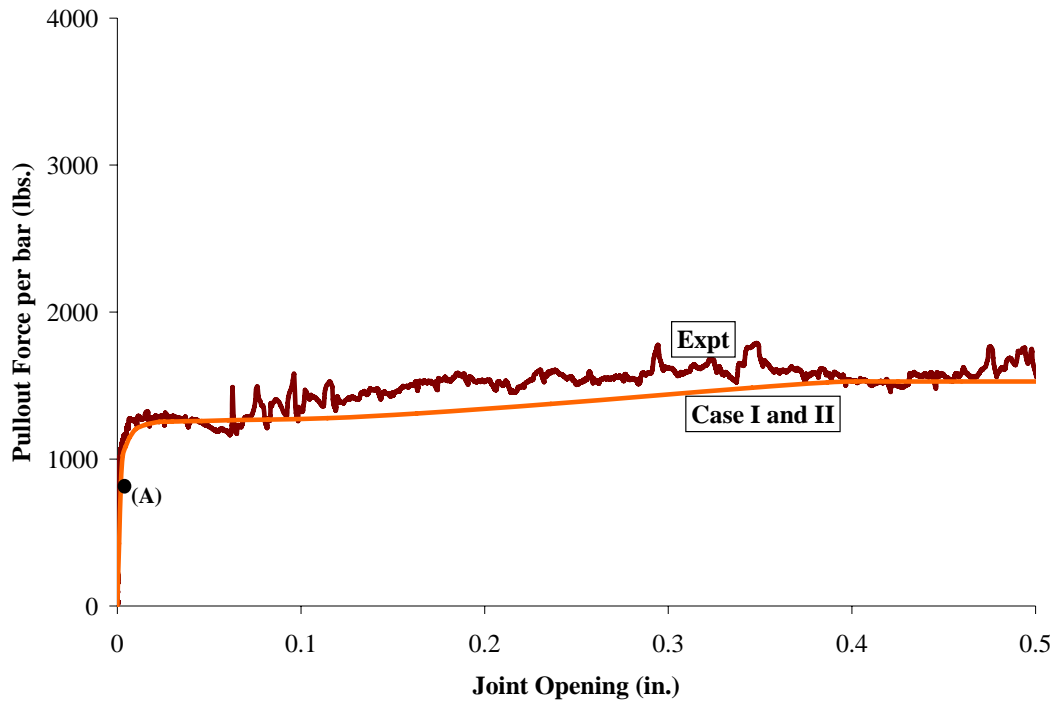
Events	5V18NU				5V18AM			
	Joint Opening (in)		Pullout Load (lbs)		Joint Opening (in)		Pullout Load (lbs)	
	(I)	(II)	(I)	(II)	(I)	(II)	(I)	(II)
(B)	0.022	0.015	1451.97	1353.50	0.032	0.017	1510.0	1290.0
(C)	0.051	0.034	1701.96	1802.57	0.047	0.036	1600.0	1640.0
(D)	0.230	0.358	2227.88	3239.90	0.208	0.260	2020.0	2470.0
(E)	0.346	0.358	2289.98	3239.90	0.352	0.368	2130.0	2610.0
(F)	0.404	0.307	2307.90	3163.28	0.439	0.347	2160.0	2650.0

Table 6.2(f): Summary of the pullout load – joint opening for cases I and II in the 5H18NU and 5H18AM tests

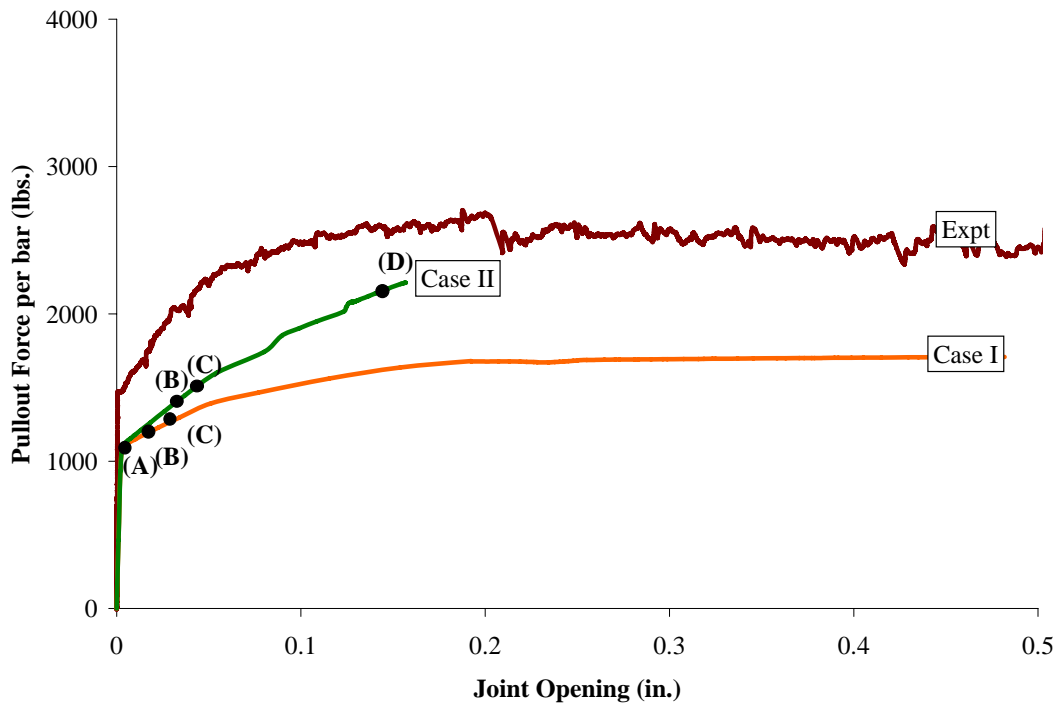
Events	5H18NU				5H18AM			
	Joint Opening (in)		Pullout Load (lbs)		Joint Opening (in)		Pullout Load (lbs)	
	(I)	(II)	(I)	(II)	(I)	(II)	(I)	(II)
(B)	0.016	0.0077	1302.90	843.0	0.016	0.016	1120.0	1180.0
(C)	0.052	0.023	1715.65	1570.0	0.046	0.046	1470.0	1620.0
(D)	0.155	0.206	2099.70	2820.0	0.146	0.147	1750.0	2090.0
(E)	0.232	-	2256.34	-	0.290	0.290	1950.0	2490.0
(F)	0.257	-	2275.36	-	0.377	0.355	2000.0	2630.0

Table 6.2(g): Summary of the pullout load – joint opening for cases I and II in the 5C18NU and 5C18AM tests

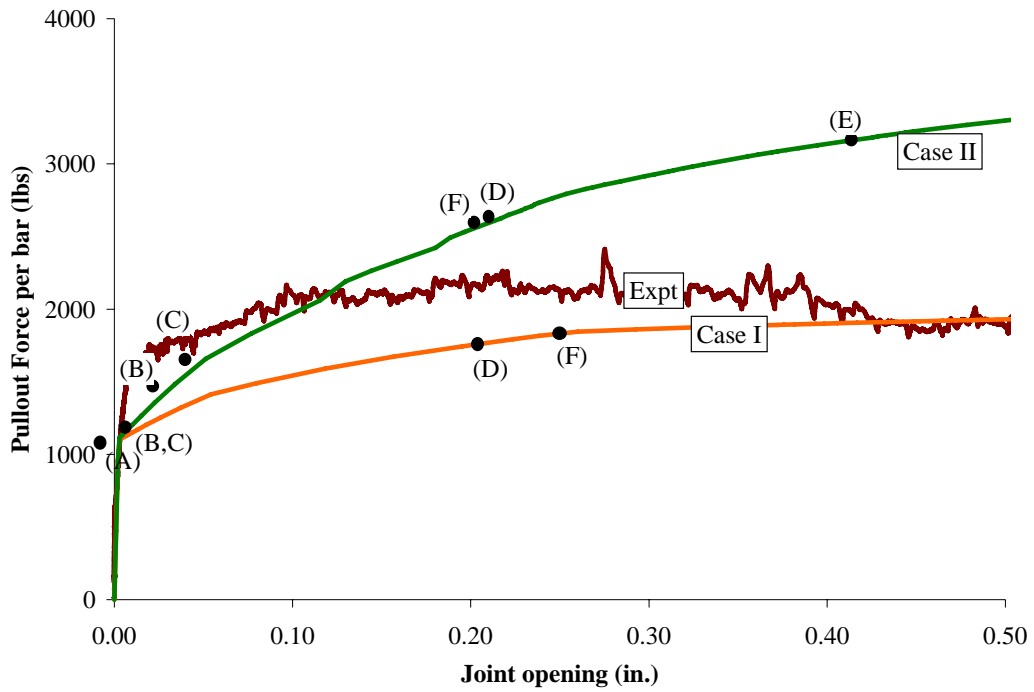
Events	5C18NU				5C18AM			
	Joint Opening (in)		Pullout Load (lbs)		Joint Opening (in)		Pullout Load (lbs)	
	(I)	(II)	(I)	(II)	(I)	(II)	(I)	(II)
(B)	0.0152	0.012	1340.0	1140.0	0.004	0.004	531.0	1550.0
(C)	0.0158	0.013	1360.0	1240.0	0.006	0.006	759.0	1810.0
(D)	0.137	0.142	2100.0	2670.0	0.012	0.013	1140.0	2270.0
(E)	0.373	0.388	2460.0	3630.0	-	0.254	-	3330.0
(F)	0.170	0.265	2230.0	3280.0	0.154	0.143	2040.0	3090.0



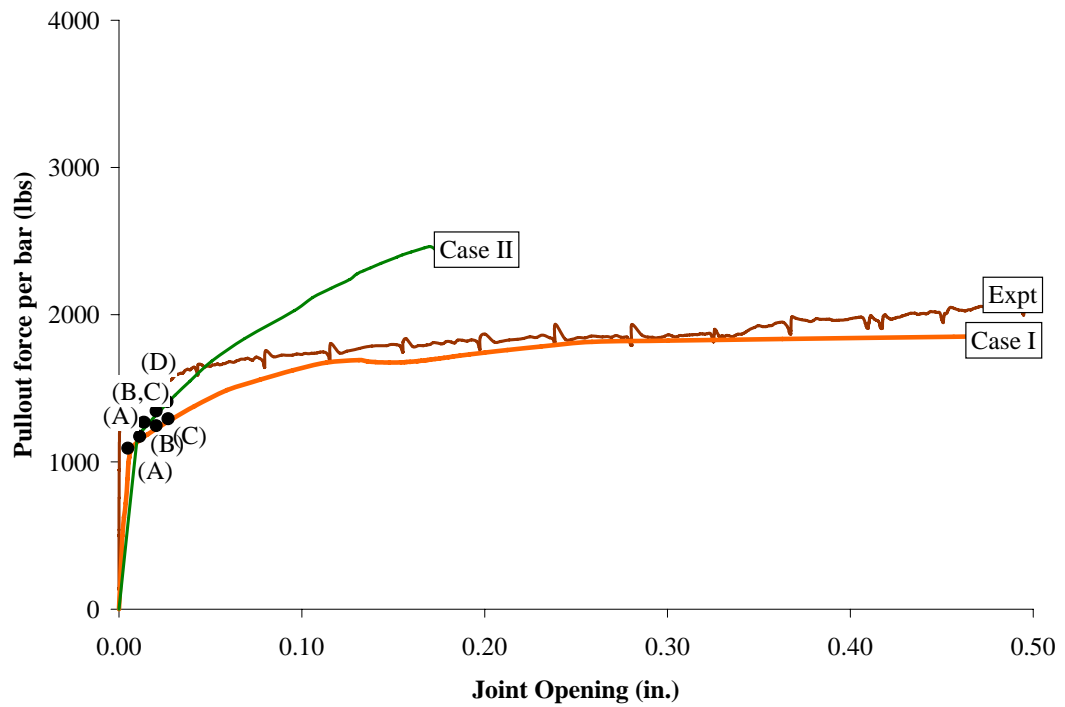
(a) Model for 1A Test



(b) Model for 1V18 Test

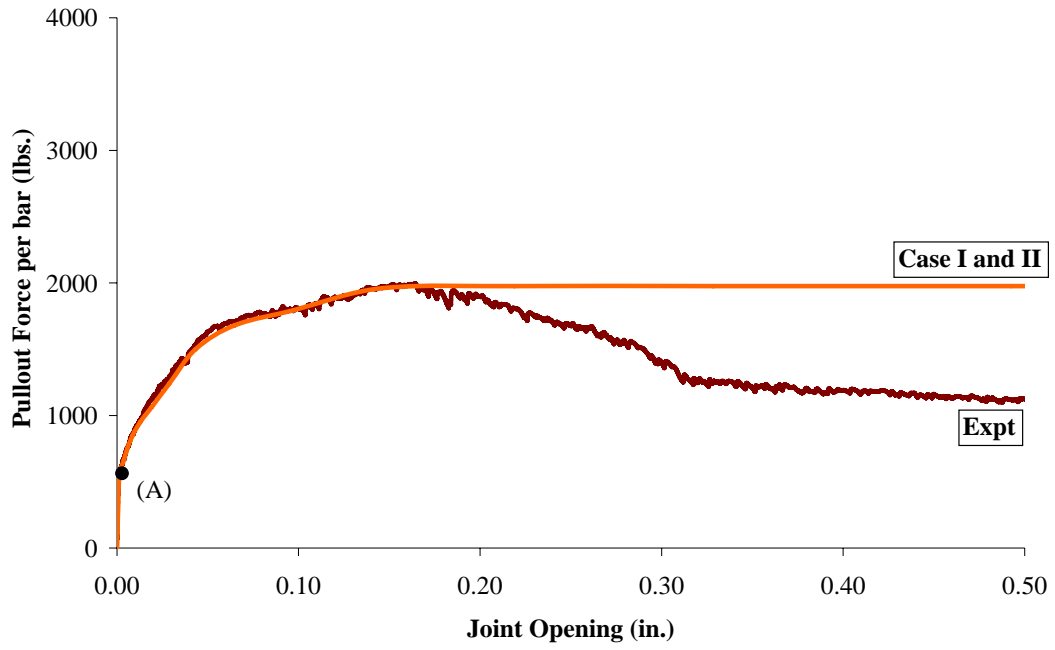


(c) Model for 1H18 Test

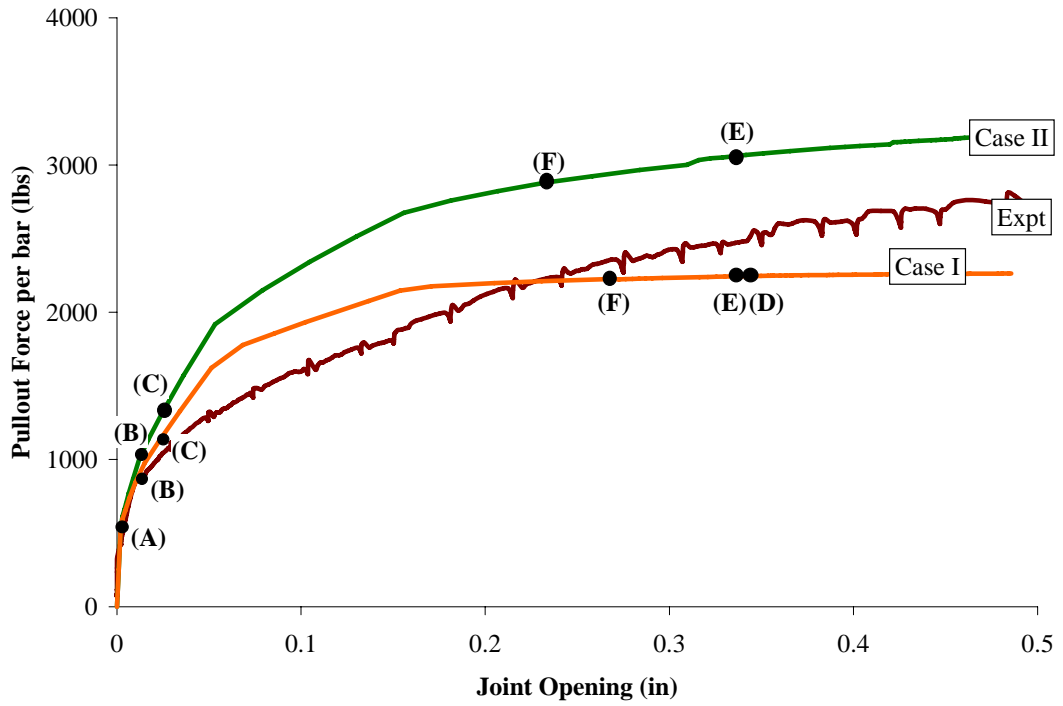


(d) Model for 1C18 Test

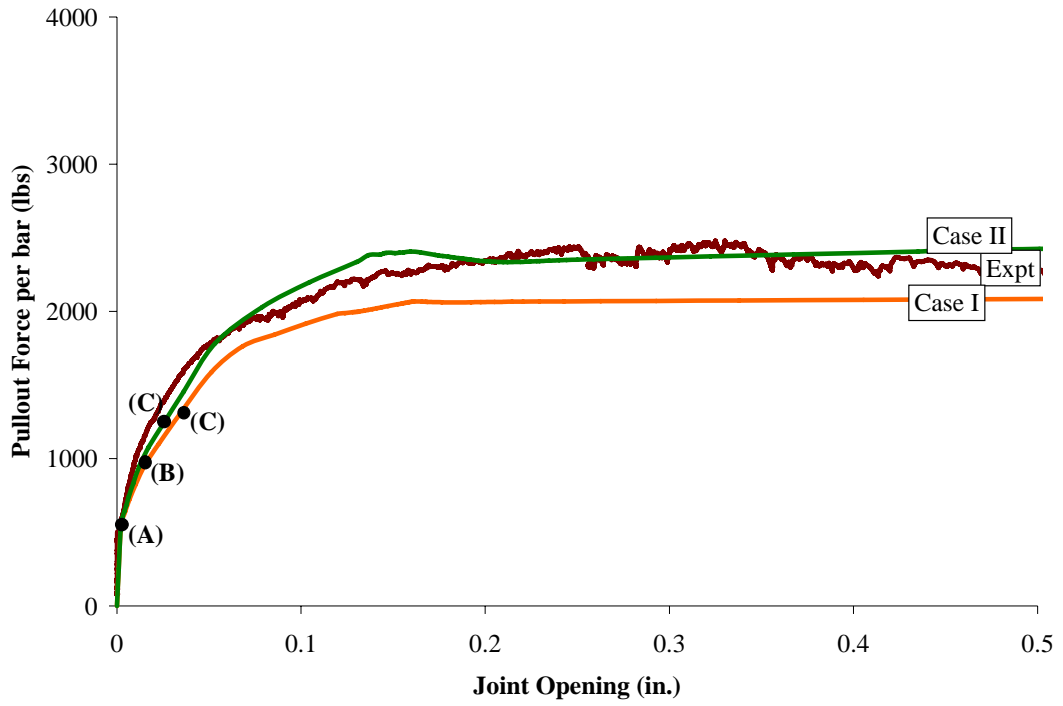
Figure 6.3: Comparison of the FEM model with the experimental data for a single dowel bar specimen



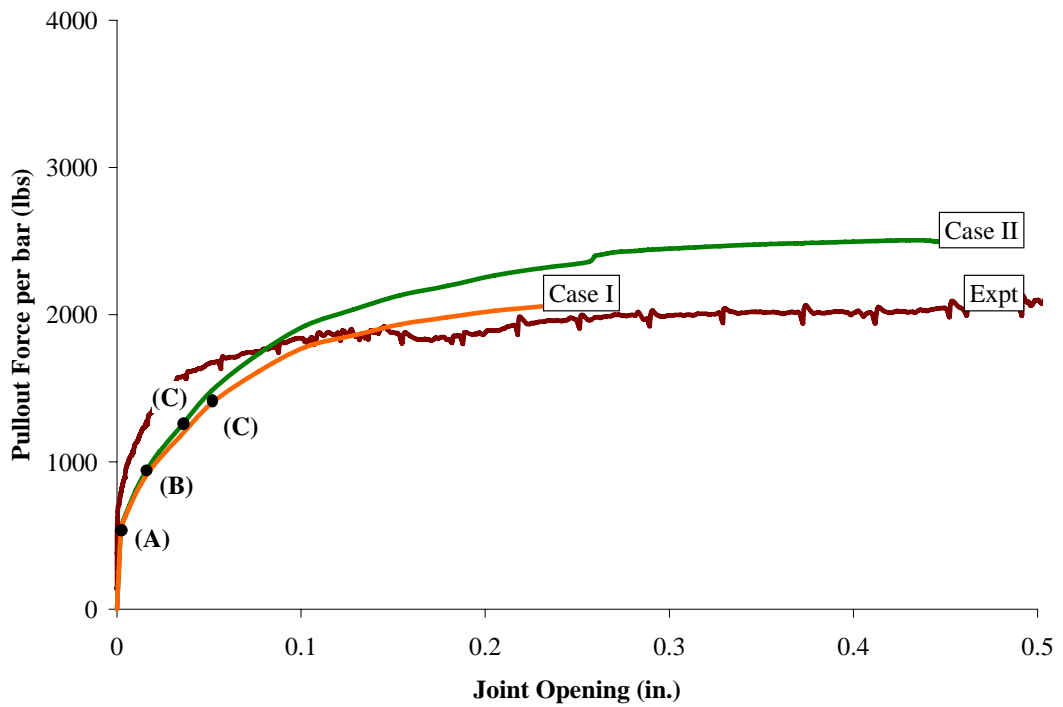
(a) Model for 2A Test



(b) Model for 2V18NU Test

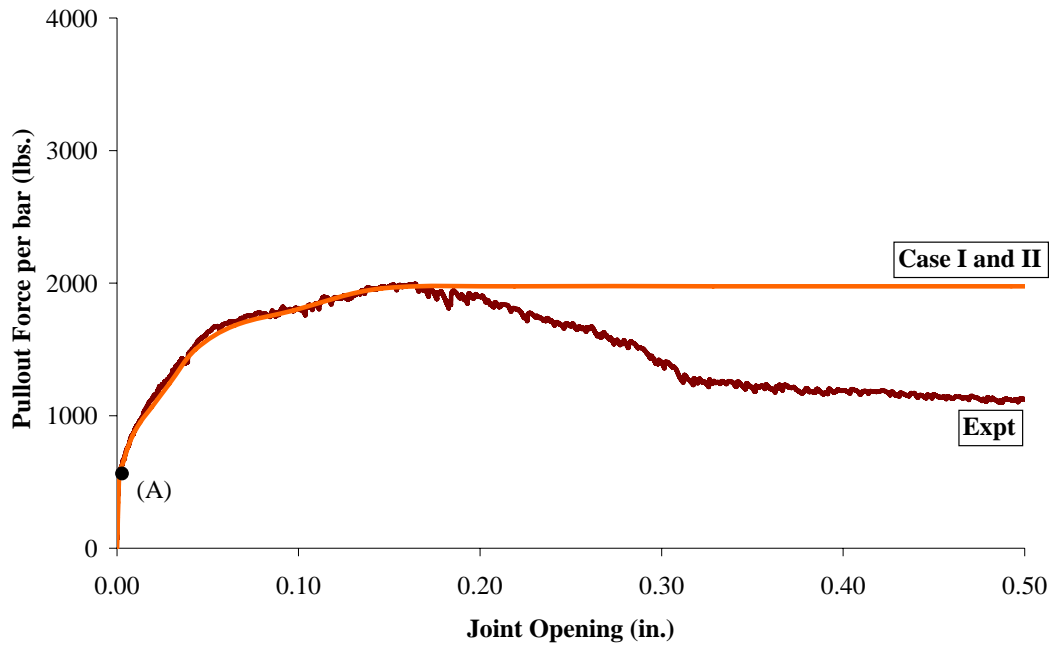


(c) Model for 2V18U Test

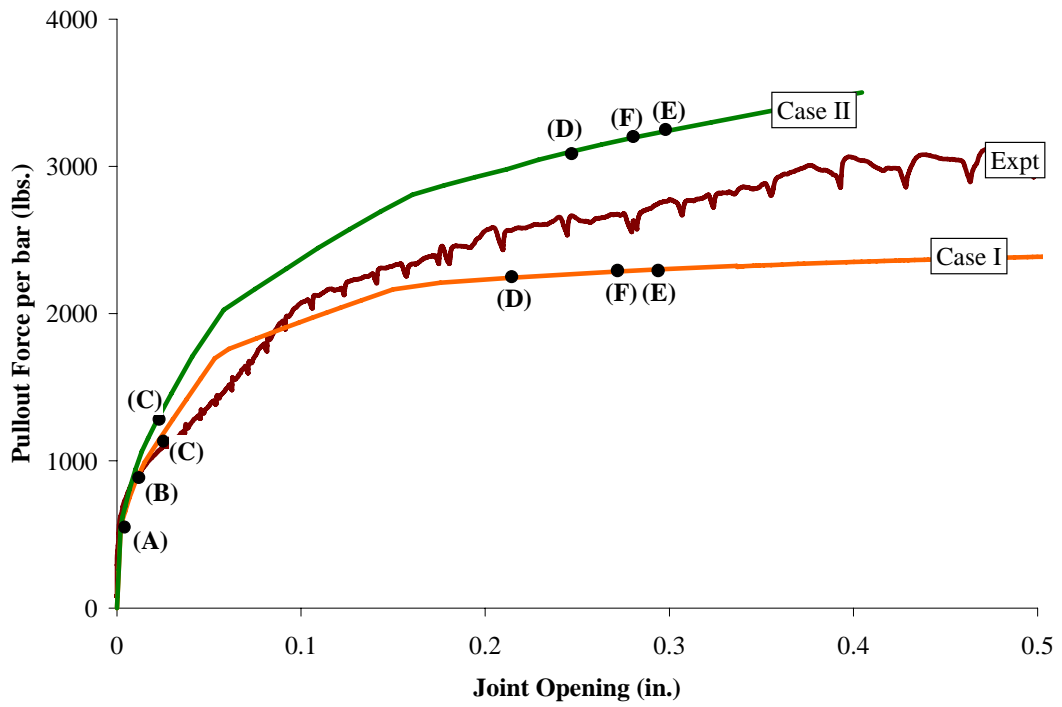


(d) Model for 2V18AM Test

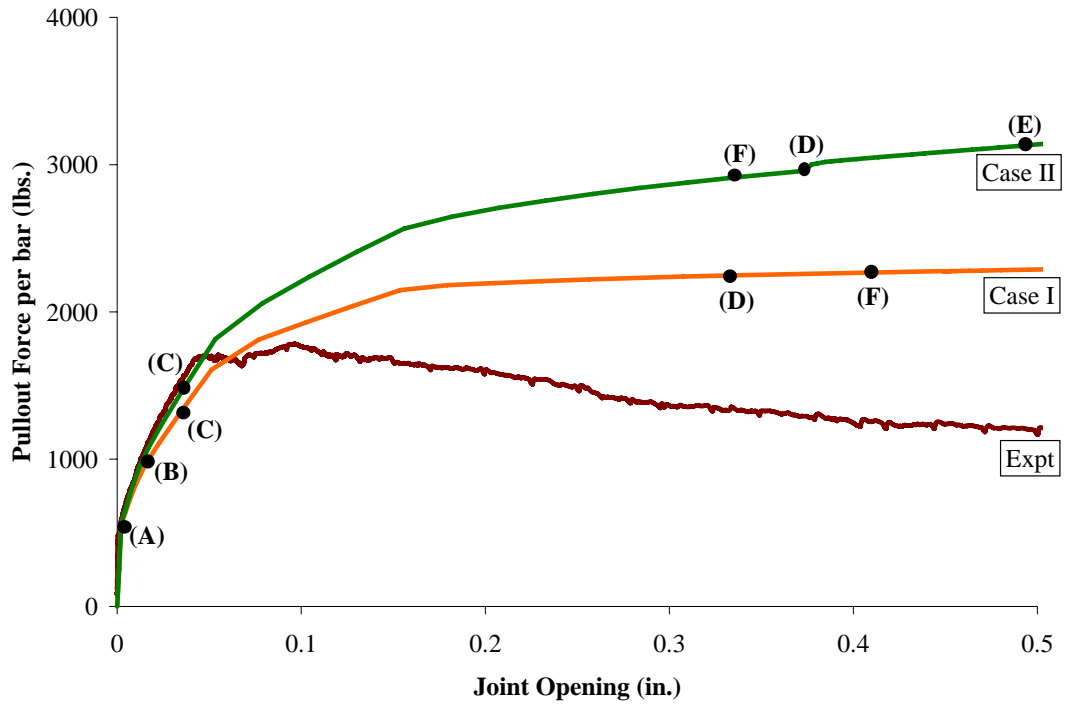
Figure 6.4: Comparison of FEM and experimental data for a two dowel bars with vertical misalignment



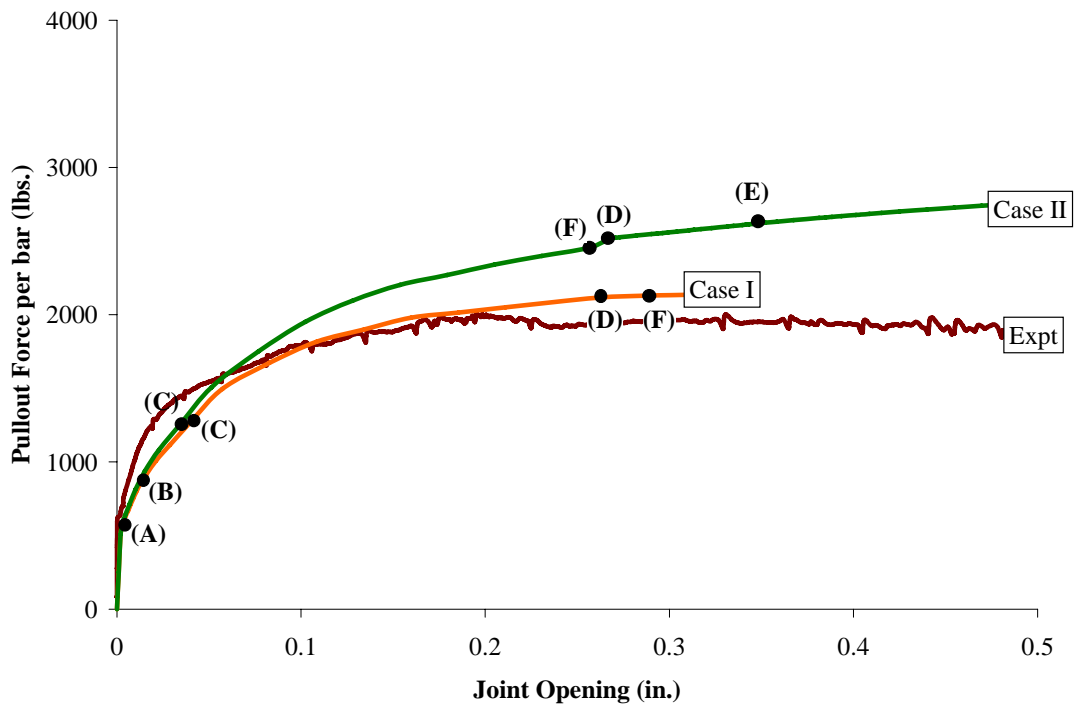
(a) Model for 2A Test



(b) Model for 2H18NU Test

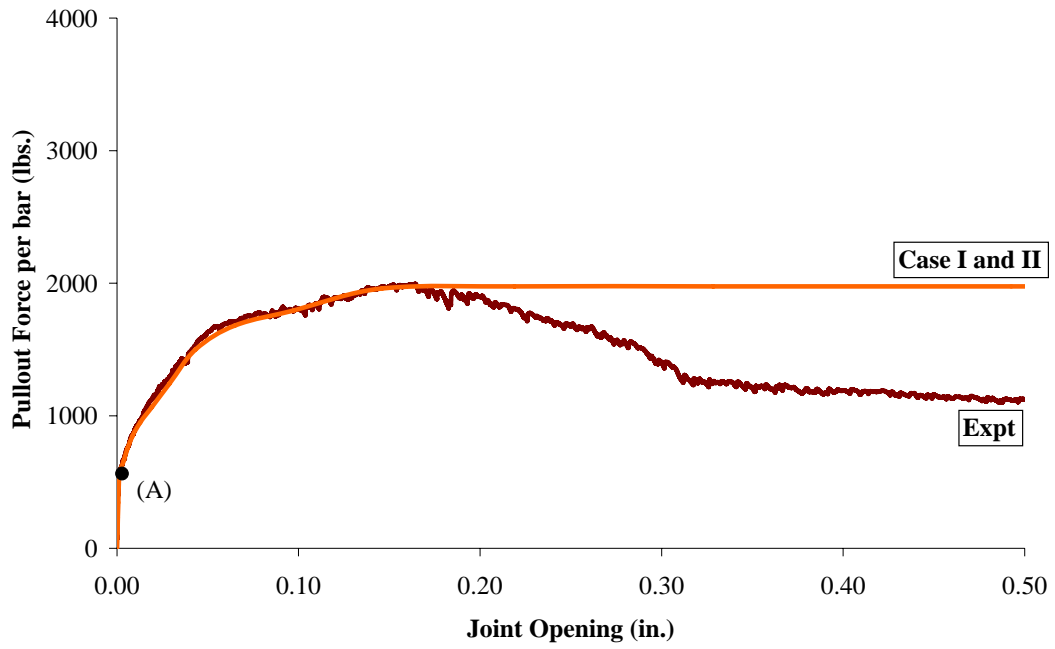


(c) Model for 2H18U Test

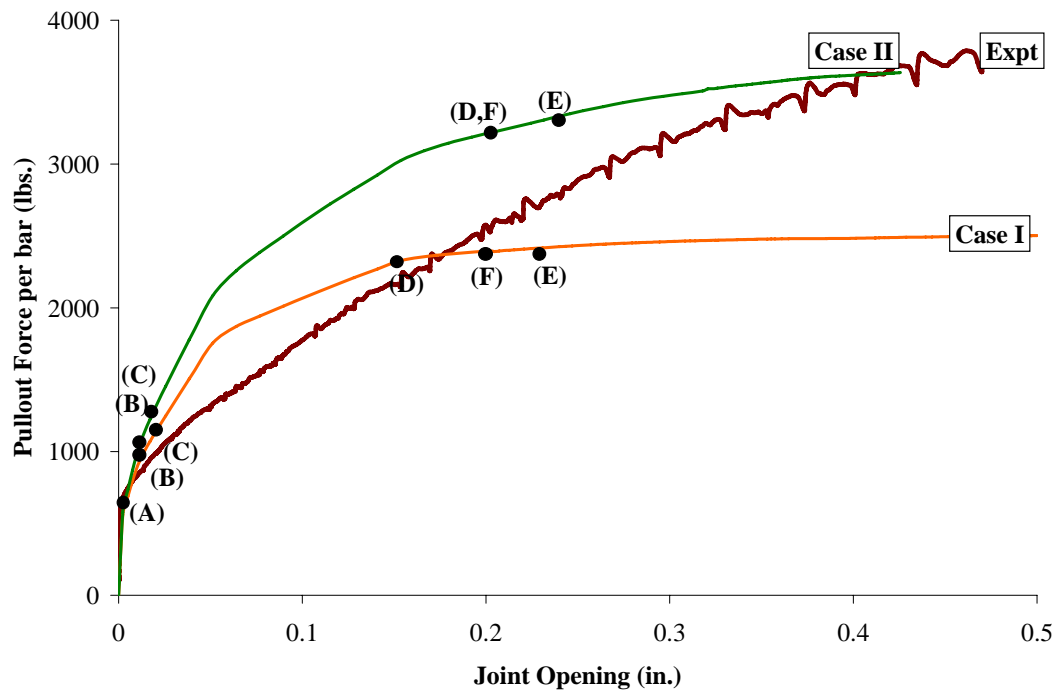


(d) Model for 2H18AM Test

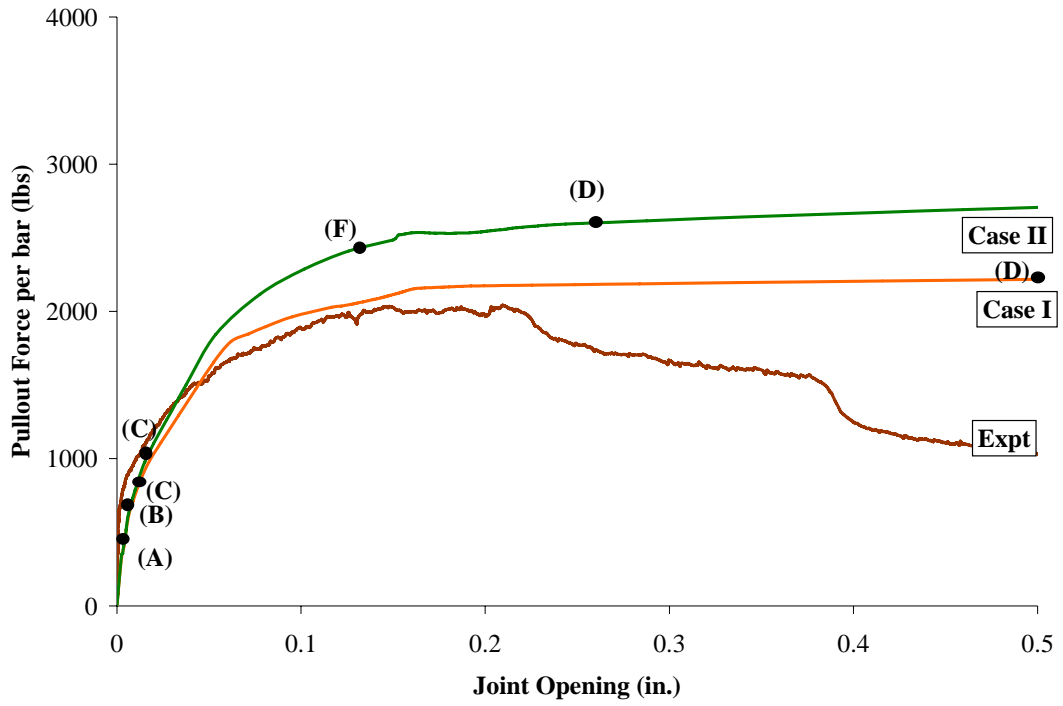
Figure 6.5: Comparison of FEM and experimental data for a two dowel bars with horizontal misalignment



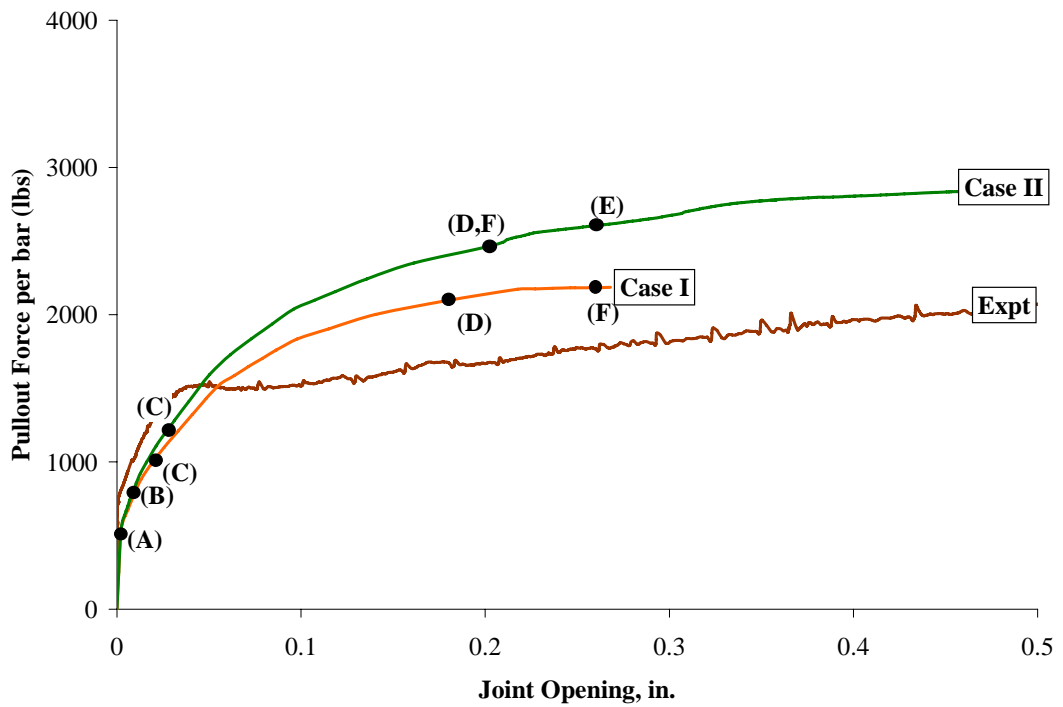
(a) Model for 2A Test



(b) Model for 2C18NU Test

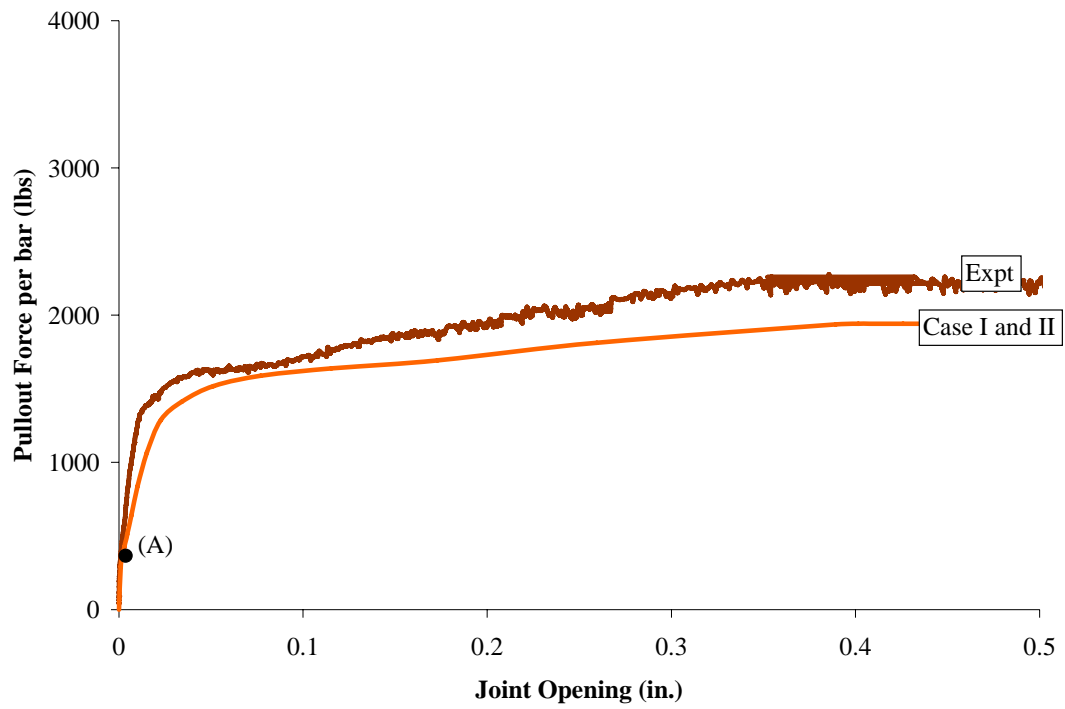


(c) Model for 2C18U Test

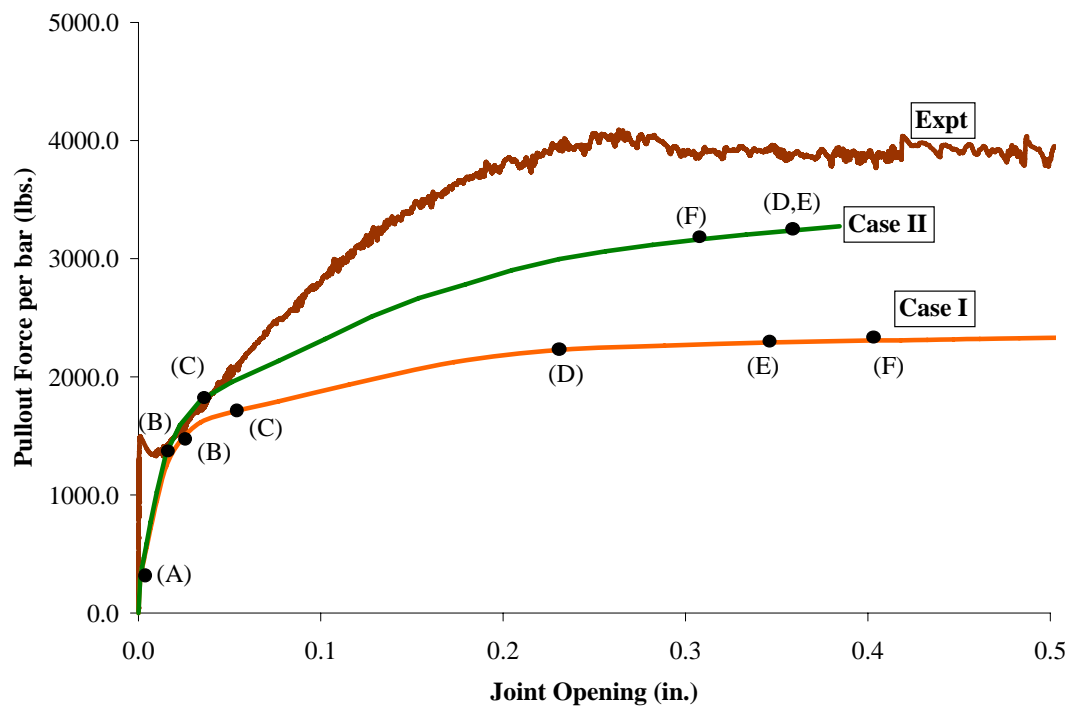


(d) Model for 2C18AM Test

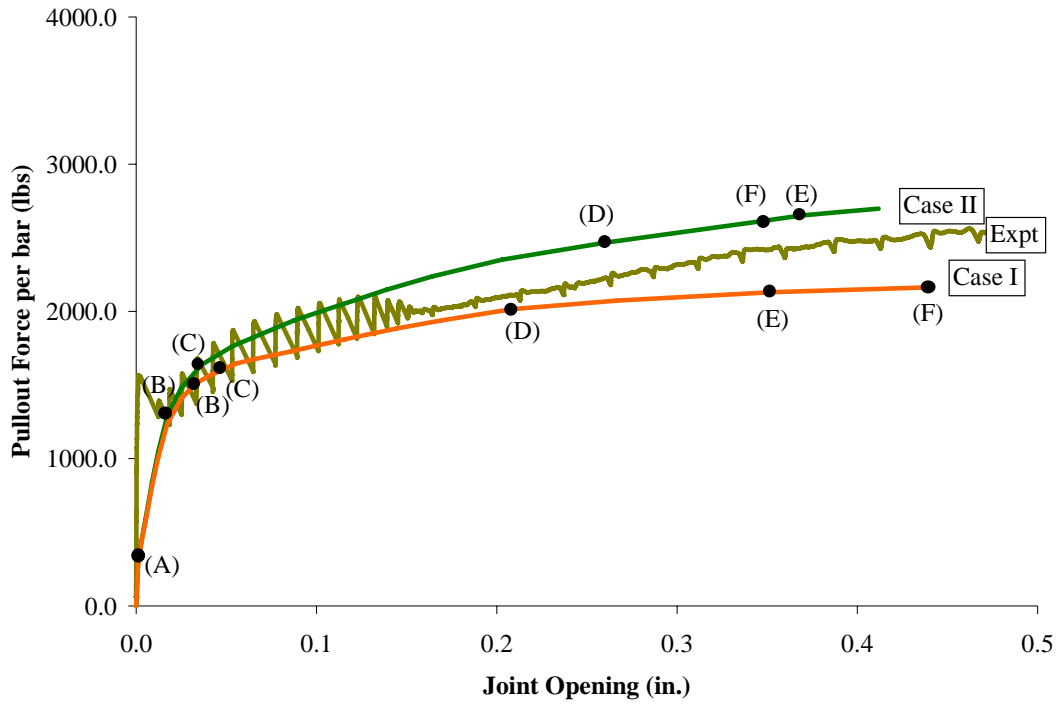
Figure 6.6: Comparison of FEM and experimental data for a two dowel bars with combined misalignment



(a) Model for 5A Test

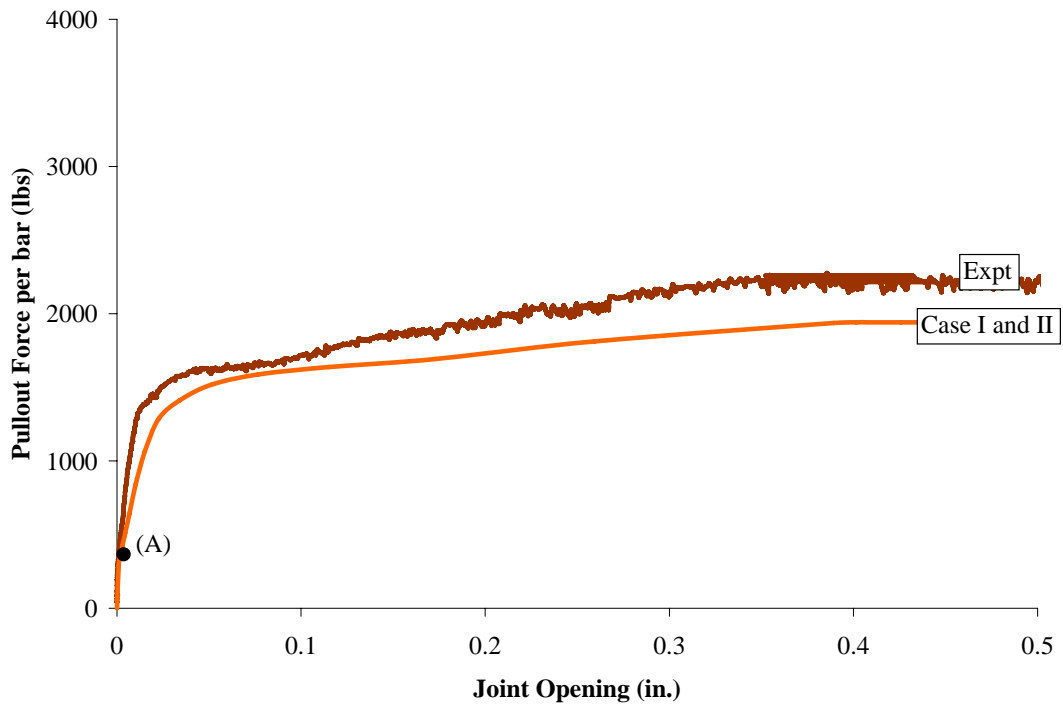


(b) Model for 5V18NU Test

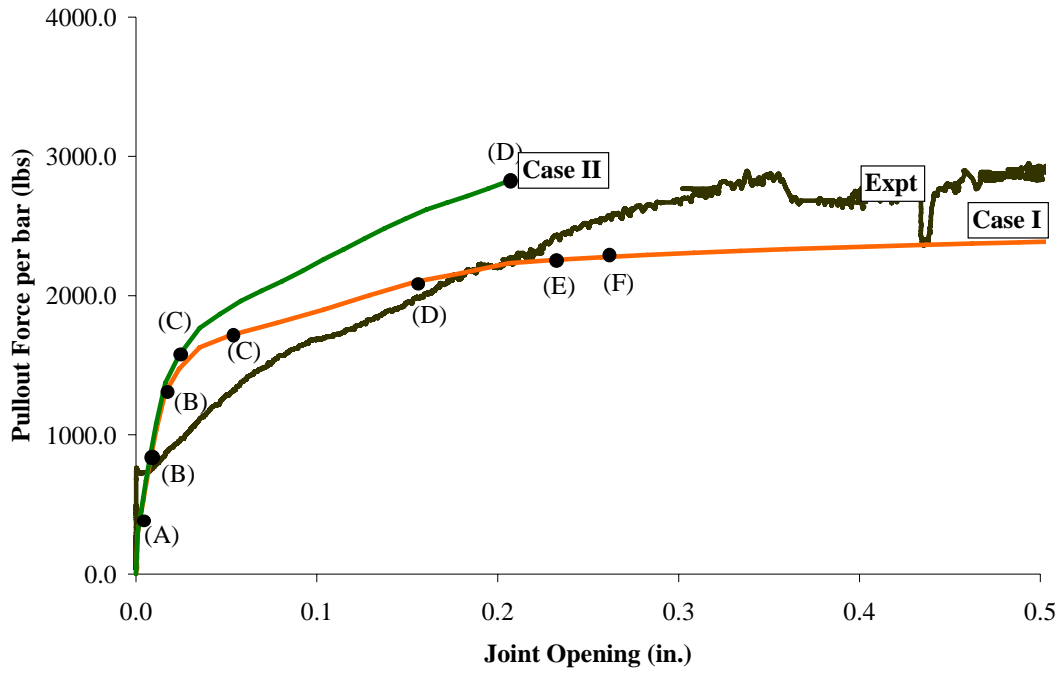


(c) Model for 5V18AM Test

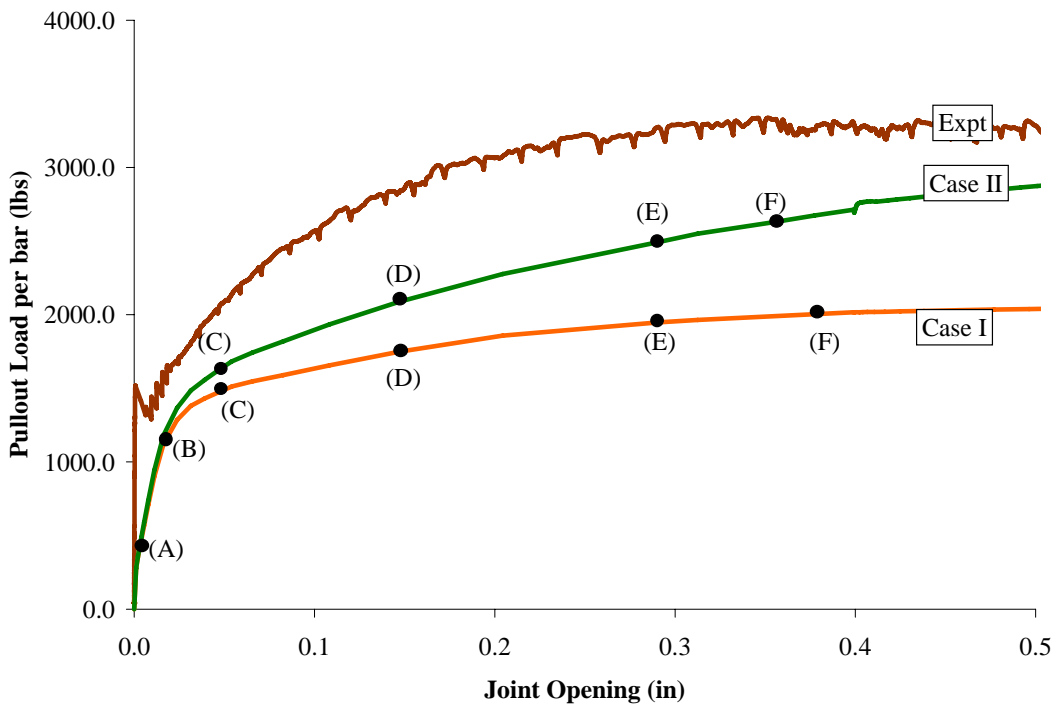
Figure 6.7: Comparison of FEM and experimental data for five dowel bars with vertical misalignment



(a) Model for 5A Test

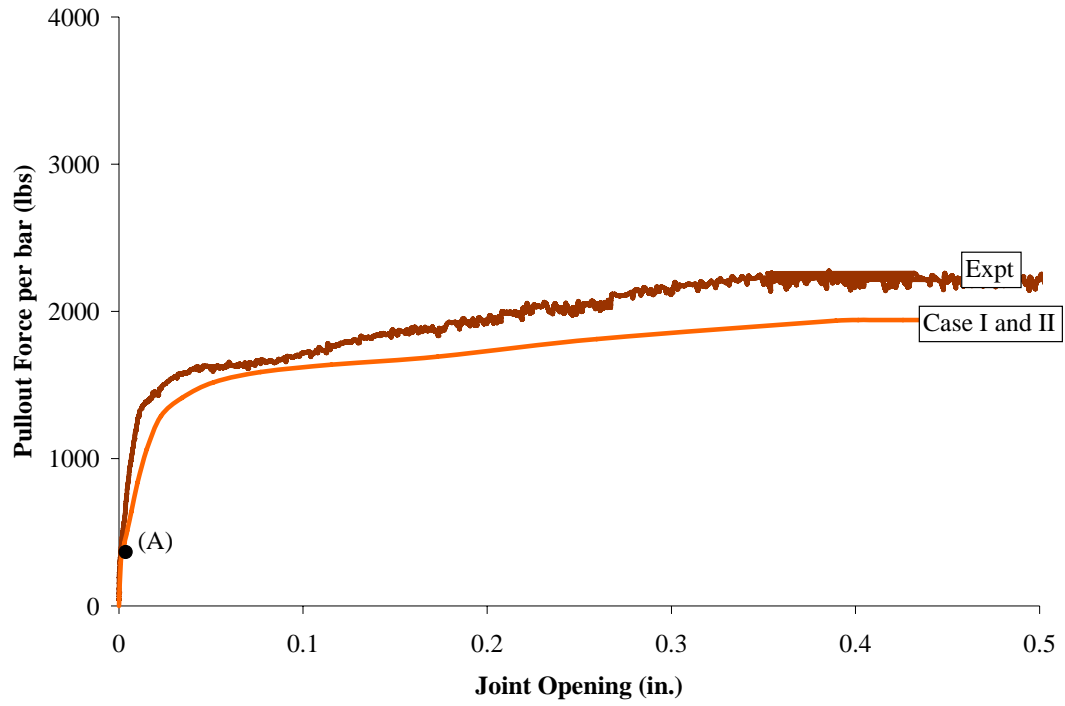


(b) Model for 5H18NU Test

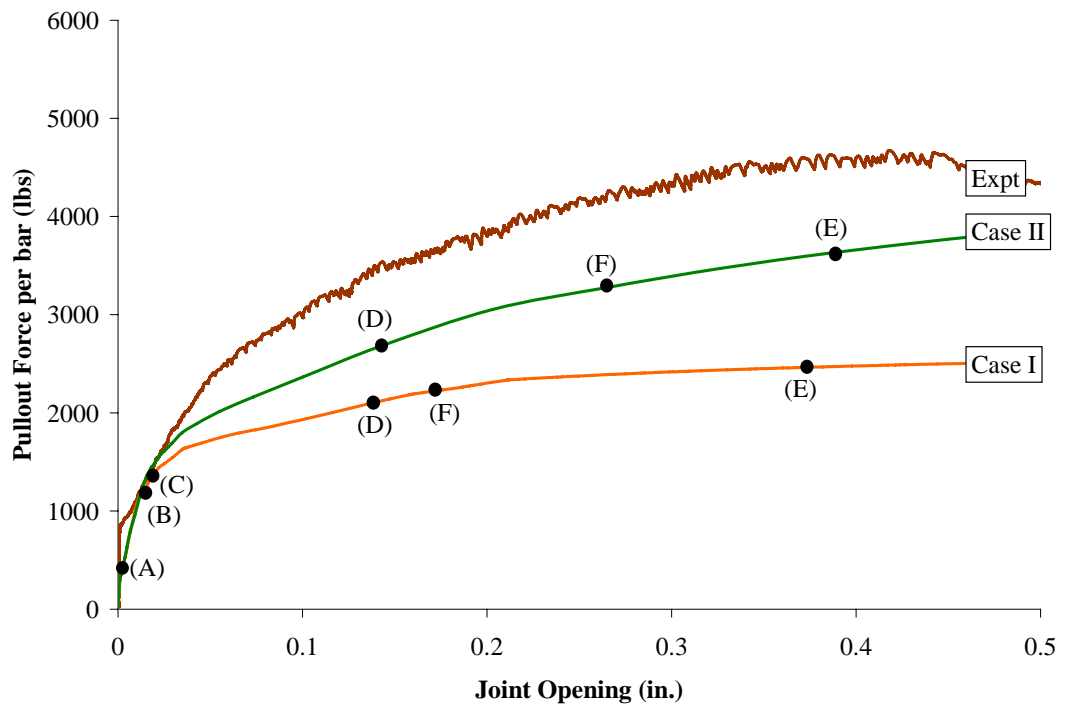


(c) Model for 5H18AM Test

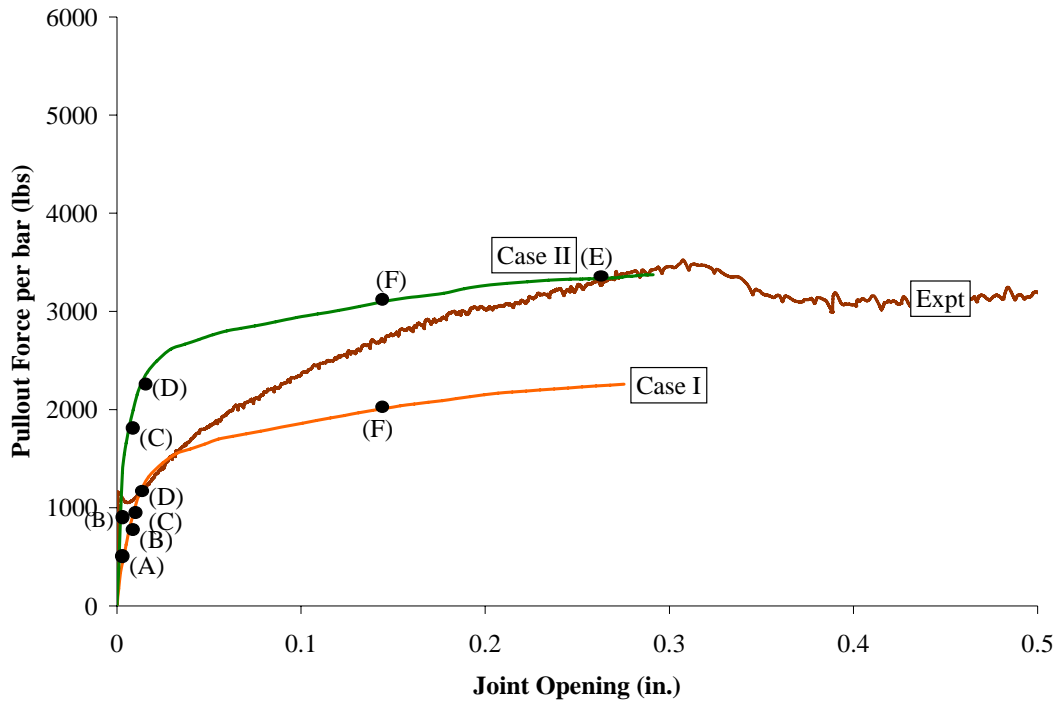
Figure 6.8: Comparison of FEM and experimental data for five dowel bars with horizontal misalignment



(a) Model for 5A Test



(b) Model for 5C18NU Test



(c) Model for 5C18AM Test

Figure 6.9: Comparison of FEM and experimental data for five dowel bars with combined misalignment

6.3.4 CONCLUDING REMARKS ON THE 3D FINITE ELEMENT ANALYTICAL MODELS WITH EVENTS / MATERIAL DAMAGE LIMIT STATES

In all the finite element analytical models, stress concentration zones occurred in concrete at the joint face around misaligned dowel bars. The results from the 3D finite element models provide significant insight into the 3D stress states and the events or damage limit states in the pullout force-joint opening behavior of concrete pavement with misaligned dowel bars. These validated models, analytical modeling approaches, and events or damage limit states definitions can be used to further investigate the effects of dowel misalignment on the stresses and structural distresses, damage in realistic concrete pavements subjected to combined traffic and thermal loads.

A parametric study on the analytical model was conducted. The parameters that were varied and the results obtained from the analyses are presented in the next section.

6.4 ANALYTICAL PARAMETRIC STUDY

Finite element models were developed for $\frac{1}{2}$ " , $\frac{1}{4}$ " and $\frac{1}{8}$ " misaligned magnitudes for one- and two- dowel bars with non-uniform, uniform and alternate orientation of misalignments. Table 6.3 shows the various cases that were considered for the analytical parametric studies. Field investigations, laboratory studies and construction specifications have shown that extremely high misalignment magnitudes are detrimental to the concrete surrounding the dowel bar and cause distresses leading to failure of the pavement slab.

Table 6.3: Summary of the Finite Element Analysis conducted

Orientation	Magnitude		1 bar	2 bars		
	(in in.)	(in rad.)		U	NU	AM
Aligned	0	0	⊙	⊙		
Vertical	1/2	18	⊙	⊙	⊙	⊙
	1/4	36	⊙	⊙	⊙	⊙
	1/8	72	⊙	⊙	⊙	⊙
Horizontal	1/2	18	⊙	⊙	⊙	⊙
	1/4	36	⊙	⊙	⊙	⊙
	1/8	72	⊙	⊙	⊙	⊙
Total			7	7	6	6

Two cases with different input parameters were considered for each of the finite element model analyses. Case I corresponds to the use of idealized friction coefficients (0.0 and 0.3 on the greased and uncoated sides) and idealized material properties (uniaxial compressive strength (f'_c) of 3500psi & tensile strength (f'_t) of 236 psi. Case II

corresponds to the use of friction coefficients measured by Shoukry (0.076 and 0.384 for greased and ungreased sides, respectively) and measured material properties of the hardened concrete specimens collected during actual laboratory tests. In all the analyses, the uniaxial compressive stress-strain curve was developed using the modified Popovics equations as given in Collins et al (1992). The fracture energy criterion developed by Hillerborg was used to model the tensile post peak failure behavior.

6.5 RESULTS AND DISCUSSION

The results obtained from the various analyses of the 3D finite element models are presented in the following subsections.

6.5.1 ONE MISALIGNED DOWEL BAR

Tables 6.4(a) and (b) present the joint openings corresponding to the occurrence of events or damage limit states for models with a single dowel bar with vertical or horizontal misalignment. Both for cases I and II are included in the tables. Figures 6.10 (a) and (b), summarize the joint opening corresponding to the occurrence of events or damage limit states. These figures illustrate the results from the finite element analyses of the models with one misaligned dowel bar.

The results indicate that for a single misaligned dowel bar, the debonding / initial event (A) occurs at 0.003 in joint opening. The post slip behavior was governed by the magnitude of misalignment. The analytical results using case I (idealized) parameters and case II (measured) parameters indicate the occurrence of events / damage limit states (B), (C) and (D).

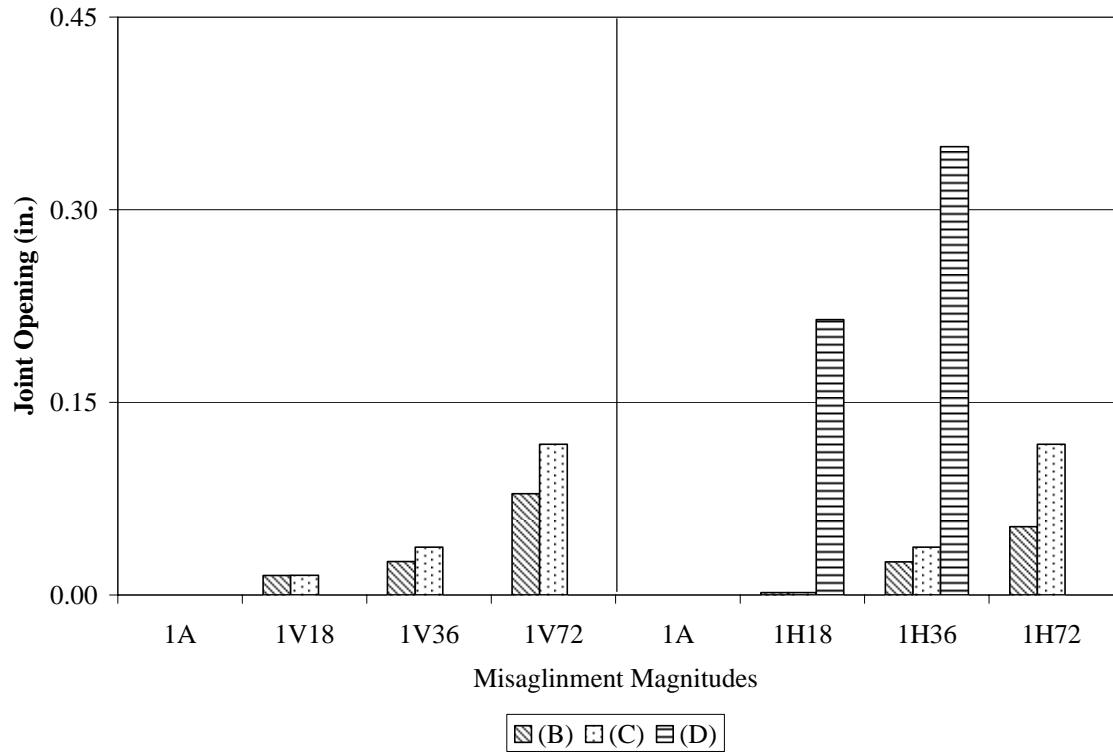
As shown in figure 6.10(a), for vertically misaligned dowel bars with Case I input parameters the occurrence of events / damage limit states (B) and (C) gets delayed as the misalignment magnitude is reduced. A similar trend is observed for models with Case II input parameters. As shown in figure 6.10(b) events / damage limit state (D) occurs for model 1V18 at joint opening of 0.15 in. As shown in figures 6.10 (a) and (b), for horizontally misaligned dowel bars with case I and case II input parameters, material events / damage limit states (B), (C) and (D) occur for the 1H18 and 1H36 analytical models. Limit state (D) does not occur in the 1H72 models using cases I and II input parameters.

**Table 6.4(a): Summary of the Damage Limit States and Joint Opening (in.) for Case I
Case I: 0.30 and 0.0**

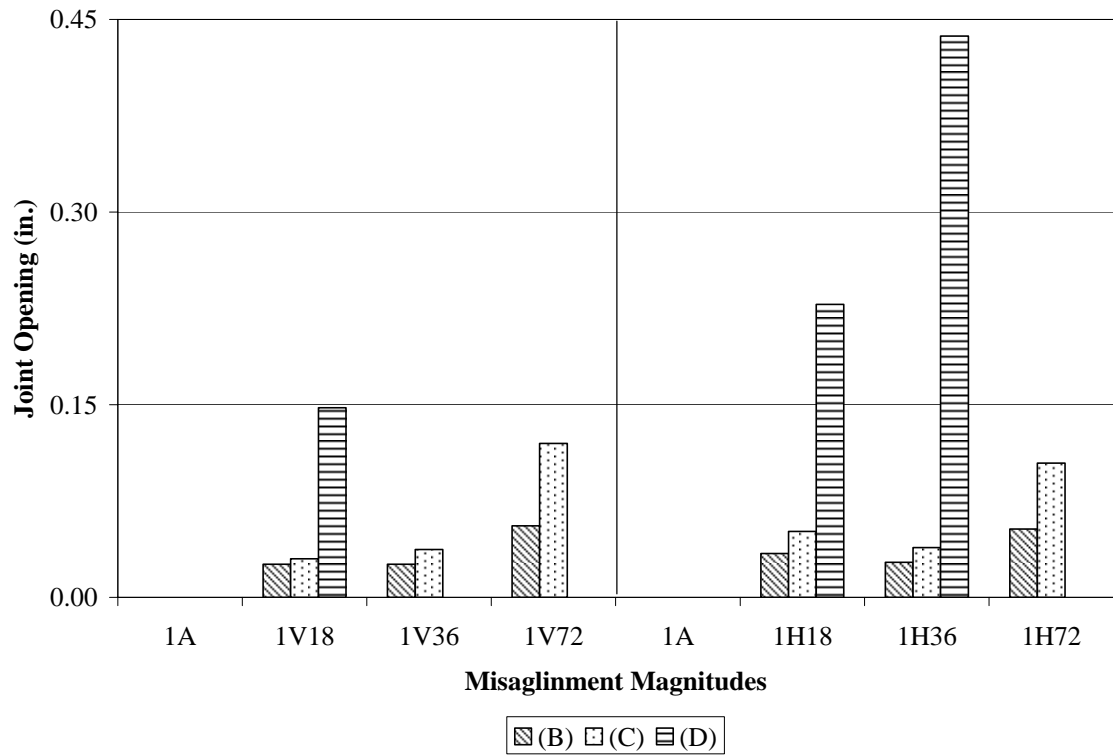
	1A	1V18	1V36	1V72	1H18	1H36	1H72
(A)	0.0030	0.0030	0.0030	0.0030	0.0030	0.0030	0.0030
(B)	-	0.0152	0.0260	0.0788	0.0018	0.0258	0.0532
(C)	-	0.0153	0.0372	0.1173	0.0018	0.0372	0.1173
(D)	-	-	-	-	0.214	0.349	-
(E)	-	-	-	-	-	-	-
(F)	-	-	-	-	0.260	-	-

**Table 6.4(b): Summary of the Damage Limit States and Joint Opening (in.) for Case II
Case II: 0.384 and 0.076**

	1A	1V18	1V36	1V72	1H18	1H36	1H72
(A)	0.003	0.0030	0.0030	0.0030	0.0030	0.0030	0.0030
(B)	-	0.0257	0.0257	0.0557	0.0342	0.0273	0.0532
(C)	-	0.030	0.0372	0.1198	0.051	0.0387	0.1045
(D)	-	0.1476	-	-	0.2281	0.437	-
(E)	-	-	-	-	0.425	-	-
(F)	-	-	-	-	0.217	-	-



(a) Case I Analysis results



(b) Case II Analysis results

Figure 6.10: Summary of Joint Opening Behavior and Limit States of single misaligned dowel bars

6.5.2 TWO MISALIGNED DOWEL BARS

Tables 6.5(a-b) and 6.6 (a-b), present the joint openings corresponding to the occurrence of events on damage limit states for models with dowel bars with vertical or horizontal misalignment. Both cases I and II input parameters are included in the tables. Figures 6.11 to 6.14 present graphical summaries of the joint opening corresponding to the occurrence of events / damage limit states (B –D) in the analysis.

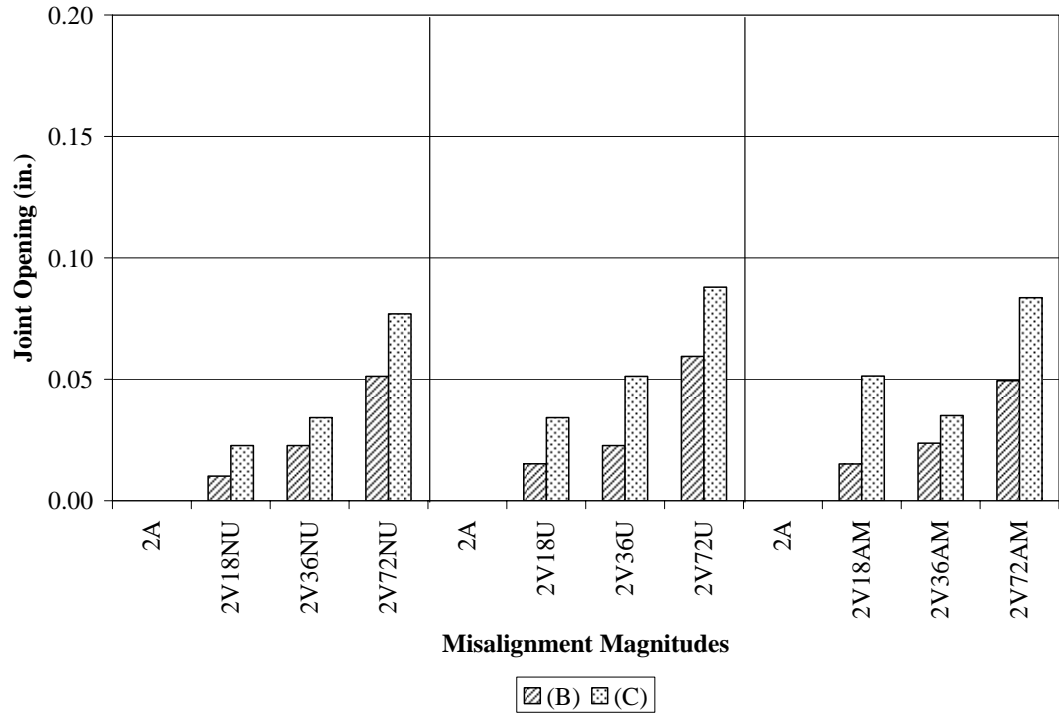
The analysis results for the models with vertically misaligned dowel bars are shown in figures 6.11 and 6.12 for case I and II input parameters. The results show that as the dowel misalignment increases from $1/72$ radians to $1/18$ radians, the events (B) and (C) occur for smaller joint openings. This trend is observed for pavements with less than 0.125 in joint opening. Events (D), (E) and (F) did not occur for models with two dowel bars with uniform or alternate misalignments up to $1/18$ rad. These events occur for models with two dowel bars with non-uniform misalignment is more detrimental than uniform or alternate misalignment. As shown in figure 6.11(b) and 6.12(b) the event or damage limit state (F) occurs first for smaller joint opening followed by events (D) and (E). Thus for non uniform vertical misalignment significant tensile cracking (F) occurs before significant crushing in compression. This endorses the finding that non-uniform vertical misalignment can be more detrimental.

Table 6.5(a): Summary of the Damage Limit States and Joint Opening (in.) for Case I with Vertically Misaligned dowel bars
Case I: 0.30 and 0.0

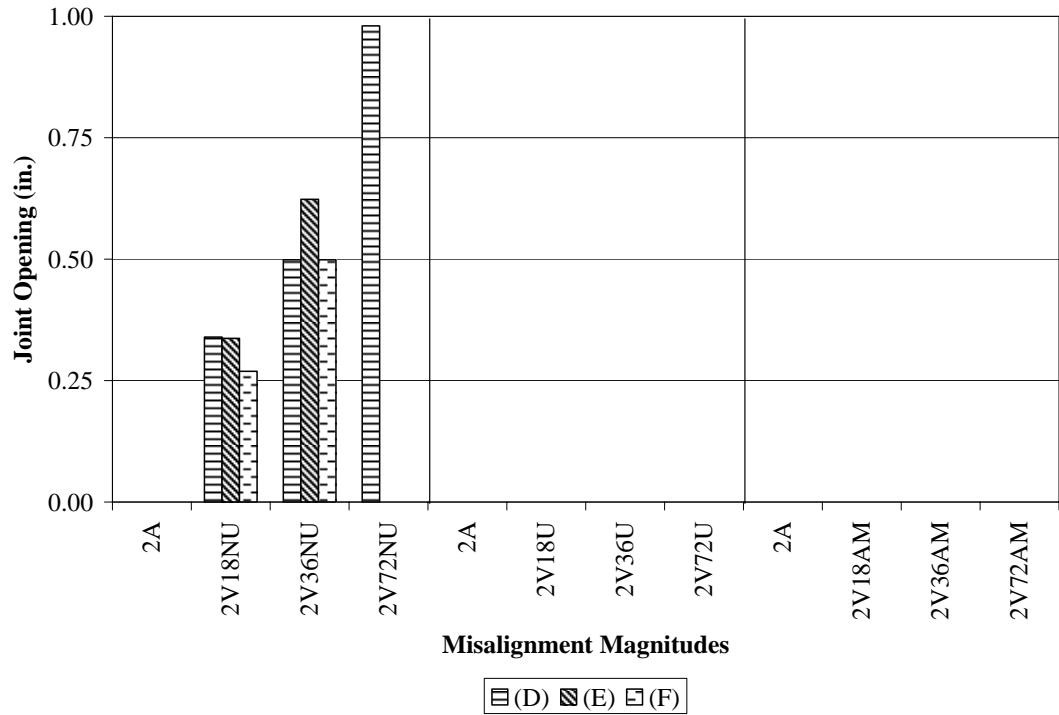
	2A	2V18NU	2V36NU	2V72NU	2V18U	2V36U	2V72U	2V18AM	2V36AM	2V72AM
(A)	0.0020	0.0020	0.0020	0.0020	0.0020	0.0020	0.0020	0.0020	0.0020	0.0020
(B)	-	0.0101	0.0227	0.0512	0.0152	0.0227	0.0594	0.0152	0.0237	0.0494
(C)	-	0.0227	0.0342	0.0769	0.0342	0.0512	0.0879	0.0513	0.0351	0.0835
(D)	-	0.3395	0.4987	0.9803	-	-	-	-	-	-
(E)	-	0.3369	0.6230	-	-	-	-	-	-	-
(F)	-	0.2691	0.4987	-	-	-	-	-	-	-

Table 6.5(b): Summary of the Damage Limit States and Joint Opening (in.) for Case II with Vertically Misaligned dowel bars
Case II: 0.384 and 0.076

	2A	2V18NU	2V36NU	2V72NU	2V18U	2V36U	2V72U	2V18AM	2V36AM	2V72AM
(A)	0.0020	0.0020	0.0020	0.0020	0.0020	0.0020	0.0020	0.0020	0.0020	0.0020
(B)	-	0.0012	0.0227	0.0512	0.0121	0.0342	0.0569	0.0152	0.0227	0.0513
(C)	-	0.0248	0.0342	0.0769	0.0247	0.0768	0.0854	0.0342	0.0512	0.1730
(D)	-	0.5525	0.7208	1.0000	-	-	-	-	-	-
(E)	-	0.3352	0.5767	-	-	-	-	-	-	-
(F)	-	0.2327	0.4613	-	-	-	-	-	-	-

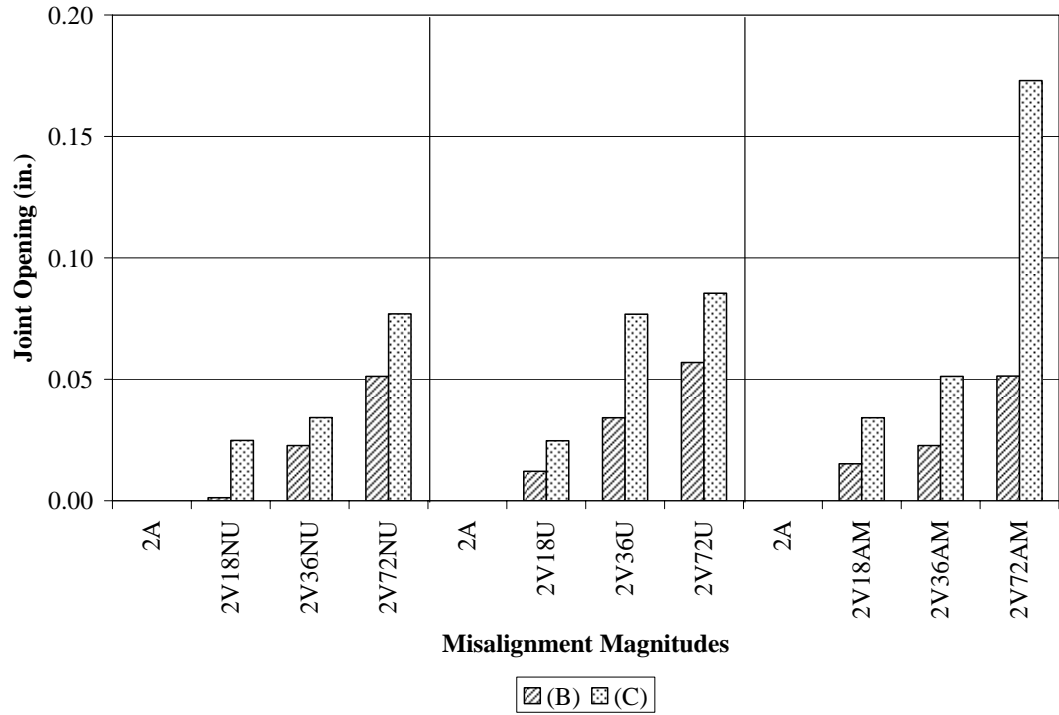


(a) Analysis results for events (B) and (C)

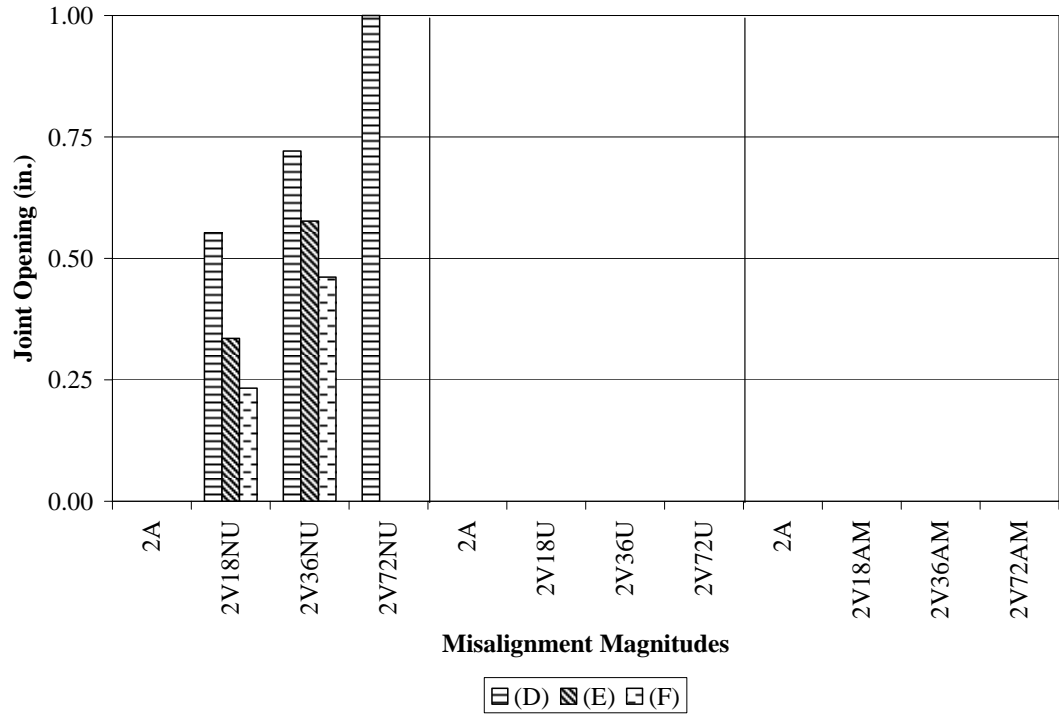


(b) Analysis results for events (D), (E) and (F)

Figure 6.11: Case I analysis summary of Joint Opening Behavior and Limit States of two vertically misaligned dowel bars



(a) Analysis results for events (B) and (C)



(b) Analysis results for events (D), (E) and (F)

Figure 6.12: Case II analysis summary of Joint Opening Behavior and Limit States of two vertically misaligned dowel bars

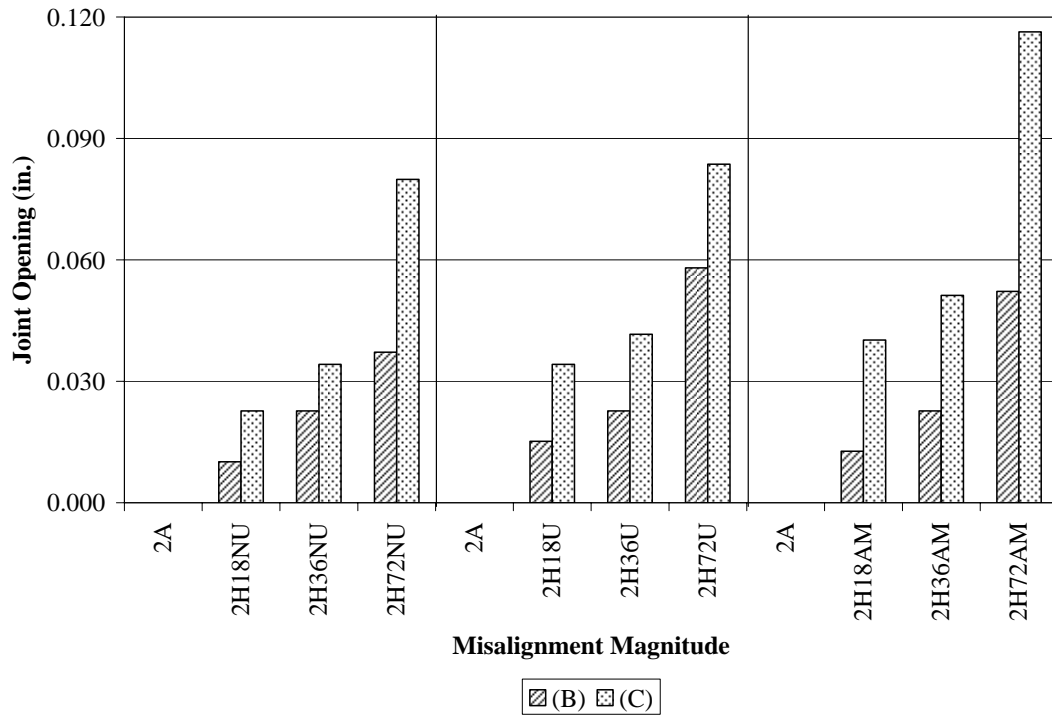
Horizontally misaligned dowel bars with case I and II input parameters are shown in figure 6.13 and 6.14. These results are similar to those for models with two vertically misaligned dowels. The results in table 6.6(a-b) and figure 6.11(a-b) and 12(a-b) show that as the dowel misalignment increases from $1/72$ radians to $1/18$ radians, the events (B) and (C) occur for smaller joint openings. This trend is observed for models with non-uniform, uniform and alternate misaligned dowel bars. Thus events (B and C) are observed for joint openings less than 0.125 in. Events (D), (E) and (F) occur for the models with uniform, non-uniform or alternate misaligned dowel bars. Figures 6.13(b) and 6.14(b) indicate that the type of dowel misalignment, i.e., the uniform, non-uniform, or alternate does not have a significant influence on the occurrence of events (D), (E) and (F) with respect to joint opening. These figures also indicate that the misalignment magnitude has a significant influence on the occurrence of events (D), (E) and (F). as shown in figure 6.13 and 6.14, as the dowel misalignment magnitude increased from $1/72$ to $1/18$ radians the events (D), E(D) and (F) occur for smaller joint openings. The event or damage limit state D occurs first followed by events (E) and (F). Thus, for horizontal misalignments, compression stress event (D) and significant crushing event (E) occur before significant cracking (F).

Table 6.6(a): Summary of the Damage Limit States and Joint Opening (in.) for Case I with Horizontally Misaligned dowel bars**CaseI: 0.30 and 0.0**

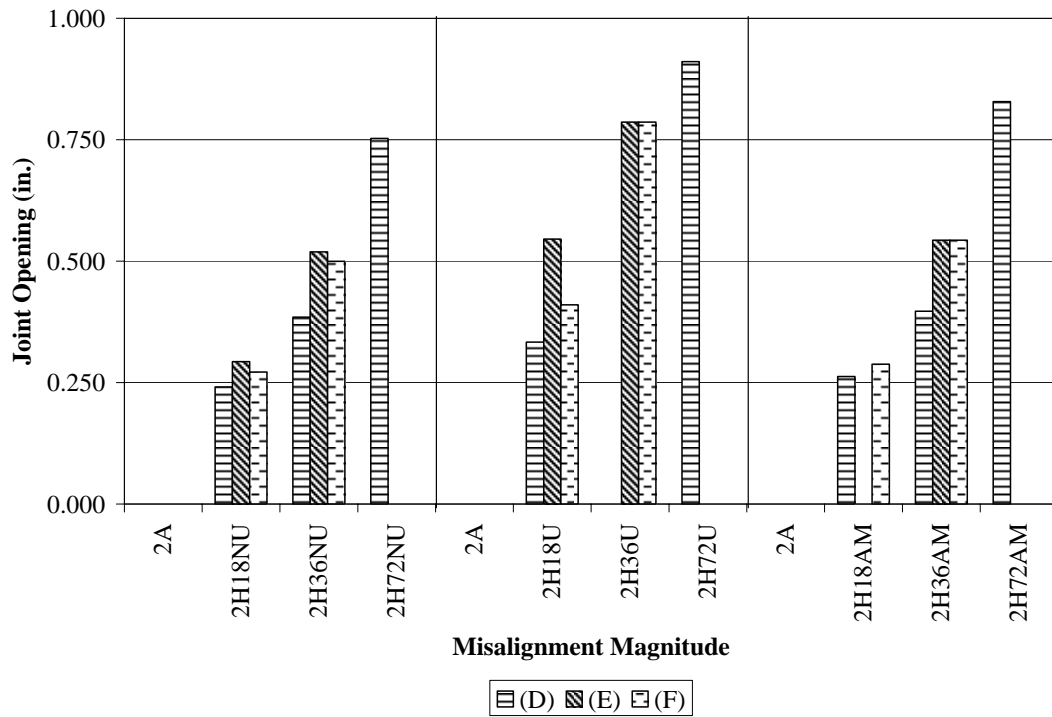
	2A	2H18NU	2H36NU	2H72NU	2H18U	2H36U	2H72U	2H18AM	2H36AM	2H72AM
(A)	0.0020	0.0020	0.0020	0.0020	0.0020	0.0020	0.0020	0.0020	0.0020	0.0020
(B)	-	0.0101	0.0227	0.0372	0.0152	0.0227	0.0580	0.0127	0.0227	0.0522
(C)	-	0.0227	0.0342	0.0799	0.0342	0.0416	0.0836	0.0402	0.0512	0.1163
(D)	-	0.2410	0.3844	0.7526	0.3332	-	0.9105	0.2623	0.3969	0.8281
(E)	-	0.2933	0.5190	-	0.5452	0.7860	-	-	0.5430	-
(F)	-	0.2717	0.4998	-	0.4101	0.7860	-	0.2879	0.5430	-

Table 6.6(b): Summary of the Damage Limit States and Joint Opening (in.) for Case II with Horizontally Misaligned dowel bars**CaseII: 0.384 and 0.076**

	2A	2H18NU	2H36NU	2H72NU	2H18U	2H36U	2H72U	2H18AM	2H36AM	2H72AM
(A)	0.0020	0.0020	0.0020	0.0020	0.0020	0.0020	0.0020	0.0020	0.0020	0.0020
(B)	-	0.0101	0.0192	0.0372	0.0121	0.0342	0.0542	0.0152	0.0203	0.0522
(C)	-	0.0219	0.0382	0.0799	0.0362	0.0769	0.0799	0.0342	0.0494	0.0779
(D)	-	0.2801	0.4326	0.7815	0.3736	0.3844	0.8680	0.2659	0.3851	0.9189
(E)	-	0.2972	0.5238	-	0.4919	0.6151	-	0.3457	0.5933	-
(F)	-	0.2460	0.6059	-	0.3352	0.7304	-	0.2563	0.5933	-

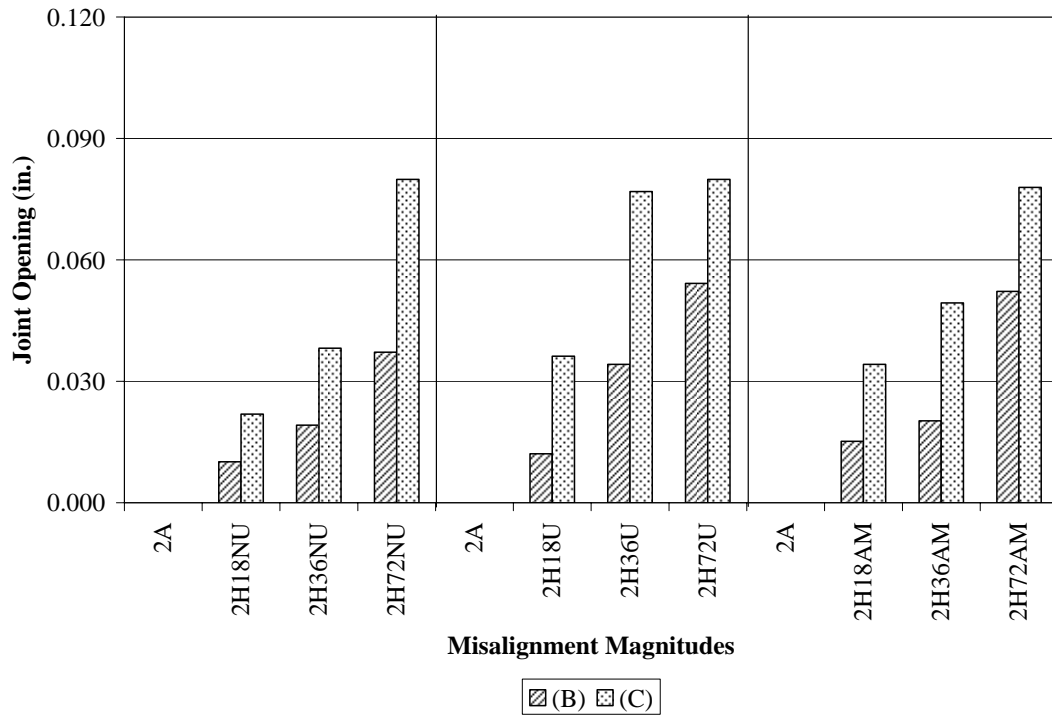


(a) Analysis results for material failure states (B) and (C)

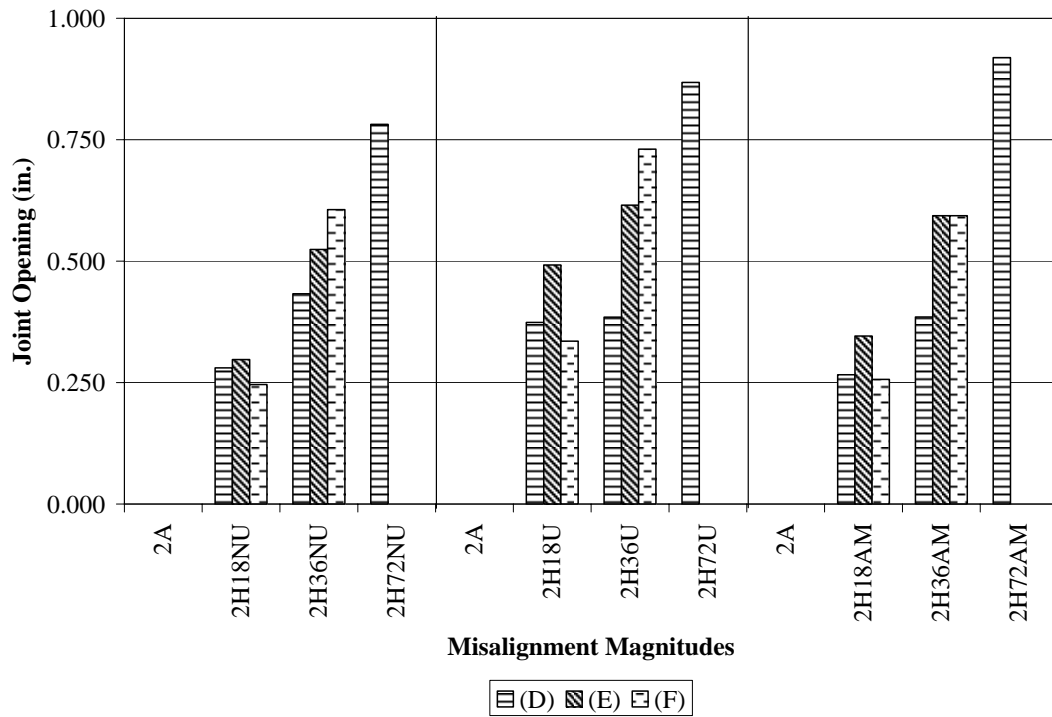


(b) Analysis results for material failure states (D), (E) and (F)

Figure 6.13: Case I analysis summary of Joint Opening Behavior and Limit States of two horizontally misaligned dowel bars



(a) Analysis results for material failure states (B) and (C)



(b) Analysis results for material failure states (D), (E) and (F)

Figure 6.14: Case II analysis summary of Joint Opening Behavior and Limit States of two horizontally misaligned dowel bars

6.5.3 CONCLUDING REMARKS ON THE RESULTS OF THE ANALYTICAL PARAMETRIC STUDIES

Three dimensional finite element models were developed and analyzed to investigate the effects of dowel misalignment magnitude and type on the behavior, 3D stress states and events or damage limit states in jointed pavements. An analytical matrix was developed to conduct the parametric studies. The parameters included were the number of misaligned dowels (1 or 2), the misalignment type (non-uniform, uniform or alternate), and the misalignment magnitude (aligned to 1/18 radians). The analytical results provide significant insight into the behavior, 3D stresses and events or damage limit states. These results indicate that:

(1) For models with one misaligned dowel bar, horizontal misalignment can be more detrimental than vertical misalignment. As the magnitude of misalignment increases, the events occur for smaller joint openings. Events B and C occur for joint openings less than 1/8 in. Event D occurs for joints with horizontally misaligned dowels or vertically misaligned dowel with 1/18 radians magnitude. Events E and F do not occur.

(2) For models with two vertically misaligned dowels, the effects of non –uniform misalignment can be more detrimental than uniform or alternate misalignment. As the misalignment magnitude increases, these events occur for smaller joint openings. Significant tensile cracking (Event F) occurs before compression crushing.

(3) For models with horizontally misaligned dowels, the misalignment orientation (uniform, non-uniform or alternate) does not have a significant influence on the occurrence of events D, E, and F. as the dowel misalignment magnitude increases, these

events occur for smaller joint openings. Compression stresses and crushing occur before significant tensile cracking.

6.6 CONCLUSIONS AND RECOMMENDATIONS

Three dimensional finite element models were developed and analyzed to investigate the effects of dowel misalignment magnitude and type on the behavior, 3D stress states and events or damage limit states in jointed pavements.

The localized material states (stress and strain) and the corresponding events A – F will have a significant influence on the *cyclic material fatigue life* at the distress locations. In the absence of experimental data and models relating the localized stresses and strains to the fatigue life of the pavement, the rational choice would be limit the localized stresses (S_{\max} and S_{\min}) to the material uniaxial stress capacities (f'_t and f'_c), i.e., to events C and D. These were the recommendations made to the Department of Transportation.

An analytical matrix was developed to conduct the parametric studies. The parameters included were the number of misaligned dowels (1 or 2), the misalignment type (non-uniform, uniform or alternate), and the misalignment magnitude (aligned to 1/18 radians). The analytical results provide significant insight into the behavior, 3D stresses and events or damage limit states. These results indicate that:

- (1) The debonding limit state occurs almost instantaneously irrespective of the dowel misalignment type, magnitude, orientation, etc. in the concrete slab.
- (2) As the misalignment magnitude (angle of skew) is reduced, the occurrence of a damage limit state is delayed as the joint is opened.

(3) These analytical models, approaches and limit states are recommended for future analytical work on realistic pavement joints with thermal and traffic loads.

(4) As the magnitude of misalignment increases, the events occur for smaller joint openings. Events B and C occur for joint openings less than 1/8 in. The effects of non – uniform misalignment can be more detrimental than uniform or alternate misalignment. Events D, E and F occur at larger joint openings. As the misalignment magnitude increases, these events occur for smaller joint openings.

CHAPTER 7

**PRELIMINARY INVESTIGATION OF LOAD EFFECTS COMBINED WITH
DOWEL MISALIGNMENTS**

7.1 INTRODUCTION

A typical JPCP consists of several components. These include multiple unreinforced concrete slabs connected by dowels that assist in transferring load and. The concrete slab rests on the base layer which distributes the load to the sub-base and the natural sub-grade, illustrated in figure 2.1 chapter 2. A preliminary investigation on the load effects combined with dowel misalignments is presented in this chapter.

The objective of this study was to understand and capture the physical behavior of typically misaligned dowel bars in a dowel jointed concrete pavement slab subjected to joint opening and truck loading. This chapter presents the assumptions and limitations of the three dimensional finite element models that are developed as a part of this study. This is followed by the development of the bond model and the boundary conditions that were used to simulate an as constructed pavement slab. Finally, this chapter presents the various typical dowel misalignment cases that were analyzed, the behavior observed in the analytical models and the results obtained from the analyses.

7.2 ASSUMPTIONS AND LIMITATIONS OF THE FINITE ELEMENT MODEL

Simple assumptions were made to model the realistic pavement slab to limit the size and computational capability of the three dimensional finite element analyses. Finite element models of three dowel bars with typical misalignment magnitudes and orientations were developed assuming that in the wheel path only three dowel bars are influenced by the

axle loads. The dowel – concrete bond interaction model developed in the earlier task of this research was used.

Like in the earlier finite element models, the pavement slab was only subjected to joint opening and not thermal cycling such as joint opening and closing. To facilitate joint opening due to thermal expansion, the concrete slab and base were not bonded to each other. The coefficient of friction between the concrete slab and the base layer was assumed zero as no calibrated laboratory or field investigation was available. Secondly, the finite element model developed in this study focuses on the effects of localized stress formation surrounding the misaligned dowel bar. The influence of fatigue loading was not considered in the finite element analyses. The wheel loads were static monotonically increasing from zero to full load and includes a dynamic impact (magnification) factor of two (Chopra, 2000). Instead of the complete truck, loading under a set of dual wheels of a tandem axle was considered.

7.3 DEVELOPMENT OF THE FINITE ELEMENT MODEL

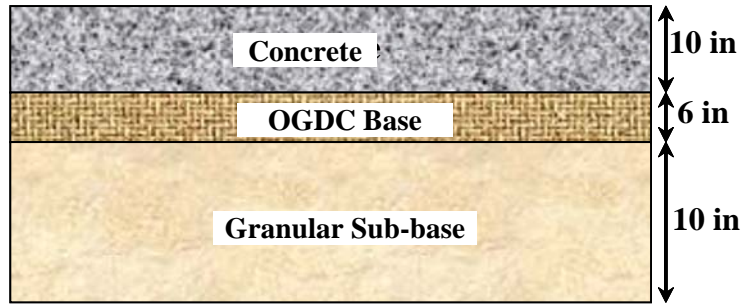
To model the concrete slab, steel dowel bar, base and sub-base layers, three dimensional (3D) first order reduced integration continuum elements (C3D8R - Bricks) were used. These elements are versatile in modeling simple linear analysis and also complex nonlinear analyses involving material nonlinearity, plasticity and large deformations. To simulate the interaction between the layers of the pavement cross-section, constraint and contact interactions in ABAQUS (2004) are used and presented in the following sections. Compared to the finite element developed in this initial study, the ILLISLAB model (Tabatabaie et. al. 1978) uses elastic homogeneous medium thick plates and elastic

material properties. It considered beam elements with limited degrees of freedom to model the dowel-concrete interaction bond. Similarly, comparing the finite element model developed in this study, the EverFE (Davids et al, 1998) software uses a twenty noded quadratic hexahedral elements to discretize the slabs and its underlying layers. Compared to using complete 3D continuum elements for both the dowel bar and concrete, the EverFE software uses an embedded flexural finite elements.

To model the complex triaxial stress states in the concrete surrounding the dowel bar, the concrete slab mesh was made up of smaller size brick elements and gradual increase in size away from the dowel bar. The base and sub-base layers are extended 12 in. on each side of the concrete slab to reduce effects of side boundary conditions on the slab response. The wheel loads were applied using discrete rigid elements (R3D4). The sub-grade is modeled as a Winkler foundation consisting of a series of springs to ground. These elements are a simple way of including the stiffness effects of a support without actually having to model the details of the support.

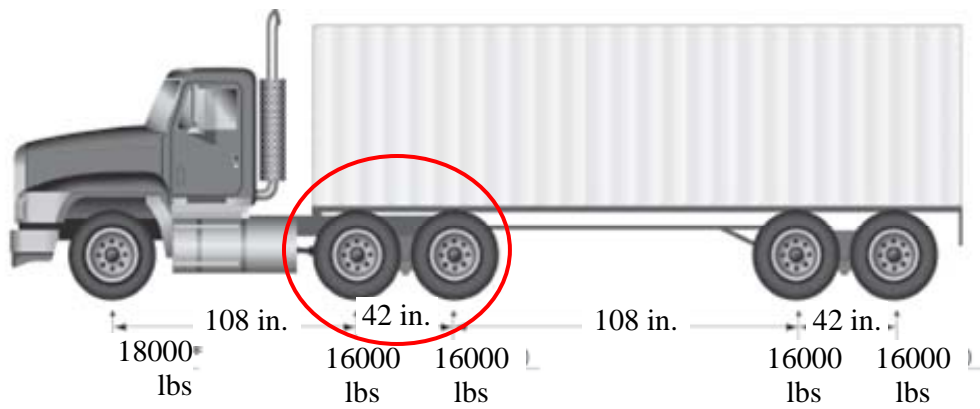
7.3.1 DIMENSIONS OF THE ANALYTICAL MODEL

A standard MDOT specified pavement cross section was considered in the finite element analyses, as shown in figure 7.1 (a). The slab dimensions for the single dowel bar and three dowel bar finite element models are shown in figures 7.1(b) and (c).

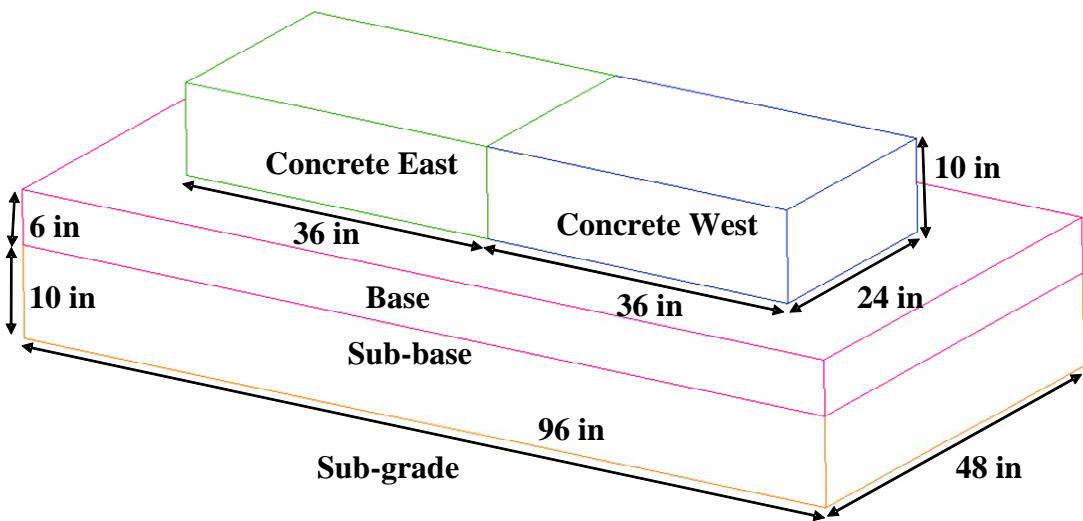


Subgrade

(a) Typical pavement cross section



(b) Typical truck loading



(c) Dimensions for a single dowel bar model

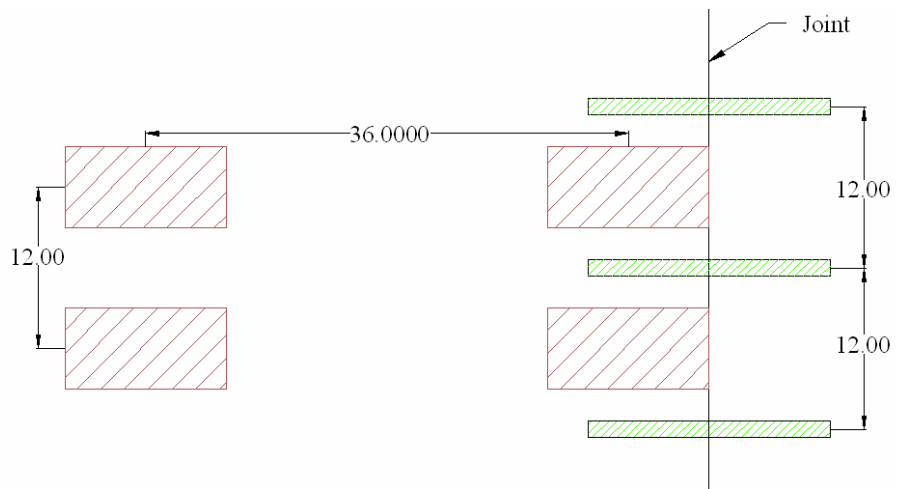
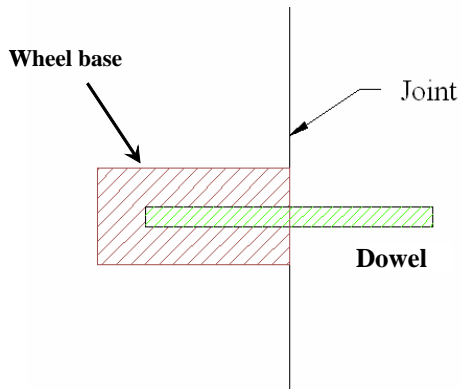
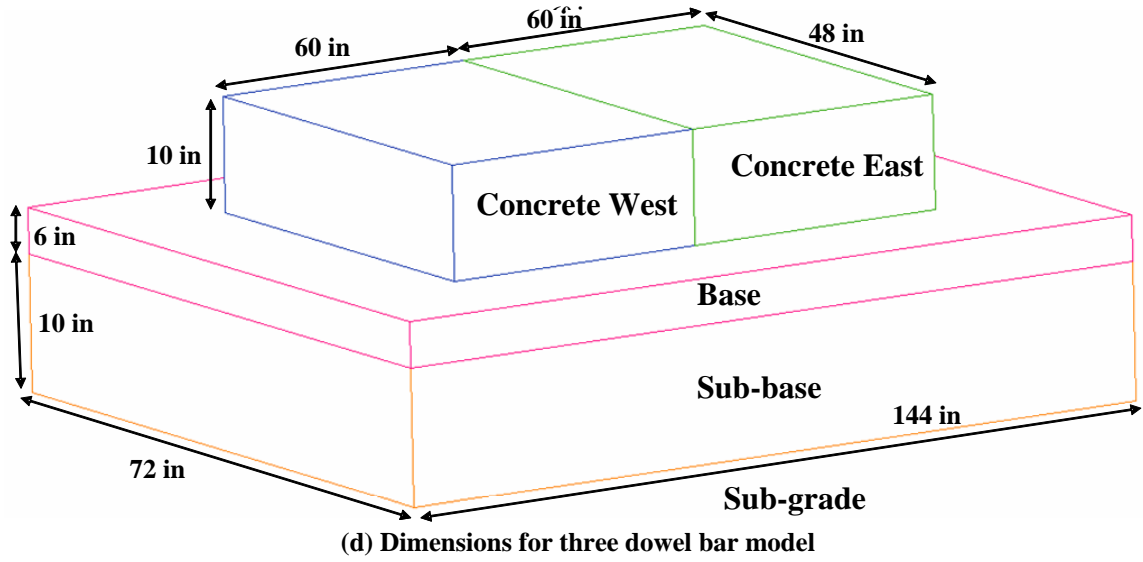


Figure 7.1: Dimensions and location of various parts of the pavement slab and wheel base in the finite element model

Single dowel bar model:

The first model consisted of a single dowel bar with skew misalignment magnitudes ranging from 0 to $1/18$ radians ($1/2$ in. over 9 in. length). The finite element model was made up of two concrete slabs 36 in. x 24 in. x 10 in. connected at the transverse joint using a single steel dowel bar 18 in. long and 1.25 in. diameter. The dowel bar is placed at mid-height and embedded 9 in. on both sides of the concrete slab. The concrete slab is supported on a base layer 96 in. x 48 in. x 6 in. and a sub-base layer of 96 in. x 48 in. x 10 in. The sub-grade is modeled using the Winkler foundation with spring stiffness of 150 psi/in.

A monotonically static load up to 16000 lbs was applied on the concrete slab, directly on top of the dowel bar on one side of the joint, as shown in figure 7.1 (c). This assumed high load was applied to understand the effects of misalignment after loading under a single dowel bar. The applied load is four times the actual wheel load of 4000 lbs. The load from one line of wheels of the dual wheel tandem gives 8000 lbs multiplied by an assumed dynamic impact factor of two.

Three dowel bar model:

The second model consisted of three dowel bars with typical skew misalignment magnitudes ranging from 0 to $1/36$ radians ($1/4$ in. over 9 in. length). The FE model is made up of two concrete slabs 60 in. x 48 in. x 10 in. connected at the transverse joint using a three steel dowel bars 18 in. long and 1.25 in. diameter. The dowel bars are spaced 12 in. on center at mid-height and embedded 9 in. on both sides of the concrete slab. The concrete slab is supported on a base layer 144 in. x 72 in. x 6 in. and a sub-base

layer of 144 in. x 72 in. x 10 in. The sub-grade is modeled using the Winkler foundation with spring stiffness of 150 psi/in. A monotonically static load of 8000 lbs on each of the wheels, as shown in figure 7.1 (d), is applied on one side of the concrete slab at the joint face. Again a dynamic magnification factor of two was assumed and multiplied to each 4000 lb. wheel load.

Table 7.1 presents the various cases that were considered in this preliminary investigation. In this table, the nomenclature used to identify a case study consists of the number of dowel bars (1 or 3), the misalignment type (Aligned, Vertical or Horizontal), the misalignment magnitude (18 represents 1/18 radians) and the misalignment orientation (NU or AM), where non uniform misalignment orientation represents all dowel bars are misaligned in opposite direction and alternate misalignment represents the only the center dowel bar having a misalignment. For example, specimen 3V72NU in Table 7.1 has all three dowel bars with non-uniform vertical misalignment of +1/72, -1/72 and +1/72 radians, i.e., 1/8 in. misalignment measured over 9 in. length of dowel.

The range of misalignment magnitudes from 0, 1/72 and 1/36 radians was chosen to minimize the number of finite element models. Also, only two types of misalignment orientations were considered, i.e., the non-uniform (NU) – worst case scenario and alternate (center misaligned - AM) misaligned dowel bars.

Table 7.1: Misalignment cases considered for single and three dowel bar loaded slabs

ID	Number of dowels	Misalignment type	Misalignment Magnitude (rad.)	Misalignment Magnitude (in.)
1A	1 dowel	Aligned	0	None
1V72		Vertical	$\frac{1}{72}$	$\frac{1}{8}$ in over 9 in.
1V36			$\frac{1}{36}$	$\frac{1}{4}$ in over 9 in
1V18			$\frac{1}{18}$	$\frac{1}{2}$ in over 9 in
1H72		Horizontal	$\frac{1}{72}$	$\frac{1}{8}$ in over 9 in.
1H36			$\frac{1}{36}$	$\frac{1}{4}$ in over 9 in
1H18			$\frac{1}{18}$	$\frac{1}{2}$ in over 9 in
3A		3 dowels	Aligned	0
3V72NU	Vertical		$+\frac{1}{72}; -\frac{1}{72}; +\frac{1}{72}$	$\frac{1}{8}$ in. over 9 in.
3V36NU			$+\frac{1}{36}; -\frac{1}{36}; +\frac{1}{36}$	$\frac{1}{4}$ in over 9 in
3V72AM			$0; -\frac{1}{72}; 0$	$\frac{1}{8}$ in. over 9 in.
3V36AM			$0; -\frac{1}{36}; 0$	$\frac{1}{4}$ in over 9 in
3H72NU	Horizontal		$+\frac{1}{72}; -\frac{1}{72}; +\frac{1}{72}$	$\frac{1}{8}$ in. over 9 in.
3H36NU			$+\frac{1}{36}; -\frac{1}{36}; +\frac{1}{36}$	$\frac{1}{4}$ in over 9 in
3H72AM			$0; -\frac{1}{72}; 0$	$\frac{1}{8}$ in. over 9 in.
3H36AM			$0; -\frac{1}{36}; 0$	$\frac{1}{4}$ in over 9 in

7.3.2 MATERIAL MODEL INPUT PARAMETERS

The concrete slabs were modeled using the concrete damaged plasticity model developed by Lubliner et al (1989), modified by Lee and Fenves (1998) and implemented in ABAQUS. Details of the various input parameters and calibration of the concrete model have already been presented in chapter 5. The steel dowel bar was modeled using an isotropic elastic multiaxial material model. The elastic modulus E_s for the models was based on results of standard ASTM (A370-97a) uniaxial tension tests on coupons

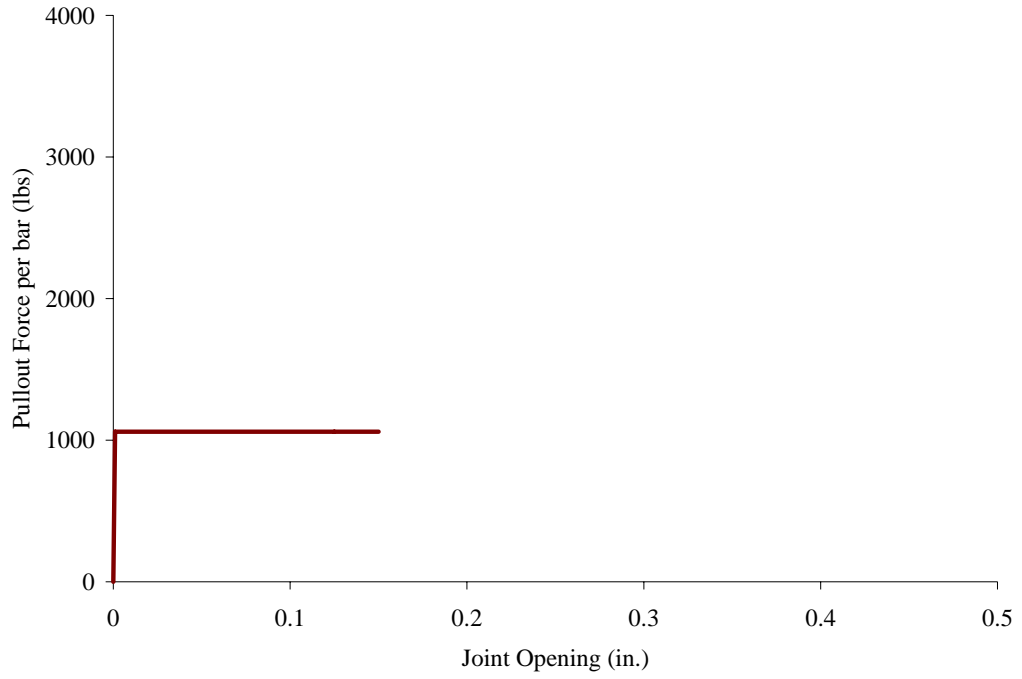
extracted from the steel dowel bars. The yield and ultimate stresses were not required because the dowel bar remained elastic throughout the analysis. The base and sub-base layers were modeled using the isotropic elastic multiaxial material model. The modulus of elasticity, poisson's ratio and density used for the material model were obtained from Shoukry (2003). Furthermore, Table 7.2 presents some of the material input parameters that were used for the concrete slab, steel dowel bar, base, sub-base and sub-grade layers.

7.3.3 INTERACTION MODELS

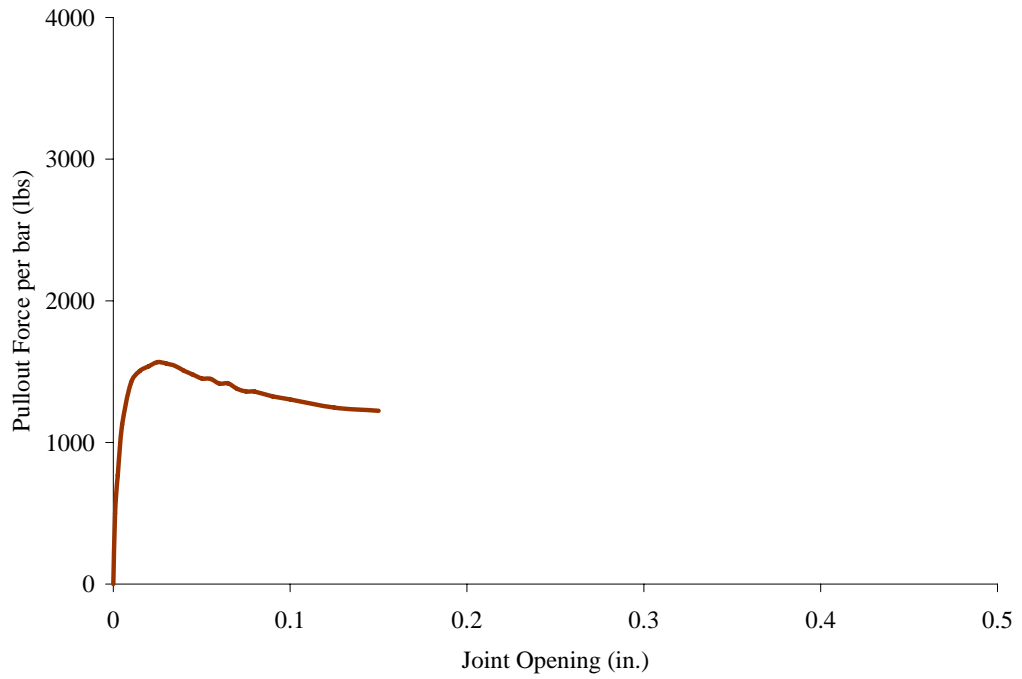
The dowel concrete bond interaction model developed in the previous task of this research study was used. The spring force vs. pullout displacement behavior for the single dowel – concrete slab model was calibrated using an idealized curve derived from the 1A experimental data, shown in figure 7.1(a). For the three dowels – concrete slab model, the spring force vs. pullout behavior was calibrated using the experimental data from the three aligned dowel bars test specimen, as shown in figure 7.2(b).

Table 7.2: Material input parameters for the single and three dowel bar finite element models

Concrete Data	
Uniaxial Compressive Strength (f'_c)	= 3500 psi
Modulus of Elasticity ($0.7 f'_c$)	= 3,372,000 psi
Tensile Strength (f'_t)	= 236 psi
Poissons ratio	= 0.18
Density	= 0.0868 lbs/in ³
Steel Data	
Type	= Billet Steel
Modulus of Elasticity	= 29,000 ksi
Poissons ratio	= 0.3
Density	= 0.282 lbs/in ³
Base Data	
Type	= Open Graded Drainage Course
Modulus of Elasticity	= 30,000 psi
Poissons ratio	= 0.3
Density	= 0.0758 lbs/in ³
Sub-base Data	
Type	= Grannular Sub-base (sand)
Modulus of Elasticity	= 15,000 psi
Poissons ratio	= 0.3
Density	= 0.0758 lbs/in ³
Subgrade Data	
Subgrade stiffness	= 150 psi/in
Modulus of elasticity	= 4000 psi
Poissons ratio	= 0.4
Density	= 0.0736 lbs/in ³



(a) Spring Force – Joint Opening for single dowel bar model



(b) Spring Force – Joint Opening for three dowel bar model

Figure 7.2: Spring Force vs. Joint Opening behavior used in the finite element models

Contact constraint equations were used between the various layers of the pavement cross-section. The OGDC layer is considered as an unbonded base, i.e., there is no friction between the concrete slab and the base layer. This constraint condition helps in modeling the OGDC base layer as a shear flexible layer that can carry normal loads (axle loads) but does not have any shear resistance thereby allowing it to simulate joint opening behavior due to thermal loads. The OGDC base layer and the granular sub-base layer are tied such that deformations in the base and sub-base layer are equal. The subgrade is modeled as an elastic Winkler foundation, i.e., a bed of elastic springs. Figure 7.3 presents the various contact conditions used in the tangential and normal directions between the concrete, base, sub-base and sub-grade layers for both the single and three misaligned dowel bars finite element models.

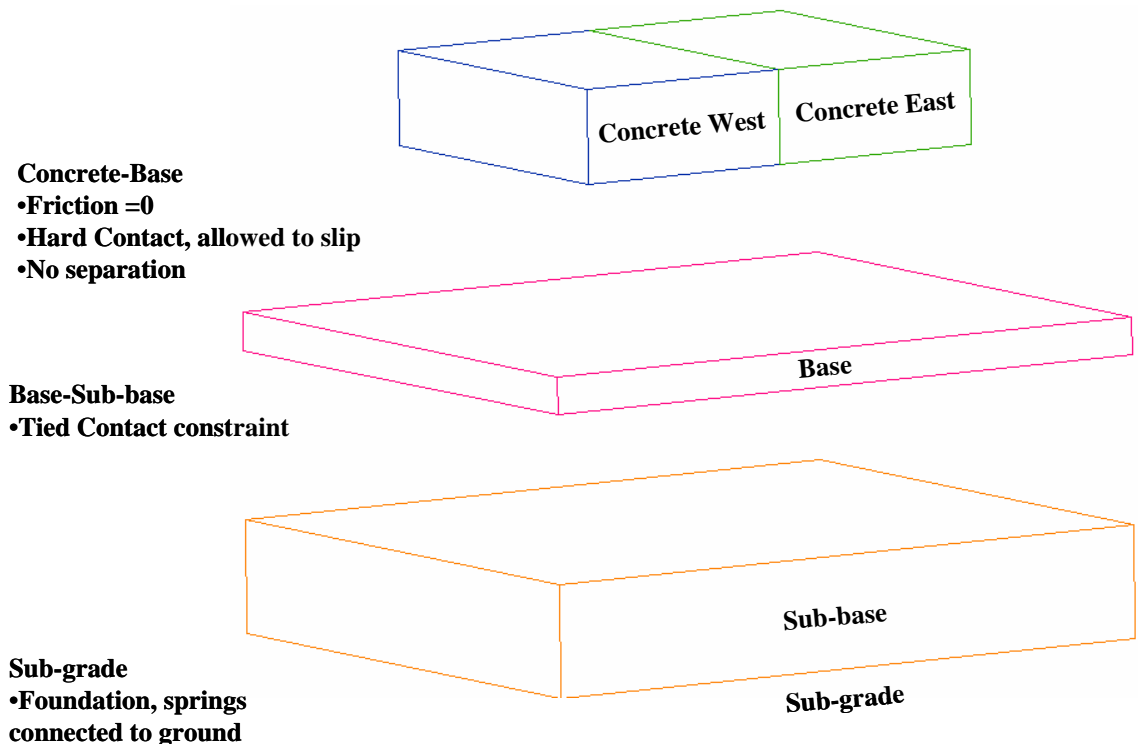


Figure 7.3: Typical constraint conditions used for the finite element model

7.3.4 LOADING AND BOUNDARY CONDITIONS

The first step of application of boundary conditions, only the gravity load is applied to allow for all the constraint conditions to take effect. The boundary and loading conditions are applied such that the model is restrained from any rigid body motion. The concrete slabs are then pulled apart to simulate a maximum joint opening of 1/8 in. due to thermal expansion of the pavement slab. This approximate joint opening was determined using the equation by Darter and Barenberg (1977),

$$\Delta L = C L (\alpha_t \Delta T + \varepsilon)$$

where, ΔL = joint opening caused by temperature change and drying shrinkage of concrete.

α_t = coefficient of thermal expansion of concrete (5 to 7 x 10⁻⁶ /°F)

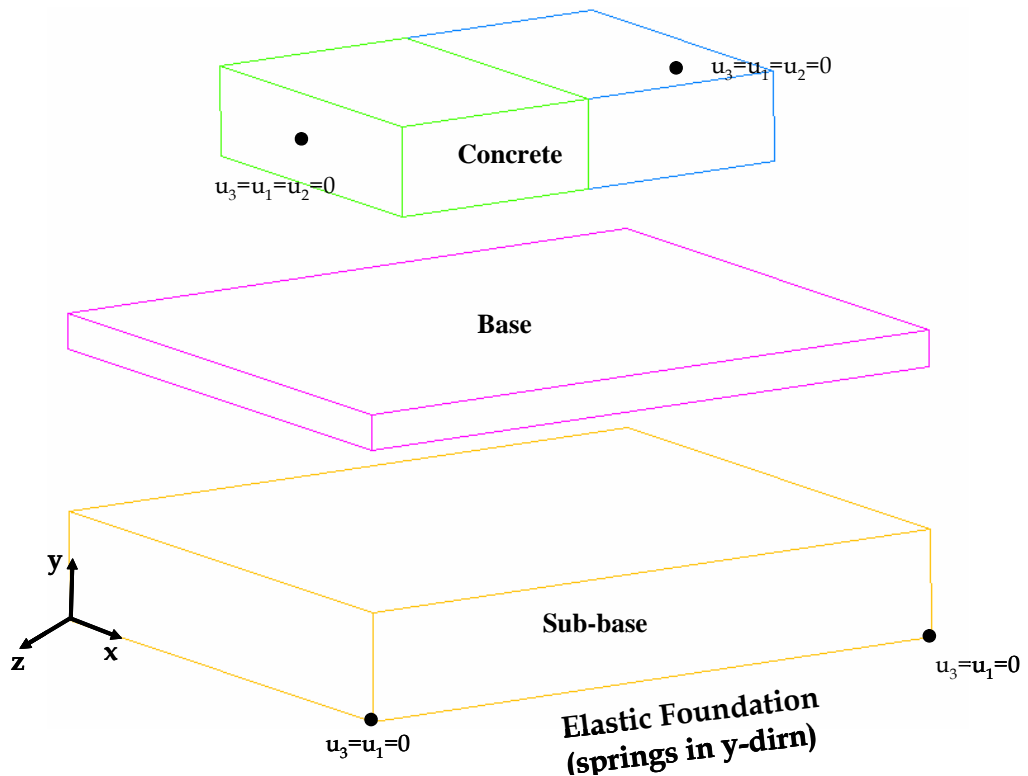
ε = drying shrinkage coefficient of concrete (0.5 to 2.5 x 10⁻⁴)

L = joint spacing or slab length = 15 ft.

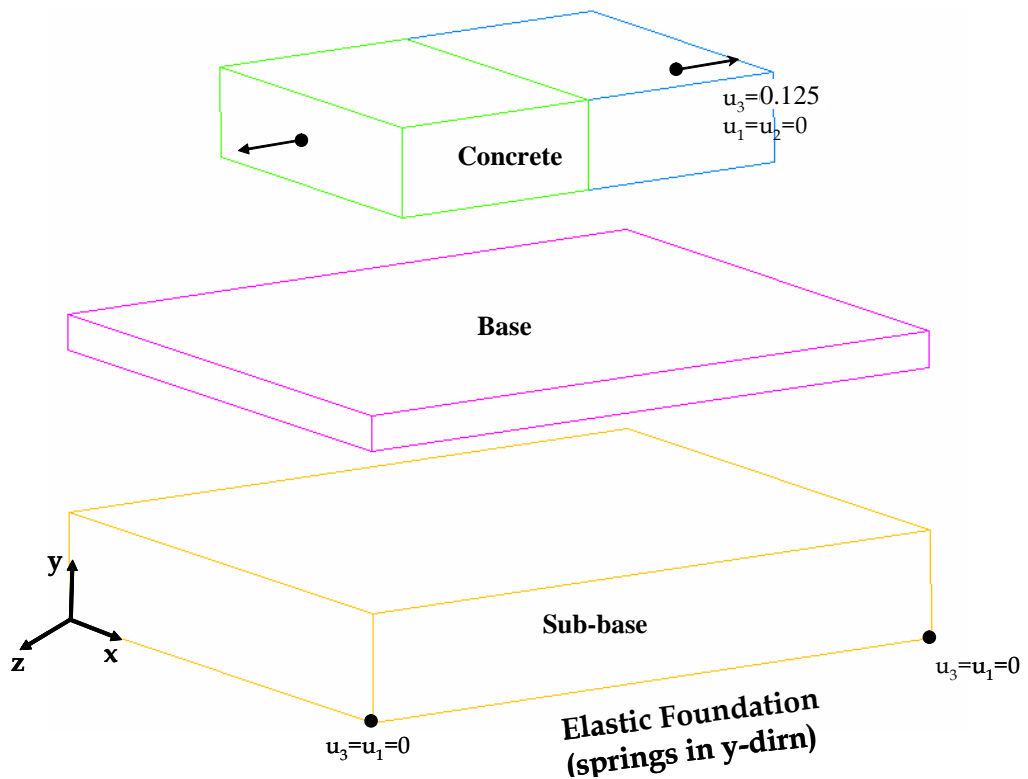
ΔT = temperature range, i.e., temperature at placement minus lowest mean monthly temperature

C = adjustment factor due to slab-subbase friction, 0.8 for granular subbase.

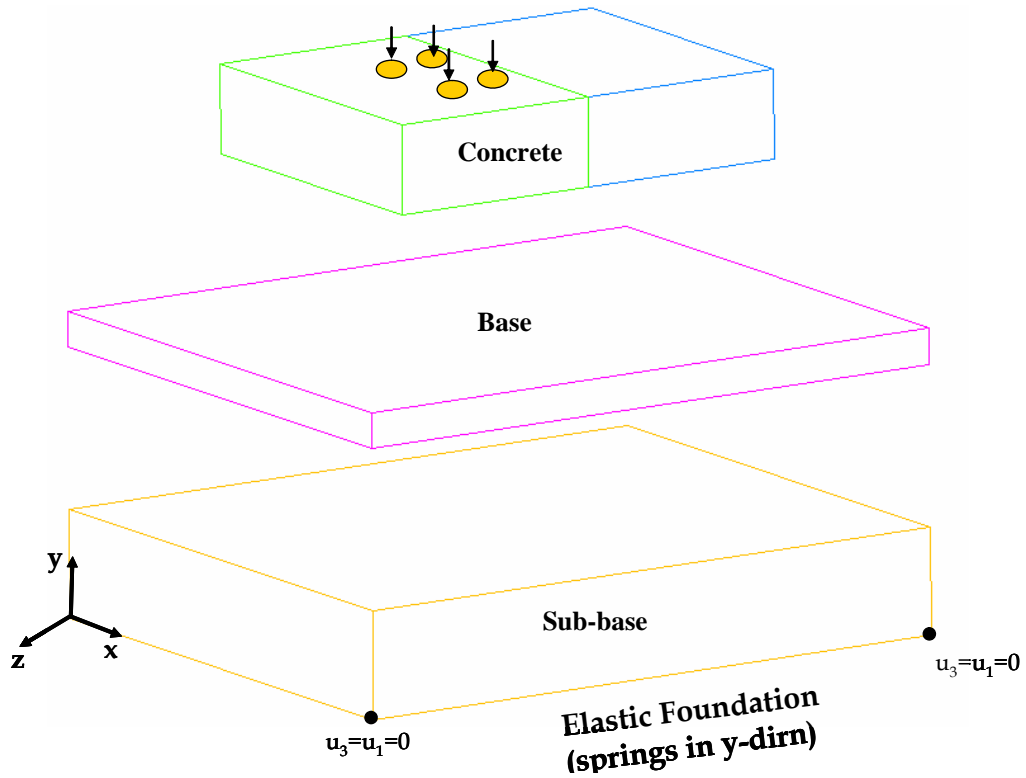
Finally, the wheel loads are applied close to the face of the joint on one side of the pavement slab. The sequence of boundary and loading conditions is shown in figure 7.4.



(a) Boundary Conditions for Step I of analysis (Gravity Loading)



(b) Boundary Conditions for Step II (Joint Opening)



(c) Boundary Conditions for Step III (wheel loading)
 Figure 7.4: Typical Boundary and Loading conditions on the pavement system

7.4 RESULTS AND DISCUSSION

The results obtained from the analytical models are summarized in this section. As observed in the FE models of the laboratory specimens, high stress concentration zones are formed in the concrete with joint opening. With the application of wheel loads on the concrete slab, the stress concentration zone in the concrete due to misalignment changes to localized bearing stresses in the concrete.

In the following sections, the results obtained from the finite element analysis of typical misaligned single and multiple dowel bars combined with loading are presented. In the results, the concrete slab where the load is applied is called the “loaded slab” (west side slab) and the opposite side is called the “unloaded side” (east side slab), as shown in Figure 7.5.

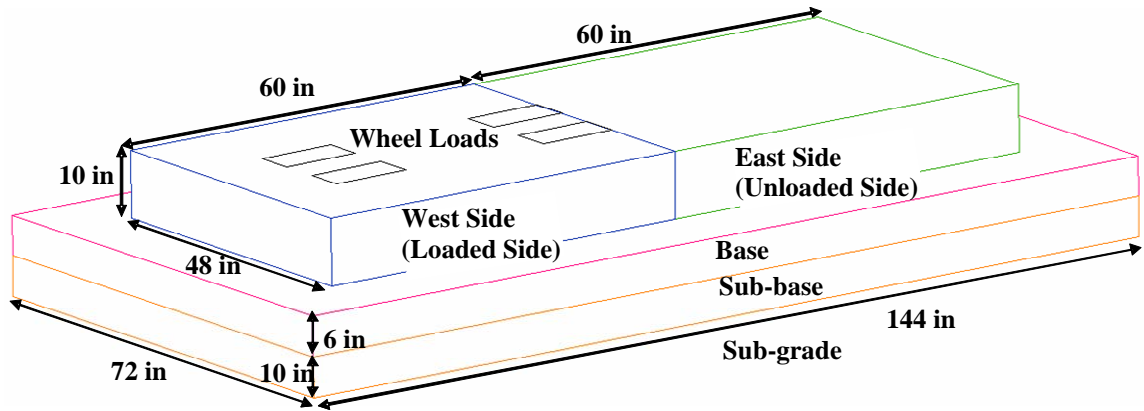


Figure 7.5: Loaded and unloaded sides of the concrete slab

Also, results with the label “before loading” are obtained after joint opening at location. The results labeled “after loading” are after the specified loading has been applied, shown in Figure 7.6 and 7.7.

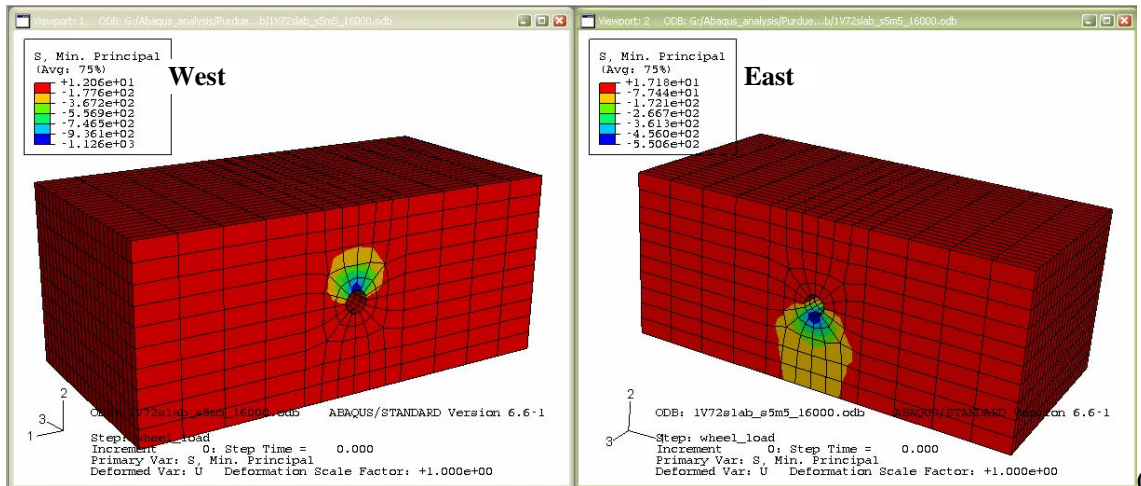
7.4.1 SINGLE DOWEL BAR MODEL

This model was developed to understand the influence of a wheel load combined with the effects of a misaligned dowel bar and joint opening on the concrete surrounding the dowel bars. The change in stress localization from a stress concentration to a bearing stress is easily understood from the results of this model.

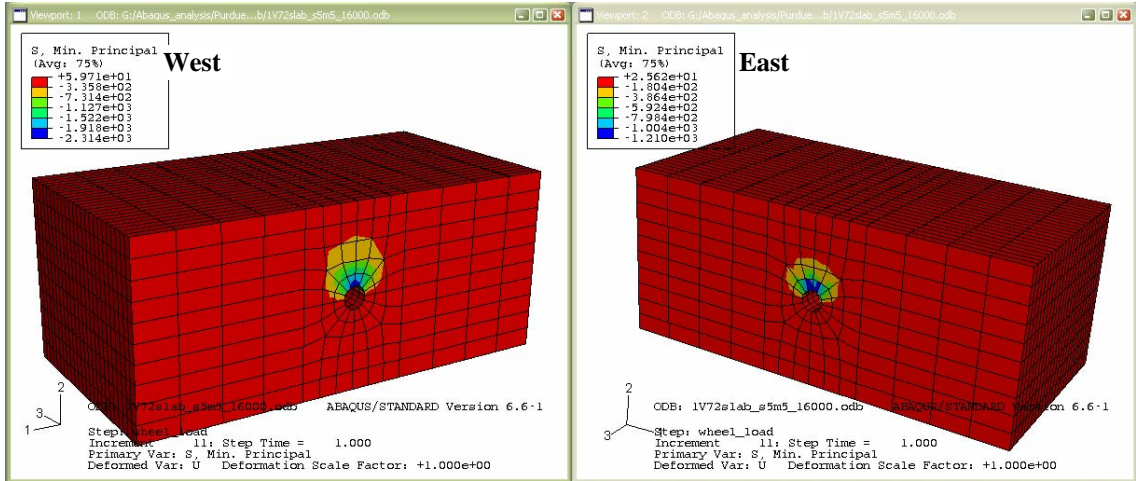
Figure 7.6 shows the minimum compressive stress zones in the concrete slab after joint opening and load application for a 1V72 finite element model. After a joint opening of 1/8 in., shown in Figure 7.6 (a), the stresses on the west and east side of the concrete slab are 1126.0 psi and 550.6 psi, respectively. The load is applied on the west side of the concrete slab and the stresses obtained after load application are 2314.0 psi and 1310.0 psi, respectively, shown in Figure 7.6 (b). Figure 7.7 shows the minimum compressive stress zones in the concrete slab in the 1H72 finite element model. Due to the misaligned dowel bar stress concentration zones are formed in a horizontal plane after joint opening

as shown in Figure 7.7 (a). These stress concentration zones change location when wheel loads are applied on the concrete slab. The bearing stress zones formed under the wheel load in concrete surrounding the dowel bar are shown in figure 7.7(b). The stresses in the concrete surrounding the dowel bar at a joint opening of 1/8 in. on the west and east side are 965.5 psi and 927.1 psi respectively. After load application the bearing stresses on the west and east side are 2392.0 psi and 1213.0 psi

There is an increase in the tensile and compressive stresses and strains magnitude after load application on both the loaded (west) and unloaded (east) side of the concrete slab. The trend showing an increase in stresses and strains for all the cases of vertically and horizontally misaligned bars is shown in figures 7.8 and 7.9

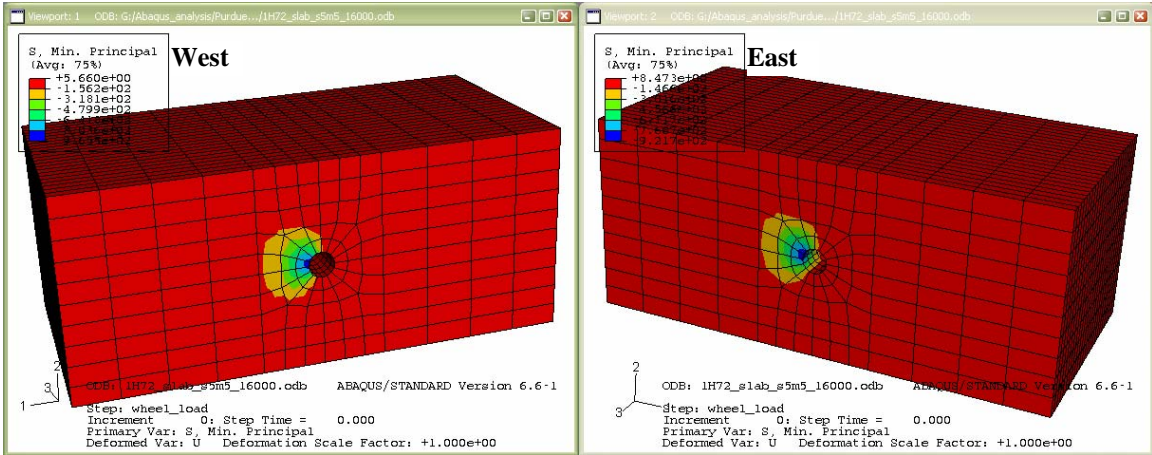


a) Stresses after a joint opening of 1/8 in.

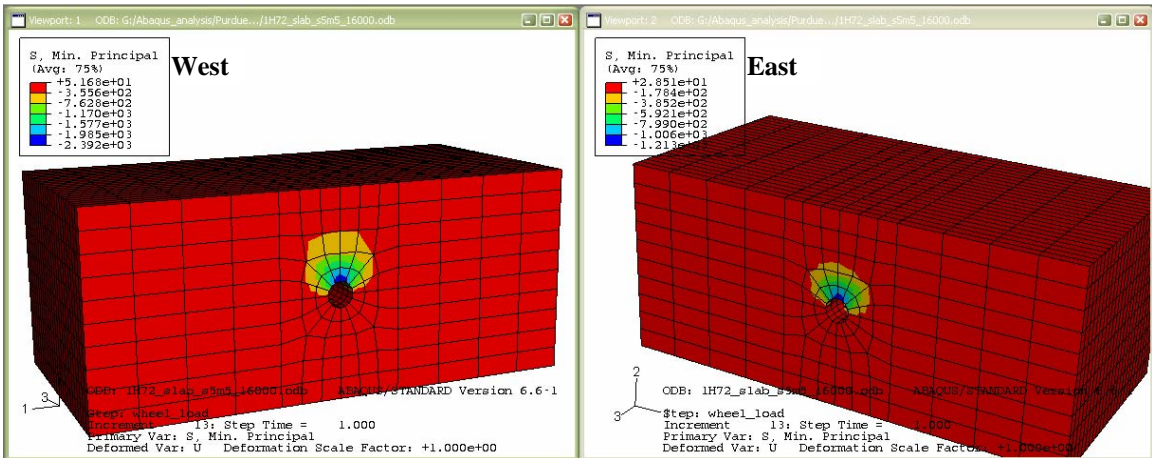


(b) Stresses after application of wheel load

Figure 7.6: Compressive stress zones in the concrete for 1V72 FE model



(a) Stresses after a joint opening of 1/8 in.



(b) Stresses after application of wheel load

Figure 7.7 Compressive stress zones in the concrete for 1H72 FE model

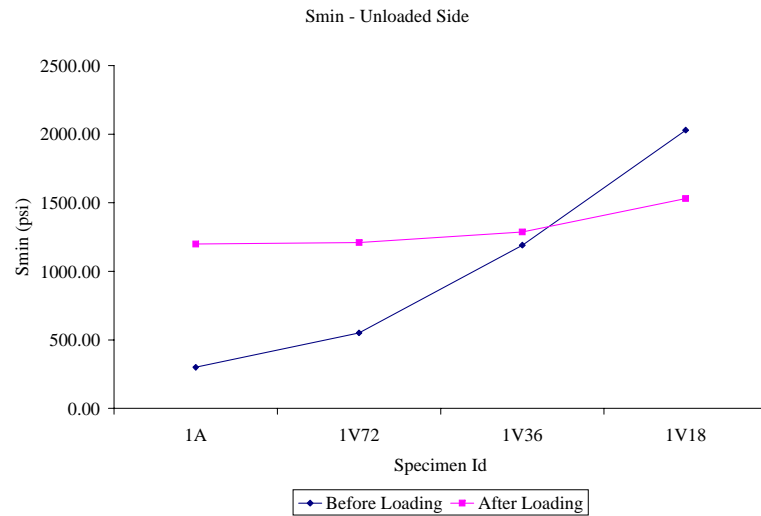
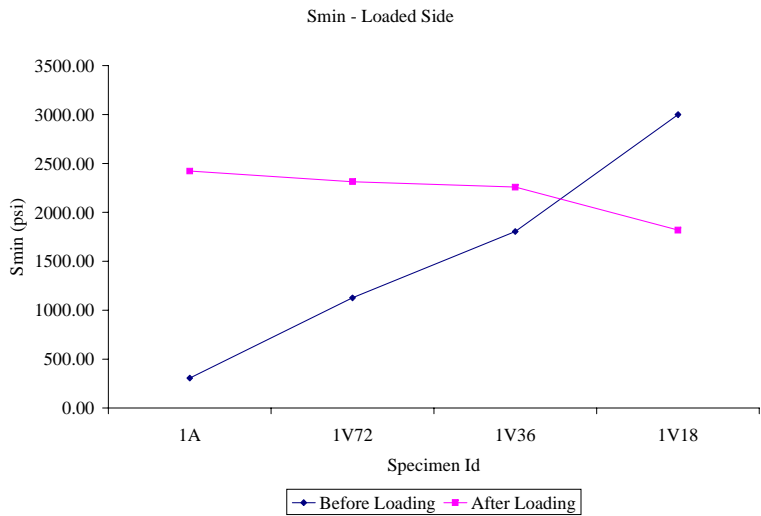
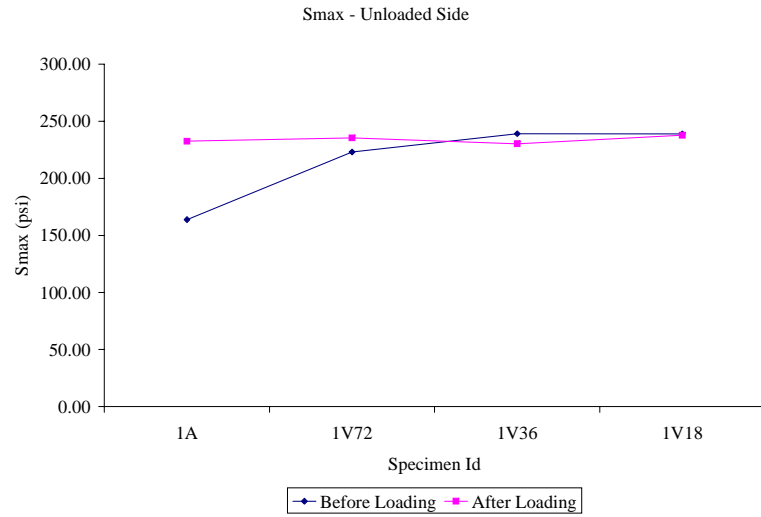


Figure 7.8 Results at location (i) and (ii) for single vertically misaligned dowel bar at 1/8" joint opening

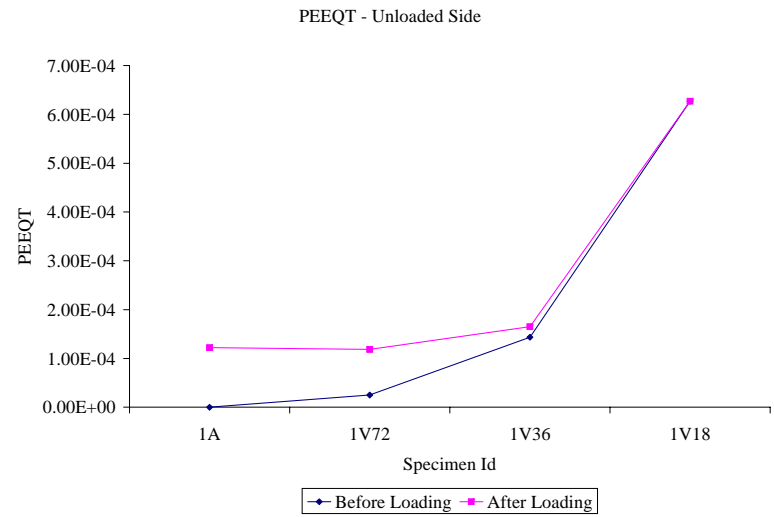
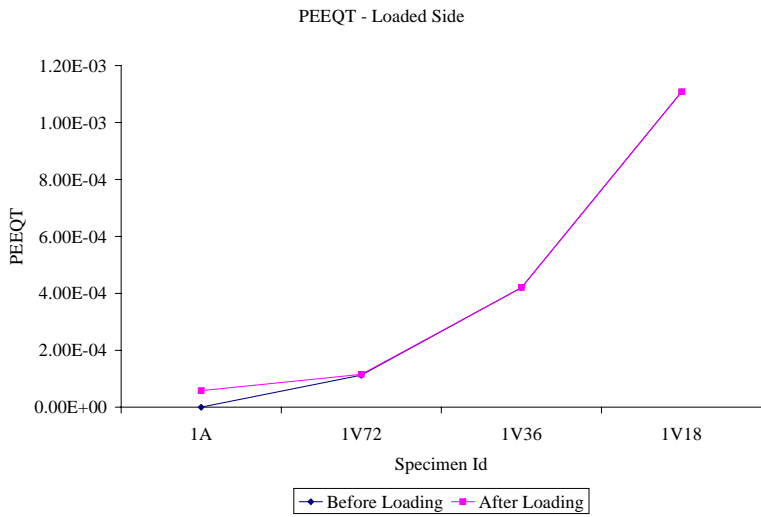
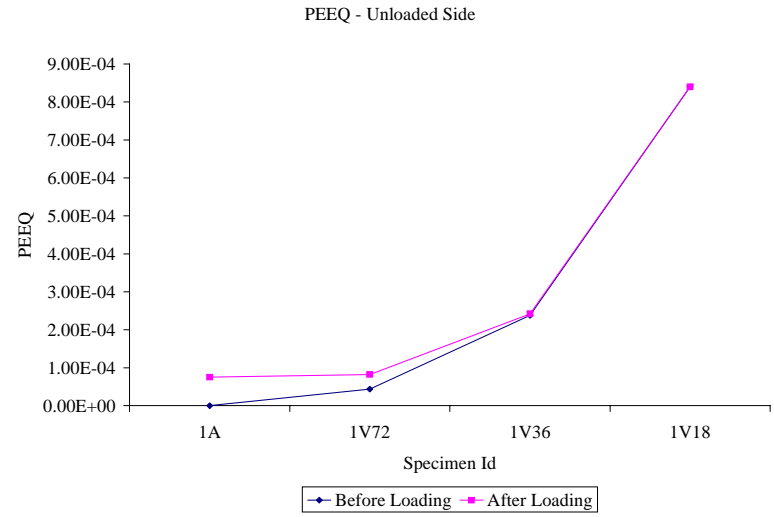
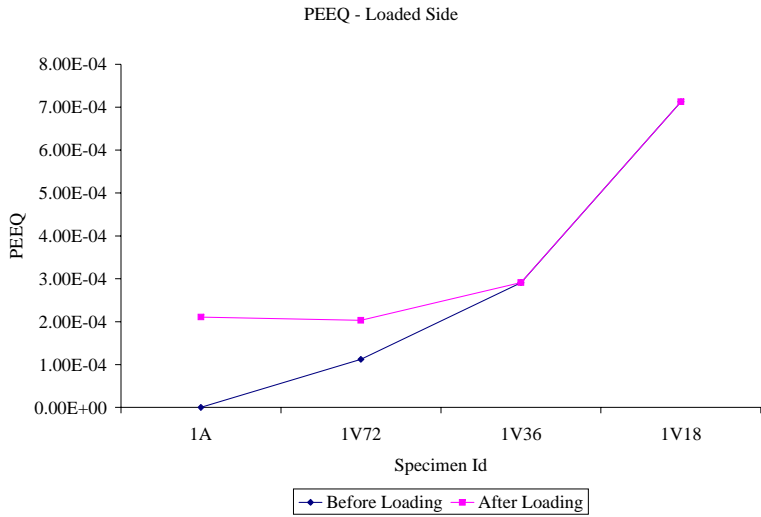


Figure 7.8 (Contd): Results at location (i) and (ii) for single vertically misaligned dowel bar at 1/8" joint opening

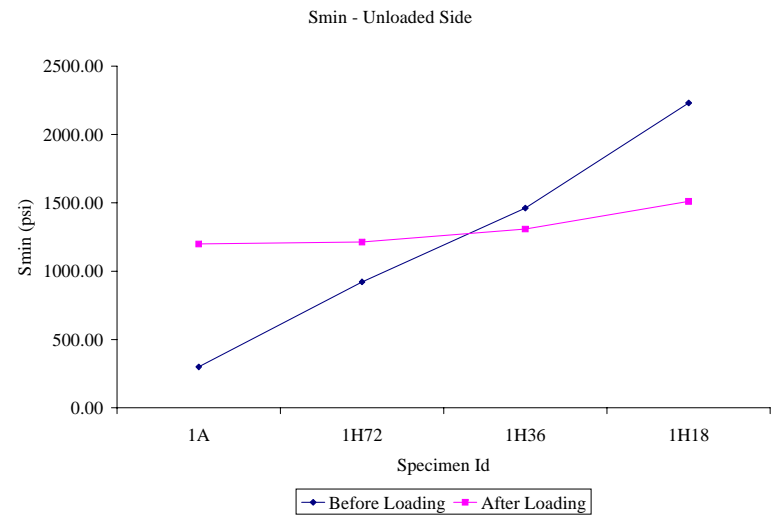
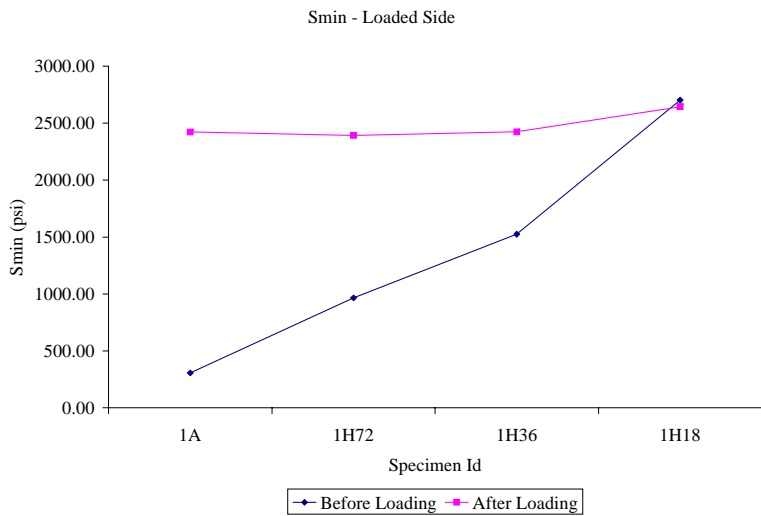
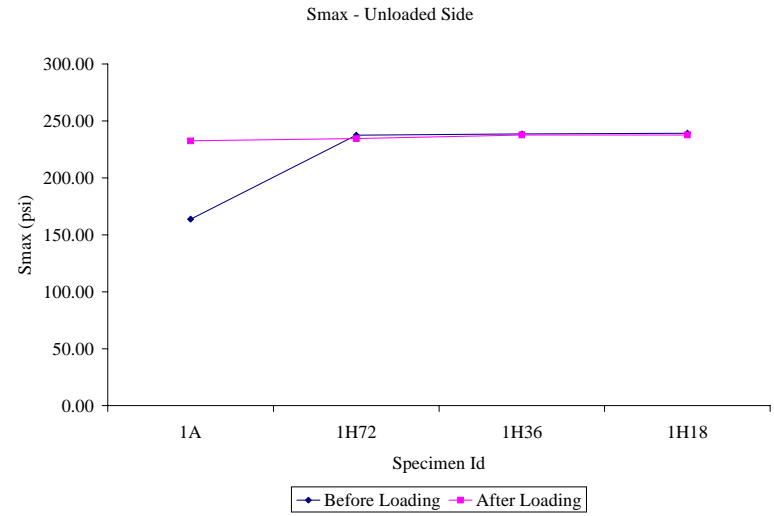


Figure 7.9 Results at location (i) and (ii) for single horizontally misaligned dowel bar at 1/8" joint opening

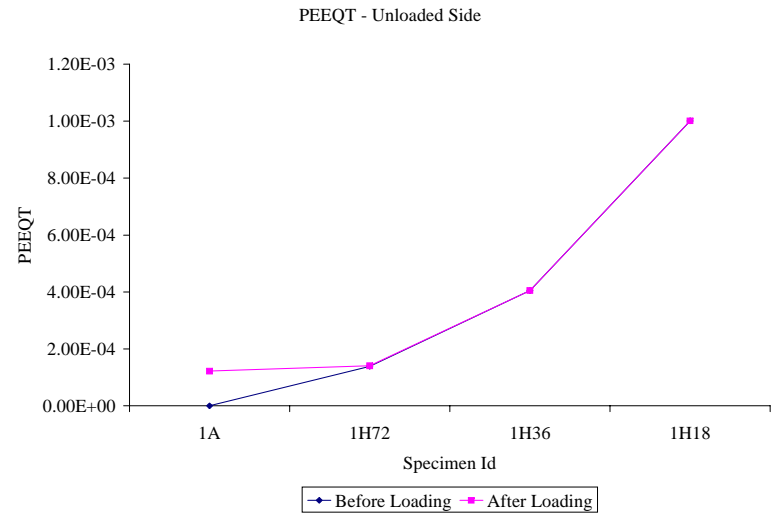
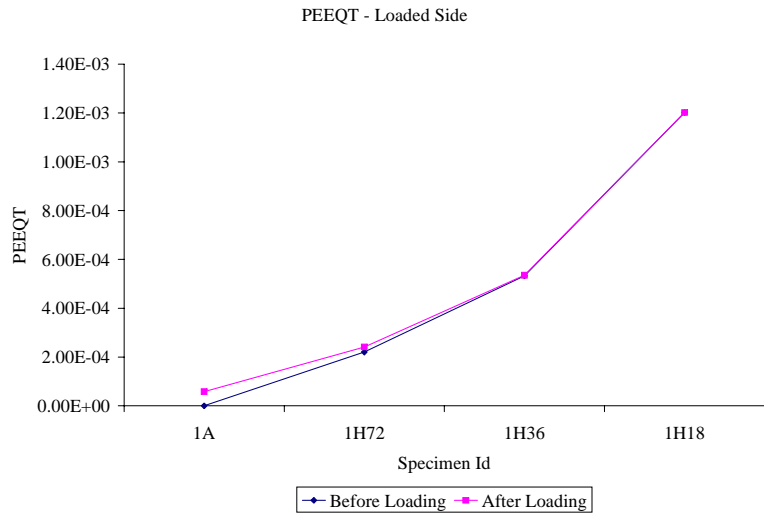
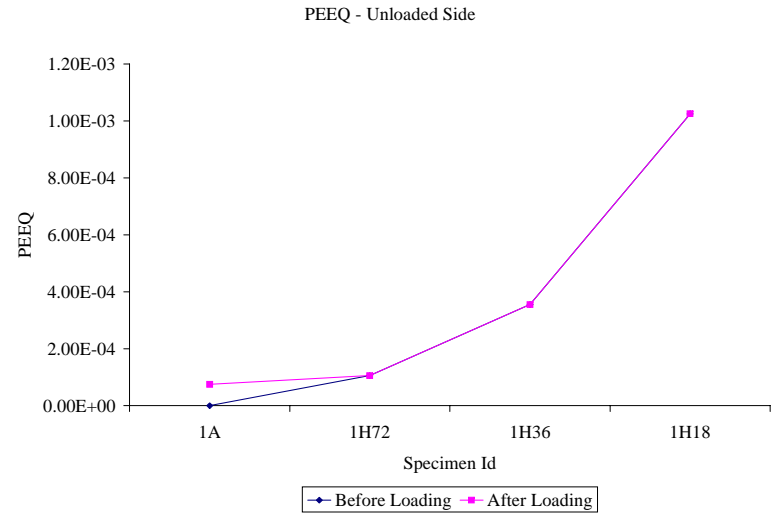
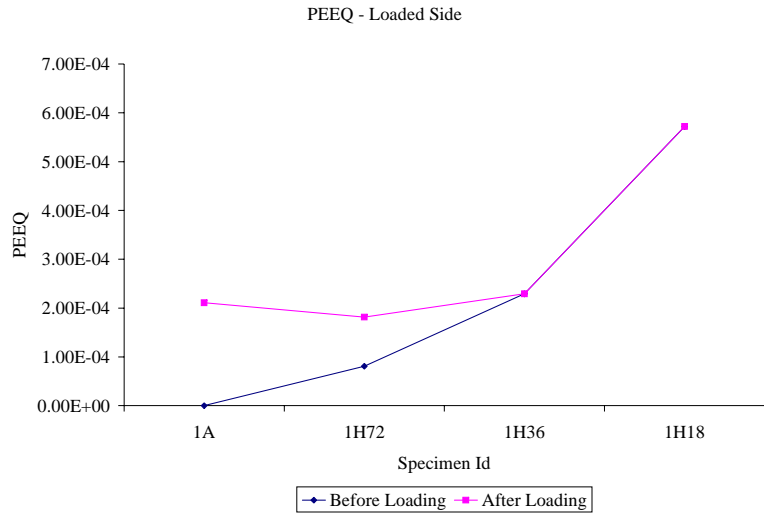


Figure 7.9 (Contd): Results at location (i) and (ii) for single horizontally misaligned dowel bar at 1/8” joint opening

7.4.2 THREE DOWEL BAR MODEL

In the three dowel bar models, the concrete pavements slabs were first pulled apart to 1/8 in and then a set of dual wheels tandem axles applied a load of 8000 lbs each on one side of the slab at the joint face. Complex multiaxial stress and strain zones were captured by the finite element analytical models and have been presented in Appendix D.

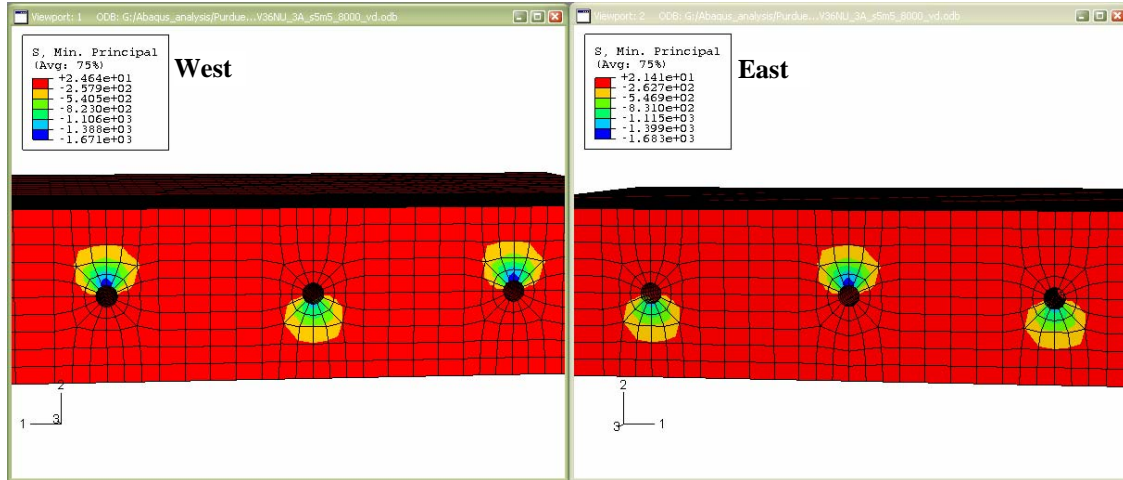
Aligned dowel bars

In the case when all the dowel bars are aligned, 3A, as the joint is opened multiaxial stress and strain states are produced in the concrete surrounding the dowel bar. The stress and strain states in this case are well below the inelastic stresses (f'_c and f'_t) and strains (PEEQ and PEEQT). There is a marginal increase in the stress states as the load is applied at the joint face. Overall, the 3A finite element analytical model showed no formation of distresses in the concrete at the joint face.

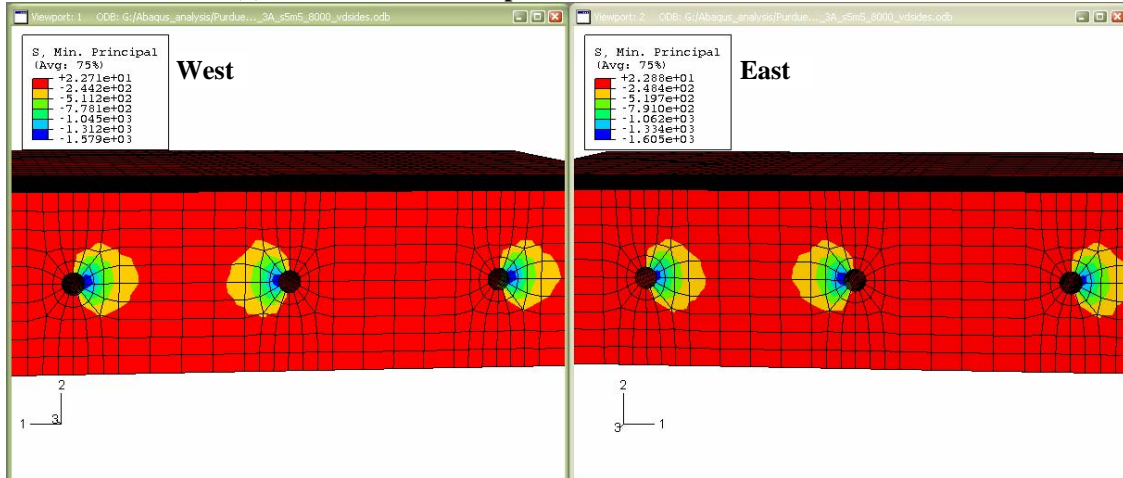
Non-Uniform orientation of dowel bars

The cases in which all the three dowel bars that were misaligned with vertical (3V36NU and 3V72NU) or horizontal (3H36NU and 3H72NU) misalignment showed the formation of high stress concentration zones in the concrete surrounding the dowel bar. These stress concentration zones formed at a joint opening of 1/8 in. near the face of the joint, as shown in figure 7.10 for 3V36NU and 3H36NU. For example, in the 3H36NU case, with load application, the stress concentration zone around the center dowel bar migrated from the side to the top of the dowel bar as shown in figures 7.10 and 7.11. The results of the 3D finite element model show that the central misaligned dowel bar is loaded more than

the outer misaligned bars. This occurs due to the redistribution of stresses and the location of the wheel loads on the concrete pavement slab. The change in stress intensity in the concrete surround the misaligned dowel bars is shown in figure 7.11 (b). The mechanics of the formation of these bearing stress zones under the misaligned dowel bar are synonymous to the ones observed in the single dowel bar finite element models.

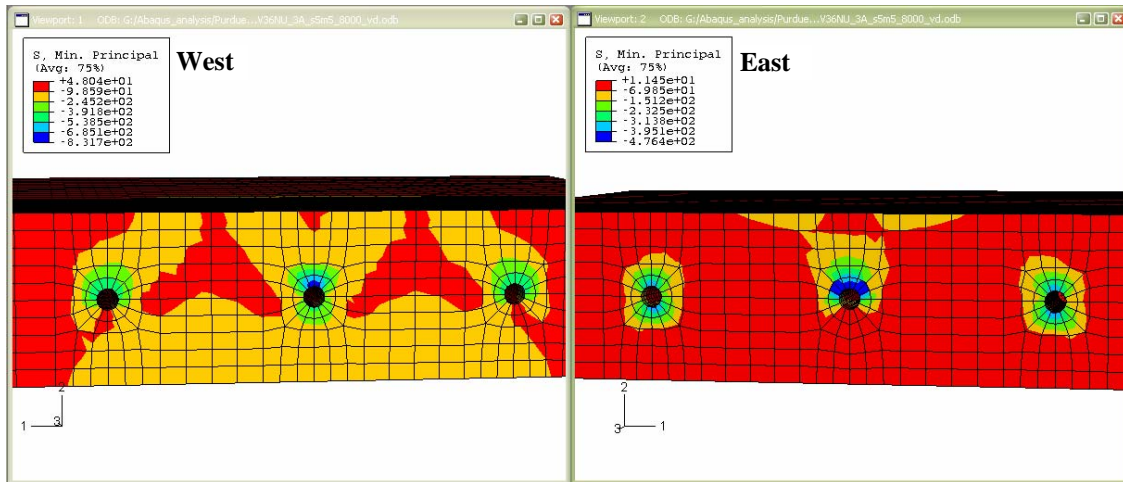


(a) Minimum Compressive Stresses in 3V36NU model

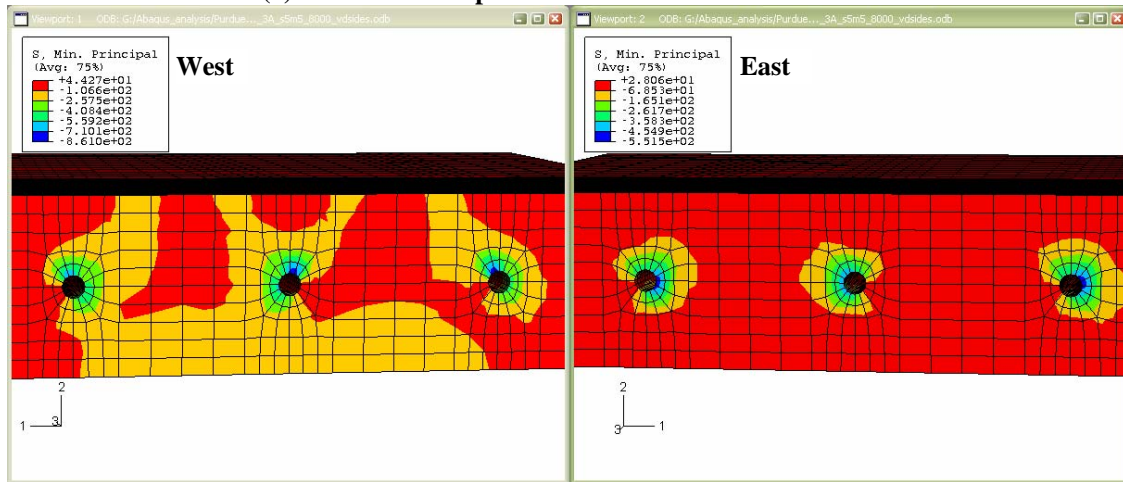


(b) Minimum Compressive Stresses in 3H36NU model

Figure 7.10: Stress concentration zones formed in concrete due to misaligned dowel bars and at joint opening (1/8 in)



(a) Minimum Compressive Stresses in 3V36NU model



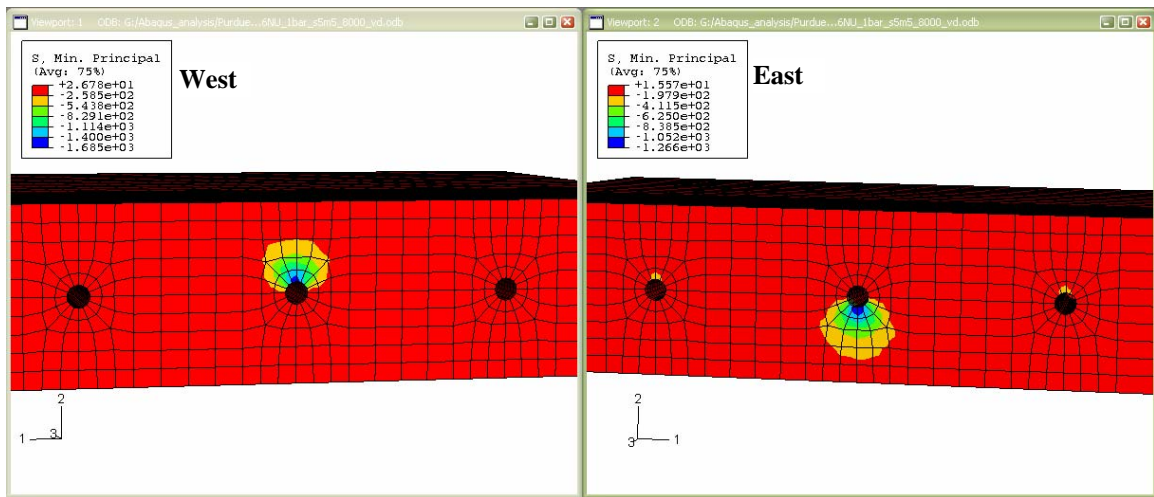
(b) Minimum Compressive Stresses in 3H36NU model

Figure 7.11: Formation of bearing stress zones in the concrete due to load application

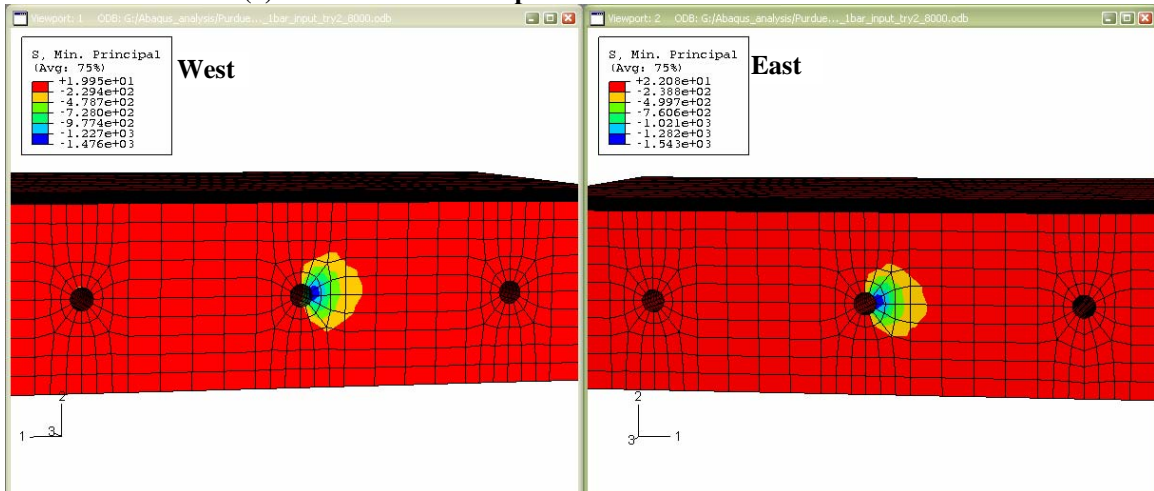
Alternate misaligned dowel bars

Similar to the non-uniform orientation of dowel bar cases, the cases with alternate misaligned dowel bars, showed the formation of very high stress concentration zones in the concrete surrounding the dowel bar. In the cases studied only the central dowel was misaligned and the outer dowels were straight. Both the vertically (3V36AM and 3V72AM) and horizontally (3H36AM and 3H72AM) misaligned dowel bar cases were studied and are presented in Appendix D. The stress concentration zones are formed at a joint opening of 1/8 in. near the face of the joint, as shown in figures 7.12 (a) and (b)

corresponding to 3V36AM and 3H36AM analytical models. With the application of wheel loads, stress concentration zones due to misalignment undergo unloading and high bearing stress zones are formed under the location of the wheel loads. Figure 7.13 shows the formation of these bearing stress contours at the end of load application on the pavement slab with 3V36AM and 3H36AM analytical models. The stresses and strains in the 3V72AM and 3H72AM models are lower compared to the results shown in figure 7.12.

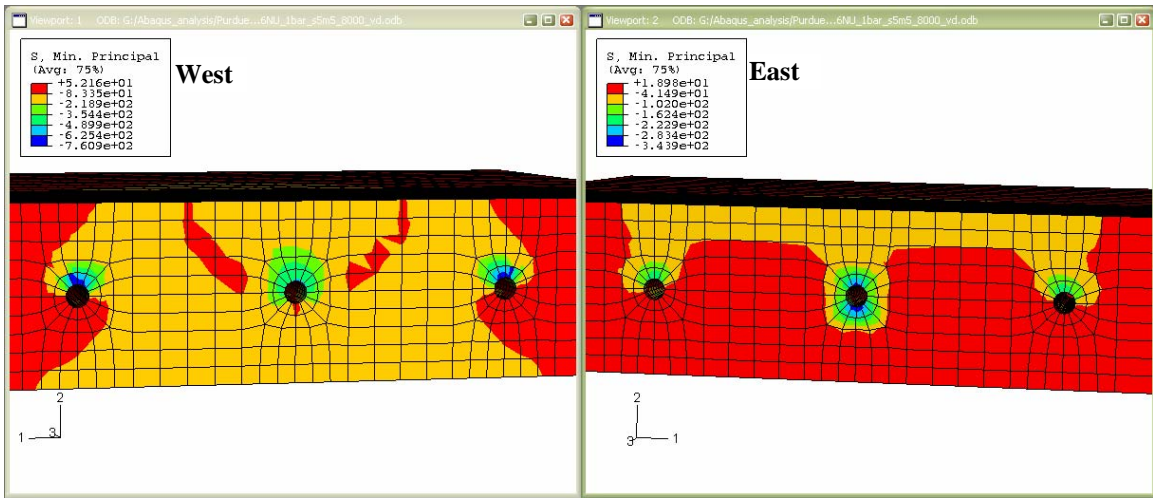


(a) Minimum Compressive Stresses in 3V36AM model

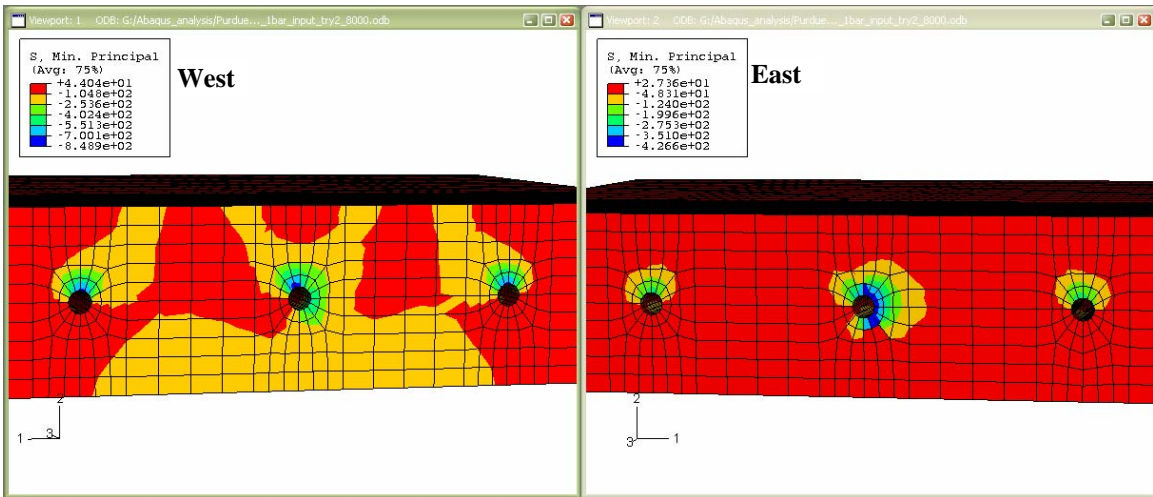


(b) Minimum Compressive Stresses in 3H36AM model

Figure 7.12: Stress concentration zones formed in concrete due to misaligned dowel bars and at joint opening (1/8 in)



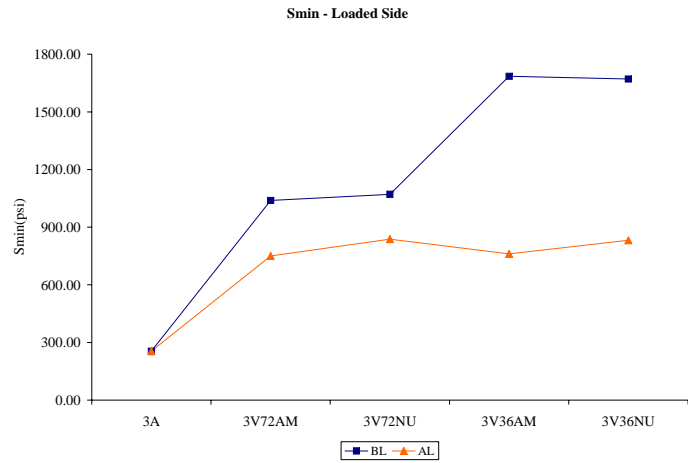
(a) Minimum Compressive Stresses in 3V36AM model



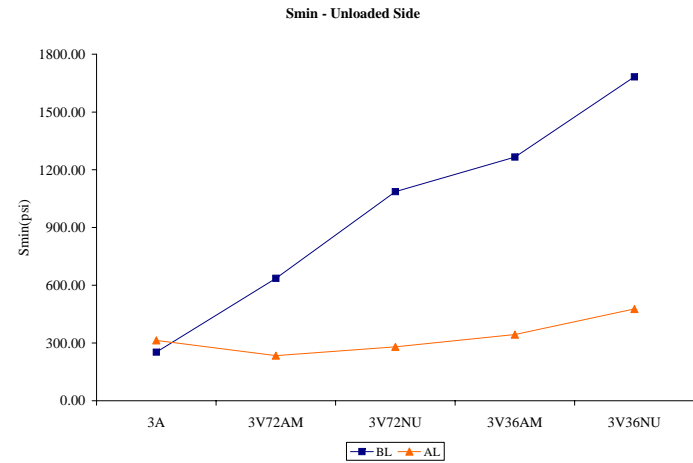
(b) Minimum Compressive Stresses in 3H36AM model

Figure 7.13: Formation of bearing stress zones in the concrete due to load application

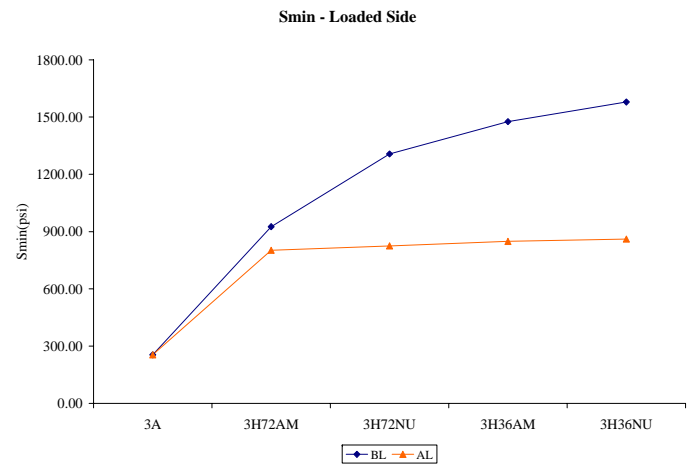
Figure 7.14 presents the formation of compressive stresses (S_{min}) in the concrete on the loaded (west) and unloaded (east) sides after joint opening and application of wheel loads. At 1/8 in joint opening before load application, there is an increase in the stress magnitude as more bars are misaligned (from alternate misalignment to non-uniform misalignment) and magnitude of misalignment is increased from 1/72 radians to



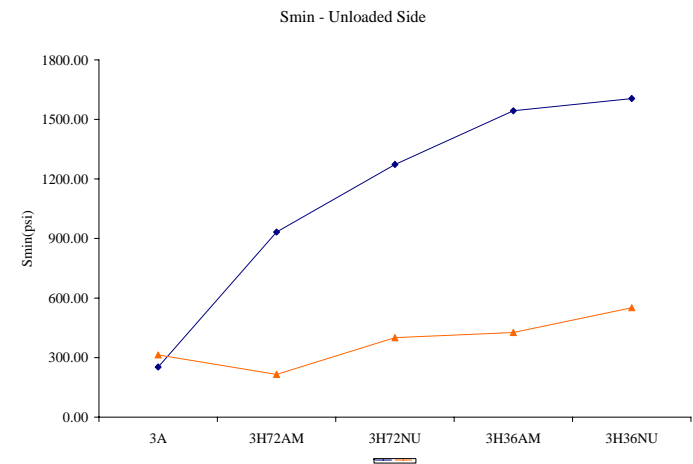
(a) Loaded side Stresses with Vertically Misaligned bars



(b) Unloaded side Stresses with Vertically Misaligned bars



(c) Loaded side Stresses with Horizontally Misaligned bars



(d) Loaded side Stresses with Horizontally Misaligned bars

Figure 7.14: Compressive stresses in the three dowel bar FE models

1/36 radians. A similar trend in bearing stresses is observed in the concrete surrounding the dowel bars after load application. The magnitude of S_{\max} , PEEQ and PEEQT after joint opening and loading are not a cause of concern because of small joint opening and load redistribution.

7.5 CONCLUDING REMARKS

The results from the analyses included the multiaxial stresses and strains in the concrete elements. These results indicated that:

- The joint opening of 0.125 in. produced stress concentration zones in joints with misaligned dowels. These zones were similar to those predicted by the finite element models with joint openings only (section 8.3 and 8.4).
- A joint opening of 0.125 in., does not produce any significant distress for the misalignment magnitudes and type considered in this portion of the study.
- Applying the wheel loading changes the stress states and the stress concentration zones (for the horizontal misalignment) finite element models.
- The inelastic strains (compression and tension) induced in the concrete by the wheel loading increase much faster after the dowel misalignment exceeds 1/36 radians.
- The pavement specimens with three dowel bars with different types and orientations of misalignment with magnitude less than or equal to 1/36 radians do not undergo significant inelastic straining in compression (crushing) or tension (cracking) for total wheel loads equal to 16000 lbs.

CHAPTER 8

SUMMARY, CONCLUSIONS, RECOMMENDATIONS AND FUTURE RESEARCH

8.1 INTRODUCTION

This chapter presents summary and conclusions of the experimental investigations, the analytical modeling, parametric studies and of the combined effects of misalignment and wheel loading.

8.2 SUMMARY AND CONCLUSIONS BASED ON EXPERIMENTAL INVESTIGATIONS

A comprehensive experimental investigation was conducted on laboratory-scale pavement specimens with aligned or misaligned dowel bars at contraction joints. The parameters included in the experimental investigations were the dowel misalignment type, magnitude, and uniformity. The experimental test matrix consisted of 54 laboratory scaled slab specimens with limited repetitions.

Pavement joint opening occurs due to thermal movements induced by changes in ambient conditions. It is a cyclic, time-varying phenomenon that depends completely on the weather (ambient) conditions. The joint in the slab specimens were created using a 1/8 in. aluminum separator plate to eliminate effects of aggregate interlock. The slab specimens in the experimental investigation were cast in steel molds to eliminate effects due to base friction and isolate distresses caused due to misaligned dowel bars. Also, no axle wheel loads were considered during the experimental investigation. The effects of

base friction and axle loads on the pavement slabs should be considered for future research.

The experimental results included the pullout force per dowel-joint opening behavior of the pavement specimens and the observed structural distresses. The experimental results indicated that:

- The pullout force per dowel-joint opening behavior of all specimens consisted of two regions: (1) the initial fully bonded region, and (2) the post-slip debonded region. Debonding or initial slip occurs typically when the pullout force per dowel exceeds 1124 -1574 lbs. This corresponds to average bond shear stress (τ_b) equal to 30.0 - 43.0 psi.
- Dowel misalignment has a small influence on the initial debond shear stress (τ_b), but it has significant influence on the post-slip pullout force per dowel-joint opening behavior.
- For all misalignment types (horizontal, vertical, or combined), the pullout force per dowel bar increases with increase in misalignment magnitude (1/36 to 1/9 radians.) and non-uniformity.
- Structural distresses in the form of concrete spalling and cracking were observed for specimens with larger dowel misalignments (greater than 1/18 radians) and non-uniformity. The severity of the structural distress increased further with the number of misaligned dowel bars at the joint.
- Specimens with horizontal (H) or combined (C) misalignments and large (greater than 1/18 radians), non-uniform dowel misalignments experienced significant structural distress in the form of spalling and transverse cracking of the slab specimens.

- Specimen with vertical (V) misalignments with large (greater than 1/18 radians), non-uniform dowel misalignments experienced structural distress in the form of spalling and uplift of the slab specimens.

The experimental results and observations provide valuable information regarding the joint opening behavior of pavement specimens with various dowel misalignment types, magnitudes, and uniformity. They provide limited information regarding the overall interaction between the dowel and the surrounding concrete. They do not provide comprehensive knowledge of the mechanics of dowel-concrete interaction. Hence, analytical investigations based on the experimental results were performed to better understand the basic dowel-concrete interaction mechanics.

The experimental investigation focused on overall pullout force per dowel-joint opening behavior on laboratory scaled concrete pavement specimens. The localized multiaxial stresses, strains and the distresses observed in the test specimens were not measured during the experimental investigation as sensors required to measure the localized stresses and strains were not embedded in the specimens. Additionally, non-destructive techniques were not used to monitor the formation of distresses within the concrete specimens at the dowel-concrete interfaces. These are some of the limitations of the experimental approach used in this research, and should be addressed by future research.

8.3 SUMMARY AND CONCLUSIONS BASED ON ANALYTICAL INVESTIGATIONS

The 3D finite element models were developed to further investigate the behavior of the pavement specimens with misaligned dowel bars. The dowel-concrete longitudinal bond model was calibrated using the experimental results for the pavement specimens with aligned dowel bars. The transverse interaction between the dowel bar and the concrete was modeled using surface-to-surface contact elements. Two cases were considered for the coefficient of friction between the dowel bar and the concrete in contact. Case I used idealized values and case II used experimentally measured values for the friction coefficient. The concrete material was modeled using a damaged plasticity model with multiaxial plasticity behavior in compression and damaged elasticity behavior in tension. The concrete material properties required to completely define this material model were based on idealized (case I) and measured (case II) values. The steel material was modeled using a multiaxial elasticity model.

The results from the 3D finite element analyses indicated that:

- The analytically predicted dowel pullout force-joint opening behavior compared favorably with the experimental measurements.
- The analytical and experimental comparisons are reasonable for all pavement specimens with different numbers, magnitudes and orientation of dowel misalignment.
- The analytical models and the analysis approach can be used to expand the experimental behavior database and conduct parametric studies.

- The analytical results indicate the formation of significant stress concentration zones in the concrete at the joint face around the misaligned dowel bars.

The comparisons focused on the overall pullout force per dowel-joint opening behavior predicted by the models and measured experimentally. The localized multiaxial stresses and strains computed by the models at the sites of stress concentration could not be verified because the corresponding measurements were not performed during the experiments. Additionally, non-destructive techniques were not used to monitor the formation of distresses within the concrete specimens at the dowel-concrete interfaces.

The analytical results (3D stresses and strains) from the finite element analyses were used to identify significant events or damage limit states occurring in the concrete material at the dowel-pavement interface. The events / damage limit states are indicated on the analytically predicted pullout force-joint opening behavior plots from event (A – F). The localized multiaxial stresses and strains and events (A – F) predicted by the numerical models could not be validated experimentally as the distresses caused were highly localized and occurred deep inside the concrete pavement specimens. The events (A – F) do not imply or suggest that they occur at the same joint opening as in real pavement specimens but it is logically assumed that these distresses and events (A – F) will occur eventually in the experimental or real pavement specimens. The relative occurrence of these events for pavement specimens with different misaligned dowel bars is probably more important than their absolute joint opening values.

8.4 SUMMARY AND CONCLUSIONS OF PARAMETRIC STUDIES

The 3D finite element models that were developed and verified using experimental results, were used to conduct analytical parametric studies. The parameters considered were the number of dowel bars (one or two), dowel misalignment magnitude (0, 1/72, 1/36 and 1/18 radians), the dowel misalignment type (vertical and horizontal) and the dowel misalignment orientation (uniform, non-uniform or alternate). The analytical matrix consisted of seven specimens with one dowel bar and nineteen specimens with two dowel bars. The results from the parametric studies indicated that:

- For models with one misaligned dowel bar, horizontal misalignment can be more detrimental than vertical misalignment.
- For models with two vertically misaligned dowels, the effects of non –uniform misalignment can be more detrimental than uniform or alternate misalignment.
- For models with horizontally misaligned dowels, the misalignment orientation (uniform, non-uniform or alternate) does not have a significant influence on the occurrence of events / material damage limit states as the dowel misalignment magnitude increases, these events occur for smaller joint openings.

8.5 SUMMARY AND CONCLUSIONS BASED ON THE STUDIES FOR MISALIGNED DOWELS COMBINED WITH WHEEL LOADING

The analytical models were modified slightly to investigate the effects of combined wheel loading and joint opening on the behavior of pavement specimen models. This was a preliminary investigation that attempted to evaluate the effects of wheel loading on the

behavior of joints with misaligned dowel bars. The models and the analysis results could not be verified due to the lack of experimental data and results. The findings of this portion of the study must be considered carefully and verified experimentally before any action.

The 3D finite element models were developed for pavement specimens with transverse joints. The pavements were supported by a base, sub-base and sub-grade layers with assumed idealized material properties. Seven pavement specimens were analyzed with transverse joints with one misaligned dowel bar. The dowel bar misalignment orientations was either vertical or horizontal, with misalignment magnitudes ranging from 0 to 1/18 radians. Nine pavement specimens were analyzed with joints with three misaligned dowel bars. The misalignment orientations were either vertical or horizontal, with non-uniform or alternate misalignment and misalignment magnitudes ranging from 0 to 1/36 radians.

The pavement specimen models were analyzed by subjecting them to a joint opening equal to 0.125 in. which simulated a change in temperature. After joint opening, the specimen models were subjected to monotonically increasing wheel loading at the joint face. The total value of wheel loading was equal to 16000 lbs, which includes the dynamic magnification factor and is conservative (four times the wheel load of 4000 lbs).

The results from the analyses included the multiaxial stresses and strains in the concrete elements. These results indicated that:

- The joint opening of 0.125 in. produced stress concentration zones in joints with misaligned dowels. These zones were similar to those predicted by the finite element models with joint openings only (section 8.3 and 8.4).

- A joint opening of 0.125 in., does not produce any significant distress for the misalignment magnitudes and type considered in this portion of the study.
- Applying the wheel loading changes the stress states and the stress concentration zones (for the horizontal misalignment) finite element models.
- The inelastic strains (compression and tension) induced in the concrete by the wheel loading increase much faster after the dowel misalignment exceeds 1/36 radians.
- The pavement specimens with three dowel bars with different types and orientations of misalignment with magnitude less than or equal to 1/36 radians do not undergo significant inelastic straining in compression (crushing) or tension (cracking) for total wheel loads equal to 16000 lbs.

8.6 RECOMMENDATIONS AND FUTURE RESEARCH

The recommendation on misalignment magnitude is based on the limitations and assumptions associated with the experimental investigation and analytical approach. The localized material states (stress and strain) and the corresponding events (A – F) will have a significant influence on the *cyclic material fatigue life* at the distress locations. In the absence of experimental data and models relating the localized stresses and strains to the fatigue life of the pavement, the rational choice would be limit the localized stresses (S_{\max} and S_{\min}) to the material uniaxial stress capacities (f'_t and f'_c), i.e., to events C and D. A misalignment tolerance range of 1/72 - 1/36 radians skew angle or 1/8 – 1/4 in. per half length of the dowel bar is recommended for construction to the Department of Transportation.

In order to develop an analytical model, experimental investigations on slab specimens with misaligned dowel bars subjected to thermal effects such as expansion and contraction of the joint is needed. Furthermore, experimental investigations can focus on laboratory scaled concrete slab specimens, to study the effects of typical misaligned dowel bars, subjected to thermal effects combined with axle loads.

The analytical models in the future studies can be developed to capture effects due to temperature gradients along the slab thickness thereby addressing issues related to curling combined with misaligned dowel bars. It is hypothesized that fatigue loading causes dowel looseness that affects the load transfer efficiency of the joint leading to joint failure. As future goals, analytical models should be developed to capture and study behavior of complex multiaxial stress states caused due to misaligned dowels, dowel looseness, environmental changes combined with axle loads.

APPENDIX A
DETAILS OF EXPERIMENTAL SETUP

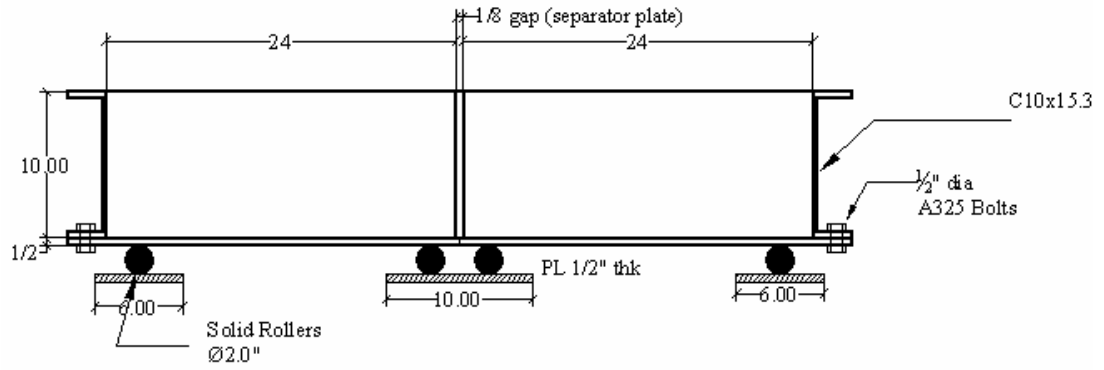


Figure A-1. Cross section of the small mold for pullout test

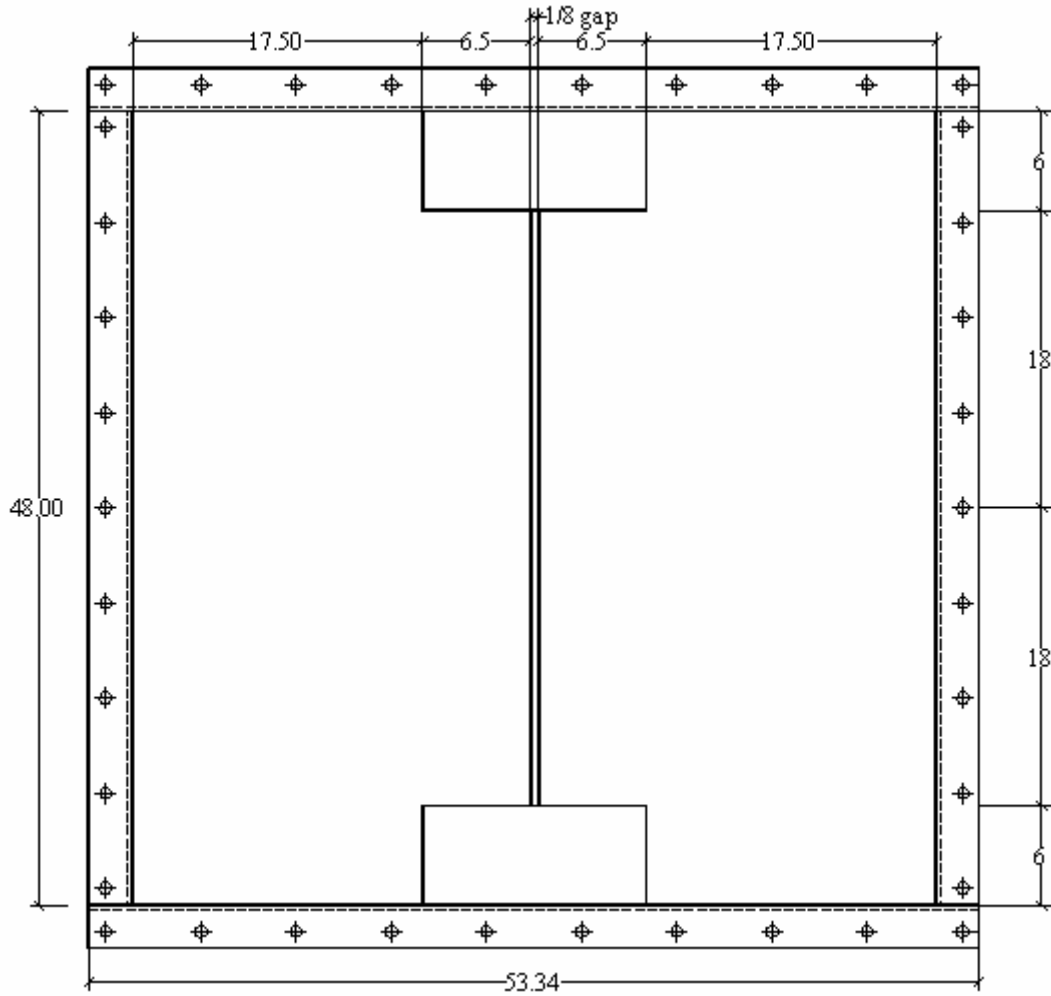


Figure A-2. Plan of the small mold with outside dimensions

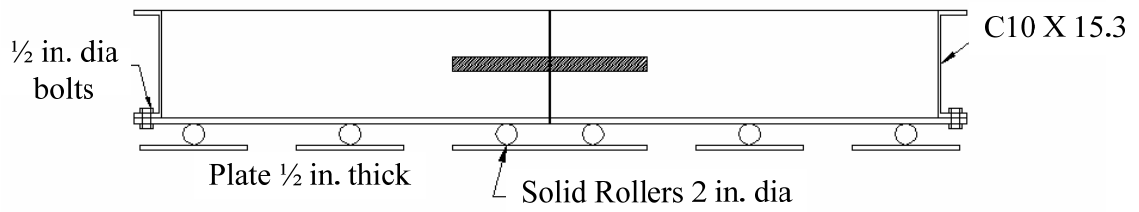


Figure A-3. Typical sectional view of the big mold

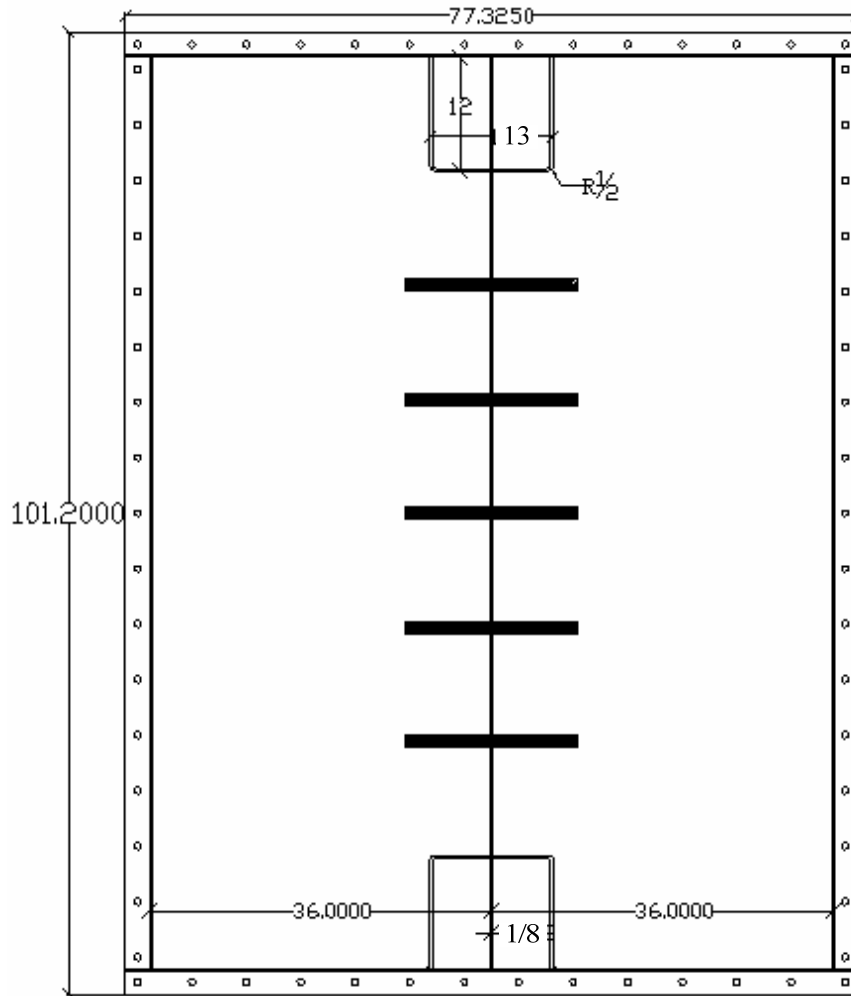


Figure A-4. Typical plan view of mold with 5 dowel bars

Table A-1. Mix Design Specifications

Specification: 2003 Standard Specifications

Grade of Concrete: P1

Intended Use of Concrete: Pavement Form

Material	Class	Specific Gravity	Absorption %
Cement	I/IA	3.13	
Fine Aggregate	2NS	2.61	1.47
Coarse Aggregate	6AA	2.66	1.50

Cement content	: 564 lb/yd ³	B/Bo	: 0.72
Air Content	(design): 6.5 %	Specification Tolerance	: 1.5 %
	(specified): 6.5 %		
R.W.C	: 1.15	Theoretical Yield	: 100.00%
Fly Ash Content, lb/yd ³	: 0		

Weight of Coarse Aggregate (Dry/Loose) lb/ft ³	Aggregate and Water Proportions Quantities, lb/yd ³ of concrete		
	Fine Aggregate (Oven Dry)	Coarse Aggregate (Oven Dry)	Total Water
88	1330	1711	288
89	1313	1730	287
90	1297	1750	286
91	1280	1769	286
92	1264	1788	285
93	1247	1808	284
94	1231	1827	283
95	1214	1847	282
96	1198	1866	281
97	1181	1886	280
98	1164	1905	279

Typical Unit Weight (dry, loose) of coarse aggregate as described above is 93 lb/ft³

Table A-2: Concrete Specimen strength at 7 days

Slab Dimensions	Number of Dowels	ID	Misalignment	Magnitude (in rad.)	Concrete Properties (7 days)		
					f'_c (psi)	f'_t (psi)	f'_b (psi)
2 slabs each - 1220 x 610 x 250 mm (48 x 24 x 10 in.)	1	1A	Aligned	0	2544	540	346
		1V9	Vertical	1/9	2544	540	346
		1V12		1/12	3880	390	458
		1V18		1/18	2544	540	346
		1V36		1/36	3328	240	491
		1H9		Horizontal	1/9	4142	440
		1H12	1/12		3880	390	458
		1H18	1/18		4142	440	438
		1H36	1/36		3328	240	491
		1C9	Combined	1/9	3764	358	551
		1C12		1/12	3396	251	698
		1C18		1/18	3530	355	-
		1C36		1/36	3673	383	636

Table A-2 (Cont'd): Concrete Specimen strength at 7 days

Slab Dimensions	Number of Dowels	ID	Misalignment	Magnitude (in rad.)	Concrete Properties (7 days)				
					f'_c (psi)	f'_t (psi)	f'_b (psi)		
2 slabs each - 48 x 24 x 10 in.	2 (Uniform)	2A	Aligned	0	3396.0	251.0	698.0		
		2V9U	Vertical	+1/9 ;+1/9	5545.0	367.0	572.0		
		2V18U		+1/18;+1/18	3654.0	217.0	534.0		
		2V36U		+1/36;+1/36	3673.0	383.0	636.0		
		2H9U	Horizontal	+1/9;+1/9	5545.0	367.0	572.0		
		2H18U		+1/18;+1/18	3654.0	217.0	534.0		
		2H36U		+1/36;+1/36	3673.0	383.0	636.0		
		2C9U	Combined	+1/9;+1/9	5545.0	367.0	572.0		
		2C18U		+1/18;+1/18	3654.0	217.0	534.0		
2 slabs each - 48 x 24 x 10 in.	2 (Non - Uniform)	2V9NU	Vertical	+1/9;-1/9	4227	317.0	400.0		
		2V12NU		+1/12;-1/12	5540	474.0	636.0		
		2V18NU		+1/18;-1/18	4931	280.0	632.0		
		2V36NU		+1/36;-1/36	4931	290.0	632.0		
		2H9NU	Horizontal	+1/9;-1/9	4227	317.0	400.0		
		2H12NU		+1/12;-1/12	5540	474.0	636.0		
		2H18NU		+1/18;-1/18	4931	280.0	632.0		
		2H36NU		+1/36;-1/36	4931	290.0	632.0		
		2C9NU	Combined	+1/9;-1/9	4227	317.0	400.0		
		2C12NU		+1/12;-1/12	5540	474.0	636.0		
		2C18NU		+1/18;-1/18	4931	280.0	632.0		
		2C36NU		+1/36;-1/36	4931	290.0	632.0		
		2 (One Bar Misaligned)	2 (One Bar Misaligned)	2V12AM	Vertical	+1/12;0	3919	336.0	481.0
				2V18AM		+1/18;0	3520	245.0	378.0
				2H12AM	Horizontal	+1/12;0	3919	336.0	481.0
2H18AM	+ 1/18;0			3520		245.0	378.0		
2C12AM	Combined			+ 1/12;0	3919	336.0	481.0		
2C18AM				+ 1/18;0	3520	245.0	378.0		

Table A-2 (Cont'd): Concrete Specimen strength at 7 days

Slab Dimensions	Number of Dowels	ID	Misalignment	Magnitude	Concrete Properties (7 days)		
					(in rad.)	f'_c (psi)	f'_t (psi)
2 slabs each - 96 x 36 x 10 in.	3 (Aligned)	3A	None	0; 0; 0	3326.6	354.02	540
	3 (Non - Uniform)	3V18NU	Vertical	+1/18;-1/18;+1/18	4931.0	290.0	632.0
		3H18NU	Horizontal	+1/18;-1/18;+1/18	3919.0	336.0	481.0
		3C18NU	Combined	+1/18;-1/18;+1/18	3520.0	245.0	378.0

Table A-2 (Cont'd): Concrete Specimen strength at 7 days

Slab Dimensions	Number of Dowels	ID	Misalignment	Magnitude	Concrete Properties (7 days)		
					(in rad.)	f'_c (psi)	f'_t (psi)
2 slabs each 2440 x 915 x 250 mm (96 x 36 x 10 in.)	5 (Aligned)	5A	Aligned	0; 0; 0; 0; 0			
	5 (Non - Uniform)	5V18NU	Vertical	+ 1/18; - 1/18; + 1/18; - 1/18; + 1/18	4822	363	491
		5H18NU	Horizontal	+ 1/18; - 1/18; + 1/18; - 1/18; + 1/18	3654	217	534
		5C18NU	Combined	+ 1/18; - 1/18; + 1/18; - 1/18; + 1/18	3396	251	698
	5 (Alternate Misaligned)	5V18AM	Vertical	+ 1/18; 0; - 1/18; 0; +1/18	3530	355	-
		5V36AM		+ 1/36; 0; - 1/36; 0; +1/36	3673	636	383
		5H18AM	Horizontal	+ 1/18; 0; - 1/18; 0; +1/18	3880	390	458
		5H36AM		+ 1/36; 0; - 1/36; 0; +1/36			
		5C18AM	Combined	+ 1/18; 0; - 1/18; 0; +1/18	4238	244	540
		5C36AM		+ 1/36; 0; - 1/36; 0; +1/36	3859.5	269.2	623.4

Table A-3. Description of Linear Variable Differential Transducer

Model	LD610-15
Excitation Voltage	± 15 V@ 18 mA maximum
Output	± 10 V DC
Stroke	± 15 mm
Total Stroke	30 mm (1.18 in.)

Table A-4. Description of the Hydraulics (Actuators RC 156 and RC 256)

Name	Capacity (ton)	Stroke (in.)	Cylinder Effective Area (in. ²)	Weight (lbs)
Actuator RC 156	15	6	3.14	15
Actuator RC 256	25	6	5.16	22

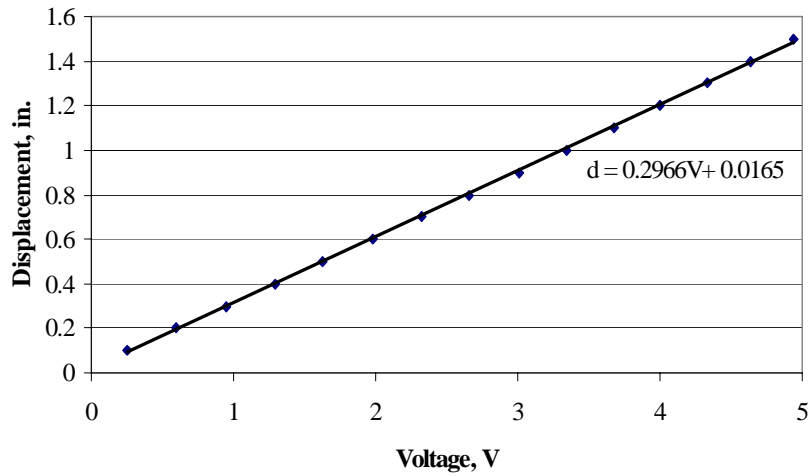


Figure A-5. Calibration of 1.5 in. slider-1

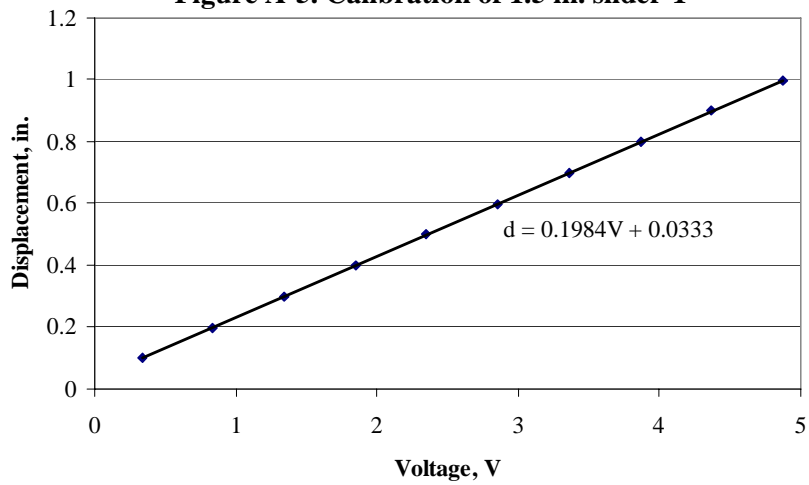


Figure A-7. Calibration of 1.0 in. slider-1

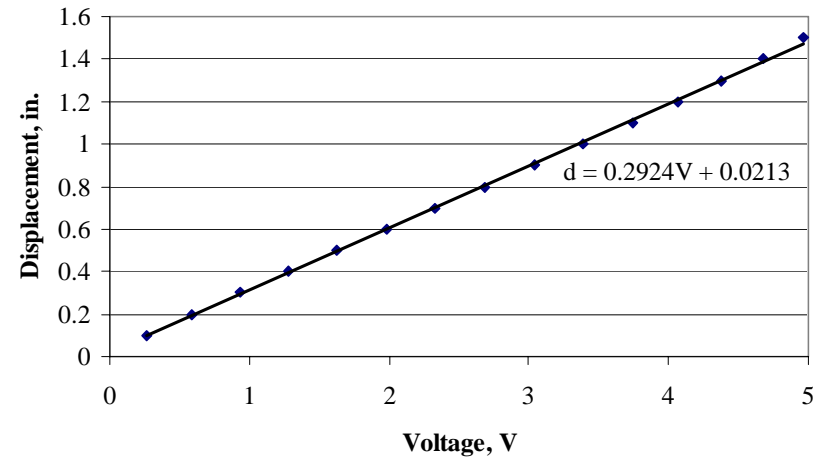


Figure A-6. Calibration of 1.5 in. slider-2

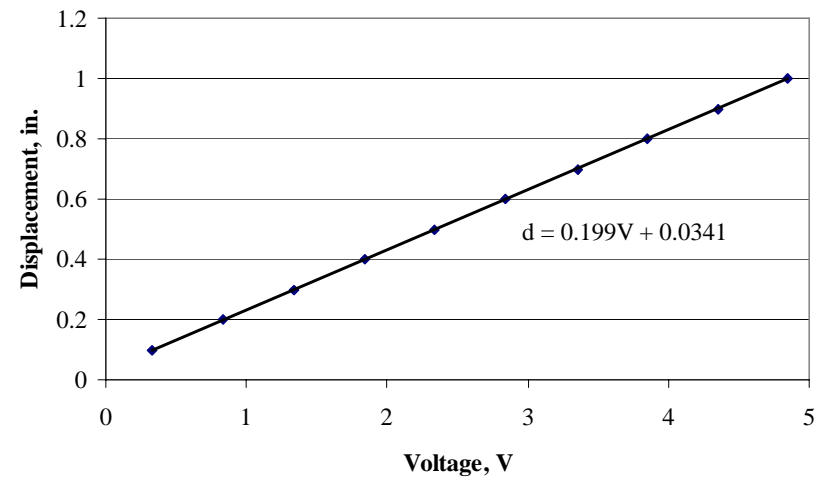


Figure A-8. Calibration of 1.0 in. slider-2

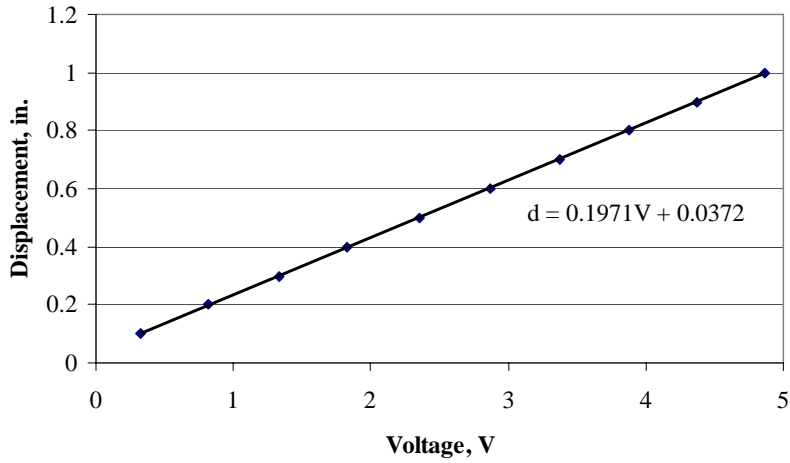


Figure A-9. Calibration of 1.0 in. slider-3

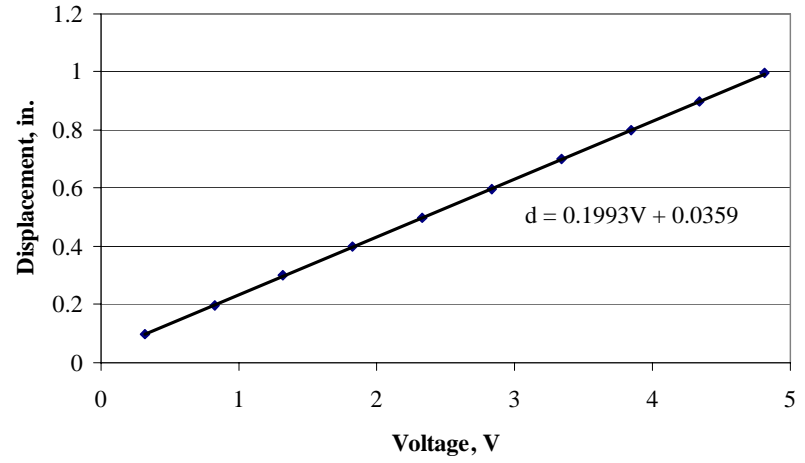


Figure A-10. Calibration of 1.0 in. slider-4

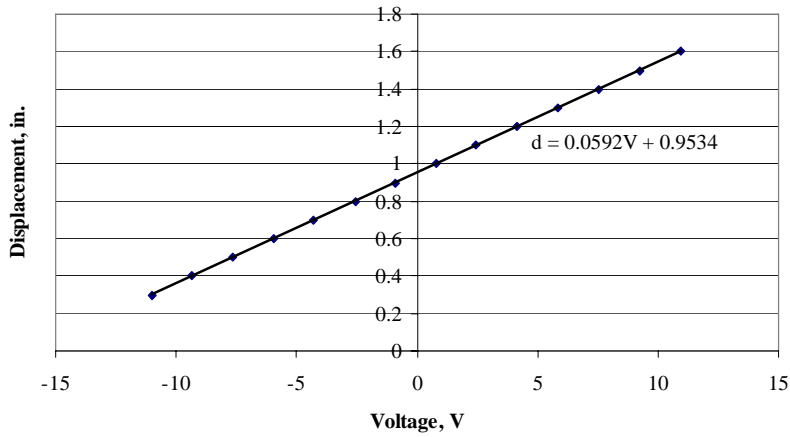


Figure A-11. Calibration of LVDT-1

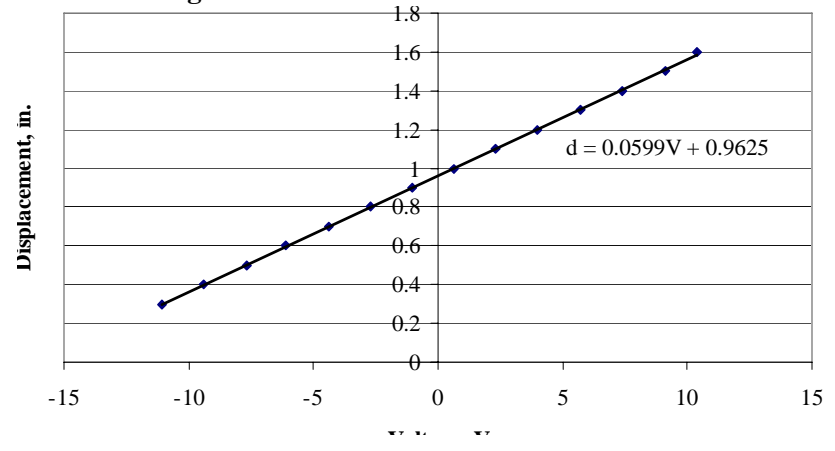


Figure A-12. Calibration of LVDT-2

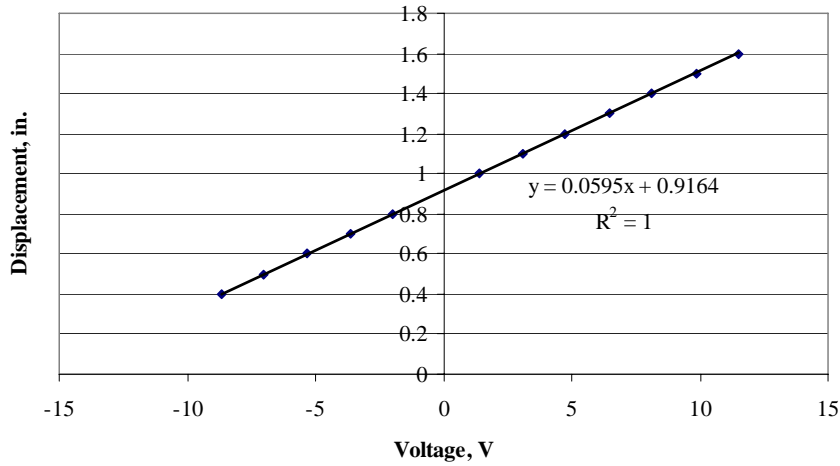


Figure A-13. Calibration of LVDT-3

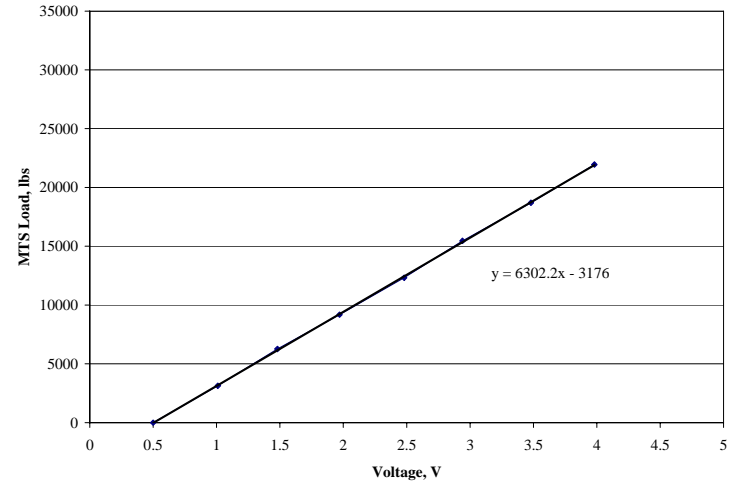


Figure A-14. Calibration of RC156 Actuator 1

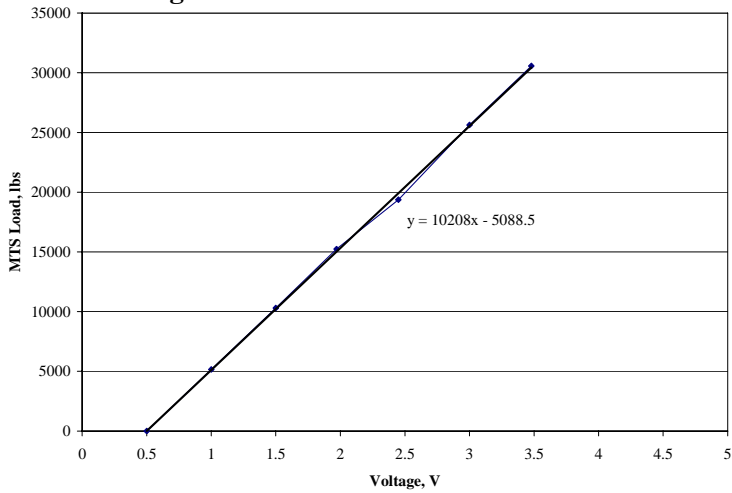


Figure A-15. Calibration of RC256 Actuator 1

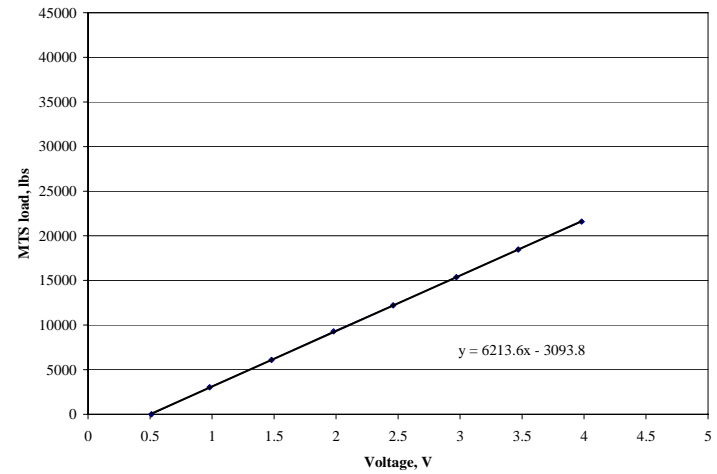


Figure A-16. Calibration of RC156 Actuator 2

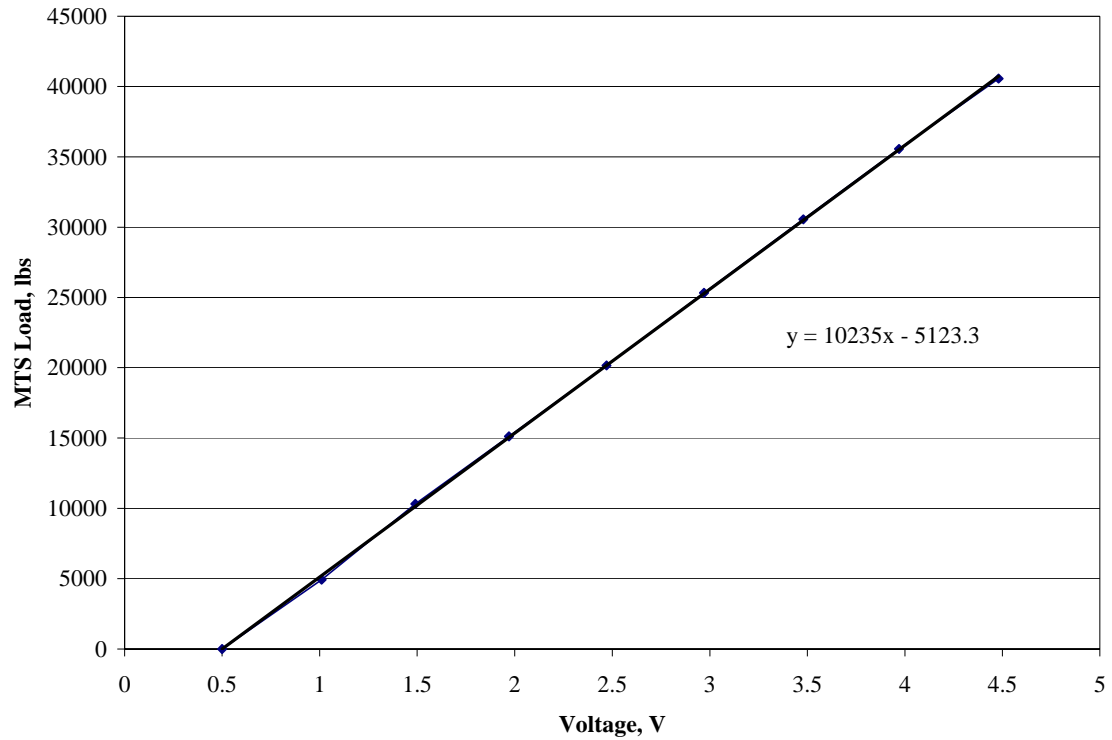


Figure A-17. Calibration of RC256 Actuator 2

Data Acquisition System

The data from the different instrumentation was collected at the rate of 6 scans per second, using a data acquisition system. The data acquisition system is capable of handling all the different instruments – sliders, LVDTs, and pressure transducers. The data flow is illustrated in Figure A-18.

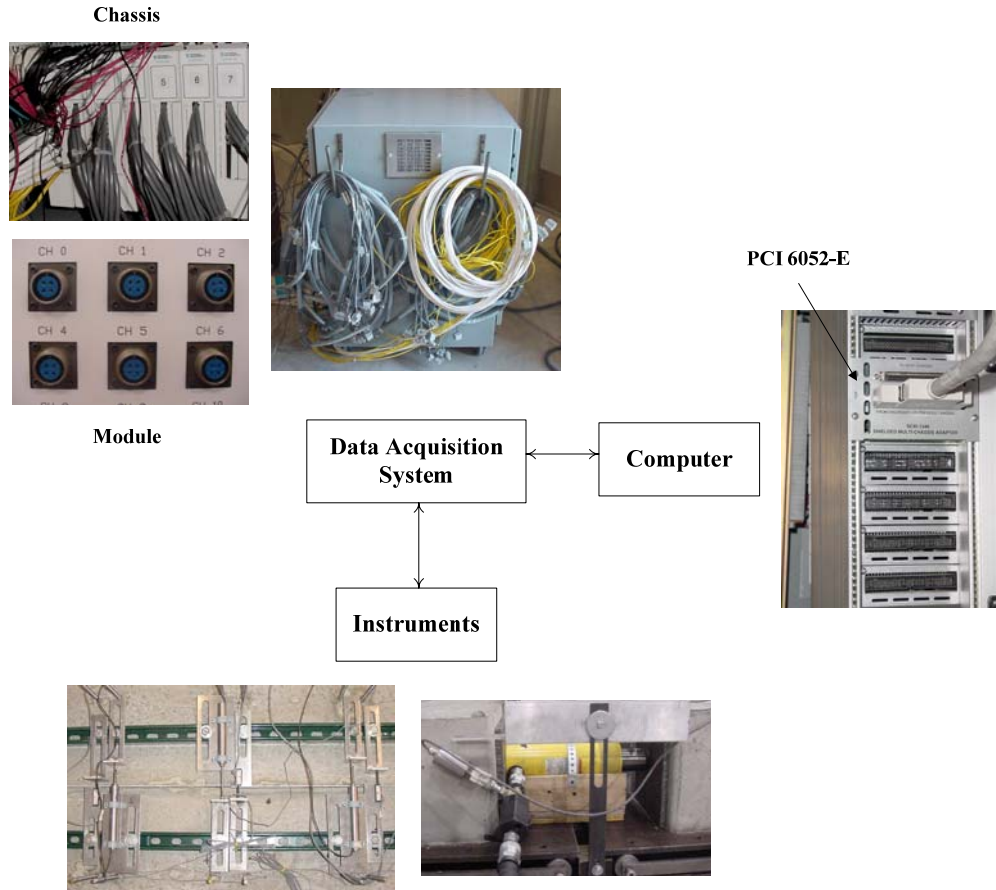


Figure A-18. Data Flow

The data acquisition system is designed to hold the chassis and provide access and power to each channel on the chassis. The chassis is the main unit which consists of all the channels of the data acquisition system. The chassis model is a SCXI-1001. The chassis consists of a series of modules connected together to form a unit. A module consists of a series of channels which are used for certain instrument types. For instance, module 1 consists of the first 32 channels and modules 2-7 all consist of eight strain gage channels. The modules are cards (SCXI-1102B or SCXI-1520) which can be individually removed from the chassis. Module 1 is a NI DAQ card termed SCXI-1102B and is the only module used in the pullout tests. Out of the 32 channels, channels 0-15 are three-wire connections, 16-25 are thermocouple connections, and channels 26-31 are four-wire

connections. The three wire connections accommodate the sliders and the pressure transducers (Channels 0-15) while the four wire connections (Channels 26-31) accommodate the LVDTs. External power supplies are linked to the data acquisition system to provide the necessary excitation voltages for the different instruments.

The calibration files corresponding to the different instrumentation are fed into the computer. The instruments are connected to the different channels on the data acquisition system using connectors and wires. As shown in Figure A-18, the connection between the computer and the data acquisition system is established using a cable and the Analog-Digital card PCI 6052-E present in the computer. Measurement and automation explorer (MAX) is a DAQ program set up by National Instruments and is responsible for the configuring the computer to read the DAQ. This data is then converted to the corresponding measurement units by the software interface (Little General Version 6.1) using the calibration files mentioned earlier. Little General run off the configuration of MAX.

APPENDIX B
MISALIGNMENT CHECK - SURVEYING SUMMARY

Table B-1. Misalignment Check Summary – One Dowel Tests

Type	Misalign- ment, in.	Misalignment through surveying, in.		Actual Misalignment, in.		Absolute Error, in.		Error, in.	
		West	East	West	East	West	East	West Side	East Side
Straight	0	5.074	5.028	5.00	5.00	0.074	0.028	>1/16 and <1/8	<1/16
		5.012	5.083	5.00	5.00	0.012	0.083	<1/16	>1/16 and <1/8
		5.028	5.022	5.00	5.00	0.028	0.022	<1/16	<1/16
V	0.25	5.168	4.804	5.25	4.75	0.082	0.054	>1/16 and <1/8	<1/16
	0.5	5.520	4.443	5.50	4.50	0.020	0.057	<1/16	<1/16
	0.75	5.816	4.312	5.75	4.25	0.066	0.062	>1/16 and <1/8	<1/16
	1	5.922	4.099	6.00	4.00	0.078	0.099	>1/16 and <1/8	>1/16 and <1/8
	2	7.046	3.062	7.00	3.00	0.046	0.062	<1/16	<1/16
H	0.25	4.983	5.105	5.00	5.00	0.017	0.105	<1/16	>1/16 and <1/8
	0.5	5.069	5.095	5.00	5.00	0.069	0.095	>1/16 and <1/8	>1/16 and <1/8
	0.75	5.100	5.082	5.00	5.00	0.100	0.082	>1/16 and <1/8	>1/16 and <1/8
	1	4.926	5.122	5.00	5.00	0.074	0.122	>1/16 and <1/8	>1/16 and <1/8
	2	4.979	4.974	5.00	5.00	0.021	0.026	<1/16	<1/16
C	0.25	5.333	4.780	5.25	4.75	0.083	0.030	>1/16 and <1/8	<1/16
	0.5	5.593	4.549	5.50	4.50	0.093	0.049	>1/16 and <1/8	<1/16
	0.75	5.821	4.237	5.75	4.25	0.071	0.013	>1/16 and <1/8	<1/16
	1	6.044	3.981	6.00	4.00	0.044	0.019	<1/16	<1/16

Table B-2. Misalignment Check Summary – Two Dowel Tests (North Dowel)

Type	Misalignment, in.	Misalignment through surveying, in.		Actual Misalignment, in.		Absolute Error, in.		Error, in.	
		West	East	West	East	West	East	West	East
Straight	0	5.042	5.068	5.000	5.000	0.042	0.068	<1/16	>1/16 and <1/8
V	0.25	5.300	4.825	5.500	4.500	0.200	0.325	>1/16 and <1/8	>1/16 and <1/8
	0.5	5.599	4.580	5.500	4.500	0.099	0.080	>1/16 and <1/8	>1/16 and <1/8
	0.75	5.779	4.244	5.750	4.25	0.029	0.006	<1/16	<1/16
	1	6.027	4.042	6	4	0.027	0.042	<1/16	<1/16
	0.5_U	5.586	4.554	5.500	4.500	0.086	0.054	>1/16 and <1/8	<1/16
	1_U	6.070	4.217	6.0	4.0	0.070	0.217	>1/16 and <1/8	>1/16 and <1/8
H	0.25	5.080	4.972	5	5	0.080	0.028	>1/16 and <1/8	<1/16
	0.5	5.069	5.065	5.000	5.000	0.069	0.065	>1/16 and <1/8	>1/16 and <1/8
	0.75	5.045	5.049	5	5	0.045	0.049	<1/16	<1/16
	1	5.049	5.036	5	5	0.049	0.036	<1/16	<1/16
	0.5_U	5.030	5.037	5.000	5.000	0.030	0.037	<1/16	<1/16
	1_U	4.959	5.049	5.0	5.0	0.041	0.049	<1/16	<1/16
C	0.25	5.308	4.808	5.500	4.500	0.192	0.308	>1/16 and <1/8	>1/16 and <1/8
	0.5	5.567	4.552	5.500	4.500	0.067	0.052	>1/16 and <1/8	<1/16
	0.75	5.797	4.261	5.750	4.250	0.047	0.011	<1/16	<1/16
	1	6.057	3.959	6.0	4.0	0.057	0.041	<1/16	<1/16
	0.5_U	5.576	4.583	5.500	4.500	0.076	0.083	>1/16 and <1/8	>1/16 and <1/8
	1_U	5.930	4.066	6.0	4.0	0.070	0.066	>1/16 and <1/8	>1/16 and <1/8
V	0,0.5	5.115	5.055	5.000	5.000	0.115	0.055	>1/16 and <1/8	<1/16
	0,0.75	5.069	5.064	5.000	5.000	0.069	0.064	>1/16 and <1/8	>1/16 and <1/8
H	0,0.5	5.070	5.050	5	5	0.070	0.050	>1/16 and <1/8	<1/16
	0,0.75	5.021	5.063	5.000	5.000	0.021	0.063	<1/16	>1/16 and <1/8
C	0,0.5	4.997	5.043	5.000	5.000	0.003	0.043	<1/16	<1/16
	0,0.75	5.047	5.057	5.000	5.000	0.047	0.057	<1/16	<1/16

Table B-3. Misalignment Check Summary – Two Dowel Tests (South Dowel)

Type	Misalign- ment, in.	Misalignment through surveying, in.		Actual Misalignment, in.		Absolute Error, in.		Error, in.	
		West	East	West	East	West	East	West	East
Straight	0	5.057	5.076	5.000	5.000	0.057	0.076	<1/16	>1/16 and <1/8
V	0.25	4.766	5.291	4.500	5.500	0.266	0.209	>1/16 and <1/8	>1/16 and <1/8
	0.5	4.430	5.547	4.500	5.500	0.070	0.047	>1/16 and <1/8	<1/16
	0.75	4.298	5.783	4.250	5.750	0.048	0.033	<1/16	<1/16
	1	4.074	6.066	4	6	0.074	0.066	>1/16 and <1/8	>1/16 and <1/8
	0.5_U	5.591	4.558	4.500	5.500	1.091	0.942	>1/16 and <1/8	>1/16 and <1/8
	1_U	6.078	4.208	6.0	4.0	0.078	0.208	>1/16 and <1/8	>1/16 and <1/8
H	0.25	5.031	4.903	5	5	0.031	0.097	<1/16	>1/16 and <1/8
	0.5	5.087	5.023	5.000	5.000	0.087	0.023	>1/16 and <1/8	<1/16
	0.75	5.095	5.025	5	5	0.095	0.025	>1/16 and <1/8	<1/16
	1	5.044	5.077	5	5	0.044	0.077	<1/16	>1/16 and <1/8
	0.5_U	5.084	5.111	4.500	5.500	0.584	0.389	>1/16 and <1/8	>1/16 and <1/8
	1_U	4.960	5.057	5.0	5.0	0.040	0.057	<1/16	<1/16
C	0.25	4.801	5.308	4.5	5.5	0.301	0.192	>1/16 and <1/8	>1/16 and <1/8
	0.5	4.600	5.534	4.500	5.500	0.100	0.034	>1/16 and <1/8	<1/16
	0.75	4.295	5.737	4.250	5.750	0.045	0.013	<1/16	<1/16
	1	4.030	5.964	4.0	6.0	0.030	0.036	<1/16	<1/16
	0.5_U	5.619	4.588	4.500	5.500	1.119	0.912	>1/16 and <1/8	>1/16 and <1/8
	1_U	5.961	3.999	6.0	4.0	0.039	0.001	<1/16	<1/16
V	0,0.5	4.581	5.548	4.500	5.500	0.081	0.048	>1/16 and <1/8	<1/16
	0,0.75	4.305	5.837	4.250	5.750	0.055	0.087	<1/16	>1/16 and <1/8
H	0,0.5	5.025	5.009	5	5	0.025	0.009	<1/16	<1/16
	0,0.75	4.935	4.959	5.000	5.000	0.065	0.041	>1/16 and <1/8	<1/16
C	0,0.5	4.589	5.472	4.500	5.500	0.089	0.028	>1/16 and <1/8	<1/16
	0,0.75	4.293	5.797	4.250	5.750	0.043	0.047	<1/16	<1/16

Table B-4. Misalignment Check Summary – Three and Five Dowel Tests

Type	Dowels Misaligned	Misalignment, in.	Misalignment through surveying, in.		Actual Misalignment, in.		Absolute Error, in.		Error, in.	
			West	East	West	East	West	East	West	East
3C	All	0.5	5.491	4.575	5.5	4.5	0.009	0.075	<1/16	>1/16 and <1/8
			4.589	5.489	4.5	5.5	0.089	0.011	>1/16 and <1/8	<1/16
			5.509	4.585	5.5	4.5	0.009	0.085	<1/16	>1/16 and <1/8
3H	All		4.988	5.075	5	5	0.012	0.075	<1/16	>1/16 and <1/8
			5.056	5.063	5	5	0.056	0.063	<1/16	>1/16 and <1/8
			4.993	5.082	5	5	0.007	0.082	<1/16	>1/16 and <1/8
3V	All		5.591	4.577	5.5	4.5	0.091	0.077	>1/16 and <1/8	>1/16 and <1/8
			4.575	5.490	4.5	5.5	0.075	0.010	>1/16 and <1/8	<1/16
			5.559	4.569	5.5	4.5	0.059	0.069	<1/16	>1/16 and <1/8
5C	Outer & Center	0.5	5.391	4.596	5.5	4.5	0.109	0.096	>1/16 and <1/8	>1/16 and <1/8
		0	4.898	5.025	5	5	0.102	0.025	>1/16 and <1/8	<1/16
		0.5	4.416	5.574	4.5	5.5	0.084	0.074	>1/16 and <1/8	>1/16 and <1/8
		0	4.976	5.059	5	5	0.024	0.059	<1/16	<1/16
		0.5	5.393	4.568	5.5	4.5	0.107	0.068	>1/16 and <1/8	>1/16 and <1/8
5H	Outer & Center	0.5	5.079	-	5	-	0.079	-	>1/16 and <1/8	-
		0	5.045	-	5	-	0.045	-	<1/16	-
		0.5	4.926	-	5	-	0.074	-	>1/16 and <1/8	-
		0	5.106	-	5	-	0.106	-	>1/16 and <1/8	-
		0.5	4.959	-	5	-	0.041	-	<1/16	-
5H	All	0.5	5.153	5.033	5.000	5.000	0.153	0.033	>1/16 and <1/8	<1/16
		0.5	5.020	5.042	5.000	5.000	0.020	0.042	<1/16	<1/16
		0.5	4.949	5.110	5.000	5.000	0.051	0.110	<1/16	>1/16 and <1/8
		0.5	5.009	5.105	5.000	5.000	0.009	0.105	<1/16	>1/16 and <1/8
		0.5	5.047	5.106	5.000	5.000	0.047	0.106	<1/16	>1/16 and <1/8
5V	Outer & Center	0.5	5.447	4.596	5.5	4.5	0.053	0.096	<1/16	>1/16 and <1/8
		0	5.038	4.993	5	5	0.038	0.007	<1/16	<1/16
		0.5	4.549	5.465	4.5	5.5	0.049	0.035	<1/16	<1/16
		0	4.930	5.018	5	5	0.070	0.018	>1/16 and <1/8	<1/16
		0.5	5.561	4.503	5.5	4.5	0.061	0.003	<1/16	<1/16

Table B-5. Horizontal Misalignment Summary – One Dowel Tests

Type	Misalign- ment, in.	Distance through surveying, in.		Actual Distance, in.		Absolute Error, in.		Error, in.	
		West	East	West	East	West	East	West	East
H	0.25	0.270	0.244	0.250	0.250	0.020	0.006	<1/16	<1/16
	0.5	0.527	0.517	0.500	0.500	0.027	0.017	<1/16	<1/16
	0.75	0.778	0.783	0.750	0.750	0.028	0.033	<1/16	<1/16
	1	1.133	1.031	1.000	1.000	0.133	0.031	>1/16 and <1/8	<1/16
	2	2.083	2.032	2.000	2.000	0.083	0.032	>1/16 and <1/8	<1/16
C	0.25	0.252	0.316	0.250	0.250	0.002	0.066	<1/16	>1/16 and <1/8
	0.5	0.448	0.475	0.500	0.500	0.052	0.025	<1/16	<1/16
	0.75_old	0.839	0.739	0.750	0.750	0.089	0.011	>1/16 and <1/8	<1/16
	0.75	0.752	0.778	0.750	0.750	0.002	0.028	<1/16	<1/16
	1	0.955	1.041	1.000	1.000	0.045	0.041	<1/16	<1/16

Table B-6. Horizontal Misalignment Summary – Two Dowel Tests (North Dowel)

Type	Misalign- ment, in.	Distance through surveying, in.		Actual Distance, in.		Absolute Error, in.		Error, in.	
		West	East	West	East	West	East	West	East
H	0.25	0.287	0.345	0.25	0.25	0.037	0.095	<1/16	>1/16 and <1/8
	0.5	0.520	0.500	0.500	0.500	0.020	0.000	<1/16	<1/16
	0.75	0.786	0.803	0.750	0.750	0.036	0.053	<1/16	<1/16
	1	0.998	0.976	1.000	1.000	0.002	0.024	<1/16	<1/16
	0.5_U	0.513	0.514	0.5	0.5	0.013	0.014	<1/16	<1/16
	1_U	1.093	1.031	1.000	1.000	0.093	0.031	>1/16 and <1/8	<1/16
C	0.25	0.276	0.276	0.250	0.250	0.026	0.026	<1/16	<1/16
	0.5	0.551	0.525	0.5	0.5	0.051	0.025	<1/16	<1/16
	0.75	0.754	0.763	0.750	0.750	0.004	0.013	<1/16	<1/16
	1	1.097	1.092	1.000	1.000	0.097	0.092	>1/16 and <1/8	>1/16 and <1/8
	0.5_U	0.552	0.479	0.5	0.5	0.052	0.021	<1/16	<1/16
	1_U	1.010	1.047	1.000	1.000	0.010	0.047	<1/16	<1/16

Table B-7. Horizontal Misalignment Summary – Two Dowel Tests (South Dowel)

Type	Misalign- ment, in.	Distance through surveying, in.		Actual Distance, in.		Absolute Error, in.		Error, in.	
		West	East	West	East	West	East	West	East
H	0.25	0.344	0.342	0.25	0.25	0.094	0.092	>1/16 and <1/8	>1/16 and <1/8
	0.5	0.486	0.505	0.500	0.500	0.014	0.005	<1/16	<1/16
	0.75	0.786	0.798	0.750	0.750	0.036	0.048	<1/16	<1/16
	1	0.983	0.961	1.000	1.000	0.017	0.039	<1/16	<1/16
	0.5_U	0.514	0.541	0.5	0.5	0.014	0.041	<1/16	<1/16
	1_U	1.021	1.021	1.000	1.000	0.021	0.021	<1/16	<1/16
C	0.25	0.259	0.277	0.250	0.250	0.009	0.027	<1/16	<1/16
	0.5	0.511	0.437	0.5	0.5	0.011	0.063	<1/16	>1/16 and <1/8
	0.75	0.762	0.736	0.750	0.750	0.012	0.014	<1/16	<1/16
	1	0.958	0.980	1.000	1.000	0.042	0.020	<1/16	<1/16
	0.5_U	0.513	0.514	0.5	0.5	0.013	0.014	<1/16	<1/16
	1_U	1.014	1.012	1.000	1.000	0.014	0.012	<1/16	<1/16
H	0.5	0.513	0.458	0.5	0.5	0.013	0.042	<1/16	<1/16
	0.75	0.693	0.762	0.750	0.750	0.057	0.012	<1/16	<1/16
C	0.5	0.473	0.477	0.5	0.5	0.027	0.023	<1/16	<1/16
	0.75	0.750	0.731	0.750	0.750	0.000	0.019	<1/16	<1/16

Table B-8. Horizontal Misalignment Summary – Three and Five Dowel Tests

Type	Dowels Misaligned	Misalignment, in.	Distance through surveying, in.		Actual Distance, in.		Absolute Error, in.		Error, in.	
			West	East	West	East	West	East	West	East
3C	All	0.5	0.517	0.526	0.5	0.5	0.017	0.026	<1/16	<1/16
		0.5	0.510	0.512	0.5	0.5	0.010	0.012	<1/16	<1/16
		0.5	0.515	0.416	0.5	0.5	0.015	0.084	<1/16	>1/16 and <1/8
3H	All	0.5	0.503	0.549	0.5	0.5	0.003	0.049	<1/16	<1/16
		0.5	0.501	0.510	0.5	0.5	0.001	0.010	<1/16	<1/16
		0.5	0.502	0.500	0.5	0.5	0.002	0.000	<1/16	<1/16
5C	Outer & Center	0.5	0.399	0.531	0.5	0.5	0.101	0.031	>1/16 and <1/8	<1/16
		0.5	-	-	-	-	-	-	-	-
		0.5	0.495	0.538	0.5	0.5	0.005	0.038	<1/16	<1/16
		0.5	-	-	-	-	-	-	-	-
		0.5	0.509	0.545	0.5	0.5	0.009	0.045	<1/16	<1/16
5H	All	0.5	0.513	0.482	0.5	0.5	0.013	0.018	<1/16	<1/16
		0.5	0.500	0.482	0.5	0.5	0.000	0.018	<1/16	<1/16
		0.5	0.499	0.540	0.5	0.5	0.001	0.040	<1/16	<1/16
		0.5	0.457	0.474	0.5	0.5	0.043	0.026	<1/16	<1/16
		0.5	0.515	0.514	0.5	0.5	0.015	0.014	<1/16	<1/16
5H	Outer & Center	0.5	0.473		0.5		0.027		<1/16	<1/16
		0.5	-	-	-	-	-	-	-	-
		0.5	0.489		0.5		0.011	0	<1/16	<1/16
		0.5	-	-	-	-	-	-	-	-
		0.5	0.507		0.5		0.007		<1/16	<1/16

APPENDIX C
RESULTS OF 3D FINITE ELEMENT MODELS

Results of 1A Finite element model

The dowel-concrete friction coefficients and material properties used in the analysis are shown in table C1. A comparison of the pullout force per bar (lbs.) vs. the joint opening (in.) is shown in figure C1. A summary of the various material failure / damage limit states is presented in Table C2.

Table C-1: Dowel-Concrete Friction Coefficients; Material Properties used and limit states obtained from the analysis.

	μ_g	μ_w	f'_c (psi)	f'_t (psi)
Case I	0.0	0.30	3500.0	236.64
Case II	0.074	0.384	2544.0	540.0

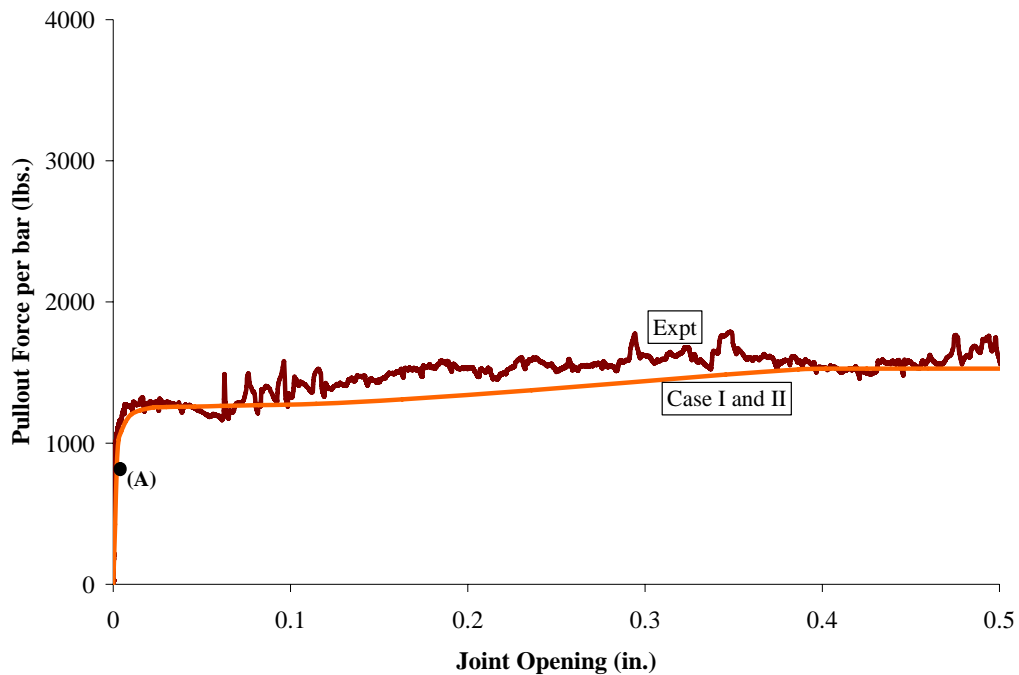


Figure C-1: Comparison of the FEM model with the experimental data for 1A specimen

Table C-2: Summary of Material Failure / Damage Limit States from the analysis

Material Damage / Limit States	Joint Opening (in.)		Pullout Load (lbs)	
	(I)	(II)	(I)	(II)
(A)	0.003	0.003	1020.0	1020.0
(B)	-	-	-	-
(C)	-	-	-	-
(D)	-	-	-	-
(E)	-	-	-	-
(F)	-	-	-	-

Results of 1V18 Finite Element Model

The dowel-concrete friction coefficients and material properties used in the analysis are shown in table C3. A comparison of the pullout force per bar (lbs.) vs. the joint opening (in.) is shown in figure C2. A summary of the various material failure / damage limit states is presented in table C4.

Table C-3: Dowel-Concrete Friction Coefficients; Material Properties used and limit states obtained from the analysis.

	μ_g	μ_w	f'_c (psi)	f'_t (psi)
Case I	0.0	0.30	3500.0	236.64
Case II	0.074	0.384	2544.0	540.0

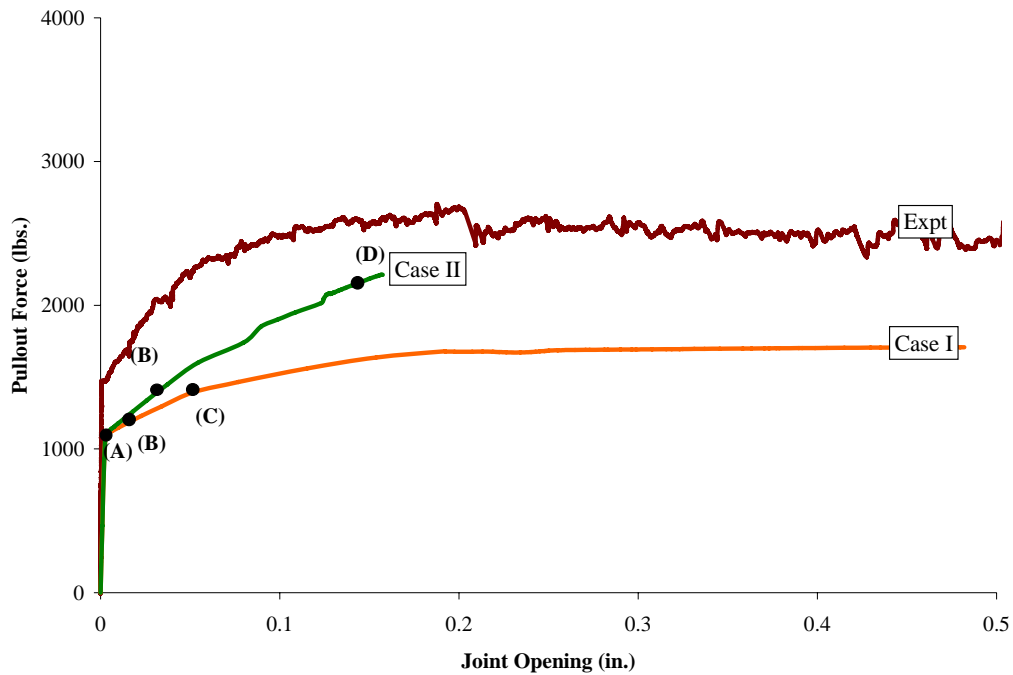


Figure C-2: Comparison of the FEM model with the experimental data for 1V18 specimen

Table C-4: Summary of Material Failure / Damage Limit States from the analysis

Material Damage / Limit States	Joint Opening (in.)		Pullout Load (lbs)	
	(I)	(II)	(I)	(II)
(A)	0.003	0.003	1100.0	1100.0
(B)	0.015	0.038	1180.0	1450
(C)	0.115	-	1560.0	-
(D)	-	0.148	-	2170
(E)	-	-	-	-
(F)	-	-	-	-

Results of 1V36 Finite Element Model

The dowel-concrete friction coefficients and material properties used in the analysis are shown in table C5. A comparison of the pullout force per bar (lbs.) vs. the joint opening (in.) is shown in figure C3. A summary of the various material failure / damage limit states is presented in table C6.

Table C-5: Dowel-Concrete Friction Coefficients; Material Properties used and limit states obtained from the analysis.

	μ_g	μ_w	f'_c (psi)	f'_t (psi)
Case I	0.0	0.30	3500.0	236.64
Case II	0.074	0.384	3328.0	240.0

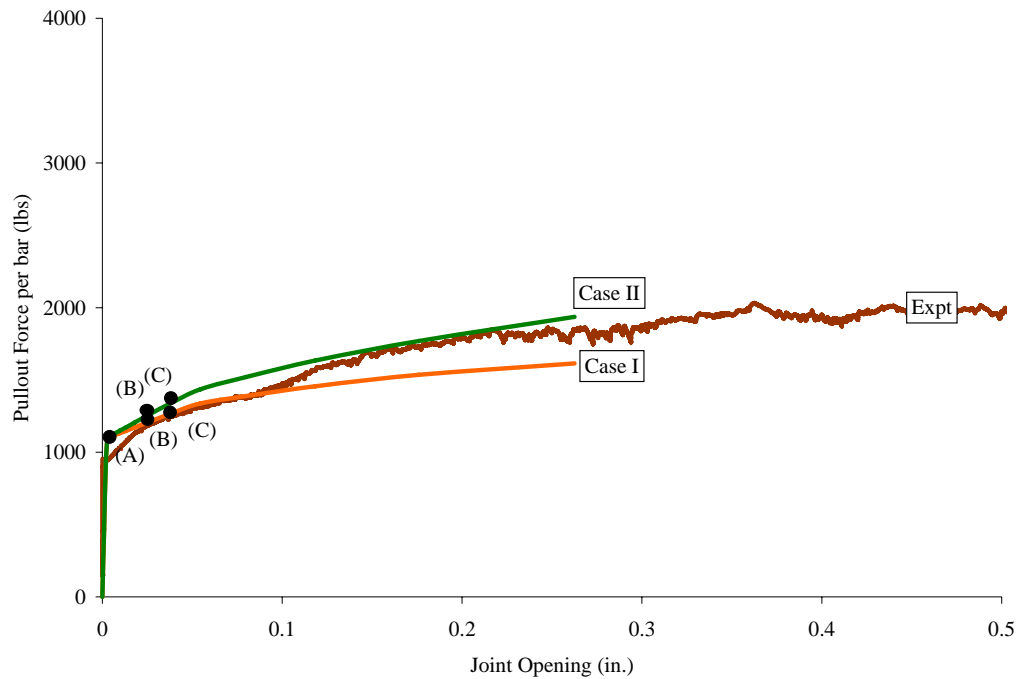


Figure C-3: Comparison of the FEM model with the experimental data for 1V36 specimen

Table C-6: Summary of Material Failure / Damage Limit States from the analysis

Material Damage / Limit States	Joint Opening (in.)		Pullout Load (lbs)	
	(I)	(II)	(I)	(II)
(A)	0.003	0.003	1100.0	1100.0
(B)	0.026	0.026	1210.0	1260.0
(C)	0.037	0.037	1260.0	1330.0
(D)	-	-	-	-
(E)	-	-	-	-
(F)	-	-	-	-

Results of 1V72 Finite Element Model

The dowel-concrete friction coefficients and material properties used in the analysis are shown in table C7. A comparison of the pullout force per bar (lbs.) vs. the joint opening (in.) is shown in figure C4. A summary of the various material failure / damage limit states is presented in table C8.

Table C-7: Dowel-Concrete Friction Coefficients; Material Properties used and limit states obtained from the analysis.

	μ_g	μ_w	f'_c (psi)	f'_t (psi)
Case I	0.0	0.30	3500.0	236.64
Case II	0.074	0.384	3500.0	236.64

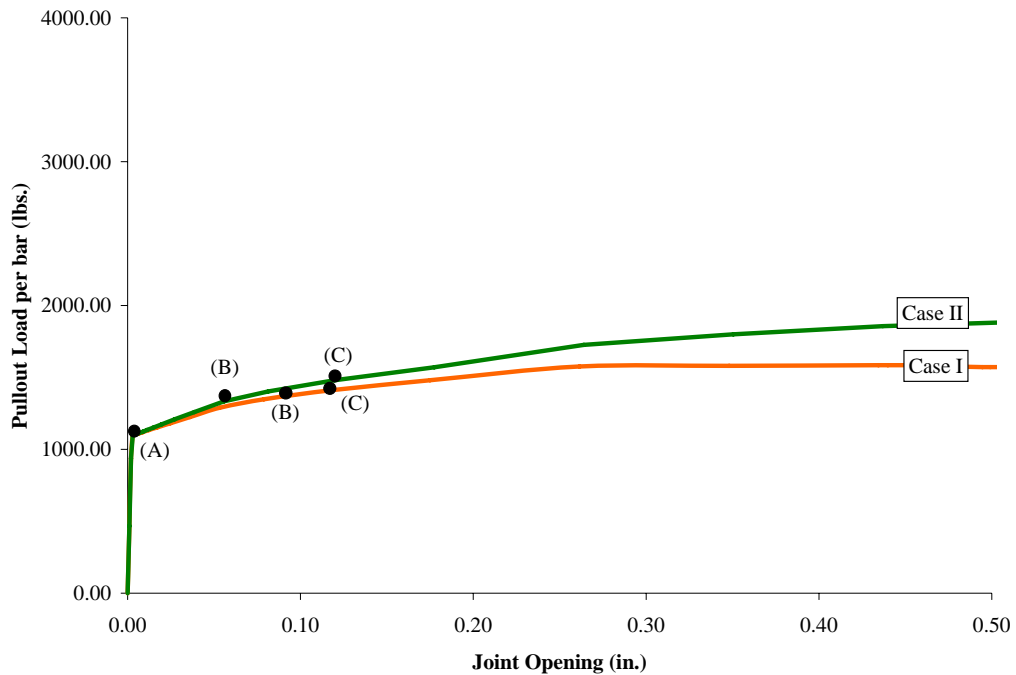


Figure C-4: Comparison of the FEM model with the experimental data for 1V72 specimen

Table C-8: Summary of Material Failure / Damage Limit States from the analysis

Material Damage / Limit States	Joint Opening (in.)		Pullout Load (lbs)	
	(I)	(II)	(I)	(II)
(A)	0.003	0.003	1100.0	1100.0
(B)	0.079	0.056	1350.0	1130.0
(C)	0.117	0.119	1410.0	1570.0
(D)	-	-	-	-
(E)	-	-	-	-
(F)	-	-	-	-

Results of 1H18 Finite Element Model

The dowel-concrete friction coefficients and material properties used in the analysis are shown in table C9. A comparison of the pullout force per bar (lbs.) vs. the joint opening (in.) is shown in figure C5. A summary of the various material failure / damage limit states is presented in table C10.

Table C-9: Dowel-Concrete Friction Coefficients; Material Properties used and limit states obtained from the analysis.

	μ_g	μ_w	f'_c (psi)	f'_t (psi)
Case I	0.0	0.30	3500.0	236.64
Case II	0.074	0.384	4142.0	440.0

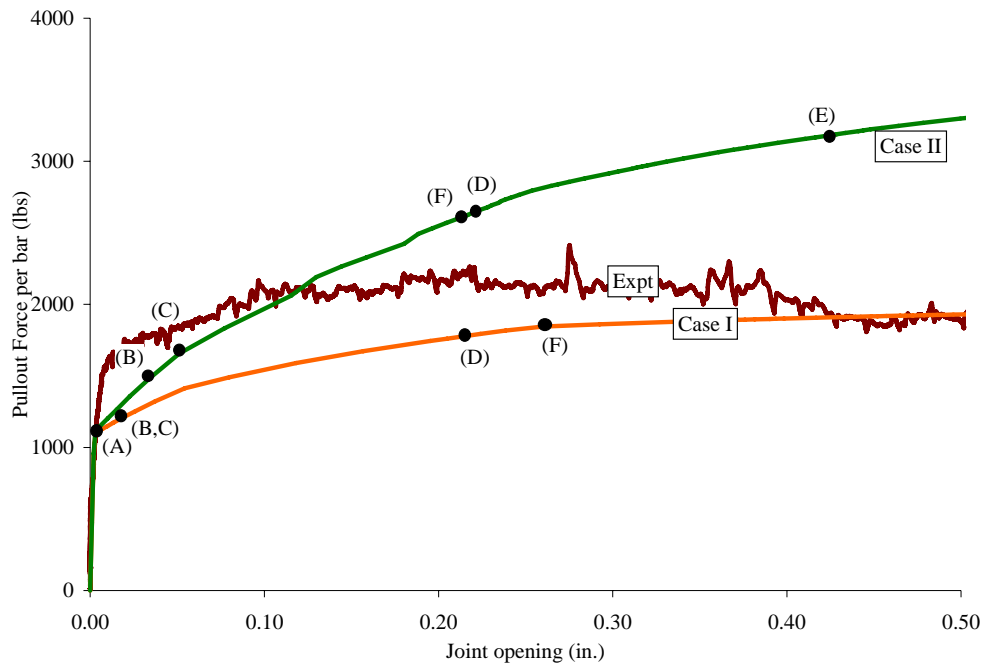


Figure C-5: Comparison of the FEM model with the experimental data for 1H18 specimen

Table C-10: Summary of Material Failure / Damage Limit States from the analysis

Material Damage / Limit States	Joint Opening (in.)		Pullout Load (lbs)	
	(I)	(II)	(I)	(II)
(A)	0.003	0.003	1100.0	1120.0
(B)	0.018	0.034	1200.0	1480.0
(C)	0.018	0.051	1200.0	1660.0
(D)	0.214	0.228	1780.0	2680.0
(E)	0.535	0.425	1940.0	3180.0
(F)	0.260	0.217	1840.0	2620.0

Results of 1H36 Finite Element Model

The dowel-concrete friction coefficients and material properties used in the analysis are shown in table C11. A comparison of the pullout force per bar (lbs.) vs. the joint opening (in.) is shown in figure C6. A summary of the various material failure / damage limit states is presented in table C12.

Table C-11: Dowel-Concrete Friction Coefficients; Material Properties used and limit states obtained from the analysis.

	μ_g	μ_w	f'_c (psi)	f'_t (psi)
Case I	0.0	0.30	3500.0	236.64
Case II	0.074	0.384	3328.0	248.0

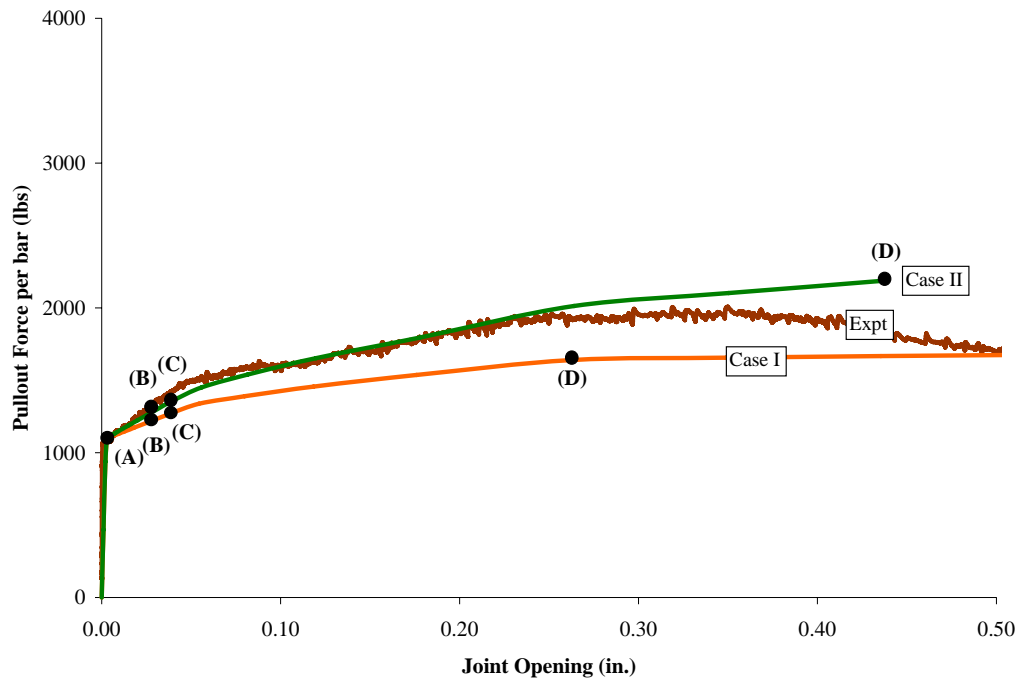


Figure C-6: Comparison of the FEM model with the experimental data for 1H36 specimen

Table C-12: Summary of Material Failure / Damage Limit States from the analysis

Material Damage / Limit States	Joint Opening (in.)		Pullout Load (lbs)	
	(I)	(II)	(I)	(II)
(A)	0.003	0.003	1100.0	1100.0
(B)	0.026	0.027	1210.0	1270.0
(C)	0.037	0.0387	1260.0	1350.0
(D)	0.349	0.4370	1660.0	2190.0
(E)	-	-	-	-
(F)	-	-	-	-

Results of 1H72 Finite Element Model

The dowel-concrete friction coefficients and material properties used in the analysis are shown in table C13. A comparison of the pullout force per bar (lbs.) vs. the joint opening (in.) is shown in figure C7. A summary of the various material failure / damage limit states is presented in table C14.

Table C-13: Dowel-Concrete Friction Coefficients; Material Properties used and limit states obtained from the analysis.

	μ_g	μ_w	f'_c (psi)	f'_t (psi)
Case I	0.0	0.30	3500.0	236.64
Case II	0.074	0.384	3500.0	236.64

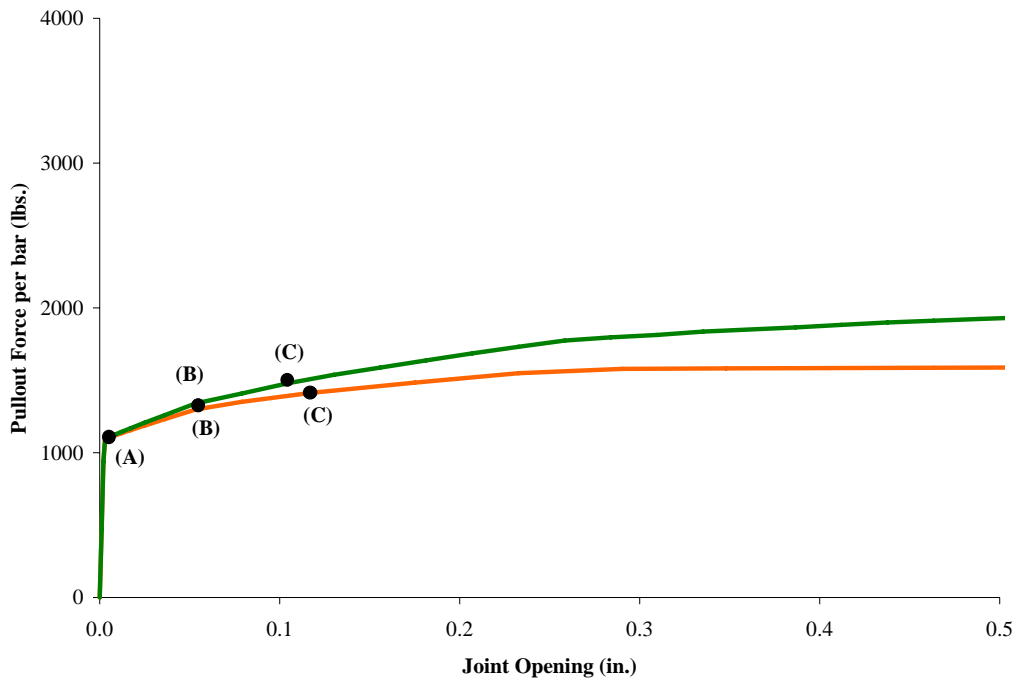


Figure C-7: Comparison of the FEM model with the experimental data for 1H72 specimen

Table C-14: Summary of Material Failure / Damage Limit States from the analysis

Material Damage / Limit States	Joint Opening (in.)		Pullout Load (lbs)	
	(I)	(II)	(I)	(II)
(A)	0.003	0.003	1100.0	1100.0
(B)	0.053	0.053	1300.0	1340.0
(C)	0.117	0.104	1410.0	1480.0
(D)	0.809	0.801	1600.0	2050.0
(E)	-	-	-	-
(F)	-	-	-	-

Results of 1C18 Finite Element Model

The dowel-concrete friction coefficients and material properties used in the analysis are shown in table C15. A comparison of the pullout force per bar (lbs.) vs. the joint opening (in.) is shown in figure C8. A summary of the various material failure / damage limit states is presented in table C16.

Table C-15: Dowel-Concrete Friction Coefficients; Material Properties used and limit states obtained from the analysis.

	μ_g	μ_w	f'_c (psi)	f'_t (psi)
Case I	0.0	0.30	3500.0	236.64
Case II	0.074	0.384	3530.0	355.0

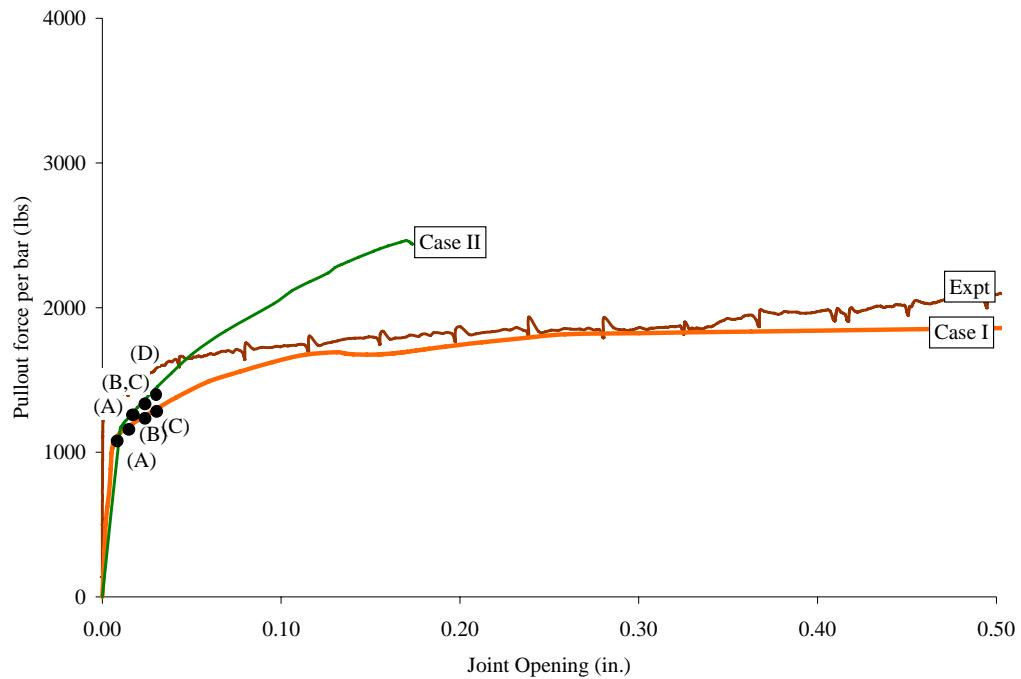


Figure C-8: Comparison of the FEM model with the experimental data for 1C18 specimen

Table C-16: Summary of Material Failure / Damage Limit States from the analysis

Material Damage / Limit States	Joint Opening (in.)		Pullout Load (lbs)	
	(I)	(II)	(I)	(II)
(A)	0.003	0.003	720.0	750.0
(B)	0.012	0.014	1160.0	1240.0
(C)	0.016	0.014	1190.0	1240.0
(D)	-	0.116	-	2180.0
(E)	-	0.126	-	2240.0
(F)	-	-	-	-

Results of 1C36 Finite Element Model

The dowel-concrete friction coefficients and material properties used in the analysis are shown in table C17. A comparison of the pullout force per bar (lbs.) vs. the joint opening (in.) is shown in figure C9. A summary of the various material failure / damage limit states is presented in table C18.

Table C-17: Dowel-Concrete Friction Coefficients; Material Properties used and limit states obtained from the analysis.

	μ_g	μ_w	f'_c (psi)	f'_t (psi)
Case I	0.0	0.30	3500.0	236.64
Case II	0.074	0.384	3328.0	240.0

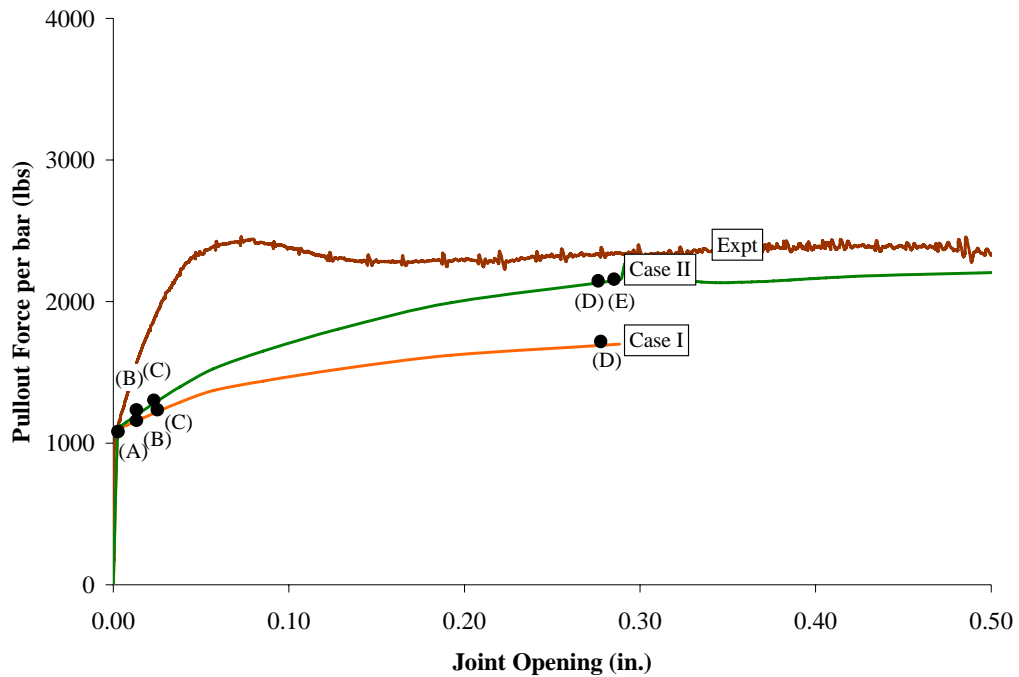


Figure C-9: Comparison of the FEM model with the experimental data for 1C36 specimen

Table C-18: Summary of Material Failure / Damage Limit States from the analysis

Material Damage / Limit States	Joint Opening (in.)		Pullout Load (lbs)	
	(I)	(II)	(I)	(II)
(A)	0.003	0.003	1100.0	1100.0
(B)	0.025	0.025	1220.0	1300.0
(C)	0.038	0.038	1290.0	1400.0
(D)	0.288	0.288	1700.0	2150.0
(E)	-	0.300	-	2220.0
(F)	-	-	-	-

Results of 2A Finite element model

The dowel-concrete friction coefficients and material properties used in the analysis are shown in table C19. A comparison of the pullout force per bar (lbs.) vs. the joint opening (in.) is shown in figure C10. A summary of the various material failure / damage limit states is presented in table C20.

Table C-19: Dowel-Concrete Friction Coefficients; Material Properties used and limit states obtained from the analysis.

	μ_g	μ_w	f'_c (psi)	f'_t (psi)
Case I	0.0	0.30	3500.0	236.64
Case II	0.074	0.384	3400.0	251.0

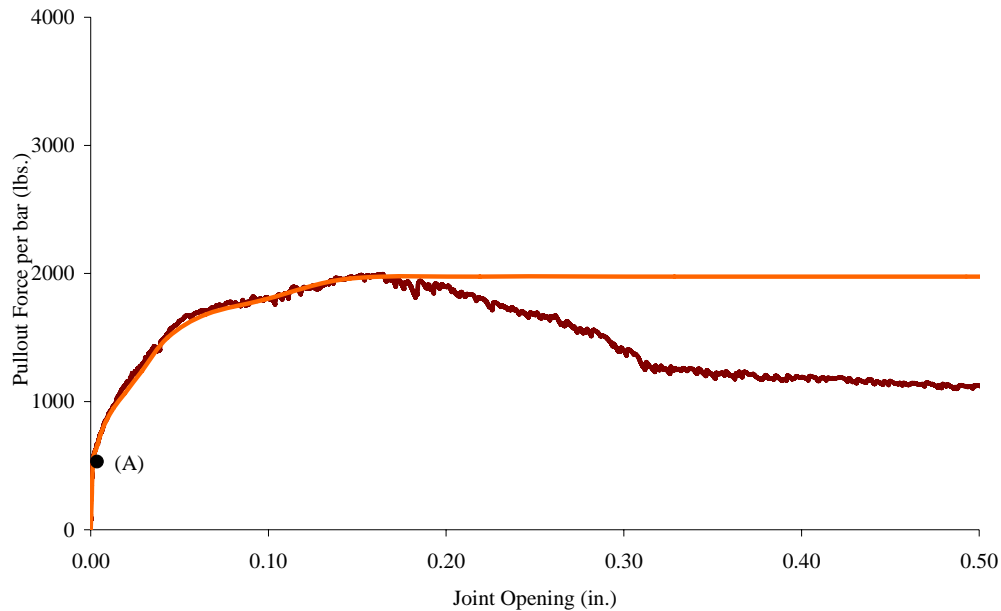


Figure C-10: Comparison of the FEM model with the experimental data for 2A specimen

Table C-20: Summary of Material Failure / Damage Limit States from the analysis

Material Damage / Limit States	Joint Opening (in.)		Pullout Load (lbs)	
	(I)	(II)	(I)	(II)
(A)	0.002	0.002	501.0	501.0
(B)	-	-	-	-
(C)	-	-	-	-
(D)	-	-	-	-
(E)	-	-	-	-
(F)	-	-	-	-

Results of 2V18NU Finite Element Model

The dowel-concrete friction coefficients and material properties used in the analysis are shown in table C21. A comparison of the pullout force per bar (lbs.) vs. the joint opening (in.) is shown in figure C11. A summary of the various material failure / damage limit states is presented in table C22.

Table C-21: Dowel-Concrete Friction Coefficients; Material Properties used and limit states obtained from the analysis.

	μ_g	μ_w	f'_c (psi)	f'_t (psi)
Case I	0.0	0.30	3500.0	236.64
Case II	0.074	0.384	4931.0	280.0

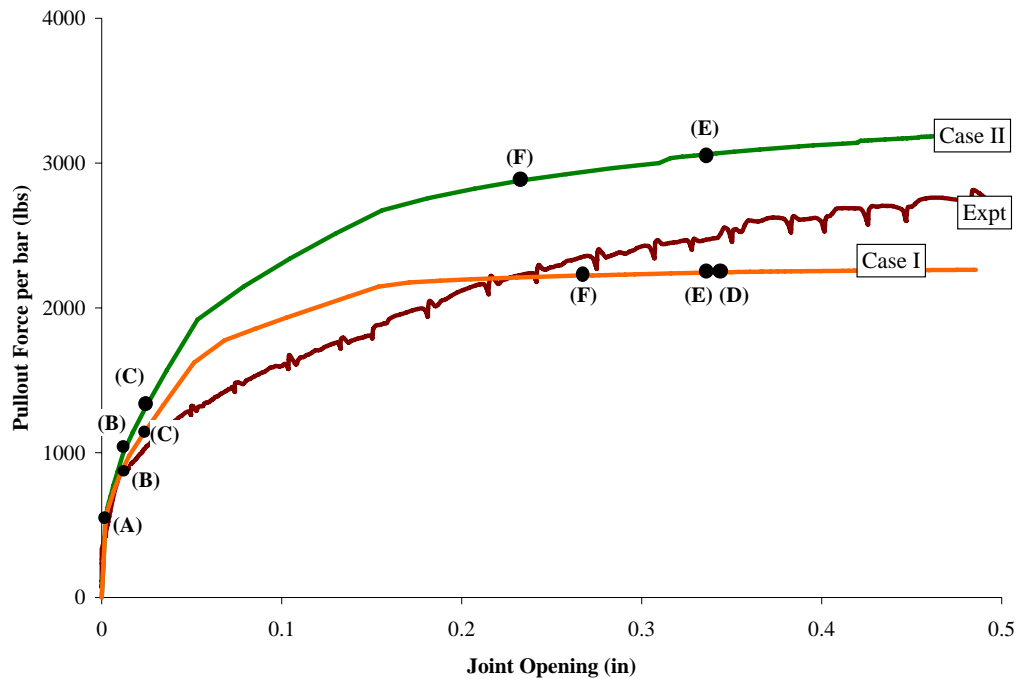


Figure C-11: Comparison of the FEM model with the experimental data for 2V18NU specimen

Table C-22: Summary of Material Failure / Damage Limit States from the analysis

Material Damage / Limit States	Joint Opening (in.)		Pullout Load (lbs)	
	(I)	(II)	(I)	(II)
(A)	0.002	0.002	513.00	525.92
(B)	0.010	0.021	846.00	1002.53
(C)	0.023	0.025	112.82	1321.06
(D)	0.339	0.552	2244.78	3247.22
(E)	0.337	0.335	2244.09	3059.84
(F)	0.269	0.233	2225.76	2880.03

Results of 2V18U Finite Element Model

The dowel-concrete friction coefficients and material properties used in the analysis are shown in table C23. A comparison of the pullout force per bar (lbs.) vs. the joint opening (in.) is shown in figure C12. A summary of the various material failure / damage limit states is presented in table C24.

Table C-23: Dowel-Concrete Friction Coefficients; Material Properties used and limit states obtained from the analysis.

	μ_g	μ_w	f'_c (psi)	f'_t (psi)
Case I	0.0	0.30	3500.0	236.64
Case II	0.074	0.384	3654.0	217.0

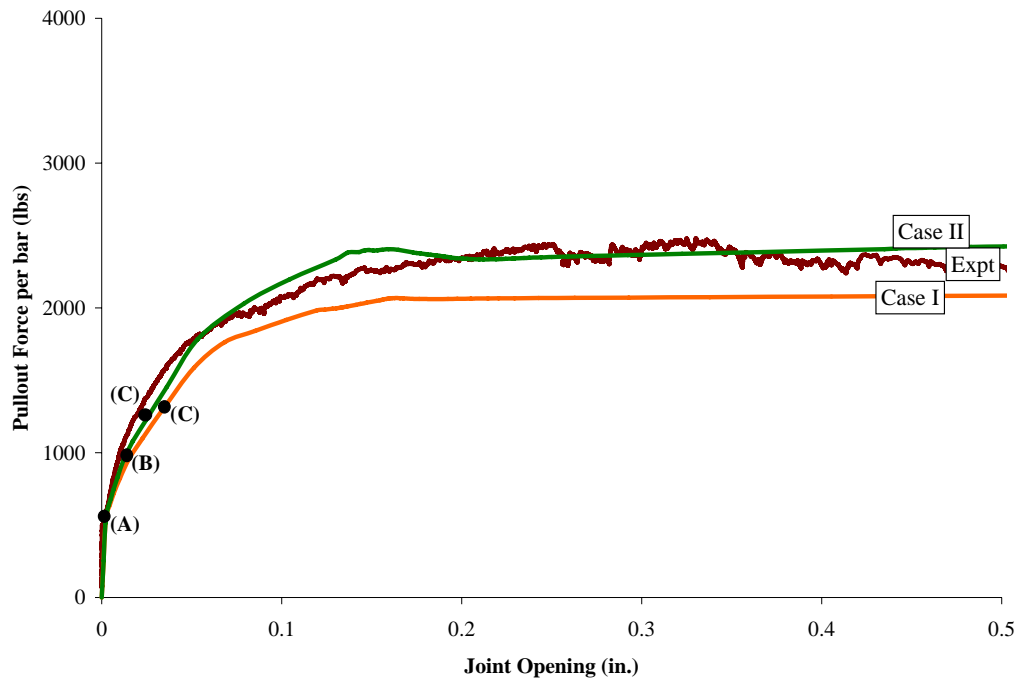


Figure C-12: Comparison of the FEM model with the experimental data for 2V18U specimen

Table C-24: Summary of Material Failure / Damage Limit States from the analysis

Material Damage / Limit States	Joint Opening (in.)		Pullout Load (lbs)	
	(I)	(II)	(I)	(II)
(A)	0.002	0.002	509.00	513.57
(B)	0.015	0.012	957.78	947.95
(C)	0.034	0.025	1302.88	1229.25
(D)	-	-	-	-
(E)	-	-	-	-
(F)	-	-	-	-

Results of 2V18AM Finite Element Model

The dowel-concrete friction coefficients and material properties used in the analysis are shown in table C25. A comparison of the pullout force per bar (lbs.) vs. the joint opening (in.) is shown in figure C13. A summary of the various material failure / damage limit states is presented in table C26.

Table C-25: Dowel-Concrete Friction Coefficients; Material Properties used and limit states obtained from the analysis.

	μ_g	μ_w	f'_c (psi)	f'_t (psi)
Case I	0.0	0.30	3500.0	236.64
Case II	0.074	0.384	3520.0	245.0

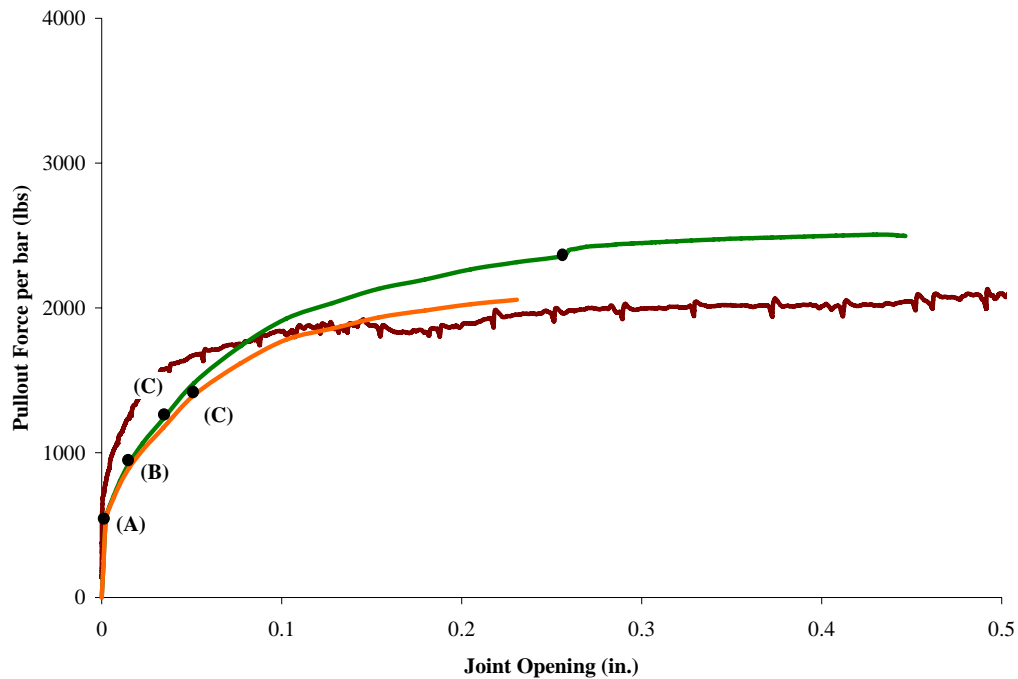


Figure C-13: Comparison of the FEM model with the experimental data for 2V18AM specimen

Table C-26: Summary of Material Failure / Damage Limit States from the analysis

Material Damage / Limit States	Joint Opening (in.)		Pullout Load (lbs)	
	(I)	(II)	(I)	(II)
(A)	0.002	0.002	505.34	507.34
(B)	0.015	0.015	893.57	925.84
(C)	0.051	0.034	1397.25	1232.84
(D)	-	-	-	-
(E)	-	-	-	-
(F)	-	-	-	-

Results of 2V36NU Finite Element Model

The dowel-concrete friction coefficients and material properties used in the analysis are shown in table C27. A comparison of the pullout force per bar (lbs.) vs. the joint opening (in.) is shown in figure C14. A summary of the various material failure / damage limit states is presented in table C28.

Table C-27: Dowel-Concrete Friction Coefficients; Material Properties used and limit states obtained from the analysis.

	μ_g	μ_w	f'_c (psi)	f'_t (psi)
Case I	0.0	0.30	3500.0	236.64
Case II	0.074	0.384	4931.0	280.0

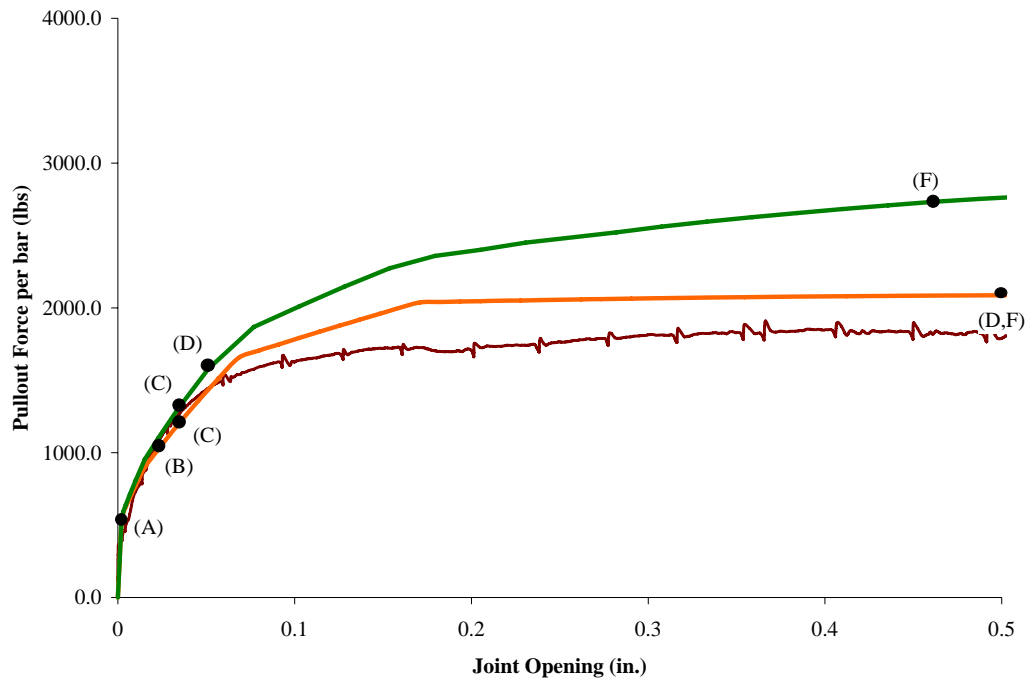


Figure C-14: Comparison of the FEM model with the experimental data for 2V36NU specimen

Table C-28: Summary of Material Failure / Damage Limit States from the analysis

Material Damage / Limit States	Joint Opening (in.)		Pullout Load (lbs)	
	(I)	(II)	(I)	(II)
(A)	0.002	0.002	504.5	512.48
(B)	0.023	0.023	1021.91	1100.62
(C)	0.034	0.034	1195.91	1306.52
(D)	0.498	0.721	2087.94	2875.67
(E)	0.623	0.577	2093.81	2808.90
(F)	0.498	0.461	2087.94	2733.14

Results of 2V36U Finite Element Model

The dowel-concrete friction coefficients and material properties used in the analysis are shown in table C29. A comparison of the pullout force per bar (lbs.) vs. the joint opening (in.) is shown in figure C15. A summary of the various material failure / damage limit states is presented in table C30.

Table C-29: Dowel-Concrete Friction Coefficients; Material Properties used and limit states obtained from the analysis.

	μ_g	μ_w	f'_c (psi)	f'_t (psi)
Case I	0.0	0.30	3500.0	236.64
Case II	0.074	0.384	3673.0	383.0

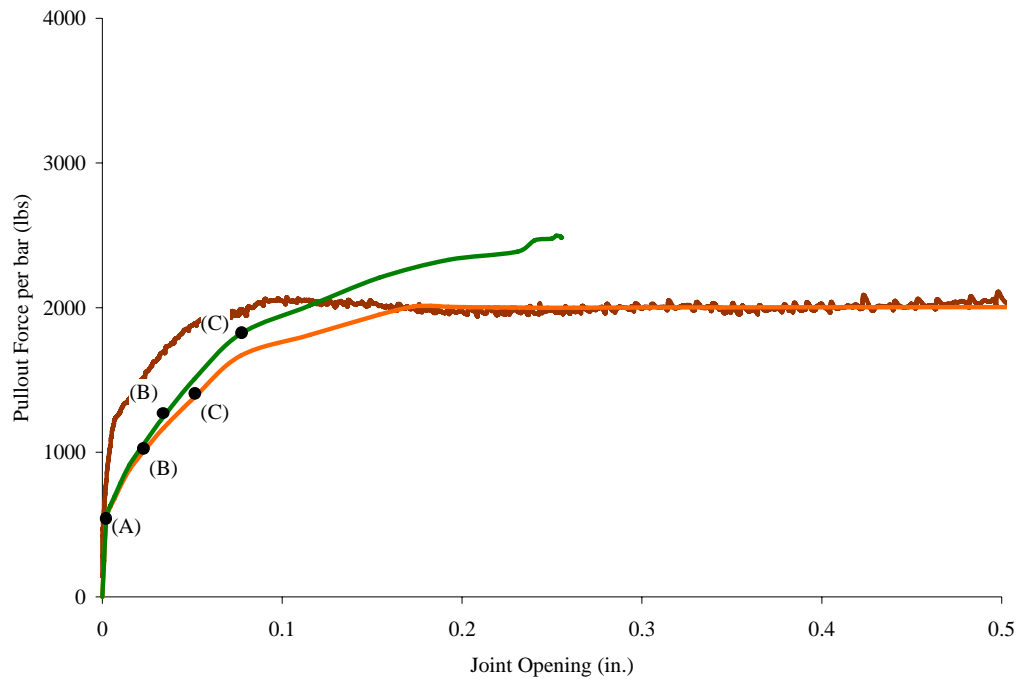


Figure C-15: Comparison of the FEM model with the experimental data for 2V36U specimen

Table C-30: Summary of Material Failure / Damage Limit States from the analysis

Material Damage / Limit States	Joint Opening (in.)		Pullout Load (lbs)	
	(I)	(II)	(I)	(II)
(A)	0.002	0.002	503.21	506.46
(B)	0.027	0.034	1003.51	1247.02
(C)	0.051	0.077	1379.87	1819.15
(D)	-	-	-	-
(E)	-	-	-	-
(F)	-	-	-	-

Results of 2V36AM Finite Element Model

The dowel-concrete friction coefficients and material properties used in the analysis are shown in table C31. A comparison of the pullout force per bar (lbs.) vs. the joint opening (in.) is shown in figure C16. A summary of the various material failure / damage limit states is presented in table C32.

Table C-31: Dowel-Concrete Friction Coefficients; Material Properties used and limit states obtained from the analysis.

	μ_g	μ_w	f'_c (psi)	f'_t (psi)
Case I	0.0	0.30	3500.0	236.64
Case II	0.074	0.384	3500.0	236.0

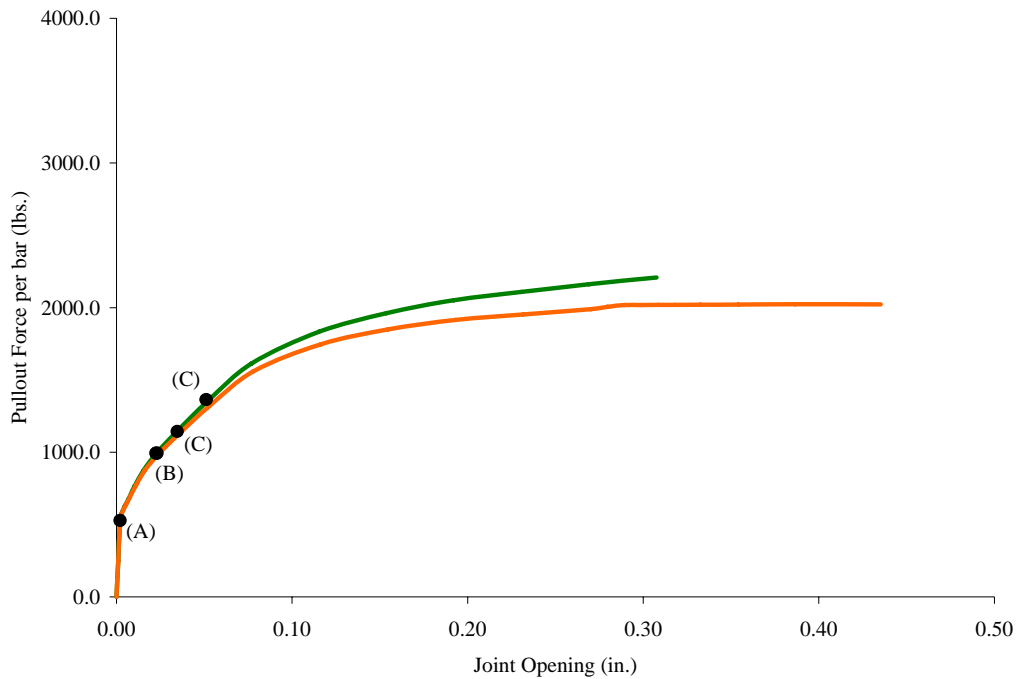


Figure C-16: Comparison of the FEM model with the experimental data for 2V36AM specimen

Table C-32: Summary of Material Failure / Damage Limit States from the analysis

Material Damage / Limit States	Joint Opening (in.)		Pullout Load (lbs)	
	(I)	(II)	(I)	(II)
(A)	0.002	0.002	501.33	502.58
(B)	0.024	0.023	984.51	993.41
(C)	0.035	0.051	1122.04	1345.74
(D)	-	-	-	-
(E)	-	-	-	-
(F)	-	-	-	-

Results of 2V72NU Finite Element Model

The dowel-concrete friction coefficients and material properties used in the analysis are shown in table C33. A comparison of the pullout force per bar (lbs.) vs. the joint opening (in.) is shown in figure C17. A summary of the various material failure / damage limit states is presented in table C34.

Table C-33: Dowel-Concrete Friction Coefficients; Material Properties used and limit states obtained from the analysis.

	μ_g	μ_w	f'_c (psi)	f'_t (psi)
Case I	0.0	0.30	3500.0	236.64
Case II	0.074	0.384	3500.0	236.64

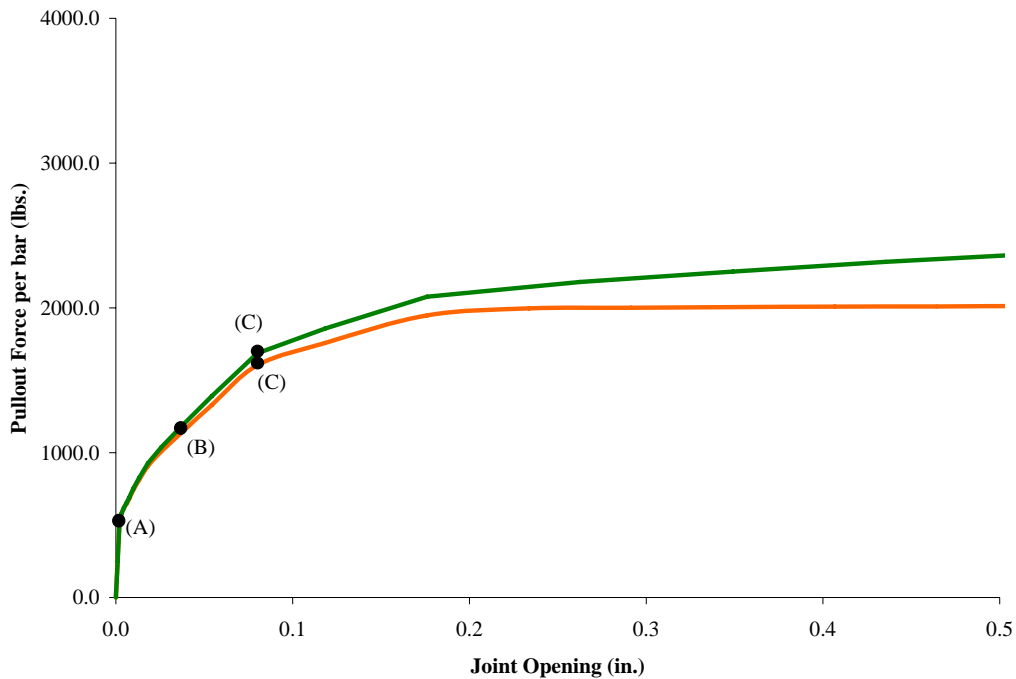


Figure C-17: Comparison of the FEM model with the experimental data for 2V72NU specimen

Table C-34: Summary of Material Failure / Damage Limit States from the analysis

Material Damage / Limit States	Joint Opening (in.)		Pullout Load (lbs)	
	(I)	(II)	(I)	(II)
(A)	0.002	0.002	500.53	501.86
(B)	0.051	0.051	1329.31	1391.04
(C)	0.077	0.077	1603.38	1686.42
(D)	-	-	-	-
(E)	-	-	-	-
(F)	-	-	-	-

Results of 2V72U Finite Element Model

The dowel-concrete friction coefficients and material properties used in the analysis are shown in table C35. A comparison of the pullout force per bar (lbs.) vs. the joint opening (in.) is shown in figure C18. A summary of the various material failure / damage limit states is presented in table C36.

Table C-35: Dowel-Concrete Friction Coefficients; Material Properties used and limit states obtained from the analysis.

	μ_g	μ_w	f'_c (psi)	f'_t (psi)
Case I	0.0	0.30	3500.0	236.64
Case II	0.074	0.384	3500.0	236.64

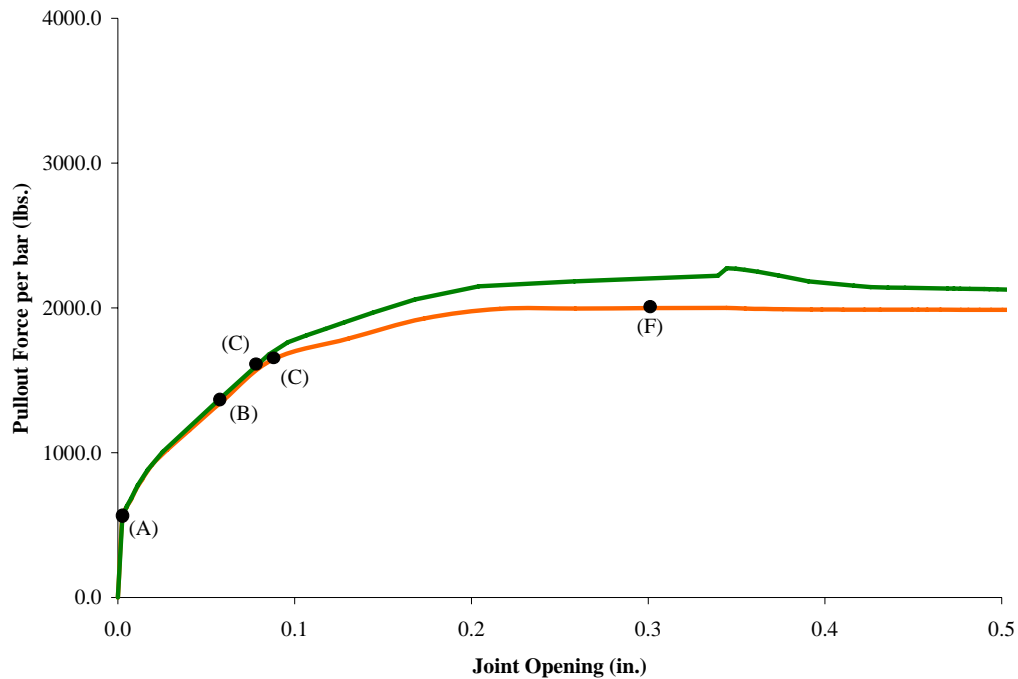


Figure C-18: Comparison of the FEM model with the experimental data for 2V72U specimen

Table C-36: Summary of Material Failure / Damage Limit States from the analysis

Material Damage / Limit States	Joint Opening (in.)		Pullout Load (lbs)	
	(I)	(II)	(I)	(II)
(A)	0.0025	0.002	555.53	557.14
(B)	0.059	0.057	1359.27	1363.32
(C)	0.088	0.085	1645.48	1678.98
(D)	-	-	-	-
(E)	-	-	-	-
(F)	-	-	-	-

Results of 2V72AM Finite Element Model

The dowel-concrete friction coefficients and material properties used in the analysis are shown in table C37. A comparison of the pullout force per bar (lbs.) vs. the joint opening (in.) is shown in figure C19. A summary of the various material failure / damage limit states is presented in table C38.

Table C-37: Dowel-Concrete Friction Coefficients; Material Properties used and limit states obtained from the analysis.

	μ_g	μ_w	f'_c (psi)	f'_t (psi)
Case I	0.0	0.30	3500.0	236.64
Case II	0.074	0.384	3500.0	236.64

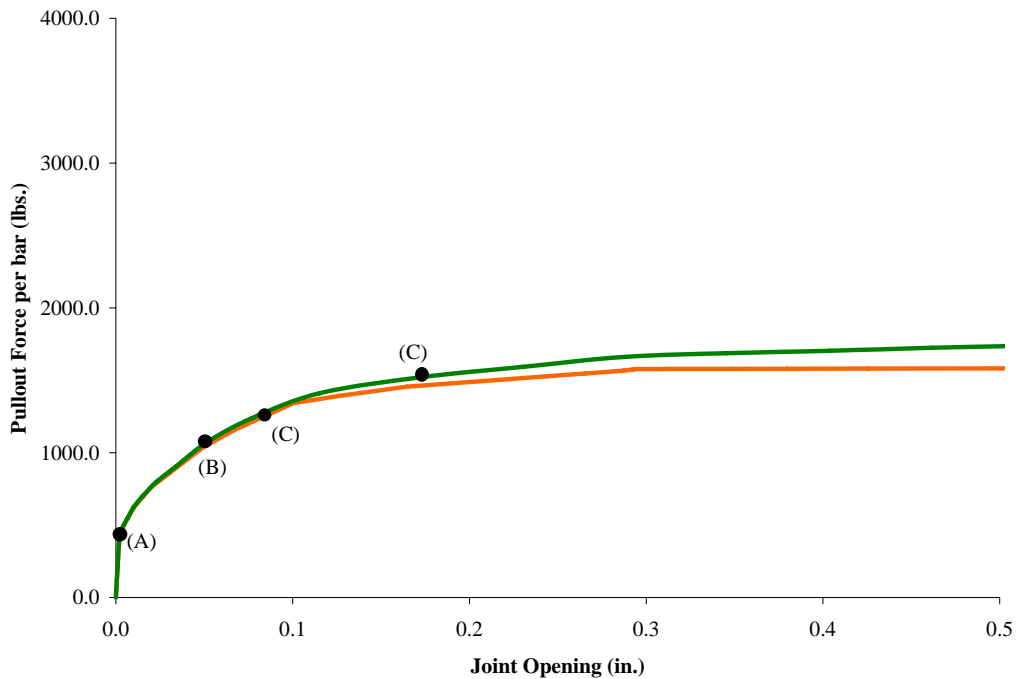


Figure C-19: Comparison of the FEM model with the experimental data for 2V72AM specimen

Table C-38: Summary of Material Failure / Damage Limit States from the analysis

Material Damage / Limit States	Joint Opening (in.)		Pullout Load (lbs)	
	(I)	(II)	(I)	(II)
(A)	0.002	0.002	412.75	413.56
(B)	0.049	0.051	1035.97	1070.28
(C)	0.083	0.173	1248.65	1522.05
(D)	-	-	-	-
(E)	-	-	-	-
(F)	-	-	-	-

Results of 2H18NU Finite Element Model

The dowel-concrete friction coefficients and material properties used in the analysis are shown in table C39. A comparison of the pullout force per bar (lbs.) vs. the joint opening (in.) is shown in figure C20. A summary of the various material failure / damage limit states is presented in table C40.

Table C-39: Dowel-Concrete Friction Coefficients; Material Properties used and limit states obtained from the analysis.

	μ_g	μ_w	f'_c (psi)	f'_t (psi)
Case I	0.0	0.30	3500.0	236.64
Case II	0.074	0.384	4931.0	280.0

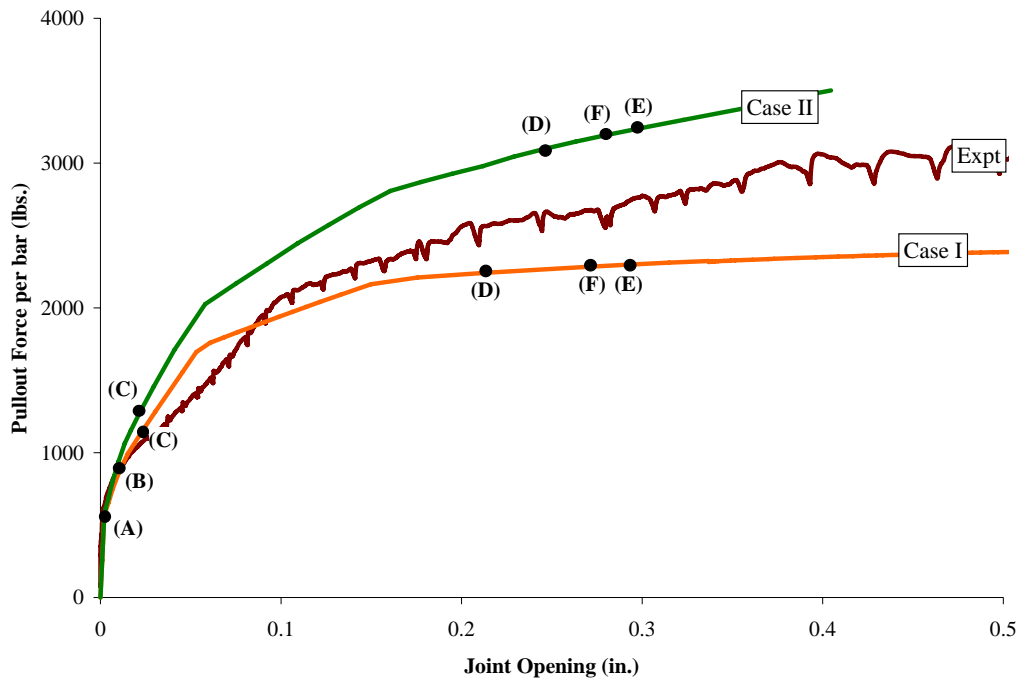


Figure C-20: Comparison of the FEM model with the experimental data for 2H18NU specimen

Table C-40: Summary of Material Failure / Damage Limit States from the analysis

Material Damage / Limit States	Joint Opening (in.)		Pullout Load (lbs)	
	(I)	(II)	(I)	(II)
(A)	0.002	0.002	516.12	529.74
(B)	0.010	0.010	859.91	943.06
(C)	0.023	0.022	1141.23	1279.29
(D)	0.214	0.280	2243.57	3139.88
(E)	0.293	0.297	2299.83	3236.9
(F)	0.272	0.246	2285.39	3098.24

Results of 2H18U Finite Element Model

The dowel-concrete friction coefficients and material properties used in the analysis are shown in table C41. A comparison of the pullout force per bar (lbs.) vs. the joint opening (in.) is shown in figure C21. A summary of the various material failure / damage limit states is presented in table C42.

Table C-41: Dowel-Concrete Friction Coefficients; Material Properties used and limit states obtained from the analysis.

	μ_g	μ_w	f'_c (psi)	f'_t (psi)
Case I	0.0	0.30	3500.0	236.64
Case II	0.074	0.384	3654.0	217.0

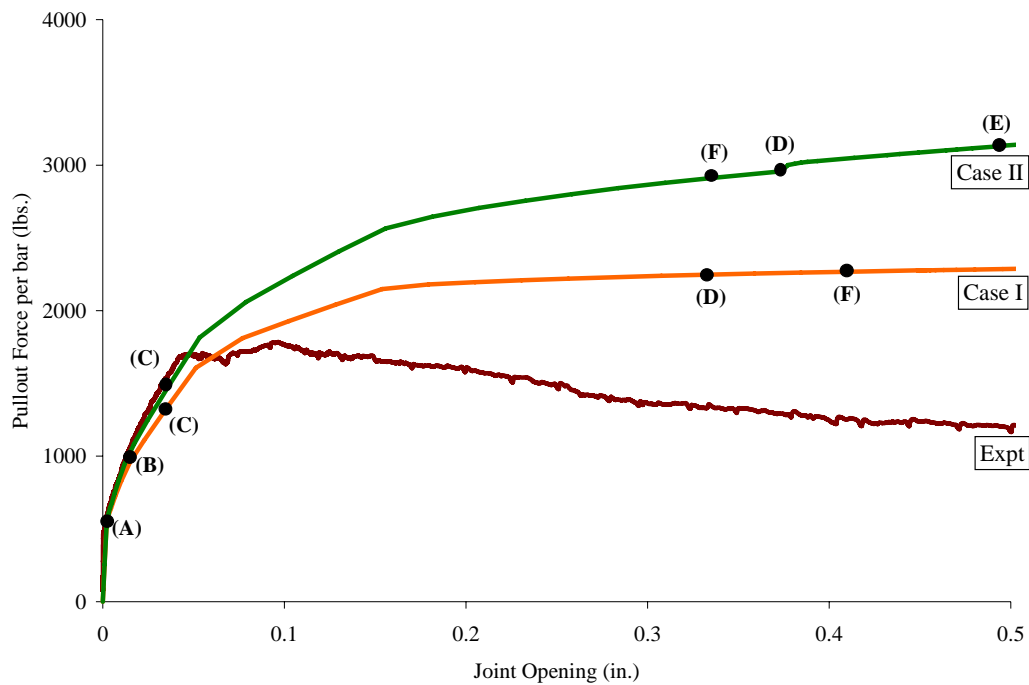


Figure C-21: Comparison of the FEM model with the experimental data for 2H18U specimen

Table C-42: Summary of Material Failure / Damage Limit States from the analysis

Material Damage / Limit States	Joint Opening (in.)		Pullout Load (lbs)	
	(I)	(II)	(I)	(II)
(A)	0.002	0.002	509.56	514.81
(B)	0.016	0.012	963.53	949.91
(C)	0.034	0.0362	1314.26	1481.65
(D)	0.333	0.374	2247.57	2957.96
(E)	0.5452	0.492	2297.17	3128.53
(F)	0.4101	0.335	2267.68	2912.34

Results of 2H18AM Finite Element Model

The dowel-concrete friction coefficients and material properties used in the analysis are shown in table C43. A comparison of the pullout force per bar (lbs.) vs. the joint opening (in.) is shown in figure C22. A summary of the various material failure / damage limit states is presented in table C44.

Table C-43: Dowel-Concrete Friction Coefficients; Material Properties used and limit states obtained from the analysis.

	μ_g	μ_w	f'_c (psi)	f'_t (psi)
Case I	0.0	0.30	3500.0	236.64
Case II	0.074	0.384	3520.0	245.0

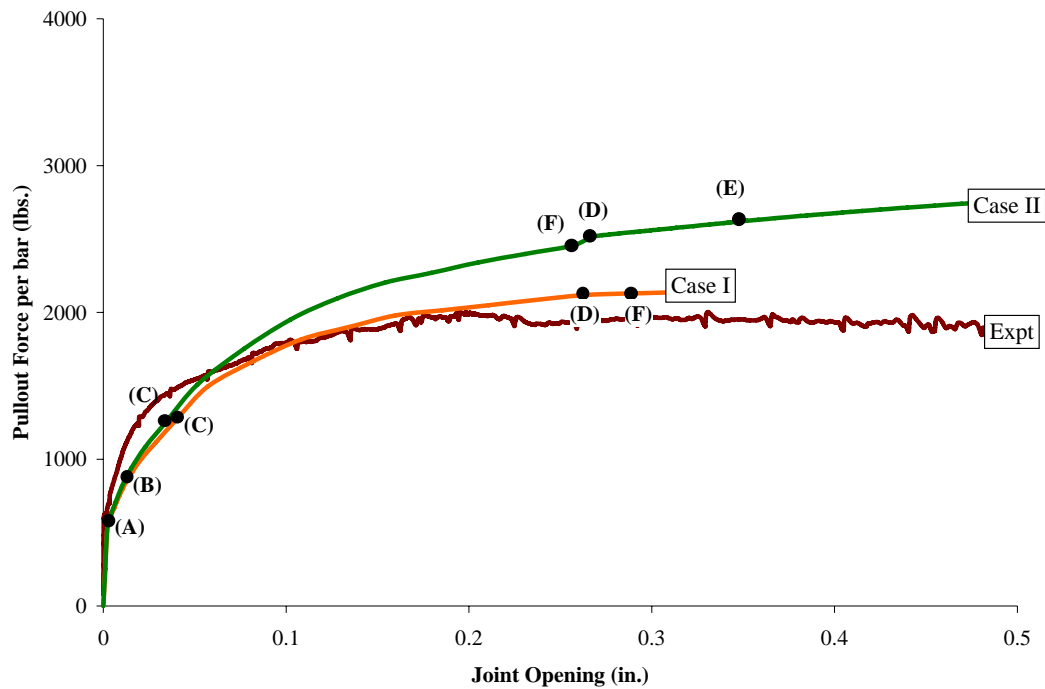


Figure C-22: Comparison of the FEM model with the experimental data for 2H18AM specimen

Table C-44: Summary of Material Failure / Damage Limit States from the analysis

Material Damage / Limit States	Joint Opening (in.)		Pullout Load (lbs)	
	(I)	(II)	(I)	(II)
(A)	0.002	0.002	505.61	508.25
(B)	0.013	0.015	852.68	937.34
(C)	0.040	0.034	1272.77	1251.89
(D)	0.262	0.266	2116.95	2507.60
(E)	-	0.348	-	2619.57
(F)	0.288	0.256	2129.46	2454.00

Results of 2H36NU Finite Element Model

The dowel-concrete friction coefficients and material properties used in the analysis are shown in table C45. A comparison of the pullout force per bar (lbs.) vs. the joint opening (in.) is shown in figure C23. A summary of the various material failure / damage limit states is presented in table C46.

Table C-45: Dowel-Concrete Friction Coefficients; Material Properties used and limit states obtained from the analysis.

	μ_g	μ_w	f'_c (psi)	f'_t (psi)
Case I	0.0	0.30	3500.0	236.64
Case II	0.074	0.384	4941.0	280.0

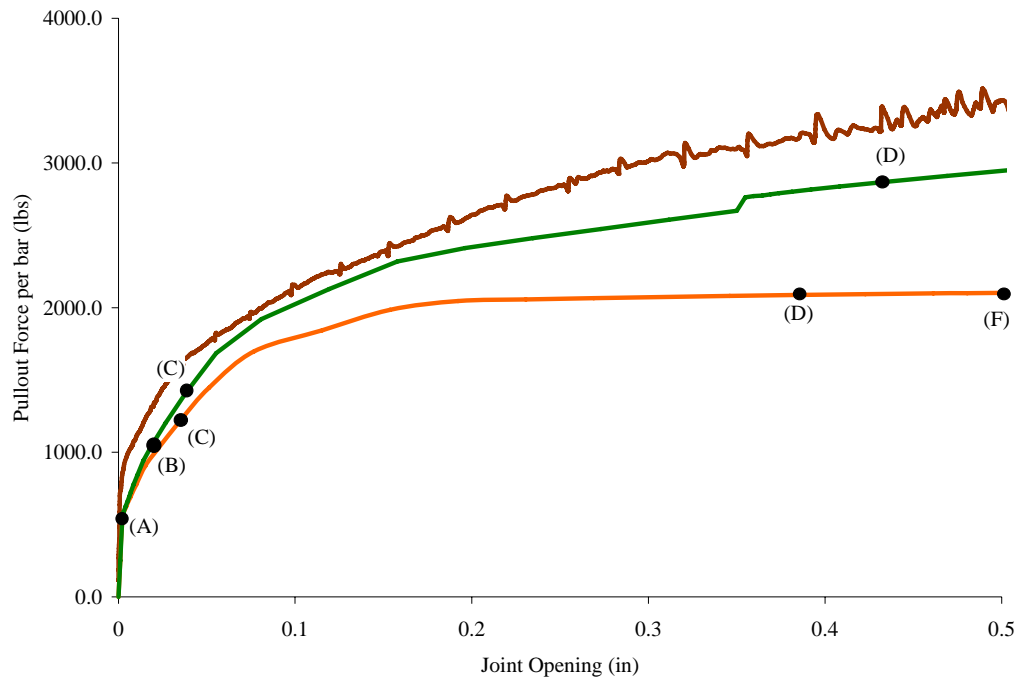


Figure C-23: Comparison of the FEM model with the experimental data for 2H36NU specimen

Table C-46: Summary of Material Failure / Damage Limit States from the analysis

Material Damage / Limit States	Joint Opening (in.)		Pullout Load (lbs)	
	(I)	(II)	(I)	(II)
(A)	0.002	0.002	504.46	509.93
(B)	0.023	0.019	1031.14	1053.07
(C)	0.034	0.038	1206.82	1410.53
(D)	0.384	0.432	2087.58	2867.48
(E)	0.519	0.524	2105.33	2972.23
(F)	0.499	0.606	2102.89	3057.04

Results of 2H36U Finite Element Model

The dowel-concrete friction coefficients and material properties used in the analysis are shown in table C47. A comparison of the pullout force per bar (lbs.) vs. the joint opening (in.) is shown in figure C24. A summary of the various material failure / damage limit states is presented in table C48.

Table C-47: Dowel-Concrete Friction Coefficients; Material Properties used and limit states obtained from the analysis.

	μ_g	μ_w	f'_c (psi)	f'_t (psi)
Case I	0.0	0.30	3500.0	236.64
Case II	0.074	0.384	3673.0	383.0

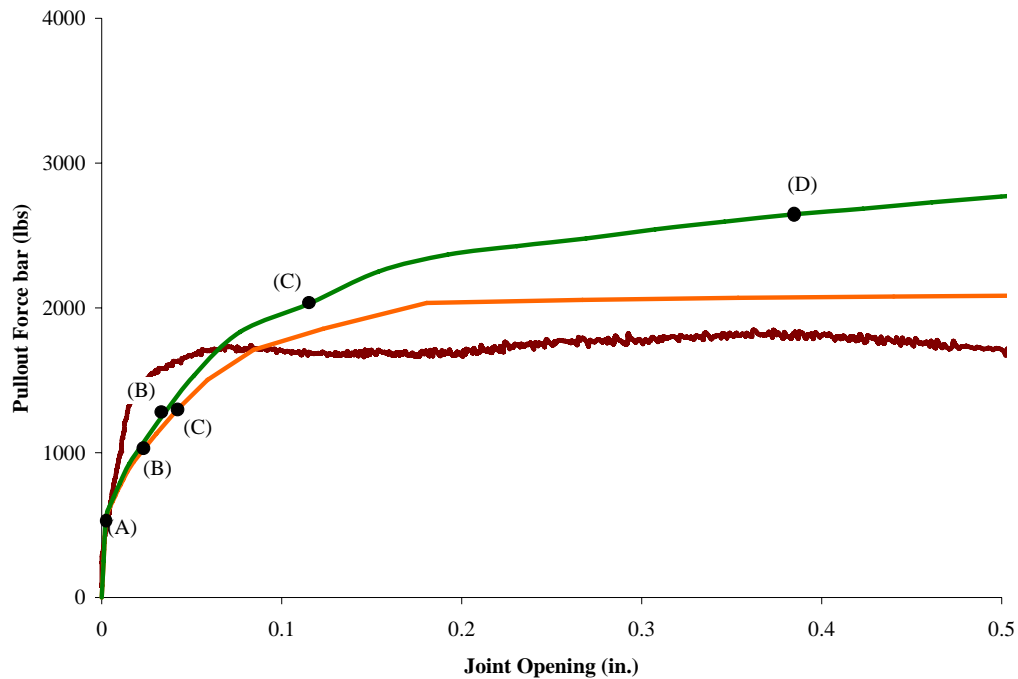


Figure C-24: Comparison of the FEM model with the experimental data for 2H36U specimen

Table C-48: Summary of Material Failure / Damage Limit States from the analysis

Material Damage / Limit States	Joint Opening (in.)		Pullout Load (lbs)	
	(I)	(II)	(I)	(II)
(A)	0.002	0.002	503.57	507.53
(B)	0.023	0.034	1014.38	1260.96
(C)	0.042	0.115	1294.47	2030.29
(D)	0.5265	0.384	2086.17	2646.19
(E)	0.7860	0.6151	2098.56	2871.68
(F)	0.7860	0.7304	2098.56	2941.00

Results of 2H36AM Finite Element Model

The dowel-concrete friction coefficients and material properties used in the analysis are shown in table C49. A comparison of the pullout force per bar (lbs.) vs. the joint opening (in.) is shown in figure C25. A summary of the various material failure / damage limit states is presented in table C50.

Table C-49: Dowel-Concrete Friction Coefficients; Material Properties used and limit states obtained from the analysis.

	μ_g	μ_w	f'_c (psi)	f'_t (psi)
Case I	0.0	0.30	3500.0	236.64
Case II	0.074	0.384	3500.0	236.64

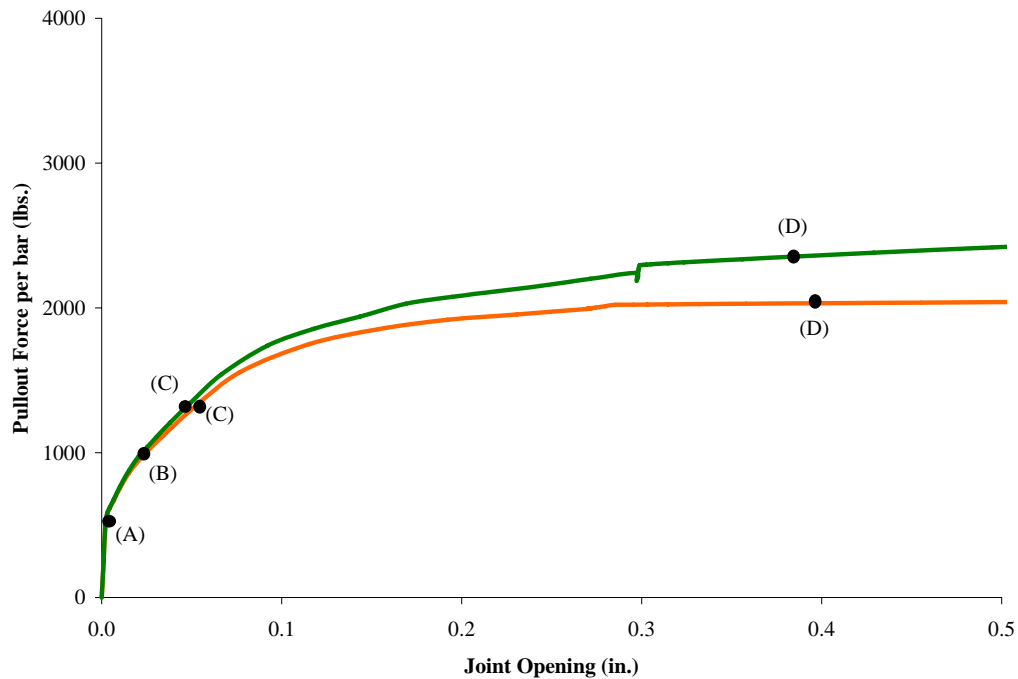


Figure C-25: Comparison of the FEM model with the experimental data for 2H36AM specimen

Table C-50: Summary of Material Failure / Damage Limit States from the analysis

Material Damage / Limit States	Joint Opening (in.)		Pullout Load (lbs)	
	(I)	(II)	(I)	(II)
(A)	0.002	0.002	501.83	503.88
(B)	0.023	0.020	977.21	969.89
(C)	0.051	0.049	1313.20	1344.32
(D)	0.397	0.385	2032.31	2355.03
(E)	0.54	0.593	2042.36	2467.74
(F)	0.54	0.593	2042.36	2467.74

Results of 2H72NU Finite Element Model

The dowel-concrete friction coefficients and material properties used in the analysis are shown in table C51. A comparison of the pullout force per bar (lbs.) vs. the joint opening (in.) is shown in figure C26. A summary of the various material failure / damage limit states is presented in table C52.

Table C-51: Dowel-Concrete Friction Coefficients; Material Properties used and limit states obtained from the analysis.

	μ_g	μ_w	f'_c (psi)	f'_t (psi)
Case I	0.0	0.30	3500.0	236.64
Case II	0.074	0.384	3500.0	236.64

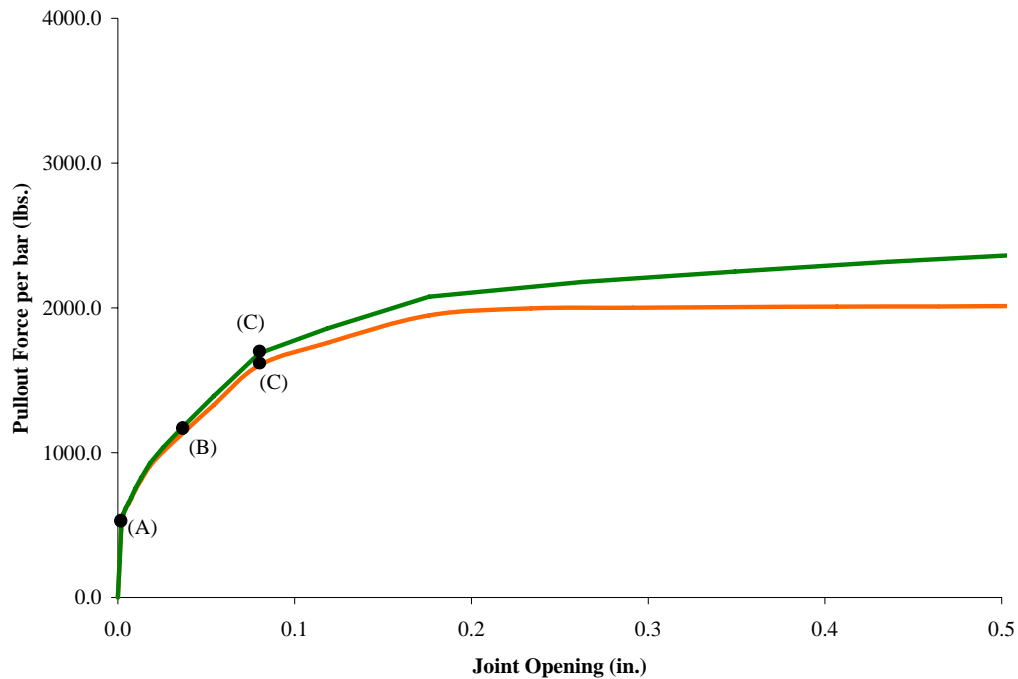


Figure C-26: Comparison of the FEM model with the experimental data for 2H72NU specimen

Table C-52: Summary of Material Failure / Damage Limit States from the analysis

Material Damage / Limit States	Joint Opening (in.)		Pullout Load (lbs)	
	(I)	(II)	(I)	(II)
(A)	0.002	0.002	500.23	501.86
(B)	0.037	0.037	1139.24	1183.07
(C)	0.078	0.079	1603.38	1686.42
(D)	0.752	0.782	2018.69	2496.33
(E)	-	-	-	-
(F)	-	-	-	-

Results of 2H72U Finite Element Model

The dowel-concrete friction coefficients and material properties used in the analysis are shown in table C53. A comparison of the pullout force per bar (lbs.) vs. the joint opening (in.) is shown in figure C27. A summary of the various material failure / damage limit states is presented in table C54.

Table C-53: Dowel-Concrete Friction Coefficients; Material Properties used and limit states obtained from the analysis.

	μ_g	μ_w	f'_c (psi)	f'_t (psi)
Case I	0.0	0.30	3500.0	236.64
Case II	0.074	0.384	3500.0	236.64

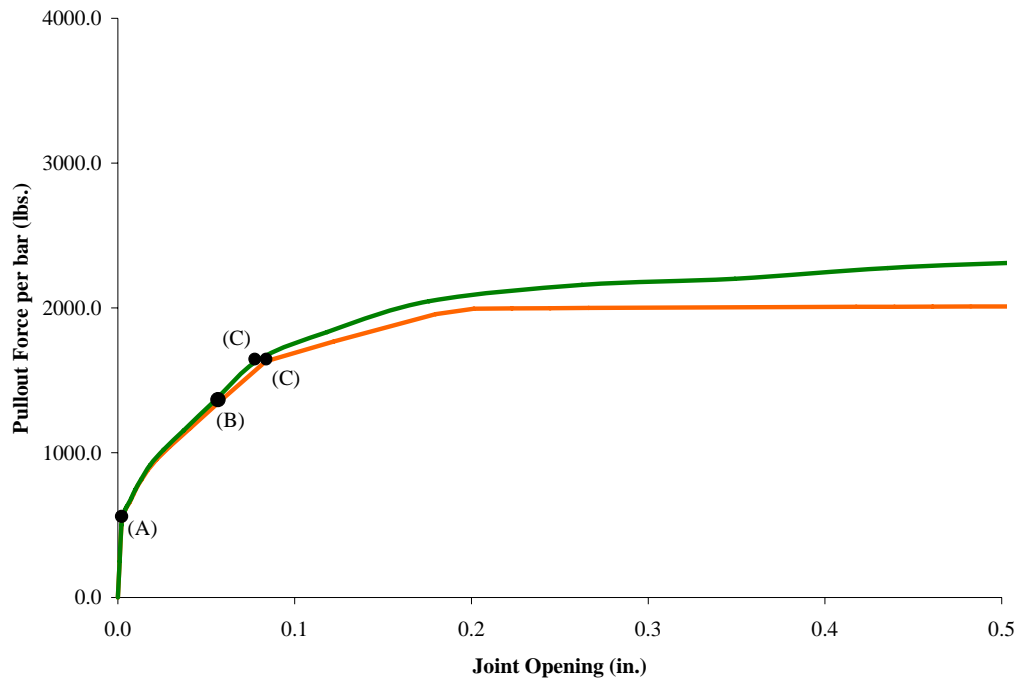


Figure C-27: Comparison of the FEM model with the experimental data for 2H72U specimen

Table C-54: Summary of Material Failure / Damage Limit States from the analysis

Material Damage / Limit States	Joint Opening (in.)		Pullout Load (lbs)	
	(I)	(II)	(I)	(II)
(A)	0.002	0.002	498.99	500.14
(B)	0.058	0.054	1357.57	1353.23
(C)	0.084	0.079	1631.36	1644.15
(D)	0.910	0.868	2018.16	2467.27
(E)	-	-	-	-
(F)	-	-	-	-

Results of 2H72AM Finite Element Model

The dowel-concrete friction coefficients and material properties used in the analysis are shown in table C55. A comparison of the pullout force per bar (lbs.) vs. the joint opening (in.) is shown in figure C28. A summary of the various material failure / damage limit states is presented in table C56.

Table C-55: Dowel-Concrete Friction Coefficients; Material Properties used and limit states obtained from the analysis.

	μ_g	μ_w	f'_c (psi)	f'_t (psi)
Case I	0.0	0.30	3500.0	236.64
Case II	0.074	0.384	3500.0	236.64

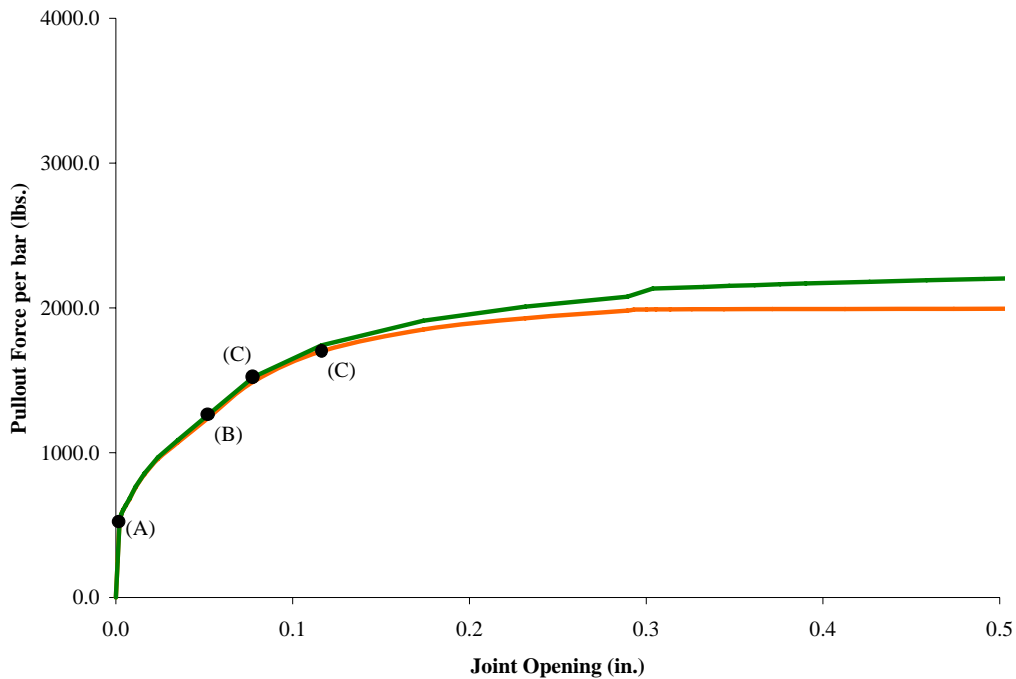


Figure C-28: Comparison of the FEM model with the experimental data for 2H72AM specimen

Table C-56: Summary of Material Failure / Damage Limit States from the analysis

Material Damage / Limit States	Joint Opening (in.)		Pullout Load (lbs)	
	(I)	(II)	(I)	(II)
(A)	0.002	0.002	500.41	501.34
(B)	0.052	0.052	1240.74	1263.06
(C)	0.116	0.078	1700.82	1522.59
(D)	0.828	0.918	1998.47	2296.83
(E)	-	-	-	-
(F)	-	-	-	-

Results of 2C18NU Finite Element Model

The dowel-concrete friction coefficients and material properties used in the analysis are shown in table C57. A comparison of the pullout force per bar (lbs.) vs. the joint opening (in.) is shown in figure C29. A summary of the various material failure / damage limit states is presented in table C58.

Table C-57: Dowel-Concrete Friction Coefficients; Material Properties used and limit states obtained from the analysis.

	μ_g	μ_w	f'_c (psi)	f'_t (psi)
Case I	0.0	0.30	3500.0	236.64
Case II	0.074	0.384	4930.0	280.0

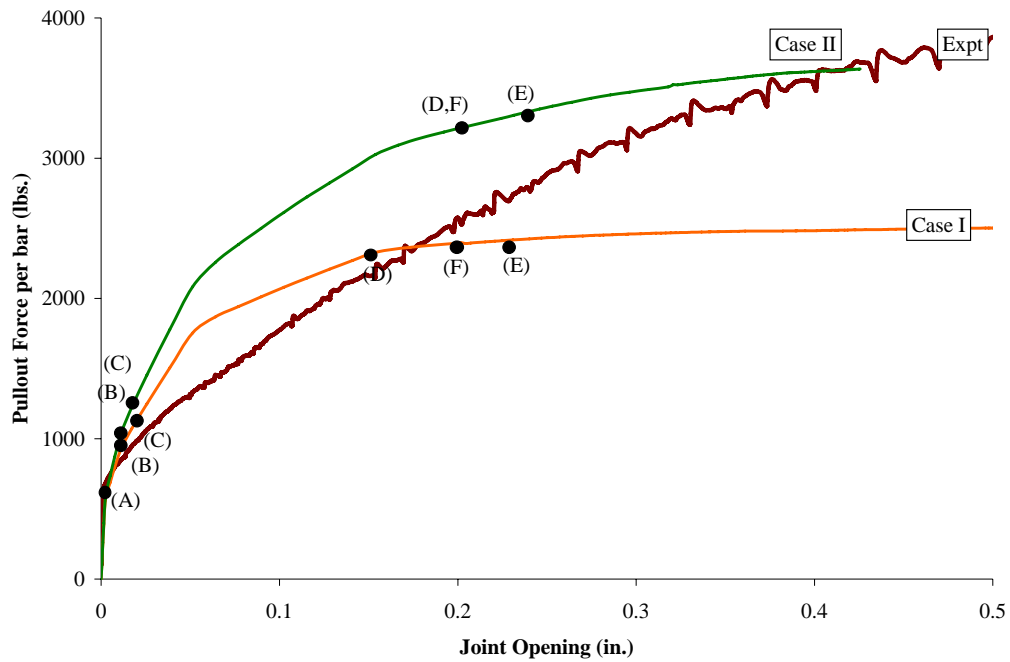


Figure C-29: Comparison of the FEM model with the experimental data for 2C18NU specimen

Table C-58: Summary of Material Failure / Damage Limit States from the analysis

Material Damage / Limit States	Joint Opening (in.)		Pullout Load (lbs)	
	(I)	(II)	(I)	(II)
(A)	0.0038	0.0038	625.0	650.0
(B)	0.014	0.014	935.0	1025.0
(C)	0.017	0.017	1070.0	1225.0
(D)	0.154	0.205	2330.0	3225.0
(E)	0.231	0.239	2415.0	3330.0
(F)	0.202	0.205	2395.0	3225.0

Results of 2C18U Finite Element Model

The dowel-concrete friction coefficients and material properties used in the analysis are shown in table C59. A comparison of the pullout force per bar (lbs.) vs. the joint opening (in.) is shown in figure C30. A summary of the various material failure / damage limit states is presented in table C60.

Table C-59: Dowel-Concrete Friction Coefficients; Material Properties used and limit states obtained from the analysis.

	μ_g	μ_w	f'_c (psi)	f'_t (psi)
Case I	0.0	0.30	3500.0	236.64
Case II	0.074	0.384	3654.0	217.0

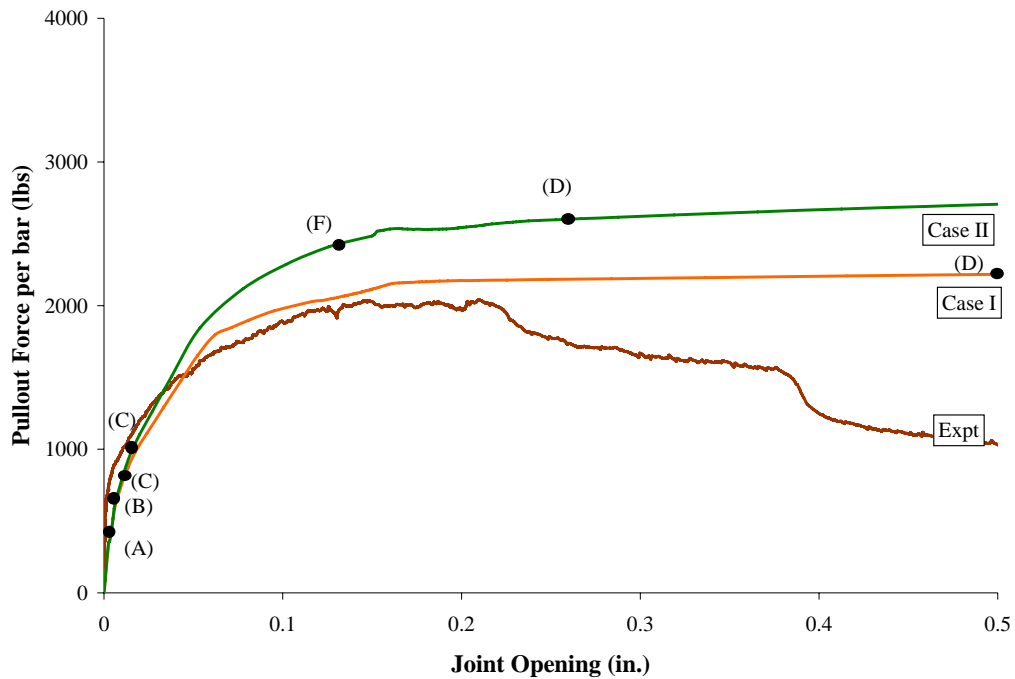


Figure C-30: Comparison of the FEM model with the experimental data for 2C18U specimen

Table C-60: Summary of Material Failure / Damage Limit States from the analysis

Material Damage / Limit States	Joint Opening (in.)		Pullout Load (lbs)	
	(I)	(II)	(I)	(II)
(A)	0.0025	0.003	460.0	460.
(B)	0.0038	0.0098	530.65	735.0
(C)	0.0075	0.015	615.0	980.0
(D)	0.534	0.253	1125.0	1165.0
(E)	-	0.126	-	2410.0
(F)	-	-	-	-

Results of 2C18AM Finite Element Model

The dowel-concrete friction coefficients and material properties used in the analysis are shown in table C61. A comparison of the pullout force per bar (lbs.) vs. the joint opening (in.) is shown in figure C31. A summary of the various material failure / damage limit states is presented in table C62.

Table C-61: Dowel-Concrete Friction Coefficients; Material Properties used and limit states obtained from the analysis.

	μ_g	μ_w	f'_c (psi)	f'_t (psi)
Case I	0.0	0.30	3500.0	236.64
Case II	0.074	0.384	3520.0	245.00

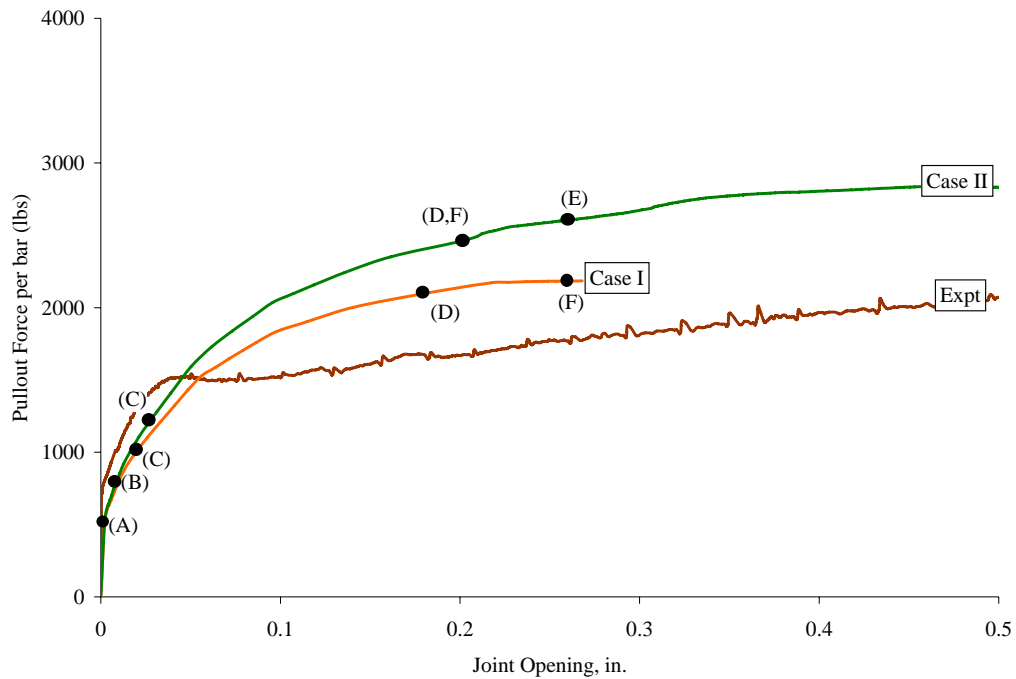


Figure C-31: Comparison of the FEM model with the experimental data for 2C18AM specimen

Table C-62: Summary of Material Failure / Damage Limit States from the analysis

Material Damage / Limit States	Joint Opening (in.)		Pullout Load (lbs)	
	(I)	(II)	(I)	(II)
(A)	0.003	0.003	585.0	585.0
(B)	0.0097	0.009	794.0	805.0
(C)	0.018	0.026	980.0	1195.0
(D)	0.179	0.200	2095.0	2455.0
(E)	-	0.259	-	2605.0
(F)	0.227	0.200	2175.0	2455.0

Results of 2C36NU Finite Element Model

The dowel-concrete friction coefficients and material properties used in the analysis are shown in table C63. A comparison of the pullout force per bar (lbs.) vs. the joint opening (in.) is shown in figure C32. A summary of the various material failure / damage limit states is presented in table C64.

Table C-63: Dowel-Concrete Friction Coefficients; Material Properties used and limit states obtained from the analysis.

	μ_g	μ_w	f'_c (psi)	f'_t (psi)
Case I	0.0	0.30	3500.0	236.64
Case II	0.074	0.384	4931.0	290.00

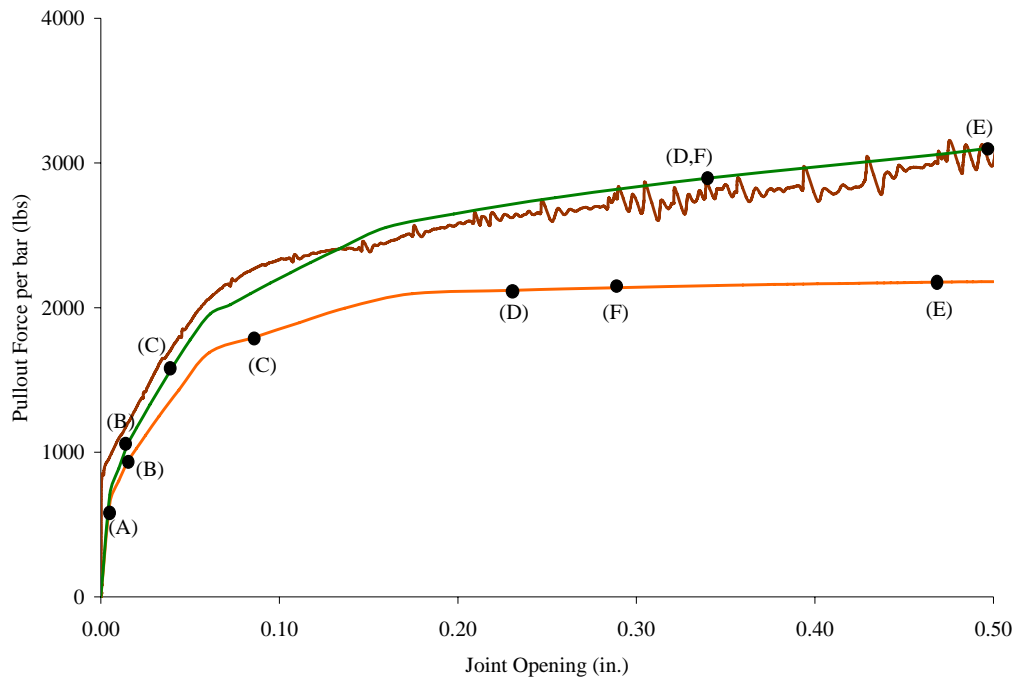


Figure C-32: Comparison of the FEM model with the experimental data for 2C36NU specimen

Table C-64: Summary of Material Failure / Damage Limit States from the analysis

Material Damage / Limit States	Joint Opening (in.)		Pullout Load (lbs)	
	(I)	(II)	(I)	(II)
(A)	0.003	0.003	550.0	575.0
(B)	0.015	0.015	935.0	1055.0
(C)	0.086	0.038	1795.0	1560.0
(D)	0.231	0.340	2120.0	2695.0
(E)	0.288	0.50	2140.0	3105.0
(F)	0.468	0.340	2175.0	2895.0

Results of 3A Finite element model

The dowel-concrete friction coefficients and material properties used in the analysis are shown in table C65. A comparison of the pullout force per bar (lbs.) vs. the joint opening (in.) is shown in figure C33. A summary of the various material failure / damage limit states is presented in table C66.

Table C-65: Dowel-Concrete Friction Coefficients; Material Properties used and limit states obtained from the analysis.

	μ_g	μ_w	f'_c (psi)	f'_t (psi)
Case I	0.0	0.30	3500.0	236.64
Case II	0.074	0.384	3326.0	354.00

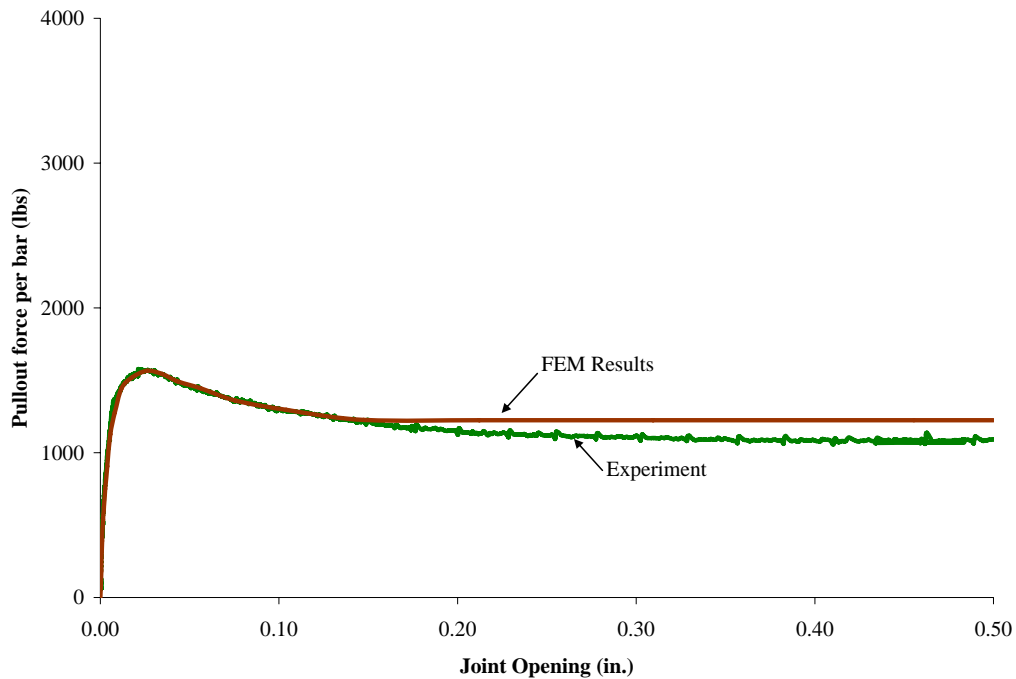


Figure C-33: Comparison of the FEM model with the experimental data for 3A specimen

Table C-66: Summary of Material Failure / Damage Limit States from the analysis

Material Damage / Limit States	Joint Opening (in.)		Pullout Load (lbs)	
	(I)	(II)	(I)	(II)
(A)	0.002	0.002	625.0	630.0
(B)	-	-	-	-
(C)	-	-	-	-
(D)	-	-	-	-
(E)	-	-	-	-
(F)	-	-	-	-

Results of 3V18NU Finite element model

The dowel-concrete friction coefficients and material properties used in the analysis are shown in table C67. A comparison of the pullout force per bar (lbs.) vs. the joint opening (in.) is shown in figure C34. A summary of the various material failure / damage limit states is presented in table C68.

Table C-67: Dowel-Concrete Friction Coefficients; Material Properties used and limit states obtained from the analysis.

	μ_g	μ_w	f'_c (psi)	f'_t (psi)
Case I	0.0	0.30	3500.0	236.64
Case II	0.074	0.384	4931.0	290.0

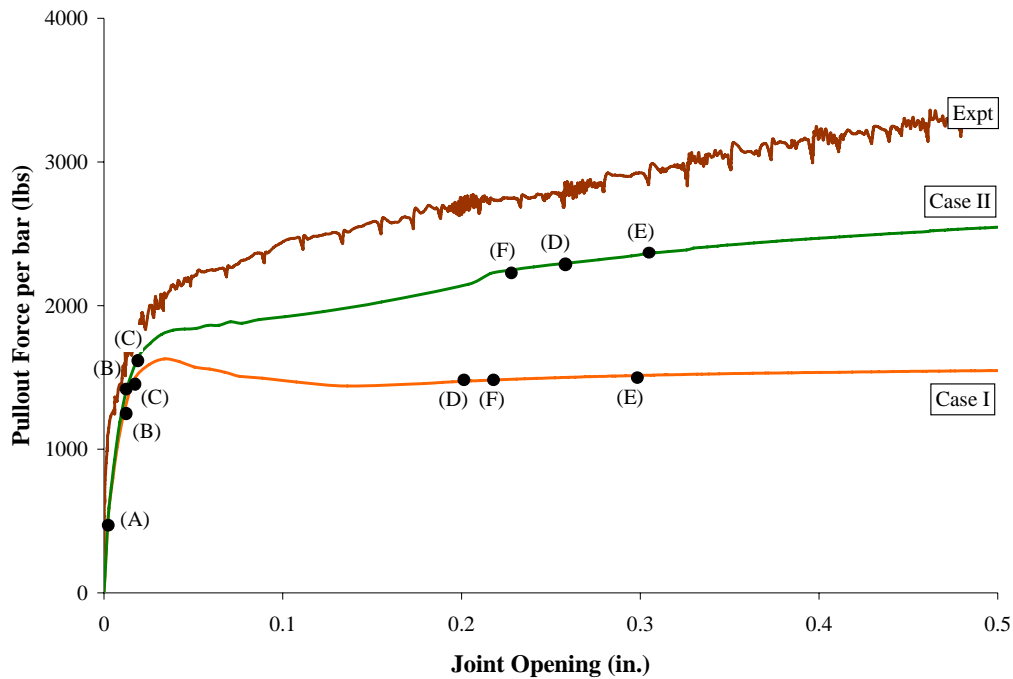


Figure C-34: Comparison of the FEM model with the experimental data for 3V18NU specimen

Table C-68: Summary of Material Failure / Damage Limit States from the analysis

Material Damage / Limit States	Joint Opening (in.)		Pullout Load (lbs)	
	(I)	(II)	(I)	(II)
(A)	0.003	0.003	600.0	620.0
(B)	0.011	0.0131	1260.0	1430.0
(C)	0.017	0.0195	1490.0	1650.0
(D)	0.200	0.259	1470.0	2300.0
(E)	0.297	0.309	1510.0	2370.0
(F)	0.219	0.228	1480.0	2250.0

Results of 3H18NU Finite element model

The dowel-concrete friction coefficients and material properties used in the analysis are shown in table C69. A comparison of the pullout force per bar (lbs.) vs. the joint opening (in.) is shown in figure C35. A summary of the various material failure / damage limit states is presented in table C70.

Table C-69: Dowel-Concrete Friction Coefficients; Material Properties used and limit states obtained from the analysis.

	μ_g	μ_w	f'_c (psi)	f'_t (psi)
Case I	0.0	0.30	3500.0	236.64
Case II	0.074	0.384	3919.0	336.0

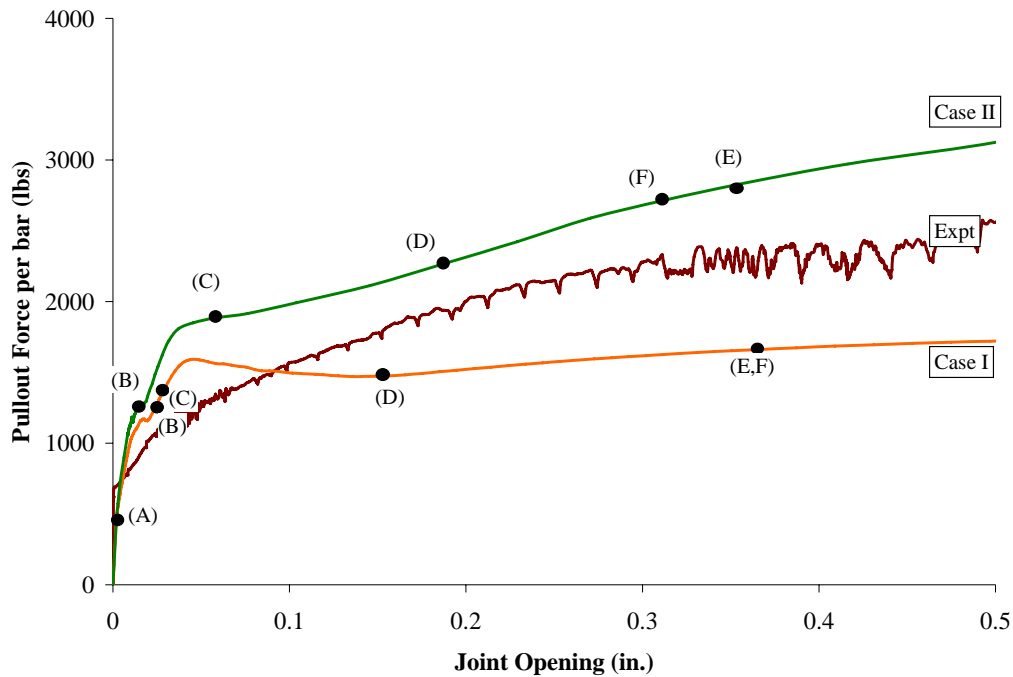


Figure C-35: Comparison of the FEM model with the experimental data for 3H18NU specimen

Table C-70: Summary of Material Failure / Damage Limit States from the analysis

Material Damage / Limit States	Joint Opening (in.)		Pullout Load (lbs)	
	(I)	(II)	(I)	(II)
(A)	0.003	0.003	557.0	610.0
(B)	0.026	0.0141	1310.0	1250.0
(C)	0.0277	0.0577	1350.0	1880.0
(D)	0.149	0.187	1470.0	2270.0
(E)	0.365	0.354	1660.0	2830.0
(F)	0.365	0.312	1660.0	2720.0

Results of 3C18NU Finite element model

The dowel-concrete friction coefficients and material properties used in the analysis are shown in table C71. A comparison of the pullout force per bar (lbs.) vs. the joint opening (in.) is shown in figure C36. A summary of the various material failure / damage limit states is presented in table C72.

Table C-71: Dowel-Concrete Friction Coefficients; Material Properties used and limit states obtained from the analysis.

	μ_g	μ_w	f'_c (psi)	f'_t (psi)
Case I	0.0	0.30	3500.0	236.64
Case II	0.074	0.384	3520.0	245.0

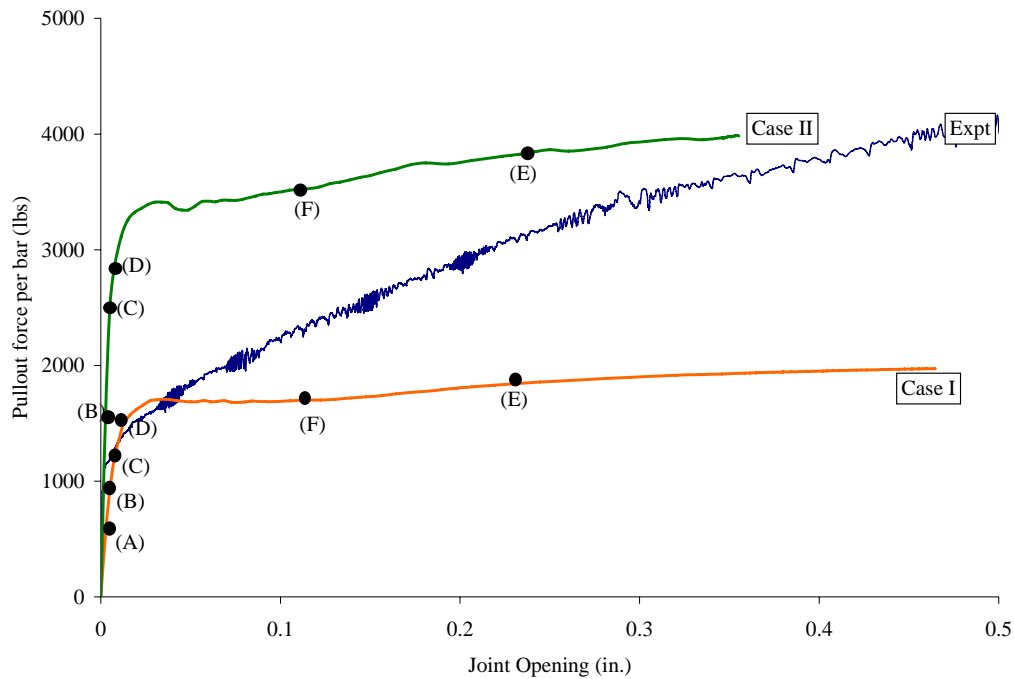


Figure C-36: Comparison of the FEM model with the experimental data for 3C18NU specimen

Table C-72: Summary of Material Failure / Damage Limit States from the analysis

Material Damage / Limit States	Joint Opening (in.)		Pullout Load (lbs)	
	(I)	(II)	(I)	(II)
(A)	0.025	0.025	540.0	1540.0
(B)	0.005	0.005	921.0	2500.0
(C)	0.075	0.075	1200.0	2850.0
(D)	0.01	0.013	1360.0	3110.0
(E)	0.232	0.238	1840.0	3840.0
(F)	0.198	0.110	1800.0	3520.0

Results of 5A Finite element model

The dowel-concrete friction coefficients and material properties used in the analysis are shown in table C73. A comparison of the pullout force per bar (lbs.) vs. the joint opening (in.) is shown in figure C37. A summary of the various material failure / damage limit states is presented in table C74.

Table C-73: Dowel-Concrete Friction Coefficients; Material Properties used and limit states obtained from the analysis.

	μ_g	μ_w	f'_c (psi)	f'_t (psi)
Case I	0.0	0.30	3500.0	236.64
Case II	0.074	0.384	3151.0	413.0

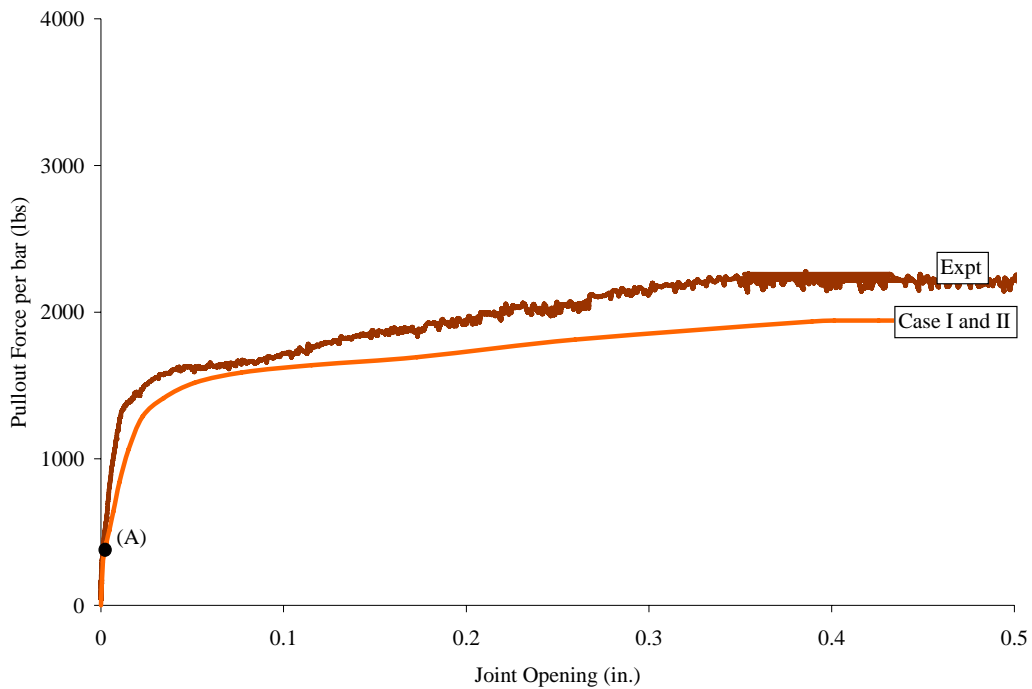


Figure C-37: Comparison of the FEM model with the experimental data for 5A specimen

Table C-74: Summary of Material Failure / Damage Limit States from the analysis

Material Damage / Limit States	Joint Opening (in.)		Pullout Load (lbs)	
	(I)	(II)	(I)	(II)
(A)	0.002	0.002	510.0	510.0
(B)	-	-	-	-
(C)	-	-	-	-
(D)	-	-	-	-
(E)	-	-	-	-
(F)	-	-	-	-

Results of 5V18NU Finite Element Model

The dowel-concrete friction coefficients and material properties used in the analysis are shown in table C75. A comparison of the pullout force per bar (lbs.) vs. the joint opening (in.) is shown in figure 38. A summary of the various material failure / damage limit states is presented in table C76.

Table C-75: Dowel-Concrete Friction Coefficients; Material Properties used and limit states obtained from the analysis.

	μ_g	μ_w	f'_c (psi)	f'_t (psi)
Case I	0.0	0.30	3500.0	236.64
Case II	0.074	0.384	4931.0	363.0

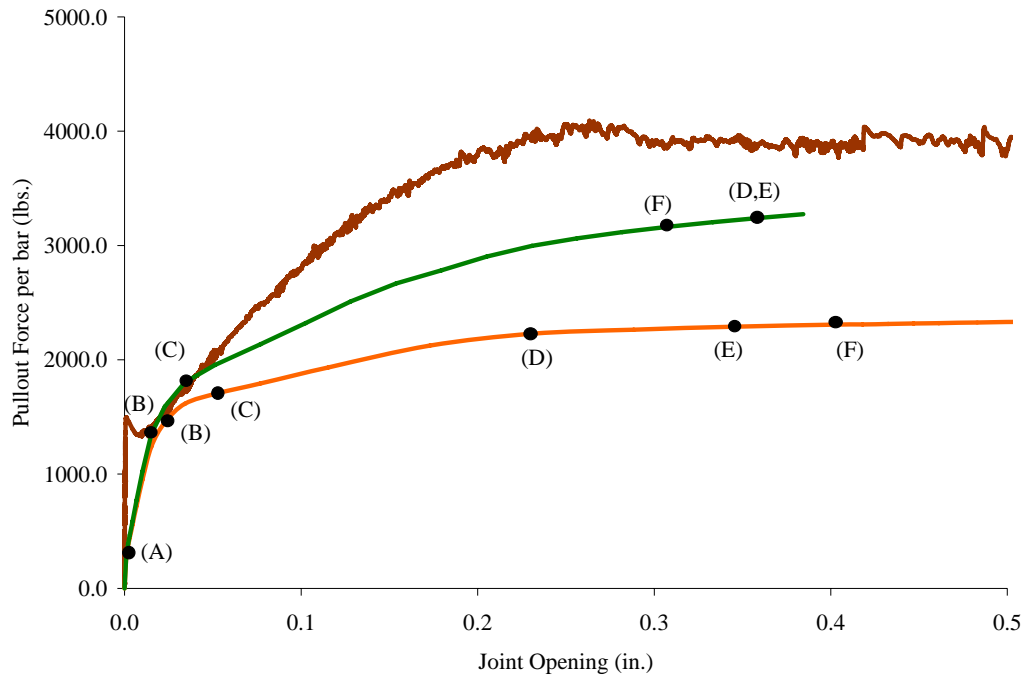


Figure C-38: Comparison of the FEM model with the experimental data for 5V18NU specimen

Table C-76: Summary of Material Failure / Damage Limit States from the analysis

Material Damage / Limit States	Joint Opening (in.)		Pullout Load (lbs)	
	(I)	(II)	(I)	(II)
(A)	0.002	0.002	379.54	388.34
(B)	0.022	0.015	1451.97	1353.50
(C)	0.051	0.034	1701.96	1802.57
(D)	0.230	0.358	2227.88	3239.90
(E)	0.346	0.358	2289.98	3239.90
(F)	0.404	0.307	2307.90	3163.28

Results of 5V18AM Finite Element Model

The dowel-concrete friction coefficients and material properties used in the analysis are shown in table C77. A comparison of the pullout force per bar (lbs.) vs. the joint opening (in.) is shown in figure C39. A summary of the various material failure / damage limit states is presented in table C78.

Table C-77: Dowel-Concrete Friction Coefficients; Material Properties used and limit states obtained from the analysis.

	μ_g	μ_w	f'_c (psi)	f'_t (psi)
Case I	0.0	0.30	3500.0	236.64
Case II	0.074	0.384	3530.0	355.0

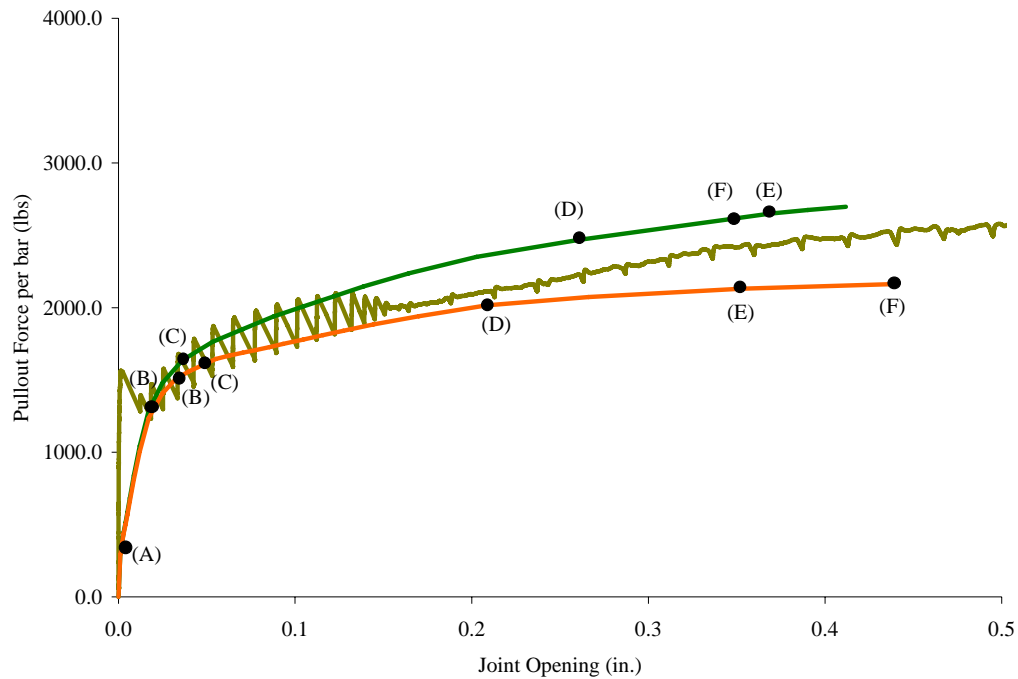


Figure C-39: Comparison of the FEM model with the experimental data for 5V18AM specimen

Table C-78: Summary of Material Failure / Damage Limit States from the analysis

Material Damage / Limit States	Joint Opening (in.)		Pullout Load (lbs)	
	(I)	(II)	(I)	(II)
(A)	0.002	0.002	374.0	378.0
(B)	0.032	0.017	1510.0	1290.0
(C)	0.047	0.036	1600.0	1640.0
(D)	0.208	0.260	2020.0	2470.0
(E)	0.352	0.368	2130.0	2610.0
(F)	0.439	0.347	2160.0	2650.0

Results of 5V36AM Finite Element Model

The dowel-concrete friction coefficients and material properties used in the analysis are shown in table C79. A comparison of the pullout force per bar (lbs.) vs. the joint opening (in.) is shown in figure C40. A summary of the various material failure / damage limit states is presented in table C80.

Table C-79: Dowel-Concrete Friction Coefficients; Material Properties used and limit states obtained from the analysis.

	μ_g	μ_w	f'_c (psi)	f'_t (psi)
Case I	0.0	0.30	3500.0	236.64
Case II	0.074	0.384	3530.0	355.0

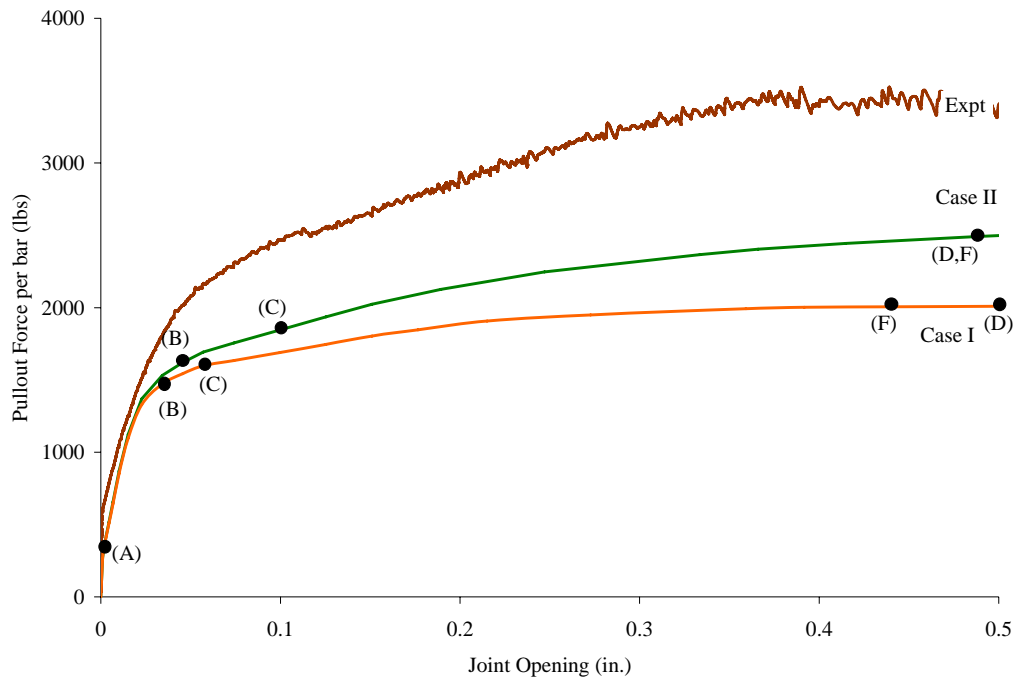


Figure C-40: Comparison of the FEM model with the experimental data for 5V36AM specimen

Table C-80: Summary of Material Failure / Damage Limit States from the analysis

Material Damage / Limit States	Joint Opening (in.)		Pullout Load (lbs)	
	(I)	(II)	(I)	(II)
(A)	0.003	0.003	419.68	424.46
(B)	0.034	0.045	1472.3	1620.3
(C)	0.056	0.099	1598.3	1845.7
(D)	0.513	0.487	2009.3	2491.64
(E)	-	-	-	-
(F)	0.440	0.487	2005.8	2491.64

Results of 5H18NU Finite Element Model

The dowel-concrete friction coefficients and material properties used in the analysis are shown in table C81. A comparison of the pullout force per bar (lbs.) vs. the joint opening (in.) is shown in figure C41. A summary of the various material failure / damage limit states is presented in table C82.

Table C-81: Dowel-Concrete Friction Coefficients; Material Properties used and limit states obtained from the analysis.

	μ_g	μ_w	f'_c (psi)	f'_t (psi)
Case I	0.0	0.30	3500.0	236.64
Case II	0.074	0.384	3654.0	217.0

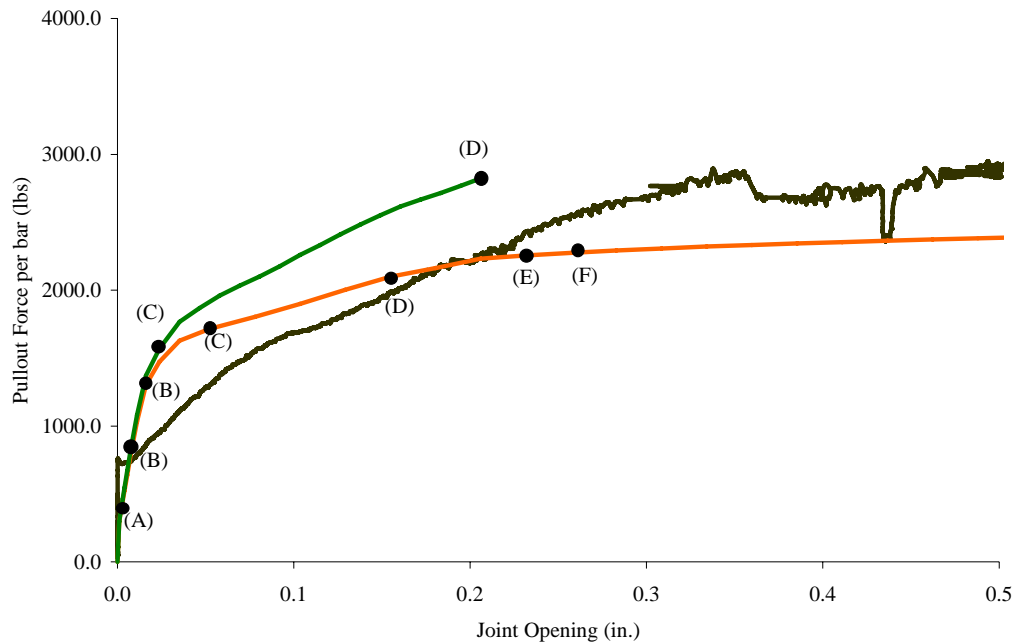


Figure C-41: Comparison of the FEM model with the experimental data for 5H18NU specimen

Table C-82: Summary of Material Failure / Damage Limit States from the analysis

Material Damage / Limit States	Joint Opening (in.)		Pullout Load (lbs)	
	(I)	(II)	(I)	(II)
(A)	0.002	0.002	380.52	386.0
(B)	0.016	0.0077	1302.90	843.0
(C)	0.052	0.023	1715.65	1570.0
(D)	0.155	0.206	2099.70	2820.0
(E)	0.232	-	2256.34	-
(F)	0.257	-	2275.36	-

Results of 5H18AM Finite Element Model

The dowel-concrete friction coefficients and material properties used in the analysis are shown in table C83. A comparison of the pullout force per bar (lbs.) vs. the joint opening (in.) is shown in figure C42. A summary of the various material failure / damage limit states is presented in table C84.

Table C-83: Dowel-Concrete Friction Coefficients; Material Properties used and limit states obtained from the analysis.

	μ_g	μ_w	f'_c (psi)	f'_t (psi)
Case I	0.0	0.30	3500.0	236.64
Case II	0.074	0.384	3880.0	390.0

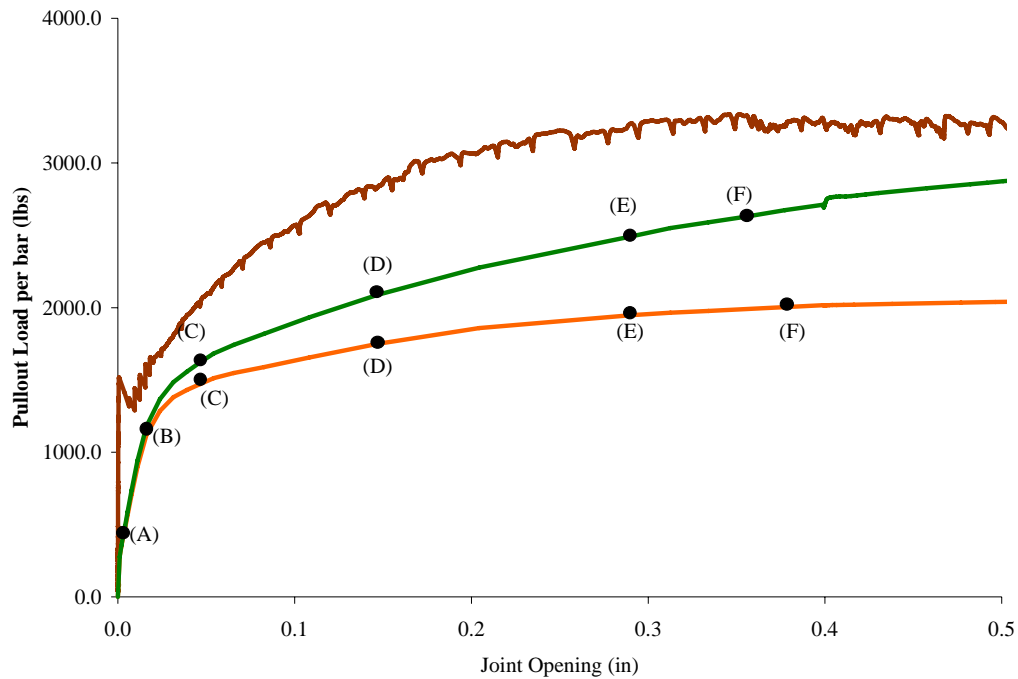


Figure C-42: Comparison of the FEM model with the experimental data for 5H18AM specimen

Table C-84: Summary of Material Failure / Damage Limit States from the analysis

Material Damage / Limit States	Joint Opening (in.)		Pullout Load (lbs)	
	(I)	(II)	(I)	(II)
(A)	0.002	0.002	352.0	357.0
(B)	0.016	0.016	1120.0	1180.0
(C)	0.046	0.046	1470.0	1620.0
(D)	0.146	0.147	1750.0	2090.0
(E)	0.290	0.290	1950.0	2490.0
(F)	0.377	0.355	2000.0	2630.0

Results of 5H36AM Finite Element Model

The dowel-concrete friction coefficients and material properties used in the analysis are shown in table C85. A comparison of the pullout force per bar (lbs.) vs. the joint opening (in.) is shown in figure C43. A summary of the various material failure / damage limit states is presented in table C86.

Table C-85: Dowel-Concrete Friction Coefficients; Material Properties used and limit states obtained from the analysis.

	μ_g	μ_w	f'_c (psi)	f'_t (psi)
Case I	0.0	0.30	3500.0	236.64
Case II	0.074	0.384	3500.0	240.0

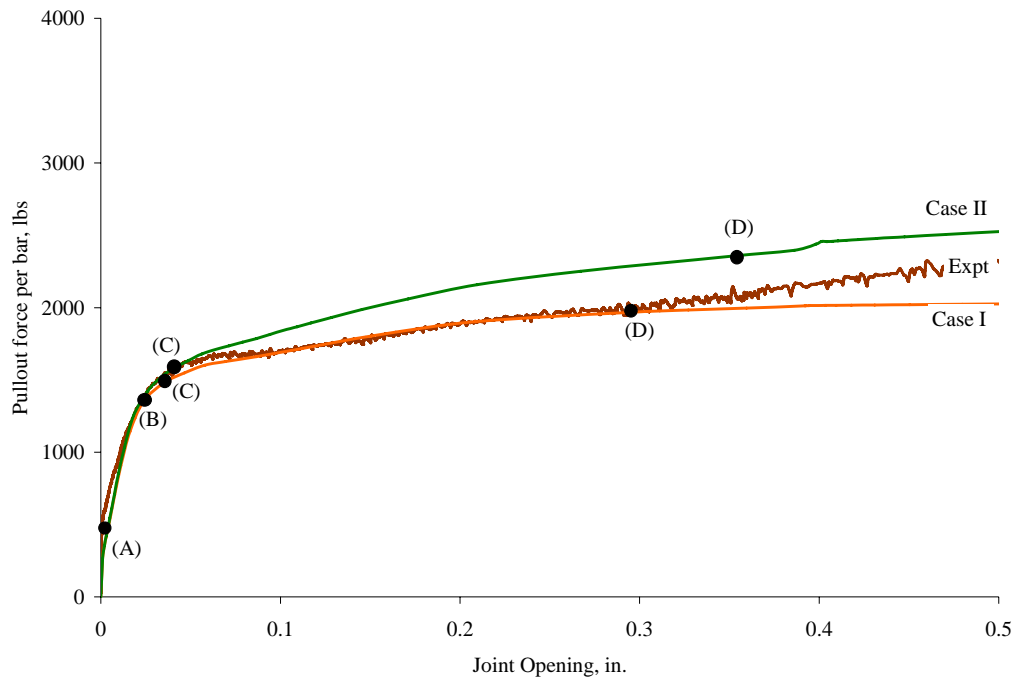


Figure C-43: Comparison of the FEM model with the experimental data for 5H36AM specimen

Table C-86: Summary of Material Failure / Damage Limit States from the analysis

Material Damage / Limit States	Joint Opening (in.)		Pullout Load (lbs)	
	(I)	(II)	(I)	(II)
(A)	0.003	0.003	418.44	422.26
(B)	0.024	0.018	1352.4	1252.1
(C)	0.035	0.041	1480.4	1585.0
(D)	0.295	0.353	1967.8	2358.4
(E)	-	-	-	-
(F)	-	-	-	-

Results of 5C18NU Finite Element Model

The dowel-concrete friction coefficients and material properties used in the analysis are shown in table C87. A comparison of the pullout force per bar (lbs.) vs. the joint opening (in.) is shown in figure C44. A summary of the various material failure / damage limit states is presented in table C88.

Table C-87: Dowel-Concrete Friction Coefficients; Material Properties used and limit states obtained from the analysis.

	μ_g	μ_w	f'_c (psi)	f'_t (psi)
Case I	0.0	0.30	3500.0	236.64
Case II	0.074	0.384	3396.0	251.0

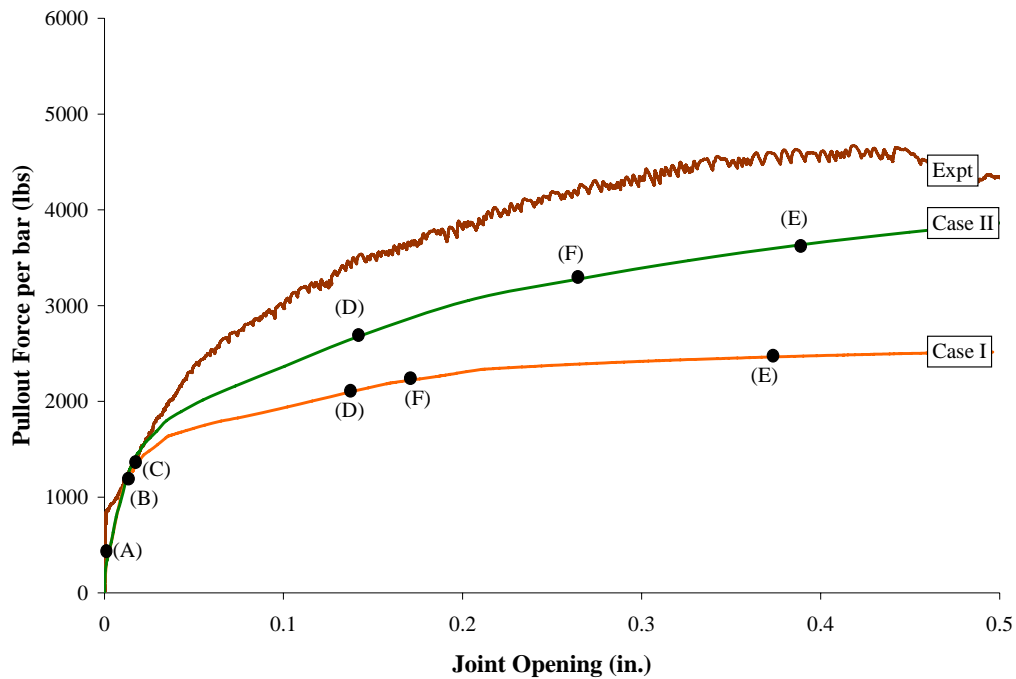


Figure C-44: Comparison of the FEM model with the experimental data for 5C18NU specimen

Table C-88: Summary of Material Failure / Damage Limit States from the analysis

Material Damage / Limit States	Joint Opening (in.)		Pullout Load (lbs)	
	(I)	(II)	(I)	(II)
(A)	0.002	0.002	383.0	385.0
(B)	0.0152	0.012	1340.0	1140.0
(C)	0.0158	0.013	1360.0	1240.0
(D)	0.137	0.142	2100.0	2670.0
(E)	0.373	0.388	2460.0	3630.0
(F)	0.170	0.265	2230.0	3280.0

Results of 5C18AM Finite Element Model

The dowel-concrete friction coefficients and material properties used in the analysis are shown in table C89. A comparison of the pullout force per bar (lbs.) vs. the joint opening (in.) is shown in figure C45. A summary of the various material failure / damage limit states is presented in table C90.

Table C-89: Dowel-Concrete Friction Coefficients; Material Properties used and limit states obtained from the analysis.

	μ_g	μ_w	f'_c (psi)	f'_t (psi)
Case I	0.0	0.30	3500.0	236.64
Case II	0.074	0.384		

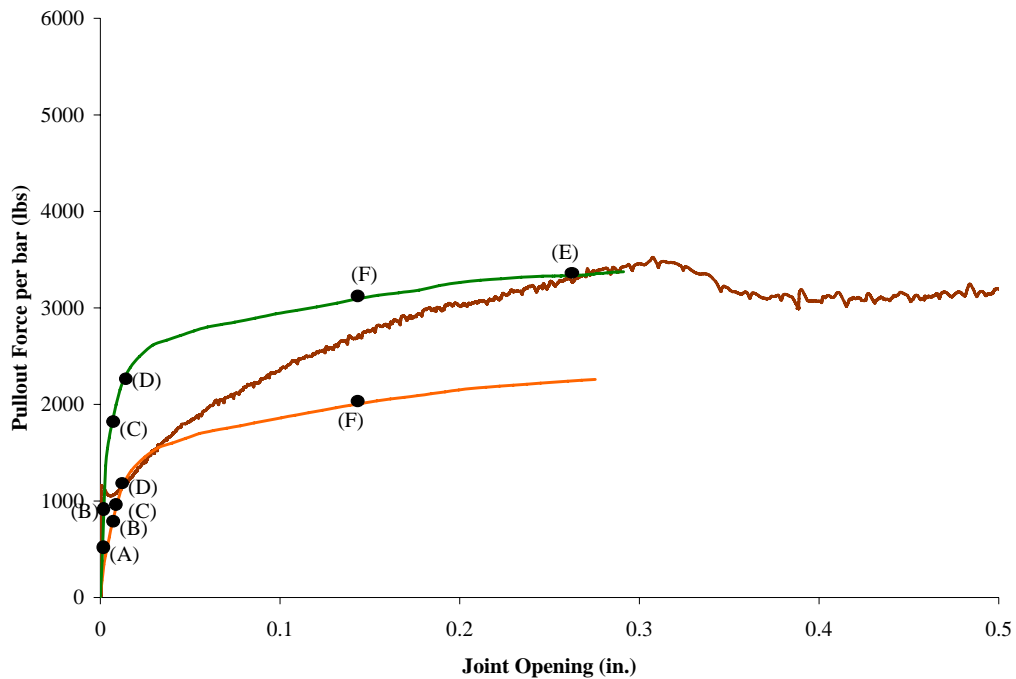


Figure C-45: Comparison of the FEM model with the experimental data for 5C18AM specimen

Table C-90: Summary of Material Failure / Damage Limit States from the analysis

Material Damage / Limit States	Joint Opening (in.)		Pullout Load (lbs)	
	(I)	(II)	(I)	(II)
(A)	0.003	0.003	439.0	1360.0
(B)	0.004	0.004	531.0	1550.0
(C)	0.006	0.006	759.0	1810.0
(D)	0.012	0.013	1140.0	2270.0
(E)	-	0.254	-	3330.0
(F)	0.154	0.143	2040.0	3090.0

Results of 5C36AM Finite Element Model

The dowel-concrete friction coefficients and material properties used in the analysis are shown in table C91. A comparison of the pullout force per bar (lbs.) vs. the joint opening (in.) is shown in figure C46. A summary of the various material failure / damage limit states is presented in table C92.

Table C-91: Dowel-Concrete Friction Coefficients; Material Properties used and limit states obtained from the analysis.

	μ_g	μ_w	f'_c (psi)	f'_t (psi)
Case I	0.0	0.30	3500.0	236.64
Case II	0.074	0.384	3860.0	269.0

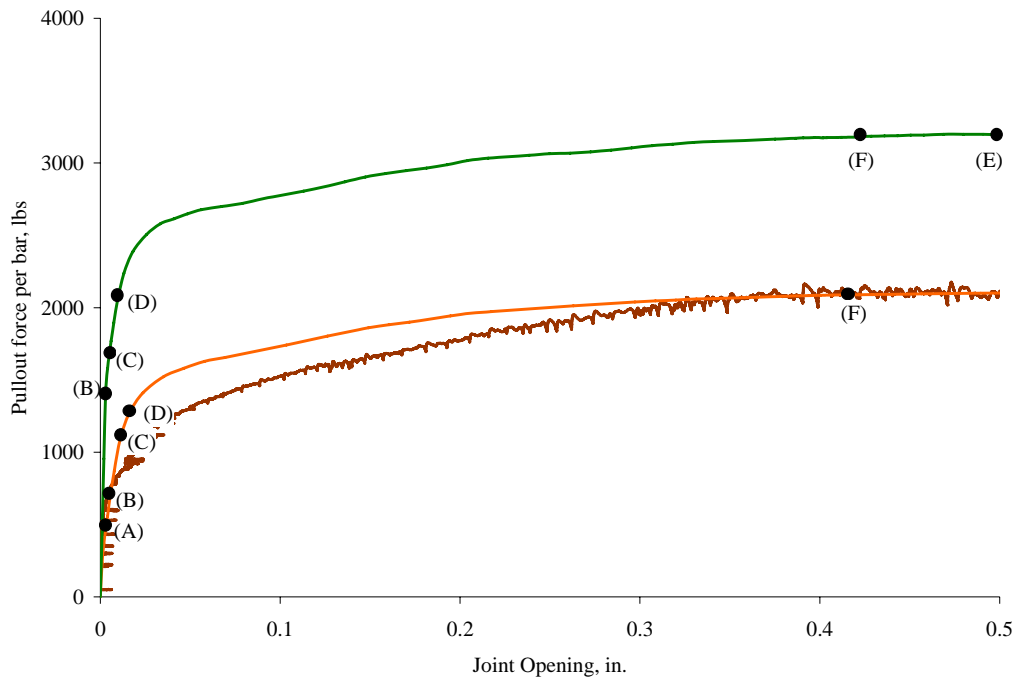


Figure C-46: Comparison of the FEM model with the experimental data for 5C36AM specimen

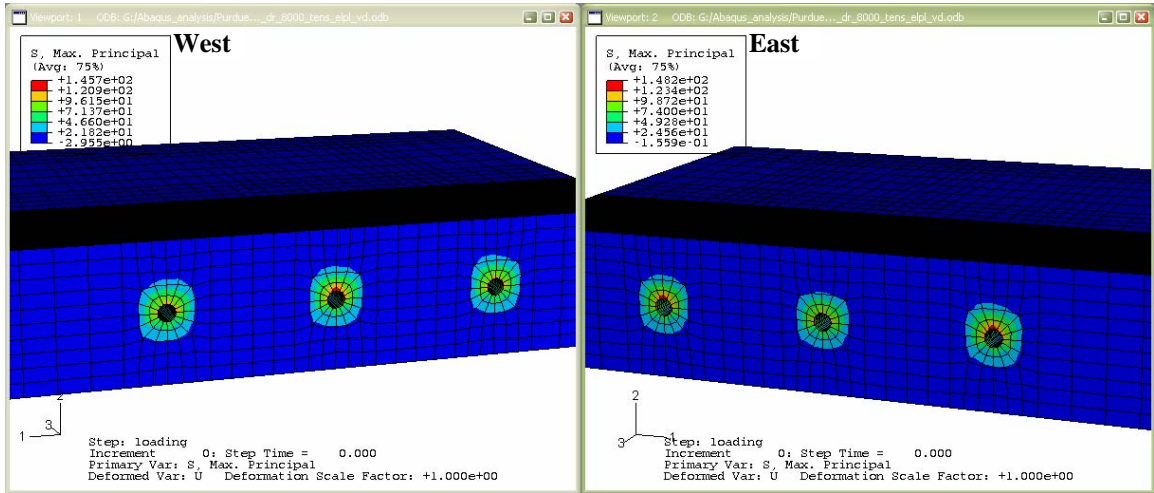
Table C-92: Summary of Material Failure / Damage Limit States from the analysis

Material Damage / Limit States	Joint Opening (in.)		Pullout Load (lbs)	
	(I)	(II)	(I)	(II)
(A)	0.003	0.003	465.0	500.0
(B)	0.005	0.006	693.0	1770.0
(C)	0.011	0.009	1100.0	2060.0
(D)	0.016	0.018	1270.0	2390.0
(E)	-	0.50	-	3200.0
(F)	0.412	0.429	2090.0	3180.0

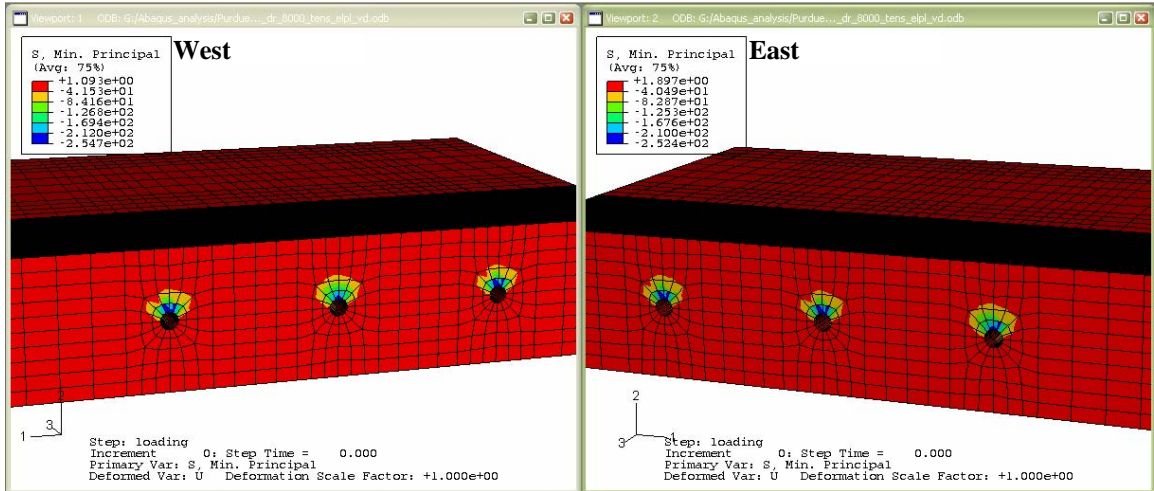
APPENDIX D

**RESULTS OF THREE DOWEL BARS WITH TYPICAL
MISALIGNMENT COMBINED WITH LOADING EFFECTS**

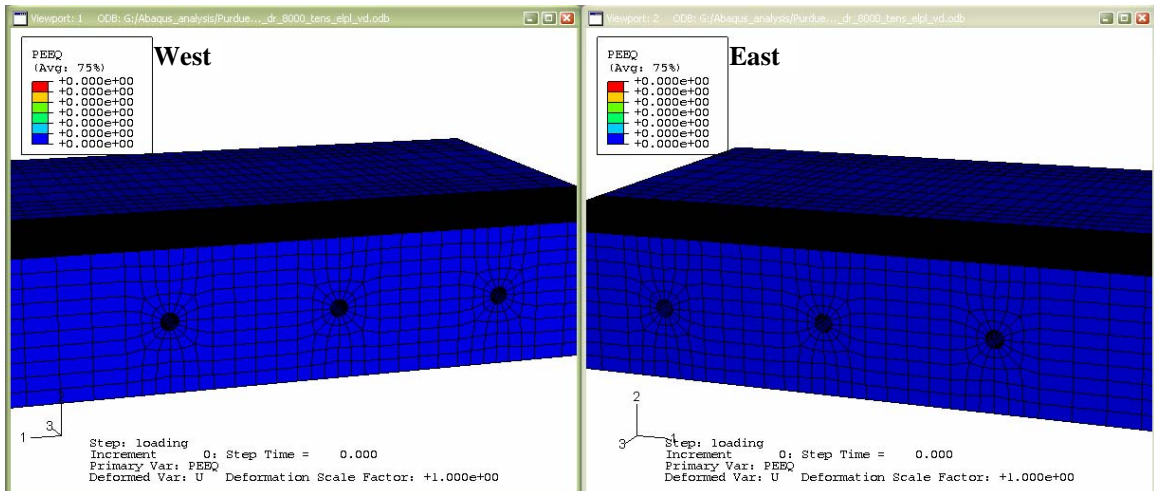
BEHAVIOR OF 3A FINITE ELEMENT MODEL



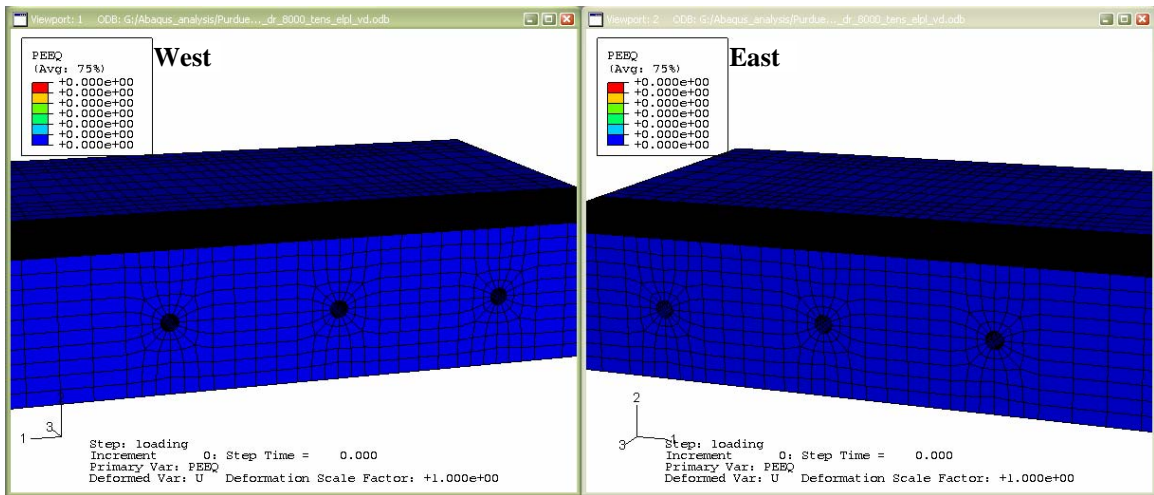
(a) Maximum Tensile Stresses at joint opening of 1/8 in.



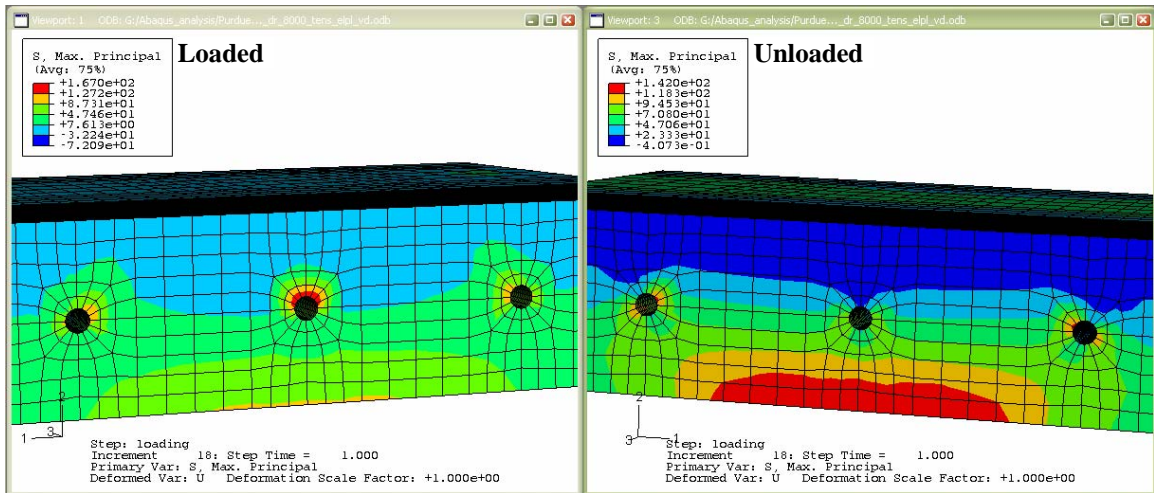
(b) Maximum Compressive Stresses at joint opening of 1/8 in.



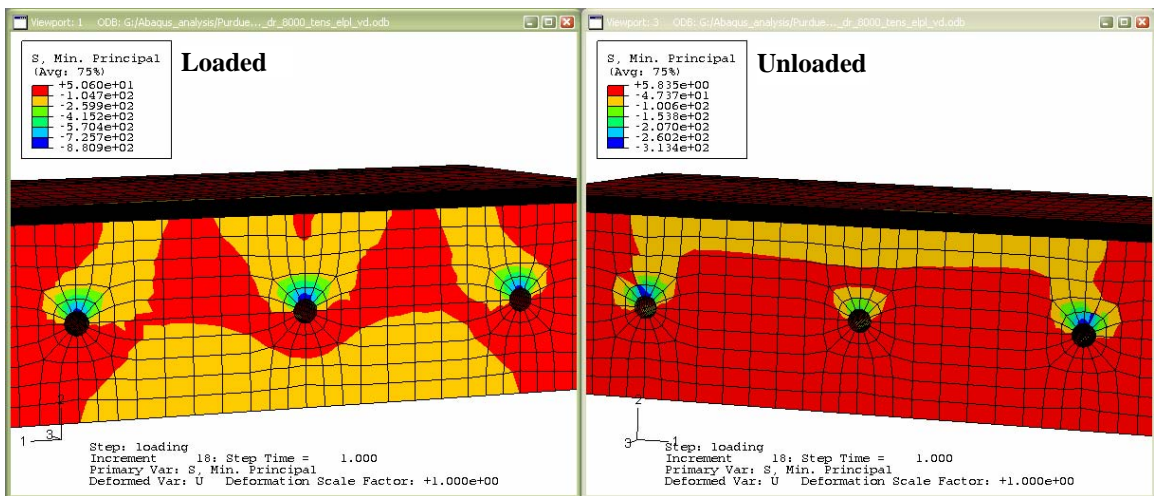
(c) Maximum Compressive Strains at joint opening of 1/8 in.



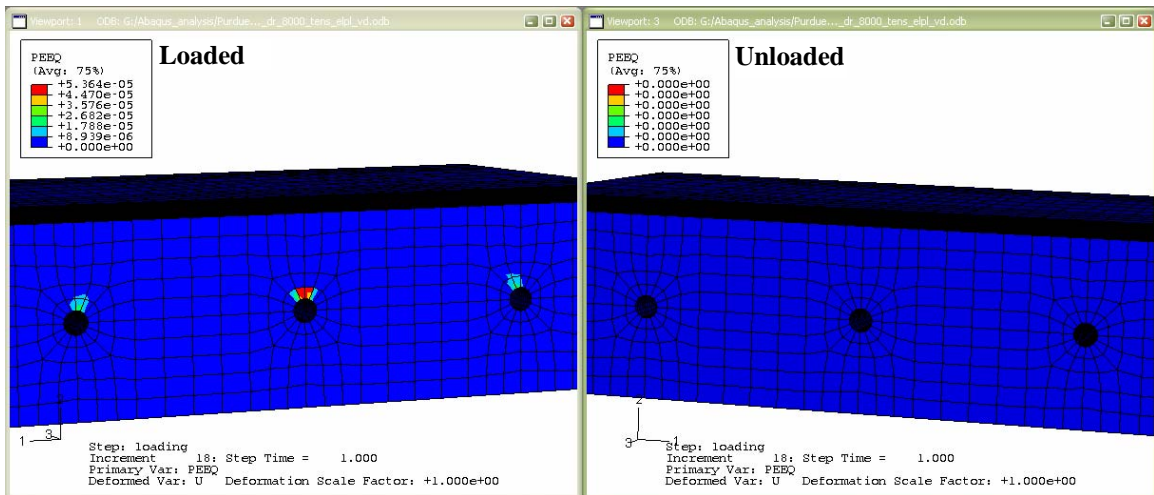
(d) Maximum Tensile Strains at joint opening of 1/8 in.
Figure D-1: Stress and Strains for 3A slab model at joint opening of 1/8 in.



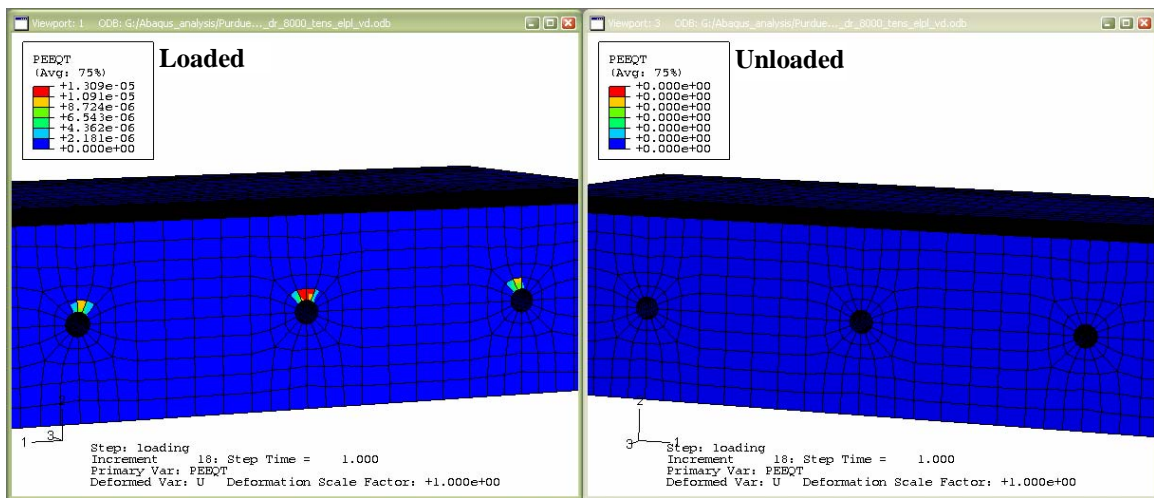
(a) Maximum Tensile Stresses at end of load application



(b) Maximum Compressive Stresses at end of load application



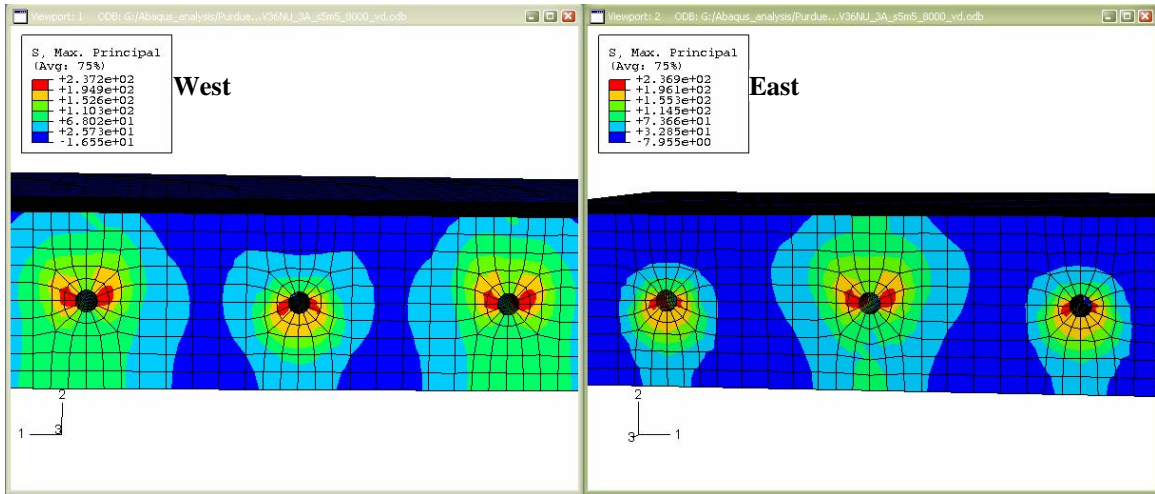
(c) Inelastic Compressive Strains at end of load application



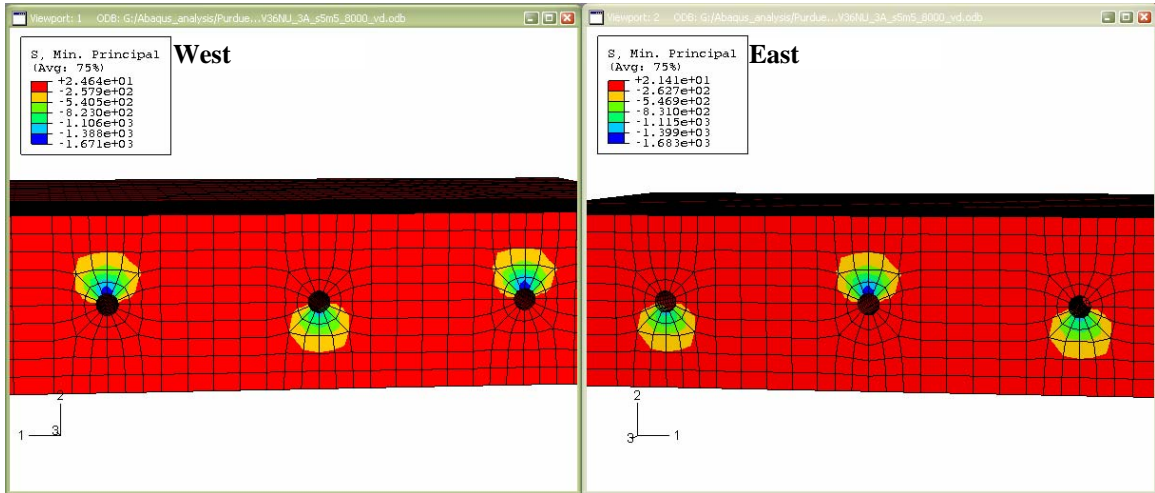
(d) Inelastic Tensile Strains at end of load application

Figure D-2: Stresses and Strains for 3A model after load application

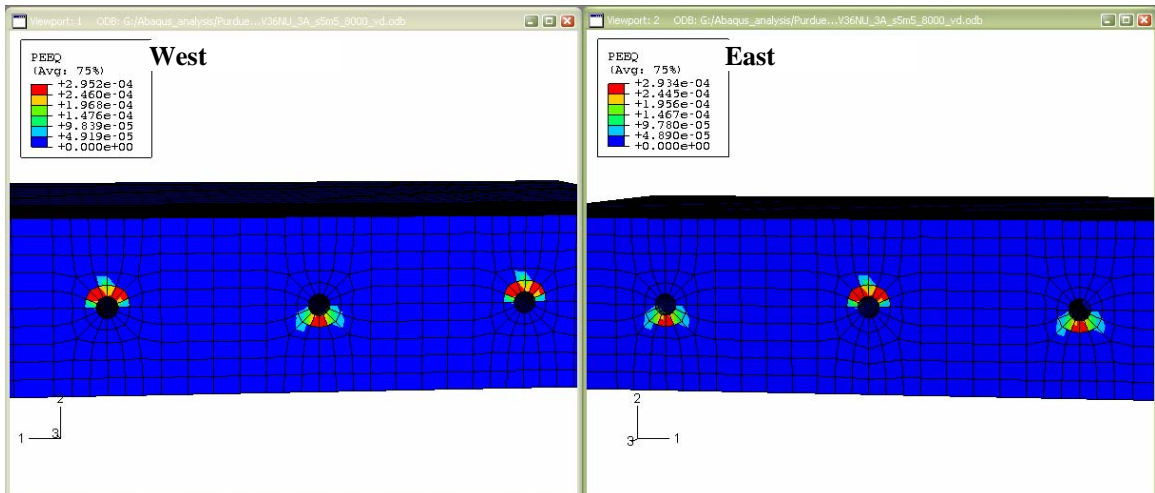
BEHAVIOR OF 3V36NU FINITE ELEMENT MODEL



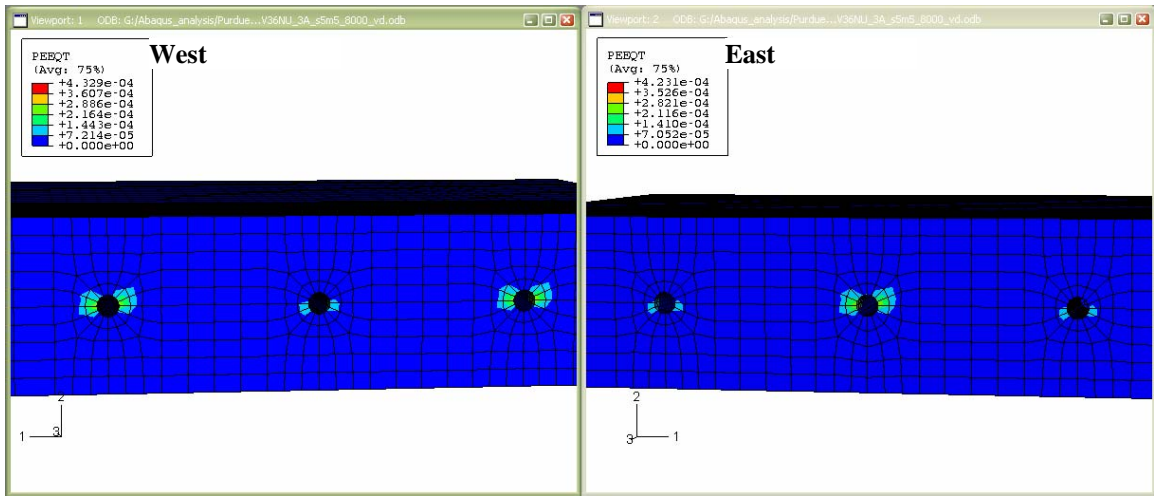
(a) Maximum Tensile Stresses at joint opening of 1/8 in.



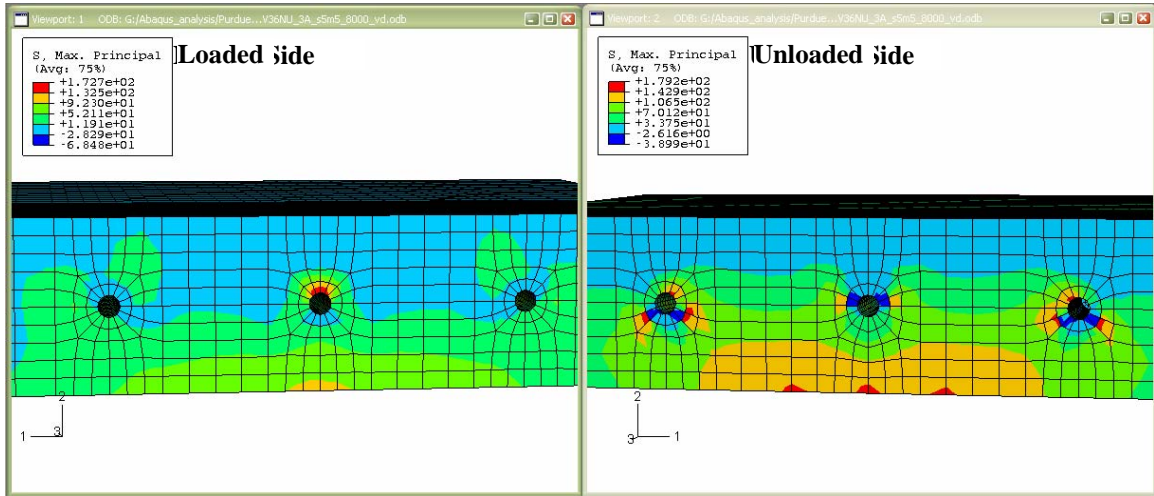
(b) Maximum Compressive Stresses at joint opening of 1/8 in.



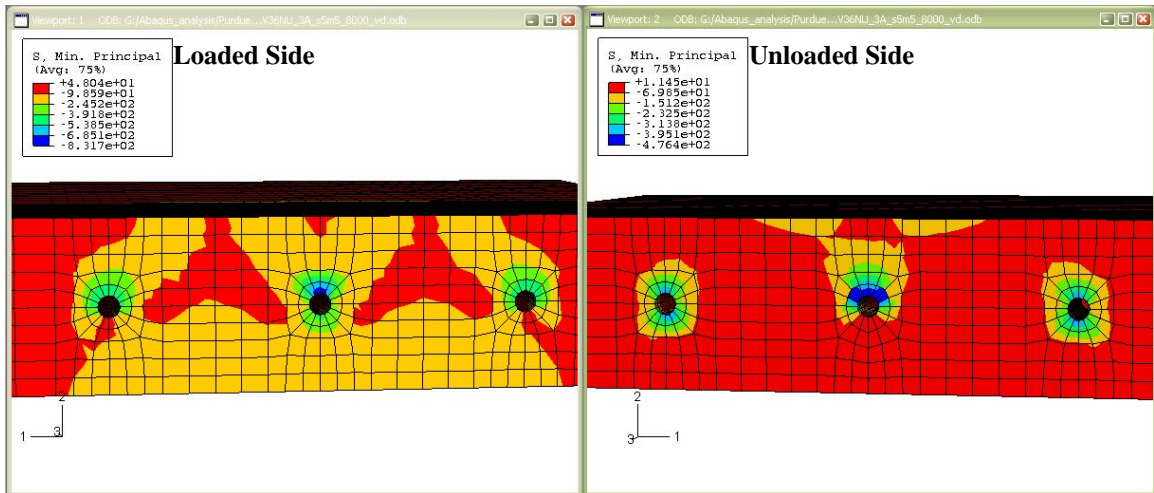
(c) Maximum Compressive Strains at joint opening of 1/8 in.



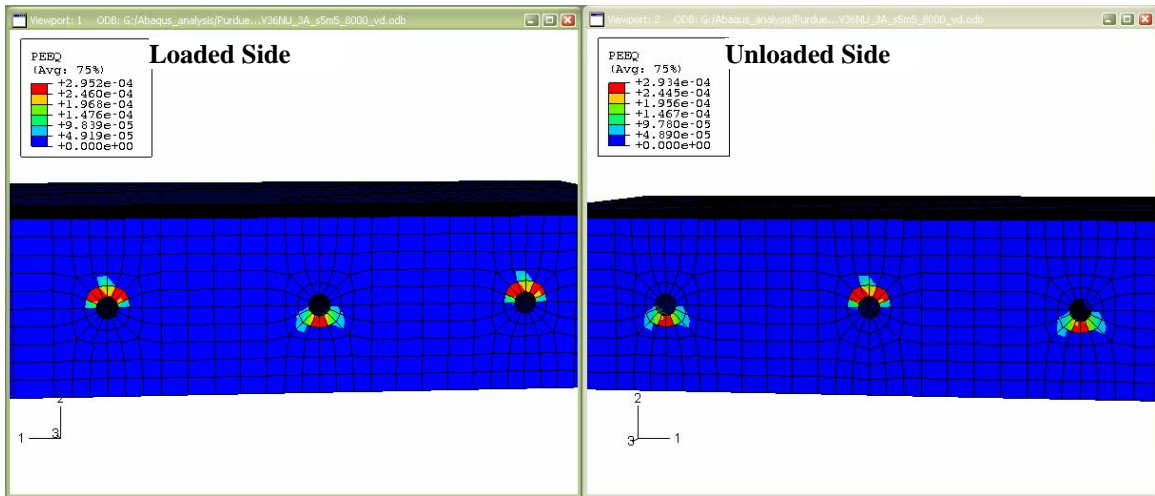
(d) Maximum Tensile Strains at joint opening of 1/8 in.
Figure D-3: Stress and Strains for 3V36NU slab model at joint opening of 1/8 in.



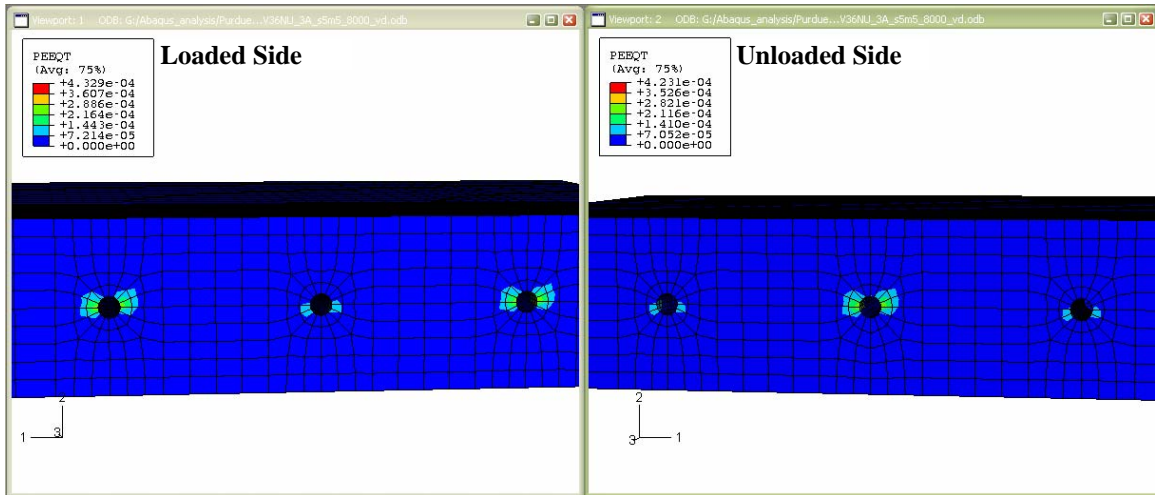
(a) Maximum Tensile Stresses at end of load application



(b) Maximum Compressive Stresses at end of load application



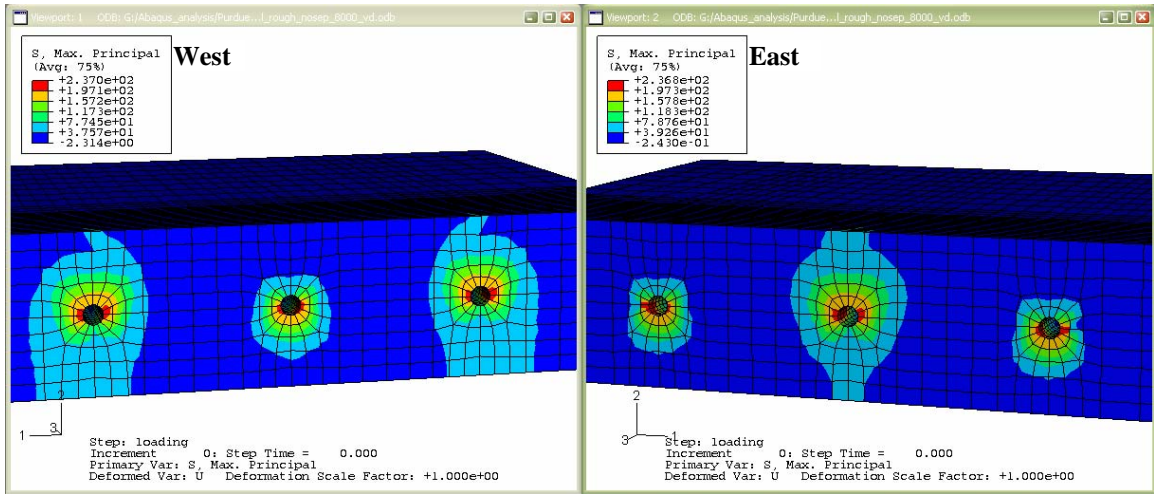
(c) Inelastic Compressive Strains at end of load application



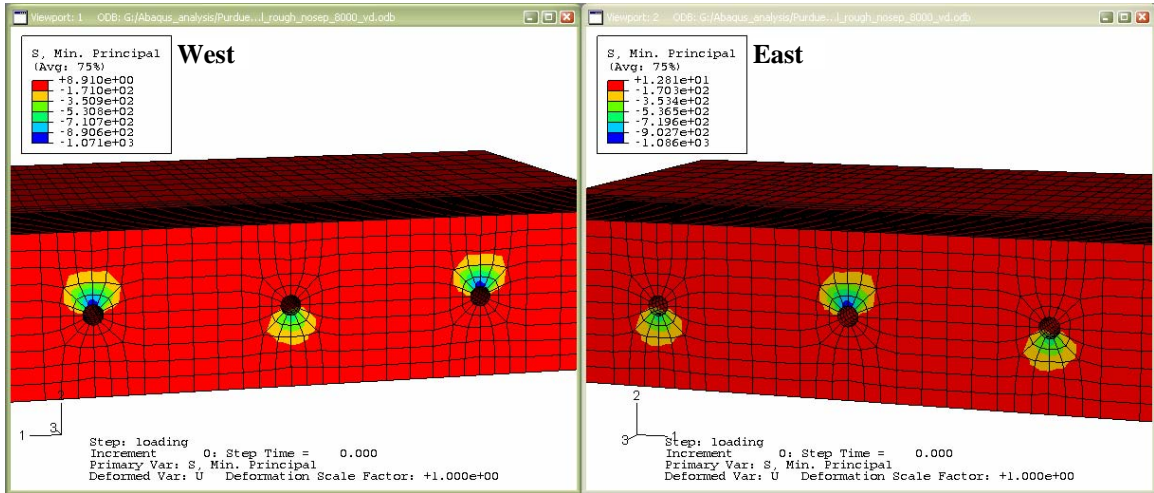
(d) Inelastic Tensile Strains at end of load application

Figure D-4: Stresses and Strains for 3V36NU model after load application

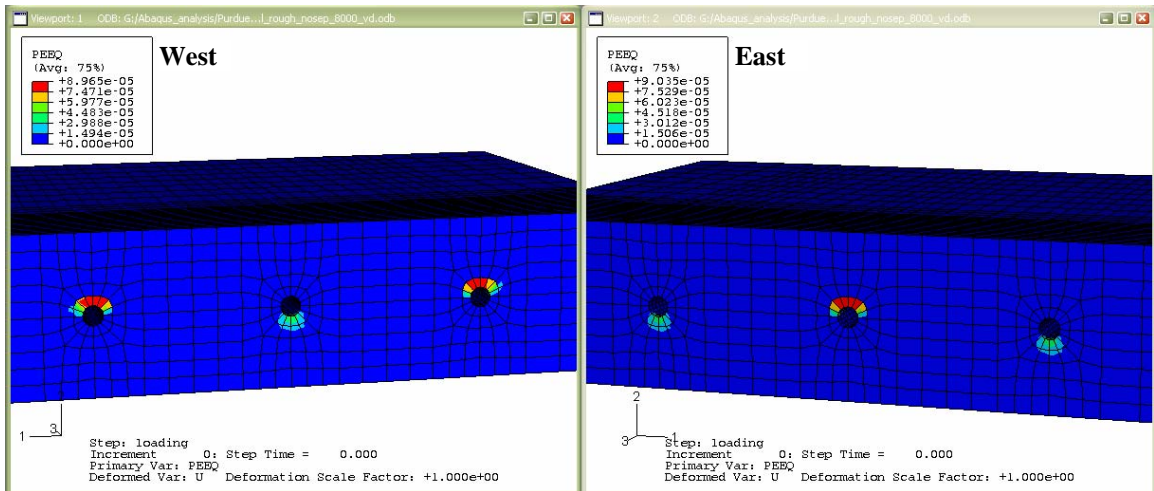
BEHAVIOR OF 3V72NU FINITE ELEMENT MODEL



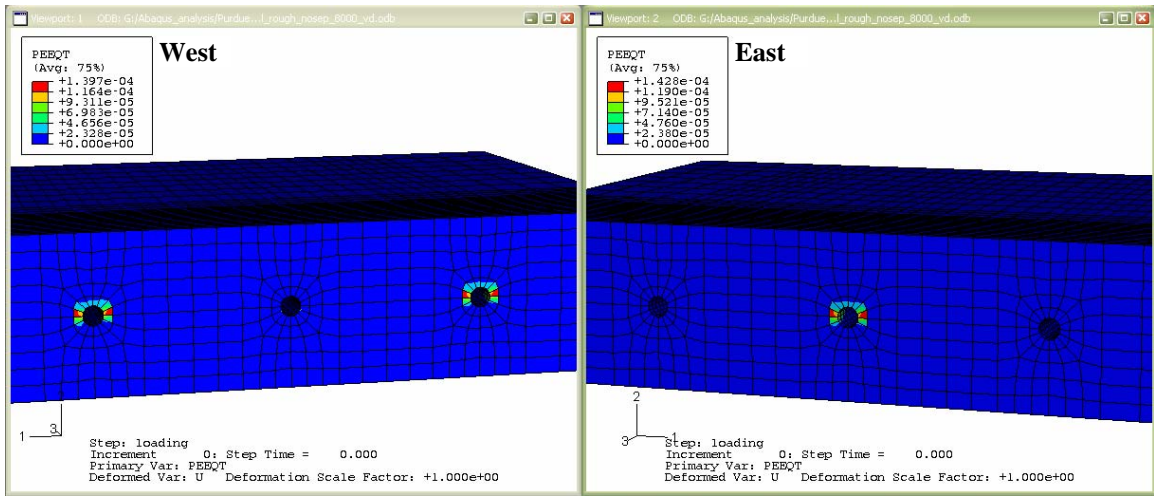
(a) Maximum Tensile Stresses at joint opening of 1/8 in.



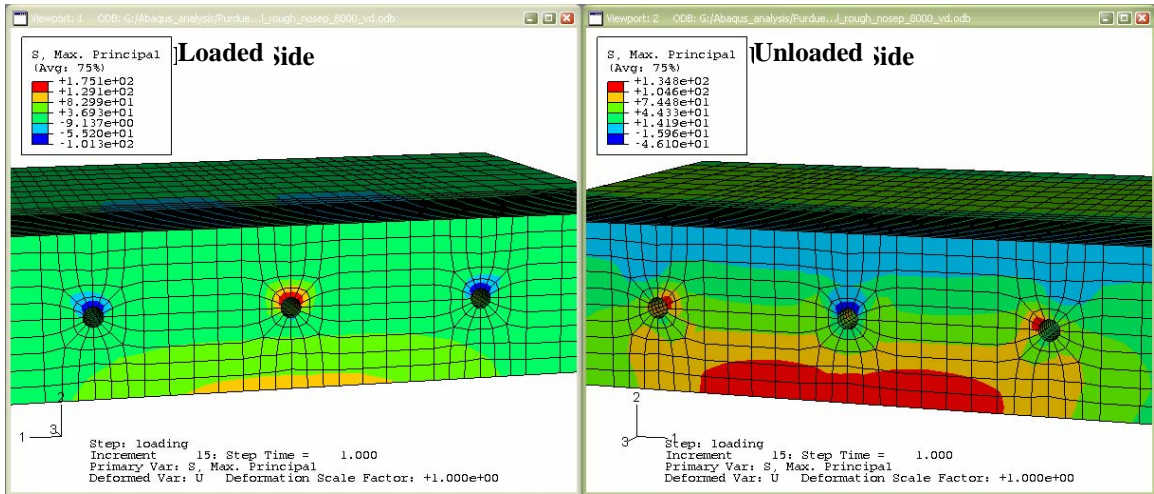
(b) Maximum Compressive Stresses at joint opening of 1/8 in.



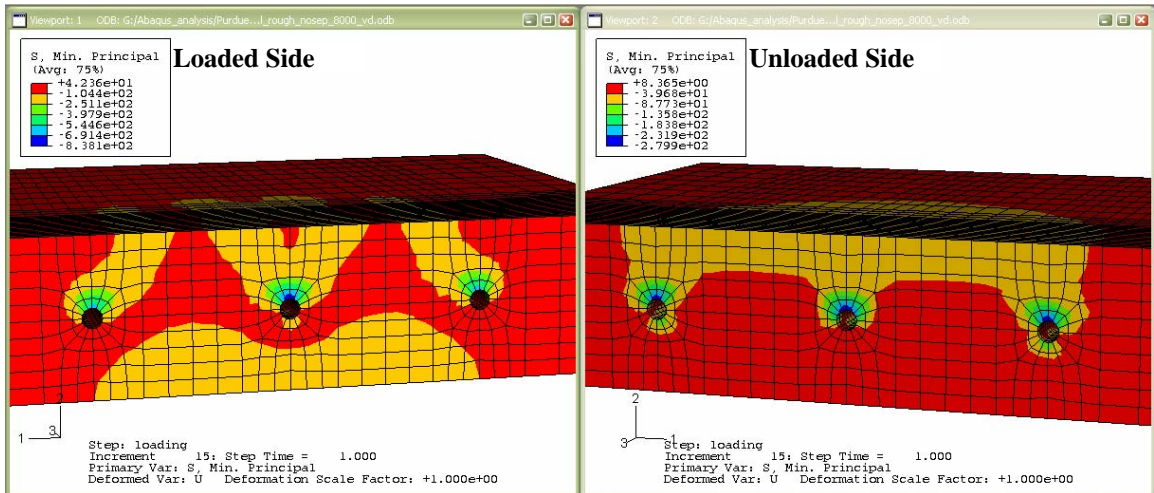
(c) Maximum Compressive Strains at joint opening of 1/8 in.



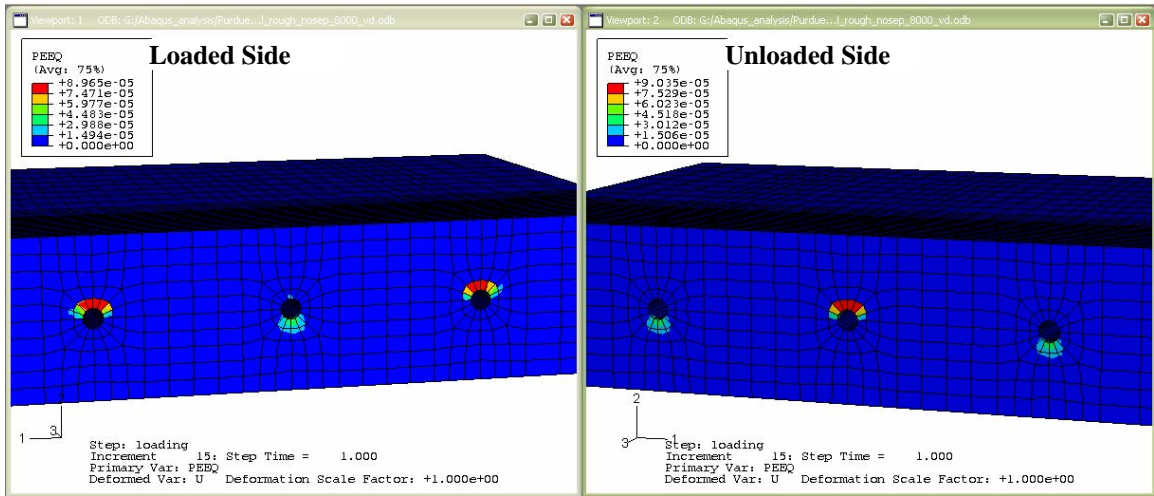
(d) Maximum Tensile Strains at joint opening of 1/8 in.
Figure D-5: Stress and Strains for 3V36AM slab model at joint opening of 1/8 in.



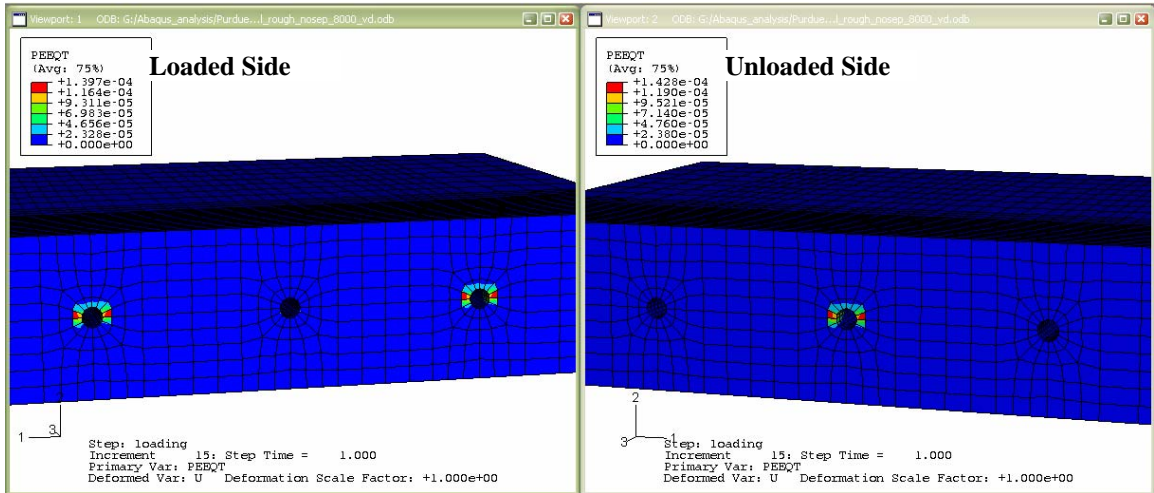
(a) Maximum Tensile Stresses at end of load application



(b) Maximum Compressive Stresses at end of load application



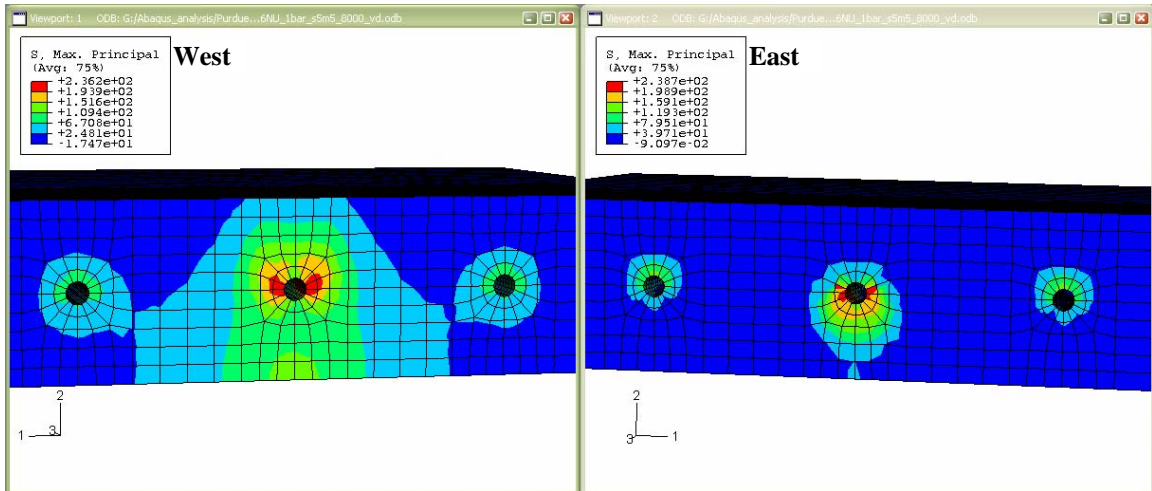
(c) Inelastic Compressive Strains at end of load application



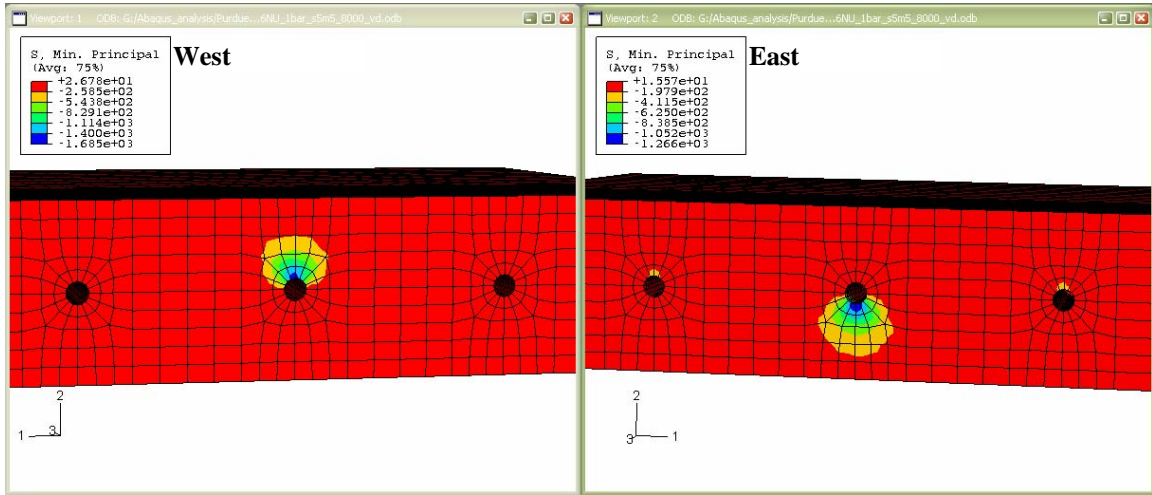
(d) Inelastic Tensile Strains at end of load application

Figure D-6: Stresses and Strains for 3V72NU model after load application

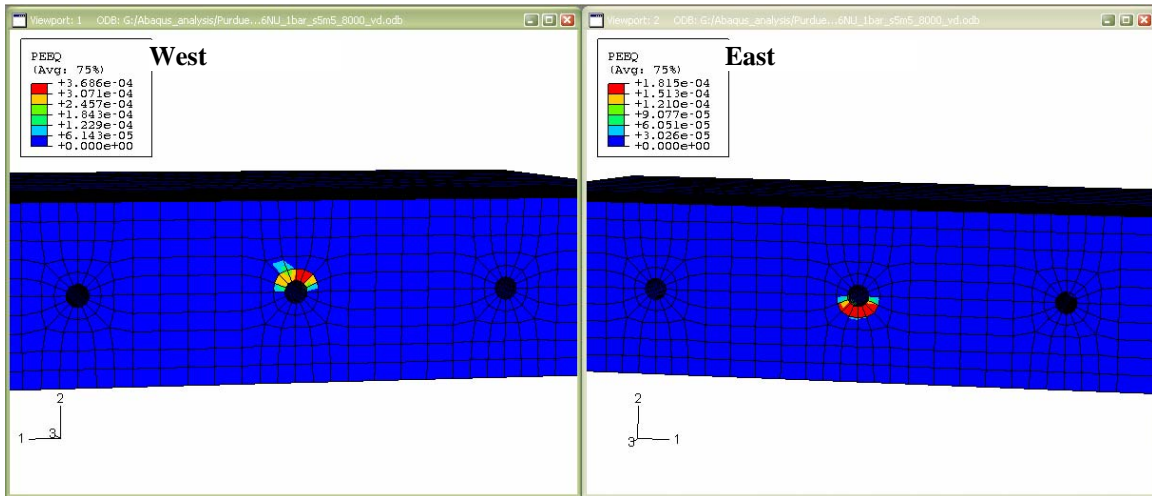
BEHAVIOR OF 3V36AM FINITE ELEMENT MODEL



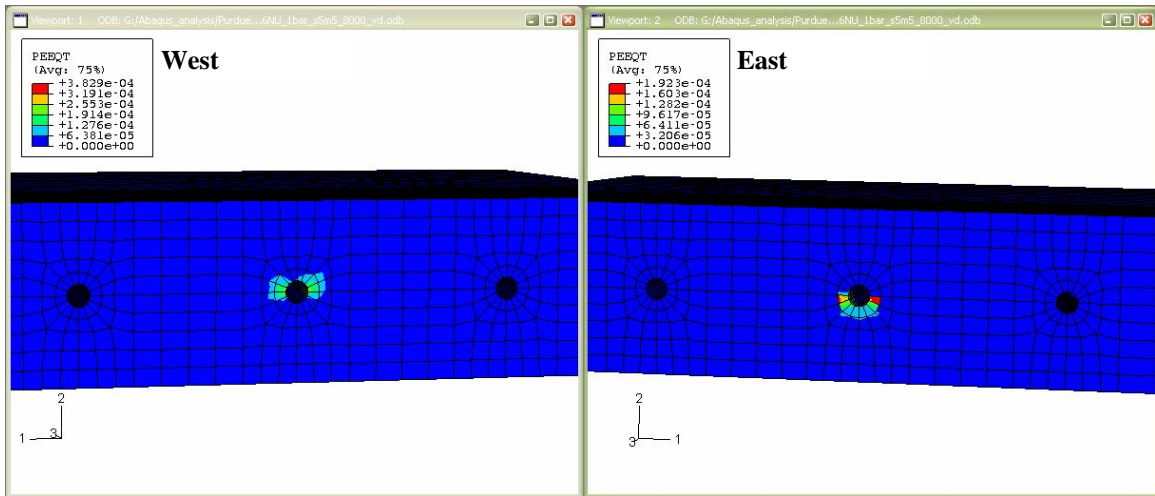
(a) Maximum Tensile Stresses at joint opening of 1/8 in.



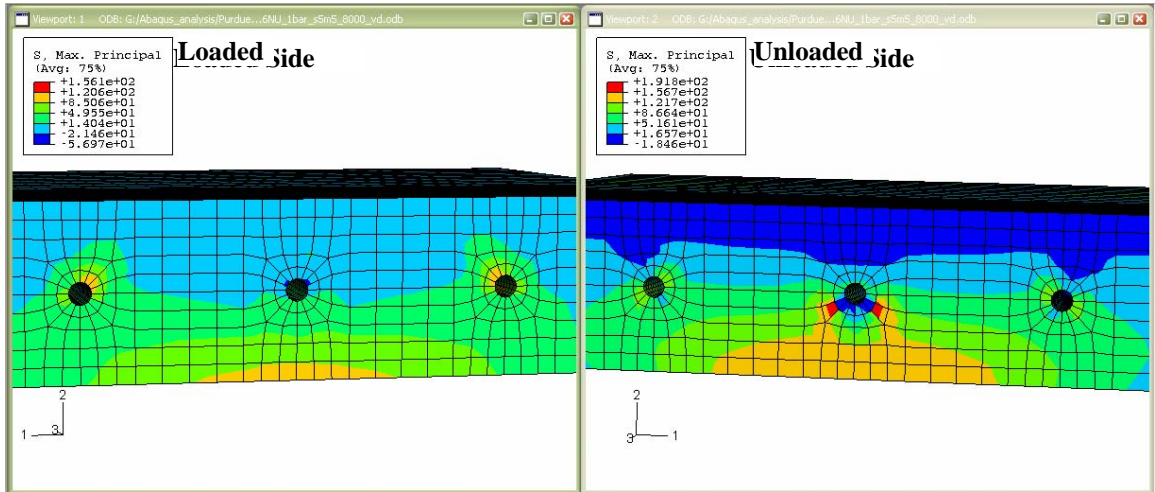
(b) Maximum Compressive Stresses at joint opening of 1/8 in.



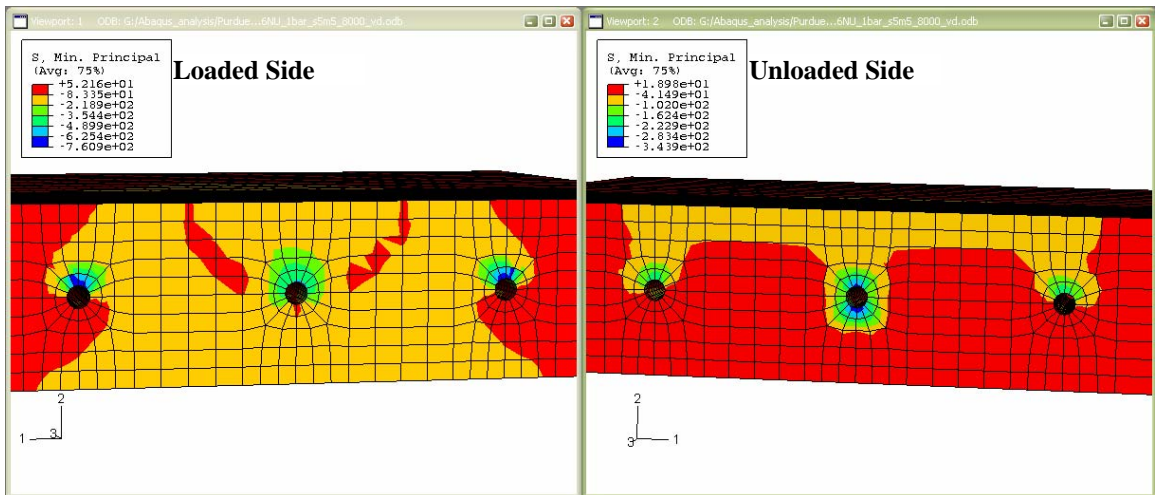
(c) Maximum Compressive Strains at joint opening of 1/8 in.



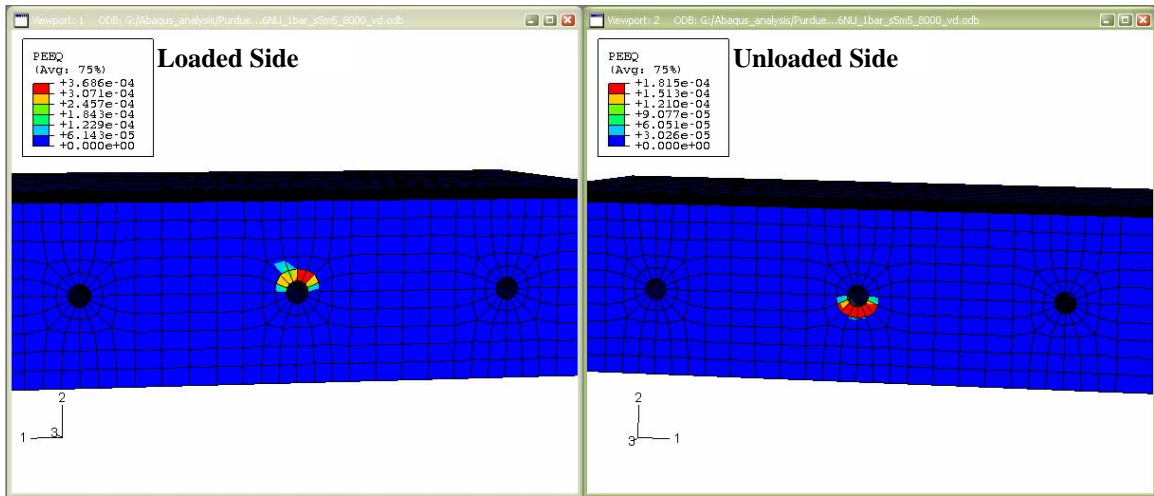
(d) Maximum Tensile Strains at joint opening of 1/8 in.
Figure D-7: Stress and Strains for 3V36AM slab model at joint opening of 1/8 in.



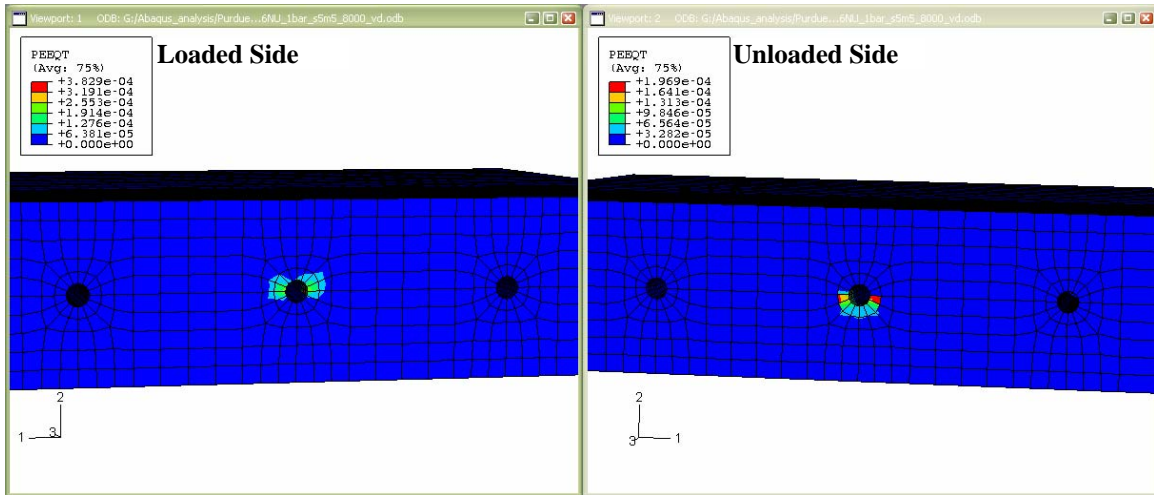
(a) Maximum Tensile Stresses at end of load application



(b) Maximum Compressive Stresses at end of load application



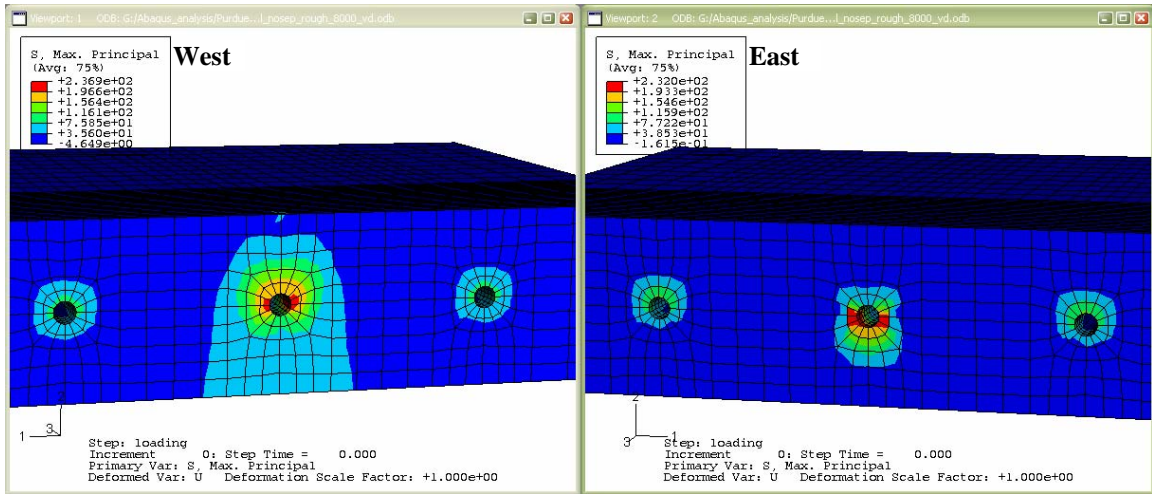
(c) Inelastic Compressive Strains at end of load application



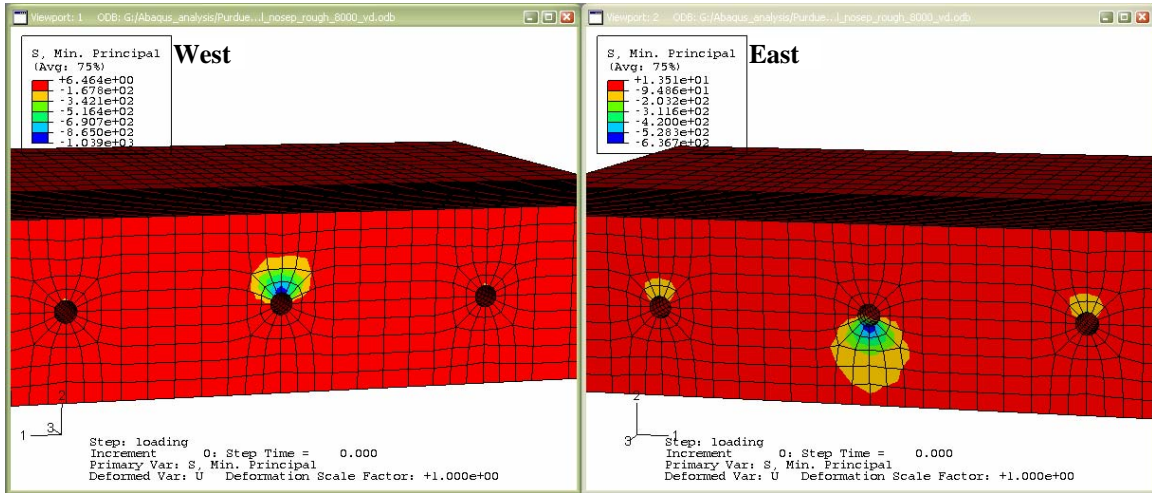
(d) Inelastic Tensile Strains at end of load application

Figure D-8: Stresses and Strains for 3V36AM model after load application

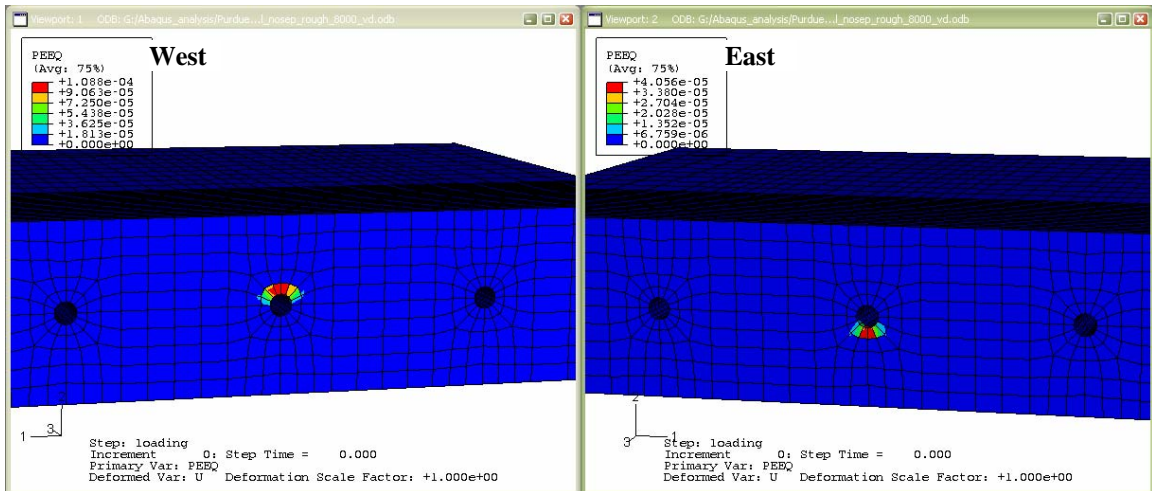
BEHAVIOR OF 3V72AM FINITE ELEMENT MODEL



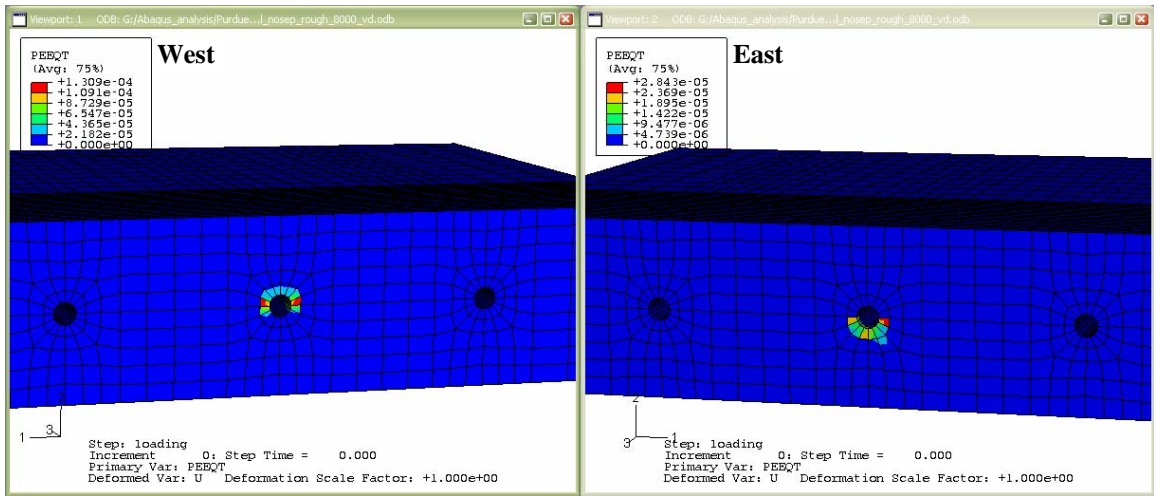
(a) Maximum Tensile Stresses at joint opening of 1/8 in.



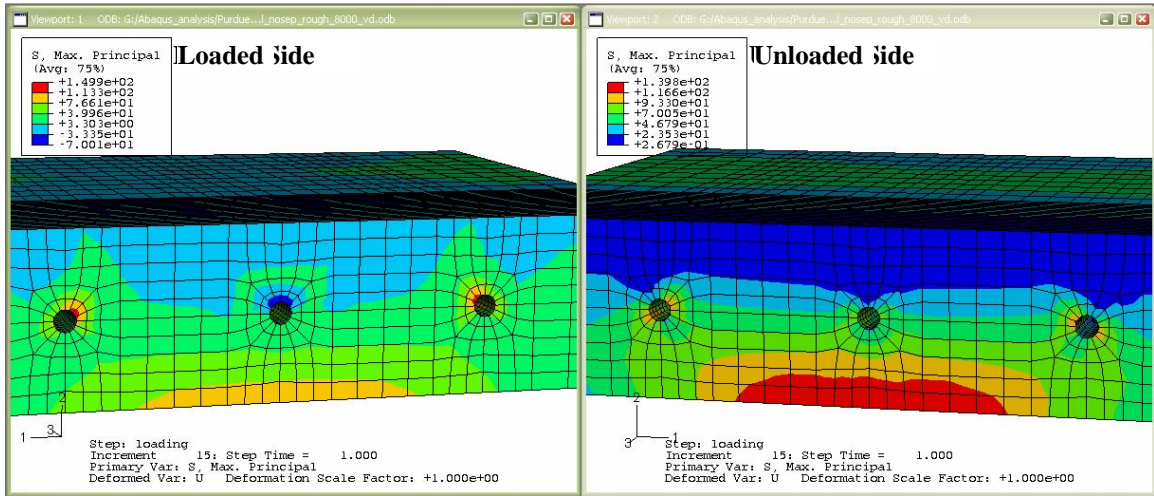
(b) Maximum Compressive Stresses at joint opening of 1/8 in.



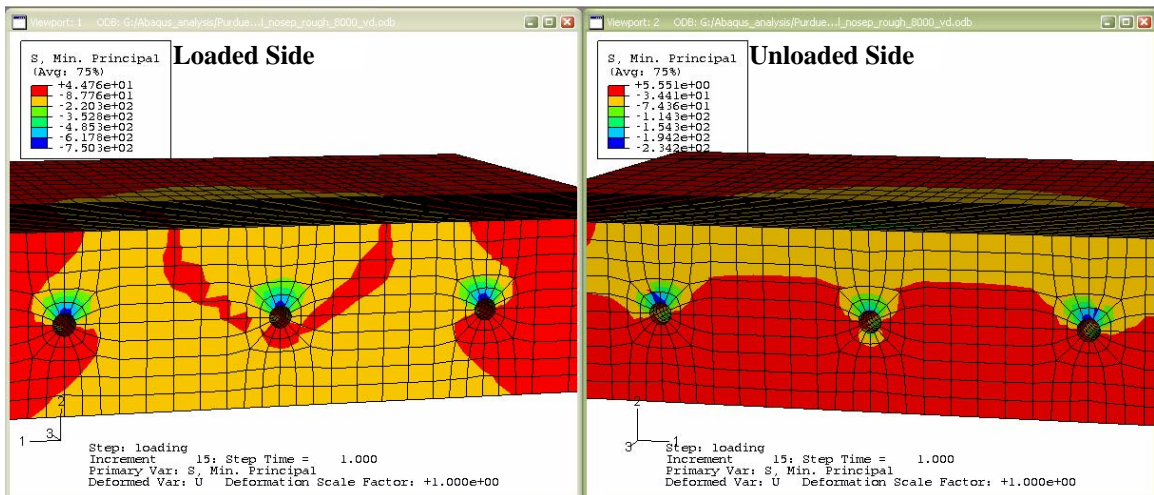
(c) Maximum Compressive Strains at joint opening of 1/8 in.



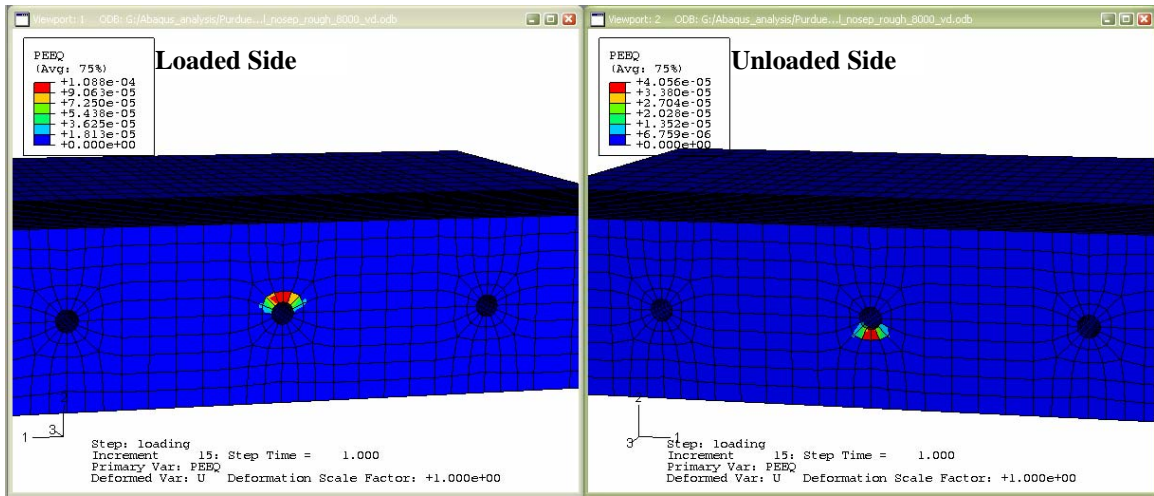
(d) Maximum Tensile Strains at joint opening of 1/8 in.
Figure D-9: Stress and Strains for 3V72AM slab model at joint opening of 1/8 in.



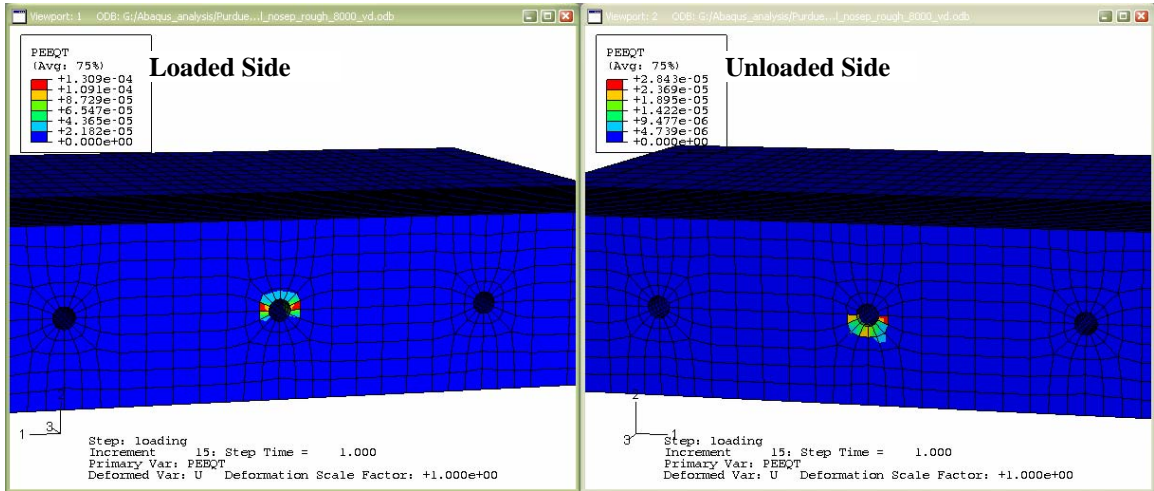
(a) Maximum Tensile Stresses at end of load application



(b) Maximum Compressive Stresses at end of load application



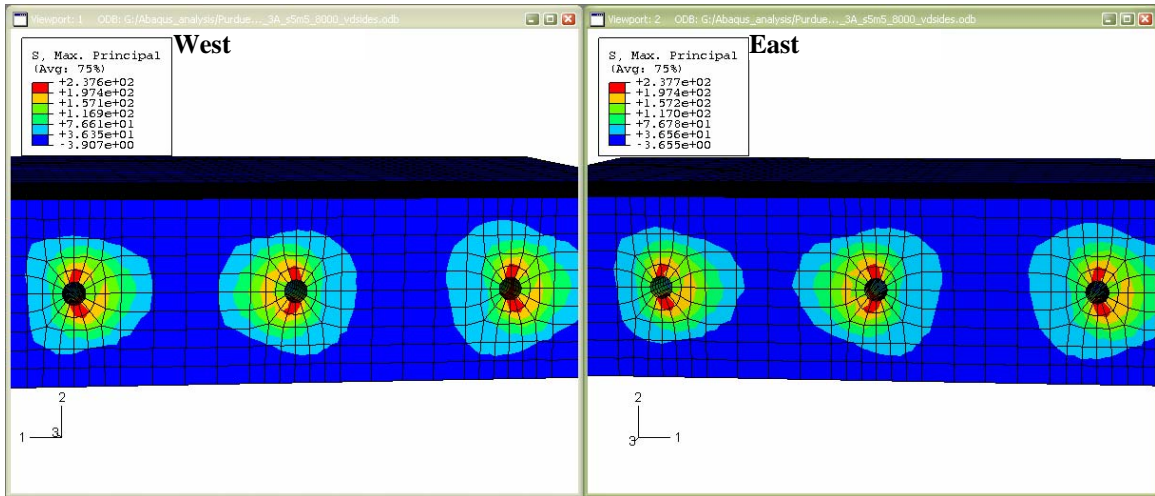
(c) Inelastic Compressive Strains at end of load application



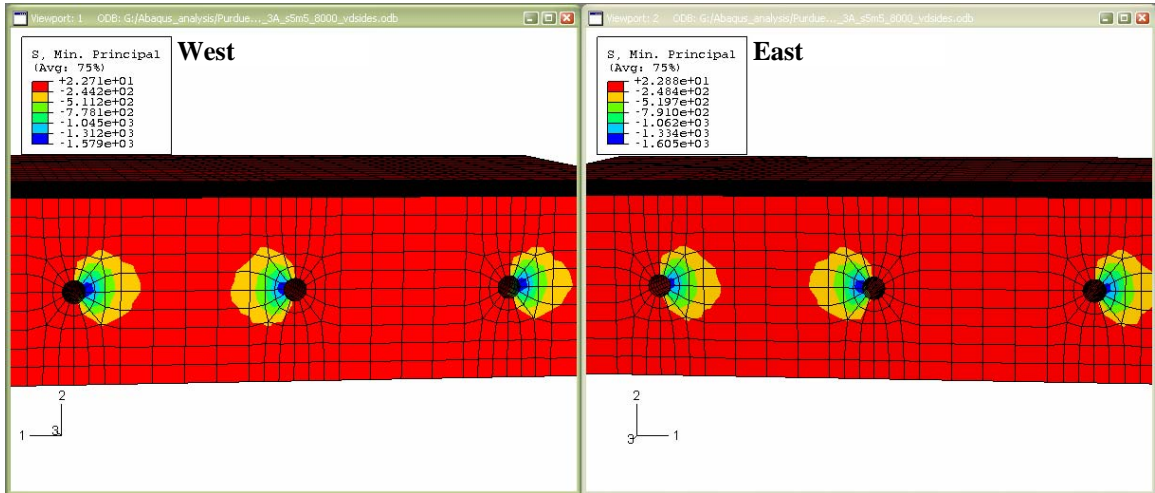
(d) Inelastic Tensile Strains at end of load application

Figure D-10: Stresses and Strains for 3V72AM model after load application

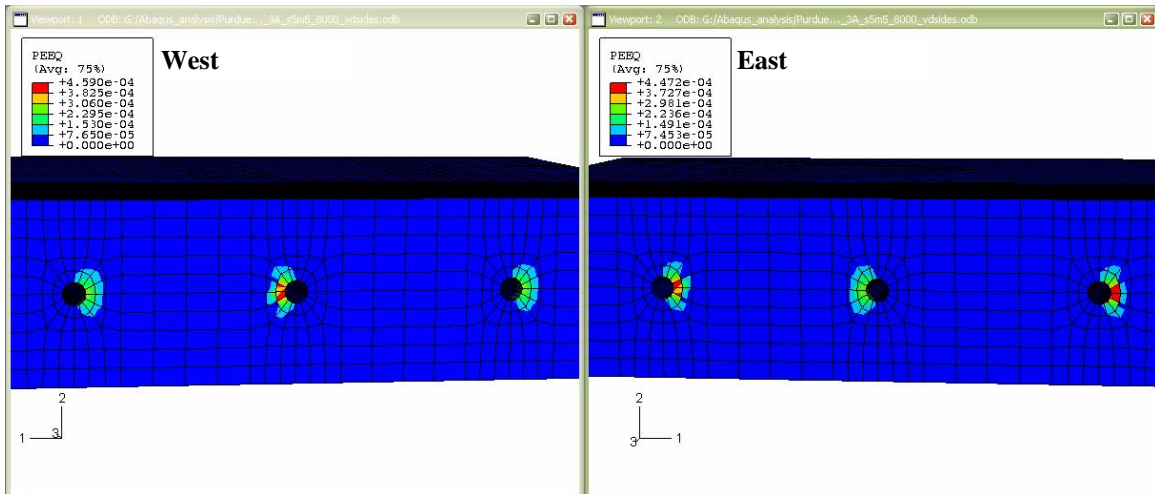
BEHAVIOR OF 3H36NU FINITE ELEMENT MODEL



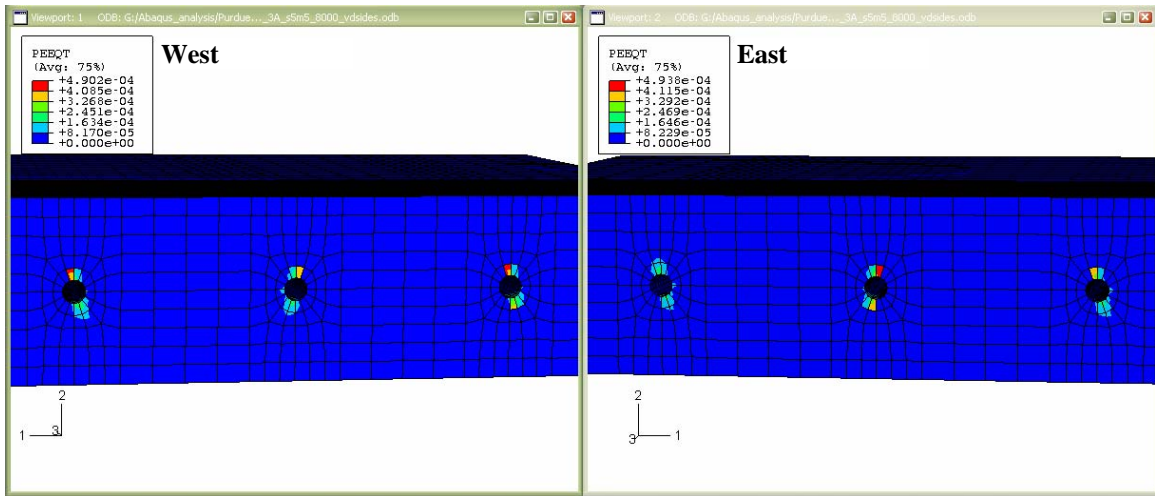
(a) Maximum Tensile Stresses at joint opening of 1/8 in.



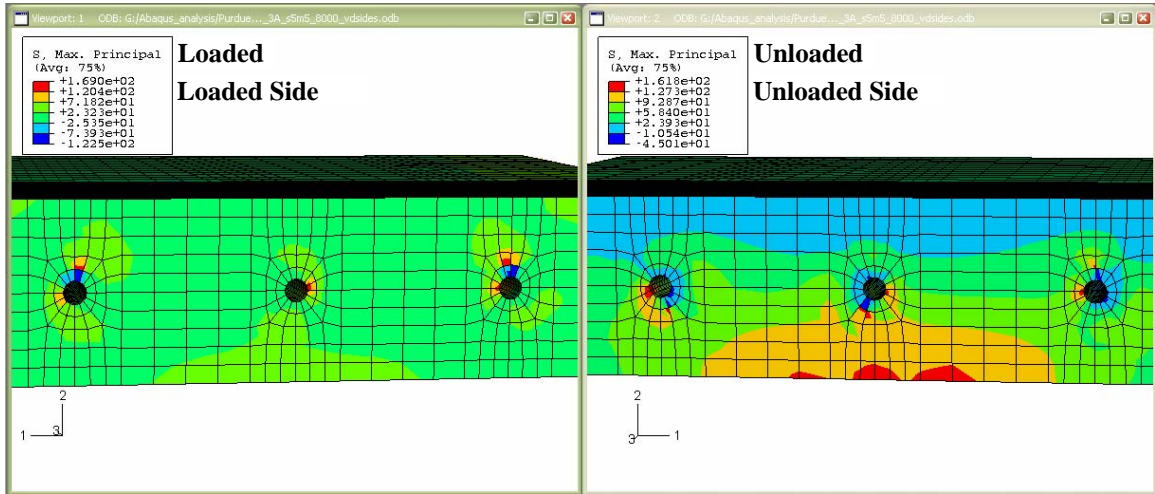
(b) Maximum Compressive Stresses at joint opening of 1/8 in.



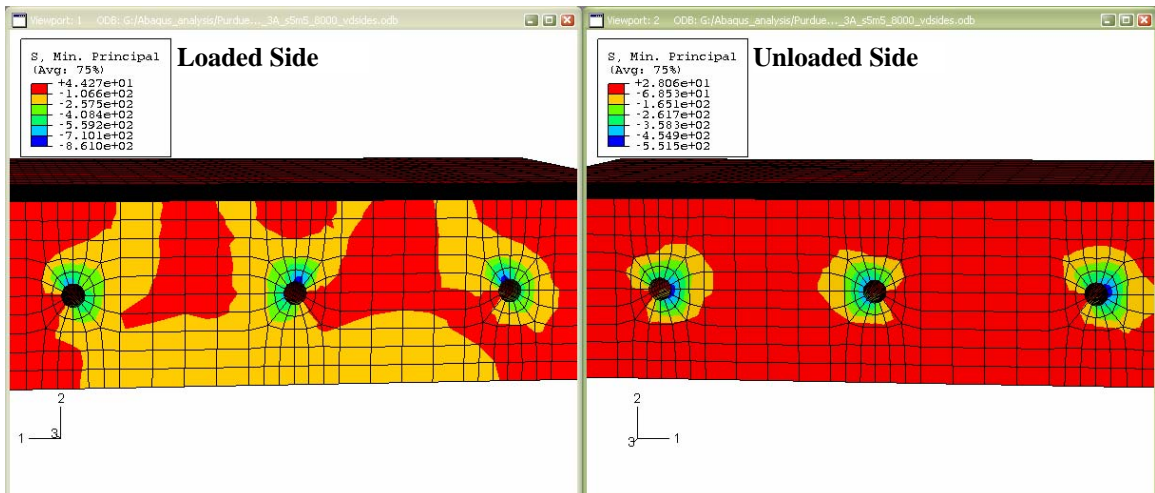
(c) Maximum Compressive Strains at joint opening of 1/8 in.



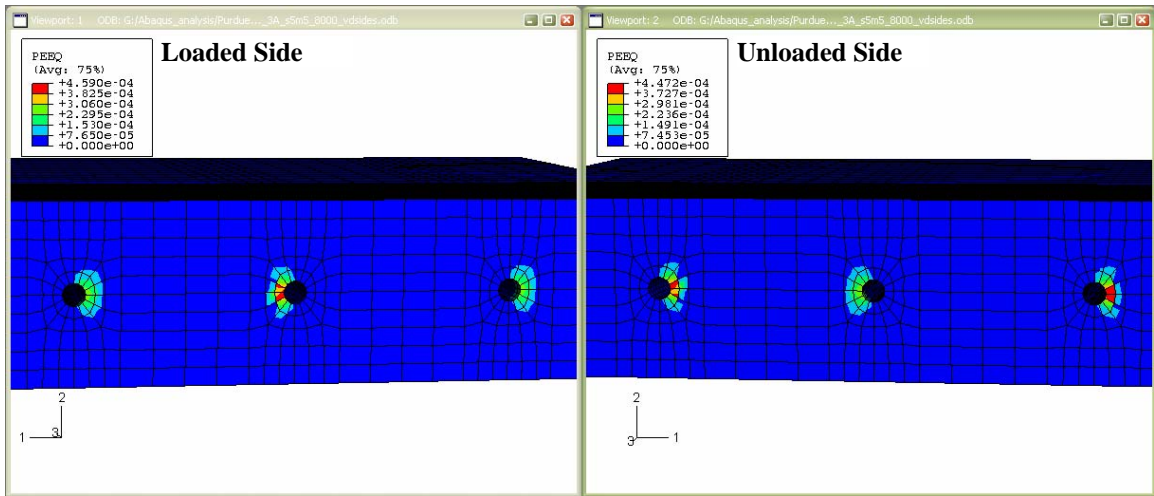
(d) Maximum Tensile Strains at joint opening of 1/8 in.
Figure D-11: Stress and Strains for 3H36NU slab model at joint opening of 1/8 in.



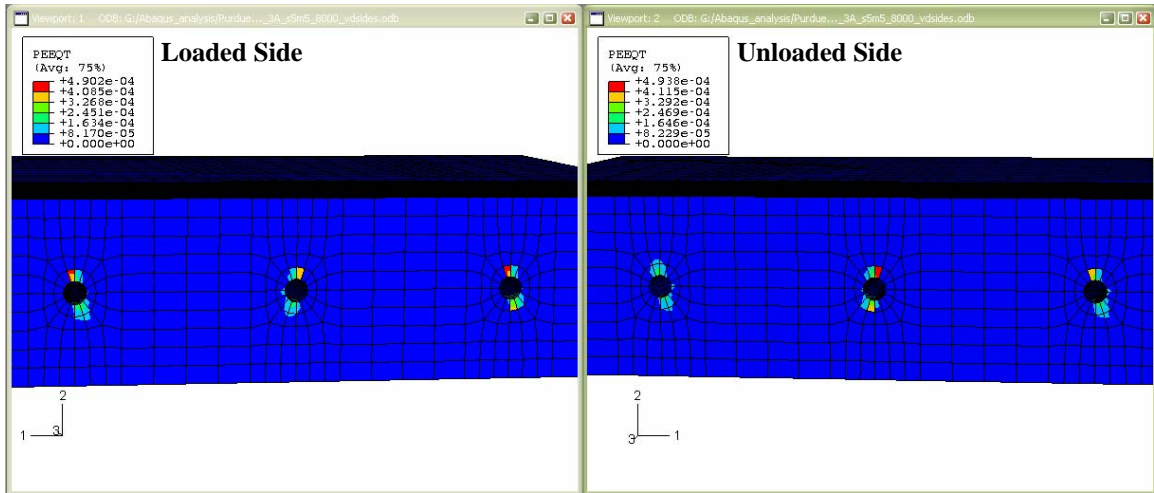
(a) Maximum Tensile Stresses at end of load application



(b) Maximum Compressive Stresses at end of load application



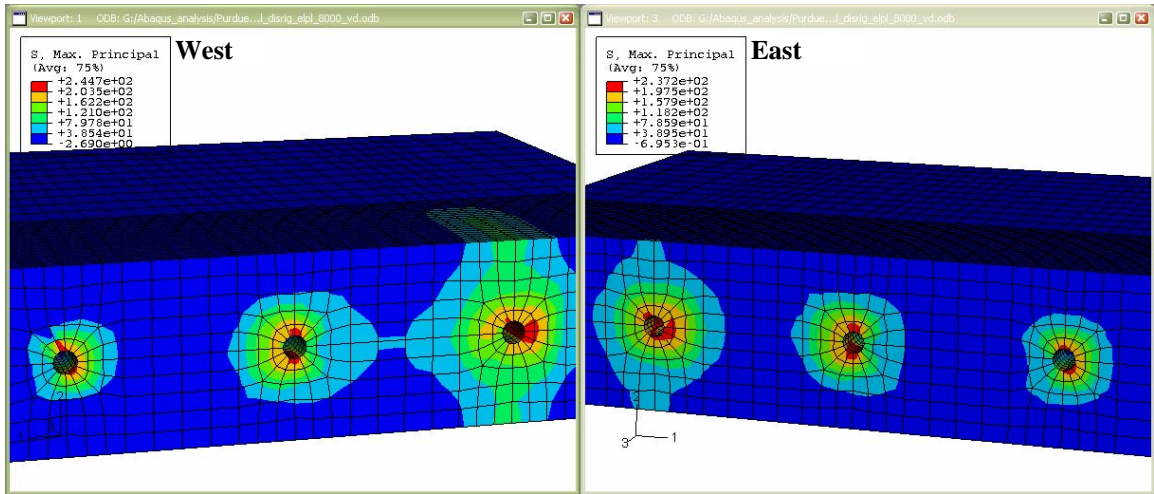
(c) Inelastic Compressive Strains at end of load application



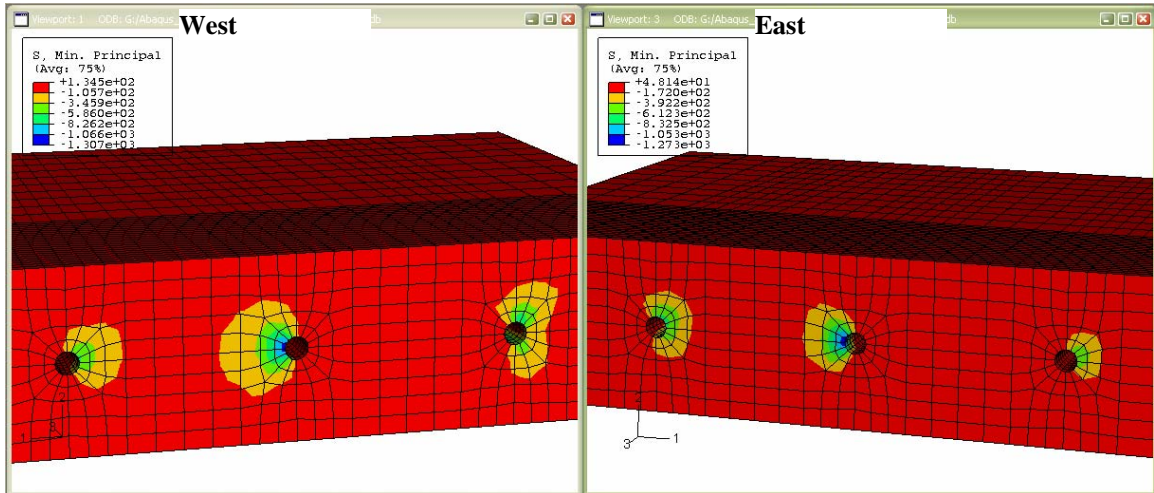
(d) Inelastic Tensile Strains at end of load application

Figure D-12: Stresses and Strains for 3H36NU model after load application

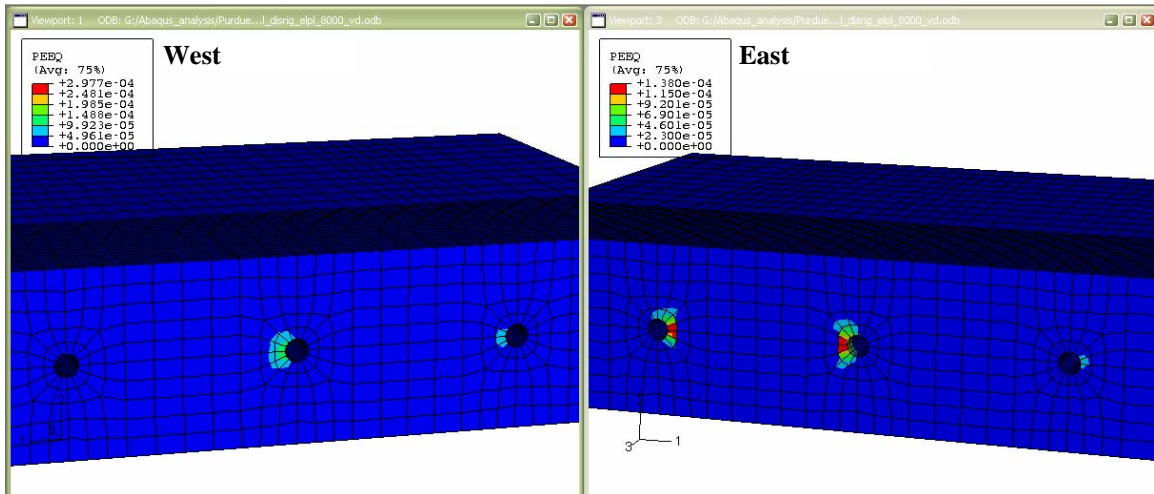
BEHAVIOR OF 3H72NU FINITE ELEMENT MODEL



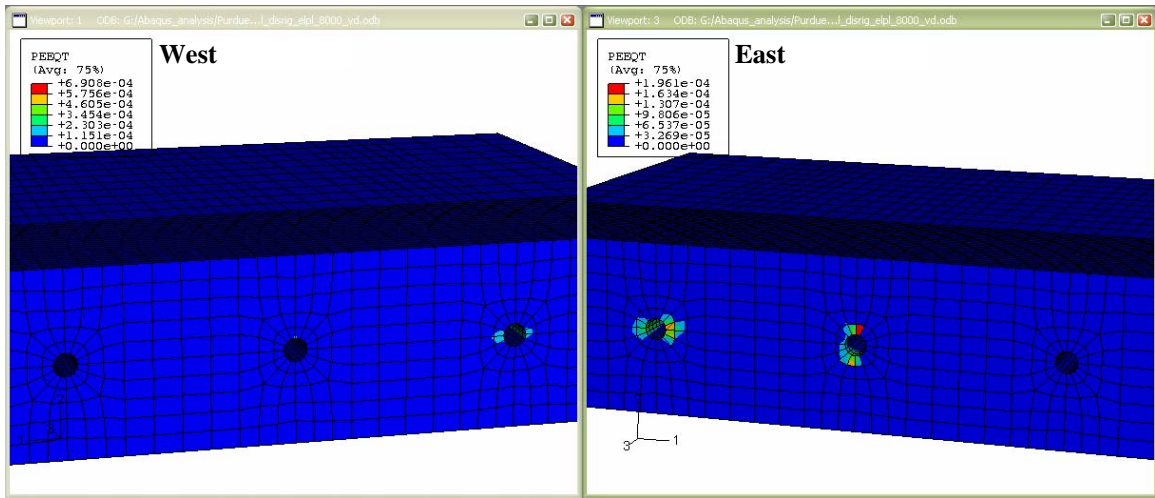
(a) Maximum Tensile Stresses at joint opening of 1/8 in.



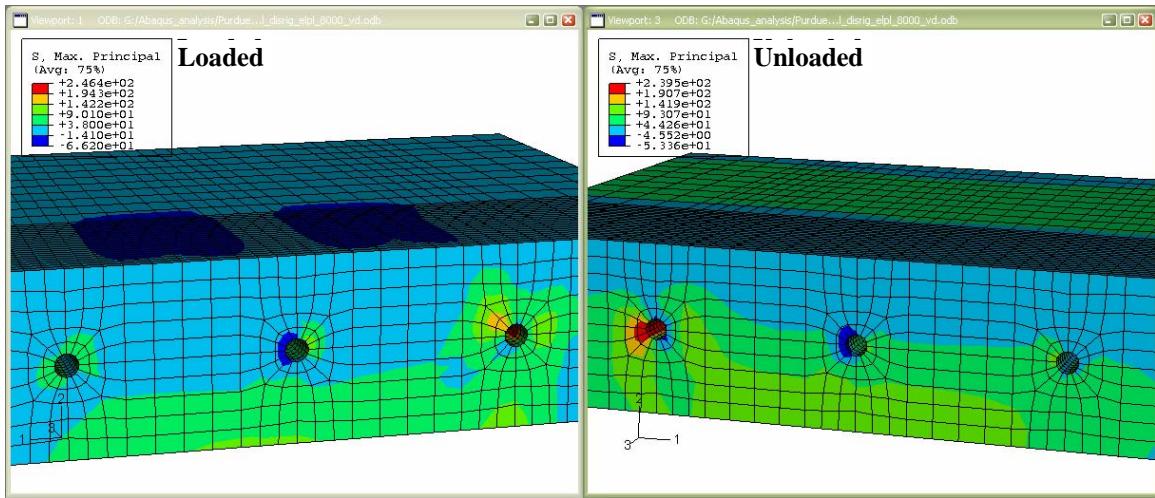
(b) Maximum Compressive Stresses at joint opening of 1/8 in.



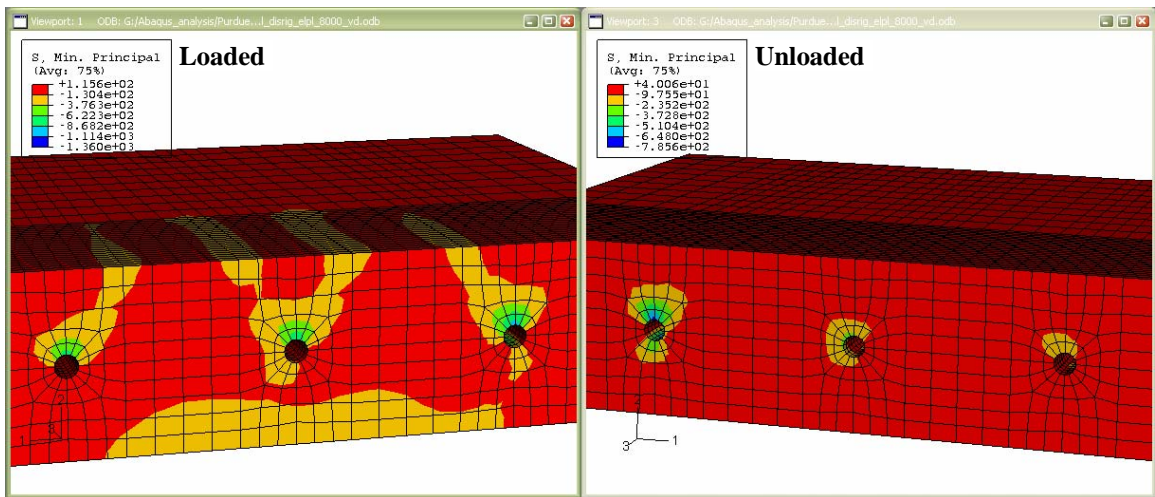
(c) Maximum Compressive Strains at joint opening of 1/8 in.



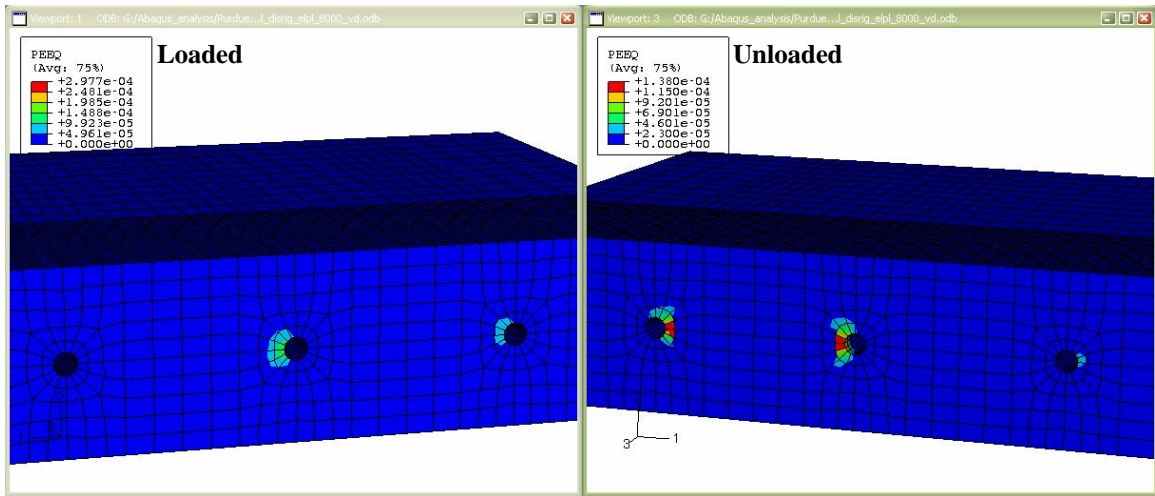
(d) Maximum Tensile Strains at joint opening of 1/8 in.
Figure D-13: Stress and Strains for 3H72NU slab model at joint opening of 1/8 in.



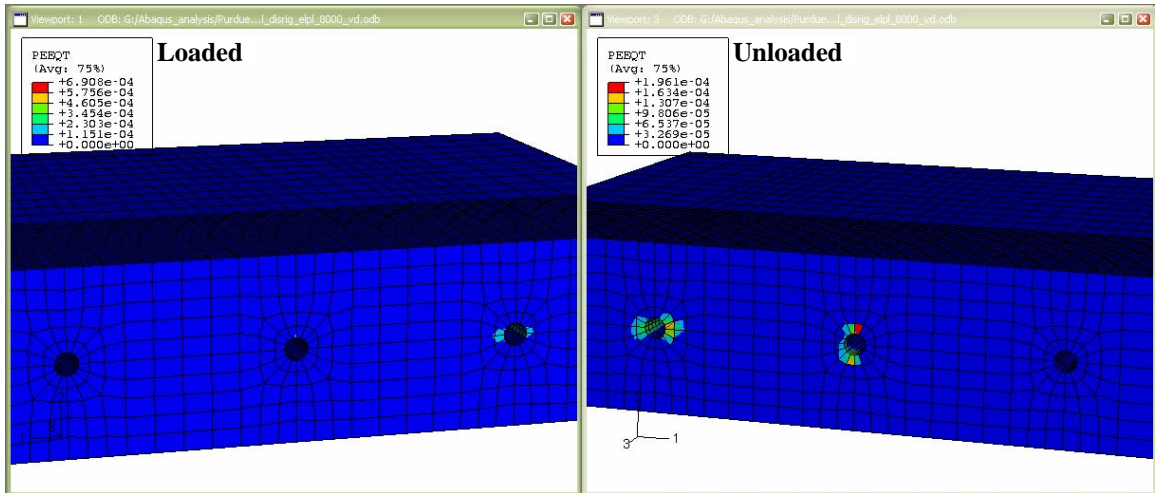
(a) Maximum Tensile Stresses at end of load application



(b) Maximum Compressive Stresses at end of load application



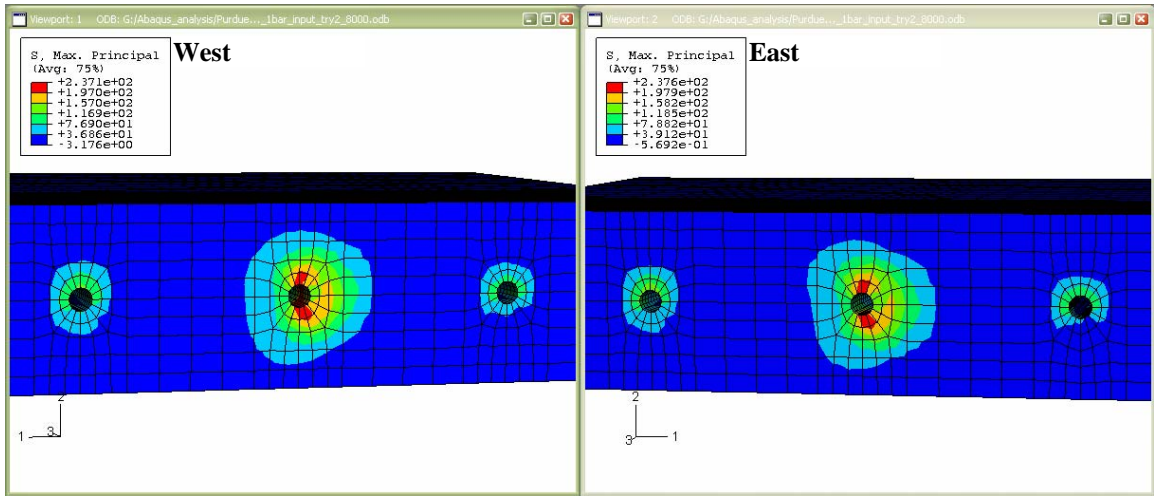
(c) Inelastic Compressive Strains at end of load application



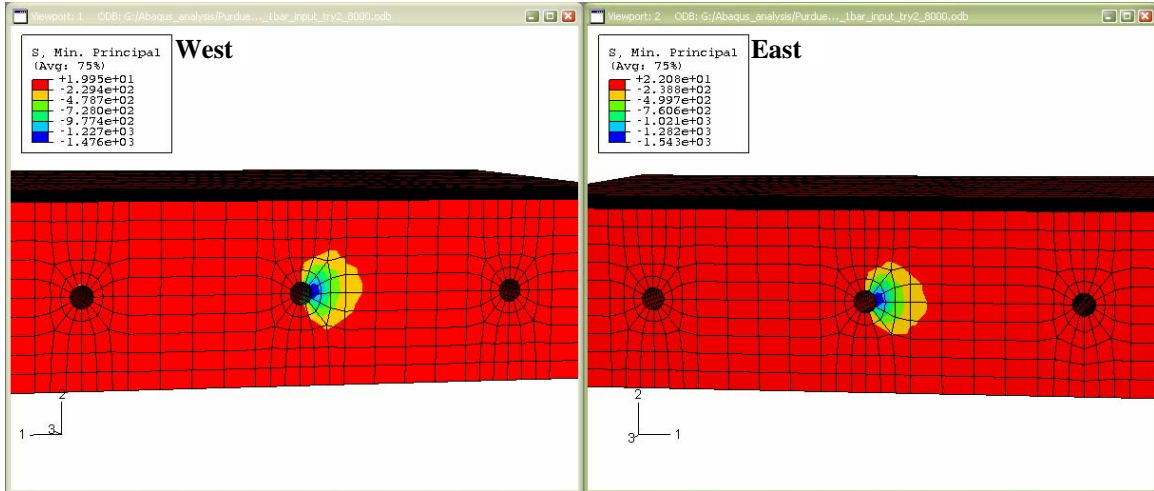
(d) Inelastic Tensile Strains at end of load application

Figure D-14: Stresses and Strains for 3H72NU model after load application

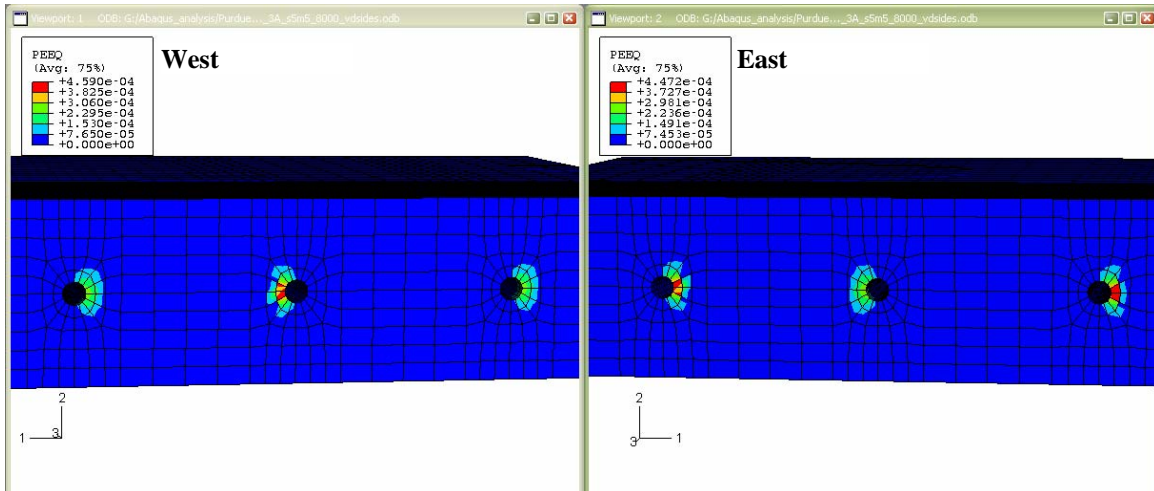
BEHAVIOR OF 3H36AM FINITE ELEMENT MODEL



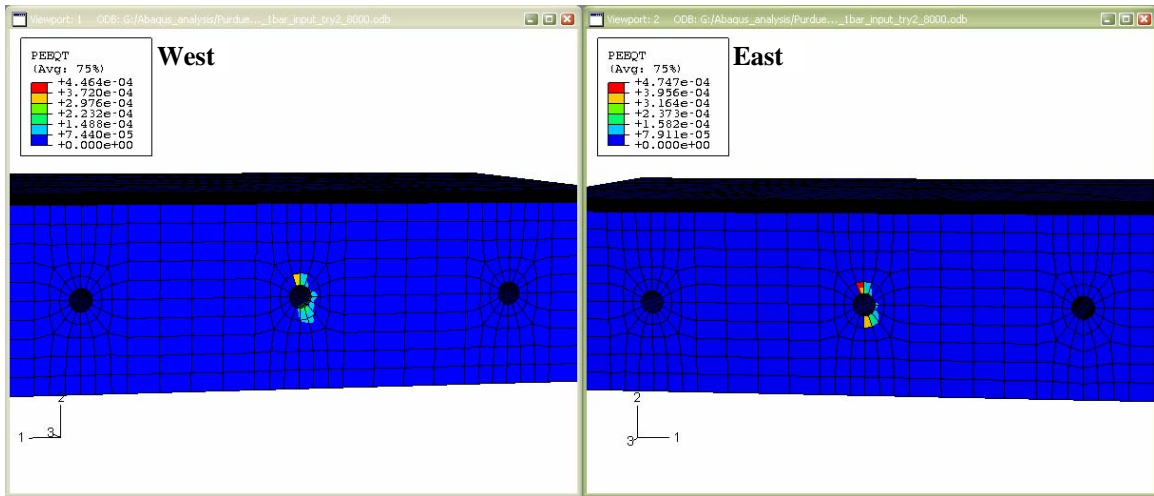
(a) Maximum Tensile Stresses at joint opening of 1/8 in.



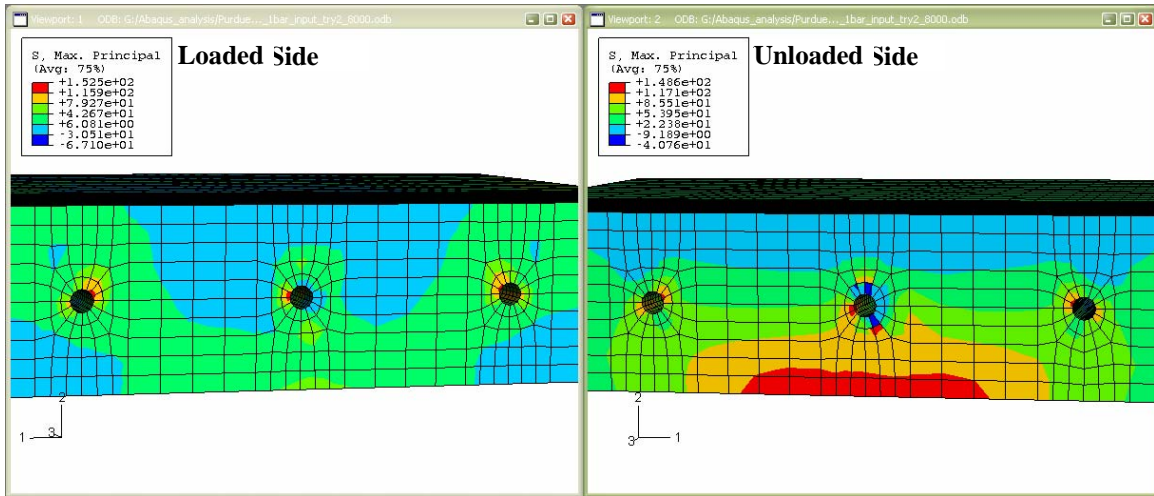
(b) Maximum Compressive Stresses at joint opening of 1/8 in.



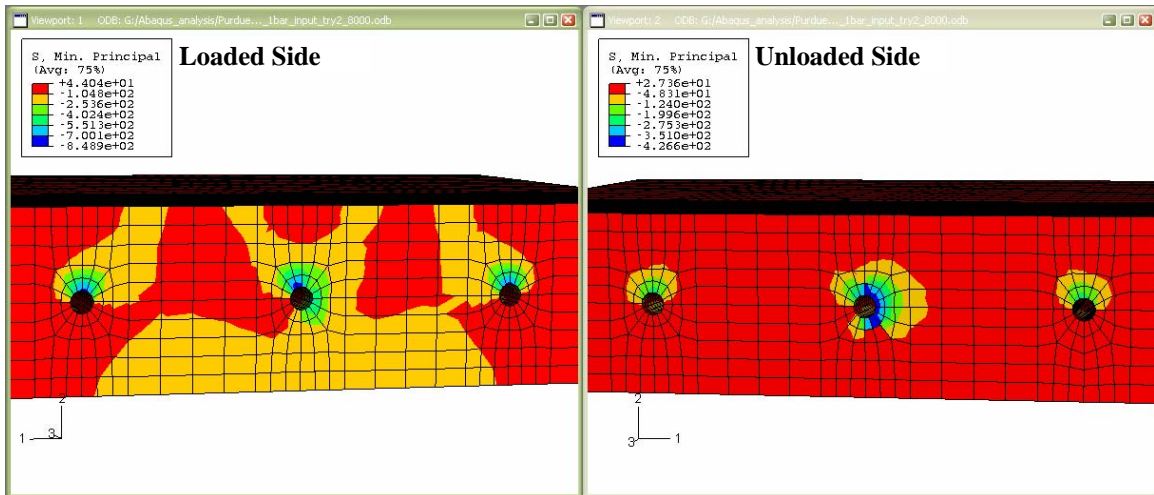
(c) Maximum Compressive Strains at joint opening of 1/8 in.



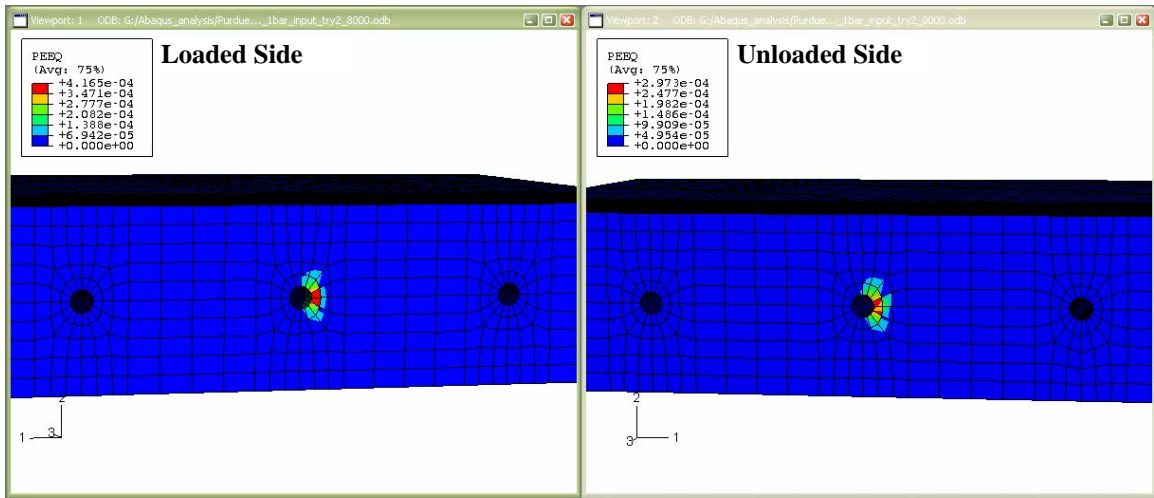
(d) Maximum Tensile Strains at joint opening of 1/8 in.
Figure D-15: Stress and Strains for 3H36AM slab model at joint opening of 1/8 in.



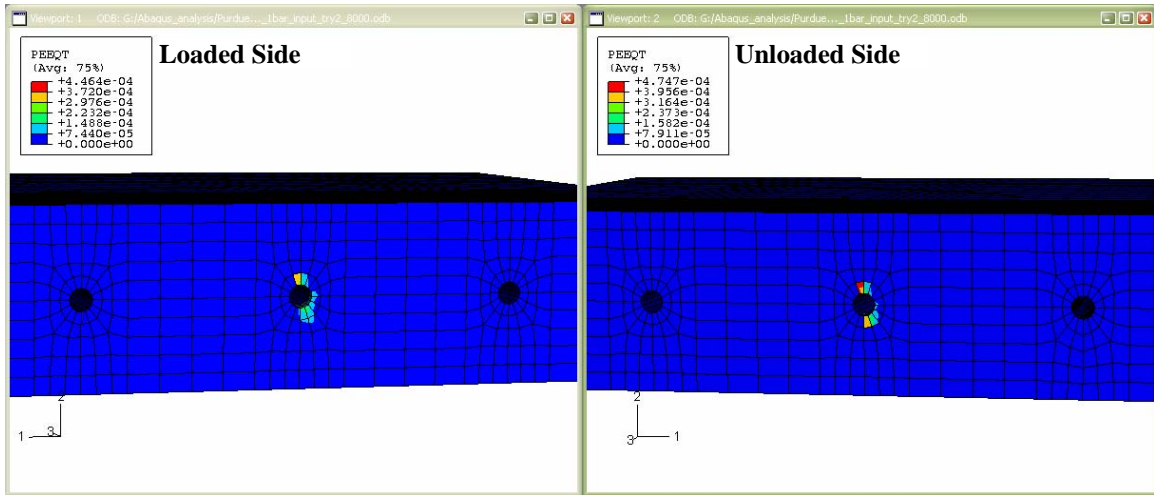
(a) Maximum Tensile Stresses at end of load application



(b) Maximum Compressive Stresses at end of load application



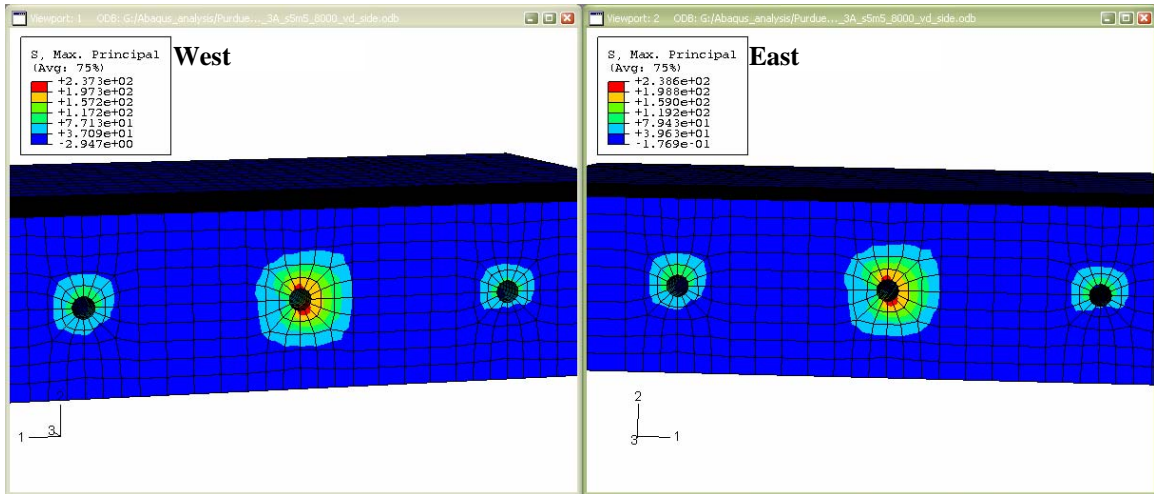
(c) Inelastic Compressive Strains at end of load application



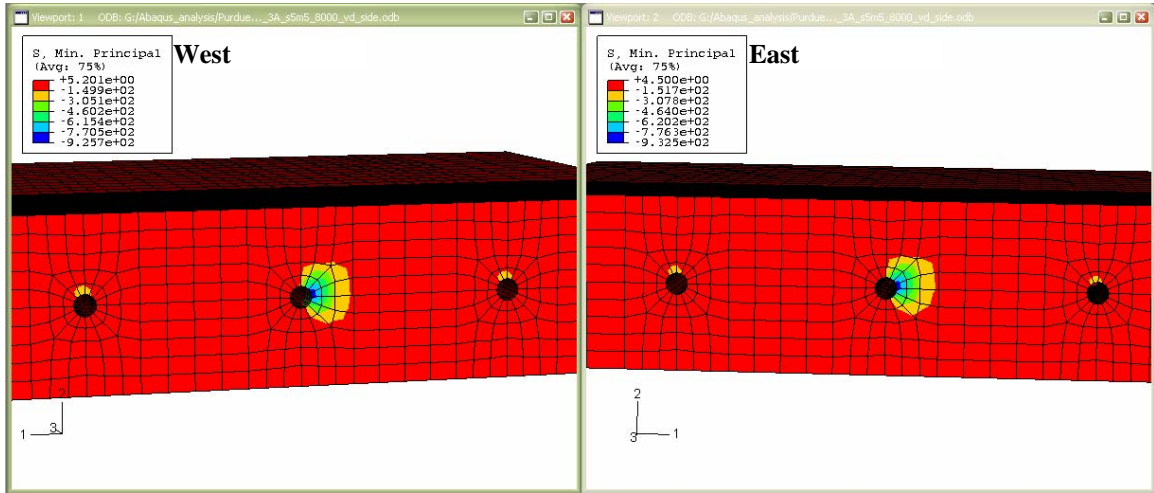
(d) Inelastic Tensile Strains at end of load application

Figure D-16: Stresses and Strains for 3H36AM model after load application

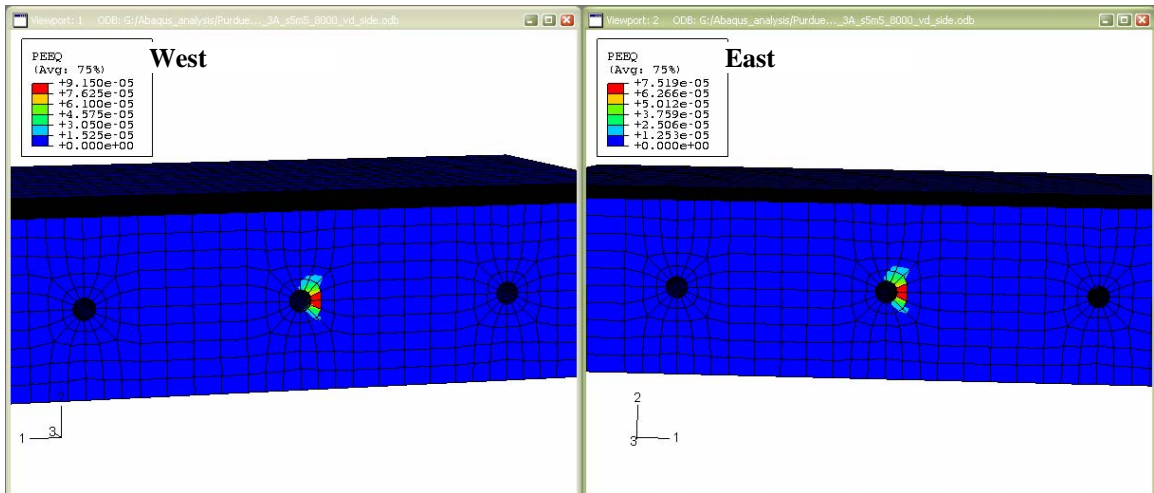
BEHAVIOR OF 3H72AM FINITE ELEMENT MODEL



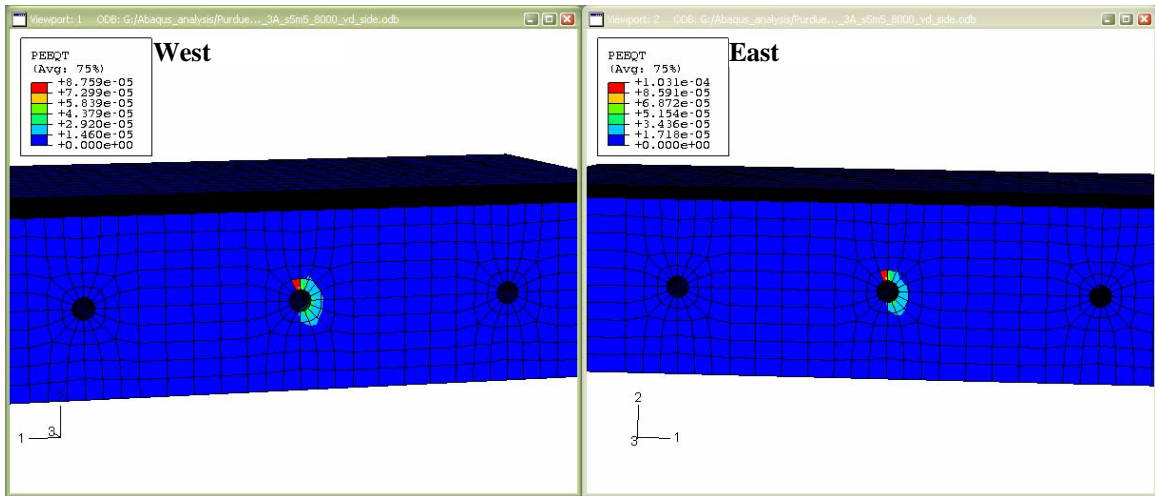
(a) Maximum Tensile Stresses at joint opening of 1/8 in.



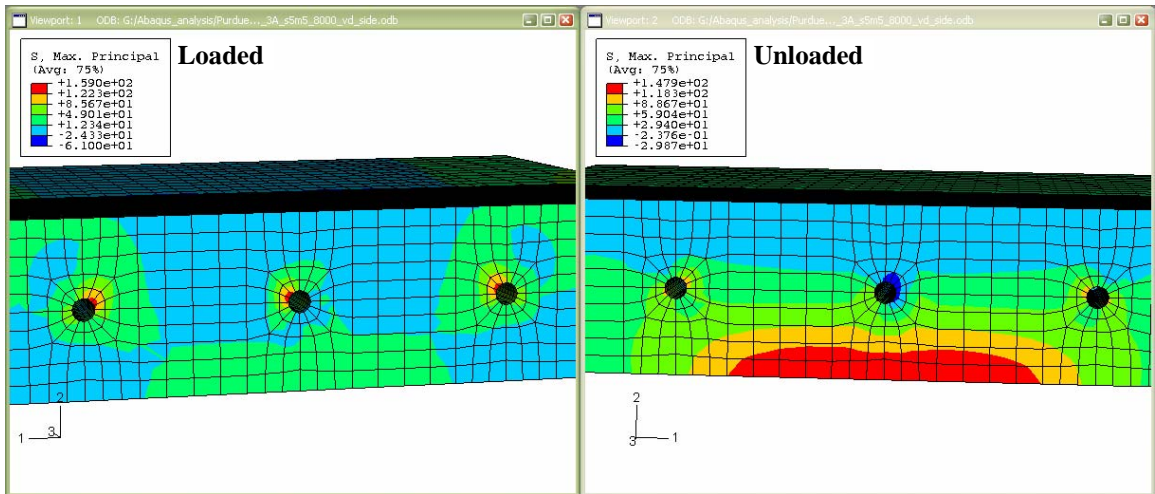
(b) Maximum Compressive Stresses at joint opening of 1/8 in.



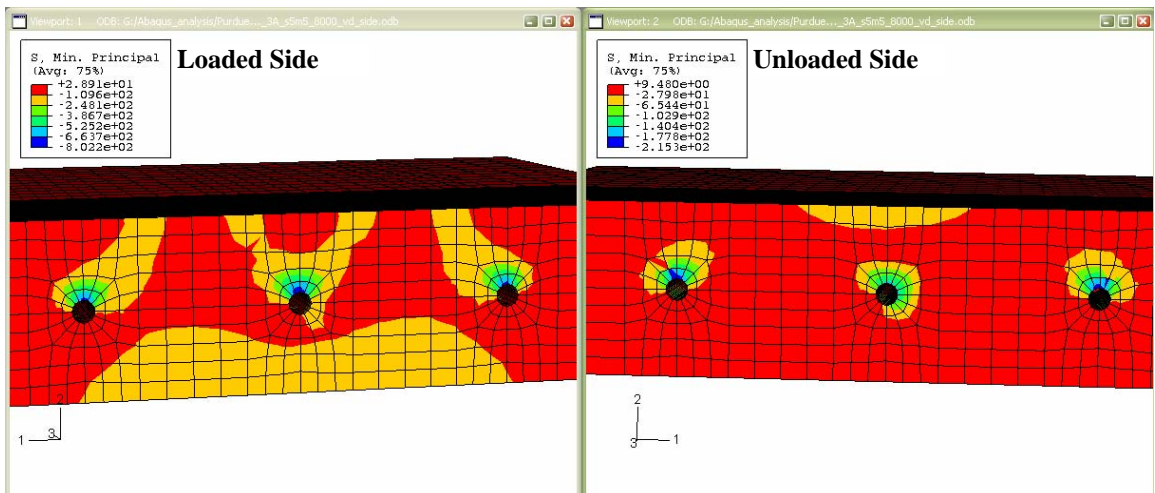
(c) Maximum Compressive Strains at joint opening of 1/8 in.



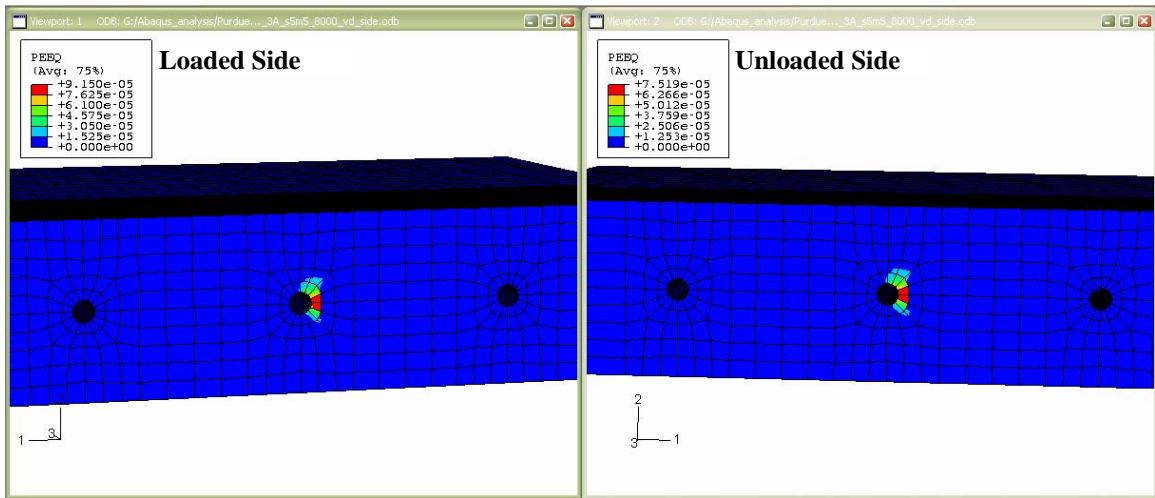
(d) Maximum Tensile Strains at joint opening of 1/8 in.
Figure D-17: Stress and Strains for 3H72AM slab model at joint opening of 1/8 in.



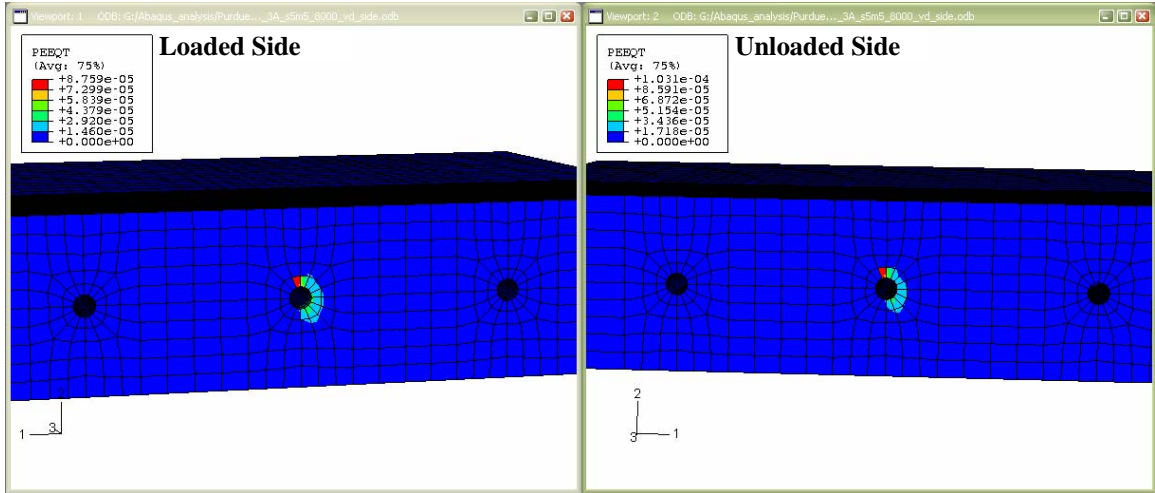
(a) Maximum Tensile Stresses at end of load application



(b) Maximum Compressive Stresses at end of load application



(c) Inelastic Compressive Strains at end of load application



(d) Inelastic Tensile Strains at end of load application

Figure D-18: Stresses and Strains for 3H72AM model after load application

APPENDIX E

CONVERGENCE STUDY OF THE 3D FINITE ELEMENT MODEL

A convergence study / mesh sensitivity study was carried out to compare the formation of the various events / material damage limit states on the dowel pullout force-joint opening behavior between a coarse and fine mesh. The 2V18NU test finite element model was used for this study. This model was primarily used as all the events / material damage limit states occurred on the dowel pullout force-joint opening behavior in the finite element model. The element size of the concrete surrounding the dowel bar in the fine mesh model was 0.25 in. (approx.) compared to an element size of 0.5 in. (approx.) in the coarse mesh.

Figure E-1 presents a comparison of the dowel pullout force per bar – joint opening behavior for the 2V18NU test specimen. As the events (A-F) form in the FE model, the joint opening and dowel pullout force per bar is presented in Table E-1. From the results of the convergence study, the magnitude of joint opening and pullout forces compare favorably with the coarse and fine mesh finite element models.

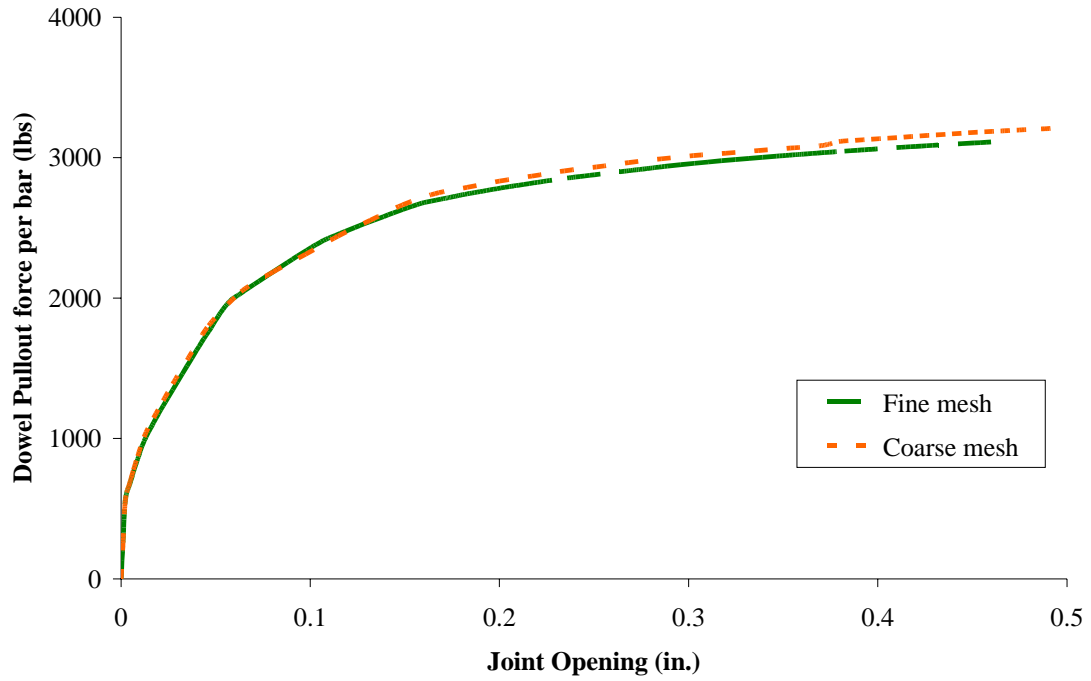


Figure E-1: Comparison of dowel pullout force-joint opening behavior for the 2V18NU coarse and fine mesh finite element model

Table E-1: Comparison of the fine and coarse mesh joint opening and dowel pullout forces

	Fine Mesh		Coarse Mesh	
	Joint Opening	Force / bar	Joint Opening	Force / bar
	(in.)	(lbs)	(in.)	(lbs)
B	0.012	979.41	0.012	1010.22
C	0.021	1271.76	0.022	1269.27
D	0.453	3137.10	0.486	3204.54
E	0.309	2987.50	0.336	3050.00
F	0.230	2865.07	0.251	2965.08

REFERENCES

- AASHTO Guide for design of pavement structures, American Association of State Highway and Transportation Officials, Washington, D.C., 1993
- Abaqus 6.5-4, Abaqus Inc., Providence, Rhode Island, USA, 2004
- American Association of State Highway and Transportation Officials (AASHTO), AASHTO Guide for Design of Pavement Structures, American Association of State Highway and Transportation Officials, Washington, D.C. 1993.
- American Concrete Institute (ACI) Committee 325, Structural Design Considerations for Pavement Joints, Journal of the American Concrete Institute, Vol. 28, No. 1, July 1956, pp. 1 – 28.
- American Concrete Paving Association, Concrete Pavement and Research Technology Update, No. 6.01, www.pavement.com/techserv/RT6.01.pdf, January 2005
- American Concrete Paving Association, Concrete Pavement Progress – Technical Tips and Techniques, ACPA, Vol. 40., No. 4., CPP-090604, www.pavement.com/CP/2004/CP-090604.pdf, September 2004
- American Concrete Paving Association, Concrete Pavement Technology Update, ACPA, FHWA-IF-04-025, www.fhwa.dot.gov/pavement/conhome.htm, August 2004.
- American Concrete Paving Association, Database of State Department of Transportation Concrete Pavement Practices, Downloaded from www.pavement.com, 2004a
- American Concrete Paving Association, Design and Construction of Joints for Concrete Highways, Technical Brief No. TB010-01P, Concrete Paving Technology, American Concrete Paving Association, 1991.
- Applied Research Associates, Guide for Mechanistic-Empirical Design of New and Rehabilitated Pavement Structures, Final Report of Project No. 1-37A, National Cooperative Highway Research Program.
- Bannantine, A. and Socie, D.F., Multiaxial fatigue life estimation technique, ASTM Special Technical Publication, No. 1122, 1992, pp. 249-275.
- Bhatti, M. A., Molinas-Vega, I. and Stoner, J.W., Nonlinear Analysis of Jointed Concrete Pavements, Transportation Research Record, No. 1629, TRB, National Research Council, Washington, November 1998, pp. 50-57.
- Bock, B.T., Okamoto, P.A., Evaluation of dowel placement using a dowel bar inserter, Proceedings of the Fourth International Conference on Concrete Pavement Design and Rehabilitation, Purdue University, West Lafayette, Indiana, April 1989, pp. 641-649

Bradbury, R.D., Reinforced Concrete Pavements, Wire Reinforcement Institute, Washington D.C., 1938.

Burati, J.L. Jr., Beeson, M.G., Hill, H.S. Jr., Comparative Analysis of Dowel Placement in Portland Cement Concrete Pavements, Transportation Research Record 924, Washington D.C., 1983.

Burnham, T., A field study of PCC joint misalignment near Fergus Fall, Minnesota, Final Report No. MN/RC-1999-29, Minnesota Department of Transportation, 1999.

California Department of Transportation, Standard Specifications for Construction of Local Streets and Roads, www.dot.ca.gov/hq/esc/oe/project_plans/HTM/stdplns-dual-new02.htm, 2002

Cashell, H.D., Performance of doweled joints under repetitive loadings, Public Roads, Vol. 30, No. 1, 1958.

Chandappa, D.C., Setunge, S. and Sanjayan, J.G., Stress versus strain relationship of high strength concrete under high later confinement, Cement and Concrete Research, Vol 29, 1999, pp 1977-1982.

Chandappa, D.C., Sanjayan, J.G. and Setunge, S., Complete triaxial stress-strain curves of high strength concrete, Journal of Materials in Civil Engineering, Vol 13, No. 3, May/June, 2001, pp. 209-215.

Channakeshava, C., Barzegar, F. and Voyiadjis, G. Z., Nonlinear FE Analysis of Plain Concrete Pavements with Doweled Joints, Journal of Transportation Engineering, Vol. 119, No. 5, September – October 1993, pp. 341-360.

Chen, W. F. and Han, D. J., Plasticity for Structural Engineers, Gau Lih Book Co., Ltd., 1995.

Chopra, A. K., Dynamics of structures – Theory and applications to earthquake engineering, Prentice Hall, Second Edition, 2000.

Collins, M., Mitchell, D. and MacGregor, J. Structural Design Considerations for high strength concrete, Network of centers of Excellence on High Performance Concrete, Toronto, 1992.

Darter, M. I., Design of zero-maintenance plain jointed concrete pavement, Report No. FHWA-RD-7-111, Federal Highway Administration, 1977.

Darter, M.I., Concrete pavement evaluation systems, NCHRP Report 277, Washington, D.C., 1985.

Darter, M.I., Design of zero maintenance plain jointed concrete pavements, Report No. FHWA-RD-7-111, Federal Highway Administration, Washington D.C., 1977.

Davids, W.G., Modeling of rigid pavements; Joint shear transfer mechanisms and finite element solution strategies, Ph. D. Thesis, University of Washington, 1998.

Davids, W. G. and Mahoney, J. P., Experimental verification of rigid pavement joint load transfer modeling with EverFE, Transportation Research Record, No. 1684, TRB, National Research Council, Washington, 1999, pp. 81-89.

Davids, W. G., Effect of dowel looseness of response of jointed concrete pavements, Journal of Transportation Engineering, Vol. 126, No. 1, January - February 2000, pp. 425-433.

Davids, W. G., Wang, Z., Turkiyyah, G., Mahoney, J. P. and Bush, D., Three dimensional finite element analysis of jointed plain concrete pavement with EveFE2.2, Transportation Research Record, No. 1853, TRB, National Research Council, Washington, 2003, pp. 92-99.

Donahue, J.P., Investigation of Dowel Bar Placement Accuracy with a Dowel Bar Inserter, Missouri Department of Transportation, Research Investigation RI01-049, May 2003.

Federal Highway Administration (FHWA), Benefits of using dowel bars, Technical Paper No. 89-03, Washington, 1989.

Federal Highway Administration (FHWA), Computer-based guidelines for concrete pavements volume-II – Design and construction guidelines and HIPERPAV II Users Manual, FHWA-HRT-04-122, February 2005

Fowler, G., and Gulden, W., Investigation of location of dowel bars placed by mechanical implantation, FHWA/RD-82/153, Georgia Department of Transportation, Office of Materials and Research, May 1983.

Friberg, B. F., Design of dowels in transverse joints of concrete pavements, Transactions ASCE, Vol. 105, 1940, pp. 1076-1095.

Guo, H., Sherwood, J. A. and Snyder, M. B., Component dowel bar model for load transfer systems in PCC pavements, Journal of Transportation Engineering, Vol. 121, No. 3, May – June 1995, pp. 289-298.

Highway Research Board, The AASHO Road Test – Report 5, Special report 61E about pavement research, Publication No. 954, Division of Engineering and Industrial Research, Washington, D.C., 1962.

Huang, Y. H., Pavement Analysis and Design, Prentice-Hall, 1993, pp. 192-200.

Illinois Department of Transportation, Standard Specifications for Road and Bridge Construction, www.dot.state.il.us/desenv/pdfs/spec2002/sec400.pdf, 2002.

Ioannides, A. M. and Korovesis, G. T., Analysis and design of slab on – grade pavement systems, *Journal of Transportation Engineering*, Vol. 118, No. 6, November – December 1992, pp. 745-768.

Ioannides, A.M., Control of faulting through joint load transfer design, *Transportation Research Record No. 1286*, 1990, pp. 49-56.

Ioannides, A.M., Thompson, M.R., and Barenberg, E.J. (1985a), Westergaard solutions reconsidered, *Transportation Research Record 1043*, Transportation Research Board, National Research Council, Washington D.C., 13 – 23.

Ioannides, A.M., Thompson, M.R., and Barenberg, E.J. (1985b), Finite element analysis of slabs-on-grade using a variety of support models, *Proceedings Third International Conference on Concrete Pavement Design and Rehabilitation*, Purdue University, 309 – 324

Iowa Department of Transportation, Standard Specifications for Road and Bridge Construction, www.eri.dot.state.ia.us/Oct_2004/GS/frames.htm, 2004.

Khazanovich, L, Buch, N. and Gotlif, A., Evaluation of Alignment Tolerances for Dowel Bars and their effects on joint performance, Final Report, 2001

Khazanovich, L. and Gotlif, A., Evaluation of joint and crack load transfer – final report, Report No. FHWA-RD-02-088, Federal Highway Administration, 2003

Kim, J. and Hjelmstad, K.D., Three dimensional finite element analysis of doweled joints for airport pavements, *Transportation Research Record*, No. 1853, TRB, National Research Council, Washington, 2003, pp. 100-109.

Kukreti, A., Taheri, M. R. and Ledesma, R. H., Dynamic Analysis of rigid Airport Pavements with Discontinuities, *Journal of Transportation Engineering*, Vol. 118, No. 3, May – June 1992, pp. 763-781.

Kupfer, H.B. and Gerstle, K. H., Behavior of concrete under biaxial stresses, *ASCE Journal of Engineering Mechanics*, Vol. 99, No. EM4, August 1973, pp. 853-866.

Kuo, C. M., Hall, K. and Darter, M., Three dimensional finite element model for analysis of concrete pavement support, *Transportation Research Record*, No.1505, TRB, National Research Council, Washington, 1995, pp. 119-127.

Lee, J., and G. L. Fenves, Plastic-Damage Model for Cyclic Loading of Concrete Structures, *Journal of Engineering Mechanics*, Vol. 124, no.8, 1998, pp. 892–900.

Lublinter, J., J. Oliver, S. Oller, and E. Oñate. A Plastic-Damage Model for Concrete, *International Journal of Solids and Structures*, Vol. 25, 1989, pp. 299–329.

Majidzadeh, K., Ilves, G. J. and McComb, R., Mechanistic Design of Rigid Pavements, *Proceedings 2th International conference on Concrete pavement design and rehabilitation*, Purdue University, West Lafayette, Indiana, 1981, pp. 87-96.

Michigan Department of Transportation, Memorandum on surface condition survey and dowel bar restraint – recycled concrete pavement research project 78B-99, December 1989.

Michigan Department of Transportation, Standard Specifications for Construction, <http://mdotwas1.mdot.state.mi.us/public/specbook>, 2003

Nishizawa, T., Fukuda, T. and Matsuno, S., A refined model of doweled joint for concrete pavements using FEM analysis, *Proceedings 4th International conference on Concrete pavement design and rehabilitation*, Purdue University, West Lafayette, Indiana, April 1989

Nochols, T.H. and Hoffman, G.L., Machine insertion of plastic coated dowel bars in PCCP, Research Project 78-9, Materials and Testing Division, Pennsylvania Department of Transportation, Harrisburg, May 1980.

Okamoto, P.A. & Bock, B.T., Evaluation of Dowel Placement Using a Dowel Bar Inserter, Construction Technology Laboratory, Inc, 1989.

Okamoto, P.A., Field evaluation of dowel placement along a section of I-45 in Texas, Transportation Research Record No. 1186, Transportation Research Board, Washington D.C., 1988, pp. 16-34.

Okamoto, P.A., Field evaluation of dowel placement along a section of I-90 near Janesville, Wisconsin, Report to Wisconsin Department of Transportation, District 1, Madison, Wisconsin, August, 1988.

Palaniswamy, R. and Shah, S. P., Fracture and stress-strain relationship of concrete under triaxial compression, *ASCE Journal of Structural Engineering*, Vol. 10, No. ST5, May 1974, pp. 901-916.

Packard, A. and Tayabji, S., Mechanistic design of concrete pavements to control joint faulting and subbase erosion, *International Seminar on Drainage and Erodibility at the Concrete Slab-Subbase Shoulder Interfaces*, Paris, March 1983.

Parry, J., Dowel bar placement: Mechanical insertion versus basket assemblies, Final Report, Study No. 88-10, Wisconsin Department of Transportation, 1989.

Poblete, Field evaluation of thermal deformations in undoweled PCC pavements slabs, Transportation Research Record No. 1207, Transportation Research Board, Washington D.C., 1988, pp. 217-228

Ross, R., A designed system of load transfer dowels for joints in PCC pavement, Final Report WI 89-05, January 1989.

Rufino, D., Mallela, J. and Darter, M.I., Dowel bar and slab size recommendations based on the mechanistic-empirical pavement design guide, Eighth International Conference on Concrete Pavements, August 2005.

Segner, E. P. Jr., and Cobbs, J.R., A Study of Misaligned Dowels in Concrete Pavements, HPR Report 32, Alabama Highway Department, Montgomery, Aug. 1967.

Shoukry, S. N. William, G.W., Riad, M.Y. and Montamarri, S. S. Report on effect of Bonding Force on Stresses in Concrete Slabs. West Virginia Department of Transportation, West Virginia, 2003

Smith, A.R. and Benham, S.W., Effects of Dowel Bar Misalignment Across Concrete Pavement Joints, Transactions, American Society of Civil Engineers, Vol. 103, 1938.

Smith, K.D., Performance of jointed pavements, Vol. I, Evaluation of concrete pavement performance and design features, Federal Highway Administration, 1990.

Snyder, M. B., Dowel load transfer systems for full depth repairs of jointed portland cement concrete pavements, Ph. D. Thesis, University of Illinois, Illinois, 1989.

Soriano, A., Dowel bar placement and displacement, Publication No. SK91-09-X, South Dakota Department of Transportation, March 1995.

Tabatabaie, A. M. and Barenberg, E. J., Finite element analysis of Jointed or cracked concrete pavements, Transportation Research Record, No. 671, TRB, National Research Council, Washington, 1978, pp. 11-19.

Tabatabaie, A. M., Longitudinal joint systems in slip-formed rigid pavements: Vol II – Analysis of load transfer systems for concrete pavements, Report No., DOT/FAA/RD-79/4, U.S. Department of Transportation, Federal Aviation Administration, Washington. D.C., 1979.

Tayabji, S. D., Dowel Placement Tolerances for Concrete Pavements, Transportation Research Record 1062, Washington D.C., 1989.

Tayabji, S. D., Dowel placement tolerances, Interim Report No. FHWA/RD-86/042, Federal Highway Administration, Washington, D.C., 1986.

Tayabji, S., Okamoto, A.P., Field evaluation of dowel placement in concrete pavements, Transportation Research Record No. 1110, Transportation Research Board, Washington D.C., 1987, pp. 101-109.

Thandaveshwara, D., A laboratory evaluation of alignment tolerances for dowel bars and their effect on joint opening behavior, M.S. Thesis, Michigan State University, Michigan, 2005.

Timoshenko, S. P. and Lessels, J. M., Applied Elasticity, Westinghouse Tech. Night School Press, East Pittsburg, Penn., 1925

Weaver, J and Clark A.J., The Effect of Dowel Bar Misalignment in the Joints of Concrete Road, Cement and Concrete Association, SBN 7210 0437 7, London, 1970.

Westergaard, H. M., Stresses in concrete pavements computed by theoretical analysis, Public Roads, Vol. 7, 1926, pp. 25-35.

Wisconsin Department of Transportation, Standard Specifications, www.dot.wisconsin.gov/business/engrserv/construction-library.htm, 2004.

Yoder, E.J. and Witzak, M.W., Principles of Pavement Design, Second Edition, John Wiley & Sons, Inc., New York, 1975.

Yoder, E.J., Principles of Pavement Design, John Wiley & Sons, Inc., New York, 1959.

Yu, H.T. and Khazanovich, L., Applied Research Associates, Final Report of used o magnetic tomography to evaluate dowel placement, Federal Highway Administration, Contract No. DTFH61-03-C-00120, February 2005.

Yu, H.T. and Kim, H.B., Use of MIT Scan 2 in dowel alignment evaluation, Proceedings of the Fifth International Conference on Pavement Technologies, Vol. II, May 2005.

Zaman, M. and Alvappillai, A., Contact element model for dynamic analysis of jointed concrete pavements, Journal of Transportation Engineering, Vol. 121, No. 5, September – October 1995, pp. 425-433.